



저작자표시-비영리-변경금지 2.0 대한민국

이용자는 아래의 조건을 따르는 경우에 한하여 자유롭게

- 이 저작물을 복제, 배포, 전송, 전시, 공연 및 방송할 수 있습니다.

다음과 같은 조건을 따라야 합니다:



저작자표시. 귀하는 원저작자를 표시하여야 합니다.



비영리. 귀하는 이 저작물을 영리 목적으로 이용할 수 없습니다.



변경금지. 귀하는 이 저작물을 개작, 변형 또는 가공할 수 없습니다.

- 귀하는, 이 저작물의 재이용이나 배포의 경우, 이 저작물에 적용된 이용허락조건을 명확하게 나타내어야 합니다.
- 저작권자로부터 별도의 허가를 받으면 이러한 조건들은 적용되지 않습니다.

저작권법에 따른 이용자의 권리는 위의 내용에 의하여 영향을 받지 않습니다.

이것은 [이용허락규약\(Legal Code\)](#)을 이해하기 쉽게 요약한 것입니다.

[Disclaimer](#)

이학박사 학위논문

Ruthenium-based Light Harvesting Complexes

루테튬 기반의 광수확 복합체 연구

2016 년 2 월

서울대학교 대학원

화학부 고분자화학전공

블라이포글 아론

Abstract

Ruthenium-based Light Harvesting Complexes

Aaron Breivogel

Polymer Chemistry, Department of Chemistry

The Graduate School

Seoul National University

Polypyridyl complexes of ruthenium(II) have a plethora of applications, e.g. in dye-sensitized solar cells and as photocatalysts. $[\text{Ru}(\text{bpy})_3]^{2+}$ is one of the most prominent ruthenium(II) complexes featuring long-lived $^3\text{MLCT}$ excited states with a lifetime of 1 μs and a luminescence quantum yield of 10%. $[\text{Ru}(\text{bpy})_3]^{2+}$ is chiral and can form stereoisomers when the ligands are substituted unsymmetrically or in the case of oligonuclear *rac/meso*-complexes. Bis(tridentate) complexes such as $[\text{Ru}(\text{tpy})_2]^{2+}$ are achiral and thus, circumvent stereoisomers. However, $[\text{Ru}(\text{tpy})_2]^{2+}$ features disappointing photophysical properties with a $^3\text{MLCT}$ lifetime of around 0.2 ns and a quantum yield $\leq 0.0007\%$. The attachment of substituents on $[\text{Ru}(\text{tpy})_2]^{2+}$ as well as the enlargement of ligand bite angles to 90° provide considerably improved properties of the emitting $^3\text{MLCT}$ states.

Following this strategy, novel bis(tridentate) ruthenium(II) complexes were developed, synthesized and characterized in this work. The attachment of ester substituents and the use of ligands with enlarged bite angles lead to $^3\text{MLCT}$ lifetimes of up to 841 ns and quantum yields of up to 1.1%. The novel bis(tridentate) complexes feature a significantly higher photostability compared to tris(bidentate) $[\text{Ru}(\text{bpy})_3]^{2+}$. The complexes were used as emitter in light-emitting electrochemical cells and show electroluminescence

with a deep red color reaching into the NIR. Likewise, the complexes were tested as light harvesters in dye-sensitized solar cells and achieve light-to-energy efficiencies of up to 0.26%.

Dinuclear, stereochemically defined ruthenium(II) complexes were oxidized in order to study the metal-metal interaction between Ru(II) and Ru(III) in the one-electron oxidized species. The different redox properties of the two ruthenium centers in the dinuclear compounds lead to a valence-localized situation with no metal-metal interaction observed. Alike, the oxidation of a mononuclear ruthenium(II) complex and its spontaneous back reduction were studied.

Energy transfer systems were synthesized via a solid-phase synthesis. A bis(terpyridine) ruthenium(II) complex serves as energy acceptor and is connected via a different number of glycine units to a coumarin chromophore serving as energy donor. Efficient energy transfer from the coumarin to the ruthenium chromophore is feasible for a small number (0, 1) of glycine units while two glycine units prevent efficient energy transfer.

Light-induced charge separation was achieved when a bis(terpyridine) ruthenium(II) complex was used as chromophore in a donor-chromophore-acceptor nanocomposite. A triphenylamine-containing block-copolymer was used as electron donor and ZnO nanorods as electron acceptor. Upon irradiation of the chromophore electrons are injected into the ZnO nanorods and electron holes are transferred to the triphenylamine-containing block-copolymer.

Keywords : ruthenium, luminescence, tridentate ligands, electron transfer, energy transfer, redox chemistry

Student Number : 2012-31263

Zusammenfassung

Polypyridylkomplexe von Ruthenium(II) besitzen eine Vielzahl von Anwendungen, z. B. in Farbstoff-sensibilisierten Solarzellen und als Photokatalysatoren. $[\text{Ru}(\text{bpy})_3]^{2+}$ ist einer der prominentesten Ruthenium(II)-Komplexe und besitzt langlebige angeregte $^3\text{MLCT}$ -Zustände mit einer Lebensdauer von 1 μs und einer Lumineszenz-Quantenausbeute von 10%. $[\text{Ru}(\text{bpy})_3]^{2+}$ ist chiral und kann Stereoisomere bilden, wenn die Liganden unsymmetrisch substituiert sind oder im Falle von oligonuklearen *rac/meso*-Komplexen. Bis-tridentate Komplexe wie $[\text{Ru}(\text{tpy})_2]^{2+}$ sind achiral und umgehen damit unerwünschte Stereoisomere. $[\text{Ru}(\text{tpy})_2]^{2+}$ besitzt jedoch enttäuschende photophysikalische Eigenschaften mit einer $^3\text{MLCT}$ -Lebensdauer von nur etwa 0.2 ns und einer Quantenausbeute von $\leq 0.0007\%$. Die Anbringung von Substituenten an $[\text{Ru}(\text{tpy})_2]^{2+}$ sowie die Aufweitung der Liganden-Bisswinkel auf 90° bewirken deutlich verbesserte Eigenschaften der emittierenden $^3\text{MLCT}$ -Zustände.

Dieser Strategie folgend wurden in der vorliegenden Arbeit neue bis-tridentate Ruthenium(II)-Komplexe entwickelt, synthetisiert und charakterisiert. Durch Anbringen von Ester-Substituenten und Verwenden von Liganden mit erweiterten Bisswinkeln konnten $^3\text{MLCT}$ -Lebensdauern von bis zu 841 ns und Quantenausbeuten von bis zu 1.1% erreicht werden. Die neuen bis-tridentaten Komplexe weisen eine deutlich erhöhte Photostabilität im Vergleich zu tris-bidentatem $[\text{Ru}(\text{bpy})_3]^{2+}$ auf.

Die Komplexe wurden als Emitter in Licht-emittierenden elektrochemischen Zellen eingebaut und zeigen Elektrolumineszenz mit einer tiefroten Farbe, die bis ins NIR reicht. Ebenso wurden die Komplexe als Lichtsammler in Farbstoff-sensibilisierten Solarzellen getestet und erreichen Licht-zu-Energie-Effizienzen von bis zu 0.26%.

Dinukleare, stereochemisch einheitliche Ruthenium(II)-Komplexe wurden oxidiert um die Metall-Metall-Wechselwirkung zwischen Ru(II) und Ru(III) in der einfach oxidierten Spezies zu untersuchen. Die unterschiedlichen Redox Eigenschaften der beiden Rutheniumzentren in den verwendeten dinuklearen Verbindungen führt zu einer valenzlokalisierten Situation in der keine Metall-Metall-Wechselwirkung beobachtet wird. Ebenso wurde die Oxidation eines einkernigen Ruthenium(II)-Komplexes sowie dessen spontane Rückreduktion untersucht.

Energietransfersysteme wurden mittels Festphasensynthese hergestellt. Dabei ist ein Bis(terpyridin)ruthenium(II)-Komplex als Energie-Akzeptor über eine unterschiedliche Anzahl an Glycineinheiten mit einem Cumarin-Chromophor als Energie-Donor verknüpft. Bei einer kleinen Zahl an Glycineinheiten (0, 1) findet effektiver Energietransfer vom Cumarin- zum Ruthenium-Chromophor statt, wogegen bei zwei Glycineinheiten ein effektiver Energietransfer verhindert ist.

Licht-induzierte Ladungstrennung wurde erreicht, indem Bis(terpyridin)ruthenium(II)-Komplexe als Chromophore in einem Donor-Chromophor-Akzeptor-Nanokomposit eingesetzt wurden. Dabei wurde ein Triphenylamin-enthaltendes Blockcopolymer als Elektronendonator und ZnO-Nanostäbchen als Elektronenakzeptor verwendet. Bei Bestrahlung des Chromophors werden Elektronen in die ZnO-Nanostäbchen injiziert und die Elektronenlöcher wandern in das Triphenylamin-enthaltende Blockcopolymer.

Abstract (in Korean)

루테늄 기반의 광수확 복합체 연구

블라이포글 아론
화학부 고분자 전공
서울대학교 대학원

루테늄(II)의 피리딘 착화합물은 염료감응 태양전지 및 광촉매 등에 다양하게 활용되어 왔다. 그 중 $[\text{Ru}(\text{bpy})_3]^{2+}$ 는 루테늄(II) 착화합물 가운데 가장 잘 알려진 착화합물로서 1 μs 수준의 긴 수명을 가진 $^3\text{MLCT}$ 여기 상태와 10 %에 달하는 발광 양자 효율이 특징이다. $[\text{Ru}(\text{bpy})_3]^{2+}$ 는 키랄성 화합물이며 리간드가 비대칭적으로 치환되거나 *rac*-, *meso*-올리고핵 착화합물을 만들게 되는 경우 입체이성질체를 가지게 된다. 이에 반해 $[\text{Ru}(\text{tpy})_2]^{2+}$ 처럼 세 자리 리간드가 두 개 결합되어 있는 착화합물의 경우 비키랄성이기 때문에 입체이성질체의 형성을 막을 수 있다. 그러나 $[\text{Ru}(\text{bpy})_3]^{2+}$ 의 광물리적 성질은 우수하지 않은 편으로 $^3\text{MLCT}$ 여기 상태 수명은 0.2 ns 정도에 불과하며 발광 양자 효율은 0.0007 % 이하이다. $[\text{Ru}(\text{bpy})_3]^{2+}$ 에 치환기를 결합시키거나 리간드의 결합각을 90° 로 늘리면 발광 능력이 있는 $^3\text{MLCT}$ 상태의 특성을 뚜렷하게 향상시킬 수 있다.

이러한 전략에 따라 본 학위논문연구에서는 새로운 루테늄(II) 착화합물을 합성 및 분석하였다. 에스터 치환기를 결합하고 더 큰 결합각을 가지는 리간드를 사용함으로써 착화합물의 $^3\text{MLCT}$ 수명 시간을 841 ns 로 늘리고 양자 효율을 1.1 % 로 향상시켰으며, 새로운 착화합물이 $[\text{Ru}(\text{bpy})_3]^{2+}$ 와 비교했을 때 상당한 수준으로 향상된 광안정성을 가짐을 확인하였다. 합성된 착화합물이 발광 전기화학 소자의 발광체로 활용되었을 때 붉은 빛에서부터 근적외선에 해당하는 영역의 빛을 전기발광하는 것을 관찰하였다. 또한 이를 염료감응 태양 전지의 광수용체로 사용하였을 때에는 소자의 빛-에너지 변환 효율이 0.26 %에 이른다는 것을 확인하였다. 일전자 산화종에서의 Ru(II)과 Ru(III) 사이 금속간 상호 작용을

연구하기 위해 이성질체 분리가 완벽하게 된 두개의 핵을 가진 루테늄(II) 착화합물을 산화시켰다. 이핵(二核) 화합물의 두 루테늄 중심원자들이 서로 다른 산화-환원 특성을 가지므로 원자가전자들이 편재화되어 금속간 상호작용은 관찰되지 않았다. 또한 이와 비슷하게 단핵(單核) 루테늄(II) 착화합물의 산화반응과 자발적인 환원과정을 연구했다.

고체상 합성법을 이용하여 bis(terpyridine) 루테늄(II) 착화합물과 쿠마린 발광체가 각각 에너지 받개와 주개로 구성된 에너지 전이 시스템을 제조하였다. 루테늄 착화합물과 쿠마린은 서로 다른 개수의 글라이신 분자 결합으로 연결되어 있는데, 글라이신 단위의 개수가 적은 경우 (0 또는 1) 쿠마린으로부터 루테늄 발광체로 효율적인 에너지 전이가 일어나지만 글라이신 단위의 개수가 2개만 되어도 에너지 전이가 차단된다.

전하 주개, 발광체, 전하 받개로 구성된 나노복합체에서 bis(terpyridine) 루테늄(II) 착화합물을 발광체로 활용했을 때 빛에 의한 전하 분리 현상을 관찰하였다. 여기서 Triphenylamine을 포함하는 블록공중합체와 ZnO 나노막대를 각각 전자 주개와 받개로 사용하였는데, 빛을 쬔어주면 발광체의 전자가 ZnO 나노막대로 주입되는 한편 정공이 triphenylamine을 포함한 블록공중합체로 전이되는 것을 확인하였다.

주요어: 루테늄, 발광(냉광), 세자리 리간드, 전자 전이, 에너지 전이, 산화-환원 반응

학번: 2012-31263

Content

1	Abbreviations	3
2	Introduction	6
3	Physicochemical Properties of Bis(tridentate) Ruthenium(II) Polypyridine Complexes	10
4	Strategies Towards Long-Living and Highly Emissive Excited States	17
5	Amide Formation and Solid-Phase Peptide Synthesis.....	20
6	Applications.....	24
7	Dye-Sensitized Solar Cells	28
7.1	Basic Principles	28
7.2	Dye Design for DSSCs	31
8	Light-Emitting Electrochemical Cells	34
9	Publications and Manuscripts	39
9.1	Contributions of Aaron Breivogel to the following manuscripts and publications	39
9.2	Thermal and Photo Reactivity of a Donor-Acceptor-Substituted Bis(terpyridine) Ruthenium(III) Complex in Acidic Solutions	41
9.3	Dinuclear Bis(terpyridine)ruthenium(II) Complexes by Amide Coupling of Ruthenium Amino Acids: Synthesis and Properties	63
9.4	Light-induced Charge Separation in a Donor-Chromophore-Acceptor Nanocomposite Poly[TPA-Ru(tpy) ₂]@ZnO.....	77
9.5	A Heteroleptic Bis(tridentate)ruthenium(II) Polypyridine Complex with Improved Photophysical Properties and Integrated Functionalizability	87
9.6	Excited State Tuning of Bis(tridentate) Ruthenium(II) Polypyridine Chromophores by Push-Pull Effects and Bite Angle Optimization: A Comprehensive Experimental and Theoretical Study.....	95
9.7	Push-Pull Design of Bis(tridentate) Ruthenium(II) Polypyridine Chromophores as Deep Red Light Emitters in Light-Emitting Electrochemical Cells	113
9.8	Anchor-Functionalized Push-Pull-Substituted Bis(tridentate) Ruthenium(II) Polypyridine Chromophores: Photostability and Evaluation as Photosensitizers	123

10	Supporting Information	140
10.1	Explanatory Notes for the Supporting Information	140
10.2	Thermal and Photo Reactivity of a Donor-Acceptor-Substituted Bis(terpyridine) Ruthenium(III) Complex in Acidic Solutions	141
10.3	Dinuclear Bis(terpyridine)ruthenium(II) Complexes by Amide Coupling of Ruthenium Amino Acids: Synthesis and Properties	179
10.4	Light-induced Charge Separation in a Donor-Chromophore-Acceptor Nanocomposite Poly[TPA-Ru(tpy) ₂]@ZnO	183
10.5	A Heteroleptic Bis(tridentate)ruthenium(II) Polypyridine Complex with Improved Photophysical Properties and Integrated Functionalizability	189
10.6	Excited State Tuning of Bis(tridentate) Ruthenium(II) Polypyridine Chromophores by Push-Pull Effects and Bite Angle Optimization: A Comprehensive Experimental and Theoretical Study.....	215
10.7	Push-Pull Design of Bis(tridentate) Ruthenium(II) Polypyridine Chromophores as Deep Red Light Emitters in Light-Emitting Electrochemical Cells.....	265
10.8	Anchor-Functionalized Push-Pull-Substituted Bis(tridentate) Ruthenium(II) Polypyridine Chromophores: Photostability and Evaluation as Photosensitizers.....	273
11	Summary and Outlook.....	289
12	List of Publications.....	295
13	Oral and Poster Presentations	296
14	Acknowledgment/Dank	297
15	Literature	298

1 Abbreviations

δ	chemical shift
ε	molar extinction coefficient
λ	wavelength
η	efficiency
τ	lifetime
$\tilde{\nu}$	wave number
Φ	quantum yield
Ac	acetyl
AM	air mass
a.u.	arbitrary units
bpy	2,2'-bipyridine
Bu	butyl
CIE	Commission Internationale de l'Éclairage, International Commission on Illumination
COSY	correlated spectroscopy
d	day
DCC	<i>N,N'</i> -dicyclohexylcarbodiimide
ddpd	<i>N,N'</i> -dimethyl- <i>N,N'</i> -dipyridin-2-ylpyridine-2,6-diamine
DIC	<i>N,N'</i> -diisopropylcarbodiimide
DFT	density functional theory
DMF	<i>N,N</i> -dimethylformamide
DSSC	dye-sensitized solar cell
$E_{1/2}$	half wave potential
EPR	electron paramagnetic resonance
em	emission
equiv	equivalent
ESI	elektro spray ionisation
Et	ethyl
EQE	external quantum efficiency
exc	excitation
Fc	ferrocene
<i>ff</i>	fill factor
Fmoc	9-fluorenyl-methoxycarbonyl
Gly	glycine
GS	ground state
h	hour/ planck constant

HMBC	heteronuclear multiple bond correlation
HOBT	1-hydroxybenzotriazole
HOMO	highest occupied molecular orbital
HR	high resolution
IEFPCM	integral equation formalism polarizable continuum model
IL	intraligand
IPCE	incident photon-to-current conversion efficiency
ISC	intersystem crossing
IVCT	intervalence charge transfer
IQE	internal quantum efficiency
<i>J</i>	coupling constant
LEC	light-emitting electrochemical cell
LED	light-emitting device
LLCT	ligand-to-ligand charge transfer
LMCT	ligand-to-metal charge transfer
LUMO	lowest unoccupied molecular orbital
M	molar (mol l^{-1})
max	maximum
MC	metal-centered
Me	methyl
min	minute
MLCT	metal-to-ligand charge transfer
mpp	maximum power point
MS	mass spectrometry
<i>m/z</i>	mass per charge
NIR	near infrared
NMR	nuclear magnetic resonance
NOESY	nuclear Overhauser effect spectroscopy
OLED	organic light-emitting device
Ph	Phenyl
phen	1,10-phenanthroline
ppy	2-phenylpyridine
PyBOP	benzotriazole-1-yl-oxy-trispyrrolidino-phosphonium hexafluorophosphate
<i>rac</i>	racemic
RT	room temperature
SCE	saturated calomel electrode
SPPS	solid-phase peptide synthesis

tBOC	<i>tert</i> -butyloxycarbonyl
tBu	<i>tert</i> -butyl
TFA	trifluoroacetic acid
THF	tetrahydrofuran
TPA	triphenylamine
tpy	2,2':6',2''-terpyridine
UV	ultraviolet
Vis	visible
vs.	versus
WOC	water oxidation catalyst

2 Introduction

Polypyridine complexes of ruthenium(II) provide a unique class of complexes with unprecedented photophysical, chemical and electrochemical properties.^[1] There is a plethora of applications dealing with polypyridine complexes of ruthenium(II) such as dye-sensitized solar cells,^[2–4] light-emitting devices,^[5–8] anticancer and photodynamic therapy,^[9–11] sensing of ions,^[12–14] sensing of small neutral molecules,^[15–17] energy transfer,^[18–20] mixed valency,^[21–26] triplet-triplet annihilation upconversion,^[27–30] and molecular data storage.^[31–33] Applications also involve photocatalytic reactions such as splitting of H₂O,^[34,35] generation of H₂,^[36–40] reduction of CO₂,^[38–40] and photocatalysis of organic redox reactions.^[39,41–45] [Ru(bpy)₃]²⁺ is one of the most prominent ruthenium(II) complexes (bpy = 2,2'-bipyridine). The absorption of a photon populates an excited ¹MLCT state (MLCT = metal-to-ligand charge transfer; Figure 1a). From this state quantitative intersystem crossing (ISC) into a ³MLCT state occurs.^[1] The long excited state lifetime ($\tau \approx 1 \mu\text{s}$) of the ³MLCT state at room temperature in solution renders [Ru(bpy)₃]²⁺ highly suitable as photoredox catalyst (Table 1).^[39,46,47] The ³MLCT state is emissive with a high luminescence quantum yield ($\Phi \approx 10\%$) which favors the application in light-emitting devices, as luminescent sensor or as imaging agent.^[47]

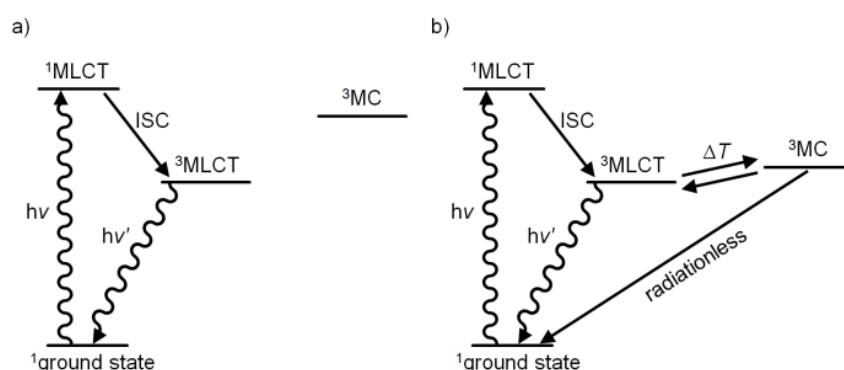
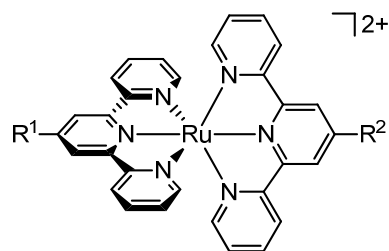


Figure 1. Qualitative Jablonski diagrams of a) [Ru(bpy)₃]²⁺ and b) [Ru(tpy)₂]²⁺ (MLCT = metal-to-ligand charge transfer, ISC = intersystem crossing, MC = metal-centered, bpy = 2,2'-bipyridine, tpy = 2,2';6',2''-terpyridine).

The properties of [Ru(bpy)₃]²⁺ can be fine tuned via ligand design. However, the chirality of [Ru(bpy)₃]²⁺ is a drawback when the bpy ligands are substituted unsymmetrically or in the case of oligonuclear *rac/meso*-complexes because stereoisomers are formed which have to be separated or avoided by complicated synthetic procedures.^[48–50] Bis(tridentate) coordination as in [Ru(tpy)₂]²⁺ ([1]²⁺, Figure 2) can avoid stereoisomers even in the case of heteroleptic complexes with 4',4'-substitution (tpy = 2,2';6',2''-terpyridine).^[51] Furthermore, the stronger chelate effect of tridentate compared to bidentate ligands is favorable in terms of complex stability.^[52,53] Despite the similar

absorption characteristics and redox potentials of $[\text{Ru}(\text{bpy})_3]^{2+}$ and $[\mathbf{1}]^{2+}$ the excited state properties differ significantly (Table 1). Unfortunately, $[\mathbf{1}]^{2+}$ has a dramatically reduced lifetime of the lowest excited $^3\text{MLCT}$ state ($\tau \approx 0.1 - 0.2$ ns) and quantum yield ($\Phi \leq 0.0007\%$; Table 1).^[54–56] The reason for the poor excited state photophysical properties is an effective radiationless deactivation via ^3MC states which are thermally populated from $^3\text{MLCT}$ states (MC = metal-centered; Figure 1b). $[\text{Ru}(\text{bpy})_3]^{2+}$ features three ligands which can create a coordination sphere that corresponds more to an ideal octahedron than in the case of $[\text{Ru}(\text{tpy})_2]^{2+}$ with two constrained ligands. Therefore the overlap between the pyridine nitrogen lone pairs and the e_g^* orbitals of Ru is higher in $[\text{Ru}(\text{bpy})_3]^{2+}$. As a result the ligand field splitting is stronger in $[\text{Ru}(\text{bpy})_3]^{2+}$ inducing less accessible ^3MC states with a higher $^3\text{MLCT}$ - ^3MC energy difference compared to $[\text{Ru}(\text{tpy})_2]^{2+}$ (Figure 1).^[54–56] In order to improve ground and especially excited state photophysical properties of bis(terpyridine) ruthenium(II) complexes extensive efforts have been made in the last two decades. Long-lived and highly emissive excited states in bis(tridentate) complexes of ruthenium(II) can be obtained by the introduction of substituents in the 4'-position of the tpy ligand.^[51] Electron-withdrawing substituents stabilize the $^3\text{MLCT}$ state compared to the ^3MC state while electron-donating substituents destabilize the ^3MC state compared to the $^3\text{MLCT}$ state. Both effects increase the $^3\text{MLCT}$ - ^3MC state energy difference and can avoid radiationless deactivation via the ^3MC state.^[57] In 4'-substituted $[(\text{EtOOC-tpy})\text{Ru}(\text{tpy})]^{2+}$ ($[\mathbf{2}]^{2+}$, Figure 2) prepared by Bolink the electron-withdrawing character of the ester group leads to a less accessible ^3MC state and a significantly higher lifetime ($\tau = 32$ ns) and a higher quantum yield ($\Phi = 0.041\%$) compared to unsubstituted $[\mathbf{1}]^{2+}$ (Table 1).^[8] Furthermore, $[\mathbf{2}]^{2+}$ has a red-shifted absorption maximum ($\lambda_{\text{max}} = 485$ nm; $\epsilon_{\text{max}} = 18140$ M⁻¹ cm⁻¹) and higher extinction coefficients compared to $[\text{Ru}(\text{bpy})_3]^{2+}$ ($\lambda_{\text{max}} = 452$ nm; $\epsilon_{\text{max}} = 13000$ M⁻¹ cm⁻¹) and $[\mathbf{1}]^{2+}$ ($\lambda_{\text{max}} = 474$ nm; $\epsilon_{\text{max}} = 10400$ M⁻¹ cm⁻¹) which is beneficial for efficient light harvesting in dye-sensitized solar cells, especially in the low energy part of the electromagnetic spectrum (Table 1).^[8]



[1]²⁺: R¹ = R² = H

[2]²⁺: R¹ = COOEt; R² = H

[3]²⁺: R¹ = COOH; R² = H

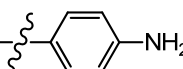
[4]²⁺: R¹ = COOEt; R² = NH₂

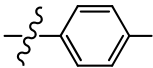
[5]²⁺: R¹ = COOH; R² = NH₂

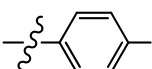
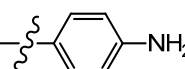
[6]²⁺: R¹ = COOEt; R² = NHCOMe

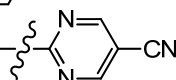
[7]²⁺: R¹ = SO₂Me; R² = OH

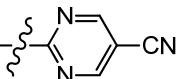
[8]²⁺: R¹ = R² = phenyl

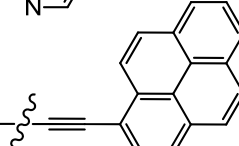
[9]²⁺: R¹ = COOEt; R² = 

[10]²⁺: R¹ = -COOH ; R² = NH₂

[11]²⁺: R¹ = -COOH ; R² = 

[12]²⁺: R¹ = H; R² = 

[13]²⁺: R¹ = R² = 

[14]²⁺: R¹ = H; R² = 

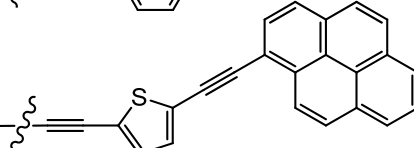
[15]²⁺: R¹ = H; R² = 

Figure 2. Bis(terpyridine) complexes of ruthenium(II).

Table 1. Photophysical and electrochemical properties of ruthenium(II) polypyridine complexes in CH₃CN at 295 K. See Figures 2 and 11 for complex numbering (bpy = 2,2'-bipyridine).

complex	absorption	emission			electrochemistry	
	λ_{\max} [nm] (ϵ [M ⁻¹ cm ⁻¹])	λ_{\max} [nm]	Φ [%]	τ [ns]	$E_{1/2}(\text{Ru}^{\text{II}}/\text{Ru}^{\text{III}})^{[\text{a}]}$ [V]	$E_{1/2}^{\text{red}} [\text{a}]$ [V]
[Ru(bpy) ₃] ²⁺ [47]	452 (13000)	615	9.4 ^[58]	1100	+0.89	-1.73
[1] ²⁺ [51]	474 (10400)	629	$\leq 0.0007^{[\text{b}]}$	0.1 – 0.2 ^[55,\text{c}]	+0.92	-1.67
[2] ²⁺ [8]	485 (18100)	667	0.041 ^[d]	32	+0.96 ^[e]	-1.27 ^[e]
[3] ²⁺ [59,60]	479 (19500)	637 ^[f]	0.02 ^[f,g]	-	+0.91	-1.69
[4] ²⁺ [61]	502 (19100)	734	0.27 ^[d]	34	+0.68	-1.54
[5] ²⁺ [61,62]	501 (20700)	739	0.18 ^[d,h]	26 (92%), 4 (8%)	+0.66	-1.60
[6] ²⁺ [63]	491 (21600)	690	0.24 ^[d]	22	+0.85	-1.55
[7] ²⁺ [51]	490 (16800)	706	0.07 ^[b]	50	+0.92	-1.53
[8] ²⁺ [51]	487 (26200)	715	0.006 ^[b]	1.0	+0.90	-1.66
[9] ²⁺ [62]	502 (35600)	707	0.053 ^[d]	23	-	-
[10] ²⁺ [62]	501 (24700)	659	0.053 ^[d]	21 (3%), 3 (97%)	-	-
[11] ²⁺ [62]	498 (26600)	664	0.030 ^[d]	23 (96%), 2 (4%)	-	-
[12] ²⁺ [64,65]	495 (31300)	713	0.13 ^[b]	200	+0.95	-1.32
[13] ²⁺ [65]	506 (42000)	705	0.17 ^[b]	231	+0.99	-1.29
[14] ²⁺ [66,67]	511 (44800)	698	0.76 ^[d]	580	-	-
[15] ²⁺ [68]	500 (25000)	710	0.3 ^[g,i]	2500	+0.94	-1.49
[16] ²⁺ [69]	463 (10000)	643 ^[j]	11.4 ^[g,j]	385 ^[j]	+0.60	-1.95
[17] ²⁺ [69]	473 (10000)	694 ^[j]	1.7 ^[g,j]	7900 ^[j]	+0.58	-1.88
[18] ²⁺ [70]	491 (14000)	700 ^[j]	3.2 ^[j,k]	3000 ^[j]	+0.71	-1.73
[19] ²⁺ [71]	553 (10000)	693 ^[j]	11.2 ^[j,k]	5500 ^[j]	+0.82	-1.52
[20] ²⁺ [72]	522 (6425)	608	30 ^[g]	3300	+1.11	-1.36
[21] ²⁺ [57]	517 (7500)	729	0.45 ^[d]	722 ^[i]	+0.81	-1.47
[22] ²⁺ [57]	539 (6360)	744	1.1 ^[d]	841 ^[i]	+0.92	-1.25
[23] ²⁺ [57]	525 (8230)	762	0.042 ^[d]	149 ^[i]	+0.64	-1.50
[24] ²⁺ [57]	546 (7810)	788	0.052 ^[d]	136 ^[i]	+0.73	-1.32

[a] Versus FcH/FcH⁺. [b] Recalculated from previously used value $\Phi = 0.028$ for [Ru(bpy)₃]Cl₂ in H₂O to the updated [Ru(bpy)₃]Cl₂ standard $\Phi = 0.040$ in H₂O.^[58] [c] Various solvents. [d] Recalculated from previously used value $\Phi = 0.062^{[73]}$ for [Ru(bpy)₃]Cl₂ in CH₃CN to the updated [Ru(bpy)₃]Cl₂ standard $\Phi = 0.094$ in CH₃CN^[58]. [e] No solvent denoted. [f] In DMF. [g] As given in the reference. [h] In acetone. [i] In PrCN. [j] In EtOH/MeOH (4:1, v/v). [k] Recalculated from previously used value $\Phi = 0.059$ for [Ru(bpy)₃]Cl₂ in CH₃CN to the updated [Ru(bpy)₃]Cl₂ standard $\Phi = 0.094$ in CH₃CN.^[58]

3 Physicochemical Properties of Bis(tridentate) Ruthenium(II) Polypyridine Complexes

The physicochemical properties of bis(tridentate) ruthenium(II) polypyridine complexes will be discussed exemplarily in more detail on the donor-acceptor substituted bis(terpyridine)complex $[4]^{2+}$ (Figure 2) prepared by Hempel and Heinze.^[61] Heteroleptic complexes such as $[4]^{2+}$ are readily synthesized in a stepwise approach. First one tpy ligand (tpy^1) coordinates to $RuCl_3$ forming the ruthenium(III) complex $(tpy^1)RuCl_3$ which can be isolated. Then the ruthenium center is reduced by *N*-ethylmorpholine from Ru^{III} to Ru^{II} in a microwave assisted reaction which enables coordination of the second tpy ligand (tpy^2) resulting in the desired heteroleptic complex $[(tpy^1)Ru(tpy^2)]^{2+}$ with *meridional* coordination.^[61] The ester group of $[4]^{2+}$ can be hydrolyzed to the carboxylic acid derivative $[5]^{2+}$ by refluxing the complex in 20% sulfuric acid which offers the possibility of orthogonal functionalization either on the acid or on the amino group. The harsh reaction procedure also underlines the high thermal and chemical stability of bis(tridentate) complexes such as $[4]^{2+}$ and $[5]^{2+}$.^[61]

Breivogel and Heinze showed that $[5]^{2+}$ is water soluble in the presence of NO_3^- ions enabling pH-dependent measurements. The Pourbaix diagram of $[5]^{2+}$ shows the redox potential $E_{1/2}$ of the Ru^{II}/Ru^{III} couple at different pH values (Figure 3) starting with 0.5 M HNO_3 in H_2O and stepwise titration with saturated aqueous NaOH. At pH = 0 – 1.6 the redox potential amounts to $E_{1/2} = 0.79$ V. Between pH 1.6 and 2.7 the redox potential drops to $E_{1/2} = 0.74$ V which is due to deprotonation of the carboxylic acid group ($pK_a = 2.7$).^[61,74] For a proton-coupled electron transfer the expected slope of the redox potential is given by $-(m/n) \times 59$ mV per pH unit (m = number of transferred protons, n = number of transferred electrons).^[75] The experimental slope amounts to approximately 46 ± 10 mV per pH unit suggesting that the electron transfer is indeed coupled to proton transfer in this pH region. The drop of the redox potential between pH 1.6 and 2.7 is rationalized by the fact that the deprotonated carboxylate group is a stronger electron donor than the protonated carboxyl group. Thus, the former can be oxidized at lower potential. From pH 2.7 – 9.5 the redox potential features a plateau with $E_{1/2} = 0.74$ V. At pH > 10 the redox potential again drops due to deprotonation of the amino group which is converted into an even stronger electron donor by deprotonation.^[61,74] Oxidation is reversible at pH < 10 and irreversible at pH > 10. DFT-calculated spin densities of ruthenium(III) complexes $[5]^{3+}$, $[5 - H]^{2+}$ and $[5 - 2 H]^+$ are depicted in Figure 4. For $[5]^{3+}$ the spin density is located at the ruthenium center with a smaller contribution at the amino nitrogen atom. The Mulliken spin densities on Ru and on the amino nitrogen atom are calculated as 0.76 and 0.11, respectively. Similarly, for one-fold deprotonated $[5 - H]^{2+}$ Mulliken spin densities amount to 0.78 and 0.10, respectively. Thus, when $[5]^{3+}$ is deprotonated at the carboxylic acid group the oxidation remains ruthenium-centered and reversible. The second deprotonation takes place at the amino group. The resulting species $[5 - 2 H]^+$ features Mulliken spin densities on Ru and the amino nitrogen atom of 0.36 and 0.51, respectively

(Figure 4). Thus, oxidation takes place at the deprotonated amino group which induces the irreversibility of the oxidation. In summary, at $\text{pH} < 10$ $[\mathbf{5}]^{2+}$ is reversibly oxidized at the ruthenium center while at $\text{pH} > 10$ the amino group is irreversibly oxidized.^[74]

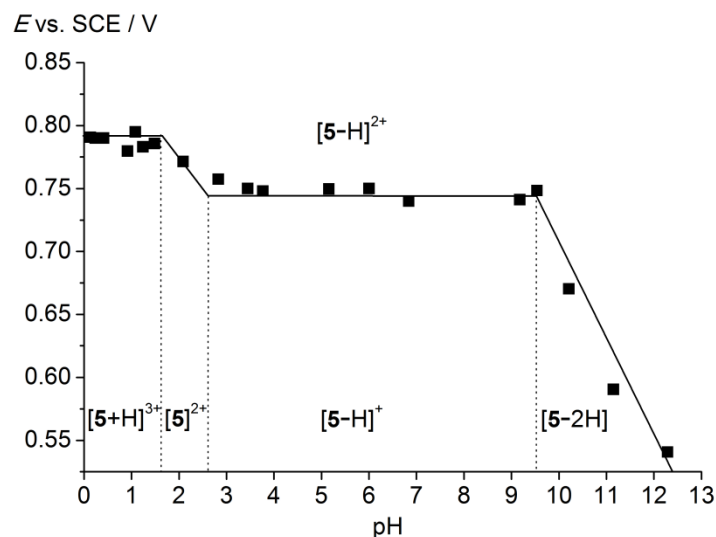


Figure 3. Pourbaix diagram of $[\mathbf{5}](\text{PF}_6)_2$ in 0.5 M HNO_3 in H_2O and stepwise titration with saturated aqueous NaOH .^[74] E (vs. SCE) $- 0.16 \approx E$ (vs. FcH/FcH^+).^[76] pK_a values are denoted by vertical dotted lines.

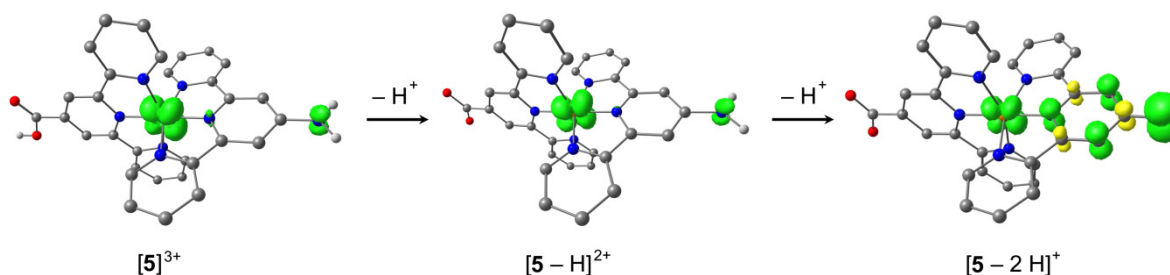


Figure 4. DFT-calculated spin density of ruthenium(III) complexes $[\mathbf{5}]^{3+}$, $[\mathbf{5} - \text{H}]^{2+}$ and $[\mathbf{5} - 2 \text{H}]^+$ (B3LYP/LANL2DZ, IEFPCM, H_2O , contour value 0.01, CH hydrogen atoms omitted).^[74]

The reversible one-electron oxidation of $[\mathbf{4}]^{2+}$ is found at $E_{1/2} = 0.68 \text{ V}$ vs. FcH/FcH^+ .^[61] The EPR spectrum of $[\mathbf{4}]^{3+}$ in frozen solution shows a rhombic signal with $g_{1,2,3} = 2.347, 2.178, 1.843$ ($\Delta g = 0.504$) confirming a characteristic Ru^{III} signature.^[57,77] The reversible one-electron reduction of $[\mathbf{4}]^{2+}$ occurs at the COOEt-substituted tpy ligand.^[57,61] The EPR spectrum of the N-acetylated analogue $[\mathbf{6}]^+$ (Figure 2) in frozen solution shows a less rhombic signal with $g_{1,2,3} = 2.005, 1.989, 1.955$ ($\Delta g = 0.050$) which is in accord with a ligand-based reduction with some ruthenium admixture.^[57] The DFT-calculated spin density of $[\mathbf{4}]^+$ confirms that oxidation takes place at the ruthenium center

(Mulliken spin density on Ru = 0.76) with some admixture from the amino nitrogen atom (Mulliken spin density on N = 0.11) while reduction is essentially localized at the tpy-COOEt ligand (Mulliken spin density on Ru = 0.10, Figure 5).

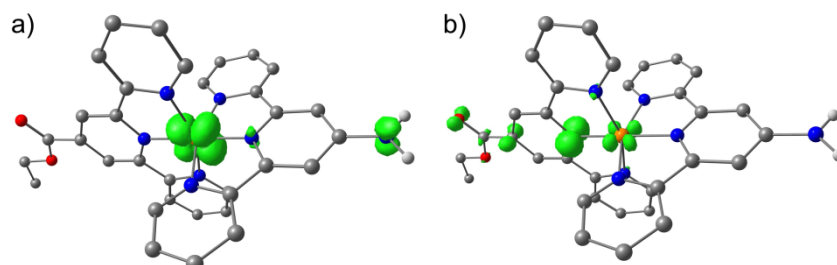


Figure 5. Spin densities of a) $[4]^{3+}$ and b) $[4]^+$ in CH_3CN calculated by DFT (B3LYP/LANL2DZ, IEFPCM, contour value 0.01 a.u., CH hydrogen atoms omitted).^[20]

Breivogel and Heinze probed the stability of ruthenium(III) complex $[4]^{3+}$ in the presence of water and coordinating OH^- ions by spectroelectrochemical measurements. The ruthenium(II) complex $[4]^{2+}$ is reversibly oxidized to the ruthenium(III) complex $[4]^{3+}$ by gradually increasing the potential and then reduced back to $[4]^{2+}$ by gradually lowering the potential (Figure 6). Upon oxidation the MLCT band of $[4]^{2+}$ at $\lambda = 502$ nm disappears while a LMCT band of $[4]^{3+}$ at $\lambda = 729$ nm rises. Seven isosbestic points are observed and confirm the clean conversion from $[4]^{2+}$ to $[4]^{3+}$. Upon back reduction the initial spectrum is fully recovered and the same isosbestic points are observed clearly demonstrating the stability of the ruthenium(II/III) complexes $[4]^{2+}$ and $[4]^{3+}$ in the presence of water and coordinating OH^- ions.^[78]

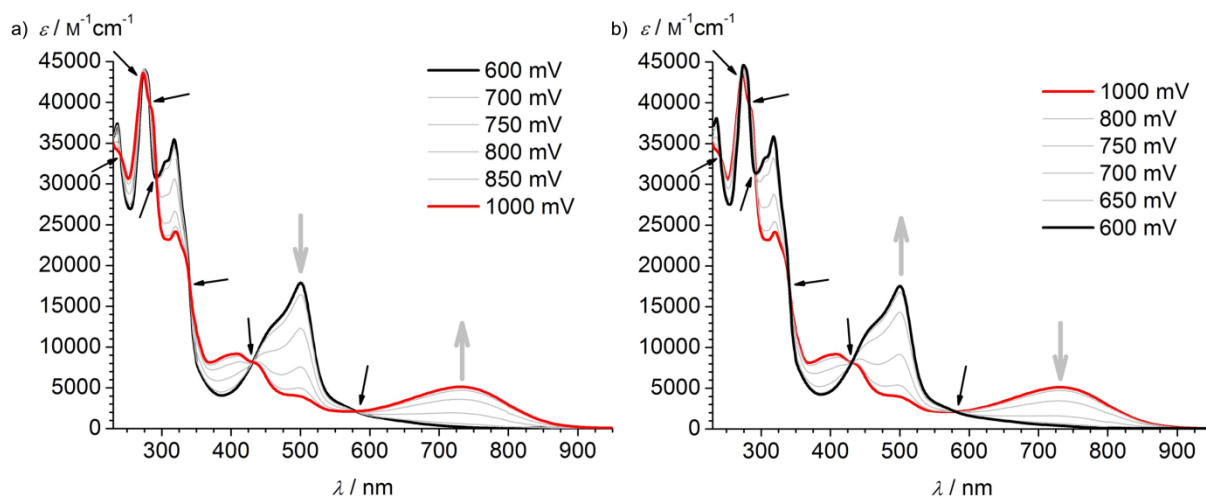


Figure 6. UV/Vis spectra during a) the electrochemical oxidation ($E = 600 \rightarrow 1000$ mV) and b) back reduction ($E = 1000 \rightarrow 600$ mV) of $[4]^{2+}$ in an OTTLE cell in 10^{-3} M NaOH and 0.1 M $[n\text{-Bu}_4\text{N}](\text{PF}_6)$ in $\text{CH}_3\text{CN}:\text{H}_2\text{O}$ (98:2, v%). Black arrows indicate isosbestic points.^[78]

The absorption spectrum of $[4]^{2+}$ features $\pi \rightarrow \pi^*$ transitions below $\lambda = 400$ nm and a characteristic metal-to-ligand charge transfer band (MLCT) with a maximum at $\lambda_{\text{max}} = 502$ nm ($\epsilon_{\text{max}} = 19100 \text{ M}^{-1} \text{cm}^{-1}$; Figure 7).^[61] TD-DFT calculations (B3LYP/LANL2DZ, IEFPCM, CH_3CN) confirm the ligand-centered character of the $\pi \rightarrow \pi^*$ transitions at $\lambda < 400$ nm and the MLCT character of the transitions at $\lambda > 400$ nm.

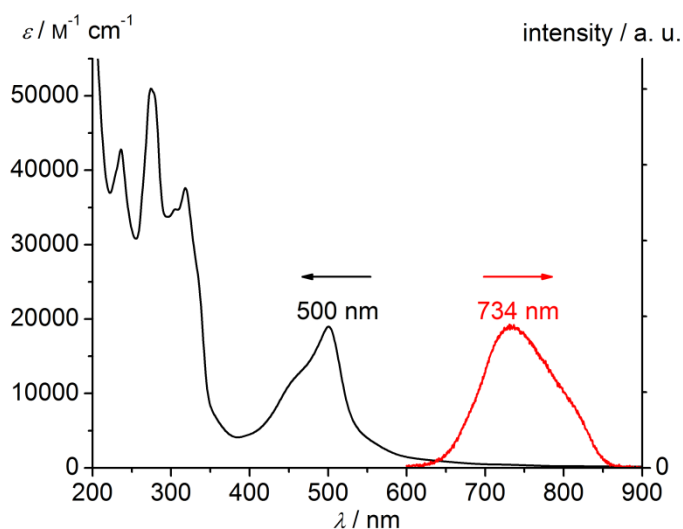


Figure 7. UV/Vis spectrum (black) and emission spectrum (red) of $[4](\text{PF}_6)_2$ in CH_3CN at 295 K.

Relevant Kohn-Sham frontier molecular orbitals of $[4]^{2+}$ are depicted in Figure 8. HOMO-2, HOMO-1, HOMO, LUMO and LUMO+1 represent the participating molecular orbitals in transitions

with $\lambda > 400$ nm. HOMO to HOMO-2 correspond to the t_{2g} orbitals in O_h symmetry and are mainly ruthenium-centered with a small contribution from the amino nitrogen atom. The contribution of the amino group is experimentally verified by Resonance Raman experiments involving the MLCT excitation.^[63] LUMO and LUMO+1 are located on the acceptor-functionalized tpy ligand. Thus, absorption is best described by a mixed $^1\text{MLCT}/^1\text{LLCT}$ character (LLCT = ligand-to-ligand charge transfer). LUMO+9 and LUMO+13 correspond to the higher energy e_g orbitals and do not participate in the MLCT absorption process (Figure 8).

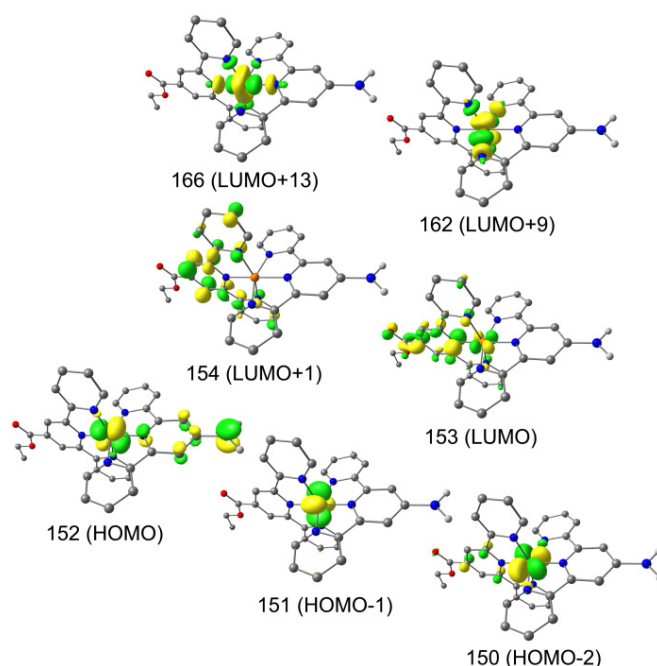


Figure 8. DFT-calculated Kohn-Sham frontier molecular orbitals (contour value 0.06 a.u.) of $[\mathbf{4}]^{2+}$ (B3LYP/LANL2DZ, IEFPCM, CH_3CN ; CH hydrogen atoms omitted).

After population of the initial $^1\text{MLCT}/^1\text{LLCT}$ state ISC into the emissive $^3\text{MLCT}$ state occurs. Breivogel and Heinze have experimentally probed excited state dynamics of $[\mathbf{4}]^{2+}$ on the ps timescale by transient absorption measurements. When excited at $\lambda_{\text{exc}} = 400$ nm the transient absorption spectra of $[\mathbf{4}]^{2+}$ show an instant ground state bleach at $\lambda = 509$ nm together with a photoinduced absorption at $\lambda = 565 - 960$ nm (Figure 9). The region of the photoinduced absorption reveals a process with a time constant of 7.2 ps at 295 K before reaching the thermalized $^3\text{MLCT}$ state. This dynamics might be associated with localization of the excited electron on the tpy-COOEt ligand, intersystem crossing or vibrational relaxation within $^1/3\text{MLCT}$ states.^[57]

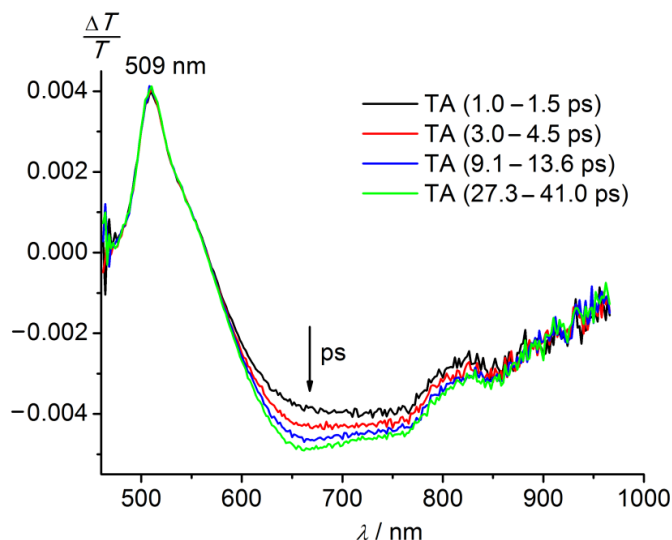


Figure 9. Transient absorption spectra of $[4]^{2+}$ (pulse $\lambda_{\text{exc}} = 400$ nm, 2600 nJ) in PrCN at 295 K.^[57]

At 295 K complex $[4]^{2+}$ shows room temperature phosphorescence from the $^3\text{MLCT}$ state at $\lambda_{\text{max}} = 734$ nm with a $^3\text{MLCT}$ lifetime of $\tau = 34$ ns and a quantum yield of $\Phi = 0.27\%$ (Figure 7).^[57] The emitting $^3\text{MLCT}$ state as well as the deactivating ^3MC state were modeled by DFT calculations by Breivogel and Heinze. The ^3MC state of $[4]^{2+}$ is higher in energy by 26.8 kJ mol^{-1} relative to the $^3\text{MLCT}$ state (Figure 10). In comparison, the corresponding triplet states of unsubstituted $[1]^{2+}$ are found to be essentially isoenergetic. While the geometry of the $^3\text{MLCT}$ state of $[4]^{2+}$ differs only slightly from the ^1GS geometry the ^3MC geometry is significantly distorted from that of the ^1GS (GS = ground state). For example, the bond lengths between Ru and the central N atom of EtOOC-tpy amount to 1.99, 2.04 and 2.17 \AA for the ^1GS , the $^3\text{MLCT}$ and the ^3MC state, respectively. The N-C-C-N dihedral angle of the EtOOC-tpy ligand amount to 0° , 0° and 13° for the ^1GS , the $^3\text{MLCT}$ and the ^3MC state, respectively, showing that the EtOOC-tpy ligand loses its planarity in the ^3MC state. The spin density of the $^3\text{MLCT}$ state is localized on the ruthenium center as well as on the EtOOC-tpy ligand while for the ^3MC state the spin density is confined to the ruthenium center (Figure 10). The connecting transition state (^3TS) between the $^3\text{MLCT}$ and the ^3MC state is calculated with an energy 31.7 kJ mol^{-1} higher than the $^3\text{MLCT}$ state. Concerning the energy, spin density and geometry the transition state resembles more the ^3MC than the $^3\text{MLCT}$ state (Figure 10).^[57]

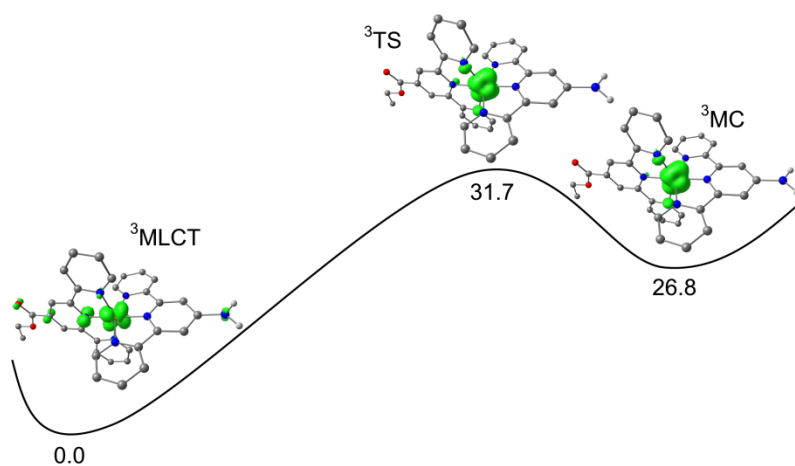


Figure 10. DFT-calculated geometries, relative energies, and spin densities of triplet states (³MLCT and ³MC) and the transition state (³TS) of [4]²⁺ (B3LYP/LANL2DZ, IEFPCM, CH₃CN; contour value 0.015 a.u.; energies in kJ mol⁻¹; CH hydrogen atoms omitted).^[57]

4 Strategies Towards Long-Living and Highly Emissive Excited States

In the bis-4'-substituted heteroleptic complex $[(\text{EtOOC-tpy})\text{Ru}(\text{tpy-NH}_2)]^{2+}$ ($[4]^{2+}$, Figure 2) the electron-donating NH_2 group destabilizes the ^3MC state compared to the $^3\text{MLCT}$ state leading to a further improvement of the excited state properties ($\tau = 34$ ns; $\Phi = 0.27\%$) compared to $[2]^{2+}$ ($\tau = 32$ ns; $\Phi = 0.041\%$; Table 1; Figure 1).^[61] The push-pull substitution of $[4]^{2+}$ induces a small HOMO-LUMO energy gap which red-shifts the absorption maximum ($\lambda_{\text{max}} = 502$ nm). In addition, the NH_2 group in $[4]^{2+}$ enlarges the chromophoric system and raises the extinction coefficient ($\epsilon_{\text{max}} = 19080 \text{ M}^{-1} \text{ cm}^{-1}$).^[61] In push-pull substituted $[7]^{2+}$ (Figure 2) the combination of an OH donor group and a SO_2Me acceptor group enables similar excited state properties ($\tau = 50$ ns; $\Phi = 0.07\%$; Table 1).^[51]

Enlargement of the chromophoric system stabilizes the $^3\text{MLCT}$ state relative to the ^3MC state. $[\text{Ru}(\text{Ph-tpy})_2]^{2+}$ ($[8]^{2+}$, Figure 2) features phenyl groups appended to the 4'-positions of the tpy ligands. The $^3\text{MLCT}$ lifetime ($\tau = 1$ ns) and quantum yield ($\Phi = 0.006\%$) of $[8]^{2+}$ are substantially enhanced compared to $[1]^{2+}$ (Table 1).^[51] The combination of donor-acceptor functionalization and an enlarged chromophoric system has been realized in complexes $[9]^{2+} - [11]^{2+}$ featuring *para*-phenylene spacers between the 4'-substituents and the tpy ligands (Figure 2). However, this combination does not lead to a synergetic effect: $[9]^{2+}$ features a lower $^3\text{MLCT}$ lifetime ($\tau = 23$ ns) and a lower quantum yield ($\Phi = 0.053\%$) compared to the phenylene-free analogue $[4]^{2+}$ (Table 1). $[10]^{2+}$ and $[11]^{2+}$ also have inferior excited state properties compared to the phenylene-free analogue $[5]^{2+}$ (Figure 2).^[61,62] The ring planes of the phenylene ring and the central pyridyl ring of a tpy ligand are twisted. Thus, the reduced π -conjugation dilutes the effect of donor-acceptor substitution.^[62] Coplanarity in extended ligands could be achieved by replacing the *para*-phenylene rings with pyrimidine groups such as in complexes $[12]^{2+}$ and $[13]^{2+}$ (Figure 2). In these complexes the enhanced π -conjugation efficiently stabilizes the $^3\text{MLCT}$ state compared to the ^3MC state which was shown by high excited state lifetimes up to $\tau = 231$ ns and quantum yields up to $\Phi = 0.17\%$ (Table 1).^[64,65]

High excited state lifetimes can also be achieved via the so-called multichromophore approach: Further chromophores such as pyrene and anthracene can have ^3IL states with energies similar to the $^3\text{MLCT}$ state (IL = intraligand). In this case a triplet-triplet equilibrium between these triplet states can significantly enhance the excited state lifetime.^[79] Deactivation from the triplet state of the organic chromophore is slow due to the spin-forbidden nature such that the organic chromophore acts as an excited state reservoir for the emitting $^3\text{MLCT}$ state.^[80] Complexes $[14]^{2+}$ and $[15]^{2+}$ (Figure 2) feature a pyrene unit as organic triplet reservoir and reach lifetimes of $\tau = 580$ and 2500 ns, respectively.^[66–68] A pronounced push-pull situation is also present in complexes $[16]^{2+}$ and $[17]^{2+}$ (Figure 11) prepared by Schubert and Berlinguette where an electron accepting tpy ligand is used in combination with a strongly σ -donating carbene ligand [2',6'-bis(3-methyl-1,2,3-triazol-4-yl-5-ylene)-pyridine] with CNC coordination. Unprecedented high excited state lifetimes and quantum yields up to $\tau = 7900$ ns and

$\Phi = 11.4\%$ have been obtained at room temperature (Table 1).^[69] Carbene donor ligands and their ruthenium complexes will not be discussed here in more detail.^[81–83]

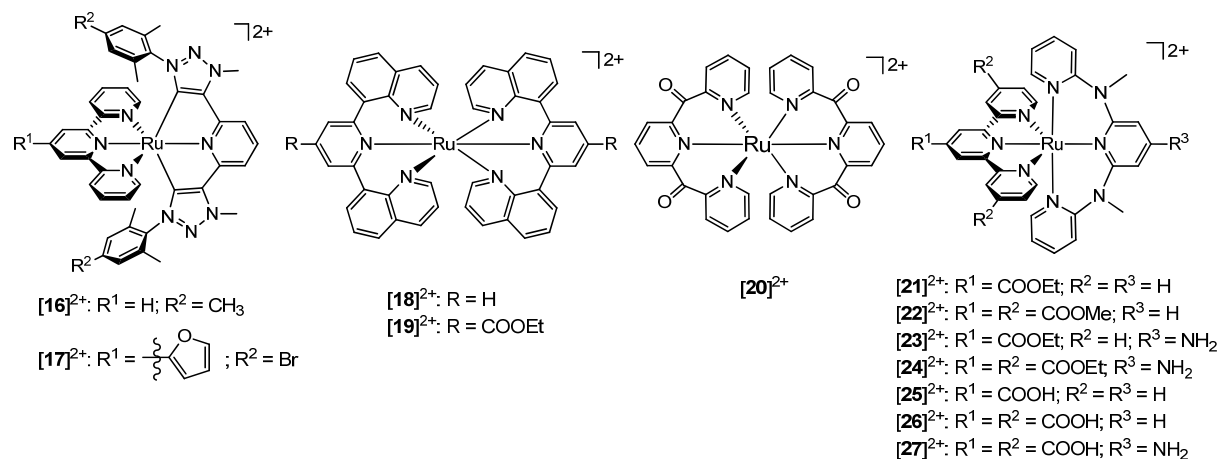


Figure 11. Bis(tridentate) complexes of ruthenium(II).

A further strategy to improve the excited state properties in (bis)tridentate complexes is the optimization of N-Ru-N bite angles. All complexes $[1]^{2+} - [17]^{2+}$ feature five-membered chelates and N-Ru-N bite angles of around 79° . The cyclometalated ligands in $[16]^{2+}$ and $[17]^{2+}$ have even smaller C-Ru-N bite angles of 77° .^[8,61,69] An ideal octahedral coordination sphere with bite angles of 90° would afford a stronger ligand field due to maximization of the overlap between the pyridine nitrogen lone pairs and the e_g^* orbitals of Ru. A stronger ligand field splitting increases the energy difference between 3MLCT and 3MC states which again hampers radiationless deactivation via the latter state (Figure 1).^[56] Hammarström et al. introduced bite angles of 90° by using six-membered chelates in $[Ru(dpq)_2]^{2+}$ ($[18]^{2+}$, Figure 11) leading to high room temperature lifetime ($\tau = 3000$ ns) and quantum yield ($\Phi = 3.2\%$) of the excited state ($dpq = 2,6\text{-di(quinolin-8-yl)pyridine}$).^[70,84] The homoleptic complex $[Ru(EtOOC-dpq)_2]^{2+}$ ($[19]^{2+}$, Figure 11) features even higher values ($\tau = 5500$ ns; $\Phi = 11\%$, Table 1).^[71] Ruben et al. introduced $[Ru(dcpp)_2]^{2+}$ ($[20]^{2+}$, Figure 11) featuring 90° bite angles and six-membered chelates by formal insertion of carbonyl spacers between the pyridine rings of the parent $[Ru(tpy)_2]^{2+}$ complex ($dcpp = 2,6\text{-di(2-carboxypyridyl)pyridine}$). $[20]^{2+}$ has a long lived 3MLCT state ($\tau = 3300$ ns) and the highest room temperature quantum yield ($\Phi = 30\%$) reported to date among bis(tridentate) ruthenium(II) complexes (Table 1).^[72]

Six-membered chelates such as in $[18]^{2+}$ and $[19]^{2+}$ are highly flexible and this can lead to undesired stereoisomers (*mer*, *cis-fac*, *trans-fac*).^[85] The mixed-ligand complex $[(EtOOC-tpy)Ru(ddpd)]^{2+}$ ($[21]^{2+}$, Figure 11) by Breivogel and Heinze overcomes the problem of stereoisomers by using the combination of a five-membered tpy and a six-membered ddpd chelate ligand ($ddpd = N,N'\text{-dimethyl-}N,N'\text{-dipyridin-2-ylpyridine-2,6-diamine}$).^[57,86] $[21]^{2+}$ can be prepared in a stepwise synthesis by first

introducing the tpy ligand to obtain the ruthenium(III) complex (EtOOC-tpy)RuCl₃ which is converted to the final, pure meridional complex [21]²⁺ by treating with the ddpd ligand. The tpy ligand only adopts a *meridional* coordination, thus forcing the ddpd ligand to adopt the *meridional* coordination as well. The bite angles of the ddpd ligand amount to 88°. Despite the presence of a tpy ligand with only 79° bite angles a quantum yield of $\Phi = 0.45\%$ and a remarkable high ³MLCT lifetime of $\tau = 722$ ns were obtained for complex [21]²⁺ at room temperature (Table 1). The synergy of the electron-accepting tpy ligand and the electron-donating ddpd ligand containing NCH₃ groups ([21]²⁺) creates a push-pull situation and shifts the maximum absorption wavelength further to lower energy ($\lambda_{\text{max}} = 517$ nm) compared to [2]²⁺ ($\lambda_{\text{max}} = 485$ nm) where the NCH₃ groups are lacking (Figure 2, Table 1). In complex [22]²⁺ the two outer pyridine rings of the tpy ligand are functionalized by additional ester groups. The maximum absorption wavelength of [22]²⁺ (Figure 11) is further red-shifted ($\lambda_{\text{max}} = 539$ nm) and even higher values for the ³MLCT lifetime ($\tau = 841$ ns) and the quantum yield ($\Phi = 1.1\%$) are obtained.^[57]

However, the increase of ³MLCT lifetimes and quantum yields by push-pull substitution tuning has a limit. A pronounced push-pull situation leads to small energy differences between the ³MLCT state and the singlet ground state (¹GS). According to the energy gap law a small ³MLCT-¹GS energy difference induces fast radiationless deactivation into the ground state.^[73,87,88] Such a strong push-pull situation is given in complexes [23]²⁺ and [24]²⁺ (Figure 11), prepared by Breivogel and Heinze, which feature an additional NH₂ group on the electron-donating ddpd ligand compared to their NH₂-free counterparts [21]²⁺ and [22]²⁺, respectively. The push-pull character of [23]²⁺ and [24]²⁺ manifests itself by the red-shifted absorption maximum and by electrochemical data when compared to [21]²⁺ and [22]²⁺, respectively (Table 1). However, the NH₂ group dramatically reduces the ³MLCT lifetimes of [23]²⁺ and [24]²⁺ by a factor of about 5 – 6 and quantum yields are reduced by an even higher factor compared to the NH₂-free analogues (Table 1). The faster excited state deactivation in [23]²⁺ and [24]²⁺ is induced by high energy oscillators (N–H). This is shown by (NH₂ → ND₂) deuteration experiments with the deuterated complexes [23^D]²⁺ and [24^D]²⁺ featuring higher quantum yields than non-deuterated [23]²⁺ and [24]²⁺, respectively.^[57] However, deuteration has only a small effect on the quantum yield. Hence, also the above mentioned ³MLCT-¹GS energy gap is responsible for radiationless deactivation of the ³MLCT state.

The tris(bidentate) benchmark complex [Ru(bpy)₃]²⁺ has been reported to be photolabile in the presence of coordinating anions such as Cl[−], Br[−], I[−], SCN[−] or NO₃[−]. In its excited state [Ru(bpy)₃]²⁺ is prone to photoinduced ligand substitution, photooxygenation and photoracemization.^[89–93] In contrast, Breivogel and Heinze showed that bis(tridentate) ruthenium(II) complexes such as [4]²⁺ and [21]²⁺ feature significantly higher photostabilities compared to [Ru(bpy)₃]²⁺ which is obviously favorable for photo applications of all kind.^[71,78]

5 Amide Formation and Solid-Phase Peptide Synthesis

Amino acid $[5]^{2+}$ and its ester $[4]^{2+}$ (Figure 2) have been introduced as building blocks in peptide synthesis by coupling 1) in solution and 2) via solid-phase peptide synthesis. Photo-induced electron transfer in derivatives of $[4]^{2+}$ with amide-appended ferrocenyl substituents has been reported.^[61] The dinuclear complex $[29]^{4+}$ is synthesized by Hempel and Heinze in solution by DCC/HOBT activation of $[28]^{2+}$ and treatment with $[4]^{2+}$ under basic conditions (Figure 12).^[26]

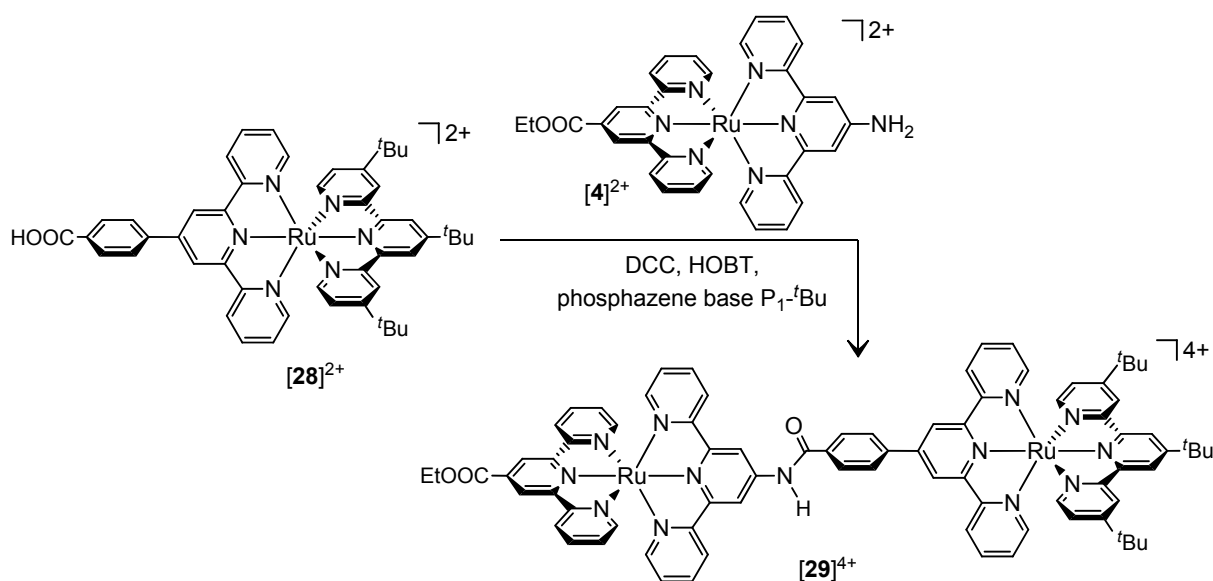


Figure 12. Synthesis of dinuclear $[29]^{4+}$ (DCC = *N,N'*-dicyclohexylcarbodiimide, HOBT = 1-hydroxybenzotriazole, $P_1\text{-}^t\text{Bu}$ = $(\text{Me}_2\text{N})_3\text{P}=\text{N}^t\text{Bu}$).^[26]

Electrochemical measurements of $[29]^{4+}$ reveal different redox potentials for the two ruthenium(II) centers with $E_{1/2} = 0.68$ and 0.91 V vs. FcH/FcH^+ . Breivogel and Heinze studied the metal-metal interaction in the mixed valence complex $[29]^{5+}$ by UV/Vis/NIR spectroscopic measurements which indicate that one-electron oxidation of $[29]^{4+}$ to $[29]^{5+}$ is localized on the $(\text{tpy})\text{Ru}(\text{tpy-}^t\text{Bu}_3)$ part of $[29]^{5+}$. The locus of oxidation can be explained by the electron-donating positive inductive effect of the ^tBu substituents. The lack of an IVCT band (IVCT = intervalence charge transfer) in the spectrum of $[29]^{5+}$ up to $\lambda = 3000$ nm reveals a negligible metal-metal interaction.^[26] Thus, $[29]^{5+}$ can be assigned to the Robin-Day-Class I.^[94] This is also confirmed by DFT-calculated spin densities with a Mulliken spin density on the Ru atom of the $(\text{tpy})\text{Ru}(\text{tpy-}^t\text{Bu}_3)$ part of 0.86 and of 0.00 for the second Ru atom (Figure 13a). In summary, the different environments of the two ruthenium(II) centers of $[29]^{4+}$ lead to a redox asymmetry which prevents metal-metal interaction. In addition, a metal-metal interaction is prevented by the *para*-phenylene bridge which enhances the distance between the metal

centers and is responsible for a poor π -orbital overlap of the *para*-phenylene ring to the amide and to the pyridine plane.^[26]

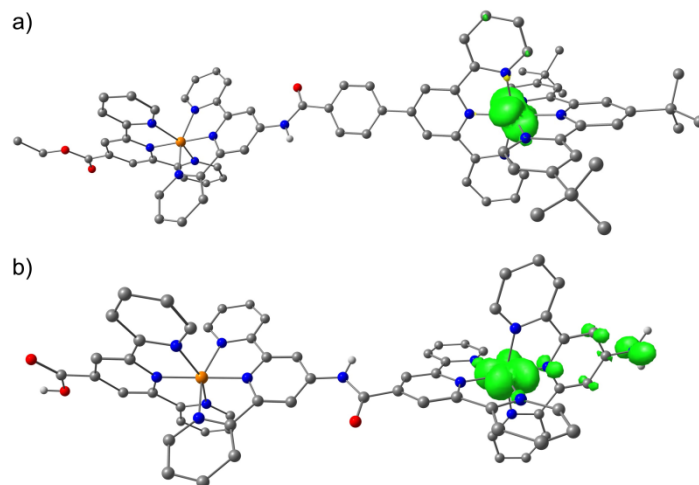


Figure 13. Spin densities of a) $[29]^{5+}$ and b) $[31]^{5+}$ in CH_3CN calculated by DFT (B3LYP/LANL2DZ, IEFPCM, contour value 0.004 a.u.). CH hydrogen atoms omitted.^[26]

Hempel and Heinze realized a smaller redox asymmetry in the dinuclear dipeptide $[31]^{4+}$ (Figure 14). The redox potentials for the two ruthenium(II) centers are $E_{1/2} = 0.80$ and 0.90 V vs. FcH/FcH^+ . $[31]^{4+}$ is synthesized by PyBOP activation of $[30]^{2+}$ and treatment with $[4]^{2+}$ under basic conditions (PyBOP = benzotriazole-1-yl-oxy-trispyrrolidino-phosphonium hexafluorophosphate). After amide bond formation the t -BOC and ethyl ester protecting groups are removed by aqueous acidic treatment to obtain $[31]^{4+}$ (Figure 14).^[26] The amide bond induces a coplanar bridging ligand allowing for a better π -orbital overlap. In addition, the lack of the *para*-phenylene spacer provides a shorter metal-metal distance compared to $[29]^{4+}$. However, UV/Vis/NIR spectroscopic measurements of $[31]^{5+}$ by Breivogel and Heinze are analogue to the situation with $[29]^{5+}$. The spectra indicate that the NH_2 -substituted bis(tpy) moiety is oxidized. This can be explained by the strong electron-donating character of the NH_2 group.^[26,61] Still no IVCT is seen, so $[31]^{5+}$ can also be assigned to the Robin-Day-Class I.^[94] The DFT-calculated spin density of $[31]^{5+}$ confirms the valence-localized situation showing spin density only on the *N*-terminal site. Mulliken spin densities of the Ru atom of the NH_2 -substituted bis(tpy) moiety, the NH_2 nitrogen atom and the second Ru atom amount to 0.76, 0.11 and 0.00, respectively (Figure 13b).^[26,57]

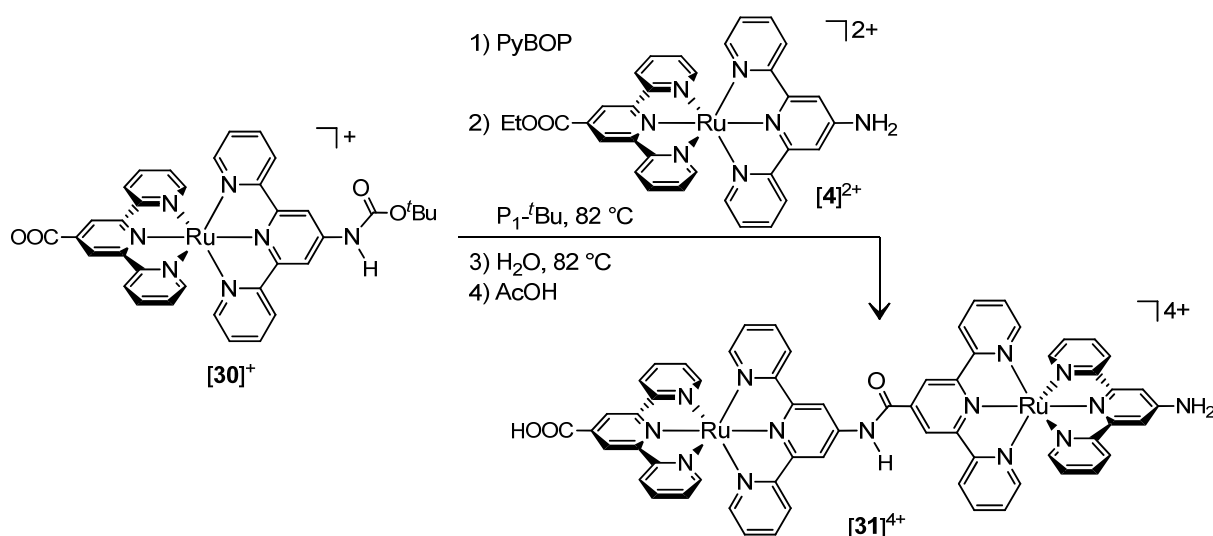


Figure 14. Synthesis of the dinuclear dipeptide $[31]^{4+}$ (PyBOP = benzotriazole-1-yl-oxy-trispyrrolidino-phosphonium hexafluorophosphate, $\text{P}_1-t\text{Bu} = (\text{Me}_2\text{N})_3\text{P}=\text{N}^t\text{Bu}$).^[26]

The introduction of $[5]^{2+}$ by solid-phase peptide synthesis has been reported by Hempel and Heinze.^[18] A general strategy is as follows: A TentaGel S resin^[95,96] with a Wang linker^[97] (**32**) is functionalized with Cl-Gly-Fmoc (Figure 15, Fmoc = fluorenylmethoxycarbonyl). The Fmoc group is cleaved by piperidine to obtain the free NH_2 group (**33**). The carboxylic acid group of $[5]^{2+}$ is activated by PyBOP and connected to the solid support via an amide bond to obtain $[34]^{2+}$ (PyBOP = benzotriazole-1-yl-oxy-trispyrrolidino-phosphonium hexafluorophosphate). Protection of the *N*-terminus of $[5]^{2+}$ is unnecessary due to the weak nucleophilicity of the aromatic NH_2 group of $[5]^{2+}$.^[18,63] For the activation of the NH_2 group of $[34]^{2+}$ strong coupling reagents such as acid chlorides are necessary in order to form an amide bond such as in $[35]^{2+}$. The aliphatic NH_2 group of $[35]^{2+}$ readily forms amide bonds with carboxylic acids $\text{R}-\text{COOH}$ by PyBOP activation. Several acids $\text{R}-\text{COOH}$ have been used, e.g. $\text{R} = \text{CH}_3$, CF_3 and coumarin-3-carboxylic acid.^[18] Finally, peptide $[36]^{2+}$ is cleaved from the solid phase by TFA to obtain the desired product $[37]^{2+}$ (TFA = trifluoroacetic acid).

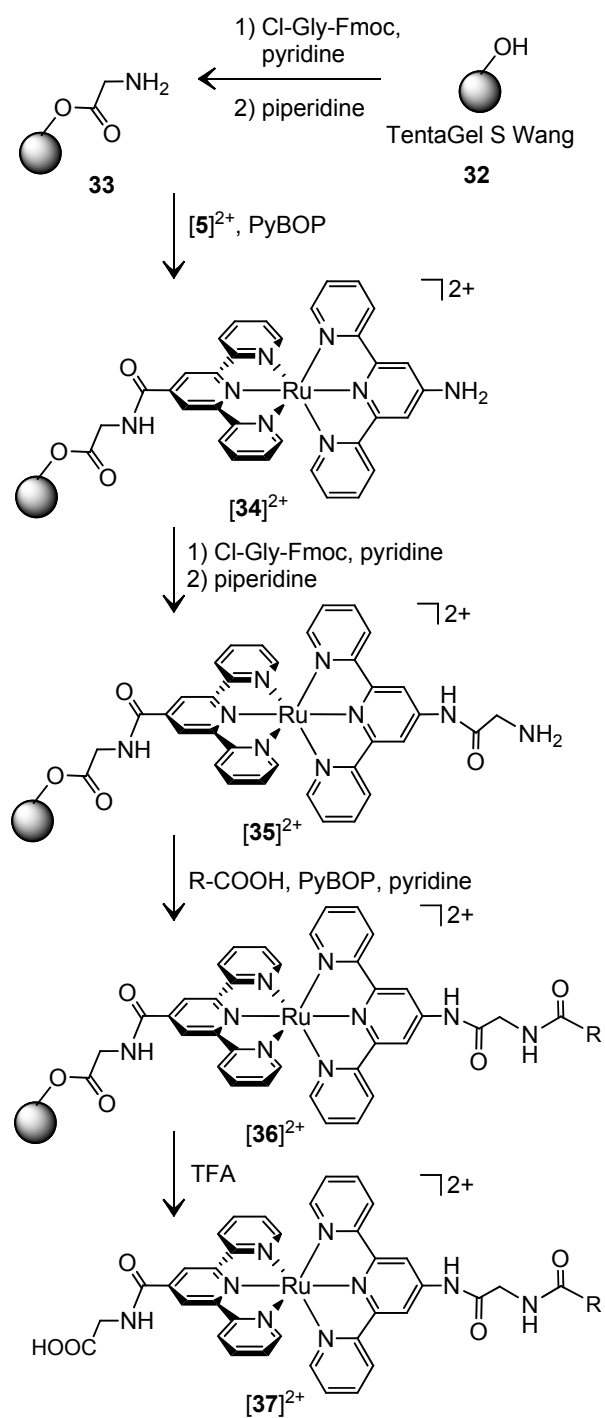


Figure 15. Solid-phase peptide synthesis including the ruthenium(II) amino acid **[5]**²⁺.^[18]

6 Applications

Polypyridine complexes of ruthenium(II), especially $[\text{Ru}(\text{bpy})_3]^{2+}$ type complexes, are suitable compounds for directional energy transfer and can act as donors and acceptors for photoinduced energy transfer.^[98] Bis(tridentate) complexes of ruthenium(II) have been incorporated into energy transfer systems using ethynyl spacers between the $[\text{Ru}(\text{tpy})_2]^{2+}$ donor and thiophene units as acceptors.^[99] Hempel and Heinze have connected the donor-acceptor substituted complex $[\mathbf{5}]^{2+}$ to organic chromophores by amide bridges via SPPS with a different number of glycine units in between (Figure 16). The use of one or none glycine unit with $n = 0$ ($[\mathbf{38}]^{2+}$) or 1 ($[\mathbf{39}]^{2+}$) allows for coplanarity of the coumarin dye and the adjacent tpy ligand which is favorable for efficient energy transfer via a Dexter mechanism.^[18] In the case of short bridges excitation of the coumarin ($[\mathbf{39}]^{2+}$, $n = 1$, $\lambda_{\text{exc}} = 422 \text{ nm}$) induces energy transfer to the $[\text{Ru}(\text{tpy})_2]^{2+}$ core while the coumarin fluorescence is efficiently quenched.^[18,20] Breivogel and Heinze measured excitation emission matrices of complexes $[\mathbf{39}]^{2+} - [\mathbf{41}]^{2+}$. The excitation emission matrix of $[\mathbf{39}]^{2+}$ clearly shows that upon excitation at $\lambda_{\text{exc}} = 400 - 500 \text{ nm}$, emission occurs at $\lambda_{\text{em}} = 670 \text{ nm}$ which corresponds to the wavelength of the coumarin-free reference $[\mathbf{41}]^{2+}$ (Figure 17). For a longer bridge ($[\mathbf{40}]^{2+}$, $n = 2$, Figure 16) efficient energy transfer is no more feasible. Excitation of the organic coumarin chromophore leads to fluorescence of the coumarin at $\lambda_{\text{exc}} = 465 \text{ nm}$ while emission from the $[\text{Ru}(\text{tpy})_2]^{2+}$ core is not observed (Figure 17).^[20]

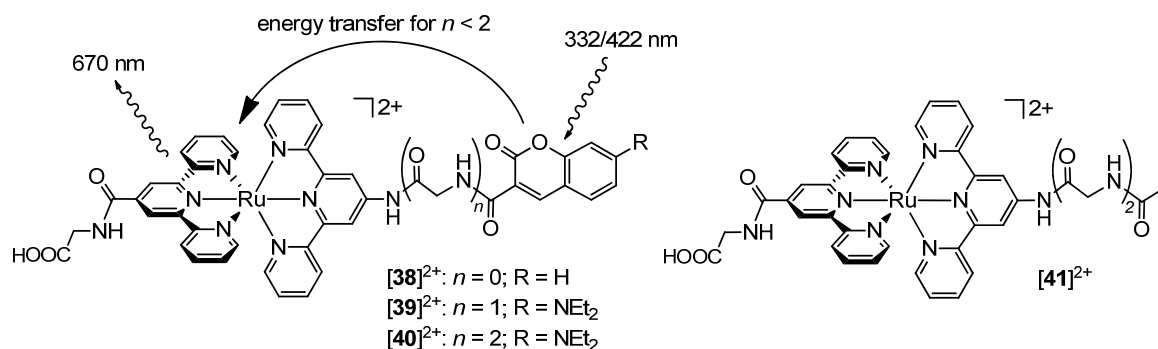


Figure 16. Bis(terpyridine) ruthenium(II) complexes for studying energy transfer.^[18,20]

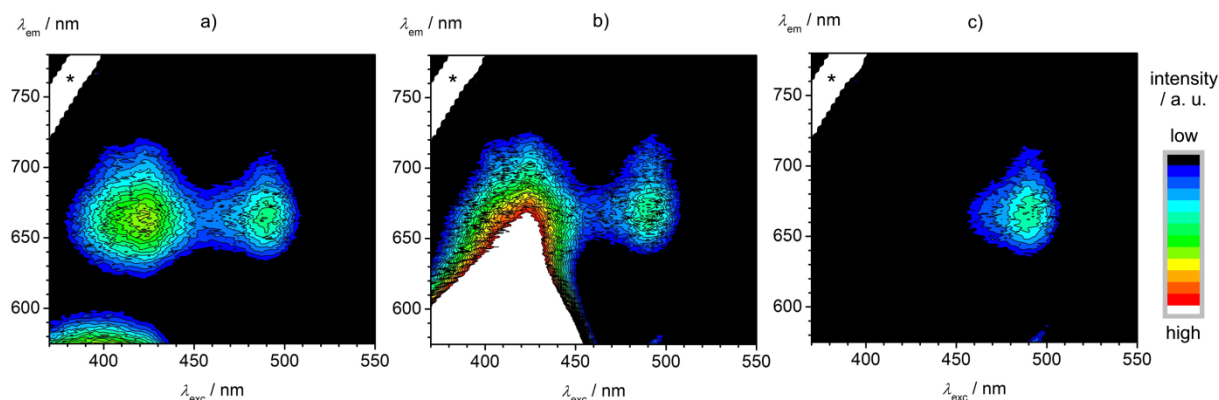


Figure 17. Excitation emission matrices of a) $[39]^{2+}$ ($n = 1$), b) $[40]^{2+}$ ($n = 2$) and c) reference complex $[41]^{2+}$. The color bar indicates the emission intensity. $*$ = $2\lambda_{\text{exc}}$.

Amino acid $[5]^{2+}$ has been used as chromophore in a donor-chromophore-acceptor electron transfer nanocomposite by zur Borg, Domanski, Breivogel, Bürger, Heinze and Zentel in order to probe light-induced charge separation.^[100] As electron donor a polymer with triphenylamine units and as electron acceptor ZnO nanorods were used. $[5]^{2+}$ was converted to tripeptide $[42]^{2+}$ by a SPPS and the amino group of $[42]^{2+}$ forms an amide bond with the pentafluorophenol activated carboxylic acid of block-copolymer **43** to give $[44]^{(2m)+}$ (Figure 18). The free COOH group in $[44]^{(2m)+}$ acts as anchor to ZnO nanorods. Upon excitation of the $[\text{Ru}(\text{tpy})_2]^{2+}$ chromophore by irradiation ($\lambda_{\text{exc}} = 488 \text{ nm}$) into its absorption band ($\lambda_{\text{max}} = 498 \text{ nm}$) excited electrons are injected into the ZnO nanorods and electron holes are generated in the triphenylamine-containing polymer. The phosphorescence of the $[\text{Ru}(\text{tpy})_2]^{2+}$ core was completely quenched. Under irradiation a significant change of the surface potential of the polymer-coated nanorods is observed via Kelvin probe force microscopy and confirms the positive charge in the polymer.^[100]

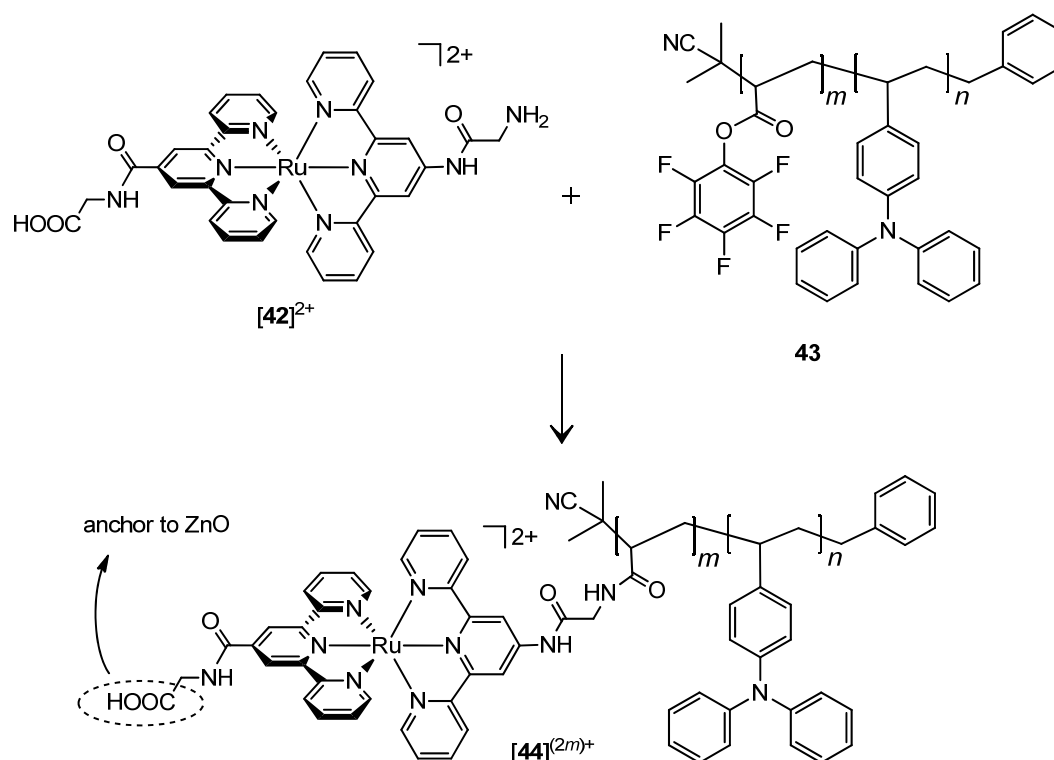


Figure 18. Synthesis of **[44]**^{(2m)+} by coupling of **[42]**²⁺ to **43** ($n \approx 50$, $m \approx 10$).^[100]

Bis(tridentate) complexes **[5]**²⁺, **[25]**²⁺, **[26]**²⁺, **[27]**²⁺, **[45]**²⁺ and **[46]**²⁺ (Figure 2, 11 and 19) have been adsorbed to TiO₂ and tested as sensitizers in dye-sensitized solar cells with an I⁻/I₃⁻ redox electrolyte by Breivogel and Heinze. The complexes feature absorption spectra comparable to the one of the standard ruthenium(II) sensitizer N719. However, the twofold positive charge of the complexes increases the I₃⁻ concentration near the TiO₂ electrode due to electrostatic interactions favoring electron recombination. Consequently, low cell power conversion efficiencies up to $\eta = 0.26\%$ were obtained with the twofold positively charged complexes. In contrast, N719 is twofold negatively charged and reaches a power conversion efficiency of $\eta = 5.03\%$ in cells under the same conditions.^[78] The charge of bis(tridentate) complexes of ruthenium(II) can be reduced by introduction of negatively charged ligands such as pyrazolyl or cyclometalated ligands such as in complexes **52** and **53** reaching power conversion efficiencies up to $\eta = 10.7\%$ (Figure 23).^[101–103] Another approach would be the use of other redox electrolytes such as positively charged metal complexes, e.g. [Co(4,4'-(*t*Bu)₂bpy)₃]^{2+/3+}.^[104]

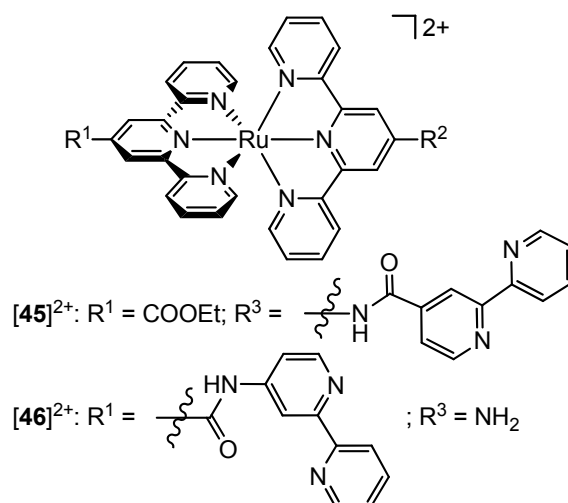


Figure 19. Complexes $[45]^{2+}$ and $[46]^{2+}$.^[77,105]

Breivogel and Heinze employed bis(tridentate) complexes $[4]^{2+}$, $[21]^{2+}$ and $[22]^{2+}$ as emitters in light-emitting electrochemical cells (LECs). A simple device structure of ITO/PEDOT:PSS/ruthenium(II) complex/Ag is used and characterized by AFM (ITO = indium tin oxide, PEDOT = 3,4-ethylenedioxythiophene, PSS = poly(styrenesulfonate), AFM = atomic force microscopy). Deep red light emission up to a maximum emission wavelength of 755 nm is achieved. To the best of our knowledge this is the lowest emission energy for LECs containing bis(tridentate) ruthenium(II) complexes.^[7,8,106] For such a low emission energy the energy gap law^[73,87,88] predicts enhanced radiationless deactivation of the excited state explaining the small external quantum efficiencies. However, dilution of the ruthenium(II) complexes in PMMA enhances the external quantum efficiencies due to less radiationless excited state deactivation.^[107]

7 Dye-Sensitized Solar Cells

7.1 Basic Principles

Dye-sensitized solar cells (DSSCs) were first reported in 1991 by O'Regan and Grätzel and provide a low cost alternative to widely used silicon-based solar cells.^[2–4] The working principle and the schematic structure of a conventional DSSC are depicted in Figure 20. A DSSC consists of a mesoporous semiconductor layer of TiO_2 (anatase) on a transparent anode such as fluorine-doped tin oxide (FTO). Molecular sensitizers are adsorbed on top of the TiO_2 particles. The porous TiO_2 structure ensures a high surface area which allows for efficient light harvesting. The porous TiO_2 network is penetrated by a liquid redox electrolyte, typically the I^-/I_3^- system in CH_3CN , which is in contact to the cathode. When light passes through the transparent anode a sensitizer is excited ($\text{S} \rightarrow \text{S}^*$) and injects an electron into TiO_2 (k_1). The electrons percolate the TiO_2 network and are collected at the anode (k_2). The oxidized sensitizer (S^+) is regenerated by the redox electrolyte (k_3). The redox electrolyte diffuses to the cathode where it is reduced (k_4). The maximum attainable voltage V_{OC} is given by the potential difference between the Fermi level of TiO_2 and the redox potential of the electrolyte, hence it is independent of the sensitizer.^[4]

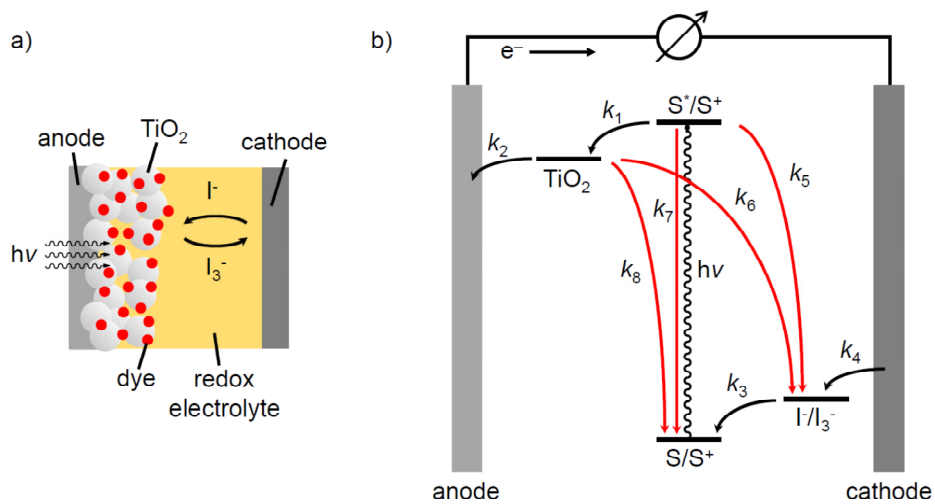


Figure 20. a) Schematic device structure and b) working principle of a DSSC. S denotes a sensitizer.

The efficiency η of a DSSC is defined by equation 1 with P_{out} being the maximum power per area that can be extracted and P_{in} being the power per area of the irradiated light.

$$(1) \quad \eta = \frac{P_{\text{out}}}{P_{\text{in}}}$$

Usually, efficiencies are referred to standardized conditions with an irradiation power of $P_{\text{in}} = 1000 \text{ W m}^{-2}$ and a sample temperature of 25°C . The standardized irradiation spectrum is the air mass (AM) 1.5 spectrum (Figure 21).^[108] The factor "1.5" indicates that the solar light passes the thickness of 1.5 atmospheres which corresponds to a zenith angle of 48.2° .

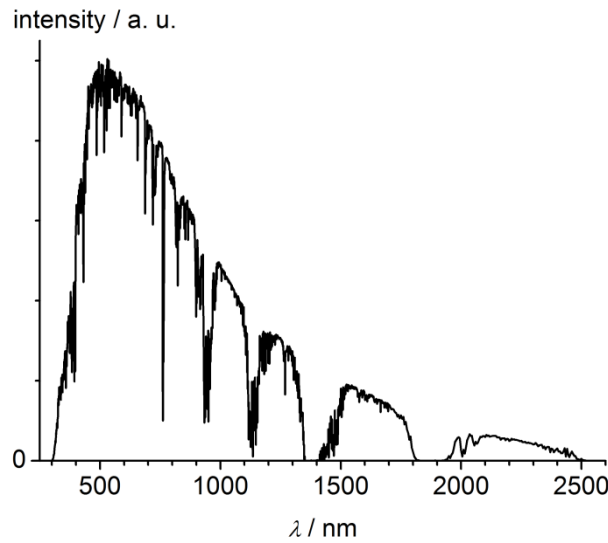


Figure 21. AM 1.5 spectrum of the sunlight reaching the surface of the earth under a zenith angle of 48.2° .^[109]

Figure 22 shows the typical behavior of a current density-voltage (I - U) curve of a DSSC. I_{sc} is the maximum current density under short circuit conditions and U_{oc} is the maximum photovoltage at open circuit conditions. At a certain point, the maximum power point (mpp), the product of the current density and the photovoltage is maximal. This point defines the maximum output power P_{out} (equation 2).

$$(2) \quad P_{\text{out}} = U_{\text{mpp}} \times I_{\text{mpp}}$$

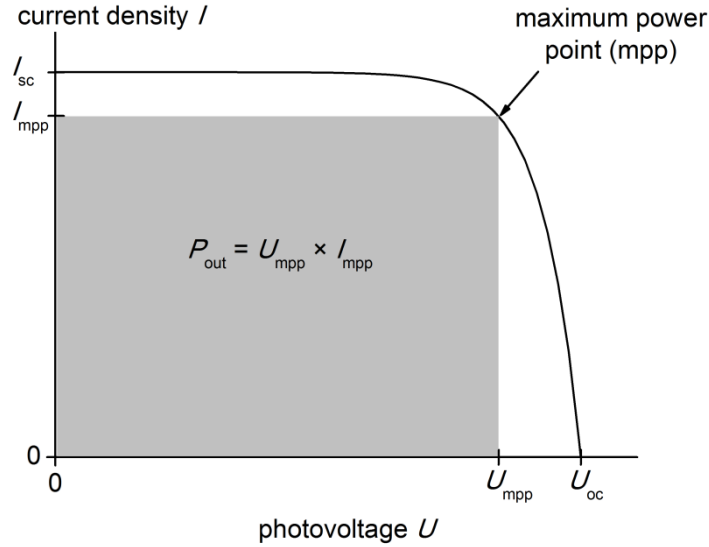


Figure 22. Current density-voltage (I - U) curve and indication of the short circuit current density (I_{sc}), the current density at the maximum power point (I_{mpp}), the open circuit voltage (U_{oc}) and the voltage at the maximum power point (U_{mpp}). The grey rectangle illustrates the maximum output power P_{out} .

The fill factor ff of a DSSC is given by equation 3 and describes the shape of the I - U curve. A rectangular shape of the I - U curve corresponds to a fill factor of $ff=1$.

$$(3) \quad ff = \frac{U_{mpp} \times I_{mpp}}{U_{oc} \times I_{sc}}$$

The incident photon-to-current conversion efficiency IPCE(λ) is defined by the number of collected electrons under short circuit conditions per number of incident photons at a given wavelength λ (equation 4).

$$(4) \quad IPCE = \frac{\# \text{ electrons out}}{\# \text{ photons in}} = \frac{\frac{I_{sc}(\lambda)}{e}}{\frac{P_{in}(\lambda)}{h\nu}} = \frac{hc}{\lambda e} \times \frac{I_{sc}(\lambda)}{P_{in}(\lambda)}$$

h denotes the Planck constant, c the velocity of light and e the elementary charge. Despite the defined DSSC parameters (equation 1 – 4) DSSC measurements of different laboratories are not directly comparable to each other because a manifold of other conditions is not standardized such as cell building procedures, solvents, additives, chemical and morphological nature of TiO_2 , electrolyte compositions and electrode materials. For a better comparison standard dyes such as N719 should generally be employed as a reference under the used conditions and compared to the investigated dyes.^[108]

7.2 Dye Design for DSSCs

Dyes for DSSCs should have a broad and intense absorption in order to efficiently harvest the sun light. Dyes should be photochemically, thermally and electrochemically stable to avoid degradation. For the immobilization on the nanoporous semiconductor anchor units such as carboxylic acids are advantageous. The LUMO of the dye needs to be higher in energy than the conduction band of TiO_2 while the HOMO of the dye needs to be lower in energy than the potential of the redox electrolyte. A high electronic directionality of the excited states is necessary for efficient electron injection into TiO_2 . This means the HOMO of the dye is located remote from TiO_2 and the LUMO is in close contact to TiO_2 .^[3] Polypyridine complexes of ruthenium(II) have been shown to be excellent sensitizers for DSSCs. Two of the best performing and most prominent complexes are the so called black dye $(\text{Bu}_4\text{N})_3[\text{Ru}(\text{Htctpy})(\text{NCS})_3]$ (**47**)^[110] and N719 $(\text{Bu}_4\text{N})_2[\text{Ru}(\text{Hdcbpy})_2(\text{NCS})_2]$ (**48**)^[111,112] (Figure 23) reaching DSSC efficiencies of $\eta = 10.4$ and 11.2% under full air mass 1.5 (AM 1.5), respectively (tctpy = 4,4',4''-tricarboxy-2,2';6',2''-terpyridine, dcbpy = 4,4'-dicarboxy-2,2'-bipyridine).^[4] Both, N719 and the black dye feature carboxylic acid/carboxylate anchor groups with a LUMO located on the anchoring ligand while the HOMO is located on the ruthenium center and the remote NCS^- ligands.^[78,113]

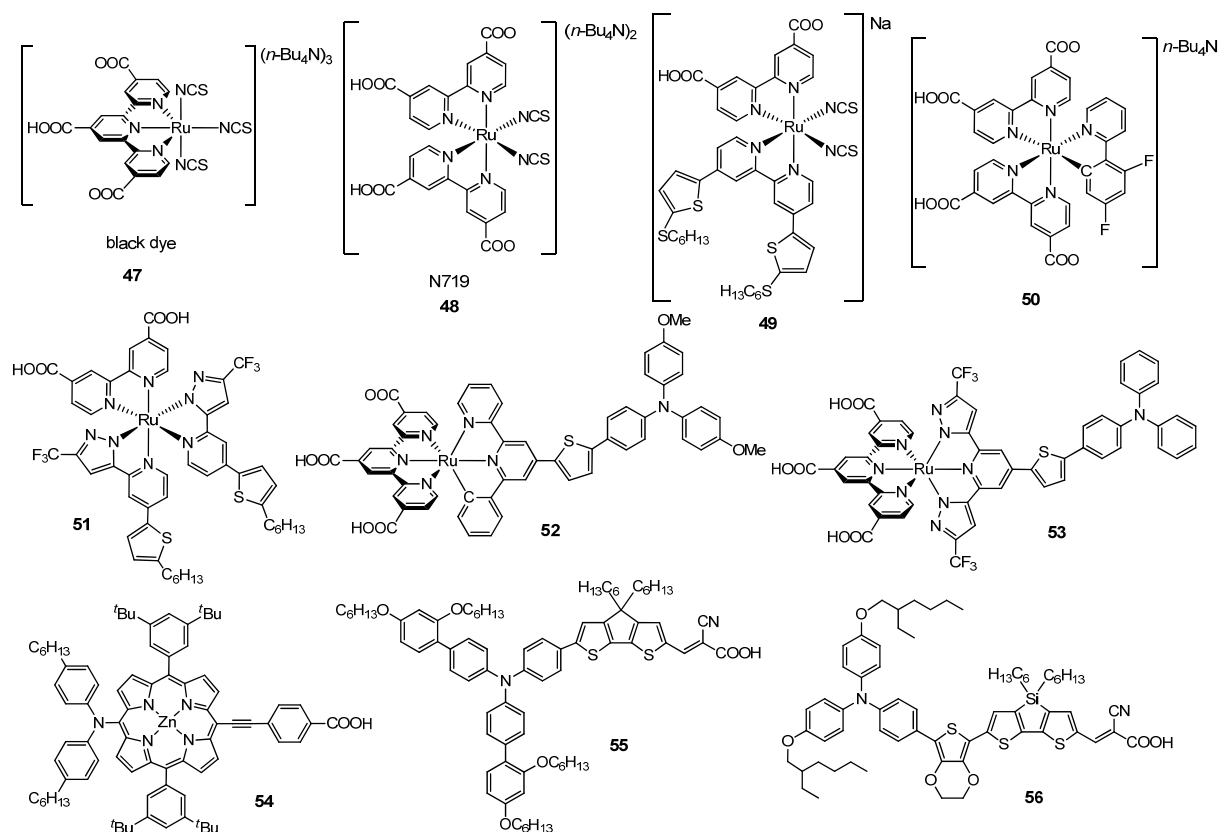


Figure 23. DSSC sensitizers **47** – **56**.

In order to improve DSSC characteristics a manifold of different design strategies for sensitizers has emerged in the last two decades. Complex **49** (Figure 23) is a derivative of N719 with thiophene units which extend the conjugated systems and significantly increase the extinction coefficients.^[114] This is beneficial as more photons can be harvested by this dye compared to N719. In addition, the long alkyl chains prevent interfacial electron recombination leading to cell efficiencies of $\eta = 11.4\%$ under full AM 1.5.^[4,114] Monodentate ligands such as NCS^- and pyridine are regarded as a drawback concerning the long term stability of sensitizers. Thermal- and photo-induced isomerization and ligand exchange has been reported for monodentate ligands leading to dye species with lower cell efficiencies.^[115–122] Attempts to avoid monodentate ligands include the use of tris(bidentate) and bis(tridentate) complexes such as **50** (Figure 23).^[4,123,124] **50** can also be seen as a derivative of N719 where both NCS^- ligands have been replaced by a bidentate cyclometalated 2-phenylpyridine ligand. DSSCs with **50** reach efficiencies of $\eta = 10.1\%$ under full AM 1.5.^[4,124] Typically, the cyclometalated ligand contributes to the HOMO of ruthenium(II) complexes while the LUMO resides on the anchor ligand. A favorable electronic directionality is thus induced when the anchor ligand is situated opposite to the cyclometalated ligand.^[125,126] Complex **51** (Figure 23) features a dcbpy ligand and two 2-pyridylpyrazole ligands. DSSCs with this complex reach efficiencies of $\eta = 9.5\%$ under full AM 1.5.^[127] However, also complexes with bidentate ligands such as bpy or 4,4'-bi-1,2,3-triazolate are prone to photo-induced ligand loss and isomerization.^[78,128,129] Furthermore, tris(bidentate) complexes of ruthenium(II) are chiral which complicates synthetic procedures as discussed above.^[48–50] In contrast, bis(tridentate) complexes are achiral and feature higher stability constants compared to their bidentate analogues.^[52,53] Bis(tridentate) complexes of ruthenium(II) have already been incorporated into DSSCs. Berlinguette et al. have employed complex **52** (Figure 23) featuring a tctpy anchor ligand and a cyclometalated pbpy ligand with an efficiency of $\eta = 8.0\%$ (pbpy = 6-phenyl-2,2'-bipyridine). The appended triarylamine moiety avoids electron recombination because after injection of an electron into TiO_2 the positive charge is shifted towards the triarylamine moiety and away from the TiO_2 surface.^[101] Chi et al. reported the neutral bis(tridentate) ruthenium(II) complex **53** (Figure 23) with a dianionic donor ligand (2,6-bis(5-pyrazolyl)pyridine) and a tctpy acceptor ligand with DSSC efficiencies up to $\eta = 10.7\%$.^[102,103] Again, the thiophene unit in **52** and **53** extends the conjugated system and increases the extinction coefficients. Bis(tridentate) coordination of ruthenium(II) leads to more robust sensitizers concerning photostability and long term stability of DSSCs.^[3,78,130,131]

To date, the highest DSSC efficiency of $\eta = 12.3\%$ could be obtained with a zinc porphyrin (**54**) in combination with **55** as organic cosensitizer (Figure 23).^[132] Also metal-free all-organic sensitizers alone can reach high DSSC performances with $\eta = 10.1\%$ being the top efficiency obtained with dye **56** (Figure 23).^[4]

Future work about DSSCs is headed towards solid-state DSSCs. In these cells the liquid electrolyte is substituted by a solid hole transporting material, typically spiro-OMeTAD (2,2'-7,7'-tetrakis(*N,N*-di-*p*-methoxyphenylamine)-9,9'-spirobifluorene). Solid-state DSSC are more robust than DSSCs containing

a liquid electrolyte because of leaking problems with the liquid electrolyte. However, solid hole transport materials have several drawbacks such as low hole mobility, increased charge recombination between the semiconductor and the hole transporting material and low interfacial contact areas between dye molecules and the solid electrolyte resulting from incomplete penetration of the hole transport material into the pores of the semiconductor.^[48] Nevertheless, new techniques in solid-state sensitized solar cells are very promising. The replacement of molecular sensitizers by perovskite $(\text{CH}_3\text{NH}_3)(\text{PbX}_3)$ ($X = \text{I}, \text{Cl}$) has lead to new record efficiencies of 14 – 15%.^[133–136]

8 Light-Emitting Electrochemical Cells

Light-emitting electrochemical cells (LECs) were introduced in 1995 by Pei and provide a low-cost alternative to conventional organic light-emitting devices (OLEDs).^[137,138] The main difference between OLEDs and LECs is the nature of the light-emitting layer which is neutral in OLEDs and ionic in LECs.^[5,139–143] In principle, an LEC can simply consist of an ionic emitting layer between two electrodes (Figure 24a). Typically, the anode material is transparent (e.g. indium tin oxide) in order to enable light output while the cathode material can be nontransparent and reflective such as silver. When a voltage is applied ions in the emitting layer start to migrate. Cations migrate towards the cathode and anions towards the anode creating ionic layers at the electrodes (Figure 24b). These charge layers efficiently lower the injection barriers for electrons and holes at the interface which allows for low turn-on and driving voltages. Electrons and holes recombine in the emitting layer forming excited electron-hole pairs, called excitons which can degrade by emitting light. In contrast, high charge injection barriers are typically present in OLEDs due to the neutral emitting layer leading to high turn-on and driving voltages. Therefore OLEDs require additional ionic layers enabling electron and hole injection and controlling electron and hole transport, thus making OLED structures more complicated and cost-intensive (Figure 24a). Furthermore, OLEDs require air-sensitive low work function metals as cathode materials such as calcium or barium in order to allow electron injection which again raises fabrication costs due to expensive encapsulation. LECs offer the possibility to be essentially independent of electrode materials due to the ionic emitting layer.^[5,139–143]

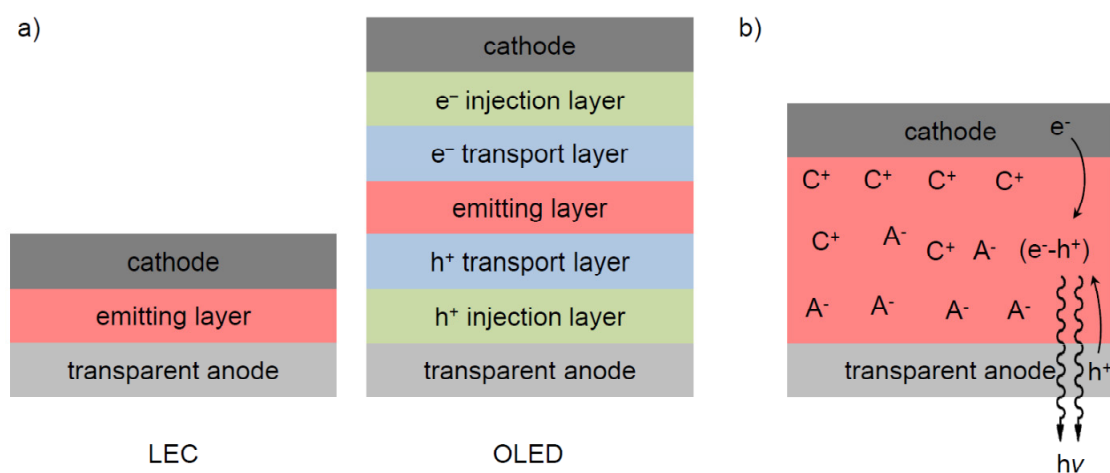


Figure 24. a) Structure of an LEC and a conventional OLED. b) Working principle of an LEC. C^+ denotes a cation and A^- an anion.

Important physical quantities in LECs are the internal quantum efficiency (IQE) which is the ratio of the number of generated photons per number of electrons passing through the cell (equation 5).

$$(5) \quad \text{IQE} = \frac{\# \text{ generated photons}}{\# \text{ electrons}}$$

Not all generated photons leave the cell due to photon reabsorption at the cathode, the emitting layer or the anode, reflection at the interface between the anode and the emitting layer or other loss mechanisms. The external quantum efficiency EQE defines the ratio of the number of photons coming out of the cell per number of electrons passing through the cell (equation 6).

$$(6) \quad \text{EQE} = \frac{\# \text{ photons out}}{\# \text{ electrons}}$$

A human eye has three color receptors. The normalized sensitivity curves $X'(\lambda)$, $Y'(\lambda)$ and $Z'(\lambda)$ of these receptors are illustrated in Figure 25.^[144]

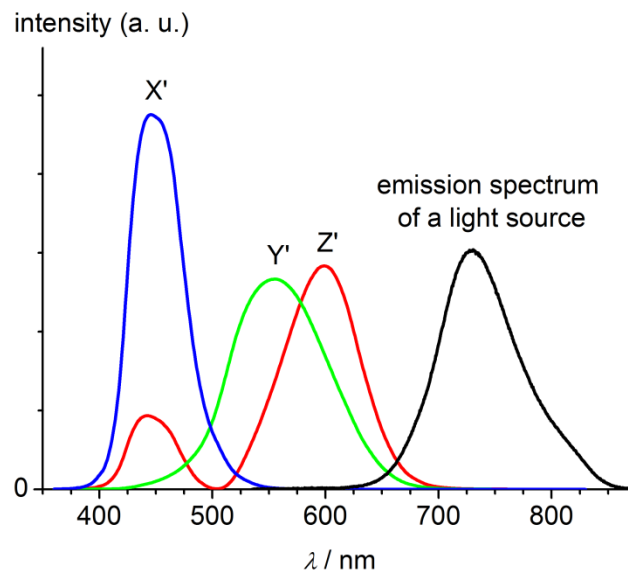


Figure 25. Integral-normalized sensitivity curves $X'(\lambda)$, $Y'(\lambda)$ and $Z'(\lambda)$ of the three color receptors of the human eye.

The color impression of an emission spectrum to the standard human eye can be defined by the CIE coordinates x and y (CIE = commission international de l'éclairage). x and y are defined by equations 7.

$$(7) \quad x = \frac{X}{X+Y+Z}; \quad y = \frac{Y}{X+Y+Z}; \quad z = \frac{Z}{X+Y+Z}; \quad x+y+z=1$$

X , Y , and Z denote the overlap of the emission spectrum with the sensitivity curve $X'(\lambda)$, $Y'(\lambda)$ and $Z'(\lambda)$, respectively. The sum of the three resulting coordinates x , y and z equals 1. For given values of x and y the value of z is predetermined. Therefore, the coordinates can be reduced to x and y . Figure 26 illustrates a chromaticity diagram which is the plot of x versus y and the corresponding colors. At $x = y = z = \frac{1}{3}$ the color impression is white. Outside of the colored area there is still a color impression to the human eye. The color merely appears with lower intensity.

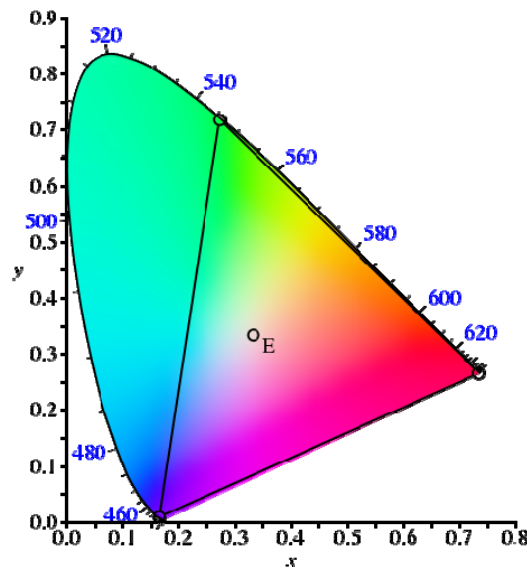


Figure 26. Chromaticity diagram.^[145]

While CIE coordinates define the color impression of a spectrum to the human eye, the luminance L describes how bright a light source appears to the human eye. The sensitivity of the human eye is wavelength-dependent and is described by the human eye response curve $V(\lambda)$ (Figure 27) with a maximum at $\lambda_{\max} = 555$ nm. Two light sources might send out the same amount of photons but with different energy (spectrum 1 and 2 in Figure 27). The light source with spectrum 1 has a larger spectral overlap with the human eye response curve than the light source with spectrum 2. Therefore, the light source with spectrum 1 appears brighter to the human eye than the light source with spectrum 2.

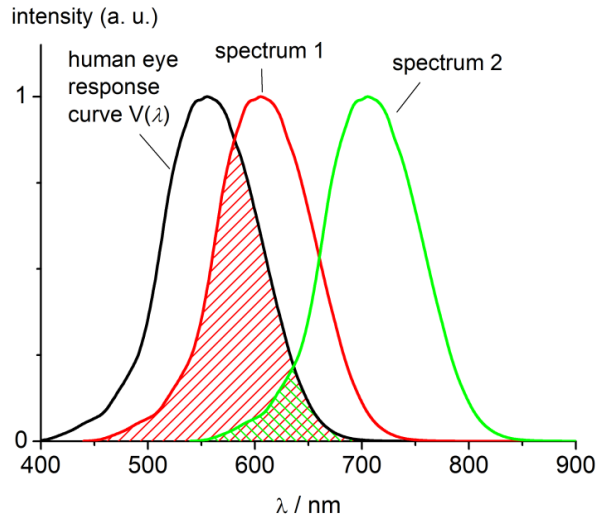


Figure 27. The human eye response curve $V(\lambda)$ has a larger overlap with spectrum 1 (red) than with spectrum 2 (green). The overlap is illustrated by red and green hatchures, respectively.

The luminance L is defined by equation 8 where $K_m = 683 \text{ lm W}^{-1}$ at 555 nm, I is the current density, R is the distance between the LEC and the photodiode, A_{LEC} is the area of the limiting aperture, $A_{\text{photodiode}}$ is the area of the photodiode, $S_{\text{emission}}(\lambda)$ is the emission spectrum and $S_{\text{responsivity}}(\lambda)$ is the responsivity of the photodiode.^[146,147]

$$(8) \quad L = \frac{K_m \cdot I_{\text{photodiode}} \cdot R^2}{A_{\text{LEC}} \cdot A_{\text{photodiode}}} \times \frac{\int_{360\text{nm}}^{830\text{nm}} V(\lambda) \cdot \frac{S_{\text{emission}}(\lambda)}{S_{\text{responsivity}}(\lambda)} d\lambda}{\int_{360\text{nm}}^{830\text{nm}} S_{\text{emission}}(\lambda) d\lambda}$$

Simple spin statistics predict that 25% of the excitons are singlet excitons and 75% are triplet excitons. However, organic materials can only convert singlet excitons into photons while triplet excitons only produce heat.^[148–151] The first LECs contained organic polymers as emitters, thus limiting the IQE to a theoretical maximum of 25%.^[137,138] Instead, when transition metal complexes are used as emitters spin-orbit coupling enables the generation of photons from both singlet and triplet excitons which raises the theoretical limit for the IQE up to 100%. The first LEC with a transition metal complex was introduced by Lee in 1996 using a $[\text{Ru}(\text{phen})_3]^{2+}$ derivative as emitter.^[152] Among ruthenium complexes, the most efficient LECs (EQE = 6.4%) were obtained by using $[\text{Ru}(\text{bpy})_3]^{2+}$ as emitter.^[153] However, the chirality of substituted tris(bidentate) complexes of ruthenium(II) is problematic as discussed above. Furthermore, $[\text{Ru}(\text{bpy})_3]^{2+}$ type complexes suffer from ligand loss in LECs which leads to degradation products in the presence of water such as $[\text{Ru}^{\text{II}}(\text{bpy})_2(\text{H}_2\text{O})_2]^{2+}$ and the oxido-bridged dimer $[\{\text{Ru}^{\text{III}}(\text{bpy})_2(\text{H}_2\text{O})\}_2\text{O}]^{4+}$.^[143,154–156] In order to enhance the emitter stability bis(tridentate) complexes of ruthenium(II) have already been used in LECs.^[7,8,107] However, EQE

values for LECs with bis(tridentate) ruthenium(II) complexes remain low which is attributed to the lower solution quantum yields of these complexes compared to $[\text{Ru}(\text{bpy})_3]^{2+}$ as discussed above.

Reasons for low EQEs in LECs are manifold: 1) Intrinsic properties of the emitter molecules such as too long luminescence lifetimes leading to saturation effects, low solution quantum yields due to deactivation via ^3MC states and vibrational coupling of the excited state to the ground state. 2) Energy transfer to impurities such as O_2 . 3) The wrong choice of cell components and high applied biases can lead to charge imbalance, saturation effects due to triplet-triplet annihilation and losses due to inefficient light outcoupling (self-absorption of the emitted light, reflection at the transparent electrode).^[157] Self-quenching of excited emitter molecules can be decreased by passivation with sterically demanding substituents^[6,158] or dilution in polymeric matrices such as PMMA (PMMA = poly(methylmethacrylate)).^[107]

To date research for ionic emitters for LECs is focused on charged iridium(III) complexes such as $[\text{Ir}(\text{ppy})_2(\text{bpy})]^+$ (**[57]**⁺, Figure 28).^[140] Iridium(III) complexes have a stronger ligand field compared to ruthenium(II) complexes as the ligand field strength increases with the quantum number in the row $3d < 4d < 5d$. Additionally, the higher charge of iridium(III) compared to ruthenium(II) also strengthens the ligand field of the former. The strong ligand field of iridium(III) complexes leads to less accessible dissociative ^3MC states and higher photostabilities compared to ruthenium(II) complexes. The lower accessibility of the ^3MC states also reduces radiationless deactivation into the ground state. Thus, solution quantum yields of iridium(III) complexes are generally higher than those of comparable ruthenium(II) complexes.^[140] For example, the use of neutral *fac*- $\text{Ir}(\text{ppy})_3$ (**58**, Figure 28) as emitter in OLEDs can be explained by its high room temperature solution quantum yield of $\Phi = 97\%$ ($\text{ppy} = 2\text{-phenylpyridine}$).^[159] Furthermore, iridium(III) complexes of the $[\text{Ir}(\text{ppy})_2(\text{bpy})]^+$ type have spatially separated frontier orbitals with the HOMO residing on the cyclometalated ppy ligands and the LUMO on the bpy ligand. This offers the possibility to separately fine tune HOMO and LUMO energies by simple ligand modifications and has lead to iridium(III) complexes with emission maxima in the entire visible spectrum.^[140] However, iridium is rare and expensive. The amount of iridium in the earth crust is around 1 ppb and the current price for 1 g iridium (99.9%) is around 70 €.

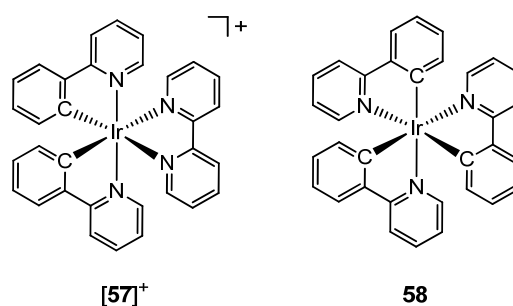


Figure 28. Iridium(III) complexes **[57]⁺** and **58** for light-emitting devices.

9 Publications and Manuscripts

9.1 Contribution of Aaron Breivogel to the Following Manuscripts and Publications

Prior to reproduction of the manuscripts and publications of my doctoral thesis I hereby clarify which contributions stem from other collaborators and which contributions stem from my own work. My contributions will be indicated by the initials "AB". Compounds mentioned herein refer to the compound numbering in the respective manuscript or publication.

Thermal and Photo Reactivity of a Donor-Acceptor-Substituted Bis(terpyridine) Ruthenium(III) Complex in Acidic Solutions: all ligand and complex syntheses, all spectroscopic and analytical measurements (NMR, MS, UV/Vis, EPR) and all DFT calculations were conducted by AB. EPR simulations were performed by Anica Wünsche von Leupoldt (group of Prof. Dr. Katja Heinze). The manuscript was written by AB.

Dinuclear Bis(terpyridine)ruthenium(II) Complexes by Amide Coupling of Ruthenium Amino Acids: Synthesis and Properties: the ruthenium complexes **1a** and **1b** were synthesized by AB and Dr. Klaus Hempel (group of Prof. Dr. Katja Heinze). Ruthenium complexes **2a**, **2b**, **2c**, **3a** and **3b** were synthesized and spectroscopically and analytically characterized by Dr. Klaus Hempel (group of Prof. Dr. Katja Heinze). All oxidation reactions (including UV/Vis spectroscopic measurements) and all DFT calculations were performed by AB. The manuscript was written by Prof. Dr. Katja Heinze.

Light-induced Charge Separation in a Donor-Chromophore-Acceptor Nanocomposite Poly[TPA-Ru(tpy)₂]@ZnO: the ruthenium complex **A** was synthesized and spectroscopically and analytically characterized by AB. Polymer syntheses and characterizations were conducted by Dr. Lisa zur Borg (group of Prof. Dr. Rudolf Zentel). Emission spectroscopy and quantum yield determinations were done by AB and Dr. Lisa zur Borg. KPFM measurements were conducted by Anna Domanski (group of Dr. Rüdiger Berger). The manuscript was written by Dr. Lisa zur Borg (~ 60%), Anna Domanski (~ 20%) and AB (~ 20%).

A Heteroleptic Bis(tridentate)ruthenium(II) Polypyridine Complex with Improved Photophysical Properties and Integrated Functionalizability: all novel compounds were synthesized and spectroscopically and analytically characterized by AB. All DFT calculations were conducted by AB. The crystal structure was solved by Dr. Christoph Förster (group of Prof. Dr. Katja Heinze). The

emission lifetimes were measured by Dr. Michael Meister (group of Dr. Frédéric Laquai). The manuscript was written by AB.

Excited State Tuning of Bis(tridentate) Ruthenium(II) Polypyridine Chromophores by Push-Pull Effects and Bite Angle Optimization: A Comprehensive Experimental and Theoretical Study: all novel compounds were synthesized and spectroscopically and analytically characterized by AB. The crystal structures were solved by Dr. Christoph Förster (group of Prof. Dr. Katja Heinze). The emission lifetimes were measured by Dr. Michael Meister and Julian Ochsmann (group of Dr. Frédéric Laquai). EPR simulations were performed by Anica Wünsche von Leupoldt (group of Prof. Dr. Katja Heinze). All DFT calculations were conducted by AB. The manuscript was written by AB.

Push-Pull Design of Bis(tridentate) Ruthenium(II) Polypyridine Chromophores as Deep Red Light Emitters in Light-Emitting Electrochemical Cells: all ruthenium complexes were synthesized by AB. After instruction from Myeongjin Park, Dongu Lee (both from the group of Prof. Dr. Changhee Lee) and Prof. Dr. Kookheon Char the LECs were built and characterized by AB. AFM measurements were performed by Stefanie Klassen (group of Prof. Dr. Angelika Kühnle). All DFT calculations were conducted by AB. The manuscript was written by AB.

Anchor-Functionalized Push-Pull-Substituted Bis(tridentate) Ruthenium(II) Polypyridine Chromophores: Photostability and Evaluation as Photosensitizers: complexes $[1]^{2+}$ – $[4]^{2+}$ were synthesized and spectroscopically and analytically characterized by AB. Complexes $[5]^{2+}$ and $[6]^{2+}$ were synthesized and spectroscopically and analytically characterized by Jan Dietrich (group of Prof. Dr. Katja Heinze). All photostability tests of the complexes were performed by AB. After instruction from Sanghyuk Wooh (group of Prof. Dr. Kookheon Char) and Prof. Dr. Kookheon Char the DSSCs were built and characterized by AB. The electron recombination lifetimes were measured by Tea Yon Kim (group of Prof. Dr. Yong Soo Kang). All DFT calculations were conducted by AB. The manuscript was written by AB.

9.2 Thermal and Photo Reactivity of a Donor-Acceptor-Substituted Bis(terpyridine) Ruthenium(III) Complex in Acidic Solutions

A. Breivogel, K. Heinze.

-to be submitted-

Thermal and Photo Reactivity of a Donor-Acceptor-Substituted Bis(terpyridine) Ruthenium(III) Complex in Acidic Solutions

Aaron Breivogel, and Katja Heinze*

Introduction

Polypyridine complexes of ruthenium(II) feature outstanding optical and electrochemical properties^[1] and are applied in a manifold of research fields: as sensitizers in dye-sensitized solar cells (DSSCs),^[2–5] phosphors in light-emitting electrochemical cells (LECs),^[6–9] molecular catalysts for water oxidation,^[10,11] hydrogen generation^[12–15] and CO₂ reduction^[12,14,16] and molecular mixed valence compounds.^[17–22] Many complexes possess mono and bidentate ligands such as NCS[−], pyridine and bpy (bpy = 2,2'-bipyridine). The use of these mono and bidentate ligands renders the complexes prone to thermal and photo induced isomerization and ligand exchange reactions leading to undesired side products.^[23–30]

Bis(tridentate) ruthenium(II) complexes are known for their high chemical and photochemical stability which is a consequence of the bis(tridentate) chelate effect.^[3,5,31–35] [Ru(tpy)₂]²⁺ is the prototype of bis(tridentate) ruthenium(II) complexes (tpy = 2,2';6',2''-terpyridine). However, poor photophysical properties prevent its use in optoelectronic applications. Excited ³MLCT states are efficiently depopulated via low lying ³MC states which leads to radiationless deactivation into the ground state ($\tau \approx 0.1 - 0.2$ ns, $\Phi \leq 0.0007\%$ ^[36], MLCT = metal-to-ligand charge transfer, MC = metal-centered).^[37–39] Electron withdrawing substituents on the 4'-position of the tpy ligand lower the energy of the ³MLCT state compared to ³MC state which is beneficial for the excited state properties. Exemplarily, 4'-ester-substituted [(EtOOC-tpy)Ru(tpy)]²⁺ features a ³MLCT lifetime of $\tau = 32$ ns and a quantum yield of $\Phi = 0.041\%$ ^[36].^[8] Addition of an electron donating substituent on the 4'-position of the unsubstituted tpy, e.g. [(EtOOC-tpy)Ru(tpy-NH₂)]²⁺ (**[1^{Et}]**²⁺, Figure 1) further enhances the lifetime ($\tau = 34$ ns) and the quantum yield ($\Phi = 0.27\%$ ^[36]).^[40,41] Such a push-pull strategy is also applied in the combination of an electron accepting tpy ligand and a strong electron donating carbene ligand leading to unprecedented emission lifetimes of up to $\tau = 7.9$ μ s and quantum yields of up to $\Phi = 17.3\%$ ^[36].^[42] ³MC state energies can also be shifted to higher values by using ligands with $\approx 90^\circ$ bite angles which allow for a better overlap between metal d orbitals and the pyridine lone pairs.^[43–47] **[1^{Et}]**²⁺ has been shown to be highly photostable under conditions where tris(bidentate) [Ru(bpy)₃]²⁺ undergoes photoaquation and photoanation.^[5] The pronounced push-pull character of **[1^{Et}]**²⁺ reduces the HOMO-LUMO gap and shifts the absorption to lower energy compared to unsubstituted [Ru(tpy)₂]²⁺ ($\lambda_{\text{max}} = 476$ ^[39] \rightarrow 502 nm^[40]). **[1^{Et}]**²⁺ and similar complexes have been used as emitters in LECs and to the best of our knowledge show the lowest emission energy for bis(tridentate)ruthenium(II) emitters in LECs.^[9] **[1^{Et}]**²⁺ has also been incorporated in energy and electron transfer systems and shows light-induced charge separation in a donor-chromophore-acceptor nanocomposite.^[16,48–50] **[1^{Et}]**²⁺ can be hydrolyzed to obtain the carboxylic acid **[1]**²⁺ (Figure 1).^[40] The carboxylic acid functionality can act as anchor to oxidic semiconductors (e.g. TiO₂) and **[1]**²⁺ has been tested as photosensitizer in DSSCs.^[5] A dinuclear analogue of **[1]**²⁺ has been used to study mixed valency in redox asymmetric compounds. However, no electronic communication between Ru^{II} and Ru^{III} has been observed in the mixed valence species.^[21,51]

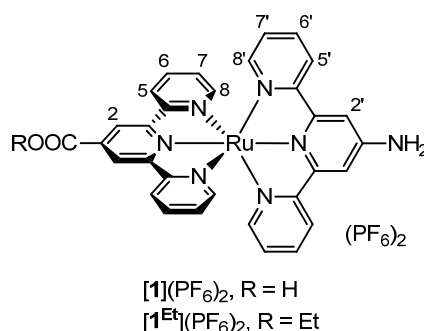


Figure 1. Bis(terpyridine)ruthenium(II) amino acid **[1]**(PF₆)₂ and its ester **[1^{Et}]**(PF₆)₂. Atom numbering for NMR assignments.

The oxidation of **[1]**²⁺ to **[1]**³⁺ is ruthenium-centered and has been reported previously.^[21,43] The stability of oxidized state is particularly important for molecular ruthenium water oxidation catalysts (WOCs) which feature high metal oxidation states during the catalytic cycle.^[52] Two main degradation pathways have been reported for molecular ruthenium WOCs: 1) Oxidative ligand degradation^[53,54] and the formation of CO and CO₂ as

decomposition products of $[\text{Ru}(\text{bpy})_3]^{3+}$ and other ruthenium complexes.^[52,55,56] 2) Ligand loss: monodentate ligands such as 4-picoline and isoquinoline are prone to ligand dissociation.^[55,57] Even bidentate bpy is oxidized to 2,2'-bipyridine-*N,N*-dioxide from $[\text{Ru}(\text{tpy})(\text{bpy})(\text{OH}_2)]^{2+}$ under catalytic conditions while no dissociation or degradation was observed for the tridentate tpy ligand.^[54,56] This indicates that the chelate effect can significantly enhance stabilities of WOCs.^[54,57]

Our work aims at maximizing the chelate effect in polypyridine complexes of ruthenium and describes the stability of the bis(tridentate) ruthenium(III) complex $[\mathbf{1}]^{3+}$. The $[\mathbf{1}^{\text{Et}}]^{2+/3+}$ couple is stable in the presence of potentially coordinating OH^- ions. However, a different reactivity is observed at low pH (in trifluoroacetic acid, H_2SO_4 and HNO_3) often in conjunction with the oxidant Ce^{IV} . After oxidation of $[\mathbf{1}]^{2+}$ to $[\mathbf{1}]^{3+}$ in acidic media an unexpected back reduction to $[\mathbf{1}]^{2+}$ is observed and described herein by means of UV/Vis, NMR and ESR spectroscopy, electrochemistry, mass spectrometry and DFT calculations.

Discussion

The ruthenium(II) complex $[\mathbf{1}](\text{PF}_6)_2$ (Figure 1) can be oxidized with $(\text{NH}_4)_2[\text{Ce}(\text{NO}_3)_6]$ in 0.5 M trifluoroacetic acid in CH_3CN .^[21] Upon oxidation the MLCT band at $\lambda_{\text{max}} \approx 500$ nm disappears and a LMCT band at $\lambda_{\text{max}} \approx 750$ nm appears with a concomitant color change from orange to green.^[21] Figure 2 compares experimental UV/Vis spectra of $[\mathbf{1}]^{2+}$ and $[\mathbf{1}]^{3+}$ in 0.125 M H_2SO_4 in H_2O with calculated stick spectra (TD-DFT, IEFPCM, H_2O). The experimental spectrum of $[\mathbf{1}]^{2+}$ features a characteristic MLCT band at $\lambda = 499$ nm ($\epsilon = 17170 \text{ M}^{-1} \text{ cm}^{-1}$). Similarly, when oxidized with $\text{Ce}(\text{SO}_4)_2$ in 0.125 M H_2SO_4 in H_2O the MLCT band disappears and a LMCT band at $\lambda = 751$ nm ($\epsilon = 6830 \text{ M}^{-1} \text{ cm}^{-1}$) appears.

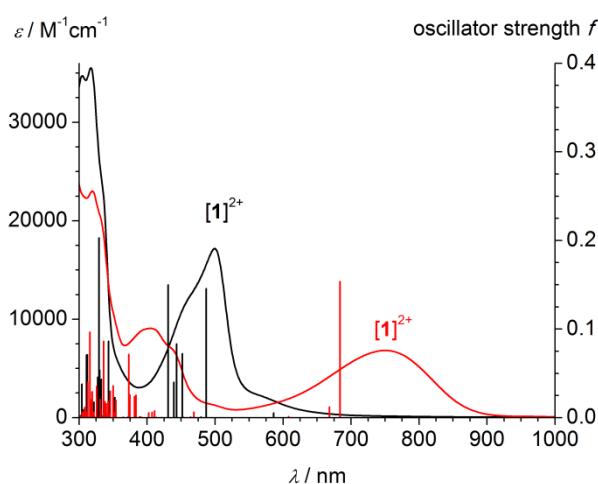


Figure 2. Experimental UV/Vis spectra of $[\mathbf{1}](\text{PF}_6)_2$ before (black) and directly after addition of $\text{Ce}(\text{SO}_4)_2$ (red) in 0.125 M H_2SO_4 in H_2O and calculated stick spectra (TD-DFT, B3LYP/LANL2DZ, IEFPCM, H_2O) of $[\mathbf{1}]^{2+}$ (black) and $[\mathbf{1}]^{3+}$ (red). For experimental details see *Oxidation 1* in the Experimental Section.

The experimental MLCT band of $[\mathbf{1}]^{2+}$ is nicely reproduced by the TD-DFT calculated stick spectrum with transitions at $\lambda = 487$ ($f = 0.1455$), 452 ($f = 0.0721$), 443 ($f = 0.0831$), 439 ($f = 0.0399$) and 431 nm ($f = 0.1498$). These transitions originate from ruthenium-centered orbitals HOMO to HOMO-2 corresponding to t_{2g} orbitals in O_h symmetry into ligand-centered orbitals LUMO to LUMO+3 residing on both tpy ligands (Figure S1 in the Supporting Information). The “ e_g ” orbitals LUMO+9 and LUMO+13 are found at higher energy. In contrast, the calculated stick spectrum of $[\mathbf{1}]^{3+}$ lacks transitions between $\lambda = 400$ and 650 nm with oscillator strengths $f \geq 0.01$. Instead, transitions are predicted at $\lambda = 684$ ($f = 0.1535$) and 668 nm ($f = 0.0118$). These transitions have predominantly LMCT character with the largest contribution stemming from the transition of molecular orbital 141 β into 144 β (Figure 3). Electron density is mainly shifted from the amino-substituted tpy ligand to the ruthenium(III) center. For more detailed results of the TD-DFT calculations of $[\mathbf{1}]^{2+}$ and $[\mathbf{1}]^{3+}$ see Figures S1 and S2 in the Supporting Information.

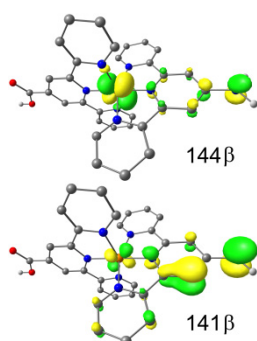


Figure 3. Relevant DFT-calculated Kohn-Sham frontier molecular orbitals of $[1]^{3+}$ (B3LYP/LANL2DZ, IEFPCM, H_2O , contour value 0.06 a. u., CH hydrogen atoms omitted).

The EPR spectrum of $[1]^{3+}$ (Figure 4) in 0.5 M trifluoroacetic acid in H_2O at 77 K is very similar to the one of its ester derivative $[1^{Et}]^{3+}$ which has already been reported.^[16] It shows a rhombic signal ($g_{1,2,3} = 2.323, 2.175, 1.865$; $\Delta g = 0.458$ by spectral simulation) and reveals that the oxidation is mainly located at the ruthenium center which is in full accordance with similar complexes of Ru^{III} .^[16,43]

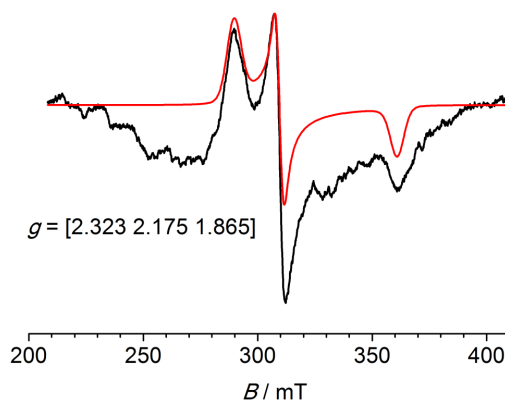


Figure 4. X-band EPR spectrum of $[1]^{3+}$ in 0.5 M trifluoroacetic acid in H_2O at 77 K. Black: experimental spectrum; red: simulation. For experimental details see *Oxidation 2* in the Experimental Section.

The DFT calculated spin density of the ruthenium(III) complex $[1]^{3+}$ is located at the ruthenium center with a smaller contribution at the amino nitrogen atom (Figure 5). The Mulliken spin densities on Ru and on the amino nitrogen atom are calculated as 0.76 and 0.11, respectively. Thus, DFT calculations substantiate the experimental finding of a largely ruthenium-centered oxidation.

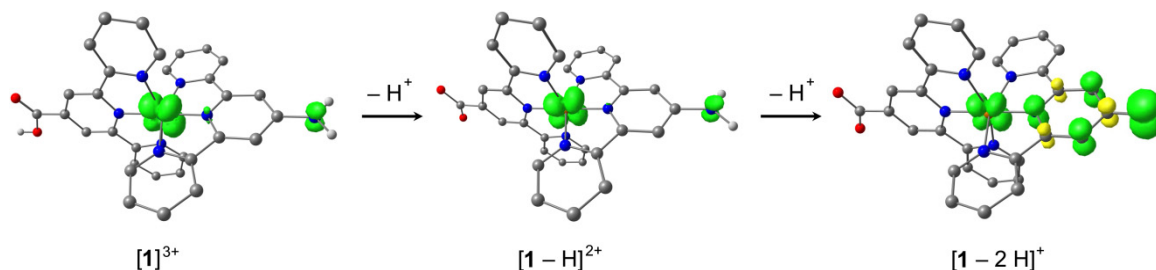


Figure 5. DFT-calculated spin density of ruthenium(III) complexes $[1]^{3+}$, $[1 - H]^{2+}$ and $[1 - 2 H]^+$ (B3LYP/LANL2DZ, IEFPCM, H_2O , contour value 0.01, CH hydrogen atoms omitted).

$[1](PF_6)_2$ is water soluble in the presence of NO_3^- ions enabling pH-dependent measurements. The Pourbaix diagram of $[1](PF_6)_2$ shows the redox potential $E_{1/2}$ of the Ru^{II}/Ru^{III} couple at different pH values (Figure 6) starting with 0.5 M HNO_3 in H_2O and stepwise titration with saturated aqueous NaOH. At pH = 0 – 1.6 the redox potential amounts to $E_{1/2} = 0.79$ V. Between pH 1.6 and 2.7 the redox potential drops which is due to deprotonation of the carboxylic acid group ($pK_a = 2.7$).^[40] For a proton-coupled electron transfer the expected

slope of the redox potential is given by $-(m/n) \times 59$ mV per pH unit (m = number of transferred protons, n = number of transferred electrons).^[52] The experimental slope amounts to approximately 46 ± 10 mV per pH unit suggesting that the electron transfer is indeed coupled to proton transfer in this pH region. The drop of the redox potential between pH 1.6 and 2.7 is rationalized by the fact that the deprotonated carboxylate group is a stronger electron donor than the protonated carboxyl group. Thus, the former can be oxidized at lower potential. From pH 2.7 – 9.5 the redox potential features a plateau with $E_{1/2} = 0.74$ V. At pH > 10 the redox potential again drops due to deprotonation of the amino group which is converted into an even stronger electron donor by deprotonation.^[40] Oxidation is reversible at pH < 10 and irreversible at pH > 10. Similar to $[1]^{3+}$ for one-fold deprotonated $[1-H]^{2+}$ Mulliken spin densities on Ru and the amino nitrogen atom amount to 0.78 and 0.10, respectively (Figure 5). Thus, when $[1]^{3+}$ is deprotonated at the carboxylic acid group the oxidation remains ruthenium-centered and reversible. However, the second deprotonation takes place at the amino group. The resulting species $[1-2H]^+$ features Mulliken spin densities on Ru and the amino nitrogen atom of 0.36 and 0.51, respectively (Figure 5). Thus, oxidation takes place at the deprotonated amino group which induces the irreversibility of the oxidation. In summary, at pH < 10 $[1]^{2+}$ is reversibly oxidized at the ruthenium center while at pH > 10 the amino group is irreversibly oxidized.

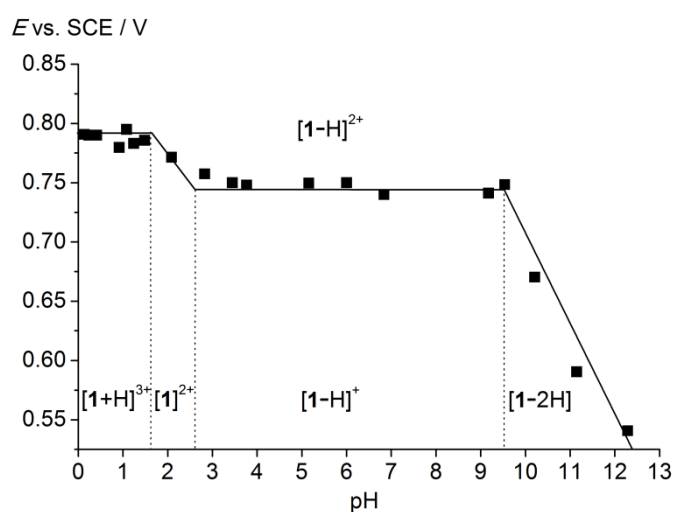


Figure 6. Pourbaix diagram of $[1](PF_6)_2$ in 0.5 M HNO_3 in H_2O and stepwise titration with saturated aqueous NaOH. E (vs. SCE) $- 0.16 \approx E$ (vs. FcH/FcH^+).^[58]

The ruthenium(III) complex $[1]^{3+}$ is stable for at least several minutes or hours in 0.5 M trifluoroacetic acid. The slow decay/back reduction of $[1]^{3+}$ can be followed by monitoring the decrease of the LMCT band. $[1](PF_6)_2$ was oxidized in 0.125 M H_2SO_4 in H_2O with $Ce(SO_4)_2 \cdot 4 H_2O$ as oxidant. Figure 7a shows solution UV/Vis spectra of $[1](PF_6)_2$ before and after the addition of 1.1 equiv $Ce(SO_4)_2$ in 0.125 M H_2SO_4 in H_2O . For experimental details see *Oxidation 1* in the Experimental Section. The MLCT band of $[1](PF_6)_2$ at $\lambda = 499$ nm ($\epsilon = 17170$ $M^{-1} cm^{-1}$) immediately disappears upon addition of 1.1 equiv $Ce(SO_4)_2$. $[1]^{3+}$ features a LMCT band at $\lambda = 751$ nm ($\epsilon = 6830$ $M^{-1} cm^{-1}$). Upon standing the UV/Vis spectra of the solution change. After seven days the MLCT band is largely recovered ($\epsilon = 15850$ $M^{-1} cm^{-1}$ at $\lambda = 499$ nm $\pm 92\%$ recovery) and the LMCT band essentially disappeared. Isosbestic points at $\lambda = 585$, 432 and 342 nm clearly indicate the recovery of $[1]^{2+}$ by conversion from $[1]^{3+}$. Possible side products seem to be optically transparent in the observed spectral region. The addition of another 1.1 equiv $Ce(SO_4)_2$ again leads to the same color change with disappearance of the MLCT band and appearance of the LMCT band at $\lambda = 751$ nm ($\epsilon = 6250$ $M^{-1} cm^{-1}$). The UV/Vis spectrum changes in the same manner as before. After four days the MLCT band is again largely recovered ($\epsilon = 13500$ $M^{-1} cm^{-1}$ at $\lambda = 499$ nm $\pm 85\%$ recovery with respect to the extinction coefficient before the second addition of $Ce(SO_4)_2$) and the LMCT band has nearly vanished (Figure 7b). The same isosbestic points are observed at $\lambda = 583$, 433 and 342 nm.

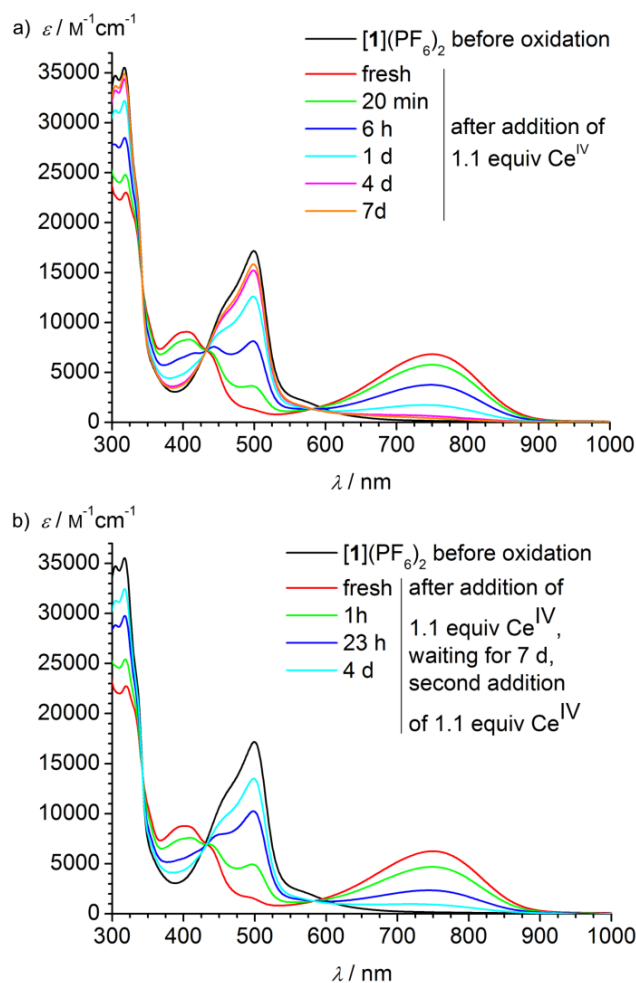


Figure 7. UV/Vis spectra of $[1](PF_6)_2$ before and after oxidation with a) 1.1 and b) 2.2 equiv $Ce(SO_4)_2$ in 0.125 M H_2SO_4 in H_2O . For experimental details see *Oxidation 1* in the Experimental Section.

$[1](PF_6)_2$ can also be oxidized in 0.125 M H_2SO_4 in $H_2O:CH_3CN$ (1:1) with $(NH_4)_2[Ce(NO_3)_6]$ as oxidant showing the same spectral behavior as in *Oxidation 1* (see *Oxidation 3* in the Experimental Section).

An excess of $Ce(SO_4)_2$ (20 equiv) was added to a solution of $[1](PF_6)_2$ (*Oxidation 4*) in 0.125 M H_2SO_4 in H_2O . The orange solution of $[1](PF_6)_2$ immediately turned green upon addition of the Ce^{IV} salt. After 1 day the solution had a yellow color. UV/Vis spectra revealed that no absorption band above $\lambda = 400$ nm was present. No ruthenium complex could be detected in an ESI mass spectrum. Thus, complete degradation seems to have occurred under these conditions.

$[1](PF_6)_2$ was oxidized in 0.5 M trifluoroacetic acid in $CH_3CN:H_2O$ (49:1) in an OTTLE cell (see *Oxidation 5* in the Experimental Section). Upon oxidation of $[1]^{2+}$ the intensity of the MLCT band is lowered (Figure 8a, $\epsilon = 19300 \rightarrow 11900 \text{ M}^{-1} \text{ cm}^{-1}$ at $\lambda_{\text{max}} = 499 \text{ nm}$). Applying higher potentials does not lead to a further decrease of the MLCT band due to diffusion in the OTTLE cell solution. The LMCT band of $[1]^{3+}$ appears at $\lambda_{\text{max}} = 733 \text{ nm}$ ($\epsilon = 2620 \text{ M}^{-1} \text{ cm}^{-1}$). During the oxidation isosbestic points are observed at $\lambda = 554, 428, 340, 292, 282, 269, 241$ and 231 nm . Upon back reduction new isosbestic points appear at $\lambda = 606, 430, 342, 292, 283, 271, 242$ and 219 nm (Figure 8a). After reaching the initial potential the MLCT band is not fully recovered ($\epsilon = 17600 \text{ M}^{-1} \text{ cm}^{-1}$ at $\lambda_{\text{max}} = 499 \text{ nm}$, 91% recovery) even when the potential is further decreased. A new shoulder is observed at $\lambda = 572 \text{ nm}$ ($\epsilon = 2540 \text{ M}^{-1} \text{ cm}^{-1}$). The appearance of this shoulder might be due to reduction of an intermediate species that is not reduced under the conditions with $Ce(VI)$ as oxidant. These results are at odds with the high redox stability of the corresponding ester $[1^{Et}](PF_6)_2$ in the presence of OH^- reported by our group.^[5] However, the redox stability of $[1^{Et}](PF_6)_2$ was measured under basic conditions while here 0.5 M trifluoroacetic acid was used. Thus, the strong acidic conditions seem to be responsible for the redox instability of the $[1]^{3+}$ complex.

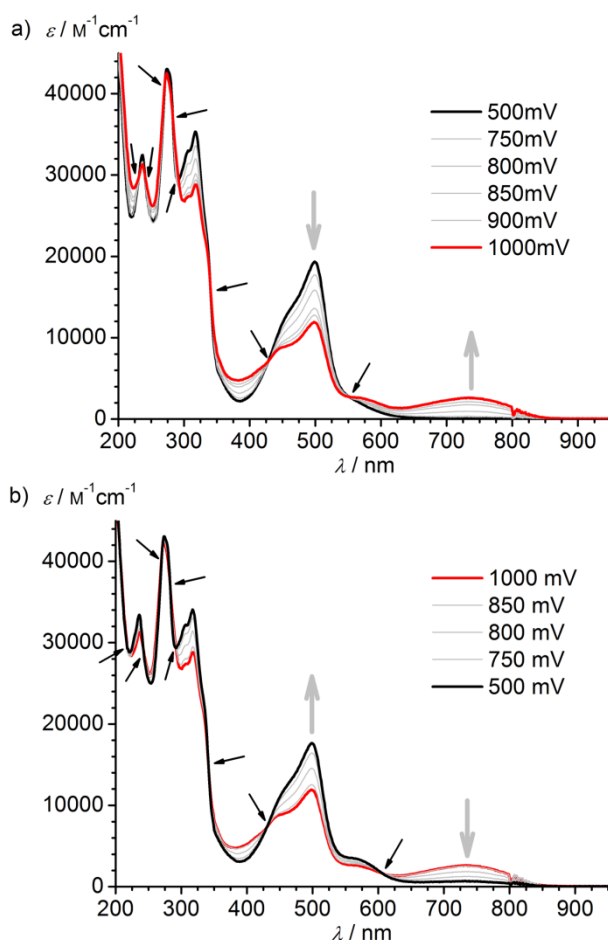


Figure 8. UV/Vis spectra during a) the electrochemical oxidation (500 \rightarrow 1000 mV) and b) back reduction (1000 \rightarrow 500 mV) of $[\mathbf{1}](\text{PF}_6)_2$ in an OTTLE cell in 0.5 M trifluoroacetic acid in $\text{CH}_3\text{CN}:\text{H}_2\text{O}$ (49:1). Black arrows indicate isosbestic points.

In an NMR experiment $[\mathbf{1}](\text{PF}_6)_2$ was oxidized with 2.0 equiv $(\text{NH}_4)_2[\text{Ce}(\text{NO}_3)_6]$ in 0.5 M trifluoroacetic acid in CH_3CN . Immediately after the addition of $(\text{NH}_4)_2[\text{Ce}(\text{NO}_3)_6]$ and the concomitant color change from orange to green the solvent was removed under reduced pressure and D_2O was added. For experimental details see *Oxidation 6* in the Experimental Section. ^1H -NMR spectra were recorded at selected time intervals after the oxidation (Figure 9). In the fresh D_2O solution no sharp resonances could be obtained in the ^1H -NMR spectrum due to the paramagnetic nature of $[\mathbf{1}]^{3+}$. Within 13 d resonances appear fitting excellently to pure $[\mathbf{1}]^{2+}$ in D_2O . Resonances for the NH_2 group are not observed due to deuteration to ND_2 . The self-exchange reaction $[\mathbf{1}]^{2+} + [\mathbf{1}]^{3+} \rightleftharpoons [\mathbf{1}]^{3+} + [\mathbf{1}]^{2+}$ is expected to be fast and leads to averaged NMR resonances in the spectra after 17 h to 13 d (Figure 9). No hint for new signals could be detected at $\delta < 6.5$ ppm within the sensitivity of the ^1H NMR experiments.

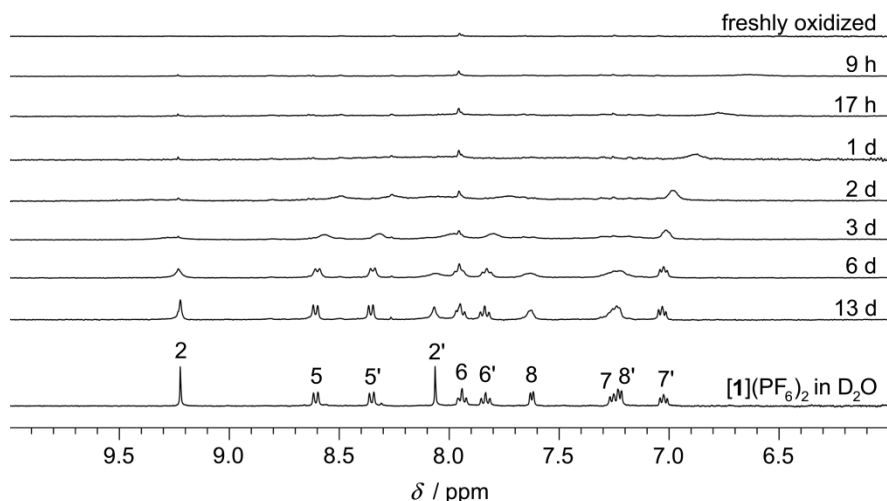
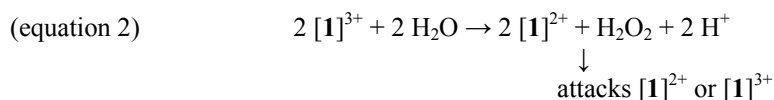
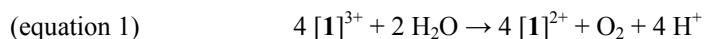


Figure 9. ^1H -NMR spectra of $[\mathbf{1}](\text{PF}_6)_2$ in D_2O after oxidation with 2.0 equiv $(\text{NH}_4)_2[\text{Ce}(\text{NO}_3)_6]$ (freshly oxidized to 13 days after oxidation). The ^1H -NMR spectrum of pure $[\mathbf{1}](\text{PF}_6)_2$ in D_2O is shown at the bottom for comparison. For experimental details see *Oxidation 6* in the Experimental Section.

After 13 days an ESI mass spectrum of the D_2O solution was recorded and showed signals with isotope distributions excellently fitting to the theoretical values for threefold deuterated $[\mathbf{1}]^{2+}$ at $m/z = 315.1$ (100%) $[M - 2 \text{PF}_6]^{2+}$, 628.1 (8%) $[M - 2 \text{PF}_6 - \text{D}]^+$ and 775.1 (70%) $[M - \text{PF}_6]^{2+}$ where M is $[(\text{DOOC-tpy})\text{Ru}(\text{tpy-ND}_2)](\text{PF}_6)_2$ (Figure 10). A signal at $m/z = 606.1$ (4%) with ruthenium isotope pattern was additionally found in the mass spectrum. This signal does not appear in the mass spectrum of neat $[\mathbf{1}](\text{PF}_6)_2$ in D_2O . So far this signal could not be assigned to a structure. In summary, the nearly quantitative reformation of $[\mathbf{1}]^{2+}$ by conversion from $[\mathbf{1}]^{3+}$ could be shown by UV/Vis, NMR and mass spectra. The question arises which reducing agent is responsible for the reduction of $[\mathbf{1}]^{3+}$. $[\text{Ru}(\text{bpy})_3]^{3+}$ and other ruthenium polypyridine complexes are reported to oxidize water to O_2 .^[10,11,59] However, the exact mechanism for the reduction of $[\text{Ru}(\text{bpy})_3]^{3+}$ to $[\text{Ru}(\text{bpy})_3]^{2+}$ is still under debate. The attack of a H_2O or OH^- molecule to the ruthenium(III) center to form a seven-coordinate species has been proposed to be the initial reaction for water oxidation.^[59] Ghosh et al. support the attack of water on a bpy ligand with further degradation of the ligand to CO_2 . The thereby generated electrons enable 92 – 95% of $[\text{Ru}(\text{bpy})_3]^{3+}$ to be reduced thermally or photochemically to $[\text{Ru}(\text{bpy})_3]^{2+}$.^[56] In the presence of colloidal RuO_2 or Co^{2+} ions $[\text{Ru}(\text{bpy})_3]^{3+}$ efficiently catalyses the photo-oxidation of H_2O to O_2 .^[60] $[\text{Ru}(\text{tpy})(\text{bpy})(\text{H}_2\text{O})]^{2+}$ and $[\text{Ru}(\text{tpy})(\text{py})_2(\text{H}_2\text{O})]^{2+}$ are efficient WOCs and already contain a water molecule in the octahedral coordination sphere (py = pyridine).^[61,62] Other ruthenium polypyridine catalysts expand their coordination sphere to a heptacoordinate pentagonal bipyramid in order to bind a water molecule to the metal.^[63–65] $[\text{Ru}(\text{tpy})_2]^{2+}$ is unable to adopt a heptacoordinate pentagonal bipyramid with a water molecule because no linear arrangement of the axial N-Ru-N bonds can be formed as is the case for bis(tridentate) complexes of ruthenium(II) with expanded ligands. This is regarded to be the reason why $[\text{Ru}(\text{tpy})_2]^{2+}$ does not catalyze water oxidation and might also be applicable for $[\mathbf{1}]^{2+}$.^[62] H_2O as reducing agent would lead to the formation of H_2O_2 , O_2^- or O_2 . The formal equations for O_2 and H_2O_2 formation are:



Oxidation of $[\mathbf{1}]^{2+}$ to $[\mathbf{1}]^{3+}$ and back reduction to $[\mathbf{1}]^{2+}$ was conducted in closed reaction vessels and the gas phases above the reaction solutions were tested for O_2 via two methods: The gas phase was bubbled slowly through a solution of $\text{IrCl}(\text{PET}_3)_3$ in d_8 -THF. $\text{Ir}(\text{O}_2)(\text{PET}_3)_3\text{Cl}$ should be formed in the presence of O_2 which was monitored by ^{31}P -NMR spectroscopy.^[66] The second method is based on a ZrO_2 -based oxygen sensor which measures the concentration of O_2 in the gas phase. Both methods reveal that no O_2 is produced during the reformation of $[\mathbf{1}]^{2+}$ from $[\mathbf{1}]^{3+}$ (*Oxidations 7 and 8*). H_2O_2 as possible intermediate in the oxidation of H_2O to O_2 is metastable in acidic solution with respect to disproportionation into H_2O to O_2 . A solution of $[\mathbf{1}](\text{PF}_6)_2$ ($1.2 \times 10^{-4} \text{ M}$) in 35% H_2O_2 in water is stable for at least 3 h (no changes in the UV/Vis spectra over time, stable MLCT band at 493 nm). However, in the presence of acid (0.1 M TFA) the ruthenium complex decomposes

within 3 h which can be seen by the absence of any UV/Vis signal above 400 nm. The theoretical maximum amount of H_2O_2 would be half the amount of $[\mathbf{1}]^{3+}$ according to equation 2. It is yet unclear whether H_2O_2 is produced during the reaction and which reaction products result from the reaction of H_2O_2 with $[\mathbf{1}]^{2+}$ or $[\mathbf{1}]^{3+}$. If H_2O_2 is produced quantitatively (0.50 equiv compared to 1.00 equiv of $[\mathbf{1}]^{2+}$), then less than 0.12 equiv (of 1.00 equiv) of $[\mathbf{1}]^{2+}$ are destroyed by 0.50 equiv of H_2O_2 (calculated from the observed 88% recovery of the MLCT band).

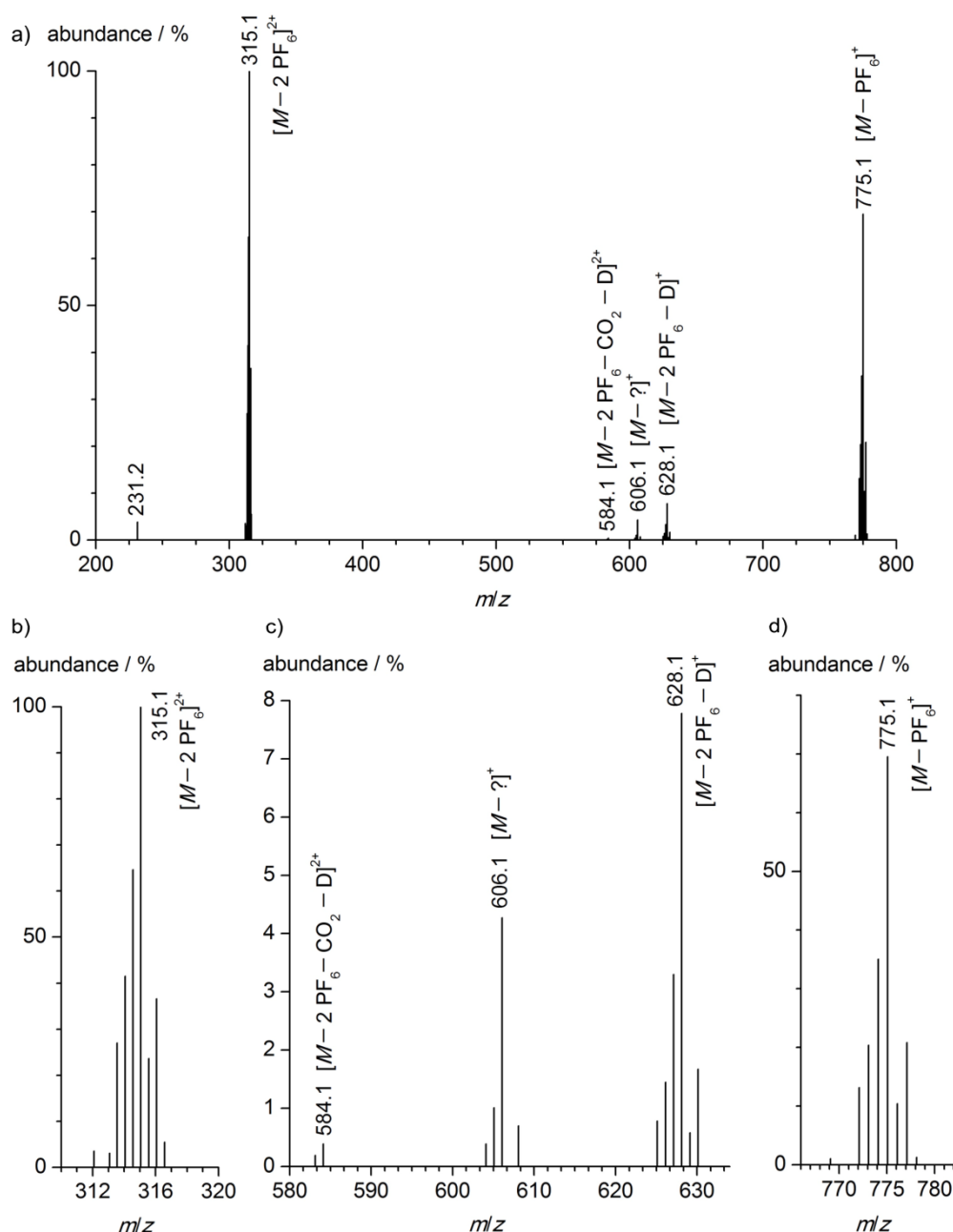


Figure 10. a) ESI⁺ mass spectrum of $[\mathbf{1}](\text{PF}_6)_2$ in D_2O 13 days after oxidation with 2.0 equiv $(\text{NH}_4)_2[\text{Ce}(\text{NO}_3)_6]$ in 0.5 M trifluoroacetic acid in CH_3CN (See *Oxidation 6* for experimental details). b) c) and d) show the respective signals with ruthenium isotope pattern. $M = [(\text{DOOC-tpy})\text{Ru}(\text{tpy-ND}_2)](\text{PF}_6)_2$.

Further experiments are necessary to clarify whether H_2O_2 is indeed formed intermediately and subsequently consumed e.g. by oxygenation of a ligand to *N*-oxides or if other electron sources are responsible for the reduction of $[\mathbf{1}]^{3+}$. For example a small part of the oxidized complex $[\mathbf{1}]^{3+}$ could decompose and generate enough electrons to reduce the majority of $[\mathbf{1}]^{3+}$ according to equation 3.

$$\text{(equation 3)} \quad n [\mathbf{1}]^{3+} + [\mathbf{1}]^{3+} \rightarrow n [\mathbf{1}]^{2+} + \text{decomposition products}$$

We tried to optimize a heptacoordinate species with one H₂O molecule coordinated to the ruthenium center of $[\mathbf{1}]^{3+}$ via DFT calculations. However, no energy minimum was found for a heptacoordinate species. Instead, only the hexacoordinate complexes " $[\text{Ru}(\kappa^3\text{-H}_2\text{N-tpy})(\kappa^3\text{-HOOC-tpy})]^{3+} + \text{H}_2\text{O}$ " and " $[\text{Ru}(\kappa^2\text{-H}_2\text{N-tpy})(\kappa^3\text{-HOOC-tpy})(\text{H}_2\text{O})]^{3+}$ " lead to energy minima in the DFT calculations (Figure 11). In the latter the amino substituted ligand coordinates to ruthenium(III) in a bidentate κ^2 -fashion via two pyridine nitrogen atoms while one outer pyridine nitrogen atom is involved in a hydrogen bond with a proton from the H₂O molecule. Indeed, the pyridine is protonated and the H₂O molecule deprotonated to OH⁻, a well known phenomenon of H₂O ligands coordinated to metal centers with high oxidation states.^[10,11] The bond length between the central pyridine nitrogen atom of the $\kappa^2\text{-H}_2\text{N-tpy}$ ligand and the ruthenium atom is increased (2.20 Å) compared to the bis(tridentate) complex (1.97 Å). The N-C-C-N dihedral angles of the $\kappa^2\text{-H}_2\text{N-tpy}$ ligand amount to 13° and 48°, respectively. In contrast the N-C-C-N dihedral angles of the $\kappa^3\text{-HOOC-tpy}$ ligand amount to $\approx 0^\circ$, similar to the bis(tridentate) complex " $[\text{Ru}(\kappa^3\text{-H}_2\text{N-tpy})(\kappa^3\text{-HOOC-tpy})]^{3+} + \text{H}_2\text{O}$ " where the dihedral angles of both tpy ligands are $\approx 0^\circ$. Hence, $[\text{Ru}(\kappa^2\text{-H}_2\text{N-tpy})(\kappa^3\text{-HOOC-tpy})(\text{H}_2\text{O})]^{3+}$ is highly distorted and activated towards potential chelate ligand loss. The bis(tridentate) complex has been calculated to be 35 kJ mol⁻¹ more stable than $[\text{Ru}(\kappa^2\text{-H}_2\text{N-tpy})(\kappa^3\text{-HOOC-tpy})(\text{H}_2\text{O})]^{3+}$. Thus, our DFT calculations support the above conclusion that bis(tpy) complexes of ruthenium(II) are not suitable for H₂O oxidation. $[\mathbf{1}]^{3+}$ is unable to adopt a heptacoordinate coordination with one H₂O molecule while the decoordination of an outer pyridine ring to form a free coordination site for H₂O is thermodynamically unfavorable. However, an energy barrier of 35 kJ mol⁻¹ can be overcome at room temperature. Especially at low pH the protonation of pyridine is favored. $[\text{Ru}(\kappa^2\text{-H}_2\text{N-tpy})(\kappa^3\text{-HOOC-tpy})(\text{H}_2\text{O})]^{3+}$ might be prone to loss of the H₂N-tpy ligand. Under acidic conditions H₂N-tpy ligand loss is irreversible due to protonation of the pyridine nitrogen atoms. Even if the reaction of " $[\text{Ru}(\kappa^3\text{-H}_2\text{N-tpy})(\kappa^3\text{-HOOC-tpy})]^{3+} + \text{H}_2\text{O}$ " to $[\text{Ru}(\kappa^2\text{-H}_2\text{N-tpy})(\kappa^3\text{-HOOC-tpy})(\text{H}_2\text{O})]^{3+}$ is slow the irreversible H₂N-tpy ligand loss of the latter is a competing pathway to the back reduction to $[\mathbf{1}]^{2+}$.

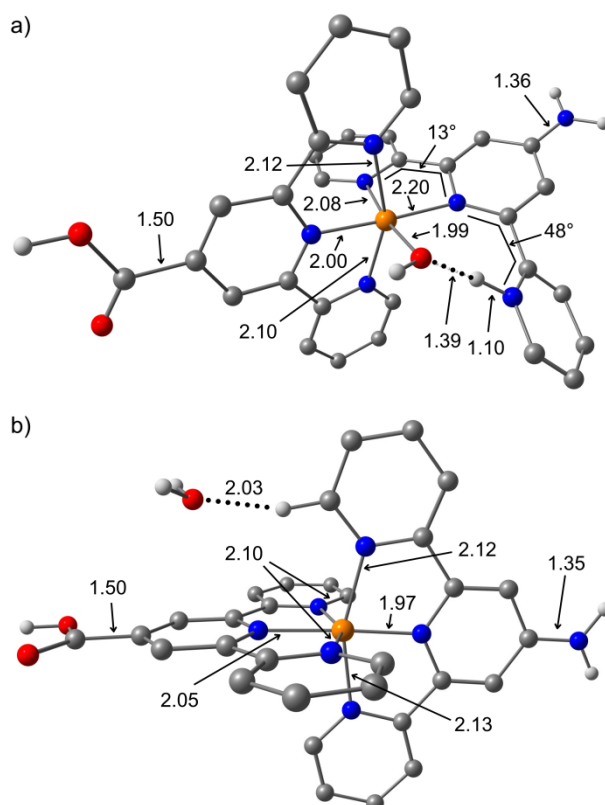


Figure 11. DFT (B3LYP/LANL2DZ, IEFPCM, H₂O, irrelevant CH hydrogen atoms omitted) optimized structures of a) $[\text{Ru}(\kappa^2\text{-H}_2\text{N-tpy})(\kappa^3\text{-HOOC-tpy})(\text{H}_2\text{O})]^{3+}$ and b) " $[\text{Ru}(\kappa^3\text{-H}_2\text{N-tpy})(\kappa^3\text{-HOOC-tpy})]^{3+} + \text{H}_2\text{O}$ ". Indicated bond lengths are given in Å.

In order to detect side products in the back reaction of $[\mathbf{1}]^{3+}$ to $[\mathbf{1}]^{2+}$ ESI mass spectra were conducted also in non-deuterated solvents before and after oxidation with $(\text{NH}_4)_2[\text{Ce}(\text{NO}_3)_6]$ in 0.5 M TFA in H₂O:CH₃CN (1:200;

Figure S3 and S4). The signal at $m/z = 249.1$ (50%) is observed before and after the oxidation and corresponds to the protonated ligand $[\text{tpy-NH}_2 + \text{H}]^+$. An unknown signal at $m/z = 605.1$ (40%) with ruthenium isotope pattern is observed besides the known signals with ruthenium isotope pattern at $m/z = 313.6$ (9%) $[M - 2 \text{PF}_6]^{2+}$, 582.2 (6%) $[M - 2 \text{PF}_6 - \text{CO}_2 - \text{H}]^+$, 626.1 (100%) $[M - 2 \text{PF}_6 - \text{H}]^+$ and 772.1 (19%) $[M - \text{PF}_6]^+$ where M is $[(\text{HOOC-tpy})\text{Ru}(\text{tpy-NH}_2)](\text{PF}_6)_2$. The signal at $m/z = 605.1$ does not appear in the ESI mass spectra before addition of $(\text{NH}_4)_2[\text{Ce}(\text{NO}_3)_6]$ (Oxidation 9, Figure S3 and S4). The signal at $m/z = 606.1$ which was observed in D_2O (Oxidation 6) indicates that one of the protons can be exchanged by deuteration. One could assume that the COOH -substituted tpy ligand is still intact while the NH_2 -substituted tpy ligand underwent a structural change. The signal at $m/z = 605.1$ would fit to a complex where the tpy-NH_2 ligand has been substituted by two CF_3COO^- anions, namely $[(\text{HOOC-tpy})\text{Ru}(\text{CF}_3\text{COO})_2]^+$. However, the signal at $m/z = 605.1$ was also found when the oxidation and back reduction of $[\mathbf{1}]^{2+}$ were performed in 0.5 M HNO_3 or 0.1 M H_2SO_4 instead of 0.5 M TFA (Oxidation 10 and 11, Figure S5 – S8). Thus, so far no complete structural assignment could be made to the signal with $m/z = 605.1$.

The reduction of $[\mathbf{1}]^{3+}$ back to $[\mathbf{1}]^{2+}$ was found to be faster in the presence of UV light ($\lambda_{\text{emiss}} = 254$ and 366 nm, Figure 12a, Oxidation 12). Upon oxidation the initial value of the extinction coefficient ϵ_{500} at $\lambda = 500$ nm dropped from $\epsilon_{500} = 16440$ to $2330 \text{ M}^{-1} \text{ cm}^{-1}$ while the extinction coefficient ϵ_{760} at $\lambda = 760$ nm rose from $\epsilon_{760} = 20$ to $6480 \text{ M}^{-1} \text{ cm}^{-1}$. After exposing the solution to UV light ($\lambda_{\text{emiss}} = 254$ and 366 nm) for 10 min the MLCT band was largely recovered ($\epsilon_{500} = 15490 \text{ M}^{-1} \text{ cm}^{-1}$, 94% recovery) and the LMCT band disappeared nearly completely ($\epsilon_{760} = 390 \text{ M}^{-1} \text{ cm}^{-1}$). In a reference measurement in the darkness a much smaller part of the MLCT band was recovered after 10 min ($\epsilon_{500} = 5420 \text{ M}^{-1} \text{ cm}^{-1}$, 33% recovery) and the LMCT band still featured a pronounced intensity ($\epsilon_{760} = 4950 \text{ M}^{-1} \text{ cm}^{-1}$). Hence, the back reduction is significantly accelerated by UV light irradiation. This points to the existence of a dissociative rate-determining step in the back reduction of $[\mathbf{1}]^{3+}$ back to $[\mathbf{1}]^{2+}$. The loss of the $\kappa^2\text{-H}_2\text{N-tpy}$ ligand of the above mentioned $[\text{Ru}(\kappa^2\text{-H}_2\text{N-tpy})(\kappa^3\text{-HOOC-tpy})(\text{H}_2\text{O})]^{3+}$ might be the responsible dissociative rate-determining step which is accelerated by light.

In a second experiment five cycles of Ce^{IV} addition and UV light treatment were conducted. The extinction coefficients ϵ_{500} and ϵ_{760} are depicted in Figure 12b (Oxidation 13). The initial value of ϵ_{500} drops upon oxidation with 1.3 equiv Ce^{IV} from $\epsilon_{500} = 16840$ to $1050 \text{ M}^{-1} \text{ cm}^{-1}$ with a concomitant rise of ϵ_{760} from $\epsilon_{760} = 110$ to $6790 \text{ M}^{-1} \text{ cm}^{-1}$. After irradiation with UV light for 10 min the extinction coefficients go back to $\epsilon_{500} = 14740 \text{ M}^{-1} \text{ cm}^{-1}$ (88% recovery) and $\epsilon_{760} = 450 \text{ M}^{-1} \text{ cm}^{-1}$. For both, ϵ_{500} and ϵ_{760} , the initial values are not reached quantitatively under these conditions. The second addition of 1.3 equiv Ce^{IV} lets ϵ_{500} drop to $2710 \text{ M}^{-1} \text{ cm}^{-1}$ and ϵ_{760} rise to $5380 \text{ M}^{-1} \text{ cm}^{-1}$. The treatment with UV light again leads to a rise of ϵ_{500} and a drop of ϵ_{760} . This procedure was conducted five times and in each step the respective starting values were not reached quantitatively (86 – 93% recovery) which is assigned to unknown side reactions such as ligand dissociation and decomposition as discussed above.

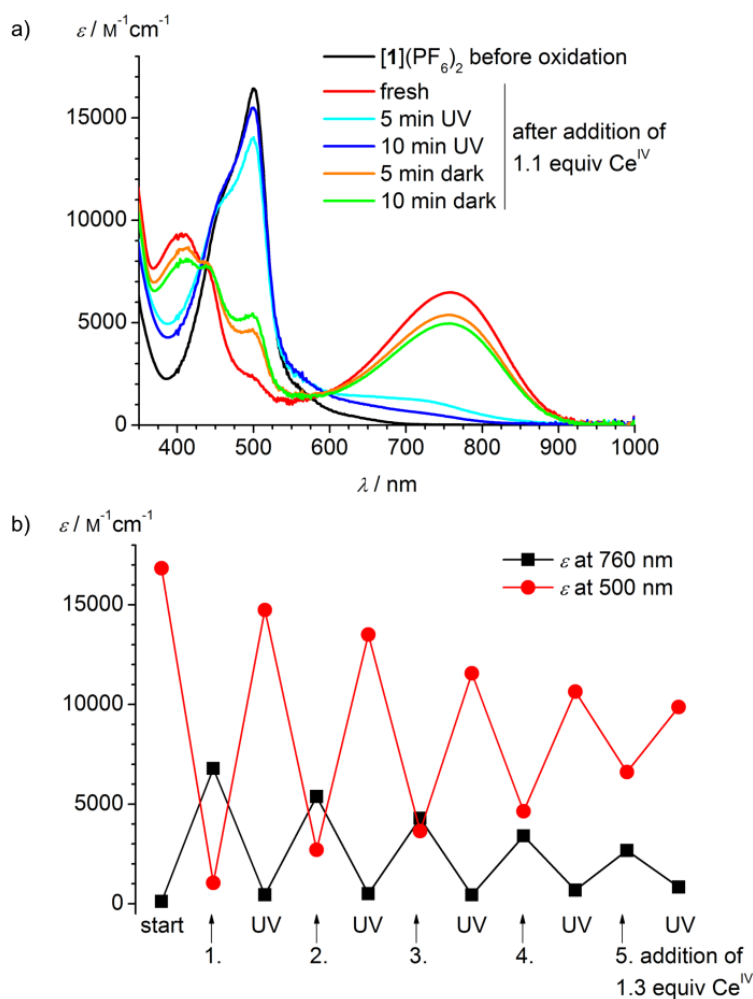


Figure 12. a) UV/Vis spectra of $[1](PF_6)_2$ before and after oxidation with 1.1 equiv $(NH_4)_2[Ce(NO_3)_6]$ in 0.11 M H_2SO_4 in $H_2O:CH_3CN$ (15:85) and treatment with UV light. For experimental details see *Oxidation 12* in the Experimental Section. b) Extinction coefficients at $\lambda = 760$ and 500 nm after alternating treatment with 1.3 equiv Ce^{IV} and UV light. For experimental details see *Oxidation 13* in the Experimental Section.

The reduction rate of $[1]^{3+}$ to $[1]^{2+}$ was also found to be higher in the presence of standard laboratory light conditions (mixture of fume hood light and scattered day light passing through the windows) than under darkness. After oxidation with 2.0 equiv $(NH_4)_2[Ce(NO_3)_6]$ in 0.5 M TFA in H_2O the temporal evolution of the extinction coefficients ϵ_{499} at $\lambda = 499$ nm and ϵ_{751} at $\lambda = 751$ nm is shown in Figure 13 (*Oxidation 14*). Under standard laboratory light conditions ϵ_{499} approaches $\sim 17800 M^{-1} cm^{-1}$ after ~ 12 h. In the darkness ϵ_{499} approaches the same value after ~ 100 h. In both cases the initial value of $\epsilon_{499} = 19600 M^{-1} cm^{-1}$ is not fully recovered (91% recovery). ϵ_{751} shows a similar behavior with the difference that the LMCT band vanishes nearly completely. The temporal evolution of ϵ_{499} and ϵ_{751} nicely fits to first order (or pseudo first order) rate laws with rate constants amounting to $k(\epsilon_{499,light}) = 20.2 h^{-1}$, $k(\epsilon_{499,dark}) = 5.2 h^{-1}$, $k(\epsilon_{751,light}) = 18.4 h^{-1}$ and $k(\epsilon_{751,dark}) = 4.9 h^{-1}$. Thus, under our conditions the reaction rate is four-fold increased under standard light conditions compared to darkness.

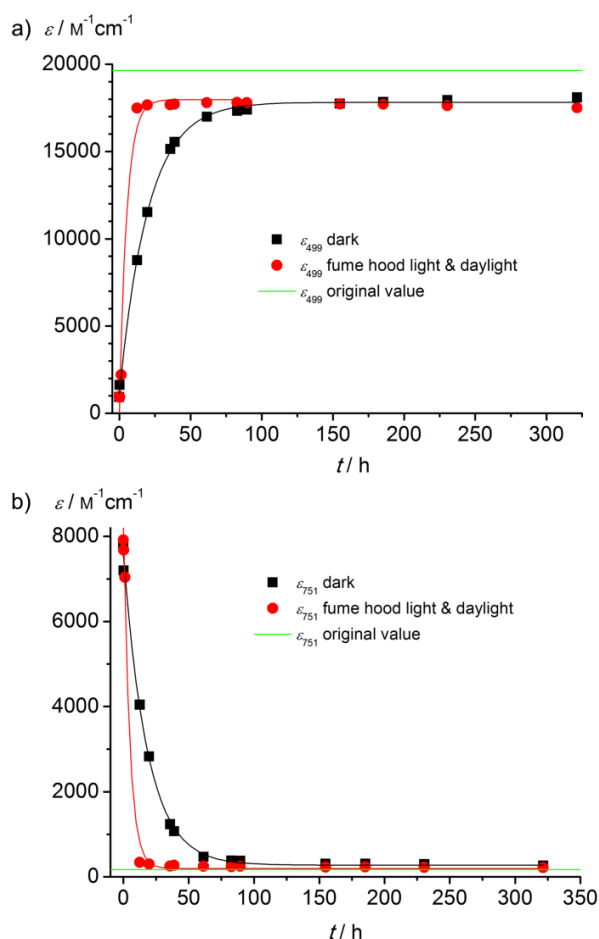
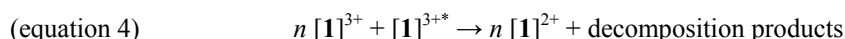


Figure 13. Temporal change of extinction coefficients at a) $\lambda = 499$ (MLCT) and b) $\lambda = 751$ nm (LMCT) after oxidation of $[\mathbf{1}](\text{PF}_6)_2$ with 2.0 equiv $(\text{NH}_4)_2[\text{Ce}(\text{NO}_3)_6]$ in 0.5 M TFA in H_2O . The solid black and red lines are monoexponential fits, respectively. For experimental details see *Oxidation 14* in the Experimental Section.

Furthermore, excited state redox potentials differ from their respective ground state redox potential by the energy of the 0–0' emission energy E_{00} and might be responsible for the faster back reduction in the presence of light.^[67] For $[\mathbf{1}](\text{PF}_6)_2$ the 0–0' emission energy was obtained by the crossing point of the normalized absorption and emission spectra at a wavelength of $\lambda = 626 \text{ nm}$ which corresponds to a redox potential shift of $\Delta E = \pm 1.98 \text{ V}$. $[\text{Ru}(\text{bpy})_3]^{2+}$ features a comparable redox potential shift of $\Delta E = \pm 2.13 \text{ V}$.^[68] Similarly, $[\mathbf{1}]^{3+}$ features excited state redox potentials that differ from its ground state redox potentials. Thus, $[\mathbf{1}]^{3+*}$ is oxidized at lower potential than $[\mathbf{1}]^{3+}$ which might be the reason for the decomposition of $[\mathbf{1}]^{3+*}$. In analogy to the slow decomposition of $[\mathbf{1}]^{3+}$ in the absence of light (equation 3), the decomposition of $[\mathbf{1}]^{3+*}$ is faster and could generate electrons that reduce the majority of $[\mathbf{1}]^{3+}$ according to:



Conclusion

The donor-acceptor-substituted bis(terpyridine)ruthenium(II) complex $[\mathbf{1}](\text{PF}_6)_2$ (Figure 1) can be chemically oxidized in acidic media by Ce^{IV} . The one electron oxidation of $[\mathbf{1}]^{2+}$ to $[\mathbf{1}]^{3+}$ is well understood and was characterized by UV/Vis and ESR spectroscopy, electrochemistry and DFT calculations. The generated $[\mathbf{1}]^{3+}$ undergoes slow spontaneous back reduction to $[\mathbf{1}]^{2+}$ without addition of a reducing agent. This was shown by UV/Vis and NMR spectroscopy and mass spectrometry. The rate of the back reaction depends on the used conditions like solvent and can be accelerated by light. However, the responsible reducing agent is yet unknown. Water as reducing agent would lead to the formation of O_2 or H_2O_2 . H_2O_2 is unstable under the used conditions and would also form O_2 or lead to further side reactions. O_2 was not detected by trapping with $\text{IrCl}(\text{PET}_3)_3$ and by gas phase measurements with a ZrO_2 -based oxygen sensor. The ruthenium complex itself ($[\mathbf{1}]^{3+}$) is assumed to behave as reducing agent as the full amount of $[\mathbf{1}]^{2+}$ is not recovered ($\approx 91 \pm 3\%$ recovery) in the back reaction

of $[1]^{3+}$ to $[1]^{2+}$. $[\text{Ru}(\kappa^2\text{-H}_2\text{N-tpy})(\kappa^3\text{-HOOC-tpy})(\text{H}_2\text{O})]^{3+}$ could be calculated by DFT and is 35 kJ mol^{-1} higher in energy than bis(tridentate) " $[\text{Ru}(\kappa^3\text{-H}_2\text{N-tpy})(\kappa^3\text{-HOOC-tpy})]^{3+} + \text{H}_2\text{O}$ ". Under acidic conditions $[\text{Ru}(\kappa^2\text{-H}_2\text{N-tpy})(\kappa^3\text{-HOOC-tpy})(\text{H}_2\text{O})]^{3+}$ might be prone to decomposition initiated by protonation of the $\kappa^2\text{-H}_2\text{N-tpy}$ ligand and subsequent irreversible ligand loss which could explain the non-quantitative recovery of $[1]^{2+}$.

Experimental Section

General Procedures. CH_3CN was distilled from CaH_2 and THF from potassium under an argon atmosphere. All reagents were used as received from commercial suppliers (Acros and Sigma-Aldrich). $\text{IrCl}(\text{PEt}_3)_3$ was prepared according to a literature procedure (see the Supporting Information).^[69] $[1](\text{PF}_6)_2$ was prepared as reported by Heinze et al.^[40] NMR spectra were recorded on a Bruker Avance DRX 400 spectrometer at 400.31 MHz (^1H) and 162.05 MHz ($^{31}\text{P}\{^1\text{H}\}$). All resonances are reported in ppm versus the solvent signal as an internal standard [D_2O (^1H , $\delta = 4.80$ ppm; $\text{d}_8\text{-THF}$ (^1H , $\delta = 1.24, 3.57$ ppm)] or versus external H_3PO_4 (85%; ^{31}P , $\delta = 0$ ppm). Electrochemical experiments were carried out on a Bio Logic SP-50 voltammetric analyzer using platinum wires as counter and working electrodes and a saturated calomel electrode as reference electrode. The measurements were carried out at a scan rate of $50 - 100 \text{ mV s}^{-1}$ for cyclic voltammetry experiments and at $50 - 200 \text{ mV s}^{-1}$ for square-wave voltammetry experiments using 0.5 M HNO_3 as the supporting electrolyte and a 10^{-3} M solution of the analyte in degassed H_2O . Potentials are referenced to the saturated calomel electrode. UV/Vis/near-IR spectra were recorded on a Varian Cary 5000 spectrometer using 1.0 cm cells (Hellma, Suprasil). ESI MS spectra were recorded on a Micromass Q-TOF-Ultima spectrometer. X-band CW ESR spectra were measured on a Miniscope MS 300 (Magnetech GmbH, Germany). g values are referenced to external Mn^{2+} in ZnS ($g = 2.118, 2.066, 2.027, 1.986, 1.946, 1.906$). Measurements were conducted at 77 K and simulations were performed with the program package EasySpin. Irradiation experiments were performed with a UV lamp (Benda, NU-4 KL, 0.18 W, $\lambda_{\text{emiss}} = 254$ and 366 nm). Solutions of $(\text{NH}_4)_2[\text{Ce}(\text{NO}_3)_6]$ and $\text{Ce}(\text{SO}_4)_2$ always were freshly prepared and used directly after complete dissolution of the salts. Dissolution was achieved via ultrasonication. Oxygen measurements were conducted with a TOS 3.0 sensor (Ionic Systems).

DFT calculations were carried out with the *Gaussian09/DFT*^[70] series of programs. The B3LYP formulation of DFT was used by employing the LANL2DZ basis set.^[70] No symmetry constraints were imposed on the molecules. The presence of energy minima or first order saddle points was checked by analytical frequency calculations. For solvent modeling, the integral-equation-formalism polarizable continuum model (IEFPCM, H_2O) was employed. In general, data obtained including solvent modeling reproduced the experimental results better than those without solvent modeling. Therefore, solvent modeling is included in all calculations in this paper. For time-dependent DFT (TD-DFT) calculations at least 50 singlet transitions ($n \geq 50$) were used. All calculations were performed without explicit counterions.

Oxidation 1. A solvent mixture of $0.125 \text{ M H}_2\text{SO}_4$ in H_2O was used. A solution of $[1](\text{PF}_6)_2$ ($3.58 \times 10^{-5} \text{ M}$, 9 ml) was prepared and a solution of $\text{Ce}(\text{SO}_4)_2 \cdot 4 \text{ H}_2\text{O}$ ($5.33 \times 10^{-4} \text{ M}$, 0.74 ml, 1.1 equiv) was added. The orange solution of $[1](\text{PF}_6)_2$ immediately turned green after the addition of the $\text{Ce}(\text{SO}_4)_2 \cdot 4 \text{ H}_2\text{O}$ solution. Within 7 d the color of the solution turned back to orange. A fresh solution of $\text{Ce}(\text{SO}_4)_2 \cdot 4 \text{ H}_2\text{O}$ ($5.51 \times 10^{-4} \text{ M}$, 0.71 ml, 1.1 equiv) was added. Again, the solution immediately turned green and then slowly changed its color to orange. The measurement was made under normal laboratory light conditions (mixture of artificial light and sunlight passing through the window).

Oxidation 2. A solvent mixture of 0.5 M trifluoroacetic acid in H_2O was used. To a solution of $[1](\text{PF}_6)_2$ ($3.21 \times 10^{-4} \text{ M}$, 1.0 ml) a solution of $(\text{NH}_4)_2[\text{Ce}(\text{NO}_3)_6]$ ($3.43 \times 10^{-2} \text{ M}$, 34.6 μl , 3.7 equiv) was added. The dark red-brown solution immediately turned dark green upon addition of the cerium salt. The mixture was frozen directly after preparation (77 K). The oxidation was performed under normal laboratory light conditions (mixture of artificial light and sunlight passing through the window).

Oxidation 3. A solvent mixture of $0.125 \text{ M H}_2\text{SO}_4$ in $\text{H}_2\text{O}:\text{CH}_3\text{CN}$ (1:1) was used. A solution of $[1](\text{PF}_6)_2$ ($4.26 \times 10^{-5} \text{ M}$, 10 ml) was prepared and a solution of $(\text{NH}_4)_2[\text{Ce}(\text{NO}_3)_6]$ ($5.62 \times 10^{-4} \text{ M}$, 0.84 ml, 1.1 equiv) was added. The orange solution of $[1](\text{PF}_6)_2$ immediately turned green after the addition of the $(\text{NH}_4)_2[\text{Ce}(\text{NO}_3)_6]$ solution. Within 18 h the color of the solution turned back to orange. 9.85 ml of the resulting solution were taken and a fresh solution of $(\text{NH}_4)_2[\text{Ce}(\text{NO}_3)_6]$ ($4.39 \times 10^{-4} \text{ M}$, 0.97 ml, 1.1 equiv) was added. Again, the solution immediately turned green and then slowly changed its color to orange. After 6 d a fresh solution of $(\text{NH}_4)_2[\text{Ce}(\text{NO}_3)_6]$ ($4.64 \times 10^{-4} \text{ M}$, 0.92 ml, 1.1 equiv) was added. Again, the solution immediately turned green and then slowly changed its color to orange. The measurement was made under normal laboratory light conditions (mixture of artificial light and sunlight passing through the window).

Figure 14a shows solution UV/Vis spectra of $[1](PF_6)_2$ before and after the addition of 1.1 equiv $(NH_4)_2[Ce(NO_3)_6]$ in 0.125 M H_2SO_4 in $H_2O:CH_3CN$ (1:1). The MLCT band of $[1](PF_6)_2$ at $\lambda = 501$ nm ($\epsilon = 16920$ M⁻¹ cm⁻¹) immediately disappears upon addition of 1.1 equiv $(NH_4)_2[Ce(NO_3)_6]$. $[1]^{3+}$ features a LMCT band at $\lambda = 753$ nm ($\epsilon = 6670$ M⁻¹ cm⁻¹). The UV/Vis spectrum rapidly changes within minutes. After 18 h the MLCT band is largely recovered ($\epsilon = 15910$ M⁻¹ cm⁻¹ at $\lambda = 500$ nm, 94% recovery) and the LMCT band essentially disappeared. Isosbestic points at $\lambda = 586$, 433 and 341 nm reveal the clean recovery of $[1]^{2+}$ by conversion from $[1]^{3+}$. The addition of another 1.1 equiv $(NH_4)_2[Ce(NO_3)_6]$ again leads to the same color change with the disappearance of the MLCT band and the appearance of the LMCT band at $\lambda = 753$ nm ($\epsilon = 6020$ M⁻¹ cm⁻¹). The UV/Vis spectrum then changes in the same manner as before. After 6 days the MLCT band is recovered ($\epsilon = 16140$ M⁻¹ cm⁻¹ at $\lambda = 500$ nm, 101% recovery) and the LMCT band has vanished (Figure 14b). The same isosbestic points are observed at $\lambda = 585$, 433 and 341. The oxidation with 1.1 equiv $(NH_4)_2[Ce(NO_3)_6]$ can also be conducted a third time with an initial LMCT band at $\lambda = 753$ nm ($\epsilon = 4070$ M⁻¹ cm⁻¹) and a recovery of the MLCT band at $\lambda = 500$ nm ($\epsilon = 14700$ M⁻¹ cm⁻¹ after 4 days, 91% recovery).

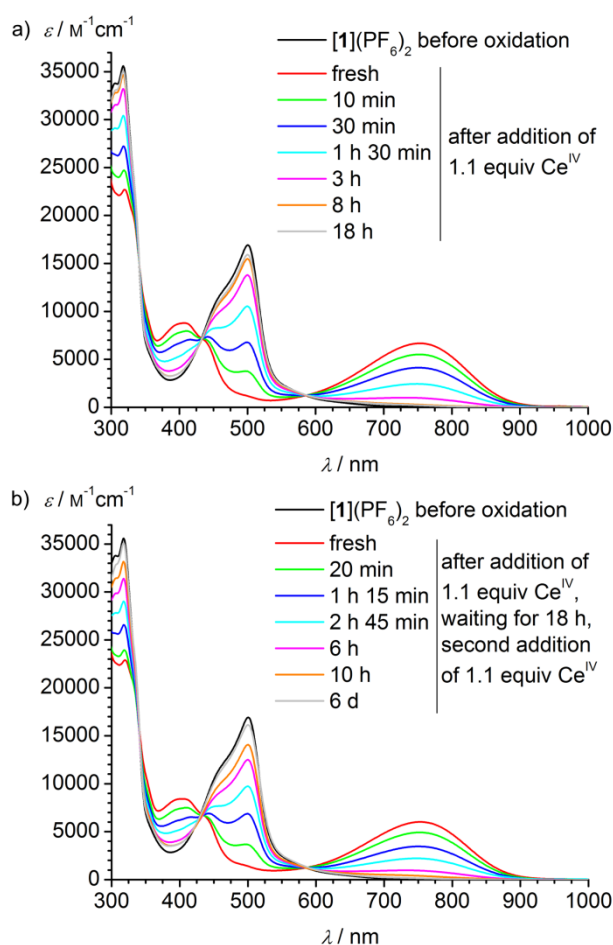


Figure 14. UV/Vis spectra of $[1](PF_6)_2$ before and after oxidation with a) 1.1 and b) 2.2 equiv $(NH_4)_2[Ce(NO_3)_6]$ in 0.125 M H_2SO_4 in $H_2O:CH_3CN$ (1:1).

Oxidation 4. A solvent mixture of 0.125 M H_2SO_4 in H_2O was used. A solution of $[1](PF_6)_2$ (3.94×10^{-4} M, 1 ml) was prepared and a solution of $Ce(SO_4)_2 \cdot 4 H_2O$ (8.11×10^{-2} M, 98.1 μ l, 20 equiv) was added. The orange solution of $[1](PF_6)_2$ immediately turned green after the addition of the $Ce(SO_4)_2 \cdot 4 H_2O$ solution. Within 1 day the color of the solution turned yellow. The measurement was made under normal laboratory light conditions (mixture of artificial light and sunlight passing through the window).

Oxidation 5. A solvent mixture of 0.5 M trifluoroacetic acid in $CH_3CN:H_2O$ (49:1) was used. A solution of $[1](PF_6)_2$ (1.20×10^{-4} M, 0.3 ml) was prepared and oxidized in an OTTLE cell by gradually increasing the potential and then reduced back by gradually lowering the potential. UV/Vis spectra were recorded during this procedure. The measurement was made under normal laboratory light conditions (mixture of artificial light and sunlight passing through the window).

Oxidation 6. A solvent mixture of 0.5 M trifluoroacetic acid in CH₃CN was used. To a solution of [1](PF₆)₂ (6.44×10^{-4} M, 2.5 ml) a solution of (NH₄)₂[Ce(NO₃)₆] (3.51×10^{-3} M, 0.92 ml, 2.0 equiv) was added. The dark red-brown solution immediately turned dark green upon addition of the cerium salt. The solvent was removed under reduced pressure. The green solid was dissolved in D₂O (0.8 ml) and ¹H NMR spectra were recorded. The dark green color of the solution slowly turned dark red-brown. After 17 h the dark red-brown color of the starting solution is seen. After 13 days an ESI mass spectrum was recorded (Figure 10). The measurements were made under normal laboratory light conditions (mixture of artificial light and sunlight passing through the window).

Oxidation 7. The whole procedure was conducted in an Ar-filled glove box. [1](PF₆)₂ (102 mg, 0.111 mmol, 1.00 equiv) was dissolved in degassed 0.5 M trifluoroacetic acid in H₂O:CH₃CN (200:1; 10 ml). A flask was filled with (NH₄)₂[Ce(NO₃)₆] powder (57 mg, 0.104 mmol, 0.94 equiv) and closed with a septum (total volume: 86 ml). The dark red-brown solution of [1](PF₆)₂ was added through the septum and the mixture was shaken thoroughly. The color turned to dark green upon dissolution of the cerium salt after shaking for a few seconds. After 5 h the solution had a dark brown color and after 17 h the solution again had the initial dark red-brown color. 24 ml of the gaseous phase were extracted by a gas-tight syringe and bubbled very slowly through a red d₈-THF solution of IrCl(PET₃)₃ (55 mM, 2.0 ml, 0.11 mmol). No color change occurred during and after the bubbling of the gaseous phase, indicating that no oxygen was present in the gaseous phase. The measurement was made under normal laboratory light conditions (mixture of artificial light and sunlight passing through the window).

For the calculation the following assumptions were made:

1) [1]³⁺ reacts quantitatively with water according to the equation 1. This assumption is reasonable because after oxidation the MLCT band regained 88% of its initial intensity.

2) The equilibrium between O₂ in the gas phase and in solution is totally on the side of the gas phase. This is reasonable due to literature known solubilities of O₂ in CH₃CN at 25 °C which amount to 8.1 mM O₂ at 1 atm (O₂ atmosphere) and 2.4 mM O₂ at 1 atm (air atmosphere).^[71,72]

3) The mixing of Ar and O₂ is ideal. This assumption is surely wrong due to different densities of Ar and O₂ ($\rho_{273K}(\text{Ar}) = 1.78 \text{ kg m}^{-3}$, $\rho_{273K}(\text{O}_2) = 1.43 \text{ kg m}^{-3}$). However, gas samples from the top of the reaction vessels were used for the attempted oxygen detection. The detected value for the O₂ concentration would then be an overestimation of the O₂ content.

4) The oxidative addition of O₂ by IrCl(PET₃)₃ is quantitative. To ensure this the gas sample was bubbled very slowly through the solution of IrCl(PET₃)₃. The reaction equation is: IrCl(PET₃)₃ + O₂ → IrCl(O₂)(PET₃)₃.

(NH₄)₂[Ce(NO₃)₆] is the limiting factor and its amount is $n(\text{Ce}) = 0.104 \text{ mmol}$. According to the equation "2 H₂O → O₂ + 4 H⁺ + 4 e⁻" four electrons are produced per molecule O₂. The reduction of [1]³⁺ requires one electron. Hence, the total amount of O₂ is $n(\text{O}_2, \text{total}) = \frac{1}{4} \times n_{\text{Ce}} = 0.026 \text{ mmol}$ which corresponds to a volume of $V(\text{O}_2, \text{total}) = n(\text{O}_2, \text{total}) \times 22.4 \text{ l mol}^{-1} = 0.58 \text{ ml}$. A sample of $V_1 = 24 \text{ ml}$ was taken out of the gas phase through the septum by a syringe. The total volume of the gas phase was $V(\text{gas phase}) = 76 \text{ ml}$. This should correspond to maximum theoretical O₂ amount of $n(\text{O}_2 \text{ in } V_1) = n(\text{O}_2, \text{total}) \times V_1 \times [V(\text{gas phase})]^{-1} = 8.2 \times 10^{-3} \text{ mmol}$.

A d₈-THF solution of IrCl(PET₃)₃ (55 mM) was prepared (see the Supporting Information). An NMR tube was filled with 2.0 ml of the IrCl(PET₃)₃ solution and the sample was bubbled very slowly through the solution. ³¹P-NMR spectra of the sample solution and of a blind sample (without cerium salt) were measured and the integrals I_x ($x = 1 - 4$, see Figure S9 of the Supporting Information) of the four relevant ³¹P resonances were determined.

The amount of produced O₂ was calculated by the following procedure:

$$\begin{aligned} n(\text{O}_2) &= \Delta n(\text{IrCl(PET}_3)_3) = n_{\text{sample}}(\text{IrCl(PET}_3)_3) - n_{\text{blind}}(\text{IrCl(PET}_3)_3) \\ &= n(\text{total amount of Ir}) \times \left[\frac{I_{1,\text{sample}} + I_{2,\text{sample}}}{I_{1,\text{sample}} + I_{2,\text{sample}} + I_{3,\text{sample}} + I_{4,\text{sample}}} - \frac{I_{1,\text{blind}} + I_{2,\text{blind}}}{I_{1,\text{blind}} + I_{2,\text{blind}} + I_{3,\text{blind}} + I_{4,\text{blind}}} \right] \\ &= 1.1 \times 10^{-4} \text{ mmol} \times \left[\frac{0.968 + 2.000}{0.968 + 2.000 + 0.077 + 0.144} - \frac{0.975 + 2.000}{0.975 + 2.000 + 0.072 + 0.140} \right] \end{aligned}$$

$$= 3.1 \times 10^{-7} \text{ mmol}$$

Thus, the experimental amount of produced O_2 was $n(\text{O}_2) = 3.1 \times 10^{-7} \text{ mmol}$. This corresponds to 0.0037% of the expected amount. Within the experimental error no oxygen was detected. In a positive sample 0.4 ml air ($3.8 \times 10^{-3} \text{ mmol O}_2$) were bubbled very slowly in an Ar atmosphere through a d_8 -THF solution of $\text{IrCl}(\text{PEt}_3)_3$ (55 mM, 0.7 ml, 39 μmol). The full conversion of $\text{IrCl}(\text{PEt}_3)_3$ into its oxygen adduct $\text{IrCl}(\text{O}_2)(\text{PEt}_3)_3$ was observed via ^{31}P -NMR spectra.

Oxidation 8. The amount of produced O_2 was also measured with a ZrO_2 -based sensor. The oxidation was performed exactly as described above (*Oxidation 7*) but in a reaction vessel with a total volume of 41 ml (instead of 86 ml) equipped with a septum, i.e. the volume of the gas phase was $V_1 = 31 \text{ ml}$. After 17 h a sample with $V_2 = 12 \text{ ml}$ was taken out of the gas phase by a syringe and injected into a reaction vessel which had a volume of $V_3 = 81 \text{ ml}$. The theoretical amount of generated O_2 is again $V(\text{O}_2, \text{total}) = 5.8 \text{ ml}$.

The theoretical maximum concentration of produced O_2 is (with the same assumptions as for *Oxidation 7*):

$$c(\text{O}_2) = \frac{V(\text{O}_2, \text{total})}{V_1} \times \frac{V_2}{V_3} \times 10^6 \text{ ppm} = \frac{5.8 \text{ ml}}{31 \text{ ml}} \times \frac{12 \text{ ml}}{81 \text{ ml}} \times 10^6 \text{ ppm} = 2782 \text{ ppm}$$

The experimentally determined concentration of produced O_2 was $0.6 \pm 1.0 \text{ ppm}$. In a blind sample (without cerium salt) the concentration of produced O_2 was $1.5 \pm 1.0 \text{ ppm}$. Again within experimental error no oxygen was detected.

Oxidation 9. A solvent mixture of 0.5 M TFA in $\text{H}_2\text{O}:\text{CH}_3\text{CN}$ (1:200) was used. A solution of $[\mathbf{1}](\text{PF}_6)_2$ ($2.95 \times 10^{-4} \text{ M}$, 1.0 ml) was prepared and a solution of $(\text{NH}_4)_2[\text{Ce}(\text{NO}_3)_6]$ ($8.19 \times 10^{-3} \text{ M}$, 72 μl , 2.0 equiv) was added. The orange solution of $[\mathbf{1}](\text{PF}_6)_2$ immediately turned green after addition of the $(\text{NH}_4)_2[\text{Ce}(\text{NO}_3)_6]$ solution. Within 2 days the color of the solution turned back to orange.

Oxidation 10. A solvent mixture of 0.5 M HNO_3 in H_2O was used. A solution of $[\mathbf{1}](\text{PF}_6)_2$ ($8.00 \times 10^{-4} \text{ M}$, 1.5 ml) was prepared and a solution of $(\text{NH}_4)_2[\text{Ce}(\text{NO}_3)_6]$ ($1.51 \times 10^{-2} \text{ M}$, 159 μl , 2.0 equiv) was added. The orange solution of $[\mathbf{1}](\text{PF}_6)_2$ immediately turned green after addition of the $(\text{NH}_4)_2[\text{Ce}(\text{NO}_3)_6]$ solution. Within 2 days the color of the solution turned back to orange.

Oxidation 11. A solvent mixture of 0.1 M H_2SO_4 in H_2O was used. A solution of $[\mathbf{1}](\text{PF}_6)_2$ ($1.1 \times 10^{-3} \text{ M}$, 1.0 ml) was prepared and a solution of $\text{Ce}(\text{SO}_4)_2 \cdot 4 \text{ H}_2\text{O}$ (16 mM, 1.34 ml, 2.0 equiv) was added. The orange solution of $[\mathbf{1}](\text{PF}_6)_2$ immediately turned green after addition of the $\text{Ce}(\text{SO}_4)_2 \cdot 4 \text{ H}_2\text{O}$ solution. Within 2 days the color of the solution turned back to orange.

Oxidation 12. A solvent mixture of 0.11 M H_2SO_4 in $\text{H}_2\text{O}:\text{CH}_3\text{CN}$ (15:85) was used. A solution of $[\mathbf{1}](\text{PF}_6)_2$ ($9.69 \times 10^{-5} \text{ M}$, 5 ml) was prepared and a solution of $(\text{NH}_4)_2[\text{Ce}(\text{NO}_3)_6]$ ($1.70 \times 10^{-3} \text{ M}$, 0.314 ml, 1.1 equiv) was added. The orange solution of $[\mathbf{1}](\text{PF}_6)_2$ immediately turned green after the addition of the $(\text{NH}_4)_2[\text{Ce}(\text{NO}_3)_6]$ solution. The freshly oxidized solution was filled into a 2 mm quartz cuvette and treated with UV light (Benda, NU-4 KL, 0.18 W, $\lambda_{\text{emiss}} = 254$ and 366 nm) and UV/Vis spectra were recorded. In a reference experiment the cuvette with the reaction mixture was kept in the dark.

Oxidation 13. A solvent mixture of 0.11 M H_2SO_4 in $\text{H}_2\text{O}:\text{CH}_3\text{CN}$ (15:85) was used. A solution of $[\mathbf{1}](\text{PF}_6)_2$ ($9.69 \times 10^{-5} \text{ M}$, 0.5 ml) was prepared and a solution of $(\text{NH}_4)_2[\text{Ce}(\text{NO}_3)_6]$ (2.56 M, 33 μl , 1.3 equiv) was added. The orange solution of $[\mathbf{1}](\text{PF}_6)_2$ immediately turned green after addition of the $(\text{NH}_4)_2[\text{Ce}(\text{NO}_3)_6]$ solution. The freshly oxidized solution was filled into a 2 mm quartz cuvette and treated with UV light (Benda, NU-4 KL, 0.18 W, $\lambda_{\text{exc}} = 254$ and 366 nm) for 10 min. Then a second portion of the same Ce^{IV} solution (2.56 M, 33 μl , 1.3 equiv) was added and again the solution was treated with UV light for 10 min. The procedure was repeated until five portions of Ce^{IV} and five periods of UV light treatments were conducted. UV/Vis spectra were recorded before, freshly after addition of Ce^{IV} and after treatment with UV light.

Oxidation 14. A solvent mixture of 0.5 M TFA in H_2O was used. A solution of $[\mathbf{1}](\text{PF}_6)_2$ ($1.10 \times 10^{-4} \text{ M}$, 3.0 ml) was prepared and a solution of $(\text{NH}_4)_2[\text{Ce}(\text{NO}_3)_6]$ ($6.09 \times 10^{-3} \text{ M}$, 109 μl , 2.0 equiv) was added. The orange solution of $[\mathbf{1}](\text{PF}_6)_2$ immediately turned green after addition of the $(\text{NH}_4)_2[\text{Ce}(\text{NO}_3)_6]$ solution. The freshly oxidized solution was filled into a 10 mm quartz cuvette and exposed to standard fume hood light conditions. In a reference experiment the cuvette with the reaction mixture was kept in the dark.

Acknowledgements

This work was supported by the International Research Training Group (IRTG 1404): Self Organized Materials for Optoelectronics supported by the Deutsche Forschungsgemeinschaft (DFG). We thank Anica Wünsche von Leupoldt for the EPR simulations.

Literature

- [1] S. Campagna, F. Puntoriero, F. Nastasi, G. Bergamini, V. Balzani, *Top. Curr. Chem.* **2007**, *280*, 117–214.
- [2] B. O'Regan, M. Grätzel, *Nature* **1991**, *353*, 737–740.
- [3] J.-F. Yin, M. Velayudham, D. Bhattacharya, H.-C. Lin, K.-L. Lu, *Coord. Chem. Rev.* **2012**, *256*, 3008–3035.
- [4] P. G. Bomben, K. C. D. Robson, B. D. Koivisto, C. P. Berlinguette, *Coord. Chem. Rev.* **2012**, *256*, 1438–1450.
- [5] A. Breivogel, S. Wooh, J. Dietrich, T. Y. Kim, Y. S. Kang, K. Char, K. Heinze, *Eur. J. Inorg. Chem.* **2014**, 2720–2734.
- [6] R. D. Costa, E. Ortí, H. J. Bolink, F. Monti, G. Accorsi, N. Armaroli, *Angew. Chem.* **2012**, *124*, 8300–8334; *Angew. Chem. Int. Ed.* **2012**, *51*, 8178–8211.
- [7] H. J. Bolink, E. Coronado, R. D. Costa, P. Gaviña, E. Ortí, S. Tatay, *Inorg. Chem.* **2009**, *48*, 3907–3909.
- [8] H. J. Bolink, L. Cappelli, E. Coronado, P. Gaviña, *Inorg. Chem.* **2005**, *44*, 5966–5968.
- [9] A. Breivogel, M. Park, D. Lee, S. Klassen, A. Kühnle, C. Lee, K. Char, K. Heinze, *Eur. J. Inorg. Chem.* **2014**, 288–295.
- [10] R. H. Crabtree *Energy Production and Storage: Inorganic Chemical Strategies for a Warming World*; Wiley-VCH: Weinheim, Germany, **2010**.
- [11] X. Liu, F. Wang, *Coord. Chem. Rev.* **2012**, *256*, 1115–1136.
- [12] M. Schulz, M. Karnahl, M. Schwalbe, J. G. Vos, *Coord. Chem. Rev.* **2012**, *256*, 1682–1705.
- [13] W. T. Eckenhoff, R. Eisenberg, *Dalton Trans.* **2012**, *41*, 13004–13021.
- [14] A. Inagaki, M. Akita, *Coord. Chem. Rev.* **2010**, *254*, 1220–1239.
- [15] T. Stoll, M. Gennari, I. Serrano, J. Fortage, J. Chauvin, F. Odobel, M. Rebarz, O. Poizat, M. Sliwa, A. Deronizer, M.-N. Collomb, *Chem. Eur. J.* **2013**, *19*, 782–792.
- [16] J. Dietrich, U. Thorenz, C. Förster, K. Heinze, *Inorg. Chem.* **2013**, *52*, 1248–1264.
- [17] S. Roeser, M. Z. Ertem, C. Cady, R. Lomoth, J. Benet-Buchholz, L. Hammarström, B. Sarkar, W. Kaim, C. J. Cramer, A. Llobet, *Inorg. Chem.* **2012**, *51*, 320–327.
- [18] L.-Z. Sui, W.-W. Yang, C.-J. Yao, H.-Y. Xie, Y.-W. Zhong, *Inorg. Chem.* **2012**, *51*, 1590–1598.
- [19] O. S. Wenger, *Chem. Soc. Rev.* **2012**, *41*, 3772–3779.
- [20] H.-J. Nie, X. Chen, C.-J. Yao, Y.-W. Zhong, G. R. Hutchison, J. Yao, *Chem. Eur. J.* **2012**, *18*, 14497–14509.
- [21] A. Breivogel, K. Hempel, K. Heinze, *Inorg. Chim. Acta* **2011**, *374*, 152–162.
- [22] C.-J. Yao, Y.-W. Zhong, J. Yao, *Inorg. Chem.* **2013**, *52*, 4040–4045.
- [23] T. P. Brewster, W. Ding, N. D. Schley, N. Hazari, V. S. Batista, R. H. Crabtree, *Inorg. Chem.* **2011**, *50*, 11938–11946.
- [24] S. Betanzos-Lara, L. Salassa, A. Habtemariam, O. Novakova, A. M. Pizarro, G. J. Clarkson, B. Liskova, V. Brabec, P. J. Sadler, *Organometallics* **2012**, *31*, 3466–3479.
- [25] S. Kämper, A. Paretzki, J. Fiedler, S. Zálaiš, W. Kaim, *Inorg. Chem.* **2012**, *51*, 2097–2104.
- [26] G. Xue, Y. Guo, T. Yu, J. Guan, X. Yu, J. Zhang, J. Liu, Z. Zou, *Int. J. Electrochem. Sci.* **2012**, *7*, 1496–1511.
- [27] A. Bahreman, B. Limburg, M. A. Siegler, E. Bouwman, S. Bonnet, *Inorg. Chem.* **2013**, *52*, 9456–9469.
- [28] P. T. Nguyen, B. X. T. Lam, A. R. Andersen, P. E. Hansen, T. Lund, *Eur. J. Inorg. Chem.* **2011**, 2533–2539.
- [29] C. Dragonetti, A. Valore, A. Colombo, D. Roberto, V. Trifiletti, N. Manfredi, M. M. Salamone, R. Ruffo, A. Abbotto, *J. Organomet. Chem.* **2012**, *714*, 88–93.
- [30] M. M. R. Choudhuri, R. J. Crutchley, *Inorg. Chem.* **2013**, *52*, 14404–14410.
- [31] C.-W. Hsu, S.-T. Ho, K.-L. Wu, Y. Chi, S.-H. Liu, P.-T. Chou, *Energy Environ. Sci.* **2012**, *5*, 7549–7554.
- [32] B. Schulze, D. Escudero, C. Friebe, R. Siebert, H. Görls, S. Sinn, M. Thomas, S. Mai, J. Popp, B. Dietzek, L. González, U. S. Schubert, *Chem. Eur. J.* **2012**, *18*, 4010–4025.
- [33] R. Hogg, R. G. Wilkins, *J. Chem. Soc.* **1962**, 341–350.
- [34] R. H. Holyer, C. D. Hubbard, S. F. A. Kettle, R. G. Wilkins, *Inorg. Chem.* **1966**, *5*, 622–625.

- [35] M. Abrahamsson, M. Jäger, R. J. Kumar, T. Österman, P. Persson, H.-C. Becker, O. Johansson, L. Hammarström, *J. Am. Chem. Soc.* **2008**, *130*, 15533–15542.
- [36] Recalculated from a previous value for [Ru(bpy)₃]Cl₂ to the updated [Ru(bpy)₃]Cl₂ standard according to A. Breivogel, C. Kreitner, K. Heinze, *Eur. J. Inorg. Chem.* **2014**, accepted.
- [37] J.-P. Sauvage, J.-P. Collin, J.-C. Chambron, S. Guillerez, C. Coudret, V. Balzani, F. Barigelletti, L. D. Cola, L. Flamigni, *Chem. Rev.* **1994**, *94*, 993–1019.
- [38] L. Hammarström, O. Johansson, *Coord. Chem. Rev.* **2010**, *254*, 2546–2559.
- [39] Y. Liu, R. Hammitt, D. A. Lutterman, R. P. Thummel, C. Turro, *Inorg. Chem.* **2007**, *46*, 6011–6021.
- [40] K. Heinze, K. Hempel, M. Beckmann, *Eur. J. Inorg. Chem.* **2006**, *10*, 2040–2050.
- [41] K. Heinze, K. Hempel, A. Breivogel, *Z. Anorg. Allg. Chem.* **2009**, *635*, 2541–2549.
- [42] D. G. Brown, N. Sanguantrakun, B. Schulze, U. S. Schubert, C. P. Berlinguette, *J. Am. Chem. Soc.* **2012**, *134*, 12354–12357.
- [43] A. Breivogel, M. Meister, C. Förster, F. Laquei, K. Heinze, *Chem. Eur. J.* **2013**, *19*, 13745–13760.
- [44] M. Abrahamsson, M. Jäger, T. Österman, L. Eriksson, P. Persson, H.-C. Becker, O. Johansson, L. Hammarström, *J. Am. Chem. Soc.* **2006**, *128*, 12616–12617.
- [45] M. Abrahamsson, M. Jäger, R. J. Kumar, T. Österman, P. Persson, H.-C. Becker, O. Johansson, L. Hammarström, *J. Am. Chem. Soc.* **2008**, *130*, 15533–15542.
- [46] F. Schramm, V. Meded, H. Fliegl, K. Fink, O. Fuhr, Z. Qu, W. Kloppe, S. Finn, T. E. Keyes, M. Ruben, *Inorg. Chem.* **2009**, *48*, 5677–5684.
- [47] G. A. Parada, L. A. Fredin, M.-P. Santoni, M. Jäger, R. Lomoth, L. Hammarström, O. Johansson, P. Persson, S. Ott, *Inorg. Chem.* **2013**, *52*, 5128–5137.
- [48] J. Dietrich, A. Wünsche von Leupoldt, M. Grabolle, U. Resch-Genger, K. Heinze, *Eur. J. Inorg. Chem.* **2013**, 3009–3019.
- [49] K. Heinze, K. Hempel, *Chem. Eur. J.* **2009**, *15*, 1346–1358.
- [50] L. zur Borg, A. L. Domanski, A. Breivogel, M. Bürger, R. Berger, K. Heinze, R. Zentel, *J. Mater. Chem. C* **2013**, *1*, 1223–1230.
- [51] C. Kreitner, K. Heinze, to be submitted.
- [52] M. D. Kärkäs, T. Åkermark, H. Chen, J. Sun, B. Åkermark, *Angew. Chem.* **2013**, *125*, 4283–4287; *Angew. Chem. Int. Ed.* **2013**, *52*, 4189–4193.
- [53] B.-L. Lee, M. D. Kärkäs, E. V. Johnston, A. K. Inge, L.-H. Tran, Y. Xu, Ö. Hansson, X. Zou, B. Åkermark, *Eur. J. Inorg. Chem.* **2010**, 5462–5470.
- [54] D. J. Wasylenko, C. Ganesamoorthy, B. D. Koivisto, M. A. Henderson, C. P. Berlinguette, *Inorg. Chem.* **2010**, *49*, 2202–2209.
- [55] M. D. Kärkäs, E. V. Johnston, E. A. Karlsson, B.-L. Lee, T. Åkermark, M. Shariatgorji, L. Ilag, Ö. Hansson, J.-E. Bäckvall, B. Åkermark, *Chem. Eur. J.* **2011**, *17*, 7953–7959.
- [56] D. Kotkar, V. Joshi, P. K. Ghosh, *Inorg. Chem.* **1986**, *25*, 4334–4335.
- [57] L. Duan, F. Bozoglian, S. Mandal, B. Stewart, T. Privalov, A. Llobet, L. Sun, *Nat. Chem.* **2012**, *4*, 418–423.
- [58] N. G. Connelly, W. E. Geiger, *Chem. Rev.* **1996**, *96*, 877–910.
- [59] P. A. Lay, W. H. F. Sasse, *Inorg. Chem.* **1985**, *24*, 4707–4710.
- [60] A. Harriman, G. Porter, P. Walters, *J. Chem. Soc., Faraday Trans. 2* **1981**, *77*, 2373–2383.
- [61] N. Kaveevivitchai, R. Zong, H.-W. Tseng, R. Chitta, R. P. Thummel, *Inorg. Chem.* **2012**, *51*, 2930–2939.
- [62] N. Kaveevivitchai, L. Kohler, R. Zong, M. E. Ojaimi, N. Mehta, R. P. Thummel, *Inorg. Chem.* **2013**, *52*, 10615–10622.
- [63] L. Duan, L. Wang, A. K. Inge, A. Fischer, X. Zou, L. Sun, *Inorg. Chem.* **2013**, *52*, 7844–7852.
- [64] L. Wang, L. Duan, B. Stewart, M. Pu, J. Liu, T. Privalov, L. Sun, *J. Am. Chem. Soc.* **2012**, *134*, 18868–18880.
- [65] H.-W. Tseng, R. Zong, J. T. Muckermann, R. Thummel, *Inorg. Chem.* **2008**, *47*, 11763–11773.
- [66] S. W. Kohl, L. Weiner, L. Schwartzburd, L. Konstantinovski, L. J. W. Shimon, Y. Ben-David, M. A. Iron, D. Milstein, *Science* **2009**, *324*, 74–77.
- [67] A. A. Vlcek, E. S. Dodsworth, W. J. Pietro, A. B. P. Lever, *Inorg. Chem.* **1995**, *34*, 1906–1913.
- [68] C. R. Bock, J. A. Connor, A. R. Gutierrez, T. J. Meyer, D. G. Whitten, B. P. Sullivan, J. K. Nagle, *J. Am. Chem. Soc.* **1979**, *101*, 4815–4824.
- [69] A. L. Casalnuovo, J. C. Calabrese, D. Milstein, *J. Am. Chem. Soc.* **1988**, *110*, 6738–6744.
- [70] M. J. Frisch, G. W. Trucks, H. B. Schlegel, G. E. Scuseria, M. A. Robb, J. R. Cheeseman, G. Scalmani, V. Barone, B. Mennucci, G. A. Petersson, H. Nakatsuji, M. Caricato, X. Li, H. P. Hratchian, A. F. Izmaylov, J. Bloino, G. Zheng, J. L. Sonnenberg, M. Hada, M. Ehara, K. Toyota, R. Fukuda, J. Hasegawa, M. Ishida, T. Nakajima, Y. Honda, O. Kitao, H. Nakai, T. Vreven, J. A. Montgomery, Jr., J. E. Peralta, F. Ogliaro, M. Bearpark, J. J. Heyd, E. Brothers, K. N. Kudin, V. N. Staroverov, R. Kobayashi, J. Normand, K. Raghavachari, A. Rendell, J. C. Burant, S. S. Iyengar, J. Tomasi, M. Cossi, N. Rega, J. M. Millam, M. Klene, J. E. Knox, J. B. Cross, V. Bakken, C. Adamo, J. Jaramillo, R.

Gomperts, R. E. Stratmann, O. Yazyev, A. J. Austin, R. Cammi, C. Pomelli, J. W. Ochterski, R. L. Martin, K. Morokuma, V. G. Zakrzewski, G. A. Voth, P. Salvador, J. J. Dannenberg, S. Dapprich, A. D. Daniels, O. Farkas, J. B. Foresman, J. V. Ortiz, J. Cioslowski, D. J. Fox *Gaussian 09*, revision A.02, Gaussian, Inc.: Wallingford CT, 2009.

[71] J. M. Achord, C. L. Hussey, *Anal. Chem.* **1980**, 52, 601–602.

[72] C. Franco, J. Olmsted III, *Talanta* **1990**, 37, 905–909.

9.3 Dinuclear Bis(terpyridine)ruthenium(II) Complexes by Amide Coupling of Ruthenium Amino Acids: Synthesis and Properties

A. Breivogel, K. Hempel, K. Heinze, *Inorg. Chim. Acta* **2011**, 374, 152–162.

DOI: 10.1016/j.ica.2011.03.046

Reprinted with permission from Elsevier, Copyright © 2011.



Dinuclear bis(terpyridine)ruthenium(II) complexes by amide coupling of ruthenium amino acids: Synthesis and properties

Aaron Breivogel^a, Klaus Hempel^b, Katja Heinze^{a,*}

^a Institute of Inorganic and Analytical Chemistry, Johannes Gutenberg-University of Mainz, Duesbergweg 10-14, 55128 Mainz, Germany

^b Department of Inorganic Chemistry, Ruprecht Karls-University of Heidelberg, Im Neuenheimer Feld 270, 69120 Heidelberg, Germany

ARTICLE INFO

Article history:

Available online 27 March 2011

Dedicated to Prof. Dr. Wolfgang Kaim on the occasion of his 60th birthday

Keywords:

Amino acids
Charge transfer
Donor–acceptor systems
Mixed-valency
Ruthenium
Terpyridine

ABSTRACT

Two redox-asymmetric amide-bridged bis(terpyridine)ruthenium(II) complexes (**3a**, **3b**) have been prepared by amide coupling of a carboxylic acid functionalized complex with an amine substituted complex and they were fully characterized by spectroscopic analyses. They emit at 692 and 750 nm at room temperature in fluid solution with quantum yields larger than 10^{-3} and $^3\text{MLCT}$ lifetimes of 22 ns. Ru···Ru distances were estimated from DFT models as 17.7 and 13.4 Å for **3a** and **3b**, respectively. Cyclic voltammetry gives two oxidation potentials for the differently substituted ruthenium sites with splittings of 0.10 and 0.23 V for **3a** and **3b**, respectively. Oxidation of **3b** with Ce^{IV} ions gives the corresponding mixed-valent $\text{Ru}^{\text{II}}\text{--}\text{Ru}^{\text{III}}$ system which is valence-localized according to NIR spectroscopic and theoretical analyses.

© 2011 Elsevier B.V. All rights reserved.

1. Introduction

The controlled assembly of multinuclear metal complexes in a precise fashion is a challenging task although several elegant solutions have been proposed, e.g. a chemistry-on-a-complex approach (complexes as ligands/complexes as metals) [1–4], solid-phase syntheses procedures [5] or supramolecular approaches [6,7]. For the first mentioned strategies rather stable metal complexes are needed while programmable labile systems can be employed in self-assembly processes.

Natural oligomeric systems often rely on directional connectors, e.g. sugar-phosphate esters in DNA/RNA or amide groups in peptides. Natural and artificial peptides with a precise amino acid sequence can be easily prepared employing adequate protection/deprotection and coupling techniques – even in an automated fashion on solid supports (solid-phase peptide synthesis) [8]. Amide connectors have been increasingly used to assemble multinuclear metal complexes in a controlled fashion [5,9–11]. As useful building blocks for metallo peptides metallo amino acids (e.g. **A** [9,12], **B** [13,14]; Scheme 1) have been developed.

Based on bis(terpyridine)ruthenium(II) fragments the ruthenium amino acid **1b** and its phenyl-elongated homologues **A** have been devised and realized (Scheme 1) [9,12]. Using ferrocene amino acid **B** [13,14] we have also reported amide bridged bis- and

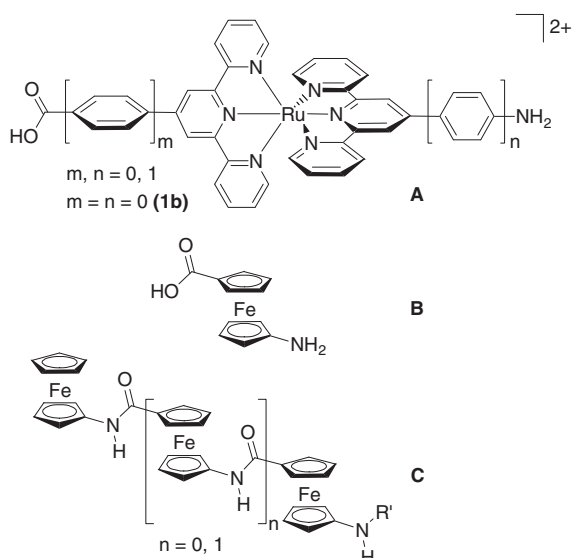
tris-ferrocenes **C** and their oxidized counterparts C^{*+} (Scheme 1) [10,11,15,16]. The neutral and the oxidized systems are potentially useful as molecular wires and as ion sensors [10,11,15–17]. Amide linked conjugates of the ruthenium amino acid **1b** and ferrocene derivatives have been shown to exhibit photoinduced electron transfer provided matching redox potentials are employed at the ferrocene electron donor site [9]. Energy transfer is observed in amide-linked conjugates of the ruthenium amino acid **1b** and matching organic chromophores (e.g. coumarins) [18].

We were then interested to study the interaction between two ruthenium centers in dinuclear systems based on ruthenium amino acid **1b**. Such long-range communication pathways in multimeric assemblies are of fundamental importance and are furthermore of potential usage in molecular electronics. Oligonuclear ruthenium complexes have been proposed as components in photochemical molecular devices, for molecular recognition, information storage, energy conversion and catalysis applications [19,20].

Mixed-valence compounds containing metallic centers in different formal oxidation states ($\text{M}^{n+}/\text{M}^{(n+1)+}$) have been widely employed to study intramolecular electron transfer (ET) processes between donor and acceptor sites and several review articles have been published [21–36]. Robin and Day classified mixed-valence systems as a function of the strength of the electronic interaction (coupling) between donor and acceptor sites [37]. Species of Class I essentially exhibit negligible metal–metal interaction while Class II compounds include species with a nonzero barrier for valence exchange. Class III systems feature fully delocalized valencies.

* Corresponding author. Fax: +49 6131 3927277.

E-mail address: katja.heinze@uni-mainz.de (K. Heinze).



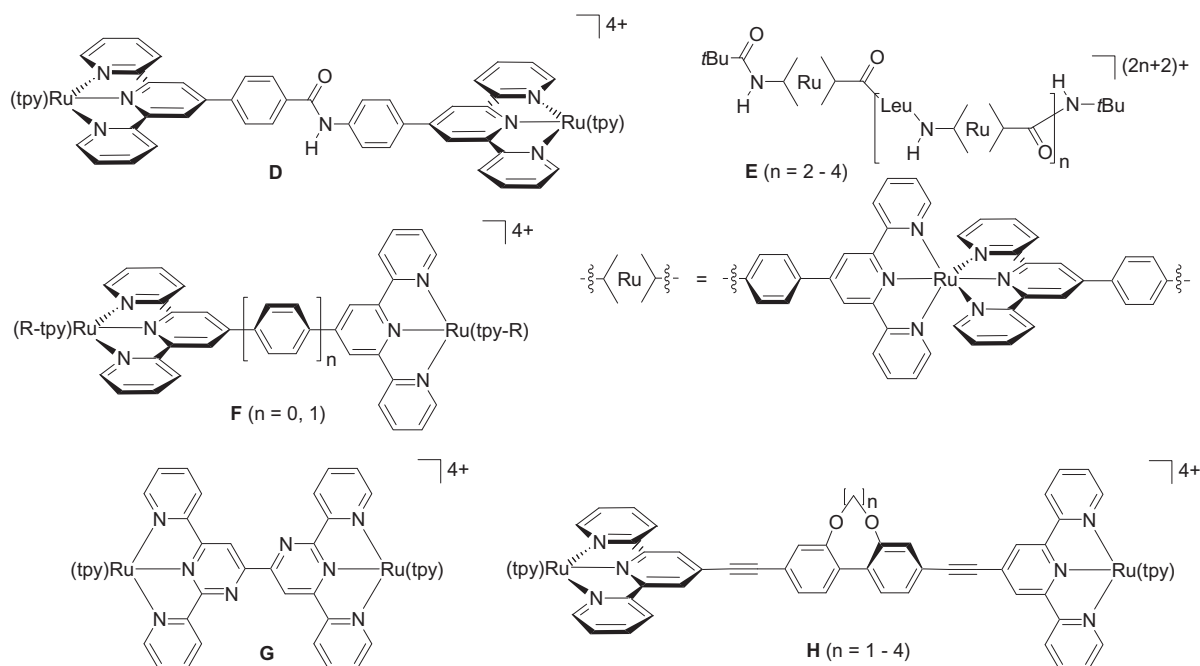
Scheme 1. Bis(terpyridine)ruthenium(II) amino acids **A** [9,12], ferrocene amino acid **B** [13,14] and oligoferroceneamides **C** [10,11,15,16].

A multitude of experimental and theoretical studies, especially on symmetrical systems with the textbook prototype being the Creutz–Taube ion $[(\text{NH}_3)_5\text{Ru}(\text{pz})\text{Ru}(\text{NH}_3)_5]^{5+}$ (py = pyrazine) [38,39], have established that the molecular architecture – mainly the distance between redox sites and the bridging ligand planarity – controls the through-bond electronic coupling [21–36].

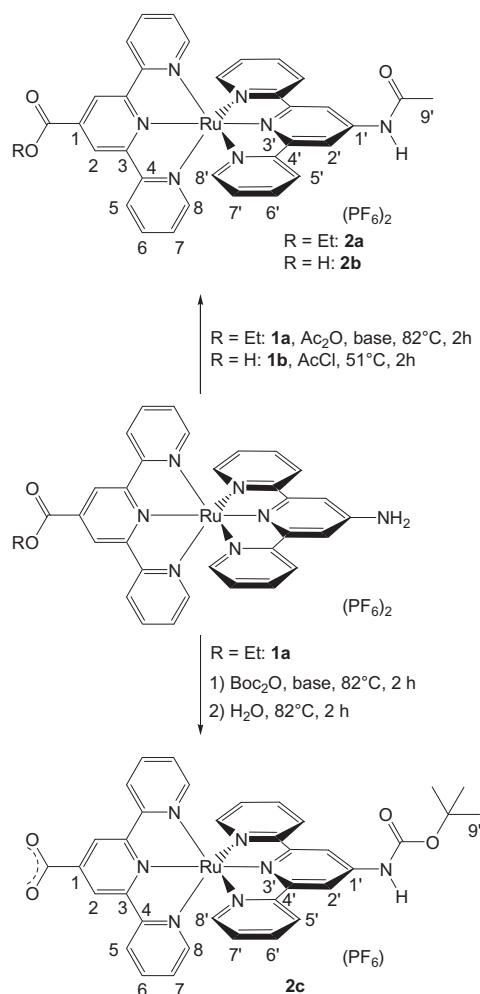
Directional electron transfer might be achieved using slightly asymmetric systems in terms of local redox potentials. This is an advanced extension of symmetrical homodinuclear systems possessing zero driving force for ET which have been thoroughly studied and are well understood [21–36]. Asymmetry can be introduced by differing metal centers (M, M'), differing terminal ligands (L, L') or asymmetrical bridging ligands (L–L'). The amide bridge considered here naturally introduces an aspect of asymmetry and directionality in oligoamides and peptides (N-terminal end → C-terminal end).

The dinuclear complex $[(\text{tpy})\text{Ru}(\text{tpy-Ph-NHCO-Ph-tpy})\text{Ru}(\text{tpy})]^{4+}$ **D** with an amide bridge and two *para*-phenylene units has been reported by Colbran (Scheme 2) [40]. As compared to mononuclear models an approximately doubled extinction coefficient (at $\lambda_{\text{max}} = 487 \text{ nm}$, $\epsilon = 50\,800 \text{ M}^{-1} \text{ cm}^{-1}$) and an unshifted absorption MLCT maximum were observed. No splitting of the (two-electron) $\text{Ru}^{\text{II}}/\text{Ru}^{\text{III}}$ couple at 1.25 V versus SCE in CH_3CN was reported. The data suggest that the ruthenium centers in **D** are isolated and electrochemically independent in the ground state. This is possibly due to the “dilution” with non-planar *para*-phenylene spacers [40]. However, no emission data has been reported to access the excited state properties. Similarly, the “expanded leucines” **E** [41] display additive extinction at 494 nm (unshifted λ_{max}) and one single $\text{Ru}^{\text{II}}/\text{Ru}^{\text{III}}$ redox couple at +1.26 V versus SCE (Scheme 2). Again, these observations are very likely due to the separation of the redoxactive $[(\text{tpy})\text{Ru}(\text{tpy})]^{2+}$ units by non-planar *para*-phenylene and leucine spacers. Based on the observation of a single oxidation wave in electrochemical experiments metal–metal interaction in dinuclear complexes **F** with ‘back-to-back’ terpyridine and *para*-phenylene bridged bis-terpyridines seems to be absent (Scheme 2). However, in spite of the non-planar bridging ligand spectroelectrochemical investigations revealed a weak electronic interaction in the mixed-valent systems **F**⁺ [42–44]. Complexes of type **F** are non emissive at room temperature similar to the parent mononuclear complex $[(\text{tpy})_2\text{Ru}]^{2+}$ [44]. Campagna and Hannan recently managed to planarize the bridging π -system by replacing two CH groups by nitrogen atoms which allows for favourable $\text{CH}\cdots\text{N}$ interactions within the bridge (Scheme 2, **G**) [4]. The planarized bridge of **G** enhances the metal–metal interaction and two $\text{Ru}^{\text{II}}/\text{Ru}^{\text{III}}$ oxidation processes were observed with $\Delta(E_{1/2}) = 90 \text{ mV}$ giving a comproportionation constant $K_C \sim 33$ for the mixed-valent cation **G**⁺. In addition a long-lived ³MLCT emission has been observed for **G** [4]. A different successful strategy to planarize the bridging ligand in terpyridine-type ruthenium complexes has been introduced by Harriman using tethers of differing lengths within the bridge (Scheme 2, **H**). Although negligible $\text{Ru}^{\text{II}}/\text{Ru}^{\text{III}}$ redox separations were found spectroelectrochemical studies revealed a weak electronic coupling (weakly coupled Class II) [45].

As an amide bridge allows for a rather coplanar arrangement of connected $\text{Ru}(\text{tpy})$ moieties we wish to address the question



Scheme 2. Selection of linear oligonuclear bis(terpyridine)ruthenium(II) complexes **D–H** (tpy = 2,2':6',2''-terpyridine, R-tpy = 4'-p-tolyl-2,2':6',2''-terpyridine or tpy).



Scheme 3. N-Acylation of ruthenium amino acid ester **1a** and ruthenium amino acid **1b–2a** [46] and **2b** and Boc protection of **1a–2c** and atom numbering for NMR assignments.

whether metal–metal communication across an amide linkage is possible in dinuclear bis(terpyridine)ruthenium complexes. We report the synthesis of two amide bridged bis(terpyridine)ruthenium(II) complexes with one single *para*-phenylene spacer (**3a**) and without any *para*-phenylene spacers (**3b**) in addition to the connecting amide unit. The synthetic starting point is the bis(terpyridine)ruthenium(II) amino acid **1b** and its ethyl ester **1a** [9]. The *para*-phenylene spacer of **3a** is expected to disrupt any π -conjugation pathway, similar to the **D** case (Scheme 2), while in **3b** the bridge is expected to be rather planar. For comparison of optical and electrochemical data the mononuclear *N*-acetyl protected bis(terpyridine)ruthenium(II) amino acid **2b** and its ethyl ester **2a** [46] are reported together with the *N*-Boc protected bis(terpyridine)ruthenium(II) amino carboxylate **2c** as versatile synthetic intermediate for the construction of dinuclear amide linked bis(terpyridine)ruthenium(II) complexes.

2. Experimental

2.1. General procedures

Chemicals were obtained from commercial suppliers and used without further purification. Bis(terpyridine)ruthenium(II) complexes **1a**, **1b** [9] and **2a** [46] were synthesized as reported. $[\text{Ru}(\text{tpy}-\text{C}_6\text{H}_4-\text{COOH})(\text{tBu}_3\text{tpy})](\text{PF}_6)_2$ has been prepared by Prof. Dr.

Sven Rau [47] IR spectra were recorded on a BioRad Excalibur FTS 3000 spectrometer using caesium iodide disks. UV/Vis spectra were recorded on a Perkin–Elmer Lambda 19 or on a Varian Cary 5000 spectrometer in 1.0 cm cells (Hellma, suprasil). FAB mass spectra were recorded with a Finnigan MAT 8400 mass spectrometer. ESI⁺ mass spectra were recorded with a Finnigan TSQ 700 triple-quadrupole or a Q-ToF Ultima API mass spectrometer (Micromass/Waters) with analyte solutions in acetonitrile. NMR spectra were obtained on a Bruker Avance DPX 200 (200 MHz, ¹H) or a Bruker Avance II 400 (400 MHz, ¹H) at 30 °C. Chemical shifts (δ /ppm) are reported with respect to residual solvent peaks as internal standards: CD_3CN ($\delta(^1\text{H}) = 1.94$ ppm, $\delta(^{13}\text{C}) = 1.24$ ppm). Cyclic voltammetry was performed on a Metrohm “Universal Mess- und Titriergefäß”, Metrohm GC electrode RDE 628, platinum electrode, SCE electrode, Princeton Applied Research potentiostat Model 273; in 0.1 M *n*Bu₄NPF₆/CH₃CN. Potentials are given relative to that of SCE. Emission spectra were recorded on a Varian Cary Eclipse spectrometer. Quantum yields were determined by comparing the areas under the emission spectra on an energy scale [cm^{-1}] recorded for optically matched solutions of the samples and the reference $\{\phi([\text{Ru}(\text{bpy})_3]^{2+}) = 0.062$ in CH₃CN} [48]; experimental uncertainty 15%. Luminescence lifetimes were determined on a PicoQuant FluoTime 100 time-correlated single-photon counting unit. Criteria for the best fit were the values of χ^2 ; experimental uncertainty 10%. Density functional calculations were carried out with the GAUSSIAN03/DFT [49] series of programs. The B3LYP formulation of density functional theory was used employing the LanL2DZ basis set [49]. All structures were characterized as minima by frequency analysis ($N_{\text{imag}} = 0$). No symmetry constraints were imposed on the molecules.

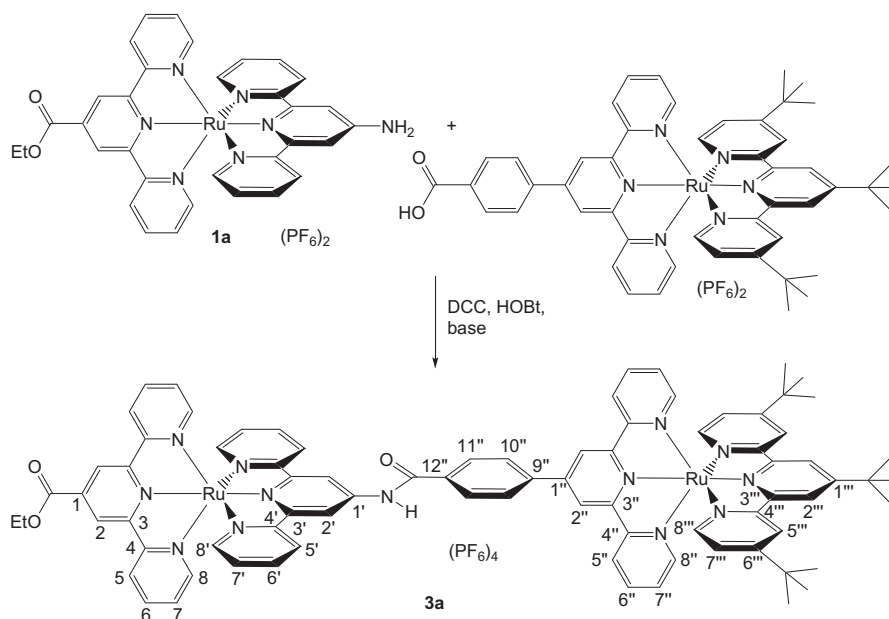
2.2. Synthesis of **2b**

Acid **1b** (150 mg, 0.16 mmol) was dissolved in acetyl chloride (20 mL) and the solution was heated under reflux for 2 h. After cooling to room temperature and removal of the solvent in vacuo the residue was dissolved in acetonitrile and the product was precipitated by the addition of diethyl ether. The product was collected by filtration, dissolved in hot water and precipitated by the addition of NH₄PF₆ (78 mg, 0.48 mmol) in water (1 mL). The product was collected by filtration and dried in vacuo to give a red powder. Yield 51% (80 mg, 0.08 mmol). Anal. Calc. $\text{C}_{33}\text{H}_{25}\text{N}_7\text{O}_3\text{RuP}_2\text{F}_{12} \cdot 4\text{H}_2\text{O}$: C, 38.46; H, 3.23; N, 9.51. Found: C, 38.63; H, 3.13; N, 9.68%. MS (FAB⁺): m/z (%) = 814 (16) $[\text{M}+\text{PF}_6]^+$. ¹H NMR (CD_3CN , 200 MHz): $\delta = 9.46$ (s, 1H, NH), 9.19 (s, 2H, H²), 8.96 (s, 2H, H^{2'}), 8.64 (d, $^3J_{\text{HH}} = 8.0$ Hz, 2H, H⁵), 8.39 (d, $^3J_{\text{HH}} = 8.0$ Hz, 2H, H^{5'}), 7.86–7.98 (m, 4H, H^{6,6'}), 7.45 (d, $^3J_{\text{HH}} = 5.2$ Hz, 2H, H⁸), 7.19–7.28 (m, 4H, H^{7,7'}), 7.11 (ddd, $^3J_{\text{HH}} = 6.6$ Hz, $^4J_{\text{HH}} = 1.20$ Hz, 2H, H^{8'}), 2.37 (s, 3H, H^{9'}). ¹³C NMR (CD_3CN , 50 MHz): $\delta = 159.4, 159.3, 158.1, 156.6$ (4 s, C^{3,3',4,4'}), 154.4 (s, C^{8'}), 154.0 (s, C⁸), 154.4 (s, C^{1'}), 139.9 (s, C^{6'}), 139.7 (s, C⁶), 137.0 (s, C¹), 129.4 (s, C⁷), 129.1 (s, C^{7'}), 126.4 (s, C⁵), 126.1 (s, C^{5'}), 124.6 (s, C²), 114.5 (s, C^{2'}), 25.5 (s, C^{9'}). COOH and NHCO were not observed. IR (CsI): $\nu = 3454$ (OH, NH), 3085 (CH_{aryl}), 2936 (CH_{alkyl}), 1711 (C=O), 1689 (amide I), 1525 (amide II), 1563 (C=N, C=C), 1246 (C–O), 841 (PF) cm^{-1} .

2.3. Synthesis of **2c**

Ester **1a** (200 mg, 0.21 mmol) and di-*tert*-butyldicarbonate (231 mg, 1.06 mmol) were dissolved in dry acetonitrile (15 mL) and phosphazene base P₁-tBu¹ [51,52] (229 mg, 0.98 mmol) was added. The solution was heated under reflux for 2 h. After the

¹ Phosphazene base P₁-tBu = *tert*-butylimino-tris(dimethylamino)-phosphorane.



Scheme 4. Amide coupling of amino acid ester **1a** and $[\text{Ru}(\text{tpy}-\text{C}_6\text{H}_4-\text{COOH})(\text{tBu}_3\text{tpy})](\text{PF}_6)_2$ to **3a** and atom numbering for NMR assignments.

addition of water (5 mL) the mixture was heated under reflux for 2 h. After cooling to room temperature and removal of the solvent in vacuo the residue was dissolved in acetonitrile and the product was precipitated by the addition of diethyl ether. The product was collected by filtration, dissolved in water and precipitated by the addition of NH_4PF_6 (78 mg, 0.48 mmol) in water (1 mL). The product was collected by filtration and dried in vacuo to give a red powder. Yield 93% (172 mg, 0.20 mmol). *Anal. Calc.* $\text{C}_{36}\text{H}_{30}\text{N}_7\text{O}_4\text{RuPF}_6 \cdot 4\text{H}_2\text{O}$: C, 45.86; H, 4.06; N, 10.40. Found: C, 45.99; H, 4.16; N, 10.71%. MS (FAB^+): m/z (%) = 726 (8) $[\text{M}]^+$. ^1H NMR (CD_3CN , 200 MHz): δ = 10.30 (s, 1H, NH), 9.32 (s, 2H, H^2), 9.26 (s, 2H, H^2), 8.61 (d, $^3J_{\text{HH}}$ = 8.0 Hz, 2H, H^5), 8.52 (d, $^3J_{\text{HH}}$ = 8.0 Hz, 2H, H^5), 7.86–7.93 (m, 4H, $\text{H}^{6,6'}$), 7.44 (d, $^3J_{\text{HH}}$ = 5.5 Hz, 2H, H^8), 7.37 (d, $^3J_{\text{HH}}$ = 5.5 Hz, 2H, H^8), 7.11–7.19 (m, 4H, $\text{H}^{7,7'}$), 1.68 (s, 9H, CH_3). ^{13}C NMR (CD_3CN , 50 MHz): δ = 167.0 (s, COO), 158.8 (s, C^3), 158.5 (s, C^3), 156.5 (s, C^4), 155.6 (s, C^4), 153.3 (s, C^{Boc}), 153.2 (s, C^8), 152.8 (s, C^8), 148.4 (s, C^1), 143.7 (s, $\text{C}^{1'}$), 138.7 (s, C^6), 138.4 (s, C^6), 128.0 (s, C^7), 127.9 (s, C^7), 125.1 (s, C^2), 124.6 (s, C^5), 123.8 (s, C^5), 112.7 (s, C^2), 82.7 (s, C_q^{Boc}), 28.0 (s, CH_3). IR (CsI): ν = 3431 (OH, NH), 3094 (CH_{aryl}), 2980 (CH_{alkyl}), 1722 (C=O), 1651 (amide I), 1564 (C=N, C=C), 1528 (amide II), 1249 (C–O), 843 (PF) cm^{-1} .

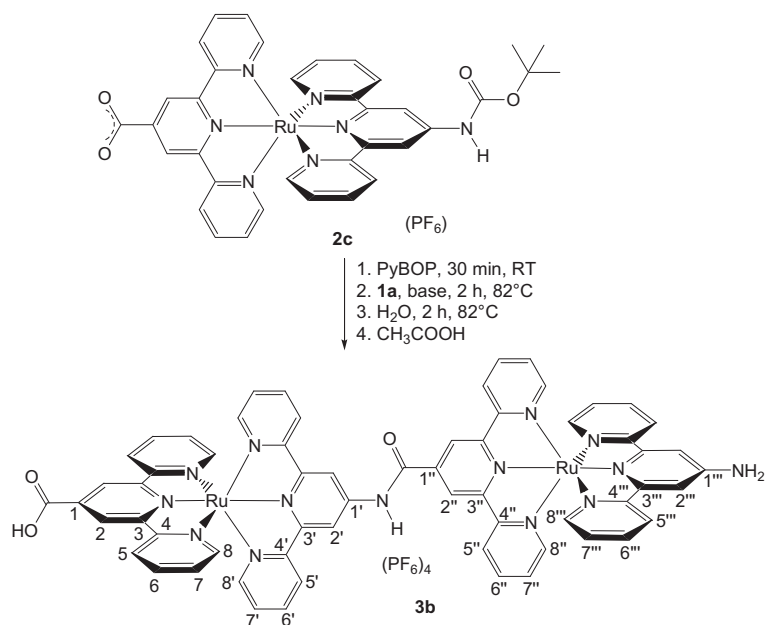
2.4. Synthesis of **3a**

$[\text{Ru}(\text{tpy}-\text{C}_6\text{H}_4-\text{COOH})(\text{tBu}_3\text{tpy})](\text{PF}_6)_2$ (150 mg, 0.13 mmol), DCC (46 mg, 0.22 mmol) and HOBT (30 mg, 0.22 mmol) were dissolved in dry acetonitrile (15 mL) and stirred for 45 min at room temperature to activate the carboxylic acid. **1a** (140 mg, 0.15 mmol) and phosphazene base $\text{P}_1\text{-tBu}$ (229 mg, 0.98 mmol) dissolved in acetonitrile (5 mL) were added and the solution was stirred for 8 h. The solution was filtered over Celite and the solvent was removed in vacuo. The residue was dissolved in hot ethanol (5 mL) and NH_4PF_6 (78 mg, 0.48 mmol) in water (1 mL) was added. After addition of excess water the precipitated product was collected by filtration. Recrystallization from ethanol/ CH_2Cl_2 and drying in vacuo gave **3a** as a red powder. Yield 46% (125 mg, 0.06 mmol). *Anal. Calc.* $\text{C}_{82}\text{H}_{75}\text{N}_{13}\text{O}_3\text{Ru}_2\text{P}_4\text{F}_{24}$ (2072.56) $\cdot \text{H}_2\text{O}$: C, 47.11; H, 3.71; N, 8.71. Found: C, 46.99; H, 3.71; N, 8.88%. MS (ESI^+): m/z (%) = 497.5 (100) $[\text{M}-\text{H}]^{3+}$, 373.4 (18) $[\text{M}]^{4+}$. ^1H NMR (CD_3CN , 200 MHz):

δ = 10.07 (s, 1H, NH), 9.33 (s, 2H, $\text{H}^{2'}$), 9.21 (s, 2H, $\text{H}^{2'}$), 9.11 (s, 2H, H^2), 8.81 (s, 2H, $\text{H}^{2''}$), 8.63–8.70 (m, 4H, $\text{H}^{5'}$, H^5), 8.41–8.52 (m, 8H, $\text{H}^{5'}$, $\text{H}^{5''}$, $\text{H}^{10'}$, $\text{H}^{11''}$), 7.97–7.99 (m, 6H, H^6 , $\text{H}^{6'}$, $\text{H}^{6''}$), 7.53 (d, $^3J_{\text{HH}}$ = 5.0 Hz, 2H, H^8), 7.25–7.31 (m, 10H, H^7 , $\text{H}^{7''}$, $\text{H}^{8'}$, $\text{H}^{8''}$, $\text{H}^{8''}$), 7.15–7.22 (m, 4H, $\text{H}^{7'}$, $\text{H}^{7''}$), 4.64 (q, $^3J_{\text{HH}}$ = 6.8 Hz, 2H, CH_2), 1.77 (s, 9H, CH_3), 1.59 (t, $^3J_{\text{HH}}$ = 6.8 Hz, 3H, CH_3), 1.33 (s, 18H, CH_3). ^{13}C NMR (CD_3CN , 50 MHz): δ = 166.8 (s, CONH), 164.5 (s, COOEt), 163.5 (s, $\text{C}^{12''}$), 162.0 (s, C^9), 158.6, 158.5, 158.3, 158.1, 156.6, 156.3, 155.5, 155.3 (8 s, $\text{C}^{3,3',3'',3'',4,4',4'',4''}$), 153.3, 152.8, 152.7, 152.2 (4 s, $\text{C}^{8,8',8'',8''}$), 147.6 (s, C^1), 146.4 (s, $\text{C}^{1'}$), 141.6 (s, C^1), 138.9, 138.6, 138.3 (3 s, $\text{C}^{6,6',6''}$), 136.7 (s, $\text{C}^{1''}$), 135.3 (s, $\text{C}^{6''}$), 129.7, 128.7, 128.3, 128.0 (4 s, $\text{C}^{7,7',7'',7''}$), 125.3, 125.0, 124.9, 124.7 (4 s, $\text{C}^{5,5',5'',5''}$), 123.2 (s, C^2), 122.4 (s, $\text{C}^{2'}$), 122.2, 121.7 (2 s, $\text{C}^{10',11''}$), 114.3 (2C) (s, $\text{C}^{2',2''}$), 63.3 (s, CH_2), 36.8 (s, C_q), 35.7 (s, C_q), 30.6 (s, CH_3), 29.9 (s, CH_3), 14.9 (s, CH_3). IR (CsI): ν = 3453 (OH, NH), 3076 (CH_{aryl}), 2968 (CH_{alkyl}), 1689 (C=O, amide I), 1612 (C=N, C=C), 1526 (amide II), 1255 (C–O), 841 (PF) cm^{-1} .

2.5. Synthesis of **3b**

Boc protected **2c** (100 mg, 0.11 mmol) and PyBOP (72 mg, 0.14 mmol) were dissolved in acetonitrile (15 mL) and stirred at room temperature for 45 min to activate the carboxylic acid. **1a** (109 mg, 0.12 mmol) and phosphazene base $\text{P}_1\text{-tBu}$ (229 mg, 0.98 mmol) dissolved in acetonitrile (5 mL) were added and the solution was heated under reflux for 2 h. Water (5 mL) was added and the mixture was heated under reflux for further 2 h. After cooling to room temperature the solvents were removed in vacuo and the residue was dissolved in acetonitrile (2 mL). Acetic acid (0.5 mL) was added and the product was precipitated by the addition of excess water. The product was collected by filtration and recrystallized from acetone/water to give a red powder. Yield 82% (170 mg, 0.09 mmol). *Anal. Calc.* $\text{C}_{62}\text{H}_{44}\text{N}_{14}\text{O}_3\text{Ru}_2\text{P}_4\text{F}_{24}$ (1815.10) $\cdot \text{C}_3\text{H}_8\text{O}$: C, 41.68; H, 2.69; N, 10.47. Found: C, 41.53; H, 2.85; N, 10.22%. MS (ESI^+): m/z (%) = 309.0 (100) $[\text{M}]^{4+}$, 411.6 (94) $[\text{M}-\text{H}]^{3+}$. ^1H NMR (CD_3CN , 200 MHz): δ = 11.30 (s, 1H, NH), 9.51 (s, 2H, $\text{H}^{2'}$), 9.45 (s, 2H, $\text{H}^{2''}$), 9.24 (s, 2H, H^2), 8.77 (d, $^3J_{\text{HH}}$ = 7.8 Hz, 2H, $\text{H}^{5'}$), 8.69 (d, $^3J_{\text{HH}}$ = 7.8 Hz, 2H, H^5), 8.61 (d, $^3J_{\text{HH}}$ = 7.8 Hz, 2H, $\text{H}^{5'}$), 8.33 (d, $^3J_{\text{HH}}$ = 7.8 Hz, 2H, $\text{H}^{5''}$), 7.86–8.07 (m, 10H, $\text{H}^{2''}$, H^6 , $\text{H}^{6'}$, $\text{H}^{6''}$, $\text{H}^{6''}$), 7.65 (d, $^3J_{\text{HH}}$ = 7.2 Hz, 2H, H^8),



Scheme 5. Amide coupling of amino acid ester **1a** and Boc protected **2c** to give fully deprotected **3b** and atom numbering for NMR assignments.

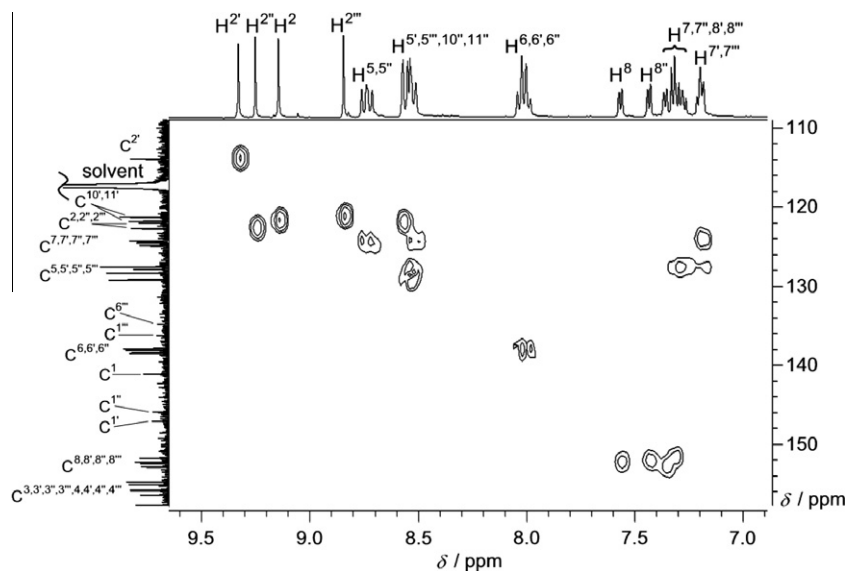


Fig. 1. Partial CH-COSY spectrum of **3a** in CD₃CN.

7.57 (ddd, $^3J_{\text{HH}} = 5.2$ Hz, $^4J_{\text{HH}} = 1.20$ Hz, 2H, H^{8''}), 7.29–7.37 (m, 8H, H⁷, H^{7''}, H⁸, H^{8'''}), 7.08–7.22 (m, 2H, H^{7'}, H^{7'''}), 5.83 (bs, 2H, NH₂). ¹³C NMR (CD₃CN, 50 MHz): δ = 165.0 (s, COOH), 159.4, 159.0, 158.8, 158.7, 158.1, 157.4, 156.3, 155.0 (8 s, C^{3,3',3'',3''',4,4',4'',4'''}), 157.1 (s, C^{1''}), 153.8 (s, C^{8'}), 153.7 (s, C^{8'''}), 153.4 (s, C^{8''}), 153.2 (s, C⁸), 147.9 (s, C^{1'}), 139.4, 139.2, 139.2, 138.8 (4 s, C^{6,6',6'',6'''}), 138.9 (s, C¹), 137.3 (s, C^{1'''}), 128.9, 128.8, 128.6, 128.0 (4 s, C^{7,7',7'',7'''}), 125.9, 125.6, 125.5, 124.9 (4 s, C^{5,5',5'',5'''}), 124.0 (s, C²), 122.6 (s, C^{2''}), 115.3 (s, C^{2'}), 109.7 (s, C^{2'''}), CONH not observed. IR (CsI): ν = 3458 (OH, NH), 3077 (CH_{aryl}), 1687 (C=O, amide I), 1562 (C=N, C=C), 1526 (amide II), 1245 (C–O), 838 (PF) cm^{−1}.

2.6. Oxidation of **1b**

A solution of **1b** (3.9×10^{-5} M) was titrated stepwise with a solution of (NH₄)₂Ce(NO₃)₆ (4.1×10^{-3} M). A solution of trifluoro-

acetic acid in acetonitrile (0.5 M) was used as solvent. During titration the colour of the solution turned from orange to yellow and finally to green. UV/Vis spectra revealed a decreasing band (MLCT) at 500 nm, an increasing band at 729 nm (LMCT) and isosbestic points at 432 und 578 nm.

2.7. Oxidation of **3a**

A solution of **3a** (1.5×10^{-5} M) was titrated stepwise with a solution of (NH₄)₂Ce(NO₃)₆ (1.8×10^{-3} M). A solution of trifluoroacetic acid in acetonitrile (0.5 M) was used as solvent. During titration the colour of the solution turned from orange to yellowish brown. UV/Vis spectra revealed a decreasing band (MLCT) at 492 nm, an increasing band at 705 nm (shoulder, LMCT) and isosbestic points at 418 und 574 nm.

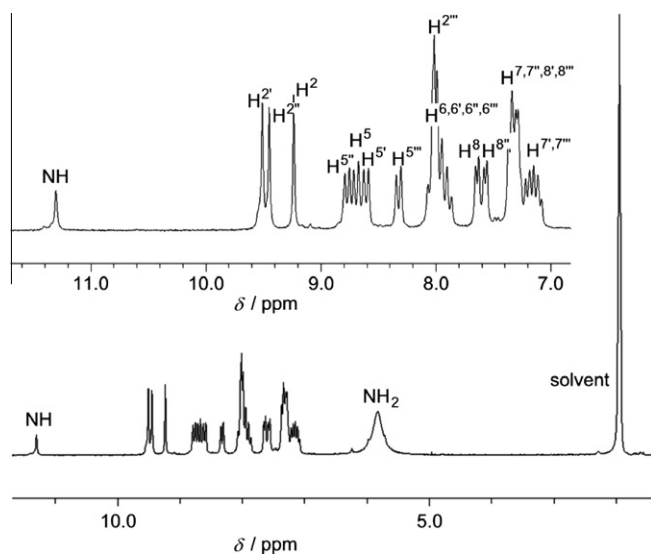


Fig. 2. ^1H NMR spectrum of **3b** in CD_3CN (bottom); aromatic region (top).

2.8. Oxidation of **3b**

A solution of **3b** (2.0×10^{-5} M) was titrated stepwise with a solution of $(\text{NH}_4)_2\text{Ce}(\text{NO}_3)_6$ (2.4×10^{-3} M). A solution of trifluoroacetic acid in acetonitrile (0.5 M) was used as solvent. During titration the colour of the solution turned from orange to yellowish brown. UV/Vis spectra revealed a decreasing band (MLCT) at 504 nm, an increasing band at 733 nm (LMCT) and isosbestic points at 436 and 583 nm.

3. Results and discussion

3.1. Syntheses of mono- and dinuclear amides

One challenge when using ruthenium amino acid **1b** or its ester **1a** in amide coupling reactions is the extremely poor nucleophilicity of the pyridylamine coordinated to the cationic ruthenium(II) center. We have tackled this problem by using a strong base to deprotonate the NH_2 group [9] or by employing highly reactive acid chlorides as acylating agents [18]. The mononuclear *N*-acetyl derivatives **2b** and **2a** [46] were prepared by acylation of the amino acid **1b** and its ester **1a**, respectively. The latter is acylated using acetic anhydride and activation of the unreactive amino group of **1a** by the phosphazene base $\text{P}_1\text{-tBu}$ (*tert*-butylimino-tris(dimethylamino)-phosphorane) [51,52] in 96% isolated yield [46] while amino acid **1b** is acylated by acetyl chloride in 51% isolated yield (Scheme 3). The Boc protected derivative **2c** is prepared by activation of **1a** with $\text{P}_1\text{-tBu}$ and reaction with Boc_2O (di-*tert*-butyl dicarbonate). As traces of water inevitably result in hydrolysis of the ester function under these alkaline conditions water was added on purpose after the Boc protection step and the carboxylate derivative **2c** was isolated in 93% yield and high purity (Scheme 3). **2c** is an excellent starting material for the construction of dinuclear ruthenium complexes from **1b** as the Boc group is compatible with the activation of NH_2 groups by strong bases.

When using amino acid ester **1a** as the amine part and a COOH -functionalized bis(terpyridine)ruthenium(II) complex without any further NH_2 group as the acid part no protection groups are necessary. Thus, coupling of **1a** with $[\text{Ru}(\text{tpy-C}_6\text{H}_4\text{-COOH})(\text{tBu}_3\text{tpy})](\text{PF}_6)_2$ [47] (tBu_3tpy = 4,4',4''-tri-*tert*-butyl-2,2':6',2''-terpyridine) is accomplished by activation of **1a** with $\text{P}_1\text{-tBu}$ and activation of

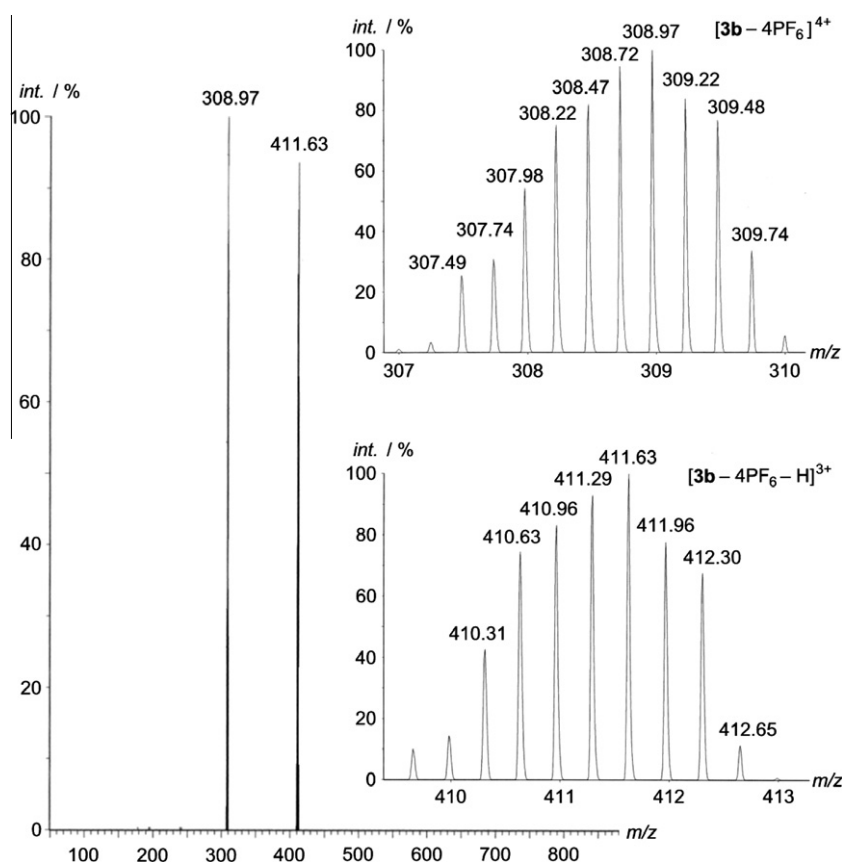


Fig. 3. ESI^+ mass spectrum of **3b** and isotopic pattern of relevant peaks.

Table 1
Optical properties of mononuclear **2a**, **2b**, **2c** and dinuclear **3a** and **3b** in CH₃CN at room temperature.

	Abs: λ_{max} (nm) ($\epsilon/\text{M}^{-1}\text{cm}^{-1}$)	Emission: λ_{max} (nm)	$\Phi \times 10^4$	τ/ns (%) ^a
2a	491 (21 600) [46]	690 [46]	16 [46]	21.7 (100) [46]
2b	493 (22 210)	699	13	21.3 (95) 4.1 (5)
2c	489 (19 990)	699	1.0	20.9 (92) 1.1 (8)
3a	496 (46 550)	692	14	21.6 (100)
3b	522 (50 620)	750	16	22.4 (99) 1.8 (1)

^a λ_{exc} = 500 nm.

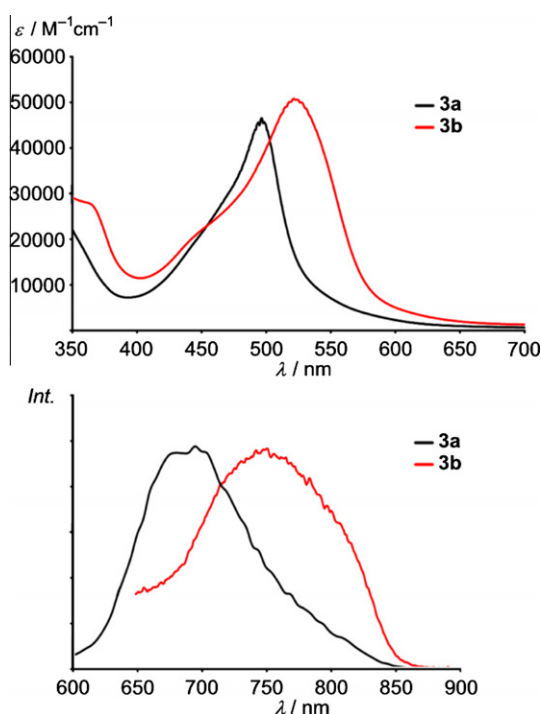


Fig. 4. Absorption spectra (top) and emission spectra (bottom) of **3a** and **3b** in CH₃CN at room temperature.

Table 2
Electrochemical data of **2a**, **2c**, **3a** and **3b** in *n*Bu₄NPF₆/CH₃CN at room temperature.

	E_{ox}^a (V)	$E_{\text{p,red}}^{a,b}$ (V)
2a	1.25	−1.15; −1.73
2c	1.27	−1.39; −1.66
3a	1.18; 1.28	−1.11; −1.24; −1.57; −1.87
3b	1.06; 1.29	−1.10; −1.32; −1.53

^a vs. SCE; $E_{1/2}(\text{FcH}/\text{FcH}^+) = 0.38$ V.

^b Pseudoreversible or irreversible reductions; peak potential given.

the acid by DCC/HOBt (DCC = *N,N'*-dicyclohexylcarbodiimide, HOBt = 1-hydroxybenzotriazole) to give dinuclear **3a** in 46% isolated yield (Scheme 4).

More challenging is the amide coupling of **1a** and **2c**. Activation of the carboxylate group of **2c** as benzotriazole ester requires slightly acidic conditions when using the standard DCC/HOBt protocol but these conditions would result in Boc deprotection. However, installing an acid-stable but base-labile Fmoc group (Fmoc = fluorenylmethoxycarbonyl) instead of Boc is prohibited as the coupling conditions with **1a** require a strong base. This dilemma is circumvented by using PyBOP (benzotriazole-1-yl-

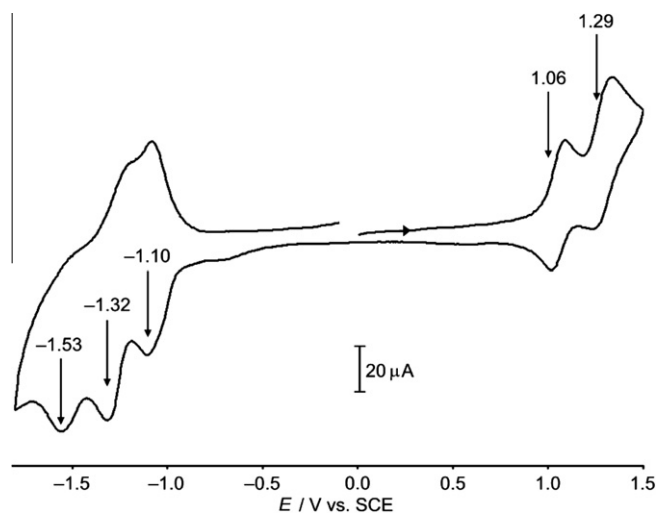


Fig. 5. Cyclic voltammogram of **3b** in CH₃CN/*n*Bu₄NPF₆.

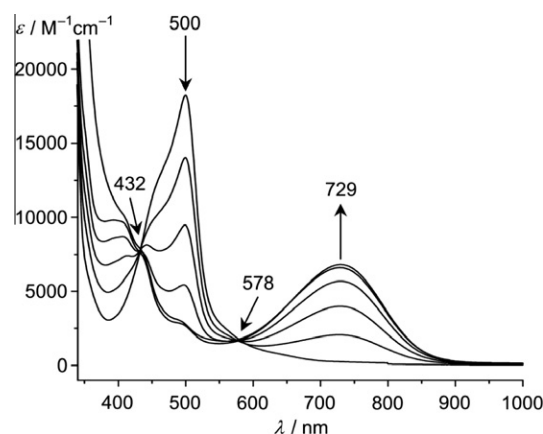


Fig. 6. UV/Vis/NIR spectra of **1b** during oxidation with Ce^{IV} in 0.5 M TFA/CH₃CN.

oxy-tris-pyrrolidino-phosphonium hexafluorophosphate) as the carboxylate activating agent for **2c** as PyBOP is compatible with the carboxylate group (Scheme 5). Thus the amino group of **1a** is activated by P₁-tBu and the carboxylate group of **2c** is activated by PyBOP to give a fully protected dinuclear complex. Addition of water hydrolyzes the ester of the dinuclear complex and acidification with acetic acid removes the Boc group giving fully deprotected **3b** in 82% overall yield (Scheme 5).

3.2. Characterization of mono- and dinuclear amides

The successful amide coupling reactions yielding the mononuclear complexes **2a–2c** are easily evidenced in the proton NMR spectra of the acetyl derivatives **2a** and **2b** as the resonances of the protons H2' are significantly shifted to lower field by about one ppm as compared to those of the starting materials **1a/1b** [9] (see Scheme 3 for atom numbering). The amide protons of **2a/2b** resonate around $\delta = 9.4$ ppm and the protons of the methyl group H9' at $\delta = 2.37$ ppm. The Boc protected derivative **2c** is characterized by the carbamate NH resonance at $\delta = 10.30$ ppm, the signal of the *tert*-butyl protons H9' at $\delta = 1.68$ ppm and the downfield shifted H2' proton resonances at $\delta = 9.26$ ppm. All other proton resonances are found at typical chemical shifts. In these mononuclear complexes the ¹³C resonances are easily assigned by CH-correlation spectroscopy (see Section 2). The FAB⁺ mass spectra

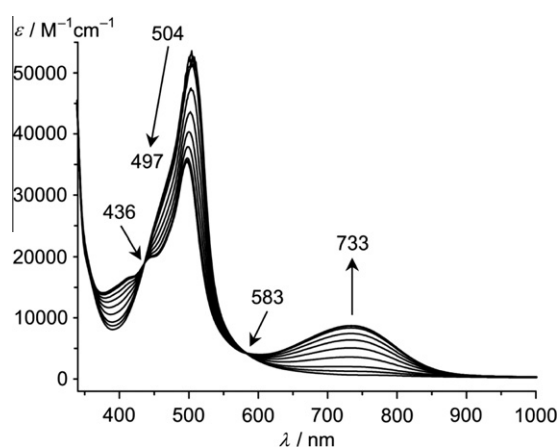


Fig. 7. UV/Vis/NIR spectra of **3b** during oxidation with Ce^{IV} in 0.5 M TFA/ CH_3CN .

of **2b** and **2c** show peaks for the compounds devoid of one hexafluorophosphate counter ion (see Section 2). As the complexes **2a–2c** tend to adsorb water (see Section 2) the IR spectra are little informative concerning characteristic NH stretching frequencies. However, characteristic group frequencies are observed for CH_{aryl} , CH_{alkyl} , $\text{C}=\text{O}$, amide I, amide II, $\text{C}-\text{O}$ and $\text{P}-\text{F}$ stretching vibrations of **2b** and **2c** (see Section 2).

As expected the ^1H NMR spectra of the dinuclear species **3a** and **3b** are somewhat more complicated and many multiplet signals are overlapping. However, 2D correlation spectroscopy allowed assigning all signal groups (Figs. 1 and 2). The amide resonances are found at $\delta = 10.07$ ppm (**3a**) and $\delta = 11.30$ ppm (**3b**) and the characteristic $\text{H}2'$ resonances are observed at $\delta = 9.33$ ppm (**3a**) and $\delta = 9.51$ ppm (**3b**). In the high field region **3a** shows the expected triplet/quartet pattern for the ethyl ester at $\delta = 1.59$ ppm and $\delta = 4.64$ ppm as well as the singlet resonances for the different *tert*-butyl groups of the terpyridine ligand at $\delta = 1.77$ ppm and $\delta = 1.33$ ppm. The amine protons of fully deprotected **3b** resonate at $\delta = 5.83$ ppm.

The ESI + mass spectra of the dinuclear complexes **3a** and **3b** display signals corresponding to quadruply charged $[\text{M}]^{4+}$ ions and triply charged $[\text{M}-\text{H}]^{3+}$ ions with correct isotopic patterns and signal spacings of $\Delta(m/z) = 0.25$ (tetracation) and $\Delta(m/z) = 0.33$ (trication) confirming the product identity and purity (Fig. 3).

IR spectroscopy confirms the presence of aliphatic CH groups in **3a** (ethyl, *tert*-butyl) and the absence of aliphatic CH groups in fully deprotected **3b**. Characteristic signatures of expected functional groups (CO , amide, PF ; see Section 2) further corroborate the constitution of **3a** and **3b**.

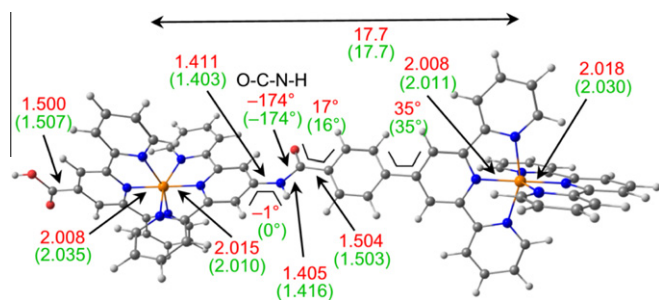


Fig. 8. Relevant DFT calculated metrical parameters of a model of **3a** (red) and $[\mathbf{3a}]^+$ (green, in parentheses) (distances in Å). (For interpretation of the references to colour in this figure legend, the reader is referred to the web version of this article.)

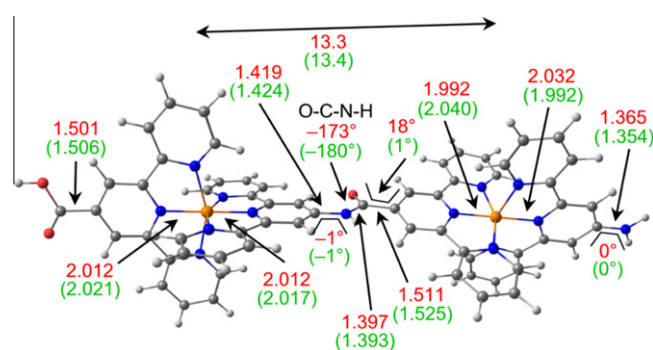


Fig. 9. Relevant DFT calculated metrical parameters of a model of **3b** (red) and $[\mathbf{3b}]^+$ (green, in parentheses) (distances in Å). (For interpretation of the references to colour in this figure legend, the reader is referred to the web version of this article.)

3.3. Optical and redox properties of mono- and dinuclear amides

The mononuclear bis(terpyridine)ruthenium(II) complexes **2a–2c** display the expected $^1\text{MLCT}$ absorption band at around $\lambda_{\text{max}} = 490$ nm ($\epsilon \approx 20\,000 \text{ M}^{-1} \text{ cm}^{-1}$) slightly hypsochromically shifted relative to the maximum of the amino acid **1b** and its ester **1a** [9,46]. For the dinuclear complexes **3a** and **3b** the extinction coefficients are more than twice as large (Table 1, Fig. 4). For **3b** a significant bathochromic shift of the $^1\text{MLCT}$ absorption band to $\lambda_{\text{max}} = 522$ nm is noted, together with a strong hyperchromic effect (Table 1). Thus, the optical properties of **3b** appear not as a simple superposition of individual spectra (e.g. of amide **2b** and ester **1a**). A straightforward explanation would be a cooperative effect of the electron donating character of the NH_2 group paired with the strong electron accepting character of the amide linked cationic bis(terpyridine)ruthenium(II) moiety (push–pull chromophore). In **3a** the electron donating effect of *tert*-butyl substituents is weaker than that of an NH_2 group and the electron accepting effect of the attached $[\text{Ru}(\text{tpy})_2]^{2+}$ unit is attenuated by the additional *para*-phenylene spacer resulting in unremarkable absorption properties.

In contrast to the parent $[(\text{tpy})_2\text{Ru}]^{2+}$ complex all compounds **2** and **3** show room temperature emission around $\lambda_{\text{max}} \approx 700$ nm in CH_3CN due to the favorable donor–acceptor substitution pattern [46,53]. The emission of **3b** is bathochromically shifted to 750 nm parallel to its low-energy absorption maximum (Table 1, Fig. 4). All compounds feature similar quantum yields (except for the carboxylate derivative **2c**, see Table 1) and $^3\text{MLCT}$ excited state lifetimes $\tau \approx 20$ ns. For carboxylic acids and carboxylate compounds **2b**, **2c** and **3b** a biexponential decay is observed which might be a result of an additional deactivation pathway to a non-emissive state, e.g. by excited state proton transfer [54,55]. Biexponential rate laws have been observed consistently in several luminescent COOH substituted derivatives of bis(terpyridine) ruthenium(II) complexes [12,18].

The cyclic voltammograms of mononuclear **2a** and **2c** (the poor solubility of the acid **2b** prevented recording of reliable CVs) show very similar reversible $\text{Ru}^{\text{II}}/\text{Ru}^{\text{III}}$ couples at ca. 1.26 V versus SCE, similar to comparable systems [53]. Two couples (pseudoreversible or irreversible) are assigned to terpyridine reductions (Table 2). The dinuclear complexes **3a** and **3b** can be oxidized twice (Fig. 5) – first at a lower potential round 1.1 V versus SCE and secondly at around 1.28 V versus SCE. The difference in oxidation potentials (0.10 V for **3a** and 0.23 V for **3b**) can be largely ascribed to the different substitution pattern and is not necessarily a sign of electronic communication or electrostatic interaction of the metal sites. However, electronic communication of the redox sites in **3b** cannot be excluded at this stage of the investigation and spectroscopic and theoretical investigations were performed.

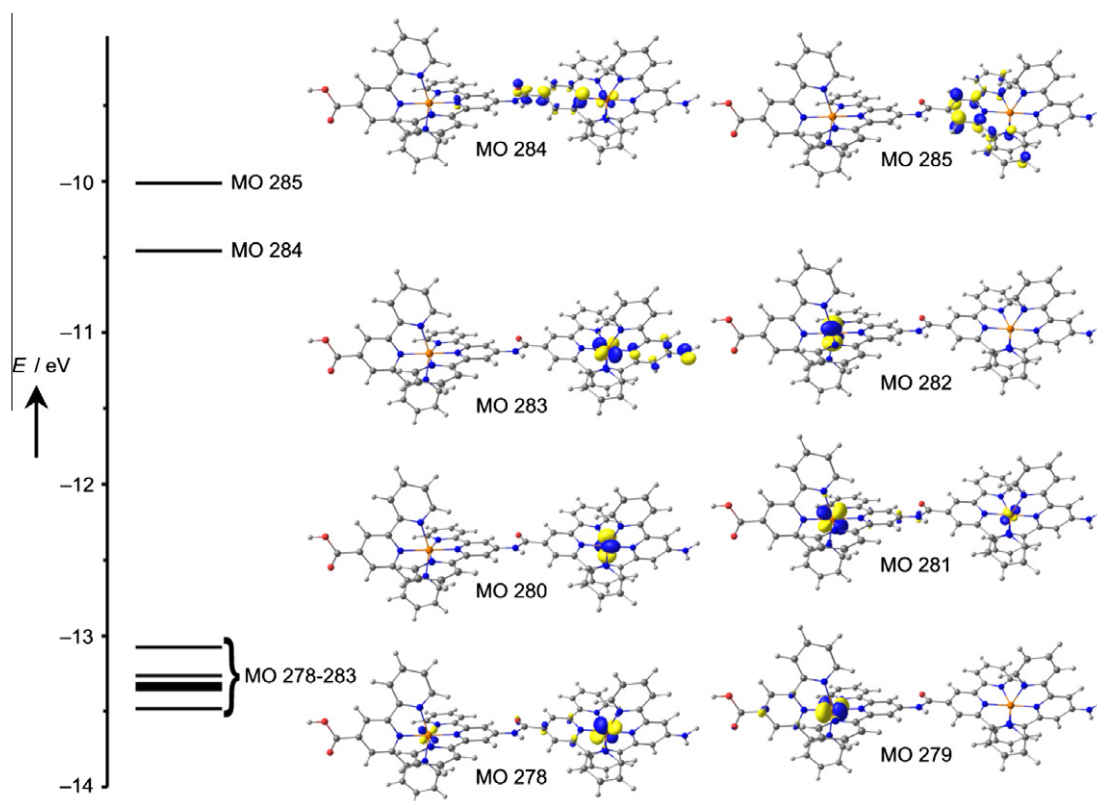


Fig. 10. MO scheme of **3b** (contour level 0.07 a.u.).

3.4. Oxidation to mixed-valent cations

In order to elucidate a possible electronic communication between ruthenium centers **3b** was titrated with diammonium cerium(IV) hexanitrates ($(\text{NH}_4)_2\text{Ce}(\text{NO}_3)_6$) in 0.5 M TFA/ CH_3CN solution. The potential of Ce^{IV} could be sufficient for the oxidation of Ru^{II} depending on the solvent employed ($E_{1/2}(\text{HClO}_4) = 1.3 \text{ V}$, $E_{1/2}(\text{H}_2\text{O}) = 0.88 \text{ V}$ versus FcH/FcH^+) [56]. For comparison the acetylated derivative **2b** and the amino acid **1b** were also treated with Ce^{IV} under the same conditions. The extremely weak basic amine function of **1b** is not protonated under these conditions [9]. In order to observe possible IVCT bands UV/Vis/NIR spectra were recorded during oxidation.

The *N*-acetylated derivative **2b** is resistant towards oxidation with Ce^{IV} under these conditions as its MLCT absorption band ($\lambda_{\text{max}} = 492 \text{ nm}$, $\epsilon = 18\,230 \text{ M}^{-1} \text{ cm}^{-1}$) remains unchanged upon addition of up to 7.2 equivalents Ce^{IV} and no new bands arise.

The amino acid **1b**, however, is oxidized by Ce^{IV} ions to the corresponding green Ru^{III} complex **[1b]⁺**. The MLCT band of **1b** ($\lambda_{\text{max}} = 500 \text{ nm}$, $\epsilon = 18\,230 \text{ M}^{-1} \text{ cm}^{-1}$) decays while a new LMCT band (**[1b]⁺**) at 729 nm ($\epsilon = 6810 \text{ M}^{-1} \text{ cm}^{-1}$) rises (Fig. 6). Isosbestic points are observed at 432 and 578 nm. The oxidation has to be done quite fast as the TFA solution of **[1b]⁺** changes with time (within hours). The nature of this slow reaction of **[1b]⁺** and the products are currently investigated in greater detail.

The data show that the amino functionalized Ruthenium complex **1b** can be oxidized by Ce^{IV} while the amido functionalized Ruthenium complex **2b** is resistant towards Ce^{IV} oxidation. Thus, it is expected that Ce^{IV} oxidizes the dinuclear NH_2 substituted complex **3b** only once – namely at the *N*-terminal end. Treating **3b** with Ce^{IV} in 0.5 M TFA solution decreases the MLCT absorption band at 504 nm from $\epsilon = 52\,690$ to $35\,350 \text{ M}^{-1} \text{ cm}^{-1}$ (now at 497 nm) and a new LMCT band at 733 nm ($\epsilon = 8720 \text{ M}^{-1} \text{ cm}^{-1}$) rises (Fig. 7). Two isosbestic points are observed at 436 and 583 nm. Addition of excess Ce^{IV}

does not further change the spectrum. Thus, the data supports the interpretation that the tetracation of **3b** is oxidized to the mixed-valent pentacation **[3b]⁺** by Ce^{IV} . No bands assignable to intervalence charge transfer bands (IVCT) are observed up to 3000 nm for **[3b]⁺**. The UV/Vis/NIR data allow us to describe the mixed-valent cation **[3b]⁺** as largely localized system (Class I) as no IVCT could be observed. The valence trapping is likely due to the quite substantial redox asymmetry at the *N*- and *C*-terminal site (estimated as 0.15 – 0.20 V from mononuclear model compounds).

Similarly, **3a** has been oxidized to **[3a]⁺** by Ce^{IV} . During oxidation isosbestic points are observed at 418 and 574 nm . The LMCT band of **[3a]⁺** is found at 705 nm together with a remaining MLCT band at 492 nm , very similar to the observations made during the **3b** \rightarrow **[3b]⁺** oxidation. Up to 3000 nm no bands attributable to IVCT have been observed also suggesting trapped valences in **[3a]⁺**.

3.5. Theoretical calculations

The ground state geometric structures of models of the dinuclear complex tetracations **3a** and **3b** were optimized at the B3LYP/LanL2DZ level and the calculated molecular structures are depicted in Fig. 8 and 9. In order to save computational costs the alkyl periphery of **3a** (*tert*-butyl and ethyl groups) has been replaced by hydrogen atoms in the model complex. The Ru–Ru distance increases from 13.4 \AA in **3b** to 17.7 \AA in **3a** due to the additional *para*-phenylene spacer. The calculations show that the amide linker in **3b** is almost perfectly planar and also co-planar to both adjacent pyridine rings so that π -conjugation is principally possible. In **3a**, however, the *para*-phenylene spacer is twisted relative to the amide plane by 17° and also relative to the pyridine plane by 35° suggesting only poor π -orbital overlap (Fig. 8).

The molecular orbital schemes of **3a** and **3b** are depicted in Fig. S1 (Supporting Information) and Fig. 10. The occupied “ t_{2g} ” orbitals of both ruthenium sites are well separated from the π^*

terpyridine orbitals in both dinuclear systems. The highest occupied molecular orbital is centered on the C-terminal site for **3a** (see Supporting Information; MO 297–299) and on the N-terminal site for **3b** (MO 283, Fig. 10) suggesting differing sites of oxidation for **3a** and **3b**. The participation of the nitrogen p-orbital in the HOMO of amino-substituted ruthenium complex **1b** has been previously suggested on the basis of Resonance Raman spectroscopic results.[46] This feature is also seen here for **3b** (MO 283, Fig. 10). Fully analogous observations have been made for amino substituted free-base porphyrins and zinc(II) porphyrinato complexes [57]. In order to clarify the site of oxidation (N-terminus, C-terminus) open-shell calculations on the oxidized complexes **[3a]⁺** and **[3b]⁺** have been performed.

No dramatic metrical changes are observed in the redox pairs **3a**/**[3a]⁺** and **3b**/**[3b]⁺** (Figs. 8 and 9) which is within expectation for Ru^{III} complexes with polypyridine ligands.[50] For the **3a**/**[3a]⁺** model some differences in Ru–N(py) distances are calculated at the C-terminal site (from 2.008 to 2.035 Å) while for **3b**/**[3b]⁺** two Ru–N(py) distances at the N-terminal site are influenced (from 1.992 to 2.040 Å and from 2.032 to 1.992 Å). In addition, the C–N(amine) bond length varies from 1.365 to 1.354 Å, similar to the changes calculated for the pair **1b**/**[1b]⁺** (Fig. S2, Supporting Information).

These DFT data suggest that the site of oxidation is mainly localized on the “C-terminal” ruthenium complex in the model of **3a** and on the “N-terminal” ruthenium site in **3b**. In amine substituted Ru^{III} complexes **[3b]⁺** and **[1b]⁺** a significant part of the additional positive charge is delocalized onto the NH₂ substituent strengthening the intrinsic iminium-like structure. This [Ru^{II}–{Ru^{III}–NH₂}]⁵⁺/[Ru^{II}–{Ru^{II}=N⁽⁺⁾H₂}]⁵⁺ description supports the class I assignment based on spectroscopic data (see Section 3.4).

4. Conclusions

Asymmetrically substituted dinuclear terpyridine ruthenium complexes **3a** and **3b** have been synthesized by amide coupling with Ru···Ru distances of 17.7 and 13.4 Å, respectively. The differences in the local redox potentials in the dinuclear complexes should increase the barrier for (thermal and optical) electron transfer in singly oxidized mixed-valent complexes. In the mixed-valent complex **[3b]⁺** with relatively small Ru···Ru distance and a rather planar bridging ligand no communication is observed by spectroscopic analysis. This finding is likely due to the redox asymmetry (ca. 0.15–0.20 V) featured in these systems with directional amide units. Future studies will focus on systems based on ruthenium amino acids with less differing redox potentials, e.g. by adjusting the substituents to –C(O)–NHR at the C-terminus and to NH–C(O)R at the N-terminus. This should result in similar redox potentials of the individual ruthenium centers due to the similar substitution pattern [(RHN–(O)C–tpy)Ru(tpy–NHC(O)–tpy)Ru(tpy–NHC(O)R)]⁴⁺ but simultaneously preserve the directionality of oligoamides and peptides (N-terminus/C-terminus).

Acknowledgments

This work was financially supported by the Deutsche Forschungsgemeinschaft (Grant No. HE 2778/5-1). We thank Prof. Dr. Sven Rau for the generous donation of a sample of [Ru(tpy–C₆H₄–COOH)(tBu₃tpy)](PF₆)₂.

Appendix A. Supplementary material

Supplementary data associated with this article can be found, in the online version, at doi:10.1016/j.ica.2011.03.046.

References

- [1] S. Campagna, G. Denti, S. Serroni, M. Ciano, A. Juris, V. Balzani, *Inorg. Chem.* 31 (1992) 2982.
- [2] K.O. Johansson, J.A. Lotoski, C.C. Tong, G.S. Hanan, *Chem. Commun.* (2000) 819.
- [3] Y.-Q. Fang, M.I.J. Polson, G.S. Hanan, *Inorg. Chem.* 42 (2003) 5.
- [4] M.I.J. Polson, F. Loiseau, S. Campagna, G.S. Hanan, *Chem. Commun.* (2006) 1301.
- [5] K. Heinze, M. Beckmann, K. Hempel, *Chem. Eur. J.* 14 (2008) 9468.
- [6] U.S. Schubert, H. Hofmeier, G.R. Newkome, *Modern Terpyridine Chemistry*, Wiley-VCH, 2006.
- [7] H. Hofmeier, U.S. Schubert, *Chem. Soc. Rev.* 33 (2004) 373.
- [8] W.C. Chan, P.D. White (Eds.), *Fmoc Solid Phase Peptide Synthesis*, Oxford University Press, Oxford, 2000.
- [9] K. Heinze, K. Hempel, M. Beckmann, *Eur. J. Inorg. Chem.* (2006) 2040.
- [10] K. Heinze, U. Wild, M. Beckmann, *Eur. J. Inorg. Chem.* (2007) 617.
- [11] K. Heinze, M. Schlenker, *Eur. J. Inorg. Chem.* (2005) 66.
- [12] K. Heinze, K. Hempel, A. Breivogel, *Z. Anorg. Allg. Chem.* 635 (2009) 2541.
- [13] L. Barišić, V. Rapić, V. Kovač, *Croat. Chem. Acta* 75 (2002) 199.
- [14] K. Heinze, M. Schlenker, *Eur. J. Inorg. Chem.* (2004) 2974.
- [15] D. Siebler, M. Linseis, T. Gasi, L.M. Carrella, R.F. Winter, C. Förster, K. Heinze, *Chem. Eur. J.* 17 (2011) 4540.
- [16] K. Heinze, D. Siebler, *Z. Anorg. Allg. Chem.* 633 (2007) 2223.
- [17] D. Siebler, C. Förster, K. Heinze, *Eur. J. Inorg. Chem.* (2010) 523.
- [18] K. Heinze, K. Hempel, *Chem. Eur. J.* 15 (2009) 1346.
- [19] V. Balzani, A. Juris, M. Venturi, S. Campagna, S. Serroni, *Chem. Rev.* 96 (1996) 759.
- [20] J.-P. Sauvage, J.-P. Collin, J.-C. Chambrun, S. Guillerez, C. Coudret, V. Balzani, F. Barigelli, L. De Cola, L. Flamigni, *Chem. Rev.* 94 (1994) 993.
- [21] C. Creutz, *Prog. Inorg. Chem.* 30 (1983) 1.
- [22] D.E. Richardson, H. Taube, *Coord. Chem. Rev.* 60 (1984) 107.
- [23] R.J. Crutchley, *Adv. Inorg. Chem.* 41 (1994) 273.
- [24] M.D. Ward, *Chem. Soc. Rev.* 24 (1995) 121.
- [25] D. Astruc, *Acc. Chem. Res.* 30 (1997) 383.
- [26] J.A. McCleverty, M.D. Ward, *Acc. Chem. Res.* 31 (1998) 842.
- [27] W. Kaim, A. Klein, M. Göckle, *Acc. Chem. Res.* 33 (2000) 755.
- [28] K.D. Demadis, C.M. Hartshorn, T.J. Meyer, *Chem. Rev.* 101 (2001) 2655.
- [29] J.-P. Launay, *Chem. Soc. Rev.* 30 (2001) 386.
- [30] B.S. Brunschwig, C. Creutz, N. Sutin, *Chem. Soc. Rev.* 31 (2002) 168.
- [31] J.T. Hupp, in: J.A. McCleverty, T.J. Meyer (Eds.), *Comprehensive Coordination Chemistry II*, Elsevier Science, Amsterdam, 2003, p. 709.
- [32] R.J. Crutchley, in: J.A. McCleverty, T.J. Meyer (Eds.), *Comprehensive Coordination Chemistry II*, Elsevier Science, Amsterdam, 2003, p. 235.
- [33] D.M. D'Alessandro, F.R. Keene, *Chem. Soc. Rev.* 35 (2006) 424.
- [34] D.M. D'Alessandro, F.R. Keene, *Chem. Rev.* 106 (2006) 2270.
- [35] (a) W. Kaim, G.K. Lahiri, *Angew. Chem.* 119 (2007) 1808; (b) W. Kaim, G.K. Lahiri, *Angew. Chem., Int. Ed.* 46 (2007) 1778.
- [36] W. Kaim, B. Sarkar, *Coord. Chem. Rev.* 251 (2007) 584.
- [37] M.B. Robin, P. Day, *Adv. Inorg. Chem. Radiochem.* 10 (1968) 247.
- [38] C. Creutz, H. Taube, *J. Am. Chem. Soc.* 91 (1969) 3988.
- [39] C. Creutz, H. Taube, *J. Am. Chem. Soc.* 95 (1973) 1086.
- [40] G.D. Storrer, S.B. Colbran, *Inorg. Chim. Acta* 284 (1999) 76.
- [41] T. Okamura, T. Iwamura, S. Seno, H. Yamamoto, N. Ueyama, *J. Am. Chem. Soc.* 126 (2004) 15972.
- [42] E.C. Constable, M.D. Ward, *J. Chem. Soc., Dalton Trans.* (1990) 1405.
- [43] J.-P. Collin, P. Lainé, J.-P. Launay, J.-P. Sauvage, A. Sour, *J. Chem. Soc., Chem. Commun.* (1993) 434.
- [44] S. Vaduvescu, P.G. Potvin, *Inorg. Chem.* 41 (2002) 4081.
- [45] A.C. Benniston, A. Harriman, P. Li, C.A. Sams, M.D. Ward, *J. Am. Chem. Soc.* 126 (2004) 13630.
- [46] K. Heinze, K. Hempel, S. Tschierlei, M. Schmitt, J. Popp, S. Rau, *Eur. J. Inorg. Chem.* (2009) 3119.
- [47] A sample of this ruthenium(II) complex has been kindly donated by Prof. Dr. Sven Rau, University of Erlangen–Nürnberg, Germany.
- [48] J.V. Caspar, T.J. Meyer, *J. Am. Chem. Soc.* 105 (1983) 5583.
- [49] M.J. Frisch, G.W. Trucks, H.B. Schlegel, G.E. Scuseria, M.A. Robb, J.R. Cheeseman, J.A. Montgomery Jr., T. Vreven, K.N. Kudin, J.C. Burant, J.M. Millam, S.S. Iyengar, J. Tomasi, V. Barone, B. Mennucci, M. Cossi, G. Scalmani, N. Rega, G.A. Petersson, H. Nakatsuji, M. Hada, M. Ehara, K. Toyota, R. Fukuda, J. Hasegawa, M. Ishida, T. Nakajima, Y. Honda, O. Kitao, H. Nakai, M. Klene, X. Li, J.E. Knox, H.P. Hratchian, J.B. Cross, C. Adamo, J. Jaramillo, R. Gomperts, R.E. Stratmann, O. Yazyev, A.J. Austin, R. Cammi, C. Pomelli, J.W. Ochterski, P.Y. Ayala, K. Morokuma, G.A. Voth, P. Salvador, J.J. Dannenberg, V.G. Zakrzewski, S. Dapprich, A.D. Daniels, M.C. Strain, O. Farkas, D.K. Malick, A.D. Rabuck, K. Raghavachari, J.B. Foresman, J.V. Ortiz, Q. Cui, A.G. Baboul, S. Clifford, J. Cioslowski, B.B. Stefanov, G. Liu, A. Liashenko, P. Piskorz, I. Komaromi, R.L. Martin, D.J. Fox, T. Keith, M.A. Al-Laham, C.Y. Peng, A. Nanayakkara, M. Challacombe, P.M.W. Gill, B. Johnson, W. Chen, M.W. Wong, C. Gonzalez, J.A. Pople, *GAUSSIAN 03*, Revision B.03, Gaussian, Inc., Pittsburgh PA, 2003.
- [50] M. Biner, H.-B. Bürgi, A. Ludi, C. Röhr, *J. Am. Chem. Soc.* 114 (1992) 5197.
- [51] (a) R. Schwesinger, C. Hasenfratz, H. Schlemper, L. Walz, E.-M. Peters, K. Peters, H.G. von Schnering, *Angew. Chem.* 105 (1993) 1420; (b) R. Schwesinger, C. Hasenfratz, H. Schlemper, L. Walz, E.-M. Peters, K. Peters, H.G. von Schnering, *Angew. Chem., Int. Ed.* 32 (1993) 1361.

- [52] R. Schwesinger, Nachr. Chem. Tech. Lab. 38 (1990) 1214.
- [53] M. Maestri, N. Armaroli, V. Balzani, E.C. Constable, A.M.W. Cargill Thompson, Inorg. Chem. 34 (1995) 2759.
- [54] G. Ulrich, F. Nastasi, P. Retailleau, F. Puntoriero, R. Ziessel, S. Campagna, Chem. Eur. J. 14 (2008) 4381.
- [55] C. Turro, S.H. Bossmann, Y. Jenkins, J.K. Barton, N.J. Turro, J. Am. Chem. Soc. 117 (1995) 9026.
- [56] N.G. Connelly, W.E. Geiger, Chem. Rev. 96 (1996) 877.
- [57] K. Heinze, A. Reinhart, Dalton Trans. (2008) 469.

9.4 Light-induced Charge Separation in a Donor-Chromophore-Acceptor Nanocomposite Poly[TPA-Ru(tpy)₂]@ZnO

L. zur Borg, A. L. Domanski, A. Breivogel, M. Bürger, R. Berger, K. Heinze, R. Zentel, *J. Mater. Chem. C* **2013**, *1*, 1223–1230.

DOI: 10.1039/c2tc00535b

Reprinted with permission from The Royal Society of Chemistry, Copyright © 2013.

Light-induced charge separation in a
donor–chromophore–acceptor nanocomposite
poly[TPA-Ru(tpy)₂]@ZnO†Cite this: *J. Mater. Chem. C*, 2013, **1**,
1223Lisa zur Borg,^a Anna L. Domanski,^{‡b} Aaron Breivogel,^{‡c} Mareike Bürger,^a
Rüdiger Berger,^b Katja Heinze^{*c} and Rudolf Zentel^{*a}

The synthesis and characterisation of a new donor–chromophore–acceptor system based on poly(vinyltriphenylamine) as the electron donor and a glycine-functionalised bis(2,2';6',2''-terpyridine) ruthenium(II) complex acting both as a chromophore and as an anchor group attached to ZnO nanorods as the electron acceptor are described. The TPA-containing block copolymer was synthesised by Reversible Addition Fragmentation Chain Transfer (RAFT) polymerisation and the ruthenium complex glycine conjugates prepared by Solid Phase Peptide Synthesis (SPPS) were attached *via* post-polymerisation esterification. GPC, NMR, IR and UV-Visible spectroscopy were used to characterise the multifunctional chromophore–donor polymer. Zinc oxide nanorods were functionalised with the block copolymer by multisite adsorption *via* the glycine COOH groups. The functionalised nanoparticles were well dispersible in organic solvents. Photoluminescence studies showed a complete quenching of the phosphorescence of the ruthenium chromophore (³MLCT state). Kelvin probe force microscopy (KPFM) was used to confirm that under continuous excitation of the Ru^{II} complex (¹MLCT) the polymer corona develops a positive charge and thus efficient charge separation between ZnO and the polymer is achieved.

Received 31st October 2012
Accepted 29th November 2012

DOI: 10.1039/c2tc00535b

www.rsc.org/MaterialsC

Introduction

Since O'Regan and Grätzel reported the first dye-sensitised solar cells (DSSCs) in 1991,¹ much effort has been devoted to enhancing their efficiency. The benefit to our environment is obvious, but the DSSCs suffer from the possibility of leaking of the I₃[−]/I[−] hole conductor dissolved in a liquid solvent. To avoid leaking, solid state dye-sensitised solar cells (ssDSSCs) were introduced in 1996.² Oligoethylene glycol methacrylate doped with lithium ions was used as a p-type conductor. In the following years, different polymers were used to improve the efficiency.^{3,4} Conducting polymers like poly(vinyltriphenylamine) (PTPA), poly(*para*-phenylene vinylene) (PPV) or poly-

(3-hexylthiophene) (P3HT) have been used as hole transporting layers.⁵ Transient absorption spectroscopy studies showed that the dye regeneration in ssDSSCs was at least one order of magnitude faster than in conventional DSSCs. However, the efficiencies of ssDSSCs remained low. The major drawback in this system is the low penetration rate of the polymer within the mesoporous film of TiO₂ nanoparticles. Several approaches were reported to increase the penetration. P3HT with carboxylate end groups has been synthesised and was used as a sensitizer in ssDSSCs.⁶ A higher adsorption of the polymer onto the TiO₂ was observed compared to methyl terminated P3HT. Oligotriarylamine groups were directly bound to ruthenium(II) polypyridine dyes, enhancing the contact between the donor and the chromophore.^{7–11} Furthermore, it has been shown that these systems show higher extinction coefficients compared to standard polypyridine complexes.¹² To further improve the ssDSSCs, a tris(2,2'-bipyridine) ruthenium(II) dye was incorporated directly inside a hole transporting PTPA and indeed these devices showed enhanced performances.¹³ However, they carry only a single ruthenium(II) complex within each polymer chain. To increase the amount of the chromophore in each polymeric chain, block copolymers with the first block based on a semi-conducting PTPA and a second block with perylene units as chromophores and separated dopamine units as anchor groups were synthesised.¹⁴ These polymers were attached to ZnO nanorods and characterised by Kelvin probe force microscopy (KPFM) on the level of the individual nanoparticle. A negative

^aInstitute of Organic Chemistry, Johannes Gutenberg-University, Duesberweg 10-14, 55099 Mainz, Germany. E-mail: Zentel@uni-mainz.de; Fax: +49-6131-3924778; Tel: +49-6131-3920361

^bMax Planck Institute for Polymer Research, Ackermannweg 10, 55128 Mainz, Germany. E-mail: berger@mpip-mainz.mpg.de; Fax: +49-6131-379100; Tel: +49-6131-379114

^cInstitute of Analytical and Inorganic Chemistry, Johannes Gutenberg-University, Duesberweg 10-14, 55128 Mainz, Germany. E-mail: katja.heinze@uni-mainz.de; Fax: +49-6131-3927277; Tel: +49-6131-3925886

† Electronic supplementary information (ESI) available: FTIR of A, P2, P3a and P3b, ¹⁹F NMR spectra of P2 and P3a, AFM of P3a@ZnO and KPFM of P3b@ZnO, atom numbering of A used for NMR assignment, UV-vis spectrum of P3b. See DOI: 10.1039/c2tc00535b

‡ These authors contributed equally to this work.

charging of the inorganic nanoparticles and a positive charging of the polymer corona were observed upon laser irradiation.¹⁴ However, a more proximate contact of the dye with the ZnO is desirable for a more efficient electron injection.

Herein, we present the synthesis of a nanoscale donor–chromophore–acceptor (D–C–A) system with a PTPA based block copolymer carrying several directional bis(terpyridine) ruthenium(II) side groups in the second block. A carboxyl group is attached to each Ru^{II} dye which binds to the oxidic surface of ZnO nanorods. This allows for a large amount of dyes in proximity to the surface of the ZnO with the direct binding of the dye to the acceptor being beneficial for an efficient electron injection and charge separation. The TPA polymer acts as a hole transporting matrix and the directional ruthenium complexes act both as light harvesting units and as anchor groups. Upon irradiation into the dye MLCT absorption band, charges are created and separated, as proven by photoluminescence (PL) spectra and KPFM measurements.

Experimental

Materials

Unless otherwise mentioned, all chemical reagents were used as purchased without any further purification. Pentafluorophenol was obtained from Fluorochem (UK). Anhydrous THF and dioxane were freshly distilled from sodium. DMF was freshly distilled from calcium hydride and not exposed to light until it was used. 2,2'-Azobis(isobutyronitrile) (AIBN) was recrystallised from diethyl ether and stored at −18 °C. Diphenyl-(4-vinylphenyl)-amine^{15a} and ZnO nanorods^{15b} were synthesised as reported in the literature.

Instrumentation

¹H NMR spectra were recorded on a Bruker 300 MHz FT NMR spectrometer. Chemical shifts (δ) are given in parts per million relative to TMS. Samples were prepared in deuterated solvents and their signals referenced to residual nondeuterated solvent signals. ¹⁹F NMR spectra were recorded on a Bruker 400 MHz FT NMR spectrometer. The molecular weight of the polymers was determined by gel permeation chromatography (GPC) in THF as the solvent and with the following equipment: pump PU 1580, auto sampler AS1555, UV detector UV 1575 (detection at 254 nm), RI detector RI 1530 from JASCO. Columns were used from MZ-Analysentechnik: MZ-Gel SDplus 10 2 Å and MZ-Gel SDplus 10 6 Å. Calibration was done using polystyrene standards purchased from Polymer Standard Services. IR spectra were recorded on a Perkin-Elmer 100 FTIR spectrometer using an ATR unit. UV-Vis spectra were recorded using a Jasco V-630 spectrophotometer (1 cm × 1 cm quartz cell). Emission spectra were recorded on a Varian Cary Eclipse spectrometer. Quantum yields were calculated by comparing the areas under the emission spectra on an energy scale/cm^{−1} recorded for optically matched solutions of the sample and the reference [Ru(bpy)₃] Cl₂ = 0.094 in CH₃CN.¹⁶ ESI MS spectra were recorded on a Micromass Q-TOF-Ultima spectrometer. TEM pictures were taken on a Philips EM-420: 120 kV with a CCD-Camera.

KPFM measurements were performed at a MFP-3D stand-alone setup (Asylum Research, Santa Barbara). In order to prevent any degradation of the sample during the KPFM measurements the setup was placed in a glove box that was continuously purged with dry nitrogen (H₂O < 0.1%, O₂ < 0.01%). For simultaneous sample illumination during the KPFM measurement the setup was equipped with a diode laser (Point Source, iFLEX2000) with a wavelength of 488 nm, an intensity of 13.3 mW on the sample, and a spot diameter of 640 μm.^{17a} We used Pt/Ir coated cantilevers with a nominal vertical resonance frequency of 70 kHz (Nanosensors, PPP-EFM). The measurements were performed in the dual pass mode at a lift height of 5 nm and with an AC voltage of 1.5 V. In KPFM, the contact potential difference (CPD) is measured which is defined as the difference in the work function between the tip and sample. By using the amplitude modulation mode for KPFM both the tip apex and the cantilever contribute to the measured CPD.^{17b} Thus, local changes in the CPD are not exclusively related to the sample area underneath the tip apex but also to the one underneath the cantilever. In case the work function of the tip remains constant, it is possible to attribute changes in the measured CPD owing to sample illumination to changes in the surface potential of the sample.²⁰ However, studies on P3HT:PCBM blends have shown that the CPD changes significantly for consecutive scanning on the same position. These shifts of the measured CPDs can be attributed to changes in the cantilever tip, such as coating thickness and adsorbates. Thus, it is important to have one surface within the scan area that does not participate in the photo-induced reaction and can therefore serve as an internal reference.^{21,22} For sample preparation, glass substrates were coated with 100 nm of ITO (99.9%, MaTeck GmbH) and cleaned in Ar plasma (PDC-002, Harrick plasma) for 2 min prior to their usage. The ITO surface acted as a reference surface for the KPFM study. A highly diluted dispersion of **P3a@ZnO** in THF was spin cast on the substrates.

Synthesis of chromophore A

The ruthenium dye [(H₂N–CH₂–CONH–tpy)Ru(tpy–CONH–CH₂–COOH)](PF₆)₂ (**A**) was synthesised from [(H₂N–tpy)Ru(tpy–COOH)](PF₆)₂ according to a solid phase peptide synthesis procedure.^{18,19} After cleavage from the TentaGel S Wang solid phase chromophore **A** was precipitated as its PF₆ salt by adding aqueous NH₄PF₆ to give **A** as a dark red powder. $\nu_{\max}/\text{cm}^{-1}$ 3090w (=C–H), 2920w (C–H), 1717m (C=O(acid)), 1663m (amide I), 1603m (C=C stretching), 1528s (amide II), 1477s (C=C stretching), 1427s, 1354s, 1289s, 1260, 1095m, 1028s, 826vs (PF₆), 789s, 752s, 555s (see Fig. S1†). ¹H NMR: δ_{H} (600 MHz; CD₃CN; Me₄Si) 9.09 (s, 2H, H²), 9.05 (s, 2H, H^{2'}), 8.59 (s, 1H, NH^b), 8.59 (m, 2H, H⁵), 8.41 (m, 2H, H^{5'}), 8.16 (m, 1H, NH^a), 7.95 (m, 2H, H⁶), 7.93 (m, 2H, H^{6'}), 7.44 (m, 2H, H⁸), 7.31 (m, 2H, H^{8'}), 7.21 (m, 2H, H⁷), 7.12 (m, 2H, H^{7'}), 4.32–4.30 (m, 2H, CH₂^a), 4.32–4.30 (m, 2H CH₂^b), NH₂ not observed probably due to protonation (for atom numbering see ESI†). $\lambda_{\text{abs,max}}(\text{DMF})/\text{nm}$ ($\epsilon/\text{dm}^3 \text{mol}^{-1} \text{cm}^{-1}$) 279 (87 900, $\pi \rightarrow \pi^*$), 311 (72 600, $\pi \rightarrow \pi^*$), 498 (29 400, MLCT), $c = 0.09 \text{ mg mL}^{-1}$. $\lambda_{\text{em,max}}(\text{DMF})/\text{nm}$

667 ($\lambda_{\text{ex}}/\text{nm}$ 498). Quantum yield $\Phi = 1.4 \times 10^{-3}$. MS (ESI⁺): $m/z = 370.6$ (22%) [$\text{M} - (\text{PF}_6)_2$]²⁺, 886.1 (100%) [$\text{M} - \text{PF}_6$]⁺.

Synthesis of P1

Diphenyl-(4-vinyl-phenyl)-amine (1.71 g, 6.3 mmol), dithiobenzoic acid benzyl ester (6.6 mg, 0.03 mmol), and 2,2'-azobis(2-methylpropionitrile) (AIBN) (0.6 mg, 4.5 μmol) were placed in a Schlenk tube and equipped with a stir bar. Dioxane (9 mL) was added and the solution was degassed by three freeze-pump-thaw cycles. The flask was then immersed in a preheated oil bath at 75 °C and the polymerisation was carried out for 42 h. The polymer was precipitated in methanol, collected by centrifugation, redissolved in THF and reprecipitated in methanol. This procedure was repeated three times. The light yellow powder **P1** (540 mg, 32%) was dried at 45 °C under reduced pressure for 12 h. $\lambda_{\text{max}}(\text{THF})/\text{nm}$ 300 ($\epsilon/\text{dm}^3 \text{ mol}^{-1} \text{ cm}^{-1}$ 205 800, $c = 0.13 \text{ mg mL}^{-1}$). GPC: $M_n = 12,800$, $M_w = 15,600$, PDI: 1.2.

Synthesis of P2

P1 (180 mg, 0.01 mmol), pentafluorophenyl acrylate (90 mg, 0.4 mmol) and AIBN (0.2 mg, 1.5 μmol) were placed in a Schlenk tube and equipped with a stir bar. Dioxane (2 mL) was added and the solution was degassed by three freeze-pump-thaw cycles. The flask was then immersed in a preheated oil bath at 80 °C and the polymerisation was carried out for 48 h. The polymer was precipitated in methanol, collected by centrifugation, redissolved in THF and reprecipitated in methanol. This procedure was repeated three times. The light yellow powder **P2** (171 mg) was dried at 45 °C under reduced pressure for 12 h. To remove the end group, the polymer (171 mg) was dissolved in dioxane (2 mL) and AIBN (47 mg, 0.28 mmol) was added. The solution was immersed in a preheated oil bath at 80 °C and stirred for 4 h. The polymer was precipitated in methanol, collected by centrifugation, redissolved in THF and reprecipitated in methanol. This procedure was repeated three times. The light yellow powder **P2** (151 mg) was dried at 45 °C under reduced pressure for 12 h. $\nu_{\text{max}}/\text{cm}^{-1}$ 3082w (=C-H), 2914w (C-H), 1784m (COOR), 1587vs, 1515vs (Ar-F), 1507vs, 1489vs, 1312s, 1272s, 1175s, 1029s, 835s, 750vs, 692vs, 623vs. ¹H NMR: δ_{H} (300 MHz; CDCl_3 ; Me_4Si) 1.55 (br, s), 1.97 (br, s), 6.54 (br), 6.87 (br). ¹⁹F NMR δ_{F} (400 MHz; CDCl_3 ; Me_4Si) -153.21 (2F, br, s, *Fortho*), -157.36 (1F, br, d, *Fpara*), -164.28 (2F, br, s, *Fmeta*). GPC: $M_n = 14,900$, $M_w = 19,000$, PDI: 1.3.

Synthesis of P3a

P2 (37 mg, 2.8 μmol) was dissolved in dry THF (0.5 mL) in a nitrogen atmosphere. **A** (88 mg, 90 μmol) was dissolved in dry DMF (0.5 mL) in a nitrogen atmosphere and triethylamine (0.01 mg, 10 μmol) was added. The solutions were combined and stirred at 45 °C for 90 h. A white precipitate was observed after some time. The polymer was precipitated in methanol, redissolved in THF and reprecipitated in methanol seven more times until the supernatant was colourless. The dark red polymer **P3a** (18 mg) was dried under reduced pressure at 45 °C for 12 h. $\lambda_{\text{max}}(\text{THF})/\text{nm}$ 300, 498 (MLCT). $\nu_{\text{max}}/\text{cm}^{-1}$ 3082w (=C-H),

2914w (C-H), 1664m (amide I), 1587vs (amide II), 1402s, 1507vs, 1489vs, 1312s, 1272s, 1175s, 835s, 780 s, 750vs, 692vs, 623vs. GPC: $M_n = 18,000$, $M_w = 22,000$, PDI: 1.2. ¹⁹F NMR δ_{F} (400 MHz; CDCl_3 ; Me_4Si) no signal.

Synthesis of P3b

P2 (300 mg, 0.02 mmol), 4-(aminomethyl)benzoic acid (139 mg, 0.9 mmol) and triethylamine (0.1 mL, 0.9 mmol) were placed in a Schlenk tube and dispersed in anhydrous DMF (2 mL). The suspension was stirred for 21 h at 80 °C in a nitrogen atmosphere and the resulting polymer was purified by dialysis against methanol (molecular weight cut off of 3.500 g mol^{-1}). **P3b** (275 mg) was obtained as a light brown powder after drying in vacuum at 45 °C for 12 h. $\lambda_{\text{max}}(\text{THF})/\text{nm}$ ($\epsilon/\text{dm}^3 \text{ mol}^{-1} \text{ cm}^{-1}$) 301 (102 400), $c = 0.16 \text{ mg mL}^{-1}$. $\nu_{\text{max}}/\text{cm}^{-1}$ 3082w (=C-H), 2914w (C-H), 1700m (amide I), 1655m (amide I), 1587vs (amide II), 1507vs, 1489vs, 1312s, 1272s, 1175s, 1029s, 835s, 750vs, 692vs, 623vs. ¹⁹F NMR δ_{F} (400 MHz; CDCl_3 ; Me_4Si) no signal.

Functionalisation of ZnO with P3a and P3b

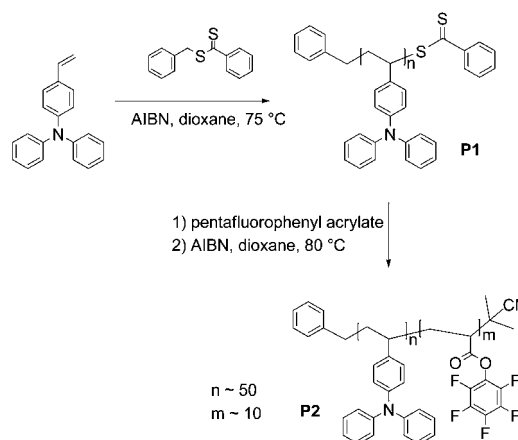
For both polymers **P3a** and **P3b** the same procedure was applied. **P3a** (15 mg) or **P3b** (15 mg) and ZnO nanorods (15 mg) were dispersed in THF (1 mL) in a Schlenk tube and degassed by three freeze-pump-thaw cycles. The tube was then immersed in a preheated oil bath at 65 °C and stirred for 18 h. The dispersion was then centrifuged at 4000 rpm for 5 min to remove the non-functionalised nanorods which precipitated. A few drops of ethanol were then added to the supernatant and the dispersion was centrifuged at 13 000 rpm for 5 min. The supernatant was removed and the precipitate redispersed in THF (0.5 mL). The washing cycle was repeated four more times. The functionalised nanoparticles **P3a@ZnO** and **P3b@ZnO** were dispersed in 1 mL anhydrous THF and kept under nitrogen and in the dark until they were used. **P3a@ZnO**: $\lambda_{\text{max}}(\text{THF})/\text{nm}$ 300, 498 (MLCT). $\lambda_{\text{em,max}}(\text{DMF})/\text{nm}$ practically no emission observed ($\lambda_{\text{ex}}/\text{nm}$ 498).

Results and discussion

Polypyridine complexes of ruthenium(II) have been extensively used as photoactive compounds in light to energy conversion devices. Compared to organic dyes they exhibit higher photo and thermal stabilities.²³ In many cases, ruthenium(II) polypyridine complexes contain bidentate (e.g. 2,2'-bipyridine) and monodentate ligands (e.g. pyridine, NCS^-). Especially monodentate ligands are believed to cause long term stability problems because of photo-induced and thermal ligand dissociation and degradation.^{24–26} We employed tridentate 2,2';6',2''-terpyridine (tpy) ligands in the ruthenium complex **A** which imparts high photo and thermal stability because of the chelating effect.^{19,27,28} In addition, the 4'-substituents on the $[\text{Ru}(\text{tpy})_2]^{2+}$ core lead to a push-pull system with the two amide substituents pointing in the same direction. This vectorial arrangement is beneficial for charge separation and charge injection into inorganic semiconductors like ZnO or TiO_2 .

The ruthenium dye conjugate $[(H_2N-CH_2-CONH-tpy)Ru(tpy-CONH-CH_2-COOH)](PF_6)_2$ (**A**) was obtained *via* a solid phase peptide synthesis (SPPS) (Scheme 1) with a TentaGel S Wang resin used as the solid phase and an Fmoc protecting group strategy.¹⁸ SPPS allows high yield and high purity over several reaction steps because the reagents can be used in excess and purification is done by a simple washing procedure. A glycine unit was attached to the resin before the ruthenium(II) complex $[(H_2N-tpy)Ru(tpy-COOH)](PF_6)_2$ was anchored to the solid support by an amide bond. As aromatic amino groups are known to be less reactive towards activated esters²⁹ the amino group of the complex was decorated with a further glycine at the *N*-terminus which provides a reactive aliphatic amine functionality. In the last step the complex was cleaved from the solid phase by trifluoroacetic acid and precipitated by addition of an aqueous NH_4PF_6 solution.

The polymer poly(vinyltriphenylamine) PTPA (**P1**) was prepared by Reversible Addition Fragmentation Chain Transfer (RAFT) polymerisation from vinyltriphenylamine (Scheme 2). PTPA is well known as a p-type semiconducting polymer and has already been used in solar cells.³⁰ The controlled radical polymerisation allows a good control of the molecular weight, a narrow polydispersity index (PDI) and the possibility to synthesise block copolymers. **P1** had a molecular weight of $13,000\text{ g mol}^{-1}$ (by GPC, polystyrene standard) and a PDI of 1.2. The second block was subsequently grafted onto **P1**, using pentafluorophenyl acrylate as the monomer and giving the block copolymer **P2**. Characterisation of **P2** by GPC (Fig. 1) showed a small shift to higher molecular weight and by referring it to the polystyrene standard, the degree of polymerisation of the first block was calculated to be around 50 ($n \approx 50$) and of the second block around 10 ($m \approx 10$). The ^{19}F NMR spectrum shows the expected resonances of the five fluorine nuclei attached to the aromatic ring (Fig. S2†). The activated pentafluorophenyl ester of **P2** can subsequently be treated with primary amines to



Scheme 2 Synthesis of **P1** and **P2** by RAFT polymerisation.

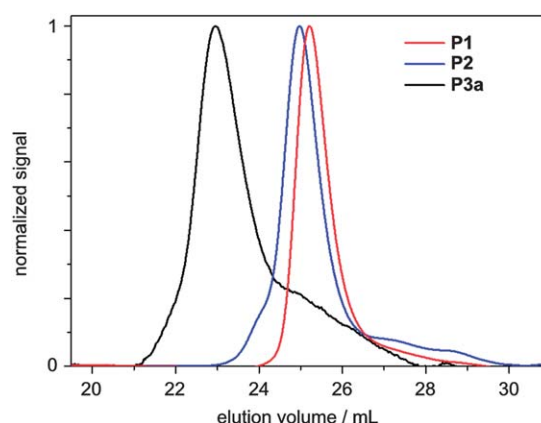
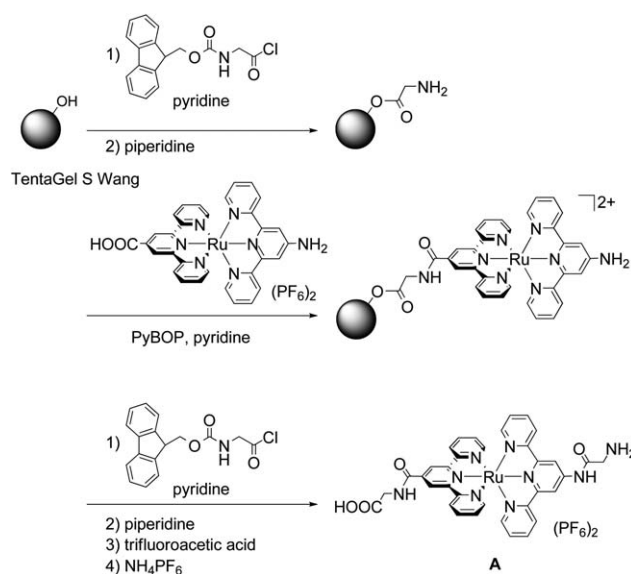


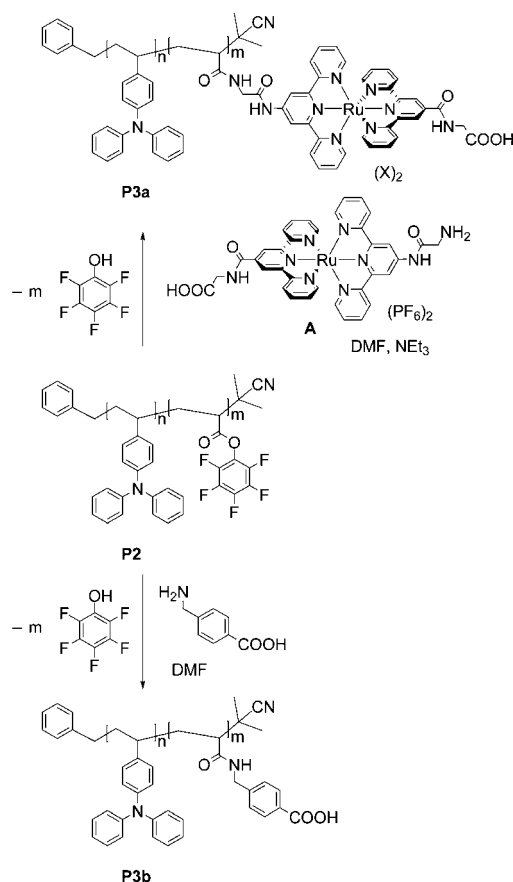
Fig. 1 GPC traces of **P1** (red), **P2** (blue) and **P3a** (black).

introduce functionalities in quantitative yields.^{31,32} The activated ester block was chosen to be relatively short ($m \approx 10$), since short anchor blocks were shown to bind the most effectively to ZnO surfaces.³³

In order to attach the ruthenium dye **A** to polymer **P2** a polymer analog reaction was carried out. The amine functionality of dye **A** readily reacts with the activated ester moieties of **P2** (Scheme 3). An excess of the dye and the polymer were dissolved in *N,N'*-dimethylformamide and heated to $45\text{ }^{\circ}\text{C}$ for 90 h. Excessive washing by precipitation/dissolving yielded the pure dark red block copolymer **P3a**. Characterisation by Fourier transform infrared (FT-IR) spectroscopy showed the absence of the ester band at 1784 cm^{-1} and the new band of amide bonds at 1664 cm^{-1} (Fig. S2†). Additionally, a ^{19}F NMR spectrum proves that all pentafluorophenyl groups were removed from the polymer (Fig. S3†). Furthermore, the PF_6 counterions were exchanged by other anions as judged by the absence of a resonance at 73.2 ppm. A significantly higher molecular weight of **P3a** was observed by GPC (Fig. 1) compared to the block copolymer **P2**, so that the covalent attachment of the dye to the polymer is proven. As a control, **P2** was treated with 4-(aminomethyl)benzoic acid giving **P3b**. The synthesis and characterisation of **P3b** are analogous to the reaction of **P2** with **A**. The



Scheme 1 Synthesis of directional chromophore **A** by SPPS.



Scheme 3 Functionalisation of **P2** with **A** to give **P3a** (top) and with 4-(aminomethyl)benzoic acid to give **P3b** (bottom).

carboxyl groups of **P3b** can also adsorb to ZnO surfaces but no charge generation is expected under irradiation with visible light.

UV-Visible and photoluminescence (PL) measurements were carried out (Fig. 2). In the absorption spectrum of **P3a** the bands at 250–350 nm arise from $\pi \rightarrow \pi^*$ transitions mainly of the triphenylamine groups and a small contribution from the ruthenium dye. The absorption of the dye in the visible region was observed at 498 nm and is attributed to the characteristic metal-to-ligand charge transfer (MLCT) of the complex.¹⁸ For **P3b** no absorption is observed in that spectral region (Fig. S8†). Photoluminescence measurements in THF ($\lambda_{\text{exc}} = 498$ nm) show that the dye functionalised polymer **P3a** emits at 667 nm, which is the same value as for the pristine dye **A** (667 nm in DMF). Thus the emission of the dye is not reductively quenched by the TPA polymer.

ZnO nanorods were synthesised according to the literature with a size distribution of several hundreds of nanometers to two micrometers.^{15b} For functionalisation with polymers **P3a** and **P3b**, the nanorods were dispersed in a small amount of THF and the respective polymer was added subsequently. The dispersion was stirred at 65 °C overnight under an inert atmosphere. Centrifugation (4000 rpm) for 2 min removed all insufficiently functionalised nanoparticles. Ethanol was then added to the clear dispersion to precipitate the nanocomposite.

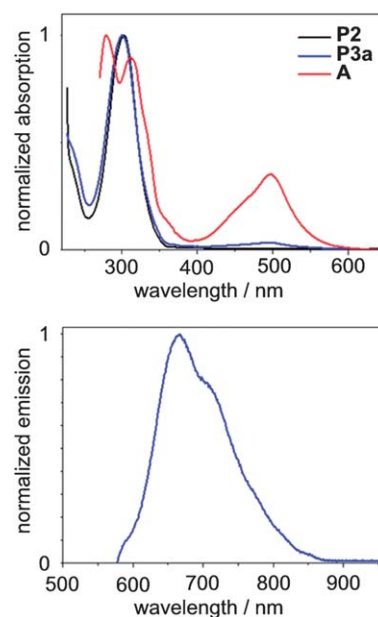


Fig. 2 UV-Vis spectra of **P2** in THF (black), **P3a** in THF (blue) and **A** in DMF (red) (top) and PL spectrum of **P3a** in THF at 498 nm excitation (bottom).

Subsequent centrifugation, redispersion and repetition of the washing cycle for several times gave the pure hybrid materials **P3a@ZnO** and **P3b@ZnO**, respectively. **P3a@ZnO** was a stable red dispersion, which showed some scattering of the light due to the large nanoparticles (length >800 nm). TEM images drop cast from the THF dispersion showed that **P3a@ZnO** nanoparticles were well dispersed and did not aggregate. In contrast, the as-synthesised sample of pristine ZnO showed strong aggregation (Fig. S4†).

The Jablonski diagram of the nanocomposite (Fig. 3) shows the estimated energy levels of the system **P3a@ZnO** together with the possible charge separation/recombination pathways in the D–C–A array.⁴² Irradiation of $\text{ZnO}-(\text{Ru})^{2+}\text{-TPA}$ at 498 nm leads to the singlet MLCT excited state $\text{ZnO}-^1(\text{Ru})^{2+*}\text{-TPA}$

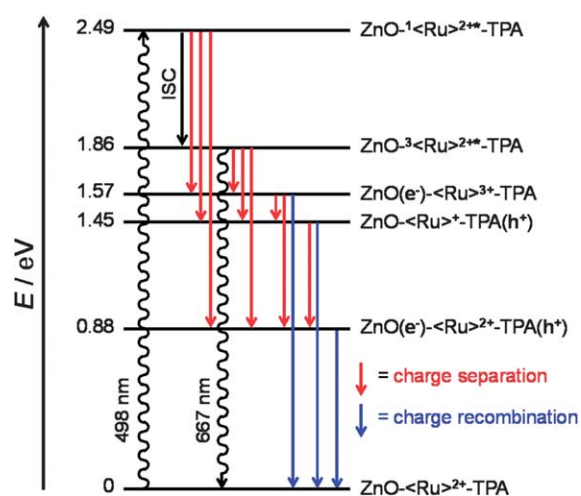


Fig. 3 Jablonski diagram of **P3a@ZnO**.

(2.49 eV), which subsequently undergoes intersystem crossing (ISC) to the triplet excited state $^3\text{MLCT ZnO}-^3\langle\text{Ru}\rangle^{2+*}\text{-TPA}$ (1.86 eV) typically with unit efficiency. Both MLCT states are thermodynamically competent to inject an electron into ZnO or to accept an electron from TPA. Photoluminescence measurements show that the phosphorescence of **P3a@ZnO** is indeed efficiently quenched as compared to **P3a** lacking the ZnO acceptor. From the singlet and triplet MLCT excited states $\text{ZnO}-^1\langle\text{Ru}\rangle^{2+*}\text{-TPA}/\text{ZnO}-^3\langle\text{Ru}\rangle^{2+*}\text{-TPA}$ the fully charge separated state $\text{ZnO}(\text{e}^-)-\langle\text{Ru}\rangle^{2+}\text{-TPA}(\text{h}^+)^{14,34}$ can principally be populated *via* the partially charge separated states $\text{ZnO}-\langle\text{Ru}\rangle^+-\text{TPA}(\text{h}^+)$ (1.45 eV) or $\text{ZnO}(\text{e}^-)-\langle\text{Ru}\rangle^{3+}\text{-TPA}$ (1.57 eV).¹⁸ In the fully charge separated state $\text{ZnO}(\text{e}^-)-\langle\text{Ru}\rangle^{2+}\text{-TPA}(\text{h}^+)$ (0.88 eV), the ZnO carries the negative and the TPA the positive charge.

By performing PL measurements the quantum yield of **P3a** was determined to be $\Phi = 2.0 \times 10^{-3}$ which is very similar to the value of **A** without TPA attachment ($\Phi = 1.4 \times 10^{-3}$).¹⁸ This shows that no luminescence quenching occurs when the dye is bound to the polymer backbone, *i.e.* photo-induced electron transfer from TPA to the excited ruthenium units $^1\langle\text{Ru}\rangle^{2+*}$ and $^3\langle\text{Ru}\rangle^{2+*}$ is inefficient in this polymer. However, after anchoring of **P3a** to ZnO, the quantum yield of the hybrid **P3a@ZnO** drops below $\Phi = 6.5 \times 10^{-5}$. This low quantum yield clearly corroborates the efficiency of the oxidative quenching in the system, *i.e.* the first electron transfer step after excitation is electron injection into ZnO, likely followed by dye regeneration by TPA.

In order to study the photo-induced interfacial charge transfer in more detail on a single particle level KPFM measurements were carried out in analogy to the measurements we performed on the D-C-A system consisting of a PTPA-perylene block copolymer covalently bound to a ZnO system.¹⁴ KPFM is a very powerful tool to detect local variations of the surface potential in the nanometer regime.³⁵ Illuminating samples with light allows studying the photo-response of optoelectronic materials.³⁶⁻⁴¹ Sample illumination of **P3a@ZnO** is realised from underneath the sample through transparent indium tin oxide (ITO) (Fig. 4a). The surface potential was first measured without illumination (Fig. 4b) on a single particle with a length of around 1 μm and a diameter of approximately 120 nm (Fig. S5†). The particle displays an approximately 45 mV higher surface potential than the surrounding ITO substrate. By subsequently comparing that to the surface potential recorded under illumination with $\lambda = 488 \text{ nm}$ (Fig. 4c), the photo-induced change in the surface potential of the **P3a@ZnO** particles is determined. Upon illumination, the surface potential on the **P3a@ZnO** particle increases. This effect was completely reversible after switching off the laser and could be observed for all particles at different positions. Upon laser illumination at a wavelength of 488 nm an electron of the chromophore is excited. Charge separation occurs at the interface of the ZnO particle by transfer of the electron to the conduction band of the ZnO. The oxidised ruthenium dye regenerates by collecting an electron from the HOMO level of the TPA polymer.

In order to quantitatively discuss this photo-response, the surface potential profile was analyzed in detail across the particle as indicated by the blue and red line for laser off and on

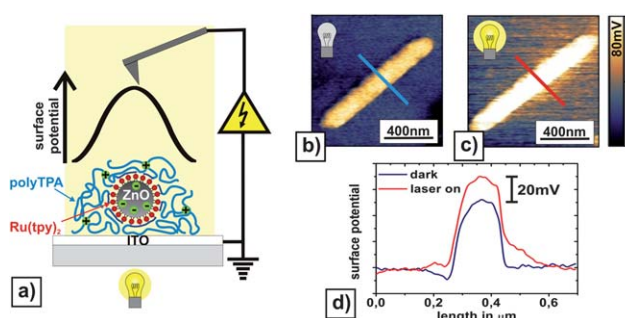


Fig. 4 Study of interfacial charge transfer by KPFM on **P3a@ZnO** spun cast from THF in the dark and under laser illumination ($\lambda = 488 \text{ nm}$). (a) Schematic of the KPFM measurement on the D-C-A system (TPA in blue, $\text{Ru}(\text{tpy})_2$ in red and ZnO in grey) under laser illumination through the ITO coated glass substrate. The surface potential on the functionalised ZnO particle upon illumination is qualitatively depicted in the upper graph. (b) and (c) Surface potential maps measured in the dark and under illumination on the same position. The measured potential values were adjusted relative to the constant potential value of the ITO at a large distance from the **P3a@ZnO**. (d) Line profiles of the surface potentials taken across the particle show an increase in surface potential of around 20 mV upon illumination.

in the corresponding surface potential images (Fig. 4d). The increase in surface potential of around 20 mV on the **P3a@ZnO** particle and up to a distance of around 100 nm around the particle was attributed to the build-up of positive charges in the TPA block as a consequence of the charge separation at the interface. Negative charges of the ZnO particle could not be detected by KPFM. This observation indicates a high grafting density of the **P3a** to the ZnO and therefore results in a densely packed and thick polymer layer. Thus, the effect of the build-up of electrons inside the ZnO on the surface potential change is shielded by the positive charges of the TPA.⁴³

The estimated energy level difference of 0.88 eV between the ground state $\text{ZnO}-\langle\text{Ru}\rangle^{2+}\text{-TPA}$ and the charge separated state $\text{ZnO}(\text{e}^-)-\langle\text{Ru}\rangle^{2+}\text{-TPA}(\text{h}^+)$ (Fig. 3) is significantly larger than the value obtained by KPFM. We attribute this difference to the screening of the positively charged TPA by the counter ions of the $\langle\text{Ru}\rangle^{2+}$ which diffuse from the D-A interface into the polymer matrix. Finally, an additional control experiment performed on **P3b@ZnO** showed no photo-response under irradiation with $\lambda = 488 \text{ nm}$ (Fig. S6†). Without the chromophore as the anchoring group at the interface between ZnO and TPA no excitons can be generated under similar conditions. Thus, for an efficient charge transfer the complete donor-chromophore-acceptor system is required.

Conclusions

Herein we demonstrated the synthesis and characterisation of a new nanoscale D-C-A system with polytriphenylamine as the electron donor (D) and a directional $[\text{Ru}^{\text{II}}(\text{tpy})_2]^{2+}$ complex as the chromophore (C) which is directly bound to ZnO nanorods as the electron acceptor (A).

The ruthenium complex $[\text{Ru}^{\text{II}}(\text{tpy})_2]^{2+}$ with tridentate ligands has a higher thermal and photostability compared to organic dyes or 2,2'-bipyridine ruthenium(II) complexes. Additionally,

the push–pull substituted terpyridine ligands induce spatially separated frontier orbitals which support the charge separation at the interphase. Since the polymer carries several chromophores within each chain, the local concentration of the light harvesting units at the ZnO surface is very high. The chromophore–acceptor contact is very intimate through the direct attachment *via* the carboxyl groups of the Ru^{II} complex. The donor–chromophore contact on the other side is enhanced by the covalent binding of the triphenylamine polymer to the chromophores. Charge separation occurs under light excitation of the chromophore and was proven by phosphorescence quenching and KPFM measurements. Based on these results, we believe that the system is especially suitable to build high performance ssDSSCs.

Acknowledgements

This work was financially supported by the International Research Training Group (IRTG): Self Organized Materials for Optoelectronics supported by the Deutsche Forschungsgemeinschaft (DFG). We thank Dr Stefan Frank for the synthesis of the ZnO nanorods and Gabi Herrmann for the preparation of the ITO coated glass substrates. In addition, we thank Esha Sengupta and Stefan Weber for discussions and the BMBF (contract # 03SF0334) for partial financial support in building up the photo-KPFM.

Notes and references

- 1 B. O'Regan and M. Grätzel, *Nature*, 1991, **353**, 737–740.
- 2 M. Matsumoto, H. Miyazaki, K. Matsuihiro, Y. Kumashiro and Y. Takaoka, *Solid State Ionics*, 1996, **89**, 263–267.
- 3 U. Bach, D. Lupo, P. Comte, J. E. Moser, F. Weissortel, J. Salbeck, H. Spreitzer and M. Grätzel, *Nature*, 1998, **395**, 583–585.
- 4 J. Boucle and J. Ackermann, *Polym. Int.*, 2012, **61**, 355–373.
- 5 W. Zhang, Y. Cheng, X. Yin and B. Liu, *Macromol. Chem. Phys.*, 2011, **212**, 15–23.
- 6 R. H. Lohwasser, J. Bandara and M. Thelakkat, *J. Mater. Chem.*, 2009, **19**, 4126–4130.
- 7 K. C. D. Robson, B. D. Koivisto, T. J. Gordon, T. Baumgartner and C. P. Berlinguette, *Inorg. Chem.*, 2010, **49**, 5335–5337.
- 8 K. C. D. Robson, B. Sporinova, B. D. Koivisto, E. Schott, D. G. Brown and C. P. Berlinguette, *Inorg. Chem.*, 2011, **50**, 6019–6028.
- 9 C. S. Karthikeyan, K. Peter, H. Wietasch and M. Thelakkat, *Sol. Energy Mater. Sol. Cells*, 2007, **91**, 432–439.
- 10 J.-H. Yum, S.-J. Moon, C. S. Karthikeyan, H. Wietasch, M. Thelakkat, S. M. Zakeeruddin, M. K. Nazeeruddin and M. Grätzel, *Nano Energy*, 2012, **1**, 6–12.
- 11 Z. Jin, H. Masuda, N. Yamanaka, M. Minami, T. Nakamura and Y. Nishikitani, *Chem. Lett.*, 2009, **38**, 44–45.
- 12 H. J. Snaith, C. S. Karthikeyan, A. Petrozza, J. Teuscher, J. E. Moser, M. K. Nazeeruddin, M. Thelakkat and M. Grätzel, *J. Phys. Chem. C*, 2008, **112**, 7562–7566.
- 13 K. Peter and M. Thelakkat, *Macromolecules*, 2003, **36**, 1779–1785.
- 14 M. Zorn, S. A. L. Weber, M. N. Tahir, W. Tremel, H. J. Butt, R. Berger and R. Zentel, *Nano Lett.*, 2010, **10**, 2812–2816.
- 15 (a) M. Behl, E. Hattemer, M. Brehmer and R. Zentel, *Macromol. Chem. Phys.*, 2002, **203**, 503–510; (b) B. Cheng, W. Shi, J. M. Russell-Tanner, L. Zhang and E. T. Samulski, *Inorg. Chem.*, 2006, **45**, 1208–1214.
- 16 K. Suzuki, A. Kobayashi, S. Kaneko, K. Takehira, T. Yoshihara, H. Ishida, Y. Shiina, S. Oishi and S. Tobita, *Phys. Chem. Chem. Phys.*, 2009, **11**, 9850–9860.
- 17 (a) S. L. Weber, H.-J. Butt and R. Berger, Electrical Characterization of Solar Cell Materials Using Scanning Probe Microscopy, in *Scanning Probe Microscopy in Nanoscience and Nanotechnology 3*, ed. B. Bhushan, Springer Berlin Heidelberg, 2013, pp. 551–573; (b) S. V. Kalinin and D. A. Bonnell, *Phys. Rev. B: Condens. Matter Mater. Phys.*, 2001, **63**, 125411.
- 18 K. Heinze and K. Hempel, *Chem.-Eur. J.*, 2009, **15**, 1346–1358.
- 19 K. Heinze, K. Hempel and M. Beckmann, *Eur. J. Inorg. Chem.*, 2006, **2006**, 2040–2050.
- 20 V. Palermo, M. Palma and P. Samorì, *Adv. Mater.*, 2006, **18**, 145–164.
- 21 E. Sengupta, A. L. Domanski, S. A. L. Weber, M. B. Untch, H.-J. Butt, T. Sauermann, H. J. Egelhaaf and R. Berger, *J. Phys. Chem. C*, 2011, **115**, 19994–20001.
- 22 A. L. Domanski, E. Sengupta, K. Bley, M. B. Untch, S. A. L. Weber, K. Landfester, C. K. Weiss, H.-J. Butt and R. Berger, *Langmuir*, 2012, **28**, 13892–13899.
- 23 A. Reynal and E. Palomares, *Eur. J. Inorg. Chem.*, 2011, **2011**, 4509–4526.
- 24 P. T. Nguyen, B. X. T. Lam, A. R. Andersen, P. E. Hansen and T. Lund, *Eur. J. Inorg. Chem.*, 2011, **2011**, 2533–2539.
- 25 T. P. Brewster, W. Ding, N. D. Schley, N. Hazari, V. S. Batista and R. H. Crabtree, *Inorg. Chem.*, 2011, **50**, 11938–11946.
- 26 S. Kämper, A. Paretzki, J. Fiedler, S. Zális and W. Kaim, *Inorg. Chem.*, 2012, **51**, 2097–2104.
- 27 A. Breivogel, C. Förster and K. Heinze, *Inorg. Chem.*, 2010, **49**, 7052–7056.
- 28 A. Breivogel, K. Hempel and K. Heinze, *Inorg. Chim. Acta*, 2011, **374**, 152–162.
- 29 K. Nilles and P. Theato, *J. Polym. Sci., Part A: Polym. Chem.*, 2010, **48**, 3683–3692.
- 30 M. Sommer, S. M. Lindner and M. Thelakkat, *Adv. Funct. Mater.*, 2007, **17**, 1493–1500.
- 31 M. Eberhardt, R. Mruk, R. Zentel and P. Théato, *Eur. Polym. J.*, 2005, **41**, 1569–1575.
- 32 M. Eberhardt and P. Theato, *Macromol. Rapid Commun.*, 2005, **26**, 1488–1493.
- 33 M. Zorn, S. Meuer, M. N. Tahir, Y. Khalavka, C. Sonnichsen, W. Tremel and R. Zentel, *J. Mater. Chem.*, 2008, **18**, 3050–3058.
- 34 E. Hattemer, *Synthesen und Charakterisierungen Arylaminhaltiger Polymere: Multifunktionelle hoch-T_g-Copolymere für photorefraktive Anwendungen*, Johannes Gutenberg-Universität, Mainz, 2000.
- 35 M. Nonnenmacher, M. P. O'Boyle and H. K. Wickramasinghe, *Appl. Phys. Lett.*, 1991, **58**, 2921–2923.

- 36 J. M. R. Weaver and H. K. Wickramasinghe, *J. Vac. Sci. Technol., B: Microelectron. Nanometer Struct.–Process., Meas., Phenom.*, 1991, **9**, 1562–1565.
- 37 H. Hoppe, T. Glatzel, M. Niggemann, A. Hinsch, M. C. Lux-Steiner and N. S. Sariciftci, *Nano Lett.*, 2005, **5**, 269–274.
- 38 J. Cao, J.-Z. Sun, J. Hong, X.-G. Yang, H.-Z. Chen and M. Wang, *Appl. Phys. Lett.*, 2003, **83**, 1896–1898.
- 39 V. Palermo, G. Ridolfi, A. M. Talarico, L. Favaretto, G. Barbarella, N. Camaioni and P. Samorì, *Adv. Funct. Mater.*, 2007, **17**, 472–478.
- 40 S. Sadewasser and M. C. Lux-Steiner, *J. Vac. Sci. Technol., B: Microelectron. Nanometer Struct.–Process., Meas., Phenom.*, 2010, **28**, C4D29–C24D33.
- 41 E. J. Spadafora, R. Demadrille, B. Ratier and B. Grevin, *Nano Lett.*, 2010, **10**, 3337–3342.
- 42 The energy levels of the Jablonski diagram were estimated from the absorption and emission maxima ($\text{ZnO}-^1\langle\text{Ru}\rangle^{2+*}\text{-TPA}$: 498 nm; 2.49 eV; $\text{ZnO}-^3\langle\text{Ru}\rangle^{2+*}\text{-TPA}$: 667 nm; 1.86 eV) as well as from potential differences of literature known energy levels and redox potentials. The conduction band of ZnO is at -4.4 eV vs. vacuum.¹⁴ The oxidation potential of the TPA units in **P3@ZnO** is estimated to be $+0.84$ V vs. NHE which is the oxidation potential of monomeric tolyldiphenylamine.³⁴ The oxidation and reduction potentials of the $\langle\text{Ru}\rangle$ unit in **P3@ZnO** were estimated to be $+1.285$ and -0.850 V vs. SCE, respectively, from the values of the molecular ruthenium dye $[(\text{H}_3\text{C-CONH-tpy})\text{Ru}(\text{tpy-CONH-CH}_2\text{-COOH})](\text{PF}_6)_2$.¹⁸ With $E(\text{vacuum})/\text{eV} = -4.44 - E(\text{NHE}) = -4.68 - E(\text{SCE})$ we estimate $\text{ZnO}-\langle\text{Ru}\rangle^+\text{-TPA}^+$ at $+1.45$ eV, $\text{ZnO}(\text{e}^-)-\langle\text{Ru}\rangle^{3+}\text{-TPA}$ at $+1.565$ eV and $\text{ZnO}(\text{e}^-)-\langle\text{Ru}\rangle^{2+}\text{-TPA}^+$ at 0.88 eV.
- 43 S. V. Kalinin and D. A. Bonnell, *Nano Lett.*, 2004, **4**, 555–560.

9.5 A Heteroleptic Bis(tridentate)ruthenium(II) Polypyridine Complex with Improved Photophysical Properties and Integrated Functionalizability

A. Breivogel, C. Förster, K. Heinze, *Inorg. Chem.* **2010**, 49, 7052–7056.

DOI: 10.1021/ic1007236

Reprinted with permission from the American Chemical Society, Copyright © 2010.

A Heteroleptic Bis(tridentate)ruthenium(II) Polypyridine Complex with Improved Photophysical Properties and Integrated Functionalizability

Aaron Breivogel, Christoph Förster, and Katja Heinze*

Institute of Inorganic Chemistry and Analytical Chemistry, Johannes Gutenberg-University of Mainz, Duesbergweg 10–14, 55128 Mainz, Germany

Received April 15, 2010

The synthesis and photophysical properties of a ruthenium(II) complex bearing an electron-accepting 2,2',6',2''-terpyridine ligand and an electron-donating *N,N'*-dimethyl-*N,N'*-dipyridin-2-ylpyridine-2,6-diamine (ddpd) ligand are presented. The heteroleptic complex is easily prepared isomerically pure and features intense low-energy metal-to-ligand charge-transfer (MLCT) absorption bands and intense room temperature ³MLCT emission with a long ³MLCT lifetime. The favorable photophysical properties are due to the strong ligand field imposed by the ddpd ligand.

Introduction

Meridional-coordinating tridentate ligands are preferred over bidentate ligands because of increased (photo)stability, absence of chirality (Δ and Λ), and simple functionalization in central mutually trans positions. For example, switching from tris(bidentate) $[\text{Ir}(\text{ppy})_2(\text{bpy})]^+$ to bis(tridentate) $[\text{Ir}(\text{phbpy})_2]^+$ has been beneficial in terms of the stability and excited-state lifetime (ppy = 2-phenylpyridine; bpy = 2,2'-bipyridine; phbpy = 6-phenyl-2,2'-bipyridine).¹ However, in ruthenium oligopyridine chemistry, $[\text{Ru}(\text{tpy})_2]^{2+}$ (**1**) shows disappointing photophysical properties [essentially nonluminescent at room temperature and a low triplet-state metal-to-ligand charge-transfer (³MLCT) lifetime] compared to $[\text{Ru}(\text{bpy})_3]^{2+}$ (**2**). Thermal population of a low-lying ³MC state of **1** provides an efficient deactivating pathway.^{2–4}

Two strategies have emerged to improve the excited-state properties of bis(tridentate) ruthenium complexes: (i) increasing the M–L orbital overlap by adjusting the bite angles from N–Ru–N < 80° in five-membered chelate rings to ~90° in

six-membered chelate rings, which raises the energy of the ³MC state relative to that of the ³MLCT state,^{5–10} and (ii) attaching an electron-withdrawing substituent to lower the oligopyridine π^* orbitals and thus the energy of the MLCT states relative to the deactivating ³MC state (which should overcompensate for the effect of increased nonradiative decay at low emission energies).^{11–14} Concomitant attachment of an electron-donating substituent at the second chelate ligand further improves the emission properties.^{14,15} These effects are clearly seen in the series $[\text{Ru}(\text{tpy})_2]^{2+}$ (**1**; $\lambda_{\text{abs/emiss}} = 474/629 \text{ nm}^{11}$) \rightarrow $[\text{Ru}(\text{EtOOC-tpy})(\text{tpy})]^{2+}$ (**3**; $485/667 \text{ nm}^{13}$) \rightarrow $[\text{Ru}(\text{EtOOC-tpy})(\text{H}_2\text{N-tpy})]^{2+}$ (**4**; $500/744 \text{ nm}^{14,15}$) (Chart 1). At room temperature, the luminescence quantum yield increases from $< 5 \times 10^{-6}$ to 2.7×10^{-4} to 1.8×10^{-3} and the excited-state lifetime from 0.25 to 32 to 34 ns.^{11,13–15} Hammarström et al. have switched five-membered chelate rings to six-membered chelate rings by employing (bipyridylpyridyl)methane derivatives (bpy-CR₂-py) instead of terpyridine.⁵ The homoleptic

*To whom correspondence should be addressed. E-mail: katja.heinze@uni-mainz.de. Fax: +49-6131-39-27277.

- (1) Tinker, L. L.; Bernhard, S. *Inorg. Chem.* **2009**, *48*, 10507.
- (2) Sauvage, J.-P.; Collin, J.-P.; Chambrion, J.-C.; Guillerez, S.; Coudret, C.; Balzani, V.; Barigelli, F.; De Cola, L.; Flamigni, L. *Chem. Rev.* **1994**, *94*, 993.
- (3) Winkler, J. R.; Netzel, T. L.; Creutz, C.; Sutin, N. *J. Am. Chem. Soc.* **1987**, *109*, 2381.
- (4) Siemeling, U.; Vor der Brüggen, J.; Vorfeld, U.; Neumann, B.; Stämmler, A.; Stämmler, H.-G.; Brockhinke, A.; Plessow, R.; Zanello, P.; Laschi, F.; Fabrizi de Biani, F.; Fontani, M.; Steenken, S.; Stapper, M.; Gurzadyan, G. *Chem.—Eur. J.* **2003**, *9*, 2819.
- (5) Abrahamsson, M.; Wolpher, H.; Johansson, O.; Larsson, J.; Kritikos, M.; Eriksson, L.; Norrby, P.-O.; Bergquist, J.; Sun, L.; Åkermark, B.; Hammarström, L. *Inorg. Chem.* **2005**, *44*, 3215.
- (6) Abrahamsson, M.; Jäger, M.; Österman, T.; Eriksson, L.; Persson, P.; Becker, H.-C.; Johansson, O.; Hammarström, L. *J. Am. Chem. Soc.* **2006**, *128*, 12616.

(7) Abrahamsson, M.; Jäger, M.; Kumar, R. J.; Österman, T.; Persson, P.; Becker, H.-C.; Johansson, O.; Hammarström, L. *J. Am. Chem. Soc.* **2008**, *130*, 15533.

(8) Jäger, M.; Kumar, R. J.; Görls, H.; Bergquist, J.; Johansson, O. *Inorg. Chem.* **2009**, *48*, 3228.

(9) Kumar, R. J.; Karlsson, S.; Streich, D.; Rolandini Jensen, A.; Jäger, M.; Becker, H.-C.; Bergquist, J.; Johansson, O.; Hammarström, L. *Chem.—Eur. J.* **2010**, *16*, 2830.

(10) Jäger, M.; Smeigh, A.; Lombeck, F.; Görls, H.; Collin, J.-P.; Sauvage, J.-P.; Hammarström, L.; Johansson, O. *Inorg. Chem.* **2010**, *49*, 374.

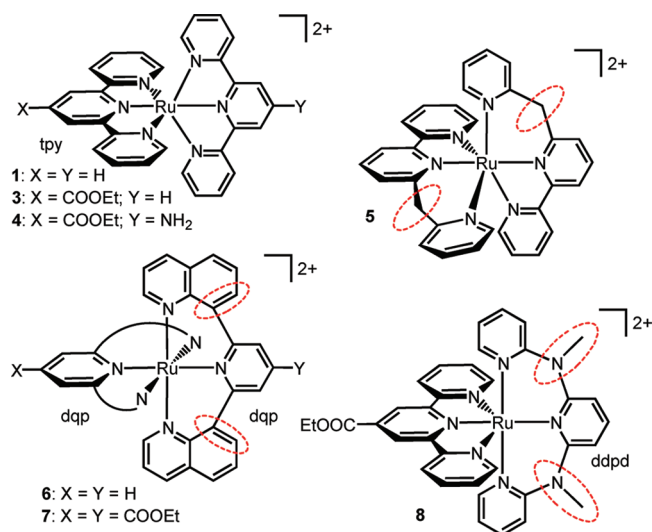
(11) Maestri, M.; Armaroli, N.; Balzani, V.; Constable, E. C.; Cargill Thompson, A. M. W. *Inorg. Chem.* **1995**, *34*, 2759.

(12) Schubert, U. S.; Hofmeier, H.; Newkome, G. R. *Modern Terpyridine Chemistry*; Wiley-VCH: Weinheim, Germany, 2006.

(13) Bolink, H. J.; Cappelli, L.; Coronado, E.; Gaviña, P. *Inorg. Chem.* **2005**, *44*, 5966.

(14) Heinze, K.; Hempel, K.; Beckmann, M. *Eur. J. Inorg. Chem.* **2006**, 2040.

(15) Heinze, K.; Hempel, K.; Tschierlei, S.; Schmitt, M.; Popp, J.; Rau, S. *Eur. J. Inorg. Chem.* **2009**, 3119.

Chart 1. Bis(tridentate) Ruthenium(II) Oligopyridine Complexes

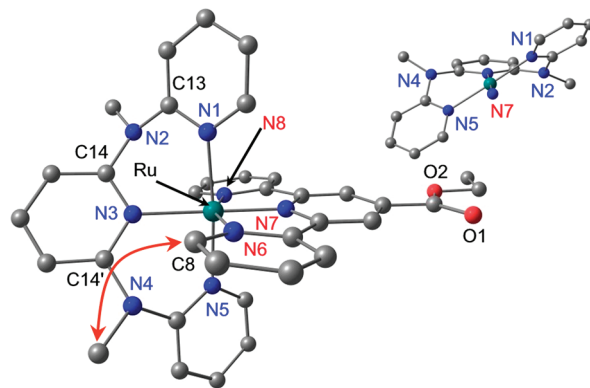
bis[bipyridylpyridyl)methane]ruthenium complex **5** features $\tau = 15$ ns and $\Phi = 10^{-3}$ ($\lambda_{\text{abs/emiss}} = 477/655$ nm; Chart 1).⁵ However, the values are still well below those of the tris-bpy complex **2** ($\tau = 1$ μ s, $\Phi = 8.9 \times 10^{-2}$),^{6,7} and **5** is still chiral. These properties have been surpassed by the homoleptic complex [Ru(dqp)₂]²⁺ (**6**, Chart 1). Almost 90° N–Ru–N bite angles are observed and excellent photophysical properties are achieved ($\Phi = 2 \times 10^{-2}$; $\tau = 3$ μ s; $\lambda_{\text{abs/emiss}} = 490/700$ nm). Further enhancement is achieved by COOEt substitution (**7**, Chart 1; $\Phi = 7 \times 10^{-2}$; $\tau = 5.5$ μ s; $\lambda_{\text{abs/emiss}} = 553/693$ nm).^{6,7}

However, these homoleptic dqp complexes show *fac/mer* stereoisomerism because of the flexible six-membered chelate rings (the *fac* isomers even come in *cis-fac* and *trans-fac* isomers), and, in addition, N₃Cl-coordinated complexes [RuCl(dqp)₂]⁺ are formed.⁸ Heteroleptic-type **6** complexes with X \neq Y (e.g., donor/acceptor substitution) are quite difficult to obtain,⁸ but very recently Hammarström et al. succeeded in incorporating dqp complexes in donor/chromophor/acceptor triads.⁹

Results and Discussion

Here we describe the synthesis and properties of the heteroleptic ruthenium oligopyridine complex **8** (Chart 1), which has several beneficial features: a 2-fold rotation axis, setup for simple functionalization in the direction of this C₂ axis,¹⁶ absence of *fac/mer* stereoisomerism, an electron-donating N,N'-dimethyl-N,N'-dipyridin-2-ylpyridine-2,6-diamine (ddpd) ligand forming six-membered chelate rings together with an electron-withdrawing 4'-(ethylcarboxy)terpyridine ligand (push–pull substitution). The methyl substituents of ddpd are necessary because tripyridylamines lacking alkyl groups at the amine are easily deprotonated, yielding chain complexes that are interesting by themselves for other reasons but undesirable for our purposes.¹⁷

First, we performed quantum chemical calculations on the homoleptic complex [Ru(ddpd)₂]²⁺ (**9**). The calculations suggest that *fac/mer* stereoisomers are analogous to those of **6**, with *mer-9* being more stable than *trans-fac-9* (31 kJ mol^{−1})

**Figure 1.** DFT (B3LYP, LANL2DZ)-optimized geometry of **8** (inset: Newman projection viewed approximately along the C₂ axis; tpy-COOEt ligand omitted). Hydrogen atoms are omitted for clarity. The arrow indicates an interligand NOE contact between protons.

and *cis-fac-9* (34 kJ mol^{−1}). Attempts to synthesize and purify **9** are indeed complicated because of the formation of *fac/mer* isomers and N₃Cl coordination. Coordinated chloride is easily removed by silver cations, but heating (dimethyl sulfoxide, reflux, microwave, 10 h) does not furnish pure *mer-9*. The photophysical properties of the *fac/mer* mixture were also disappointing ($\lambda_{\text{abs/emiss}} = 393/468$ nm, very weak emission). Thus, we switched to the mixed donor/acceptor-substituted ruthenium(II) complex **8** with an electron-donating ddpd ligand and an electron-withdrawing EtOOC-tpy ligand. **8** is easily prepared from RuCl₃(EtOOC-tpy)^{18–20} and ddpd in a microwave-assisted synthesis at 80 °C (after chloride abstraction with silver nitrate and precipitation with NH₄PF₆) as a purple powder in 62% yield.

High-resolution electrospray ionization [(HR)ESI] mass spectrometry (MS), IR spectrometry, multinuclear and correlation NMR spectroscopy, and elemental analysis are consistent with the formulated structure of **8**. Because the tpy ligand only coordinates in a meridional fashion, *fac/mer* stereoisomers are absent. A single resonance is observed for the N–CH₃ hydrogen, carbon, and nitrogen nuclei, respectively (Supporting Information). Singlet ground-state density functional theory (DFT) calculations on **8** reveal that the N–Ru–N angles involving the ddpd ligand are around 88° while the corresponding angles involving the tpy ligand are around 79° (Figure 1). The six-membered chelate rings of the ddpd ligand form boat conformations, resulting in an overall small twist of the ddpd ligand, with one terminal pyridine ring pointing up and the other one pointing down relative to the plane of the central pyridine ring (Figure 1, inset). Similarly, the N–CH₃ groups point up and below the central pyridine plane (H₃C–N2–C14–N3/H₃C–N4–C14'–N3 = 150.4°/150.2°), which allows for an nuclear Overhauser enhancement (NOE) contact to the tpy proton H8 vis-à-vis (indicated by an orange-colored arrow, Figure 1). Gratifyingly, the DFT-calculated metrical parameters match those obtained from a single-crystal X-ray diffraction analysis of **8** [triclinic, *P* $\bar{1}$; N1–Ru–N3/N5–Ru–N3 = 87.5°/87.7°; N6–Ru–N7/N7–Ru–N8 = 79.6°/79.7°; H₃C–N2–C14–N3/H₃C–N4–C14'–N3 = 156.2°/153.2°; the atom numbering refers to that used in Figure 1 for the sake of comparison].

(16) Heinze, K.; Hempel, K. *Chem.—Eur. J.* **2009**, *15*, 1346.

(17) Yin, C.; Huang, G.-C.; Kuo, C.-K.; Fu, M.-D.; Lu, H.-C.; Ke, J.-H.; Shih, K.-N.; Huang, Y.-L.; Lee, G.-H.; Yeh, C.-Y.; Chen, C.-h.; Peng, S.-M. *J. Am. Chem. Soc.* **2008**, *130*, 10090.

(18) Fallahpour, R.-A. *Synthesis* **2000**, *8*, 1138.

(19) Fallahpour, R.-A. *Eur. J. Inorg. Chem.* **1998**, 1205.

(20) Fallahpour, R.-A.; Neuburger, M.; Zehnder, M. *New J. Chem.* **1999**, *23*, 53.

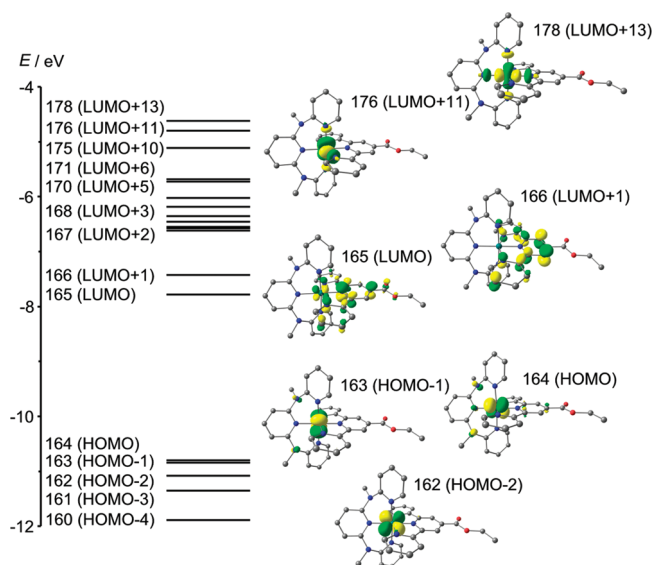


Figure 2. Molecular orbital diagram of **8** and some relevant molecular orbitals (contour value 0.06 au).

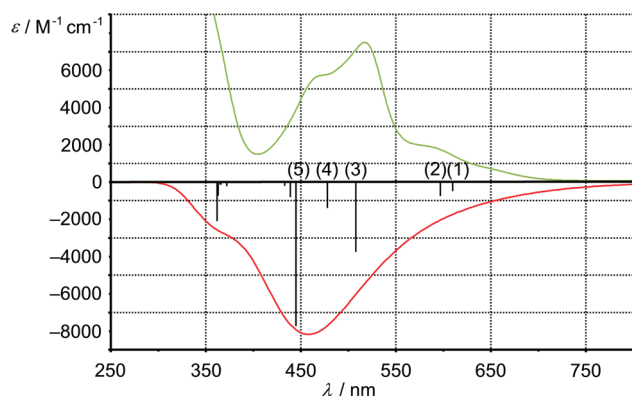


Figure 3. Experimental electronic absorption spectrum of **8** in CH_3CN (top) and calculated stick spectrum (TD-DFT, IEFPCM, CH_3CN) of **8** (the intensity of the sticks is proportional to the calculated oscillator strength, and the calculated spectrum is composed of δ functions at the excitation energies) (bottom).

Kohn–Sham frontier orbitals of the singlet ground state of **8** are shown in Figure 2. The lowest unoccupied molecular orbitals (LUMOs) of **8** are mainly localized on the EtOOC -tpy ligand, while the highest occupied molecular orbitals (HOMOs) are essentially ruthenium-based orbitals (t_{2g} in octahedral symmetry) with some ddpd contribution (especially the nitrogen atoms of the $\text{N}-\text{CH}_3$ groups). The experimental electronic spectrum of **8** is dominated by intense $\pi \rightarrow \pi^*$ transitions at $\lambda < 350$ nm (Supporting Information). The broad absorption band around $\lambda = 500$ nm corresponds to several MLCT transitions (Figure 3).²¹ On the basis of time-dependent DFT (TD-DFT) calculations (gas-phase and polarizable continuum solvation model, CH_3CN)²¹ on **8** involving the first 12 spin-allowed singlet excitations, the most intense peaks in the visible spectral region are assigned to MLCT “ $t_{2g}(\text{Ru}) \rightarrow \pi^*(\text{tpy-COOEt})$ ” transitions, e.g., transitions (3), (4), and (5) involve mainly HOMO, HOMO–1, and HOMO–2 (d_{Ru}) to LUMO and LUMO+1 [$\pi^*(\text{tpy-COOEt})$] transitions at 508, 478, and 445 nm (Figures 2 and 3).

(21) Jakubikova, E.; Chen, W.; Dattelbaum, D. M.; Rein, F. N.; Rocha, R. C.; Martin, R. L.; Batista, E. R. *Inorg. Chem.* **2009**, *48*, 10720.

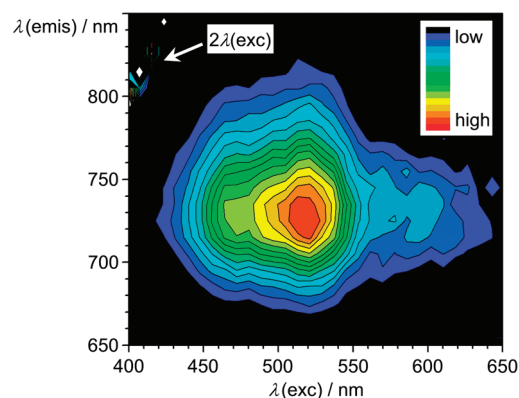


Figure 4. Excitation emission matrix of **8**.

The TD-DFT results compare well with the experimental data of **8** ($\lambda_{\text{abs}} = 517$ nm; $\epsilon = 7500 \text{ M}^{-1} \text{ cm}^{-1}$; Figure 3). The difference between experimental and calculated absorption maxima of $\Delta E = 0.35$ eV (gas phase) [$\Delta E = 0.30$ eV (CH_3CN)] is similar to the one obtained for **1** using the same method [$\Delta E = 0.38$ eV (acetone)].²¹ The experimental maximum of **8** is bathochromically shifted by 1275 cm^{-1} relative to that of **3** because of the π -electron-donating effect of ddpd, raising the energy of the Ru d orbitals.

The room temperature emission is also shifted from 667 nm (**3**) to 729 nm (**8**),¹³ with the maximum intensity observed upon excitation of the $^1\text{MLCT}$ transitions (Figure 4). The excitation spectrum closely follows the absorption spectrum in the visible spectral region. In spite of the lower $^3\text{MLCT}$ energy, **8** features a more than 10-fold higher quantum yield compared to **3** [$\Phi = 3.0 \times 10^{-3}$ (**8**)]. Also, the $^3\text{MLCT}$ lifetime has dramatically increased to $\tau = 722(5)$ ns (**8**). This is appreciable considering the fact that a lower $^3\text{MLCT}$ energy should lead to faster nonradiative decay.^{22,23}

In frozen butyronitrile at 77 K, emission is observed at higher energy and with a higher lifetime [$\lambda_{\text{emiss}} = 707$ nm; $\tau = 3309(15)$ ns]. The first observation is due to the lower stabilization of the excited state in the frozen matrix, and the second finding is due to less accessible thermal deactivation pathways. The DFT-calculated energy difference between the $^3\text{MLCT}$ state and the ground state (gas phase) amounts to 1.64 eV (756 nm for the $0 \rightarrow 0$ transition), in quite good agreement with the experiment.²¹

The photophysical properties of **8** are thus dramatically improved when compared to those of **1** and are approaching those of **2** ($\Phi = 6.2 \times 10^{-2}$; $\tau = 962 \text{ ns}$).^{24,25}

The $\text{Ru}^{\text{II/III}}$ oxidation of **8** is found at $E_{1/2} = 0.81$ V (vs Fc/Fc^+). Thus, **8** is harder to oxidize than **4** ($E_{1/2} = 0.68 \text{ V}$)¹⁴ but easier to oxidize than **1** ($E_{1/2} = 0.92 \text{ V}$)¹¹ or **3** ($E_{1/2} = 0.96 \text{ V}$).¹³ This reflects the stronger donor ability of ddpd as compared to tpy, raising the energy of the Ru d levels. **8** is reduced at $E_{1/2} = -1.40$ V in a quasi-two-electron process, precluding assignments to individual ligands.

To place the ddpd ligand in the context of other donor ligands, a computational analysis was conducted. The net donor strength ($\sigma + \pi$) is estimated from DFT-calculated A_1 carbonyl stretching modes of tricarbonyl(nickel) fragments

(22) Meyer, T. J. *Pure Appl. Chem.* **1986**, *58*, 1193.

(23) Caspar, J. V.; Meyer, T. J. *J. Phys. Chem.* **1983**, *87*, 952.

(24) Caspar, J. V.; Meyer, T. J. *J. Am. Chem. Soc.* **1983**, *105*, 5583.

(25) Ding, Z.; Wellington, R. G.; Brevet, P. F.; Girault, H. H. *J. Phys. Chem.* **1996**, *100*, 10658.

coordinated to the ligands.^{26,27} On this basis, the ddpd ligand was ranked between trimethylamine and N-heterocyclic carbene ligands (Supporting Information).

Conclusion

We have prepared a novel heteroleptic ruthenium(II) complex with a terpyridine acceptor ligand and a meridional-coordinating tridentate ddpd donor ligand. The latter forms six-membered chelate rings with the metal center. This ligand combination results in long-wavelength absorption and emission as well as an extended ³MLCT lifetime of 722 ns.

The effects of ddpd are 3-fold: improved σ -orbital overlap with Ru “e_g” orbitals due to $\approx 90^\circ$ bite angles (LUMO+11 and LUMO+13; Figure 2) raising their energies and thus the energy of the deactivating ³MC state, increased σ -donation boosting this effect, and increased π donation raising the energy of the Ru “t_{2g}” orbitals and resulting in quite low absorption and emission energies. These aspects of ddpd will also be exploited in other ddpd metal complexes currently prepared in our group. The use of **8** and functionalized derivatives in organic light-emitting devices, dye-sensitized solar cells (DSSCs), or biolabeling applications is actively pursued in our group.

Experimental Section

General Procedures. CH₃CN and dioxane were distilled from CaH₂ and sodium, respectively. All reagents were used as received from commercial suppliers (Acros and Sigma-Aldrich). Microwave heating was performed in a Discover Benchmate Plus (CEM Synthesis) single-mode microwave cavity, producing continuous irradiation at 2.455 GHz with 100 W (maximum power). Reaction mixtures were stirred with a magnetic stir bar during irradiation. The temperature and irradiation power were monitored during the course of the reaction. NMR spectra were recorded on a Bruker Avance DRX 400 spectrometer at 400.31 MHz (¹H), 100.66 MHz (¹³C{¹H}), and 40.56 MHz (¹⁵N). All resonances are reported in ppm versus the solvent signal as an internal standard [CD₃CN (¹H, δ = 1.94; ¹³C, δ = 1.24 ppm)] or versus external CH₃NO₂ (90% in CDCl₃; ¹⁵N, δ = 0 ppm). IR spectra were recorded with a BioRad Excalibur FTS 3100 spectrometer as KBr disks. Electrochemical experiments were carried out on a BioLogic SP-50 voltammetric analyzer using platinum wires as counter and working electrodes and 0.01 M Ag/AgNO₃ as the reference electrode. The measurements were carried out at a scan rate of 150 mV s⁻¹ for cyclic voltammetry experiments and at 50–200 mV s⁻¹ for square-wave voltammetry experiments using 0.1 M (*n*Bu₄N)(PF₆) as the supporting electrolyte in CH₃CN. Potentials are referenced to the ferrocene/ferrocenium couple ($E_{1/2}$ = 85 \pm 5 mV under the experimental conditions). UV/vis/near-IR spectra were recorded on a Varian Cary 5000 spectrometer using 1.0 cm cells (Hellma, Suprasil). Emission spectra were recorded on a Varian Cary Eclipse spectrometer. Quantum yields were determined by comparing the areas under the emission spectra on an energy scale/cm⁻¹ recorded for optically matched solutions of the sample and the reference {[Ru(bpy)₃]²⁺} = 0.062 in CH₃CN}.²⁴ For time-resolved photoluminescence measurements, a solution (c = 4.5 \times 10⁻⁶ M in butyronitrile) was filled into a homemade cuvette (tin-plated copper with quartz windows; indium-sealed; 4 mm optical path length) inside a nitrogen-filled glovebox and the cuvette was sealed and transferred to a home-built cryostat. It was kept under a dynamic vacuum (typically 10⁻⁶ mbar) for

low-temperature experiments. The sample was excited by the 517 nm output of an optical parametric oscillator (OPO; GWU Lasertechnik) itself pumped by the frequency-tripled (10 Hz) output of a pulsed Nd:YAG nanosecond laser (INDI Quanta Ray Spectra Physics). The luminescence of the sample was dispersed by a Shamrock SR-303i spectrograph with a 150 L/mm grating and detected by a gated intensified CCD detector (Andor IStar DH740 ICCD camera). The solution was illuminated with the laser beam from the detector side, and measurements were conducted at room temperature (295 K) and liquid-nitrogen temperature (77 K). Single exponentials were used to fit the experimental data. Field desorption (FD) MS spectra were recorded on a FD Finnigan MAT90 spectrometer. ESI MS spectra were recorded on a Micromass Q-TOF-Ultima spectrometer. Elemental analyses were performed by the microanalytical laboratory of the chemical institutes of the University of Mainz.

Crystal Structure Determination. Intensity data were collected with a Bruker AXS Smart1000 CCD diffractometer with an APEX II detector and an Oxford cooling system and corrected for absorption and other effects using Mo K α radiation (λ = 0.710 73 Å) at 173(2) K. The diffraction frames were integrated using the *SAINT* package, and most were corrected for absorption with *MULABS*.^{28,29} The structures were solved by direct methods and refined by the full-matrix method based on F^2 using the *SHELXTL* software package.^{30,31} All non-hydrogen atoms were refined anisotropically, while the positions of all hydrogen atoms were generated with appropriate geometric constraints and allowed to ride on their respective parent carbon atoms with fixed isotropic thermal parameters. The asymmetric unit of a crystal of **8** contains one molecule of an acetonitrile solvent and two [PF₆]⁻ counterions, one of which is disordered over two positions (site occupancy 0.73:0.27). Crystallographic data (excluding structure factors) for the structure reported in this paper have been deposited with the Cambridge Crystallographic Data Centre as supplementary publication no. CCDC-773229. Copies of the data can be obtained free of charge upon application to CCDC, 12 Union Road, Cambridge CB2 1EZ, U.K. [fax (0.44) 1223-336-033; e-mail deposit@ccdc.cam.ac.uk].

DFT calculations were carried out with the *Gaussian03*/DFT³² series of programs. The B3LYP formulation of DFT was used by employing the LANL2DZ basis set.³² No symmetry constraints were imposed on the molecules. For solvent modeling, the integral-equation-formalism polarizable continuum model (IEFPCM) was employed.

(28) *SMART Data Collection and SAINT-Plus Data Processing Software for the SMART System*, various versions; Bruker Analytical X-ray Instruments, Inc.; Madison, WI, 2000.

(29) Blessing, B. *Acta Crystallogr.* **1995**, *A51*, 33.

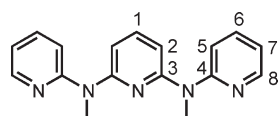
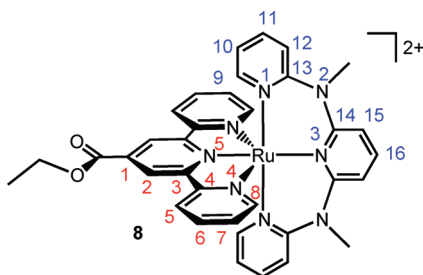
(30) Sheldrick, G. M. *SHELXTL*, version 5.1; Bruker AXS: Madison, WI, 1998.

(31) Sheldrick, G. M. *SHELXL-97*; University of Göttingen: Göttingen, Germany, 1997.

(32) Frisch, M. J.; Trucks, G. W.; Schlegel, H. B.; Scuseria, G. E.; Robb, M. A.; Cheeseman, J. R.; Montgomery, J. A.; Vreven, T., Jr.; Kudin, K. N.; Burant, J. C.; Millam, J. M.; Iyengar, S. S.; Tomasi, J.; Barone, V.; Mennucci, B.; Cossi, M.; Scalmani, G.; Rega, N.; Petersson, G. A.; Nakatsuji, H.; Hada, M.; Ehara, M.; Toyota, K.; Fukuda, R.; Hasegawa, J.; Ishida, M.; Nakajima, T.; Honda, Y.; Kitao, O.; Nakai, H.; Klene, M.; Li, X.; Knox, J. E.; Hratchian, H. P.; Cross, J. B.; Adamo, C.; Jaramillo, J.; Gomperts, R.; Stratmann, R. E.; Yazyev, O.; Austin, A. J.; Cammi, R.; Pomelli, C.; Ochterski, J. W.; Ayala, P. Y.; Morokuma, K.; Voth, G. A.; Salvador, P.; Dannenberg, J. J.; Zakrzewski, V. G.; Dapprich, S.; Daniels, A. D.; Strain, M. C.; Farkas, O.; Malick, D. K.; Rabuck, A. D.; Raghavachari, K.; Foresman, J. B.; Ortiz, J. V.; Cui, Q.; Baboul, A. G.; Clifford, S.; Cioslowski, J.; Stefanov, B. B.; Liu, G.; Liashenko, A.; Piskorz, P.; Komaromi, I.; Martin, R. L.; Fox, D. J.; Keith, T.; Al-Laham, M. A.; Peng, C. Y.; Nanayakkara, A.; Challacombe, M.; Gill, P. M. W.; Johnson, B.; Chen, W.; Wong, M. W.; Gonzalez, C.; Pople, J. A. *Gaussian 03*, revision B.03; Gaussian, Inc.: Pittsburgh, PA, 2003.

(26) Tolman, C. A. *Chem. Rev.* **1977**, *77*, 313.

(27) Shi, Q.; Thatcher, R. J.; Slattery, J.; Sauari, P. S.; Whitwood, A. C.; McGowan, P. C.; Douthwaite, R. E. *Chem.—Eur. J.* **2009**, *15*, 11346.

Chart 2. Atom Numbering of ddpd for NMR Assignment**Chart 3.** Atom Numbering of **8** for NMR Assignment

Synthesis of ddpd (Chart 2). Potassium bis(trimethylsilyl)-amide (5.670 g, 28.42 mmol, 2.6 equiv) was dissolved in dioxane (100 mL) under argon. After the addition of *N*-methylpyridin-2-ylamine (3.00 mL, 29.2 mmol, 2.7 equiv), the solution turned yellow. A solution of 2,6-dibromopyridine (2.555 g, 10.79 mmol, 1.0 equiv) in dioxane (30 mL) was added, and the mixture was heated to reflux for 64 h, resulting in a brown solution. After cooling to room temperature, water (250 mL) was added, and the aqueous phase was extracted three times with tetrahydrofuran/Et₂O (1:1, 100 mL). The combined organic phases were washed three times with a 1 M aqueous Na₂CO₃ solution and finally dried over MgSO₄. After removal of the solvent under reduced pressure, the product was purified by column chromatography (silica gel, 3:1 petroleum ether 40–60/ethyl acetate), yielding a yellow viscous liquid. Yield: 2.82 g (9.68 mmol, 90%). ¹H NMR (CD₃CN, 300 K): δ 8.29 (m, 2 H, H⁸), 7.57 (m, 2 H, H⁶), 7.50 (t, ³J_{HH} = 8.0 Hz, 1 H, H¹), 7.26 (m, 2 H, H⁵), 6.89 (m, 2 H, H⁷), 6.71 (d, ³J_{HH} = 8.0 Hz, 2 H, H³), 3.50 (s, 6 H, CH₃). ¹³C{¹H} NMR (CD₃CN, 300 K): δ 158.7 (s, C⁴), 157.2 (s, C³), 148.8 (s, C⁸), 139.8 (s, C¹), 137.8 (s, C⁶), 117.9 (s, C⁷), 116.3 (s, C⁵), 106.6 (s, C²), 36.3 (s, CH₃). MS (FD): *m/z* 291.2 (100%) [M]⁺. HR-MS (ESI⁺): Calcd for C₁₇H₁₇N₅Na: *m/z* 314.1382. Obsd: *m/z* 314.1375. Elem anal. Calcd for C₁₇H₁₇N₅ (291.35): C, 70.08; H, 5.88; N, 24.04. Found: C, 70.12; H, 5.52; N, 24.34.

Synthesis of **8 (Chart 3).** A solution of ddpd (216.4 mg, 0.743 mmol, 1.5 equiv) in ethanol (15 mL) was added to RuCl₃·(EtOOC-tpy)^{33–35} (251.0 mg, 0.490 mmol, 1.0 equiv). After the addition of *N*-ethylmorpholine (0.20 mL, 0.18 mg, 3.2 equiv), the mixture was sonicated for 1 min and heated to reflux in a laboratory microwave oven for 15 min (80 °C). The mixture was filtered over Celite (1.5 cm; diameter 3.5 cm) and rinsed with ethanol. The solvent was removed under reduced pressure, and the dark-red-brown residue was dissolved in ethanol (3 mL). The addition of an aqueous solution of NH₄PF₆ (239.0 mg, 1.466 mmol, 3.0 equiv, 3 mL of H₂O) resulted in the precipitation of a purple solid. After the precipitate was washed with water, the precipitate was dissolved in CH₃CN (10 mL) and a solution of AgNO₃ (52 mg, 0.31 mmol, 0.4 equiv) in CH₃CN

(10 mL) was added. The mixture was refluxed for 4 h. The resulting AgCl was removed by filtration, and the filtrate was concentrated to 3 mL under reduced pressure. The addition of an aqueous solution of NH₄PF₆ (156.0 mg, 0.957 mmol, 2.0 equiv, 3 mL of H₂O) resulted in the precipitation of a purple solid, which was collected by filtration and dried under reduced pressure. Yield: 298.6 mg (0.3023 mmol, 62%). Crystals suitable for single-crystal X-ray diffraction were obtained by the slow diffusion of diethyl ether into a solution of **8** in CH₃CN. ¹H NMR (CD₃CN, 300 K): δ 8.97 (s, 2 H, H²), 8.56 (m, 2 H, H⁵), 8.27 (t, ³J_{HH} = 8.2 Hz, 1 H, H¹⁶), 8.11 (m, 2 H, H⁸), 8.02 (m, 2 H, H⁶), 7.61 (m, 2 H, H¹¹), 7.56 (d, ³J_{HH} = 8.2 Hz, 2 H, H¹⁵), 7.47 (m, 2 H, H⁷), 7.17 (m, 2 H, H¹²), 6.57 (m, 2 H, H¹⁰), 6.42 (m, 2 H, H⁹), 4.58 (q, ³J_{HH} = 7.1 Hz, 2 H, CH₂CH₃), 3.46 (s, 6 H, N-CH₃), 1.52 (t, ³J_{HH} = 7.1 Hz, 3 H, CH₂CH₃). ¹³C{¹H} NMR (CD₃CN, 300 K): δ 164.9 (s, C=O), 159.8, 159.7 (2s, C³, C¹³), 158.7 (s, C⁴), 157.2 (s, C¹⁴), 155.1 (s, C⁸), 149.4 (s, C⁹), 141.8 (s, C¹⁶), 140.2 (s, C¹¹), 139.2 (s, C⁶), 136.3 (s, C¹), 128.0 (s, C⁷), 125.7 (s, C⁵), 123.8 (s, C²), 121.5 (s, C¹⁰), 116.3 (s, C¹²), 113.6 (s, C¹⁵), 63.7 (s, CH₂CH₃), 41.8 (s, NCH₃), 14.6 (s, CH₂CH₃). ¹H-¹⁵N HMBC (CD₃CN, 300 K): δ -288.1 (N²), -168.6 (N¹), -162.2 (N³), -142.2 (N⁴), -85.8 (N⁵). MS (ESI⁺): *m/z* 349.1 (7%) [M - 2PF₆]²⁺, 843.1 (100) [M - PF₆]⁺. HR-MS (ESI⁺): Calcd for C₃₅H₃₂F₆N₈O₂P₂Ru: *m/z* 837.1366. Obsd: *m/z* 837.1360. IR (KBr): $\tilde{\nu}$ 3432 (br, crystal water), 3092 (m, CH_{ar}), 2922 (m, CH_{al}), 1729 (s, CO_{ester}), 1603 (s), 1583 (m), 1492 (m), 1454 (s), 1441 (s), 1372 (m), 1343 (s), 1280 (m), 1254 (s), 1126 (m), 1100 (m), 1023 (m), 841 (vs, PF), 768 (m), 752 (m), 560 (s) cm⁻¹. UV/vis (CH₃CN): λ_{abs} (ε) 517 (7500), 319 (28 800), 276 (34 700), 236 (29 900), 205 nm (31 500 M⁻¹ cm⁻¹). Emission (CH₃CN, 295 K, λ_{exc} = 517 nm): λ_{emiss} = 729 nm [τ = 722(5) ns]. Emission (CH₃-CH₂-CH₂-CN, 77 K, λ_{exc} = 517 nm): λ_{emiss} = 707 nm [τ = 3309(15) ns]. Quantum yield (CH₃CN, λ_{exc} = 469 nm, 295 K): Φ = 0.003. CV (CH₃CN): *E*_{1/2} = +0.81 (1e), -1.40 V (2e) vs Fc/Fc⁺. Elem anal. Calcd for C₃₅H₃₂F₁₂N₈O₂P₂Ru (987.68)·5H₂O: C, 39.00; H, 3.93; N, 10.40. Found: C, 39.03; H, 3.60; N, 10.40.

Acknowledgment. This work was supported by the Deutsche Forschungsgemeinschaft (Grant HE 2778/5-2). We thank Dr. F. Laquai and M. Meister (Max Planck Institute for Polymer Research, Mainz) for measuring the excited-state lifetime of **8**.

Supporting Information Available: X-ray crystallographic data for complex **8** in CIF format, X-ray structure of complex **8** (Figure S1), crystal and structure refinement data for complex **8** (Table S1), bond lengths and angles of complex **8** (Table S2), IR spectrum, UV/vis absorption and emission spectra, ¹H NMR spectrum, ¹³C{¹H} NMR spectrum, HH COSY, NOESY, CH COSY, ¹³C-¹H HMBC, and ¹⁵N-¹H HMBC of **8** (Figures S2–S10), Cartesian coordinates of *cis-fac-9*, *trans-fac-9*, *mer-9*, the singlet ground state of **8**, the ³MLCT state of **8**, graphical representation of the frontier orbitals of **8**, results of the TD-DFT (singlet) calculation of **8** (gas phase and CH₃CN), Cartesian coordinates of Ni(CO)₃L complexes [L = κN(central pyridine)-ddpd, κN(terminal pyridine)-ddpd, NMe₃, NHC (1,3-dimethyl-2,3-dihydro-1*H*-imidazol-2-ylidene), PMe₃, PH₃, PF₃, pyridine, NH₃, CH₃CN, CH₃NC, correlation of A₁ stretching frequencies with C–O distances in Ni(CO)₃L complexes. This material is available free of charge via the Internet at <http://pubs.acs.org>.

(33) Fallahpour, R.-A. *Synthesis* **2000**, 8, 1138.(34) Fallahpour, R.-A. *Eur. J. Inorg. Chem.* **1998**, 1205.(35) Fallahpour, R.-A.; Neuburger, M.; Zehnder, M. *New J. Chem.* **1999**, 23, 53.

9.6 Excited State Tuning of Bis(tridentate) Ruthenium(II) Polypyridine Chromophores by Push-Pull Effects and Bite Angle Optimization: A Comprehensive Experimental and Theoretical Study

A. Breivogel, M. Meister, C. Förster, F. Laquai, K. Heinze, *Chem. Eur. J.* **2013**, *19*, 13745–13760.

DOI: 10.1002/chem.201302231

Reprinted with permission from John Wiley and Sons, Copyright © 2013.

Excited State Tuning of Bis(tridentate) Ruthenium(II) Polypyridine Chromophores by Push–Pull Effects and Bite Angle Optimization: A Comprehensive Experimental and Theoretical Study

Aaron Breivogel,^[a] Michael Meister,^[b] Christoph Förster,^[a] Frédéric Laquai,^[b] and Katja Heinze*^[a]

Abstract: The synergy of push–pull substitution and enlarged ligand bite angles has been used in functionalized heteroleptic bis(tridentate) polypyridine complexes of ruthenium(II) to shift the ¹MLCT absorption and the ³MLCT emission to lower energy, enhance the emission quantum yield, and to prolong the ³MLCT excited-state lifetime. In these complexes, that is, [Ru(ddpd)(EtOOC-tpy)][PF₆]₂, [Ru(ddpd-NH₂)(EtOOC-tpy)][PF₆]₂, [Ru(ddpd){(MeOOC)₃-tpy}][PF₆]₂, and [Ru(ddpd-NH₂){(EtOOC)₃-tpy}][PF₆]₂ the combination of the electron-accepting 2,2';6',2''-terpyridine (tpy) ligand

equipped with one or three COOR substituents with the electron-donating *N,N'*-dimethyl-*N,N'*-dipyridin-2-ylpyridine-2,6-diamine (ddpd) ligand decorated with none or one NH₂ group enforces spatially separated and orthogonal frontier orbitals with a small HOMO–LUMO gap resulting in low-energy ¹MLCT and ³MLCT states. The extended bite angle of the ddpd ligand increases the ligand field splitting and

pushes the deactivating ³MC state to higher energy. The properties of the new isomerically pure mixed ligand complexes have been studied by using electrochemistry, UV/Vis absorption spectroscopy, static and time-resolved luminescence spectroscopy, and transient absorption spectroscopy. The experimental data were rationalized by using density functional calculations on differently charged species (charge *n* = 0–4) and on triplet excited states (³MLCT and ³MC) as well as by time-dependent density functional calculations (excited singlet states).

Keywords: density functional calculations • excited states • ligands • luminescence • ruthenium

Introduction

Polypyridine complexes of ruthenium(II) have attracted great interest due to their outstanding and tunable photo-physical and electrochemical properties combined with high thermal and chemical robustness.^[1] They are used as light harvesters in dye-sensitized solar cells,^[2–4] luminescent emitters in light-emitting electrochemical cells,^[5–7] possible anticancer and imaging agents in phototherapy,^[8–10] sensors for ions^[11–16] and small molecules,^[17,18] photocatalysts for water splitting,^[19,20] hydrogen production,^[21–24] CO₂ reduction,^[21,23,25] and many other chemical reactions,^[23,26–29] components in mixed valence systems,^[30–35] light upconversion systems^[36–39] and molecular memory devices.^[40–42]

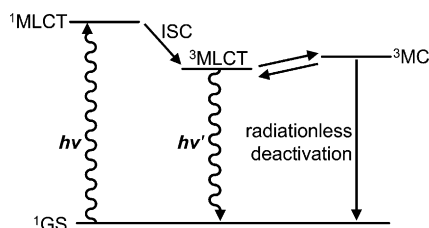
The most prominent ruthenium(II) polypyridine complexes are [Ru(bpy)₃]²⁺ (bpy = 2,2'-bipyridine) and its analogues thanks to their high ³MLCT state lifetimes ($\tau \approx 1 \mu\text{s}$) and luminescence quantum yields ($\Phi \approx 10\%$) at room temperature in solution.^[1,43] However, the intrinsic chirality of Δ, Λ -[Ru(bpy)₃]²⁺ leads to the formation of stereoisomers for unsymmetrically substituted bpy ligands, which heavily complicates synthetic procedures.^[44,45] In contrast, [Ru(tpy)₂]²⁺ ([5]²⁺, tpy = 2,2';6',2''-terpyridine) type complexes are achiral and can be synthesized free of stereoisomers even in the case of unsymmetrical substitution of the tpy 4'-positions.^[46] Additionally, the tridentate coordination should provide a higher photo and chemical stability compared with the bidentate mode with respect to ligand substitution. Despite the structural similarity of the parent complexes [Ru(bpy)₃]²⁺ and [Ru(tpy)₂]²⁺, the triplet metal-to-ligand charge transfer (³MLCT) lifetime of the latter is dramatically reduced due to an efficient radiationless deactivation through triplet metal-centered (³MC) states ($\tau \approx 0.1$ – 0.2 ns , $\Phi \leq 0.0005\%$; Scheme 1).^[47–49]

Two strategies have emerged to impede radiationless deactivation in bis(tridentate) ruthenium(II) complexes and to improve ³MLCT lifetimes and luminescence quantum yields:

[a] A. Breivogel, Dr. C. Förster, Prof. Dr. K. Heinze
Institute of Inorganic Chemistry and Analytical Chemistry
Johannes Gutenberg-University of Mainz
Duesbergweg 10-14, 55128 Mainz (Germany)
Fax: (+49) 6131-39-27-277
E-mail: katja.heinze@uni-mainz.de

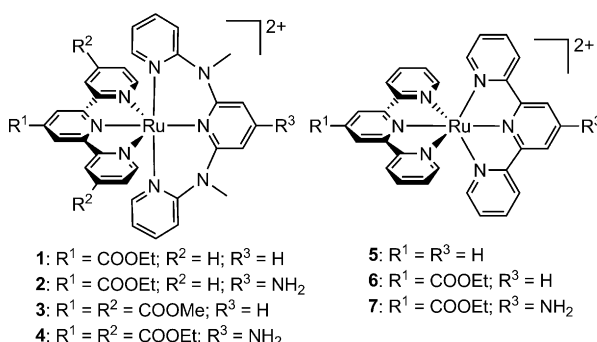
[b] M. Meister, Dr. F. Laquai
Max Planck Institute for Polymer Research
Ackermannweg 10, 55128 Mainz (Germany)

Supporting information for this article is available on the WWW under <http://dx.doi.org/10.1002/chem.201302231>.



Scheme 1. Qualitative Jablonski diagram of Ru^{II} oligopyridine complexes (GS = ground state, MLCT = metal-to-ligand charge transfer, ISC = inter-system crossing, MC = metal-centered).

- 1) Push–pull substituents at the 4-position of the central pyridine rings: Electron-withdrawing substituents lower the ³MLCT state energy, whereas electron-donating substituents raise the ³MC state energy, which increases the energy difference between the two states.^[46] For example, the bis-4'-substituted complex [(EtOOC-tpy)Ru(tpy-NH₂)]²⁺ (**[7]**²⁺, Scheme 2) possesses a significantly higher lifetime (τ = 34 ns) and a higher quantum yield (Φ = 0.18 %) compared with unsubstituted [Ru(tpy)₂]²⁺. This amino acid derivative **[7]**²⁺ has been successfully in-



Scheme 2. Bis(tridentate) ruthenium(II) oligopyridine complexes.

corporated in peptidic energy and electron-transfer systems and shows light-induced charge separation in a donor–chromophore–acceptor nanocomposite.^[25,50–54] Exceptionally high room temperature emission lifetimes and quantum yields were obtained by Schubert and Berlinguette et al. by using heteroleptic bis(tridentate) ruthenium(II) complexes incorporating electron-accepting tpy and strongly σ -electron-donating tridentate bis-(carbene)pyridine ligands (τ up to 7.9 μ s, Φ up to 11 %).^[55]

- 2) Enlargement of N–Ru–N bite angles: Typically, N–Ru–N bite angles in tpy complexes of ruthenium are around 79°. Larger bite angles (ideally 90°) would create a stronger ligand field splitting due to the better overlap between the Ru d orbitals and the pyridine nitrogen lone pairs. In a stronger ligand field the ³MC–³MLCT energy difference increases and the deactivating ³MC states are less accessible.^[48] Bite angles of close to 90° could be achieved by Hammarström et al. in [Ru(dqp)₂]²⁺ (dqp =

2,6-di(quinolin-8-yl)pyridine) with a high lifetime and quantum yield at room temperature (τ = 3.0 μ s, Φ = 2 %).^[56] The 4'-substituted analogue [Ru(dqp-COOEt)₂]²⁺ even surpasses the values of the latter (τ = 5.5 μ s, Φ = 7 %) and [Ru(dqp)₂]²⁺ complexes have already been used in donor–acceptor arrays with long-lived photoinduced charge-separated states.^[57,58] A homoleptic analogue of [Ru(tpy)₂]²⁺ containing carbonyl bridges between the pyridine rings synthesized by Ruben et al. shows bite angles of 90° and, to the best of our knowledge, features the highest reported room temperature quantum yield for a bis(tridentate) ruthenium(II) complex (τ = 3.3 μ s, Φ = 30 %).^[59] Ligands with large bite angles like dqp are flexible and therefore can lead to the formation of stereoisomers (*mer*, *cis-fac*, *trans-fac*).^[60] For this reason we developed the heteroleptic bis(tridentate) ruthenium(II) complex **[1]**[PF₆]₂ (Scheme 2), which is the first example for the combination of a tpy ligand and a ddpd ligand (ddpd = *N,N'*-dimethyl-*N,N'*-dipyridin-2-ylpyridine-2,6-diamine, **11**). The tpy ligand only allows for a *meridional* coordination of both ligands and avoids the formation of undesired stereoisomers. The ddpd ligand is a tpy analogue and shows large bite angles due to the additional NCH₃ bridges between the pyridine rings. The ³MLCT room temperature lifetime of **[1]**[PF₆]₂ and its room temperature quantum yield are significantly higher than for comparable bis(tpy) complexes (τ = 722 ns, Φ = 0.45 %).^[7,61]

Herein, we apply the push–pull strategy to the complex **[1]**[PF₆]₂ by stepwise boosting its push–pull substitution pattern with additional electron-accepting (–COOR) and electron-donating (–NH₂) substituents (**[1]**[PF₆]₂–**[4]**[PF₆]₂, Scheme 2). The amino and the (hydrolyzed) ester groups can be easily functionalized and principally connected to semiconductors, polymers, biomolecules, or potential catalysts in a directional way.^[25,50–53] A 2,2';6',2''-terpyridine (R¹R²-tpy) ligand as electron acceptor and a R³-ddpd ligand as electron donor are used in combination with additional substituents on both tridentate ligands enhancing their acceptor or donor strength, respectively. This choice of acceptor and donor abilities should lead to a small HOMO–LUMO gap, which should shift the MLCT absorption and emission energies towards the red spectral region. Additionally, the different donor–acceptor characteristics of the *meridional* coordinating ligands should enforce spatially separated (orthogonal) frontier orbitals and should equip the systems with a high electronic directionality. The second strategy aims at shifting the energy of the thermally accessible ³MC state, which is a funnel for radiationless deactivation,^[48] to higher values by employing the ddpd ligand with its large bite angle. Thus, to enhance the emission quantum yield and ³MLCT state lifetime, the ³MC–³MLCT energy difference is increased by increasing the energy of the ³MC state and by decreasing the energy of the ³MLCT state. As the latter strategy also decreases the energy between the emitting ³MLCT state and the ground state ¹GS, the effects of the

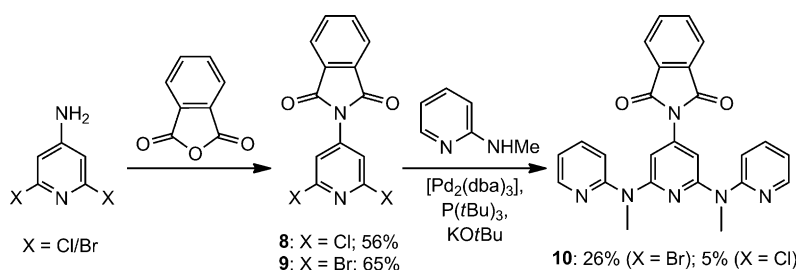
energy gap law^[62–64] also need to be considered (Scheme 1). The properties of $[1]^{2+}$ – $[4]^{2+}$ and bis(tpy) reference complexes $[5]^{2+}$ – $[7]^{2+}$ will be disclosed by electrochemistry, UV/Vis, static and time-resolved emission, transient absorption spectroscopy, and by DFT calculations (Scheme 2).

Results and Discussion

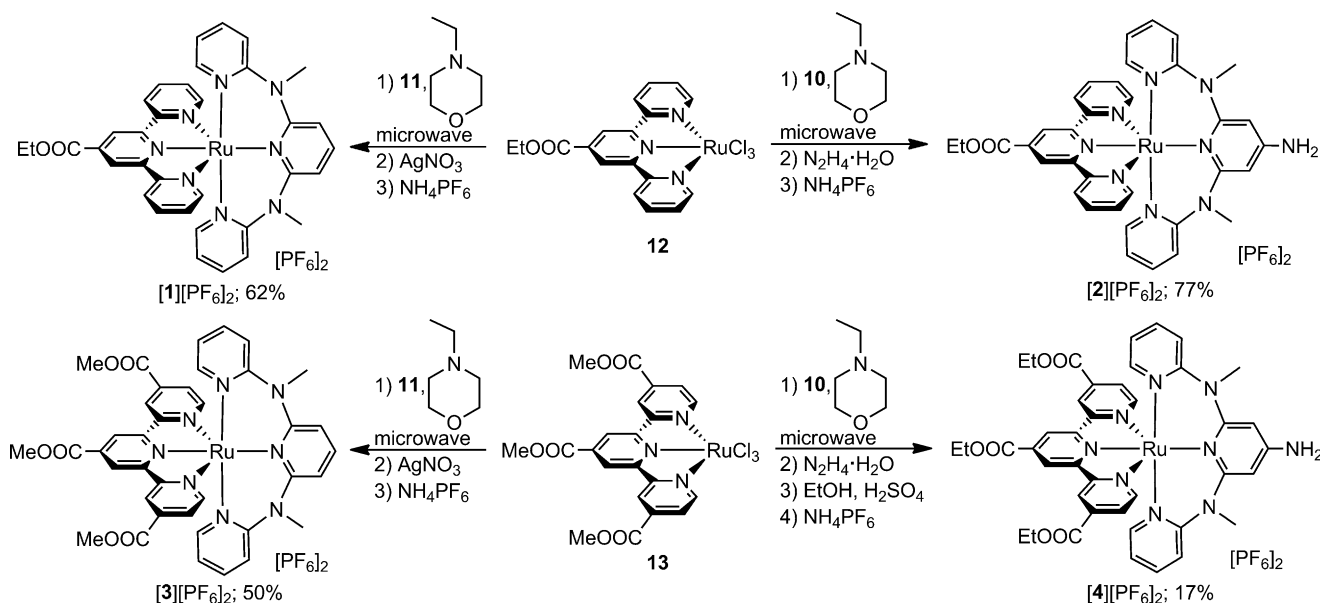
Ligand and complex synthesis and analytical characterization: The terpyridine ligands EtOOC-tpy and (MeOOC)₃-tpy, the unsubstituted ddpd ligand **11**, the trichlorido ruthenium(III) complexes **12** and **13**, and the heteroleptic complex $[1][PF_6]_2$ have been reported previously.^[61,65–67] The synthesis of the new amino-functionalized ddpd ligand precursor **10** is depicted in Scheme 3. The N-protected ligand **10** was prepared by a Pd-catalyzed Buchwald–Hartwig amination of 2,6-dichloro-4-phthalimidopyridine **8** or its bromo derivative **9**. The reasons for this protecting-group strategy are outlined in the Supporting Information. All compounds **8**–**11**^[61] were characterized by using mass spectrometry, infrared (Figure S1–S4, the Supporting Information), ¹H, ¹³C, and ¹⁵N NMR 1D- and 2D spectroscopy (Figure S5–S16, the

Supporting Information) and elemental analysis. Single crystals of **8** and **9** have been obtained and X-ray diffraction analyses show a dihedral angle of 43° between the pyridine and the phthalimido substituent in both cases (Figures S17 and S18, Tables S1–S3, the Supporting Information).

The syntheses of heteroleptic ruthenium(II) complexes $[1][PF_6]_2$ – $[4][PF_6]_2$ are depicted in Scheme 4. Starting from the trichlorido(terpyridine)ruthenium(III) precursors **12** and **13**^[65–67] all mixed ligand complexes were obtained in isomerically pure form (*mer*) in a microwave-assisted reaction with the respective ddpd ligand **10** or **11** in ethanol and *N*-ethylmorpholine as reducing agent. For a successful synthesis of $[1]^{2+}$ ^[61] and $[3]^{2+}$ comprising the unsubstituted ddpd ligand **11** the chloride ions have to be removed with AgNO₃ as AgCl. In the last step, the complexes $[1][PF_6]_2$ and $[3][PF_6]_2$ are precipitated by addition of an aqueous NH₄PF₆ solution. For $[2]^{2+}$ and $[4]^{2+}$ bearing the N-protected amino ligand **10** the phthalimido group is partially deprotected during the microwave-assisted reaction to give a mixture of phthalimide, monoethylester monoamide, and free amino group functionality of the coordinated ddpd ligand. Full deprotection is achieved in situ by treating the mixture with hydrazine hydrate. The use of AgNO₃ to remove the chloride anions proved unnecessary. During the hydrazine deprotection to give $[4]^{2+}$, the methyl ester groups are partially hydrolyzed. Therefore, the free acid groups are re-alkylated by treating the mixture with ethanol and sulfuric acid to obtain $[4]^{2+}$ as pure tris(ethylester). All complexes $[1][PF_6]_2$ – $[4][PF_6]_2$ were characterized by using ESI and HR-ESI mass



Scheme 3. Synthesis of functionalized ddpd ligand **10**.



Scheme 4. Synthesis of the heteroleptic ruthenium(II) complexes $[1][PF_6]_2$ – $[4][PF_6]_2$.

spectrometry, infrared, ^1H , ^{13}C and ^{15}N NMR 1D and 2D spectroscopy, and elemental analysis. For all complexes, the ion peaks for $[M-\text{PF}_6]^+$ and for $[M-2\text{PF}_6]^{2+}$ were observed in the ESI mass spectrum with m/z values and isotope distributions fitting excellently to the theoretical values. Moreover, the HR-ESI spectra verify the molecular formulae of all the complex cations (see the Experimental Section). ^1H NMR spectral data of $[1][\text{PF}_6]_2$ – $[4][\text{PF}_6]_2$ are summarized in the Supporting Information (Table S4) and the corresponding spectra of $[2][\text{PF}_6]_2$ – $[4][\text{PF}_6]_2$ are shown in Figures S19–S21. All NMR data confirm the presence of a single stereoisomer in each case, namely, the *meridional* one. Exemplarily, the ^1H NMR spectrum of $[2][\text{PF}_6]_2$ and its atom numbering are depicted in Figure 1. All resonances of the pyridine protons appear in the expected range from $\delta=6$ to 9 ppm. The most downfield-shifted resonance is assigned to H^2 and appears as a singlet at $\delta=8.95$ ppm. The amino protons resonate at $\delta=5.72$ and the protons of the bridging NCH_3 unit at $\delta=3.36$ ppm. Compared with $[1]^{2+}$ ($\delta=7.56$ ppm)^[61] the resonance of H^{15} in $[2]^{2+}$ is shifted to higher field ($\delta=6.80$ ppm) due to the presence of the NH_2 group as expected.^[68] For the NCH_3 moieties a single resonance is observed for each of the ^1H , ^{13}C and ^{15}N nuclei in the respective NMR spectra. The two NCH_3 units in the ddpd ligand point up and below the plane of the central pyridine plane, respectively, enforcing an interligand nuclear Overhauser effect (NOE) between NCH_3 of the ddpd ligand and H^8 of the tpy ligand vis-à-vis. $^{13}\text{C}\{^1\text{H}\}$ NMR spectra of $[1][\text{PF}_6]_2$ – $[4][\text{PF}_6]_2$ show resonances of all carbon atoms (Table S5 and Figures S22–S24, the Supporting Information). The ^{13}C resonances were successfully assigned by using 2D NMR correlation spectroscopy. ^{15}N – ^1H HMBC spectral data of $[1][\text{PF}_6]_2$ – $[4][\text{PF}_6]_2$ and of ligands **10**, **11**, and EtOOC-tpy are summarized in Table S6 and Figures S15, S16, and S25–S27 (the Supporting Information). All ^{15}N resonances, including pyridyl, amino, and phthalimido nitrogen

atoms have been identified and assigned by correlation to the respective adjacent hydrogen nuclei. The coordinating pyridine nitrogen atoms of the ligands are much more affected by Ru^{2+} coordination (coordination shift) than the remote and non-coordinating NCH_3 ^{15}N nuclei substantiating that the NCH_3 groups remain indeed non-coordinated.

Solid-state IR spectra of complexes $[1][\text{PF}_6]_2$ – $[4][\text{PF}_6]_2$ show very strong bands at 841 – 843 cm^{-1} , which are assigned to the PF stretching vibration of the counterions. Functional groups of the cations are identified by strong bands at 1726 – 1734 cm^{-1} belonging to C=O stretching vibrations of the ester moieties and by bands at 3400 – 3468 cm^{-1} and 3240 cm^{-1} assigned to asymmetric and symmetric NH stretching vibrations (Figure S28–S30, the Supporting Information).

Single crystals of $[2][\text{PF}_6]_2$ and $[3][\text{PF}_6]_2$ were obtained by diffusion of diethyl ether into an acetonitrile solution of the complexes. The single-crystal X-ray diffraction analysis of $[1][\text{PF}_6]_2$ has been described previously.^[61] Selected bond lengths and angles obtained by X-ray diffraction and from DFT optimized geometries are summarized in Table 1. All complex cations $[1]^{2+}$ – $[3]^{2+}$ exhibit *meridional* coordination of the tridentate ligands as expected (Figure 2 and the Supporting Information, Figures S31–S32 and Tables S7–S9). Cations $[1]^{2+}$ – $[3]^{2+}$ feature very similar Ru–N bond lengths and N–Ru–N bond angles. The shortest Ru–N distance in $[1]^{2+}$ – $[3]^{2+}$ is the one between ruthenium and the central tpy-nitrogen atom N2 (1.94 – 1.95 Å) due to the small bite angle of tpy. All other Ru–N bond lengths in $[1]^{2+}$ – $[3]^{2+}$ are around 2.07 – 2.09 Å . The DFT-calculated values are about 0.03 – 0.04 Å longer (1.98 Å for Ru–N2 and 2.11 – 2.12 Å for all other Ru–N bonds) but reproduce the short central Ru–N(tpy) distance. The N–Ru–N bite angles are well reproduced by DFT calculations with tpy bite angles of 79 – 80° and ddpd bite angles of 87 – 88° . The latter nearly approach the value of an ideal octahedron (90°) allowing for an opti-

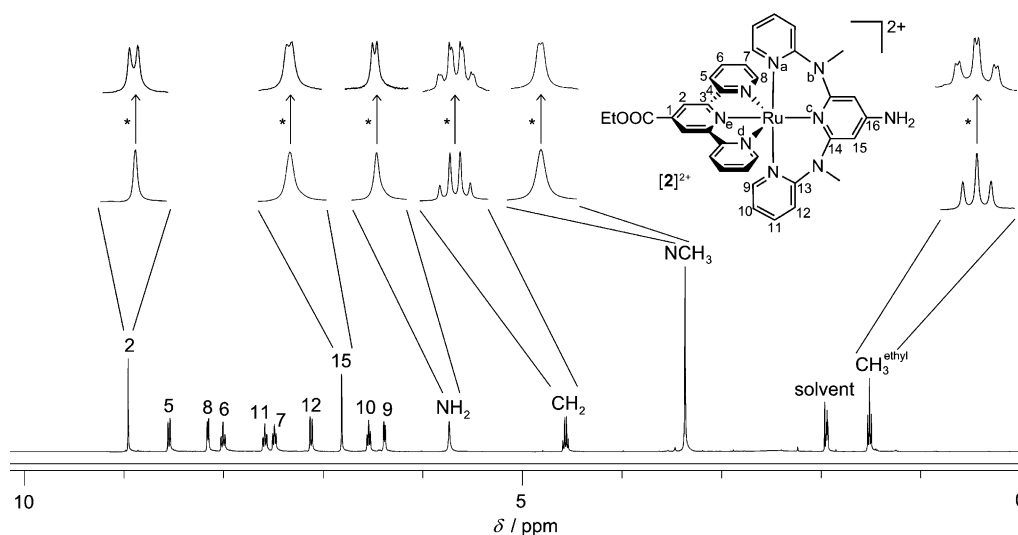


Figure 1. ^1H NMR spectrum of $[2][\text{PF}_6]_2$ and atom numbering in CD_3CN . The asterisk (*) indicates the splitting of the proton resonances of $[2]^{2+}$ after addition of chiral $(\Delta\text{-TRISPHAT})^-$ counterions.

Table 1. Experimental (X-ray diffraction) and DFT calculated (singlet ground state, B3LYP/LANL2DZ, IEFPCM in CH₃CN), selected bond lengths [Å] and angles [°] of [1]²⁺–[4]²⁺.

	[1] ²⁺ exp	[1] ²⁺ DFT	[2] ²⁺ exp	[2] ²⁺ DFT	[3] ²⁺ exp	[3] ²⁺ DFT	[4] ²⁺ DFT
Ru–N1	2.079(2)	2.117	2.0804(17)	2.114	2.0777(15)	2.109	2.107
Ru–N2	1.944(2)	1.983	1.9465(16)	1.980	1.9481(14)	1.984	1.982
Ru–N3	2.078(2)	2.117	2.0869(16)	2.116	2.0921(15)	2.108	2.107
Ru–N4	2.076(2)	2.119	2.0750(16)	2.118	2.0800(15)	2.119	2.119
Ru–N5	2.078(2)	2.114	2.0806(16)	2.113	2.0858(15)	2.114	2.111
Ru–N6	2.072(2)	2.119	2.0766(16)	2.118	2.0784(15)	2.119	2.118
N1–Ru–N2	79.68(8)	79.23	79.80(7)	79.28	79.84(6)	79.28	79.33
N1–Ru–N3	159.22(8)	158.46	159.53(7)	158.56	159.10(6)	158.59	158.72
N2–Ru–N5	178.29(9)	179.85	178.19(7)	179.91	177.18(6)	179.95	179.92
N4–Ru–N5	87.51(8)	87.55	87.33(6)	87.28	87.34(6)	87.54	87.31
N4–Ru–N6	174.70(8)	175.12	174.83(6)	174.56	174.74(6)	175.04	174.58

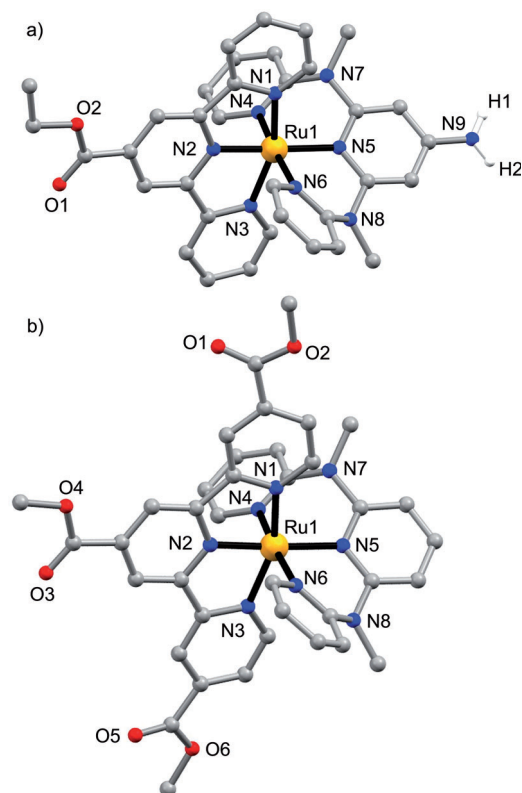


Figure 2. Molecular structures of cations of a) [2]²⁺ and b) [3]²⁺ in the solid state (CH hydrogen atoms omitted).

mal σ -overlap of metal d orbitals (“ e_g ”) with the lone pairs of the ddpd nitrogen donor atoms. The coordinated ddpd ligand is slightly twisted with the NCH₃ groups pointing up and below the plane of the central pyridine ring as already deduced from the nuclear Overhauser effect (NOE) data.

To explore this helical twist of the coordinated ddpd ligand, a solution of [2][PF₆]₂ was treated with the chiral anion [Δ-tris(tetrachloro-1,2-benzenediolato)phosphate(V)] ((Δ-TRISPHAT)[−]).^[45,69] This splits the ¹H NMR resonances of [2]²⁺ (H², H¹⁵, NH₂, CH₂, NCH₃, CH₃; Figure 1; Figure S33, the Supporting Information) into two signal sets

(≈1.0:1.3 by integration of ¹H NMR spectrum) revealing the helical chirality of [2]²⁺. The formation of diastereomeric ion pairs is a result of the electrostatic attraction between the cations and anions leading to a high proximity between [2]²⁺ and the (Δ-TRISPHAT)[−] or [PF₆][−] counterions. Indeed, the solid-state structures of [2][PF₆]₂ and [3][PF₆]₂ reveal that the [PF₆][−] counterions are situated in chiral “pockets” formed by the tridentate ligands (Figure 3). The two [PF₆][−] counterions with the shortest Ru...P distance (≈6 Å) lie vis-à-vis on both sides of the ruthenium atom. Each hexafluorophosphate is embraced by two neighboring pyridine rings of one chelate ligand and by one additional pyridine ring of the other tridentate ligand, respec-

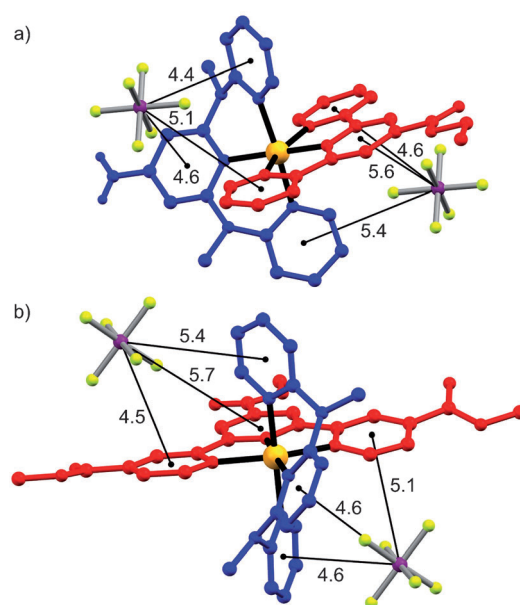


Figure 3. Arrangement of cations and the two nearest [PF₆][−] counterions of a) [2]²⁺ and b) [3]²⁺ in the solid state (red: tpy, blue: ddpd, CH hydrogen atoms omitted). Distances between the phosphorus atoms and the center of the surrounding pyridine rings are indicated in Å.

tively, with distances between the phosphorus atom and the center of the pyridine rings of 4.4–5.7 Å. Similar contact ion pairs are expected for the (Δ-TRISPHAT)[−] anion and [2]²⁺ with the anion inserted into the chiral “pockets” of the cation.

Electrochemistry of [1][PF₆]₂–[4][PF₆]₂ and reference complexes: Electrochemical data of [1][PF₆]₂–[4][PF₆]₂ are obtained by cyclic and square wave voltammetry in acetonitrile solution and [n-Bu₄N][PF₆] as the supporting electrolyte. All potential values are referenced to the Fc/Fc⁺ couple. Electrochemical data of all complexes [1][PF₆]₂–[7][PF₆]₂ are summarized in Table 2 (Figures S34–S36, the Supporting Information). Exemplarily, Figure 4 depicts cyclic and square wave voltammograms of [4][PF₆]₂. The reversible one-elect-

Table 2. Electrochemical data^[a] of complexes **[1]**[PF₆]₂–**[7]**[PF₆]₂.

	$E_{1/2}$ ddpd/ddpd ⁺	$E_{1/2}$ Ru ^{II} /Ru ^{III}	$E_{1/2}$ tpy/tpy [–]
[1] [PF ₆] ₂ ^[a]	+1.80 ^[b]	+0.81	–1.47, –2.09 ^[b]
[2] [PF ₆] ₂ ^[a]	+1.73 ^[b]	+0.64	–1.50, –2.11 ^[b] , –2.21 ^[b]
[3] [PF ₆] ₂ ^[a]	+1.80 ^[b]	+0.92	–1.25 ^[b] , –1.70 ^[b]
[4] [PF ₆] ₂ ^[a]	+1.70 ^[b]	+0.73	–1.32, –1.75
[5] [PF ₆] ₂ ^{[46][a]}	–	+0.92	–1.67
[6] [PF ₆] ₂ ^{[7][c]}	–	+0.96	–1.27, –1.45
[7] [PF ₆] ₂ ^{[53,70][a]}	–	+0.68	–1.54, –1.99

[a] In CH₃CN in V versus Fc/Fc⁺. [b] Irreversible, E_p given. [c] No solvent denoted.

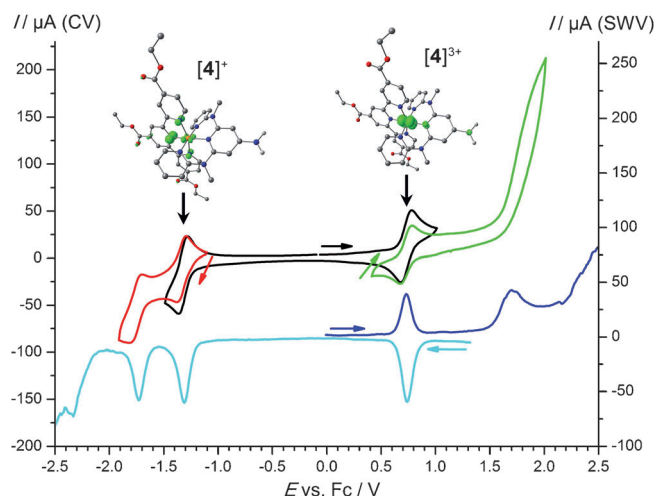


Figure 4. Cyclic voltammogram (top) and square wave voltammogram (bottom) of **[4]**[PF₆]₂ in CH₃CN; 0.1 M *n*Bu₄[PF₆]. The inset structures show the DFT calculated spin densities (contour value 0.01 au) of the reduced and oxidized species **[4]**⁺ and **[4]**³⁺, respectively.

tron oxidation of **[4]**²⁺ to **[4]**³⁺ at 0.73 V is assigned to the Ru^{II/III} redox couple in analogy to similar complexes.^[7,53,54,61] To further confirm this assignment, DFT calculations (B3LYP/LANL2DZ, IEFPCM, CH₃CN) were performed on singly oxidized species **[1]**³⁺–**[4]**³⁺ and on bis(tpy) ruthenium reference compounds **[5]**³⁺–**[7]**³⁺ (without (PF₆)[–] counterions, multiplicity $M=2$). Indeed, the spin density is largely located on the ruthenium atom with Mulliken spin densities calculated as 0.85, 0.78, 0.83, 0.77, 0.88, 0.88, and 0.76 for **[1]**³⁺–**[7]**³⁺, respectively (Figure S37, the Supporting Information). For **[2]**³⁺, **[4]**³⁺, and **[7]**³⁺ bearing NH₂ groups, a small amount of spin density is delocalized onto the nitrogen atom of the NH₂ group (Mulliken spin density on N: 0.06, 0.07, and 0.11), which underlines the electron-donating character of the amino group in these complexes (Figure 4).^[25,53,54] This electron donation is experimentally clearly observed in the oxidation potentials of complexes with and without an NH₂ group **[2]**²⁺/**[1]**²⁺, **[4]**²⁺/**[3]**²⁺ and **[7]**²⁺/**[6]**²⁺ (Table 2).^[7,53,54,61] On the other hand, comparing the Ru^{II/III} potential of complexes with one or three ester substituents **[1]**²⁺/**[3]**²⁺ and **[2]**²⁺/**[4]**²⁺ reveals that their electron-withdrawing nature hampers the largely metal-centered oxidation by roughly 0.1 V.

The second experimentally observed oxidation of **[1]**²⁺–**[4]**²⁺ at 1.70–1.80 V is irreversible. DFT calculations of doubly oxidized complexes **[1]**⁴⁺–**[4]**⁴⁺ ($M=3$) and reference compounds **[5]**⁴⁺–**[7]**⁴⁺ are depicted in Figure S38 (the Supporting Information). The spin density in bis(tpy) complexes **[5]**⁴⁺ and **[6]**⁴⁺ is located almost entirely on the metal center and for **[7]**⁴⁺ also partly on the NH₂ group. However, in ddpd complexes **[1]**⁴⁺–**[4]**⁴⁺ a significant amount of spin density is delocalized onto the nitrogen atoms of the NCH₃ groups. Therefore, we assign the second oxidation in complexes **[1]**²⁺–**[4]**²⁺ to the irreversible oxidation of the NCH₃ groups of the ddpd ligands. Again, the second oxidation potential of NH₂-containing ddpd complexes **[2]**²⁺ and **[4]**²⁺ is lower than that of their NH₂-free counterparts **[1]**²⁺ and **[3]**²⁺, respectively (Table 2).

Two reduction waves are observed for **[1]**²⁺–**[4]**²⁺ and assigned to ligand-based reductions.^[53,61] The first reduction is clearly centered on the tpy ligand as it is strongly affected by the number of ester substituents on the tpy ligand (**[1]**²⁺/**[3]**²⁺; **[2]**²⁺/**[4]**²⁺) and only marginally affected by the presence of NH₂ groups on the ddpd ligand (**[1]**²⁺/**[2]**²⁺; **[3]**²⁺/**[4]**²⁺). The second reduction follows the trend of the first reduction, with triesters **[3]**⁺ and **[4]**⁺ being much more easily reduced than **[1]**⁺ and **[2]**⁺ (Table 2). This leads to the conclusion that both the first and the second reduction are related to the tpy ligands.

DFT calculated spin densities of the singly reduced species **[1]**⁺–**[7]**⁺ ($M=2$) and doubly ($M=3$) reduced species **[1]**⁰–**[7]**⁰ are depicted in Figures S39 and S40 of the Supporting Information, respectively. As spin densities are mainly localized on the tpy ligand(s) in all cases the experimental assignment to tpy reductions is confirmed. In some cases the singlet species **[1]**⁰–**[7]**⁰ ($M=1$) are calculated slightly lower in energy than their triplet counterparts ($M=3$). Thus, for a pictorial comparison, the highest occupied molecular orbitals (HOMOs) of these singlet species were also calculated (the Supporting Information, Figure S40). The HOMOs of **[1]**⁰–**[4]**⁰ ($M=1$) are fully localized on the (ROOC)_{*n*}-tpy ligand leading to the same conclusion as the spin density in the triplet species.

Exemplarily, complex **[2]**²⁺ was chemically oxidized by ammonium cerium(IV) nitrate to **[2]**³⁺ and reduced by decamethylcobaltocene to **[2]**⁺. EPR spectra of the resulting radicals were measured at 77 K. The radical **[2]**³⁺ gives a rhombic signal ($g_{1,2,3}=2.4440, 2.2694, 2.0300$; $\Delta g=0.4140$ by spectral simulation; Figure S41, the Supporting Information). This signal is in full accordance with similar complexes of Ru^{III}^[52] and the DFT calculations of **[2]**³⁺ (Figure S37, the Supporting Information). For the one-electron-reduced radical **[2]**⁺ a less rhombic signal is obtained ($g_{1,2,3}=2.0089, 1.9865, 1.9720$; $\Delta g=0.0387$ by spectral simulation; Figure S42, the Supporting Information). The reduced g anisotropy points to a ligand-based reduction with some ruthenium admixture,^[25,52] which is fully corroborated by DFT calculations for **[2]**⁺ (Mulliken spin density of 0.10 on Ru; Figure S39, the Supporting Information).

In summary, oxidation occurs at the ruthenium center (plus some ddpd-NH₂ admixture for [2]²⁺ and [4]²⁺), whereas reduction is confined to the tpy ligand. Consequently, oxidation is favored by NH₂ substitution at ddpd, whereas reduction is facilitated by COOR substitution at tpy leading to the smallest difference between oxidation and reduction potentials in [4]²⁺ in the series [1]²⁺–[4]²⁺ (Table 2). This electronic situation should also be reflected in the optical properties.

Optical properties of [1][PF₆]₂–[4][PF₆]₂ and reference complexes: Experimental UV/Vis data together with time-dependent (TD) DFT (IEFPCM, CH₃CN) calculated stick spectra showing the oscillator strength *f* of the calculated transitions are graphically depicted in Figure 5 and numerically listed in Table 3.

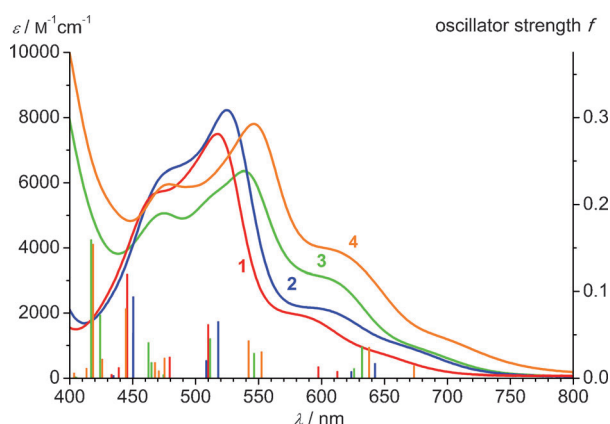


Figure 5. Experimental UV/Vis spectra and calculated stick spectra (TD-DFT, IEFPCM, CH₃CN) of [1]²⁺–[4]²⁺ in CH₃CN.

The absorption spectra of [1][PF₆]₂–[4][PF₆]₂ in acetonitrile show ligand-centered $\pi \rightarrow \pi^*$ transitions below $\lambda = 350$ nm. In the visible spectral region characteristic metal-to-ligand charge transfer (MLCT) bands with maxima at $\lambda_{\text{max}} = 517$ –546 nm and further maxima (or shoulders) at around $\lambda \approx 470$, 600, and 665 nm are found. Similar to the electrochemical data, the MLCT maxima are affected by the ligand type and the ligand-substitution pattern.

Replacing a tpy ligand by ddpd ([6]²⁺ \rightarrow [1]²⁺; [7]²⁺ \rightarrow [2]²⁺) causes a bathochromic shift of the MLCT band (485^[7] \rightarrow 517 nm,^[61] 502^[53] \rightarrow 525 nm) due to the electron-donating NCH₃ groups, which raise the energy of the (mainly ruthenium-centered) HOMO, leaving the lowest occupied molecular orbital (LUMO) of the tpy acceptor essentially unaffected. This results in a smaller HOMO–LUMO gap (Table 3). Attaching electron-donating NH₂ groups to the ddpd ligand further decreases the HOMO–LUMO gap ([1][PF₆]₂ \rightarrow [2][PF₆]₂; [3][PF₆]₂ \rightarrow [4][PF₆]₂, Table 3, Figure 6). Installing more electron-withdrawing ester substituents at the acceptor tpy ligand also results in bathochromically shifted MLCT absorptions ([1]²⁺ \rightarrow [3]²⁺; [2]²⁺ \rightarrow [4]²⁺, Table 3, Figure 5). The strongest push–pull combination is realized in [4]²⁺,

Table 3. UV/Vis data of complexes [1][PF₆]₂–[7][PF₆]₂ in CH₃CN and TD-DFT data (B3LYP/LANL2DZ, IEFPCM in CH₃CN) data.

	Experimental MLCT λ_{max} [nm] (ϵ [M ⁻¹ cm ⁻¹])	$\pi \rightarrow \pi^*$ λ_{max} [nm] (ϵ [M ⁻¹ cm ⁻¹])	DFT ^[a] λ [nm] (<i>f</i>)
[1][PF ₆] ₂	630 (1000, sh), 582 (1900, sh), 517 (7500), 473 (5700, sh)	319 (28800), 276 (34700), 236 (29900), 205 (31500)	596.70 (0.0116), 507.85 (0.0576), 478.37 (0.0215), 444.82 (0.1188)
[2][PF ₆] ₂	648 (1200, sh), 595 (2200, sh), 525 (8230), 475 (6300, sh)	323 (26700), 273 (42000), 238 (43600)	642.20 (0.0167), 623.45 (0.0072), 517.71 (0.0649), 508.21 (0.0198), 450.24 (0.0937), 450.08 (0.0516)
[3][PF ₆] ₂	687 (800, sh), 603 (3100, sh), 539 (6360), 508 (5400, sh), 475 (5060)	340 (31000), 292 (34200), 210 (52400)	631.34 (0.0356), 625.10 (0.0106), 545.59 (0.0283), 510.71 (0.0451), 464.10 (0.0174), 461.70 (0.0405), 423.32 (0.0725), 416.11 (0.1591)
[4][PF ₆] ₂	696 (1200, sh), 622 (3700, sh), 546 (7810), 479 (5960)	341 (32000), 292 (37200), 223 (45600)	674.37 (0.0139), 638.74 (0.0352), 553.25 (0.0300), 543.00 (0.0428), 476.16 (0.0226), 468.56 (0.0175), 445.44 (0.0797), 426.62 (0.0214), 419.40 (0.1538)
[5][PF ₆] ₂ ^[49]	476 (14400)	308 (57400), 269 (38800)	555.80 (0.0063), 489.74 (0.0144), 471.01 (0.1314), 441.43 (0.0262), 426.47 (0.1782), 425.02 (0.0372), 415.02 (0.0447)
[6][PF ₆] ₂ ^[7]	485 (18140)	309 (51690), 272 (42450), 225 (39620)	502.22 (0.0151), 502.22 (0.0151), 456.98 (0.0526), 429.73 (0.1659), 428.54 (0.0190), 428.54 (0.0192), 425.14 (0.0297), 425.14 (0.0297)
[7][PF ₆] ₂ ^[53]	502 (19080)	318 (37610), 306 (34760), 274 (50990), 236 (42800)	572.52 (0.0064), 483.95 (0.1485), 453.79 (0.0593), 446.09 (0.0838), 439.61 (0.0411), 432.21 (0.1618)

[a] Highest calculated oscillator strengths *f* at $\lambda > 400$ nm (TD-DFT, IEFPCM, CH₃CN). For a complete list see the Supporting Information.

which displays its MLCT band at the lowest energy in the reported series, consistent with the redox data. We note that [1]²⁺–[4]²⁺ have more structured MLCT absorption bands than their bis(tpy) counterparts [6]²⁺ and [7]²⁺. Extinction coefficients at the band maxima of [1]²⁺–[4]²⁺ are significantly lower than for [6]²⁺ and [7]²⁺,^[7,53,54] which might be due to the fact that the low-energy MLCT excitations only involve tpy ligands but no ddpd ligands. The extinction coefficients of the amino derivatives [2]²⁺, [4]²⁺,

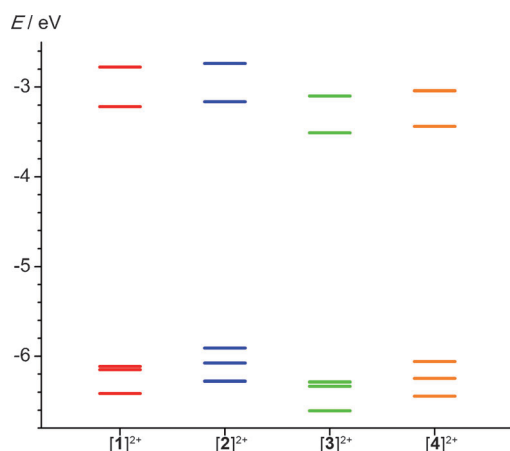


Figure 6. Energies of relevant frontier molecular orbitals (HOMO-2, HOMO-1, HOMO, LUMO, and LUMO + 1) of $[1]^{2+}$ – $[4]^{2+}$.

and $[7]^{2+}$ are consistently larger than that of their respective NH_2 -free parent complexes $[1]^{2+}$, $[3]^{2+}$, and $[6]^{2+}$. This is based on the enlarged chromophore system, which extends onto the NH_2 group in $[2]^{2+}$, $[4]^{2+}$, and $[7]^{2+}$.

The Kohn–Sham frontier molecular orbitals have been calculated by using DFT (B3LYP/LANL2DZ, IEFPCM, CH_3CN) for $[1]^{2+}$ – $[4]^{2+}$ and their energies are presented in Figure 6. Figure 7 exemplarily depicts the frontier molecular

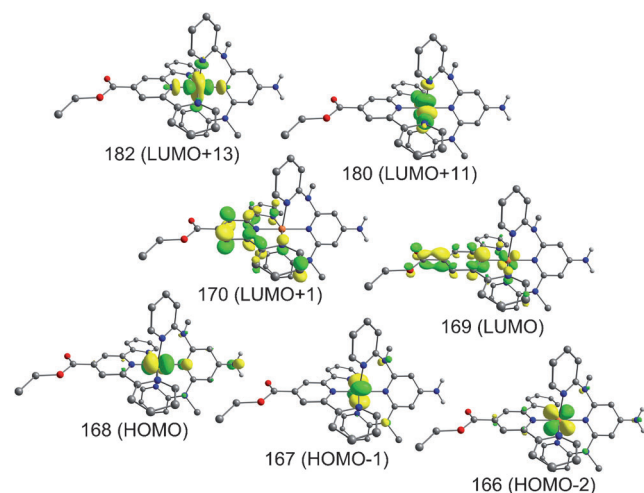


Figure 7. Relevant Kohn–Sham frontier molecular orbitals (contour value 0.06 au) of $[2]^{2+}$ (CH hydrogen atoms omitted).

orbitals of $[2]^{2+}$. HOMO to HOMO-2 are essentially ruthenium-centered corresponding to the t_{2g} orbitals in O_h symmetry, whereas LUMO and LUMO + 1 are localized on the tpy ligand.^[55] The “ e_g ” orbitals LUMO + 11 and LUMO + 13 are found at a higher energy. Introduction of an NH_2 group at the ddpd ligand ($[1]^{2+} \rightarrow [2]^{2+}$) raises the HOMO energy by $\Delta E_{\text{HOMO}} = 0.21$ eV, whereas the LUMO energy is hardly affected ($\Delta E_{\text{LUMO}} = 0.05$ eV). Similar values are calculated for the pair $[3]^{2+} \rightarrow [4]^{2+}$ ($\Delta E_{\text{HOMO}} = 0.23$; $\Delta E_{\text{LUMO}} = 0.07$ eV). Installing more ester substituents at the tpy ligand lowers

the LUMO energy more than the HOMO energy ($[1]^{2+} \rightarrow [3]^{2+}$: $\Delta E_{\text{LUMO}} = 0.29$; $\Delta E_{\text{HOMO}} = 0.17$ eV and $[2]^{2+} \rightarrow [4]^{2+}$: $\Delta E_{\text{LUMO}} = 0.27$; $\Delta E_{\text{HOMO}} = 0.15$ eV) resulting in a net smaller HOMO–LUMO gap consistent with a bathochromically shifted MLCT absorption (Figures 5 and 6). The HOMO of the NH_2 -substituted ddpd complexes $[2]^{2+}$ and $[4]^{2+}$ extends onto the NH_2 group similar to that of $[7]^{2+}$ and thus enhances the transition dipole moment leading to higher extinction coefficients (Table 3).^[54]

The absorption spectra of $[1]^{2+}$ – $[4]^{2+}$ were also estimated by TD-DFT calculations including a polarizable solvent continuum model.^[55,71,72] The characteristic experimental bandshape with four discernible features (Table 3, Figure 5) is reproduced as MLCT transitions originating from the metal-centered orbitals (HOMO to HOMO-2) to the tpy-based π^* orbitals (LUMO and LUMO + 1). For $[2]^{2+}$ the MLCT band is composed of four sets of transitions centered at 450.1 ($f = 0.0516$)/450.2 ($f = 0.0937$), 508.2 ($f = 0.0198$)/517.5 ($f = 0.0649$), 623.5 ($f = 0.0072$), and 642.2 nm ($f = 0.0167$). The bathochromic shift and the shape of the MLCT band of $[4]^{2+}$ is also fully reproduced by the TD-DFT calculation by 468.6 ($f = 0.0175$)/476.2 ($f = 0.0226$), 543.0 ($f = 0.0428$)/553.3 ($f = 0.0300$), 638.7 ($f = 0.0352$), and 674.4 ($f = 0.0139$). Furthermore, the individual sum of oscillator strengths Σf at $\lambda > 400$ nm increases by attaching an amino group ($\Sigma f = 0.2408$ ($[1]^{2+}$) \rightarrow 0.2564 ($[2]^{2+}$) and $\Sigma f = 0.4153$ ($[3]^{2+}$) \rightarrow 0.4410 ($[4]^{2+}$)). The total experimental integrated intensity $\int I$ of the MLCT absorption bands was calculated on an energy scale (cm^{-1}). In the range $\lambda = 400$ – 1000 nm ($25\,000$ – $10\,000$ cm^{-1}), the integrated intensity $\int I$ increases in the same direction ($\int I = 3.57 \times 10^7 \text{ M}^{-1} \text{ cm}^{-2}$ ($[1]^{2+}$) \rightarrow $4.01 \times 10^7 \text{ M}^{-1} \text{ cm}^{-2}$ ($[2]^{2+}$) and $\int I = 4.58 \times 10^7 \text{ M}^{-1} \text{ cm}^{-2}$ ($[3]^{2+}$) \rightarrow $5.86 \times 10^7 \text{ M}^{-1} \text{ cm}^{-2}$ ($[4]^{2+}$)). The high absorptivity in the visible spectral region up to 700 nm of the amino-substituted complexes $[2]^{2+}$ and $[4]^{2+}$ would be especially beneficial for harvesting the low-energy red light in dye-sensitized solar cells. For reference compounds $[5]^{2+}$ – $[7]^{2+}$, the sums of the oscillator strengths Σf at $\lambda > 400$ nm ($\Sigma f = 0.3463$ ($[5]^{2+}$) $< \Sigma f = 0.4395$ ($[6]^{2+}$) $< \Sigma f = 0.5026$ ($[7]^{2+}$)) is also nicely in accordance with the trend of their respective experimental extinction coefficients of their lowest-energy MLCT band (Table 3).

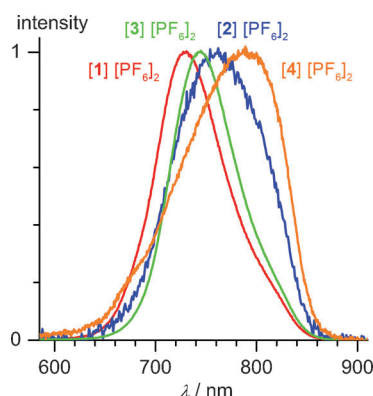
Emission data of $[1][\text{PF}_6]_2$ – $[7][\text{PF}_6]_2$ are summarized in Table 4. In a solution of CH_3CN at room temperature, complexes $[1]^{2+}$ – $[4]^{2+}$ emit red to near-infrared light with emission maxima at $\lambda_{\text{max}} > 720$ nm bathochromically shifted in the series $[1]^{2+} < [3]^{2+} < [2]^{2+} < [4]^{2+}$ ($\lambda_{\text{max}} = 729, 744, 762$, and 788 nm; Figure 8). Both the amino groups at the push-substituted side and the ester groups at the pull-substituted side act in a cooperative manner and lower the energy of the emitting $^3\text{MLCT}$ state. The mixed ligand complex $[2]^{2+}$ emits at significantly lower energy than the bis(tpy) complex $[7]^{2+}$ ($[2]^{2+}$: $\lambda_{\text{max}} = 762$ nm; $[7]^{2+}$: $\lambda_{\text{max}} = 734$ nm), which is essentially due to the electron-donating NCH_3 groups present in the ddpd ligand.

Emission energies were estimated by using DFT calculations (B3LYP/LANL2DZ, IEFPCM, CH_3CN) as energy difference of the energy of the optimized $^3\text{MLCT}$ state and the

Table 4. Experimental and DFT calculated emission data of complexes [1][PF₆]₂–[7][PF₆]₂.

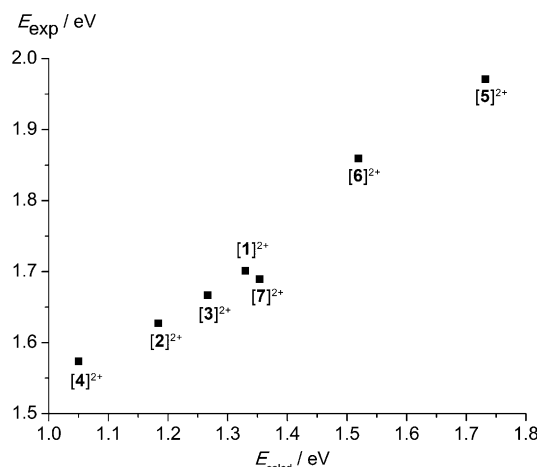
	Experimental			DFT ^[d]		
	$\lambda_{\text{max},295\text{K}}^{[a]}$ [nm] ($E_{\text{max},295\text{K}}$ [eV])	$\Phi_{295\text{K}}^{[a]}$ [%] (λ_{ex} [nm])	$\tau_{295\text{K}}$ [ns]	$\lambda_{\text{max},77\text{K}}^{[b]}$ [nm] ($E_{\text{max},77\text{K}}$ [eV])	$\tau_{77\text{K}}^{[b]}$ [ns]	$\tau_{\text{TA}}^{[b,c]}$ [ps]
[1][PF ₆] ₂	729 (1.70)	0.45 (469.0)	722 ^[b]	707 (1.75)	3309	9.3
[2][PF ₆] ₂	762 (1.63)	0.042 (474.5)	149 ^[b]	749 (1.66)	1123	8.4
[3][PF ₆] ₂	744 (1.67)	1.1 (467.5)	841 ^[b]	728 (1.70)	3251	16.7
[4][PF ₆] ₂	788 (1.57)	0.052 (467.5)	136 ^[b]	779 (1.59)	1002	7.5
[5][PF ₆] ₂ ^[49]	629 (1.97)	≤ 0.0005 (n.a.)	≈ 0.1–0.2 ^[e]	n.a.	10600	n.a.
[6][PF ₆] ₂ ^{[7][f]}	667 (1.86)	0.027 (n.a.)	32	n.a.	n.a.	8.7
[7][PF ₆] ₂ ^[54]	734 (1.69)	0.18 (n.a.)	34 ^[a]	702 (1.77)	n.a.	7.2

[a] In CH₃CN. [b] In PrCN. [c] Time constants from picosecond TA spectroscopy at 295 K. [d] Calculated from the energy difference of the optimized ³MLCT state and the singlet state with ³MLCT geometry. [e] Various solvents. [f] No solvent denoted.

Figure 8. Normalized emission spectra of [1][PF₆]₂–[4][PF₆]₂ in CH₃CN at room temperature.

energy of the singlet ground state at the ³MLCT state geometry. Figure 9 shows a clear correlation of the DFT-calculated values of [1]²⁺–[7]²⁺ with the experimentally determined ones. Thus, the DFT derived conclusions corroborate the experimental findings and underpin the successful push–pull concept to manipulate absorption and emission energies.

All mixed ligand complexes [1]²⁺–[4]²⁺ display high room temperature emission quantum yields and long ³MLCT-state lifetimes in fluid solution in comparison to the essentially non-emissive bis(tpy) complex [5]²⁺ (Table 4). Recently, cyclometalated ligands as strong donors in ruthenium(II) complexes have been reported with quantum yields of 0.001–0.025 % and lifetimes of 1–30 ns.^[73,74] The significantly higher values for [1]²⁺–[4]²⁺ are based on a synergetic effect of the push–pull substitution (lower ³MLCT state) and the stronger ligand field imposed by the ddpd ligand with the large bite angle (higher ³MC state). However, for the low-energy emitting complexes [2]²⁺ and [4]²⁺ a further effect is noted. The lower emission energy of the amino-substituted complexes renders them susceptible to radiationless deactivation to the ground state (energy-gap law^[62–64]) especially due to the presence of high-energy oscillators such as the N–H stretch (≈ 3450 cm^{−1}). This detrimental effect of the NH₂ group significantly reduces the quantum yield and room temperature ³MLCT lifetime ([1]²⁺ → [2]²⁺ $\tau_{295\text{K}}$ = 722 → 149 ns and [3]²⁺ → [4]²⁺ $\tau_{295\text{K}}$ = 841 → 136 ns; Fig-

Figure 9. DFT calculated and experimental emission energies (E_{max} at 295 K) of [1]²⁺–[4]²⁺ and reference compounds [5]²⁺–[7]²⁺ in CH₃CN. Experimental emission data of [5]²⁺ and [6]²⁺ were taken from the literature.^[17,49]

(asymmetric/symmetric)) in the solid-state IR spectra. Hence, high-energy N–H oscillators (≈ 3450 cm^{−1}) are replaced by lower-energy N–D oscillators (≈ 2630 cm^{−1}). Intersystem crossing from the ³MLCT state to the ¹GS ground state is feasible through the second vibrational NH overtone of the ¹GS ([2]²⁺/[4]²⁺) and through the third ND overtone ([2^D]²⁺/[4^D]²⁺; Figure 11). As multiphonon deactivation is more probable for fewer phonons, the deuterated derivatives are less prone to quenching by high-energy vibrations (Figure 11). Indeed, deuteration of the amino group significantly increases the quantum yields ([2]²⁺ → [2^D]²⁺: Φ = 0.042 → 0.100 %; [4]²⁺ → [4^D]²⁺: Φ = 0.052 → 0.073 %). Possibly, the replacement of C–H in the ligands by C–D would further improve the quantum yield and lifetime but this is beyond the scope of this study.^[75–78]

³MLCT lifetimes for [1]²⁺–[4]²⁺ ($\tau_{77\text{K}}$ = 3309, 1123, 3251, 1002 ns) at 77 K in frozen butyronitrile are higher than room temperature lifetimes by a factor of 4–8 (Table 4, Figure 10) showing that deactivation through thermally accessible ³MC states is still a deactivation pathway at room temperature in fluid solution. The presence of an amino group reduces $\tau_{77\text{K}}$ by a factor of approximately three ([1]²⁺

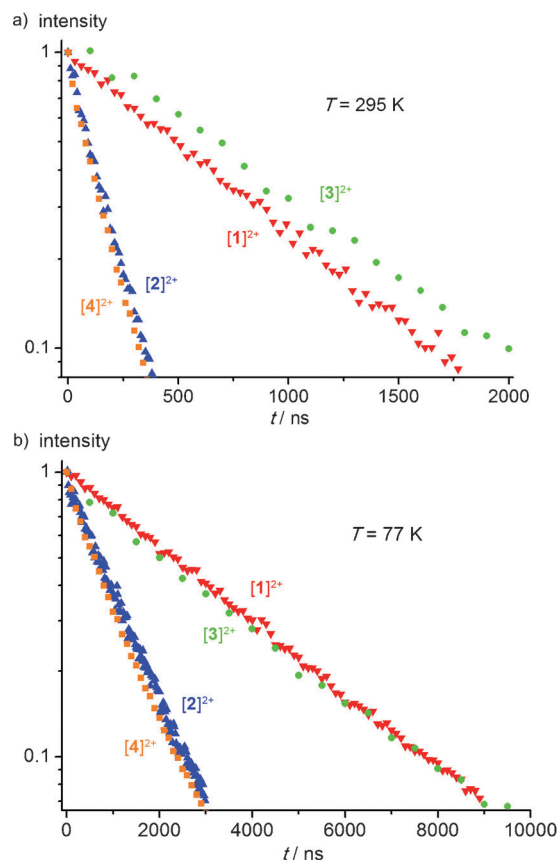


Figure 10. Monoexponential emission decay of $[1]^{2+}$ – $[4]^{2+}$ in PrCN a) at 295 K and b) at 77 K.

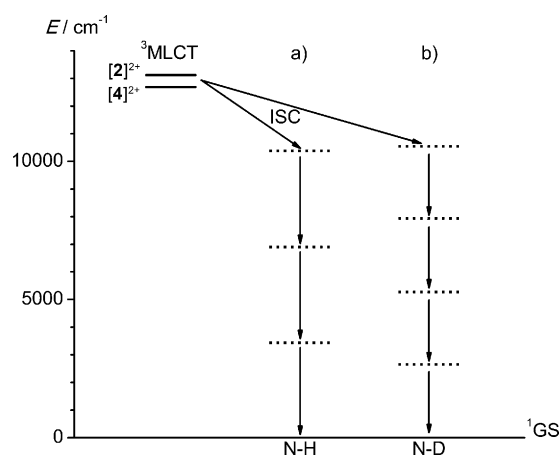


Figure 11. Proposed radiationless deactivation from the vibrationally relaxed $^3\text{MLCT}$ states of $[2]^{2+}$ and $[4]^{2+}$ (estimated by $\lambda_{\text{max,emis}}$ at 295 K) into their respective ground states (^1GS) in the presence of a) N–H and b) N–D harmonic oscillators.

$\rightarrow[2]^{2+}$; $[3]^{2+} \rightarrow [4]^{2+}$). Emission maxima at 77 K are shifted to higher energy ($\Delta E = 0.02$ – 0.05 eV) compared with room temperature values because the excited state is less stabilized in the frozen matrix than in solution, which also prolongs the lifetime at low temperature (energy-gap law).

In summary, emission quantum yields and $^3\text{MLCT}$ lifetimes are improved by 1) using the push–pull concept decreasing the energy of the $^3\text{MLCT}$ state and 2) increasing the ligand bite angle to strengthen the ligand field and thus raising the energy of the deactivating ^3MC state. The first approach, however, seems to reach its limits at around 750 nm emission energy due to the energy-gap law in this type of complexes, especially when high-energy oscillators are present.

DFT modeling of excited triplet states: Relevant electronic triplet states $^3\text{MLCT}$ and ^3MC have been successfully modeled by DFT methods for all complexes $[1]^{2+}$ – $[7]^{2+}$ (Figure 12), except for the ^3MC state of $[4]^{2+}$, which we were unable to localize. It appears that the ^3MC state of $[4]^{2+}$ corresponds only a very shallow minimum, which connects to the $^3\text{MLCT}$ state without a significant barrier. In addition, we were able to locate the transition states (^3TS) for the excited state equilibrium between $^3\text{MLCT}$ and ^3MC

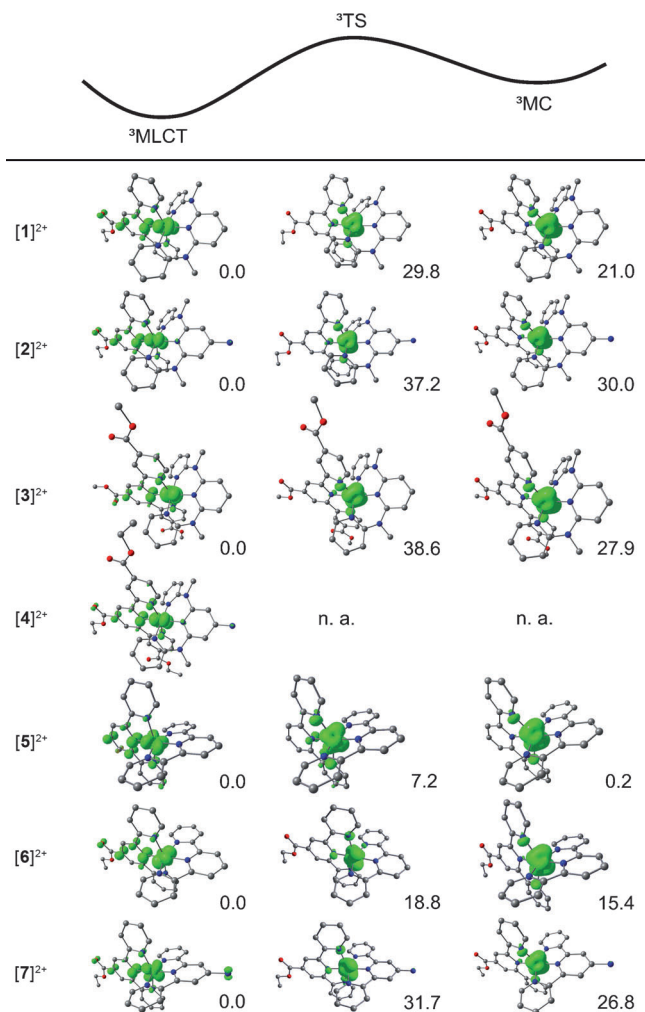


Figure 12. Geometries, relative energies, and spin densities of triplet states ($^3\text{MLCT}$ and ^3MC) as well as the connecting transition state (^3TS) of $[1]^{2+}$ – $[7]^{2+}$. Contour value 0.01; energies in kJ mol⁻¹; hydrogen atoms are omitted.

states for all complexes $[1]^{2+}$ – $[7]^{2+}$ except $[4]^{2+}$. Optimized geometries and spin densities of the triplet states are depicted in Figure 12 together with their energy relative to the $^3\text{MLCT}$ state. Selected bond lengths and angles are summarized in Table S10 (the Supporting Information). For complexes $[1]^{2+}$ – $[7]^{2+}$ (except $[5]^{2+}$), the Ru–N2 bond is slightly elongated (0.02–0.05 Å) from the ^1GS to the $^3\text{MLCT}$ state, whereas the Ru–N5 bond *trans* to N2 is slightly shortened (0.01–0.06 Å). Consequently, bite angles of the ester substituted tpy ligand (N1–Ru–N2, N2–Ru–N3) in the $^3\text{MLCT}$ state (77–78°) are slightly smaller than in the ^1GS state (79°). The majority of the spin density in the $^3\text{MLCT}$ state is located on the ester substituted tpy ligand and on the ruthenium atom as can be seen from Mulliken spin density values (Table S11, the Supporting Information) and spin densities (Figure 12). The elongation of the Ru–N2 bond as well as the spin density distribution clearly demonstrate that the excited $^3\text{MLCT}$ state is located on both the ruthenium atom as well as on the tpy ligand as expected from electrochemical and optical investigations.

Geometries of ^3MC states are obtained as local energy minima. The Ru–N bond lengths of the ester substituted tpy ligand of $[1]^{2+}$ – $[4]^{2+}$, $[6]^{2+}$ and $[7]^{2+}$ are significantly longer in the ^3MC state than in the $^3\text{MLCT}$ state, whereas for the second ligand (ddpd or tpy) the Ru–N bond lengths change only marginally. N–Ru–N angles with the ester-substituted tpy ligand are smaller due to the larger distance between the ruthenium atom and the ester-substituted ligand. Furthermore, dihedral angles (N1–C–C–N2 and N2–C–C–N3) of the ester substituted tpy ligand are significantly larger in the ^3MC state than in the ^1GS and $^3\text{MLCT}$ states. Spin density plots (Figure 12) and Mulliken spin densities (Table S11, Supporting Information) show that the ^3MC state is predominantly located on the ruthenium atom with only small contributions from both ligands, which corresponds to the expected spin density of a “(t_{2g}) $^5(e_g)^1$ ” electronic configuration (see “ e_g ” orbitals LUMO+11 and LUMO+13 in Figure 7). All ^3MC states are calculated to be higher in energy than corresponding $^3\text{MLCT}$ states. For bis(tpy) complexes $[6]^{2+}$ and $[7]^{2+}$ the energy difference amounts to 15.4 and 26.8 kJ mol $^{-1}$, respectively. Substituting one tpy ligand in $[6]^{2+}$ and $[7]^{2+}$ by a ddpd ligand ($[1]^{2+}$ and $[2]^{2+}$) raises the energy difference between the ^3MC and the $^3\text{MLCT}$ state by 3–6 kJ mol $^{-1}$ ($[6]^{2+} \rightarrow [1]^{2+}$: 15.4 \rightarrow 21.0 kJ mol $^{-1}$; $[7]^{2+} \rightarrow [2]^{2+}$: 26.8 \rightarrow 30.0 kJ mol $^{-1}$). This finding is in accordance with experimental $^3\text{MLCT}$ lifetimes, which are higher for the ddpd complexes $[1]^{2+}$ and $[2]^{2+}$ compared with $[6]^{2+}$ and $[7]^{2+}$ (Table 4). Additionally, the ^3MC – $^3\text{MLCT}$ energy difference of a given complex type dramatically increases by push–pull substitution ($[7]^{2+}$ (26.8 kJ mol $^{-1}$) > $[6]^{2+}$ (15.4 kJ mol $^{-1}$) > $[5]^{2+}$ (0.2 kJ mol $^{-1}$); $[2]^{2+}$ (30.0 kJ mol $^{-1}$) \approx $[3]^{2+}$ (27.9 kJ mol $^{-1}$) > $[1]^{2+}$ (21.0 kJ mol $^{-1}$)). The calculated transition states ^3TS are more similar to the ^3MC than to the $^3\text{MLCT}$ states with respect to energies, bond lengths, N–Ru–N angles and N–C–C–N dihedral angles as well as from spin density distributions, suggesting a late transition state on the reaction coordinate. The homoleptic complex $[\text{Ru}(\text{tpy})_2]^{2+}$

($[5]^{2+}$) is unique when compared with heteroleptic analogues due to its higher symmetry. In the ^1GS , both ligands have similar Ru–N bond lengths, whereas in the $^3\text{MLCT}$ state, one central pyridine nitrogen atom moves towards and the other central pyridine nitrogen atom moves away from the ruthenium atom, indicating that the excited state is distorted and the spin density is localized on one of the two tpy ligands. Spin densities are higher on the tpy ligand with the shorter central Ru–N bond. With respect to the ^3TS and the ^3MC state, complex $[5]^{2+}$ is similar to the aforementioned heteroleptic complexes.^[79]

Early-time dynamics by transient absorption spectroscopy:

Before reaching the $^3\text{MLCT}$ state and its thermal equilibration with the ^3MC state, the Franck–Condon excited $^1\text{MLCT}$ state has to undergo localization of the excited electron onto a single oligopyridyl ligand, intersystem crossing (ISC), solvent reorganization, and vibrational relaxation.^[1] Early-time dynamics occurring shortly after excitation to the Franck–Condon state and before reaching the emitting $^3\text{MLCT}$ state and the deactivating ^3MC state were probed by picosecond transient absorption (TA) spectroscopy for $[1]^{2+}$ – $[4]^{2+}$, and $[6]^{2+}$ and $[7]^{2+}$ at 298 K in CH₃CN (pulse λ_{exc} = 400–425 nm). The TA spectra of $[2]^{2+}$ and $[7]^{2+}$ are exemplarily depicted in Figure 13 (Figures S43–S46 in the Supporting Information for $[1]^{2+}$, $[3]^{2+}$, $[4]^{2+}$, and $[6]^{2+}$). All complexes exhibit ground-state bleaching from 480 to 550 nm and absorption features of the MLCT state from 550 to 1000 nm similar to the reported data of $[\text{Ru}(\text{tpy})_2]^{2+}$ in CH₃CN.^[49,80]

To assign absorption and bleaching in the TA spectra, UV/Vis spectra of chemically oxidized and reduced $[2]^{2+}$ were recorded (Figure S47, the Supporting Information). In $[2]^{3+}$ the MLCT band at 450–550 nm is replaced by LMCT bands at 600–950 nm with maxima at 647 (4300 M $^{-1}$ cm $^{-1}$) and at 770 nm (3100 M $^{-1}$ cm $^{-1}$).^[34] In the reduced form $[2]^+$ absorption bands appear at 372 (27500 M $^{-1}$ cm $^{-1}$) and 466 nm (18600 M $^{-1}$ cm $^{-1}$). Similar absorptions are also present in the spectra of reduced $[\text{Ru}(\text{tpy})_2]^{2+}$ complexes.^[25,52] A third absorption band of $[2]^+$ is found at 695 nm (4100 M $^{-1}$ cm $^{-1}$). The absorption features of $[2]^+$ are tentatively assigned to the coordinated tpy radical ligand. The difference spectrum “[2] $^{2+} - 1/2$ ([2] $^{3+} + [2]^+$)” emulates the TA spectrum concerning ground state bleach at 530 nm and excited state absorption at 560–900 nm (Figure 13). Thus, the excited $^3\text{MLCT}$ state of $[2]^{2+}$ is well formulated by $[\text{Ru}^{\text{III}}(\text{ddpd-NH}_2)(\text{EtOOC-tpy}^{(-)})]^{2+}$, with the spin density localized on the tpy ligand and a Ru^{III} center.

Time-resolved transient absorption features evolve within the first picoseconds after the laser pulse. The time constants of $[1]^{2+}$ – $[4]^{2+}$, and $[6]^{2+}$ and $[7]^{2+}$ are summarized in Table 4. TA spectra of $[\text{Ru}(\text{bpy})_3]^{2+}$ had revealed that no significant changes occur in the spectrum within ≈ 0.3 ps after a laser pulse with λ_{exc} = 475 nm.^[81] On the other hand, time constants of 5 ps had been observed by TA measurements for $[\text{Ru}(\text{dmb})_3]^{2+}$ (dmb = 4,4'-dimethyl-2,2'-bipyridine) when irradiated at 400 nm and had been assigned to

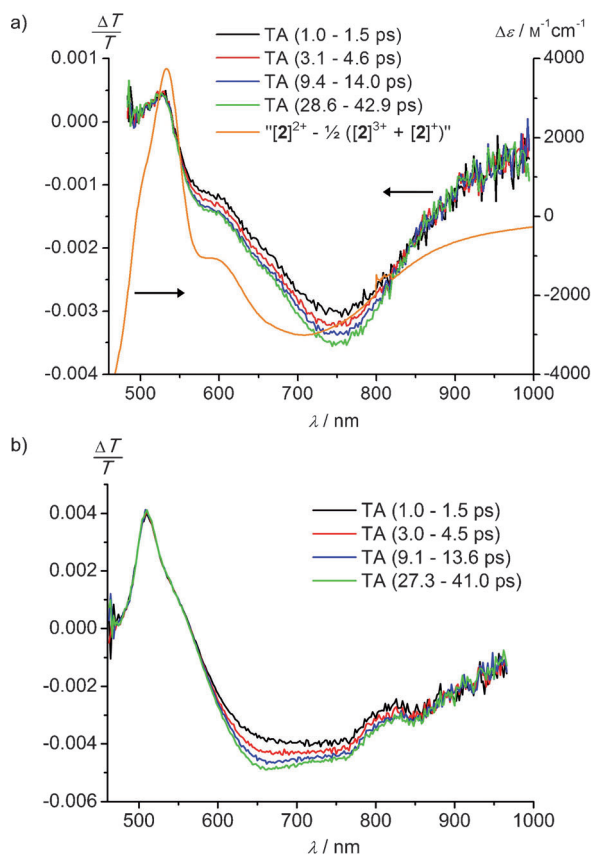


Figure 13. Transient absorption spectra of a) $[2]^{2+}$ (pulse $\lambda_{\text{exc}}=425$ nm, 2050 nJ) with difference spectrum $[[2]^{2+}-\frac{1}{2}([2]^{3+}+[2]^{1+})]$ and b) $[7]^{2+}$ (pulse $\lambda_{\text{exc}}=400$ nm, 2600 nJ) in PrCN at 295 K.

vibrational cooling within the $^3\text{MLCT}$ state.^[82] A time constant of 2 ps had been found for $[\text{Ru}(\text{tpy})_2]^{2+}$ and had been assigned to the equilibrium between $^3\text{MLCT}$ and ^3MC states. This interpretation is clearly not applicable for $[1]^{2+}$ – $[4]^{2+}$, and $[6]^{2+}$ and $[7]^{2+}$ because the $^3\text{MLCT}/^3\text{MC}$ equilibration occurs in the nanosecond regime. For heteroleptic $[\text{Ru}(\text{tpy})(\text{ttpy})]^{2+}$ (ttpy = 4'-(4-methylphenyl)-2,2':6',2''-terpyridine) a 3 ps dynamics had been discussed to be an interligand electron-transfer process.^[80] Whatever the exact nature of the observed dynamics in $[1]^{2+}$ – $[4]^{2+}$ and $[6]^{2+}$ and $[7]^{2+}$ (localization of the electron on the tpy ligand, ISC, or vibrational relaxation within MLCT states), all these processes together from the $^1\text{MLCT}$ Franck–Condon state to the thermalized $^3\text{MLCT}$ state are completed within several picoseconds in all cases. The thermalized $^3\text{MLCT}$ state equilibrates with the ^3MC state, relaxes to the ground state by radiationless deactivation through high-energy oscillators, or emits a photon.

Conclusion

Heteroleptic bis(tridentate) ruthenium(II) complexes $[1]^{2+}$ – $[4]^{2+}$ with long $^3\text{MLCT}$ lifetimes (up to 841 ns) and high quantum yields (up to 1.1%) have been synthesized by using the combination of an electron-accepting tpy and an

electron-donating ddpd ligand. The favorable push–pull substitution of the complexes leads to a small HOMO–LUMO gap, a spatial separation of the frontier orbitals, and to low-energy absorption and emission. The large 88° bite angle of ddpd ligands induces a strong ligand field and increases the energy difference between $^3\text{MLCT}$ and ^3MC states, thus reducing radiationless decay pathways through the latter state. Excited states of $[1]^{2+}$ – $[4]^{2+}$ have been probed experimentally by using ultrafast transient absorption spectroscopy and theoretically by DFT calculations. The $^1\text{MLCT} \rightarrow ^3\text{MLCT}$ relaxation occurs within picoseconds, whereas the $^3\text{MLCT} \rightarrow ^3\text{MC}$ equilibration is shifted to the nanosecond timescale (Scheme 1). The fairly long lifetime of >100 ns of the $^3\text{MLCT}$ state of complexes $[1]^{2+}$ – $[4]^{2+}$ should allow for efficient electron-transfer processes in solution or at semiconductor interfaces. Furthermore, the quantum yields together with the functional groups present will allow labeling applications in the field of luminescent sensors and in other luminescent devices. Future applications of $[1]^{2+}$ – $[4]^{2+}$ are dye-sensitized solar cells, light-emitting electrochemical cells, labeling, and photocatalysis. This research is currently being pursued in our group and results will be reported in due course.

Experimental Section

General procedures: Dioxane, diethyl ether, and petroleum ether (b.p. 40 – 60°C) were distilled from sodium, CH_3CN and CH_2Cl_2 from CaH_2 , and THF from potassium under an argon atmosphere. All reagents were used as received from commercial suppliers (Acros and Sigma–Aldrich). Microwave heating was performed in a Discover Benchmate Plus (CEM Synthesis) single-mode microwave cavity, producing continuous irradiation at 2.455 GHz with 100 W (maximum power). Reaction mixtures were stirred with a magnetic stir bar during irradiation. The temperature and irradiation power were monitored during the course of the reaction. NMR spectra were recorded on a Bruker Avance DRX 400 spectrometer at 400.31 MHz (^1H), 100.66 MHz ($^{13}\text{C}\{^1\text{H}\}$), and 40.56 MHz (^{15}N). All resonances are reported in ppm versus the solvent signal as an internal standard (CD_3CN (^1H , $\delta=1.94$; ^{13}C , $\delta=1.24$ ppm); CD_2Cl_2 (^1H , $\delta=5.32$); $[\text{D}_6]\text{DMSO}$ (^1H , $\delta=2.50$; ^{13}C , $\delta=39.43$ ppm)) or versus external CH_3NO_2 (90% in CDCl_3 , $\delta=380.23$ ppm vs. $\text{NH}_3(\text{l})$) and referenced to NH_3 (^{15}N , $\delta=0$ ppm). IR spectra were recorded with a BioRad Excalibur FTS 3100 spectrometer as KBr or CsI disks. Electrochemical experiments were carried out on a Bio Logic SP-50 voltammetric analyzer using platinum wires as counter- and working electrodes and 0.01 M Ag/AgNO_3 as reference electrode. The measurements were carried out at a scan rate of 100 – 333 mV s^{-1} for cyclic voltammetry experiments and at 25 – 333 mV s^{-1} for square-wave voltammetry experiments using 0.1 M $[\text{nBu}_4\text{N}][\text{PF}_6]$ as the supporting electrolyte and a 10^{-3} M solution of the sample in dry and degassed CH_3CN . Potentials are referenced to the ferrocene/ferrocenium couple ($E_{1/2}=90 \pm 5$ mV under experimental conditions). UV/Vis/near-IR spectra were recorded on a Varian Cary 5000 spectrometer using 1.0 cm cells (Hellma, Suprasil). Emission spectra were recorded on a Varian Cary Eclipse spectrometer. Quantum yields were determined by comparing the areas under the emission spectra on an energy scale cm^{-1} recorded for optically matched solutions of the sample and the reference $\Phi([\text{Ru}(\text{bpy})_3]\text{Cl}_2)=0.094$ in deaerated CH_3CN .^[83] Time-resolved photoluminescence measurements were recorded with a gated intensified charge-coupled device camera (Andor IStar iCCD Detector DH740 ICCD) connected to a spectrograph (Andor Shamrock SR-303i) employing gratings with 150 or 300 lines per millimeter. Photoexcitation at wavelengths corresponding to the maximum absorption of the complexes in solution was

provided by 10 ns pulses of an optical parametric oscillator (GWU VisIR2 OPO System) pumped by the third harmonic of a Nd:YAG Laser (Spectra-Physics Quanta Ray-INDI) at a repetition rate of 10 Hz. Solutions ($c = 5 \times 10^{-6}$ M) in degassed butyronitrile were prepared under a nitrogen atmosphere. The measurements were performed at 295 and 77 K in a self-made indium sealed brass cuvette with quartz windows and an optical path of 1 mm. Single exponentials were used to fit the experimental data. Transient absorption measurements were performed with a home-built pump-probe setup.^[84] To measure a time range up to 3 ns with a resolution of ≈ 100 fs, the output of a commercial titanium:sapphire amplifier (Coherent LIBRA HE, 3.5 mJ, 1 kHz, 100 fs) was split with one portion used to generate a 400–425 nm excitation pulse using an optical parametric amplifier (Coherent OPerA Solo), and another used to generate a 1300 nm seed pulse (output of an optical parametric amplifier (Coherent OPerA Solo)) for white-light generation in the visible to NIR (500–1000 nm) in a c-cut 3 mm thick sapphire window. The variable delay of up to 3 ns between pump and probe was introduced by using a broad-band retroreflector mounted on a mechanical delay stage. The excitation pulse was chopped at 500 Hz, while the white light pulses were dispersed onto a linear silicon (Hamamatsu NMOS linear image sensor S3901) photodiode. The array was read out at 1 kHz. Adjacent diode readings corresponding to the transmission of the sample after an excitation pulse and without an excitation pulse were used to calculate $\Delta T/T$. Samples were excited with fluences between 50 and 500 $\mu\text{J cm}^{-2}$. No fluence dependent kinetics were observed. The complexes were dissolved in degassed butyronitrile ($c = 0.2\text{--}0.6$ mM) under a nitrogen atmosphere and measured in a quartz cuvette with 1 mm optical path length. Field desorption (FD) mass spectra were recorded on a FD Finnigan MAT90 spectrometer. ESI mass spectra were recorded on a Micromass Q-TOF-Ultima spectrometer. X-band CW ESR spectra were measured on a Miniscope MS 300 (Magnetech GmbH, Germany). g values are referenced to external Mn^{2+} in ZnS ($g = 2.118, 2.066, 2.027, 1.986, 1.946, 1.906$). Measurements were conducted at 77 K and simulations were performed with the program package EasySpin.^[85] Elemental analyses were performed by the microanalytical laboratory of the chemical institutes of the University of Mainz.

Crystal structure determinations: Intensity data were collected with a Bruker AXS Smart 1000 CCD diffractometer with an APEX II detector and an Oxford cooling system and corrected for absorption and other effects using $\text{MoK}\alpha$ radiation ($\lambda = 0.71073 \text{ \AA}$) at 173(2) K. The diffraction frames were integrated using the SAINT package, and most were corrected for absorption with MULABS.^[86,87] The structures were solved by direct methods and refined by the full-matrix method based on F^2 using the SHELXTL software package.^[88,89] All non-hydrogen atoms were refined anisotropically, whereas the positions of all hydrogen atoms were generated with appropriate geometric constraints and allowed to ride on their respective parent carbon atoms with fixed isotropic thermal parameters. The asymmetric unit of a crystal of $[\mathbf{3}][\text{PF}_6]_2$ contains one molecule of an acetonitrile solvent and one molecule of diethylether. Both $[\text{PF}_6]^-$ counterions and one ester group are disordered over two positions (site occupancy 0.55:0.45 (P1); 0.68:0.32 (P2); 0.76:0.24 (ester)). In the refinement one $[\text{PF}_6]^-$ counterion (P1) of $[\mathbf{3}][\text{PF}_6]_2$ restraints were applied (same, simu, delu). Crystallographic data (excluding structure factors) for the structure reported in this paper have been deposited as CCDC-930312 ($[\mathbf{2}][\text{PF}_6]_2$), CCDC-930313 ($[\mathbf{3}][\text{PF}_6]_2$), CCDC-930310 ($\mathbf{8}$) and CCDC-930311 ($\mathbf{9}$). These data can be obtained free of charge from The Cambridge Crystallographic Data Centre via www.ccdc.cam.ac.uk/data_request/cif.

DFT calculations: Calculations were performed by using the Gaussian 09/DFT^[90] series of programs. The B3LYP formulation of DFT was used employing the LANL2DZ basis set.^[90] No symmetry constraints were imposed on the molecules. The presence of energy minima or first order saddle points was checked by analytical frequency calculations. The integral-equation-formalism polarizable continuum model (IEFPCM, CH_3CN) was employed for solvent modeling. As data obtained including solvent modeling reproduced the experimental results better than those without solvent modeling the IEFPCM formalism is used in all calculations in this paper. In TD-DFT calculations at least 100 singlet transitions ($n \geq 100$) were calculated. For thermodynamic energy values, the sum of

electronic and thermal free-energies ($T = 298.15 \text{ K}$) from the output file was used. All calculations were performed without explicit counterions and solvent molecules.

Syntheses: The synthesis of $[\text{Ru}(\text{ddpd})(\text{EtOOC-tpy})][\text{PF}_6]_2$ ($[\mathbf{1}][\text{PF}_6]_2$), $[\text{RuCl}_3(\text{EtOOC-tpy})]$ ($\mathbf{12}$) and ddpd ($\mathbf{11}$) have been reported previously.^[61] $[\text{RuCl}_3(\text{MeOOC-tpy})]$ ($\mathbf{13}$) was synthesized according to literature procedures.^[55,66,67] Syntheses of $\mathbf{8}$, 4-amino-2,6-dibromopyridine, $\mathbf{9}$ and $\mathbf{10}$ can be found in the Supporting Information.

$[\text{Ru}(\text{ddpd-NH}_2)(\text{EtOOC-tpy})][\text{PF}_6]_2$ ($[\mathbf{2}][\text{PF}_6]_2$): $[\text{RuCl}_3(\text{EtOOC-tpy})]$ ($\mathbf{12}$, 103.7 mg, 0.2022 mmol, 1.0 equiv) and $\mathbf{10}$ (95.4 mg, 0.219 mmol, 1.1 equiv) were suspended in ethanol (15 mL). The dark red-brown suspension was ultrasonicated for 1 min and *N*-ethylmorpholine (0.15 mL, 1.2 mmol, 5.9 equiv) was added. The mixture was heated to reflux in a laboratory microwave oven for 30 min (80 °C). The mixture was filtered over Celite (1.5 cm; \varnothing 3.5 cm) and rinsed with ethanol. The solvent was removed under reduced pressure, and the dark-purple solid was dissolved in ethanol (5 mL). Addition of diethylether (50 mL) resulted in the precipitation of a dark-purple solid, which was filtered and dissolved in ethanol (25 mL). Hydrazine hydrate (50 μL , 1.0 mmol, 5.1 equiv) was added and the mixture was heated to reflux (16 h). After cooling to room temperature a second portion of hydrazine hydrate (70 μL , 1.4 mmol, 7.1 equiv) was added. The mixture was heated to reflux (17 h), cooled to room temperature and the solvent was removed under reduced pressure. The dark purple solid was dissolved in ethanol (2 mL) and precipitated by adding diethylether (26 mL). The solid was filtered and dissolved in water (11 mL). The dark-purple product was precipitated by the addition of an aqueous solution of NH_4PF_6 (166.2 mg, 1.020 mmol, 5.0 equiv, 13 mL). The precipitate was filtered, washed with water (10 mL) and diethyl ether (30 mL) and dried under reduced pressure. A dark-purple powder was obtained. Yield: 155.2 mg (0.1548 mmol, 77 %). $^1\text{H NMR}$ (CD_3CN , 300 K): $\delta = 8.95$ (s, 2H, H^2), 8.54 (m, 2H, H^5), 8.15 (m, 2H, H^8), 8.00 (m, 2H, H^6), 7.58 (m, 2H, H^{11}), 7.48 (m, 2H, H^7), 7.12 (m, 2H, H^{12}), 6.80 (s, 2H, H^{15}), 6.54 (m, 2H, H^{10}), 6.38 (m, 2H, H^9), 5.72 (br, s, 2H, NH_2), 4.57 (q, $^3J_{\text{HH}} = 7.1 \text{ Hz}$, 2H, CH_2CH_3), 3.36 (s, 6H, NCH_3), 1.51 ppm (t , $^3J_{\text{HH}} = 7.1 \text{ Hz}$, 3H, CH_2CH_3); $^{13}\text{C}\{^1\text{H}\}$ NMR (CD_3CN , 300 K): $\delta = 165.0$ (s, C=O), 160.2 (s, C^{13}), 160.0 (s, C^{16}), 159.1 (s, C^3), 158.8 (s, C^4), 156.8 (s, C^{14}), 155.0 (s, C^8), 149.3 (s, C^9), 140.0 (s, C^{11}), 138.8 (s, C^6), 135.1 (s, C^1), 127.8 (s, C^7), 125.4 (s, C^5), 123.6 (s, C^2), 121.1 (s, C^{10}), 116.2 (s, C^{12}), 98.7 (s, C^{15}), 63.5 (s, CH_2CH_3), 41.4 (s, NCH_3), 14.5 ppm (s, CH_2CH_3); $^1\text{H-}^{15}\text{N}$ HMBC (CD_3CN , 300 K): $\delta = 297.2$ (N^6), 238.6 (N^4), 212.7 (N^9), 183.1 (N^5), 90.1 (N^3), 72.1 ppm (NH_2) ppm; MS (ESI⁺): m/z 356.6 (100 %) $[\text{M}-2\text{PF}_6]^{2+}$, 858.2 (25 %) $[\text{M}-\text{PF}_6]^+$; HR-MS (ESI⁺): m/z calcd for $\text{C}_{35}\text{H}_{33}\text{F}_6\text{N}_9\text{O}_2\text{P}_2\text{Ru}^+$: 852.1475; found: 852.1500; IR (CsI): $\tilde{\nu} = 3468$ (m, NH), 3400 (m, NH), 3240 (w, NH), 3125 (w, NH, CH), 2920 (m, CH), 2853 (w, CH), 1726 (s, C=O), 1641 (s, NH_2 , NH, C=C), 1620 (s, NH, C=N), 1605 (s, NH, C=N), 1574 (m, NH, C=N), 1462 (s, CH_3 , CH_2), 1433 (s, CH_3 , CH_2), 1367 (s, CH_3), 1344 (s, C-N), 1327 (s, C-N), 1281 (s, C-N, C-O-C), 1254 (s, C-N, C-O-C), 1170 (m, C-N, C-O-C), 1132 (m, C-N, C-O-C), 1097 (m, C-O-C), 1049 (m, C-O-C), 1026 (m, C-O-C), 966 (w), 843 (vs, PF), 781 (m), 767 (m), 650 (w), 613 (w), 559 (s), 527 cm^{-1} (w); UV/Vis (CH_3CN): λ_{abs} (ϵ) = 525 (8230), 323 (26 700), 273 (42 000), 238 nm ($43 600 \text{ M}^{-1} \text{ cm}^{-1}$); emission (CH_3CN , 295 K, $\lambda_{\text{exc}} = 525 \text{ nm}$): $\lambda_{\text{emiss}} = 762 \text{ nm}$ [$\tau = 149(2) \text{ ns}$]; emission ($\text{CH}_3\text{CH}_2\text{CH}_2\text{CN}$, 77 K, $\lambda_{\text{exc}} = 525 \text{ nm}$): $\lambda_{\text{emiss}} = 749 \text{ nm}$ [$\tau = 1123(9) \text{ ns}$]; Φ (CH_3CN , $\lambda_{\text{exc}} = 474.5 \text{ nm}$, 295 K): 0.00042 %; CV (CH_3CN): $E_{1/2} = +1.73$ (1e, irrev.), $+0.64$ (1e, rev.), -1.50 (1e, rev.), -2.11 (1e, irrev.), -2.21 (1e, irrev.) vs. Fc/Fc^+ ; elemental analysis calcd (%) for $\text{C}_{35}\text{H}_{33}\text{F}_6\text{N}_9\text{O}_2\text{P}_2\text{Ru} \cdot 1/2 \text{Et}_2\text{O}$: C 42.74, H 3.68, N 12.12; found: C 42.97, H 3.48, N 11.96.

$[\text{Ru}(\text{ddpd})((\text{MeOOC})_3\text{-tpy})][\text{PF}_6]_2$ ($[\mathbf{3}][\text{PF}_6]_2$): A solution of $\mathbf{11}$ (524.7 mg, 1.801 mmol, 2.1 equiv) in methanol (40 mL) was added to $[\text{RuCl}_3((\text{MeOOC})_3\text{-tpy})]$ ($\mathbf{13}$, 523.1 mg, 0.851 mmol, 1.0 equiv). *N*-ethylmorpholine (1.50 mL, 11.9 mmol, 13.9 equiv) was added, the black mixture was ultrasonicated (1 min) and heated to reflux in a laboratory microwave oven for 30 min (70 °C). A dark purple-brown solution was obtained which was filtered over Celite (1.5 cm; \varnothing 3.0 cm) and rinsed with methanol. The solvent was removed under reduced pressure, and the viscous dark purple-brown residue was dissolved in methanol (10 mL). Addition of an aqueous solution of NH_4PF_6 (5.768 g, 35.39 mmol, 41.6 equiv,

100 mL) led to the precipitation of a dark purple-brown solid which was filtered and washed with a dilute aqueous solution of NH_4PF_6 (50.5 mg in 100 mL; pale-brown filtrate). The filtrate was washed with dioxane (≈ 200 mL) until the filtrate was colorless (the color of the filtrate turned from dark-green to colorless). The black residue on the filter paper was redissolved in acetone. The solvent of the dark purple solution was removed under reduced pressure and the residue was dissolved in CH_3CN , filtered again and the filter was washed with CH_3CN (a dark-green residue remained on the filter paper). The solvent was removed under reduced pressure and the residue was dissolved in acetone (10 mL). Dioxane (90 mL) was added and the mixture was concentrated to half of its volume under reduced pressure. The suspension was filtered (greenish filtrate). The solid residue was dried in vacuo. AgNO_3 (0.5025 g, 2.958 mmol, 3.5 equiv) and absolute CH_3CN (43 mL) were added and the solution was heated to reflux (30 min) under an argon atmosphere. After cooling to room temperature AgCl was filtered and washed with CH_3CN . The solvent of the combined filtrates was removed under reduced pressure and the residue was dissolved in CH_3CN (14 mL). An aqueous solution of NH_4PF_6 (1.037 g, 6.362 mmol, 7.5 equiv, 10 mL) was added and the dark-purple product precipitated. CH_3CN was removed under reduced pressure and the suspension was filtered, washed with diethyl ether, and dried in vacuo. A dark-purple powder was obtained. Yield: 464 mg (0.426 mmol, 50 %). ^1H NMR (CD_3CN , 300 K): δ = 9.17 (s, 2H, H^2), 8.99 (m, 2H, H^3), 8.30 (t, $^3J_{\text{HH}} = 8.2$ Hz, 1H, H^{16}), 8.28 (m, 2H, H^8), 7.91 (m, 2H, H^7), 7.62 (m, 2H, H^{11}), 7.60 (d, $^3J_{\text{HH}} = 8.2$ Hz, 2H, H^{15}), 7.19 (m, 2H, H^{12}), 6.56 (m, 2H, H^{10}), 6.36 (m, 2H, H^9), 4.13 (s, 3H, H^{19}), 3.99 (s, 6H, H^{18}), 3.48 ppm (s, 6H, NCH_3); $^{13}\text{C}\{^1\text{H}\}$ NMR (CD_3CN , 300 K): δ = 165.2 (s, $\text{C}=\text{O}^{\text{center}}$), 164.8 (s, $\text{C}=\text{O}^{\text{outer}}$), 159.7 (s, C^4), 159.5 (s, C^{13}), 159.3 (s, C^5), 157.1 (s, C^{14}), 155.8 (s, C^8), 149.2 (s, C^9), 142.1 (s, C^{16}), 140.4 (s, C^{11}), 140.0 (s, C^6), 136.4 (s, C^1), 126.8 (s, C^7), 124.8 (s, C^2), 124.7 (s, C^5), 121.6 (s, C^{10}), 116.6 (s, C^{12}), 113.7 (s, C^{15}), 54.1 (s, $\text{OCH}_3^{\text{center}}$), 53.9 (s, $\text{OCH}_3^{\text{outer}}$), 41.7 ppm (s, NCH_3); ^1H - ^{15}N HMBC (CD_3CN , 300 K): δ = 294.4 (N^c), 249.1 (N^d), 216.2 (N^e), 209.2 (N^a), 92.0 (N^b) ppm. MS (ESI $^+$): m/z = 400.2 (84 %) [$M-2$ PF $_6$] $^{2+}$, 945.3 (100 %) [$M-\text{PF}_6$] $^+$; HR-MS (ESI $^+$): m/z calcd for $\text{C}_{38}\text{H}_{34}\text{F}_6\text{N}_8\text{O}_6\text{P}_2\text{Ru}^+$: 939.1319; found: 939.1343; IR (CsI): $\tilde{\nu}$ = 3120 (w, CH), 2959 (w, CH), 2922 (w, CH), 2853 (w, CH), 1734 (s, $\text{C}=\text{O}$), 1607 (m, $\text{C}=\text{N}$), 1582 (w, $\text{C}=\text{N}$), 1491 (m, $\text{C}=\text{N}$), 1450 (m, CH_3), 1408 (m, CH_3), 1358 (s, CH_3 , C-N), 1337 (s, C-O-C), 1308 (m, C-N, C-O-C), 1238 (s, C-N, C-O-C), 1165 (w, C-N, C-O-C), 1123 (m, C-N, C-O-C), 1099 (m, C-N), 841 (vs, PF), 768 (m), 727 (w), 613 (w), 559 (s), 538 (w), 467 (w), 444 (w), 349 (w) cm^{-1} ; UV/Vis (CH_3CN): λ_{abs} (ϵ) = 539 (6360), 475 (5060), 340 (31 000), 292 (34 200), 210 nm (52 400 $\text{M}^{-1}\text{cm}^{-1}$); emission (CH_3CN , 295 K, $\lambda_{\text{exc}} = 539$ nm): $\lambda_{\text{emiss}} = 744$ nm [$\tau = 841(26)$ ns]. Emission ($\text{CH}_3\text{CH}_2\text{CH}_2\text{CN}$, 77 K, $\lambda_{\text{exc}} = 539$ nm): $\lambda_{\text{emiss}} = 728$ nm [$\tau = 3251(55)$ ns]; Φ (CH_3CN , $\lambda_{\text{exc}} = 467.5$ nm, 295 K): 0.011 %; CV (CH_3CN): $E_{1/2} = +1.80$ (1e, irrev.), $+0.92$ (1e, rev.), -1.25 (1e, irrev.), -1.70 (1e, irrev.) vs. Fc/Fc^+ ; elemental analysis calcd (%) for $\text{C}_{38}\text{H}_{34}\text{F}_{12}\text{N}_8\text{O}_6\text{P}_2\text{Ru}\cdot\text{H}_2\text{O}\cdot\frac{1}{2}\text{Et}_2\text{O}$: C 41.97, H 3.61, N 9.79; found: C 41.22, H 3.33, N 8.79.

[$\text{Ru}(\text{ddpd}-\text{NH}_2)\{(\text{EtOOC})_3\text{tpy}\}\}[\text{PF}_6]_2$ [**4**]/ $[\text{PF}_6]_2$: [$\text{RuCl}_3\{(\text{MeOOC})_3\text{tpy}\}$] (**13**, 141.9 mg, 0.2308 mmol, 1.0 equiv) and ddpd-phthalimide (**10**, 98.6 mg, 0.2259 mmol, 1.0 equiv) were placed in a flask and ethanol (15 mL) was added. The dark red-brown suspension was ultrasonicated (1 min) and *N*-ethylmorpholine (0.15 mL, 1.2 mmol, 5.2 equiv) was added. The mixture was heated to reflux in a laboratory microwave oven for 30 min (80 °C). A dark-purple solution was obtained that was filtered over Celite (1.5 cm; diameter 3.5 cm) and rinsed with ethanol. The solvent was removed under reduced pressure, the solid residue was dissolved in CH_3CN (5 mL) and precipitated by the addition of diethyl ether (100 mL). After filtration and washing with diethyl ether half of the obtained solid was used for further treatment. The solid was dissolved in ethanol (25 mL) and hydrazine hydrate (1.00 mL, 20.6 mmol, 178 equiv) was added. The mixture was heated to reflux (18 h). After cooling to room temperature the solvent was removed under reduced pressure. The dark-purple solid was dissolved in water (13 mL) and a dark-purple solid was precipitated by the addition of an aqueous NH_4PF_6 (1.088 g, 6.675 mmol, 58 equiv, 10 mL) solution. A pH of 7 was adjusted with concentrated H_2SO_4 , the suspension was filtered and the solid was washed with water. The solid was dissolved in CH_3CN (2.5 mL) and pre-

cipitated by the addition of dioxane (25 mL). After filtration and washing with distilled dioxane and distilled diethyl ether, the solid was dried in a vacuo and dissolved in absolute ethanol (25 mL). Concentrated H_2SO_4 (0.25 mL) was added and the mixture was heated to reflux (21 h). After cooling to room temperature, an aqueous solution of NH_4PF_6 (1.552 g, 9.521 mmol, 84 equiv, 10 mL) was added. Ethanol was removed under reduced pressure and the precipitate was filtered, washed with water and dried in a vacuo. A dark-purple powder was obtained. Yield: 19.9 mg (0.0187 mmol, 17 %). ^1H NMR (CD_3CN , 300 K): δ = 9.15 (s, 2H, H^2), 8.96 (m, 2H, H^3), 8.31 (m, 2H, H^8), 7.91 (m, 2H, H^7), 7.59 (m, 2H, H^{11}), 7.13 (m, 2H, H^{12}), 6.82 (s, 2H, H^{15}), 6.52 (m, 2H, H^{10}), 6.30 (m, 2H, H^9), 5.77 (br, s, 2H, NH_2), 4.60 (q, $^3J_{\text{HH}} = 7.1$ Hz, 2H, $\text{CH}_2\text{CH}_3^{\text{center}}$), 4.45 (q, $^3J_{\text{HH}} = 7.1$ Hz, 4H, $\text{CH}_2\text{CH}_3^{\text{outer}}$), 3.36 (s, 6H, NCH_3), 1.54 (t, $^3J_{\text{HH}} = 7.1$ Hz, 3H, $\text{CH}_2\text{CH}_3^{\text{center}}$), 1.41 ppm (q, $^3J_{\text{HH}} = 7.1$ Hz, 6H, $\text{CH}_2\text{CH}_3^{\text{outer}}$); $^{13}\text{C}\{^1\text{H}\}$ NMR (CD_3CN , 300 K): δ = 164.8 (s, $\text{C}=\text{O}^{\text{center}}$), 164.4 (s, $\text{C}=\text{O}^{\text{outer}}$), 160.0 (s, C^{13}), 159.8 (s, C^4), 159.6 (s, C^3), 159.3 (s, C^{16}), 156.7 (s, C^{14}), 155.7 (s, C^8), 149.2 (s, C^9), 140.3 (s, C^{11}), 140.0 (s, C^6), 135.8 (s, C^1), 126.7 (s, C^7), 124.6 (s, C^2), 124.4 (s, C^5), 121.2 (s, C^{10}), 116.5 (s, C^{12}), 98.8 (s, C^{15}), 63.6 (s, $\text{CH}_2\text{CH}_3^{\text{center}}$), 63.5 (s, $\text{CH}_2\text{CH}_3^{\text{outer}}$), 41.3 (s, NCH_3), 14.6 (s, $\text{CH}_2\text{CH}_3^{\text{center}}$), 14.4 ppm (s, $\text{CH}_2\text{CH}_3^{\text{outer}}$); ^1H - ^{15}N HMBC (CD_3CN , 300 K): δ = 296.6 (N^c), 249.7 (N^d), 209.9 (N^e), 181.7 (N^a), 89.5 (N^b), 72.7 ppm (NH_2); MS (ESI $^+$): m/z = 428.6 (100 %) [$M-2$ PF $_6$] $^{2+}$, 1002.2 (55 %) [$M-\text{PF}_6$] $^+$; HR-MS (ESI $^+$): m/z calcd for $\text{C}_{41}\text{H}_{41}\text{F}_6\text{N}_9\text{O}_6\text{P}_2\text{Ru}^+$: 996.1898; found: 996.1891; IR (CsI): $\tilde{\nu}$ = 3109 (w, CH), 2957 (w, CH), 2926 (m, CH), 2855 (w, CH), 1726 (s, $\text{C}=\text{O}$), 1636 (m, NH, $\text{C}=\text{C}$, $\text{C}=\text{N}$), 1607 (m, NH, $\text{C}=\text{N}$), 1574 (w, NH, $\text{C}=\text{N}$), 1556 (w, NH, $\text{C}=\text{N}$), 1464 (m, CH), 1441 (w, CH), 1408 (m), 1364 (s, CH, C-N), 1325 (s, C-O-C), 1304 (m, C-N, C-O-C), 1238 (s, C-N, C-O-C), 1169 (w, C-N, C-O-C), 1117 (m, C-N, C-O-C), 1051 (w, C-N, C-O-C), 1016 (w, C-O-C), 843 (vs, PF), 768 (w), 615 (w), 559 (m) cm^{-1} ; UV/Vis (CH_3CN): λ_{abs} (ϵ) = 546 (7810), 479 (5960), 341 (32 000), 292 (37 200), 223 nm (45 600 $\text{M}^{-1}\text{cm}^{-1}$); emission (CH_3CN , 295 K, $\lambda_{\text{exc}} = 546$ nm): $\lambda_{\text{emiss}} = 788$ nm [$\tau = 136(3)$ ns]; emission ($\text{CH}_3\text{CH}_2\text{CH}_2\text{CN}$, 77 K, $\lambda_{\text{exc}} = 546$ nm): $\lambda_{\text{emiss}} = 779$ nm [$\tau = 1002(17)$ ns]; Φ (CH_3CN , $\lambda_{\text{exc}} = 467.5$ nm, 295 K): 0.00052 %; CV (CH_3CN): $E_{1/2} = +1.70$ (1e, irrev.), $+0.73$ (1e, rev.), -1.32 (1e, rev.), -1.75 (1e, rev.) vs. Fc/Fc^+ ; elemental analysis calcd (%) for $\text{C}_{41}\text{H}_{41}\text{F}_{12}\text{N}_9\text{O}_6\text{P}_2\text{Ru}\cdot 5\text{EtOH}$: C 44.48, H 5.20, N 9.15; found: C 44.76, H 5.06, N 8.78.

Anion exchange with Δ -TRISPHAT: ^1H NMR spectra of [**2**]/ $[\text{PF}_6]_2$ (2.7 mg, 2.7 μmol , 1 equiv) in CD_3CN (0.55 mL) were measured before and after addition of tetra(*n*-butyl)ammonium(Δ -tris(tetrachloro-1,2-benzenediolato) phosphate(V)) (4.8 mg, 4.7 μmol , 1.8 equiv). A small but clear splitting of around $\Delta\delta = 0.01$ ppm is obtained for the proton resonances of H^2 , H^{15} , NH_2 , CH_2 , NCH_3 , and $\text{CH}_3^{\text{ethyl}}$ in the presence of (Δ -TRISPHAT) $^-$ (see Figure 1). The ^{31}P NMR spectrum revealed no splitting of the phosphorus resonance of (Δ -TRISPHAT) $^-$ at $\delta = -81.6$ ppm.

Deuteration: A few milligrams of [**2**]/ $[\text{PF}_6]_2$ or [**4**]/ $[\text{PF}_6]_2$ were dissolved in dry CD_3CN (0.5 mL). D_2O (99.96 % D, 2–3 drops) was then added. A proton NMR spectrum revealed the instantaneous absence of the NH_2 resonance due to proton–deuterium exchange. The solvent was removed under reduced pressure and the resulting deuterated complex was kept under a dry argon atmosphere. Solid-state IR spectra of [**2**]/ $[\text{PF}_6]_2$ or [**4**]/ $[\text{PF}_6]_2$ revealed the presence of N–D vibrational bands and the absence of N–H vibrational bands (the Supporting information, Figures S48 and S49).

[**2**]/ $[\text{PF}_6]_2$: IR (CsI): $\tilde{\nu}$ = 3120 (w, CH), 2984 (w, CH), 2924 (w, CH), 2851 (w, CH), 2631 (w, ND_{asym}), 2477 (w, ND_{sym}), 1728 (s, $\text{C}=\text{O}$), 1628 (s, $\text{C}=\text{C}$, $\text{C}=\text{N}$), 1605 (s, $\text{C}=\text{N}$), 1574 (m, $\text{C}=\text{N}$), 1477 (s, CH), 1462 (s, CH), 1435 (m, CH_3 , CH_2), 1368 (m, CH_3), 1344 (s, C-N), 1335 (s, C-N), 1283 (s, C-N, C-O-C), 1258 (s, C-N, C-O-C), 1175 (m, C-N, C-O-C), 1134 (m, C-N, C-O-C), 1105 (w, C-O-C), 1047 (m, C-O-C), 1026 (w, C-O-C), 1013 (w, C-O-C), 980 (w), 843 (vs, PF), 781 (m), 766 (s), 557 (s), 527 cm^{-1} (w); Φ (CH_3CN , $\lambda_{\text{exc}} = 472.2$ nm, 295 K): 0.0010 %.

[**4**]/ $[\text{PF}_6]_2$: IR (CsI): $\tilde{\nu}$ = 3105 (w, CH), 2955 (m, CH), 2926 (m, CH), 2855 (m, CH), 2629 (w, ND_{asym}), 2475 (w, ND_{sym}), 1732 (s, $\text{C}=\text{O}$), 1628 (s, $\text{C}=\text{C}$, $\text{C}=\text{N}$), 1607 (m, $\text{C}=\text{N}$), 1576 (w, $\text{C}=\text{N}$), 1553 (w, $\text{C}=\text{N}$), 1464 (s, CH), 1416 (w, CH), 1371 (m, CH, C-N), 1310 (s, C-N, C-O-C), 1246 (s, C-N, C-O-C), 1184 (m, C-N, C-O-C), 1134 (s, C-N, C-O-C), 1049 (w, C-N,

C-O-C), 1024 (w, C-O-C), 986 (m), 843 (vs, PF), 768 (m), 557 cm⁻¹ (s); Φ (CH₃CN, λ_{exc} = 477.4 nm, 295 K): 0.00073 %.

Oxidation and reduction of [2][PF₆]₂: For UV/Vis oxidation measurements a solution of [2][PF₆]₂ (7.7×10^{-5} M) was titrated with a solution of (NH₄)₂[Ce(NO₃)₆] (3.0×10^{-2} M) in 0.5 M trifluoroacetic acid in water. UV/Vis reduction measurements were performed by titration of a solution of [2][PF₆]₂ (1.3×10^{-4} M, 0.5 mL) with a solution of [Co(Cp*)₂] (2.0×10^{-3} M) in CH₃CN. For EPR oxidation measurements a solution of (NH₄)₂[Ce(NO₃)₆] (5.0×10^{-2} M, 3.1 equiv) was added to a solution of [2][PF₆]₂ (1.3×10^{-3} M, 0.5 mL) in CH₃CN. EPR reduction was performed by addition of a solution of [Co(Cp*)₂] (1.0×10^{-2} M, 3.0 equiv) to a solution of [2][PF₆]₂ (1.7×10^{-3} M) in CH₃CN. For all EPR measurements the solution was immediately frozen to 77 K in an EPR tube. [2]⁺: EPR: $g_{1,2,3}$ = 2.0089, 1.9865, 1.9720; Δg = 0.0387 by spectral simulation; Figure S42, the Supporting Information). [2]³⁺: EPR: $g_{1,2,3}$ = 2.4440, 2.2694, 2.0300; Δg = 0.4140 by spectral simulation; Figure S41, the Supporting Information).

Acknowledgements

This work was supported by the International Research Training Group (IRTG 1404): Self Organized Materials for Optoelectronics supported by the Deutsche Forschungsgemeinschaft (DFG). M.M. thanks the Max Planck Graduate Center for support and F.L. (all Max Planck Institute for Polymer Research of Mainz, Germany) thanks the Max Planck Society for funding a Max Planck Research group. We thank Anica Wünsche von Leupoldt for the EPR simulations, Regine Jung-Pothmann for the X-ray data collection (all Johannes Gutenberg-University of Mainz, Germany), Julian Ochsmann (MPI-P Mainz) for transient absorption measurements and Prof. Dr. Doris Kunz (Eberhard Karls-University of Tübingen, Germany) for helpful discussions.

- [1] S. Campagna, F. Puntoriero, F. Nastasi, G. Bergamini, V. Balzani, *Top. Curr. Chem.* **2007**, *280*, 117–214.
- [2] B. O'Regan, M. Grätzel, *Nature* **1991**, *353*, 737–740.
- [3] J.-F. Yin, M. Velayudham, D. Bhattacharya, H.-C. Lin, K.-L. Lu, *Coord. Chem. Rev.* **2012**, *256*, 3008–3035.
- [4] P. G. Bomben, K. C. D. Robson, B. D. Koivisto, C. P. Berlinguette, *Coord. Chem. Rev.* **2012**, *256*, 1438–1450.
- [5] R. D. Costa, E. Ortí, H. J. Bolink, F. Monti, G. Accorsi, N. Armaroli, *Angew. Chem.* **2012**, *124*, 8300–8334; *Angew. Chem. Int. Ed.* **2012**, *51*, 8178–8211.
- [6] H. J. Bolink, E. Coronado, R. D. Costa, P. Gaviña, E. Ortí, S. Tatay, *Inorg. Chem.* **2009**, *48*, 3907–3909.
- [7] H. J. Bolink, L. Cappelli, E. Coronado, P. Gaviña, *Inorg. Chem.* **2005**, *44*, 5966–5968.
- [8] L. Marcélis, J. Ghesquière, K. Garnir, A. K.-D. Mesmaeker, C. Moucheron, *Coord. Chem. Rev.* **2012**, *256*, 1569–1582.
- [9] M. R. Gill, J. A. Thomas, *Chem. Soc. Rev.* **2012**, *41*, 3179–3192.
- [10] H. Komatsu, K. Yoshihara, H. Yamada, Y. Kimura, A. Son, S.-i. Nishimoto, K. Tanabe, *Chem. Eur. J.* **2013**, *19*, 1971–1977.
- [11] C. Bhaumik, D. Saha, S. Das, S. Baitalik, *Inorg. Chem.* **2011**, *50*, 12586–12600.
- [12] L. M. Hancock, E. Marchi, P. Ceroni, P. D. Beer, *Chem. Eur. J.* **2012**, *18*, 11277–11283.
- [13] T. Kundu, A. D. Chowdhury, D. De, S. M. Mobin, V. G. Puranik, A. Datta, G. K. Lahiri, *Dalton Trans.* **2012**, *41*, 4484–4496.
- [14] S. Khatua, D. Samanta, J. W. Bats, M. Schmittel, *Inorg. Chem.* **2012**, *51*, 7075–7086.
- [15] H.-J. Mo, Y. Shen, B.-H. Ye, *Inorg. Chem.* **2012**, *51*, 7174–7184.
- [16] Z.-B. Zheng, Z.-M. Duan, Y.-Y. Ma, K.-Z. Wang, *Inorg. Chem.* **2013**, *52*, 2306–2316.
- [17] R. Zhang, Z. Ye, G. Wang, W. Zhang, J. Yuan, *Chem. Eur. J.* **2010**, *16*, 6884–6891.
- [18] H. Chen, X. Li, Y. Wu, W. Gao, R. Bai, *Dalton Trans.* **2012**, *41*, 13292–13297.
- [19] R. H. Crabtree, *Energy Production and Storage: Inorganic Chemical Strategies for a Warming World*, Wiley-VCH, Weinheim, **2010**.
- [20] X. Liu, F. Wang, *Coord. Chem. Rev.* **2012**, *256*, 1115–1136.
- [21] M. Schulz, M. Karnahl, M. Schwalbe, J. G. Vos, *Coord. Chem. Rev.* **2012**, *256*, 1682–1705.
- [22] W. T. Eckenhoff, R. Eisenberg, *Dalton Trans.* **2012**, *41*, 13004–13021.
- [23] A. Inagaki, M. Akita, *Coord. Chem. Rev.* **2010**, *254*, 1220–1239.
- [24] T. Stoll, M. Gennari, I. Serrano, J. Fortage, J. Chauvin, F. Odobel, M. Rebarz, O. Poizat, M. Sliwa, A. Deronizer, M.-N. Collomb, *Chem. Eur. J.* **2013**, *19*, 782–792.
- [25] J. Dietrich, U. Thorenz, C. Förster, K. Heinze, *Inorg. Chem.* **2013**, *52*, 1248–1264.
- [26] S. Ohzu, T. Ishizuka, Y. Hirai, S. Fukuzumi, T. Kojima, *Chem. Eur. J.* **2013**, *19*, 1563–1567.
- [27] H. Nitadori, T. Takahashi, A. Inagaki, M. Akita, *Inorg. Chem.* **2012**, *51*, 51–62.
- [28] P. Guillo, O. Hamelin, P. Batat, G. Jonusauskas, N. D. McClenaghan, S. Ménage, *Inorg. Chem.* **2012**, *51*, 2222–2230.
- [29] F. Li, M. Yu, Y. Jiang, F. Huang, Y. Li, B. Zhang, L. Sun, *Chem. Commun.* **2011**, *47*, 8949–8951.
- [30] S. Roeser, M. Z. Ertem, C. Cady, R. Lomoth, J. Benet-Buchholz, L. Hammarström, B. Sarkar, W. Kaim, C. J. Cramer, A. Llobet, *Inorg. Chem.* **2012**, *51*, 320–327.
- [31] L.-Z. Sui, W.-W. Yang, C.-J. Yao, H.-Y. Xie, Y.-W. Zhong, *Inorg. Chem.* **2012**, *51*, 1590–1598.
- [32] O. S. Wenger, *Chem. Soc. Rev.* **2012**, *41*, 3772–3779.
- [33] H.-J. Nie, X. Chen, C.-J. Yao, Y.-W. Zhong, G. R. Hutchison, J. Yao, *Chem. Eur. J.* **2012**, *18*, 14497–14509.
- [34] A. Breivogel, K. Hempel, K. Heinze, *Inorg. Chim. Acta* **2011**, *374*, 152–162.
- [35] C. J. Yao, Y.-W. Zhong, J. Yao, *Inorg. Chem.* **2013**, *52*, 4040–4045.
- [36] P. Ceroni, *Chem. Eur. J.* **2011**, *17*, 9560–9564.
- [37] T. N. Singh-Rachford, F. N. Castellano, *Coord. Chem. Rev.* **2010**, *254*, 2560–2573.
- [38] W. Wu, S. Ji, W. Wu, J. Shao, H. Guo, T. D. James, J. Zhao, *Chem. Eur. J.* **2012**, *18*, 4953–4964.
- [39] P. Hanczyc, B. Norden, M. Samoc, *Dalton Trans.* **2012**, *41*, 3123–3125.
- [40] P. Ceroni, G. Bergamini, V. Balzani, *Angew. Chem.* **2009**, *121*, 8668–8670; *Angew. Chem. Int. Ed.* **2009**, *48*, 8516–8518.
- [41] J. Lee, H. Chang, S. Kim, G. S. Bang, H. Lee, *Angew. Chem.* **2009**, *121*, 8653–8656; *Angew. Chem. Int. Ed.* **2009**, *48*, 8501–8504.
- [42] K. Terada, K. Kanaizuka, V. M. Iyer, M. Sannodo, S. Saito, K. Kobayashi, M.-a. Haga, *Angew. Chem.* **2011**, *123*, 6411–6415; *Angew. Chem. Int. Ed.* **2011**, *50*, 6287–6291.
- [43] A. Juris, V. Balzani, F. Barigelli, S. Campagna, P. Belser, A. von Zelewsky, *Coord. Chem. Rev.* **1988**, *84*, 85–277.
- [44] C. Fu, M. Wenzel, E. Treutlein, K. Harms, E. Meggers, *Inorg. Chem.* **2012**, *51*, 10004–10011.
- [45] E. Meggers, *Chem. Eur. J.* **2010**, *16*, 752–758.
- [46] M. Maestri, N. Armaroli, V. Balzani, E. C. Constable, A. M. W. Cargill Thompson, *Inorg. Chem.* **1995**, *34*, 2759–2767.
- [47] J.-P. Sauvage, J.-P. Collin, J.-C. Chambron, S. Guillerez, C. Coudret, V. Balzani, F. Barigelli, L. D. Cola, L. Flamigni, *Chem. Rev.* **1994**, *94*, 993–1019.
- [48] L. Hammarström, O. Johansson, *Coord. Chem. Rev.* **2010**, *254*, 2546–2559.
- [49] Y. Liu, R. Hammitt, D. A. Lutterman, R. P. Thummel, C. Turro, *Inorg. Chem.* **2007**, *46*, 6011–6021.
- [50] K. Heinze, K. Hempel, *Chem. Eur. J.* **2009**, *15*, 1346–1358.
- [51] L. zur Borg, A. L. Domanski, A. Breivogel, M. Bürger, R. Berger, K. Heinze, R. Zentel, *J. Mater. Chem. C* **2013**, *1*, 1223–1230.
- [52] J. Dietrich, A. Wünsche von Leupoldt, M. Grabolle, U. Resch-Genger, K. Heinze, *Eur. J. Inorg. Chem.* **2013**, 3009–3019.
- [53] K. Heinze, K. Hempel, M. Beckmann, *Eur. J. Inorg. Chem.* **2006**, 2040–2050.
- [54] K. Heinze, K. Hempel, S. Tschierlei, M. Schmitt, J. Popp, S. Rau, *Eur. J. Inorg. Chem.* **2009**, 3119–3126.

- [55] D. G. Brown, N. Sanguantrakun, B. Schulze, U. S. Schubert, C. P. Berlinguette, *J. Am. Chem. Soc.* **2012**, *134*, 12354–12357.
- [56] M. Abrahamsson, M. Jäger, T. Österman, L. Eriksson, P. Persson, H.-C. Becker, O. Johansson, L. Hammarström, *J. Am. Chem. Soc.* **2006**, *128*, 12616–12617.
- [57] M. Abrahamsson, M. Jäger, R. J. Kumar, T. Österman, P. Persson, H.-C. Becker, O. Johansson, L. Hammarström, *J. Am. Chem. Soc.* **2008**, *130*, 15533–15542.
- [58] R. J. Kumar, S. Karlsson, D. Streich, A. R. Jensen, M. Jäger, H.-C. Becker, J. Bergquist, O. Johansson, L. Hammarström, *Chem. Eur. J.* **2010**, *16*, 2830–2842.
- [59] F. Schramm, V. Meded, H. Fliedl, K. Fink, O. Fuhr, Z. Qu, W. Klopfer, S. Finn, T. E. Keyes, M. Ruben, *Inorg. Chem.* **2009**, *48*, 5677–5684.
- [60] M. Jäger, R. J. Kumar, H. Görls, J. Bergquist, O. Johansson, *Inorg. Chem.* **2009**, *48*, 3228–3238.
- [61] A. Breivogel, C. Förster, K. Heinze, *Inorg. Chem.* **2010**, *49*, 7052–7056.
- [62] T. J. Meyer, *Pure Appl. Chem.* **1986**, *58*, 1193–1206.
- [63] J. V. Caspar, T. J. Meyer, *J. Am. Chem. Soc.* **1983**, *105*, 5583–5590.
- [64] J. V. Caspar, T. J. Meyer, *J. Phys. Chem.* **1983**, *87*, 952–957.
- [65] M. K. Nazeeruddin, P. Péchy, T. Renouard, S. M. Zakeeruddin, R. Humphry-Baker, P. Comte, P. Liska, L. Cevey, E. Costa, V. Shklover, S. Spiccia, G. B. Deacon, C. A. Bignozzi, M. Grätzel, *J. Am. Chem. Soc.* **2001**, *123*, 1613–1624.
- [66] L. Giribabu, T. Bessho, M. Srinivasu, C. Vijaykumar, Y. Soujanya, V. G. Reddy, P. Y. Reddy, J.-H. Yum, M. Grätzel, M. K. Nazeeruddin, *Dalton Trans.* **2011**, *40*, 4497–4504.
- [67] J. Dehaut, J. Husson, L. Guyard, *Green Chem.* **2011**, *13*, 3337–3340.
- [68] M. Hesse, H. Meier, B. Zeeh, *Spektroskopische Methoden in der organischen Chemie*, Thieme, Stuttgart, **1991**.
- [69] S. Sharma, F. Lombeck, L. Eriksson, O. Johansson, *Chem. Eur. J.* **2010**, *16*, 7078–7081.
- [70] $E(\text{vs. Fe/Fe}^+)/V = E(\text{vs. SCE})/V - 0.4\text{ V}$.
- [71] E. Jakubikova, W. Chen, D. M. Dattelbaum, F. N. Rein, R. C. Rocha, R. L. Martin, E. R. Batista, *Inorg. Chem.* **2009**, *48*, 10720–10725.
- [72] T. Österman, P. Persson, *Chem. Phys.* **2012**, *407*, 76–82.
- [73] B. Schulze, D. Escudero, C. Friebe, R. Siebert, H. Görls, S. Sinn, M. Thomas, S. Mai, J. Popp, B. Dietzek, L. González, U. S. Schubert, *Chem. Eur. J.* **2012**, *18*, 4010–4025.
- [74] W.-W. Yang, Y.-W. Zhong, S. Yoshikawa, J.-Y. Shao, S. Masaoka, K. Sakai, J. Yao, M.-a. Haga, *Inorg. Chem.* **2012**, *51*, 890–899.
- [75] J. Van Houten, R. J. Watts, *J. Am. Chem. Soc.* **1975**, *97*, 3843–3844.
- [76] J. Van Houten, R. J. Watts, *J. Am. Chem. Soc.* **1976**, *98*, 4853–4858.
- [77] S. F. McClanahan, J. R. Kincaid, *J. Am. Chem. Soc.* **1986**, *108*, 3840–3841.
- [78] T. E. Keyes, C. M. O'Connor, U. O'Dwyer, C. G. Coates, P. Callaghan, J. J. McGarvey, J. G. Vos, *J. Phys. Chem. A* **1999**, *103*, 8915–8920.
- [79] T. Österman, M. Abrahamsson, H.-C. Becker, L. Hammarström, P. Persson, *J. Phys. Chem. A* **2012**, *116*, 1041–1050.
- [80] J. T. Hewitt, P. J. Vallet, N. H. Damrauer, *J. Phys. Chem. A* **2012**, *116*, 11536–11547.
- [81] N. H. Damrauer, G. Cerullo, A. Yeh, T. R. Boussie, C. V. Shank, J. K. McCusker, *Science* **1997**, *275*, 54–57.
- [82] N. H. Damrauer, J. K. McCusker, *J. Phys. Chem. A* **1999**, *103*, 8440–8446.
- [83] K. Suzuki, A. Kobayashi, S. Kaneko, K. Takehira, T. Yoshihara, H. Ishida, Y. Shiina, S. Oishi, S. Tobita, *Phys. Chem. Chem. Phys.* **2009**, *11*, 9850–9860.
- [84] F. Etzold, I. A. Howard, N. Forler, D. M. Cho, M. Meister, H. Mangold, J. Shu, M. R. Hansen, K. Müllen, F. Laquai, *J. Am. Chem. Soc.* **2012**, *134*, 10569–10583.
- [85] S. Stoll, A. Schweiger, *J. Magn. Reson.* **2006**, *178*, 42–55.
- [86] *SMART Data Collection and SAINT-Plus Data Processing Software for the SMART System, various versions*, Bruker Analytical X-ray Instruments, Madison, **2000**.
- [87] R. H. Blessing, *Acta Crystallogr. A* **1995**, *51*, 33–38.
- [88] G. M. Sheldrick, *SHELXTL, Version 5.1*, Bruker AXS, Madison, **1998**.
- [89] G. M. Sheldrick, *SHELXL-97*, University of Göttingen, Göttingen, **1997**.
- [90] Gaussian 09, Revision A.02, M. J. Frisch, G. W. Trucks, H. B. Schlegel, G. E. Scuseria, M. A. Robb, J. R. Cheeseman, G. Scalmani, V. Barone, B. Mennucci, G. A. Petersson, H. Nakatsuji, M. Caricato, X. Li, H. P. Hratchian, A. F. Izmaylov, J. Bloino, G. Zheng, J. L. Sonnenberg, M. Hada, M. Ehara, K. Toyota, R. Fukuda, J. Hasegawa, M. Ishida, T. Nakajima, Y. Honda, O. Kitao, H. Nakai, T. Vreven, J. A. Montgomery, Jr., J. E. Peralta, F. Ogliaro, M. Bearpark, J. J. Heyd, E. Brothers, K. N. Kudin, V. N. Staroverov, R. Kobayashi, J. Normand, K. Raghavachari, A. Rendell, J. C. Burant, S. S. Iyengar, J. Tomasi, M. Cossi, N. Rega, J. M. Millam, M. Klene, J. E. Knox, J. B. Cross, V. Bakken, C. Adamo, J. Jaramillo, R. Gomperts, R. E. Stratmann, O. Yazyev, A. J. Austin, R. Cammi, C. Pomelli, J. W. Ochterski, R. L. Martin, K. Morokuma, V. G. Zakrzewski, G. A. Voth, P. Salvador, J. J. Dannenberg, S. Dapprich, A. D. Daniels, Ö. Farkas, J. B. Foresman, J. V. Ortiz, J. Cioslowski, D. J. Fox, Gaussian, Inc., Wallingford CT, **2009**.

Received: June 12, 2013

Published online: September 2, 2013

9.7 Push-Pull Design of Bis(tridentate) Ruthenium(II) Polypyridine Chromophores as Deep Red Light Emitters in Light-Emitting Electrochemical Cells

A. Breivogel, M. Park, D. Lee, S. Klassen, A. Kühnle, C. Lee, K. Char, K. Heinze, *Eur. J. Inorg. Chem.* **2014**, 288–295.

DOI: 10.1002/ejic.201301226

Reprinted with permission from John Wiley and Sons, Copyright © 2013.

DOI:10.1002/ejic.201301226

Push-Pull Design of Bis(tridentate) Ruthenium(II) Polypyridine Chromophores as Deep Red Light Emitters in Light-Emitting Electrochemical Cells

Aaron Breivogel,^[a] Myeongjin Park,^[b] Donggu Lee,^[b] Stefanie Klassen,^[c] Angelika Kühnle,^[c] Changhee Lee,^[b] Kookheon Char,^[d] and Katja Heinze*^[a]

Dedicated to Professor Rudolf Zentel on the occasion of his 60th birthday

Keywords: Ruthenium / Molecular electronics / Tridentate ligands / Luminescence / N ligands

Light-emitting electrochemical cells (LECs) with a simple device structure were prepared by using heteroleptic bis(tridentate) ruthenium(II) complexes [1](PF₆)₂–[3](PF₆)₂ as emitters. The push-pull substitution shifts the emission energy to low energy, into the NIR region. The devices emit deep red light up to a maximum emission wavelength of 755 nm [CIE (International Commission on Illumination) coordinates: x = 0.731, y = 0.269 for [3](PF₆)₂], which, to the best of our knowledge, is the lowest emission energy for LECs containing

bis(tridentate) ruthenium(II) complexes. A device structure of ITO/PEDOT:PSS/ruthenium(II) complex/Ag was used, and the thickness of the emitting layer was measured by AFM [ITO: indium tin oxide, PEDOT: poly(3,4-ethylenedioxythiophene), PSS: poly(styrenesulfonate), AFM: atomic force microscopy]. To enhance the external quantum efficiency (EQE), cells were fabricated with and without poly(methyl methacrylate) (PMMA) as additive in the emitting layer.

Introduction

Light-emitting electrochemical cells (LECs) provide a low-cost alternative to conventional organic light emitting devices (OLEDs) due to their simple device structures and solution processability. LECs feature an ionic emitting layer that enables low turn-on and driving voltages, as well as independence of the work function of electrode materials.^[1–6] LECs introduced in 1995 by Pei contained organic polymers as emitters.^[7,8] While for all-organic emitters spin statistics predicts a maximum internal quantum efficiency

of 25%, transition metal complexes have a theoretical limit of 100%, because in the latter both singlet and triplet excitons can lead to light emission.^[9–12] The first LEC with an ionic transition metal complex was reported in 1996 by Lee employing a [Ru(phen)₃]²⁺ derivative as emitter (phen: 1,10-phenanthroline).^[13] The use of ruthenium(II) complexes as emitters is reasonable because of their outstanding photo-physical and electrochemical properties combined with their high thermal and chemical stabilities.^[14] So far [Ru(bpy)₃]²⁺ (bpy: 2,2'-bipyridine) and its analogues are the most studied ruthenium(II) polypyridine complexes because they have high ³MLCT (MLCT: metal-to-ligand charge transfer) excited state lifetimes ($\tau \approx 1 \mu\text{s}$) and luminescence quantum yields ($\Phi \approx 10\%$) at room temperature in solution.^[14–16] [Ru(bpy)₃]²⁺ and its derivatives have already been used in LECs showing high external quantum efficiencies (EQEs) of up to 6.4%.^[17–20]

However, [Ru(bpy)₃]²⁺ is chiral (Δ , Λ), and unsymmetrical substitution of bpy ligands leads to the formation of stereoisomers, which complicates synthetic procedures.^[21,22] The formation of stereoisomers can be avoided by using tridentate, meridional coordinating ligands. For instance achiral [Ru(tpy)₂]²⁺ (tpy: 2,2';6',2''-terpyridine) gives rise to only a single isomer even in the case of unsymmetrical substitution of the tpy 4'-positions.^[23] Additionally, the tridentate coordination provides a higher photostability and

[a] Institute of Inorganic Chemistry and Analytical Chemistry, Johannes Gutenberg University of Mainz, Duesbergweg 10-14, 55128 Mainz, Germany
E-mail: katja.heinze@uni-mainz.de
<http://www.ak-heinze.chemie.uni-mainz.de/>

[b] Department of Electrical and Computer Engineering, Inter-University Semiconductor Research Center, Seoul National University, 1 Gwanak-ro, Gwanak-gu, Seoul 151-744, Korea

[c] Institute of Physical Chemistry, Johannes Gutenberg University of Mainz, Duesbergweg 10-14, 55099 Mainz, Germany

[d] The National Creative Research Initiative Center for Intelligent Hybrids, The WCU Program on Chemical Convergence for Energy and Environment, School of Chemical and Biological Engineering, Seoul National University, 1 Gwanak-ro, Gwanak-gu, Seoul, 151-744, Korea

Supporting information for this article is available on the WWW under <http://dx.doi.org/10.1002/ejic.201301226>.

chemical stability relative to the bidentate mode.^[24,25] This should prevent thermal and photoinduced ligand exchange, favoring longevity of luminescent and solar cell devices.^[26–29] Degradation products due to ligand loss have been identified in LECs with $[\text{Ru}(\text{bpy})_3]^{2+}$ complexes, namely bis(aqua)complex $[\text{Ru}(\text{bpy})_2(\text{H}_2\text{O})_2]^{2+}$ and oxido-bridged dimer $[\{\text{Ru}(\text{bpy})_2(\text{H}_2\text{O})\}_2\text{O}]^{4+}$, which have been formed by photoaquation in the presence of water.^[6,30–32] A better stabilization towards (photo) ligand substitution might be achieved by using tridentate ligands.

Unfortunately, excited state features of $[\text{Ru}(\text{tpy})_2]^{2+}$ in solution are very unfavorable ($\tau \approx 0.1\text{--}0.2\text{ ns}$, $\Phi \leq 0.0005\%$) because of rapid radiationless deactivation of the radiative $^3\text{MLCT}$ states via thermally accessible ^3MC states (MC: metal-centered; Figure 1).^[33,34] Increased excited state lifetimes τ and quantum yields Φ have been obtained by structurally modifying $[\text{Ru}(\text{tpy})_2]^{2+}$ in order to increase the energy difference between the $^3\text{MLCT}$ and ^3MC states and hence to avoid radiationless deactivation via the latter states. Push-pull substitution like that in $[(\text{EtOOC-tpy})\text{-Ru}(\text{tpy-NH}_2)]^{2+}$ (**[1]**(PF_6)₂, Figure 2) is favorable, as the electron-withdrawing ester group lowers the energy of the $^3\text{MLCT}$ state while the electron-donating amino group increases the energy of the ^3MC state, thus reducing radiationless deactivation via the latter state and enhancing the excited state lifetime and luminescence quantum yield significantly ($\tau = 34\text{ ns}$, $\Phi = 0.18\%$).^[23,35–37] Another strategy employs a strong ligand field to increase the energy difference between the $^3\text{MLCT}$ and ^3MC states. This can be achieved by N–Ru–N bite angles of 90° as in an ideal octahedron allowing for an optimal overlap of ruthenium and nitrogen orbitals. The N–Ru–N bite angle of tpy is 79° because its five-membered chelate rings result in a suboptimal orbital overlap.^[38] Hammarström et al. designed a complex $\{[\text{Ru}(\text{dqp})_2]^{2+}$; dqp: 2,6-di(quinolin-8-yl)pyridine} with six-membered chelate rings and 90° bite angles featuring high room-temperature lifetime and quantum yield in solution ($\tau = 3.0\text{ }\mu\text{s}$, $\Phi = 2\%$).^[39,40] The substituted complex $[\text{Ru}(\text{dpq-COOEt})_2]^{2+}$ with ester substituents on the 4'-positions reaches even higher values ($\tau = 5.5\text{ }\mu\text{s}$, $\Phi = 7\%$).^[41] Ruben et al. incorporated carbonyl bridges between the pyridine rings of $[\text{Ru}(\text{tpy})_2]^{2+}$ and thus obtained six-membered chelate rings and 90° bite angles leading to high $^3\text{MLCT}$ lifetimes and, to the best of our knowledge, to the highest re-

ported quantum yield of bis(tridentate) ruthenium(II) complexes ($\tau = 3.3\text{ }\mu\text{s}$, $\Phi = 30\%$).^[42] Bis(tridentate) ruthenium(II) complexes have been incorporated in LECs, but until now only complexes with small bite angles (ca. 79°) and hence low solution luminescence quantum yields have been utilized, leading to low EQEs ($\leq 0.1\%$) of the devices.^[43–45]

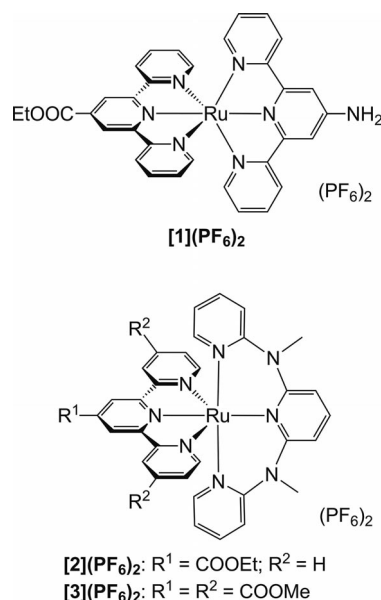


Figure 2. Bis(tridentate) ruthenium(II) oligopyridine complexes **[1](PF₆)₂–[3](PF₆)₂.**

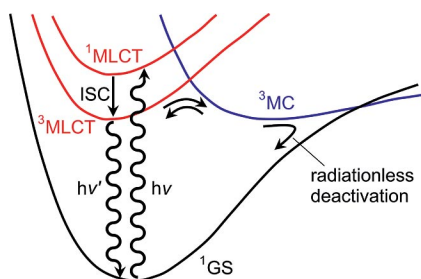


Figure 1. Jablonski diagram of ruthenium(II) polypyridine complexes (GS: ground state, MLCT: metal-to-ligand charge transfer, ISC: intersystem crossing, MC: metal centered).

In this paper, we incorporate bis(tridentate) ruthenium(II) complexes **[1](PF₆)₂–[3](PF₆)₂** as low-energy emitters in LECs (Figure 2). **[1](PF₆)₂–[3](PF₆)₂** are photostable and chemically stable as a result of their tridentate coordination mode; they feature a sophisticated push-pull substitution with high directionality due to electron-withdrawing ester and electron-donating amino groups.^[35–37,46–48] The push-pull substitution lowers the HOMO–LUMO gap (and hence increases the energy difference between the $^3\text{MLCT}$ and ^3MC states) and leads to emission in the red spectral region ($\lambda_{\text{em}} = 729\text{--}744\text{ nm}$, Table 1).^[35,36,46,47] Red light and NIR emission are particularly favorable for noninvasive bioimaging, telecommunication, night-vision-readable displays, downconversion and triplet–triplet annihilation up-conversion.^[1,2,49–57] However, according to the energy gap law, low-energy emission is correlated to low luminescence quantum yields and short luminescence lifetimes due to effective radiationless deactivation into the ground state.^[58–60] In spite of their low emission energy, complexes **[1](PF₆)₂–[3](PF₆)₂** possess comparably high luminescence lifetimes and quantum yields at room temperature in solution ($\tau = 34, 722,$ and 841 ns ; $\Phi = 0.18, 0.45,$ and 1.1% , Table 1). While complex **[1](PF₆)₂** consists of two tpy ligands with 79° N–Ru–N bite angles, complexes **[2](PF₆)₂** and **[3](PF₆)₂** consist of a tpy ligand and a ddpd ligand (ddpd: *N,N'*-dimethyl-*N,N'*-dipyridin-2-ylpyridine-2,6-diamine).^[35,46,47] The larger bite angle (88°) of the latter ligand favors the

high luminescence lifetimes and quantum yields of [2]-(PF₆)₂ and [3](PF₆)₂ (Φ = 0.45 and 1.1 %, Table 1) and their choice as red light to NIR emitters in LECs.

Table 1. Electrochemical and photophysical properties of complexes [1](PF₆)₂–[3](PF₆)₂.^[35–37,46]

	[1](PF ₆) ₂	[2](PF ₆) ₂	[3](PF ₆) ₂
$E_{1/2}^{\text{ox}}/\text{V}[\text{a}]$	+0.68	+0.81	+0.92
$E_{1/2}^{\text{red}}/\text{V}[\text{a}]$	–1.54, –1.99	–1.47, –2.09 ^[b]	–1.25 ^[b] , –1.70 ^[b]
$\lambda_{\text{abs}}/\text{nm}$ ($\epsilon/\text{M}^{-1}\text{cm}^{-1}$) ^[c]	502 (19080)	517 (7500)	539 (6360), 475 (5060)
$\lambda_{\text{em},295\text{ K}}/\text{nm}[\text{c}]$	734	729	744
$\Phi_{295\text{ K}}/\%$ ^[c]	0.18	0.45	1.1
$\tau_{295\text{ K}}/\text{ns}$	34 ^[c]	722 ^[d]	841 ^[d]

[a] In 0.1 M $[n\text{Bu}_4\text{N}][\text{PF}_6]$ in CH₃CN vs. Fc/Fc⁺. [b] Irreversible, E_p given. [c] In CH₃CN. [d] In PrCN.

Results and Discussion

The electrochemical and photophysical properties of complexes [1](PF₆)₂–[3](PF₆)₂ have been described previously and are summarized in Table 1.^[35–37,46] The oxidation potential, $E_{1/2}^{\text{ox}}$, follows the order [1](PF₆)₂ < [2](PF₆)₂ < [3](PF₆)₂ (Table 1). [1](PF₆)₂ is oxidized at the lowest potential because of the electron-donating effect of the NH₂ substituent. [3](PF₆)₂ is oxidized at the highest potential because of the electron-withdrawing effect of the three ester groups.^[46] The first reduction potential, $E_{1/2}^{\text{red}}$, follows the same order [1](PF₆)₂ < [2](PF₆)₂ < [3](PF₆)₂ (Table 1) for the same reasons as those for the trend in $E_{1/2}^{\text{ox}}$. The oxidation of [1](PF₆)₂–[3](PF₆)₂ is reversible on the time scale of electrochemical experiments, while reduction is only reversible for [1](PF₆)₂ and [2](PF₆)₂ on this time scale. The reduction of [3](PF₆)₂ seems to be only quasi-reversible.^[35,36,46] Thus, for all complexes sufficient reversibility in oxidation and reduction processes is given for the application in LECs.

HOMO and LUMO energies of emitting compounds [1](PF₆)₂–[3](PF₆)₂ were estimated from electrochemical redox potentials (Table 1) and are depicted in Figure 3.^[61] The parent $[\text{Ru}(\text{tpy})_2]^{2+}$ complex has a HOMO–LUMO energy gap of ΔE = 2.59 eV with E_{HOMO} = –6.00 eV and E_{LUMO} = –3.41 eV.^[23] The effect of donor–acceptor substitution in [1](PF₆)₂ can be clearly seen as the electron-withdrawing ester group lowers the LUMO energy (E_{LUMO} = –3.54 eV) while the electron-donating amino group raises the HOMO energy (E_{HOMO} = –5.76 eV) resulting in a smaller ΔE = 2.22 eV compared to that of $[\text{Ru}(\text{tpy})_2]^{2+}$. [2](PF₆)₂ and [3](PF₆)₂ have lower HOMO and LUMO energies than [1](PF₆)₂ because of the strong electron-donating effect of the primary amino group present in [1]-(PF₆)₂.^[35–37,46] [3](PF₆)₂ has even lower HOMO and LUMO energies than [2](PF₆)₂, which results from the electron-withdrawing character of the additional ester groups on the tpy ligand. The push-pull effect is most pronounced in [3](PF₆)₂, leading to the smallest HOMO–LUMO energy gap in this series (E_{HOMO} = –6.00 eV, E_{LUMO} = –3.83 eV,

ΔE = 2.17 eV). HOMO and LUMO energies were also obtained by DFT calculations and are summarized in Figure 3.

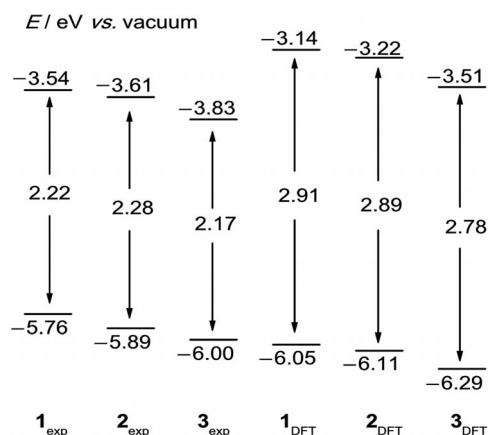


Figure 3. HOMO and LUMO levels of complexes [1](PF₆)₂–[3](PF₆)₂ from experimentally determined redox potentials in CH₃CN^[35,46] and from DFT calculations (B3LYP/LANL2DZ, IEFPCM, CH₃CN).

HOMO energies calculated by DFT (B3LYP/LANL2DZ, IEFPCM, CH₃CN) are lower (0.2–0.3 eV) and LUMO energies are higher (0.3–0.4 eV) than values obtained from electrochemical data. Nevertheless, the trend of the HOMO and LUMO energies (E_{HOMO} and E_{LUMO}) is correctly reproduced: $[1]^{2+} > [2]^{2+} > [3]^{2+}$.

The injection of electrons and holes from opposite electrodes leads to the formation of radical species. Electron capture and loss both occur on the doubly charged ruthenium complex cation. Reduction is located at the ester-substituted tpy ligands, while oxidation is essentially confined to the ruthenium center.^[35,46–48] Spin densities calculated by DFT are exemplarily depicted for complex $[3]^{2+}$ in its reduced and oxidized forms ($[3]^+$ and $[3]^{3+}$; Figures 4a and 4b). The plot illustrates the location of reduction and oxidation processes in $[3]^{2+}$. Electron transfer from $[3]^+$ to $[3]^{3+}$ leads to one ^{1,3}MLCT excited state species ^{1,3} $[3]^{2+}$ and $[3]^{2+}$ in the ground state.^[62] The excited ¹MLCT state undergoes efficient ISC to the ³MLCT state (Figure 1).^[16] Finally, the ³MLCT state emits light upon returning to the singlet ground state $[3]^{2+}$ (Figure 1). The spin density of $[3]^{2+}$ is located on both the ruthenium center and the ester-substituted tpy ligand (Figure 4c), which is in accord with a ruthenium(III) center and a one-electron-reduced tpy ligand.

LECs incorporating [1](PF₆)₂–[3](PF₆)₂ were built with a configuration of ITO/PEDOT:PSS/ruthenium(II) complex/Ag [Figure 5; ITO: indium tin oxide; PEDOT: poly(3,4-ethylenedioxythiophene); PSS: poly(styrenesulfonate)]. PEDOT:PSS was found to increase reproducibility^[45] and shows a HOMO energy level of E_{HOMO} = –5.1 eV.^[63] Ag was used as cathode material because it greatly improves lifetimes of LECs compared to other electrode materials like Al.^[20] Cells were fabricated with and without 20% (w/w) PMMA in the emitting layer [PMMA: poly(methyl methacrylate)]. PMMA acts as insulator, improves the film

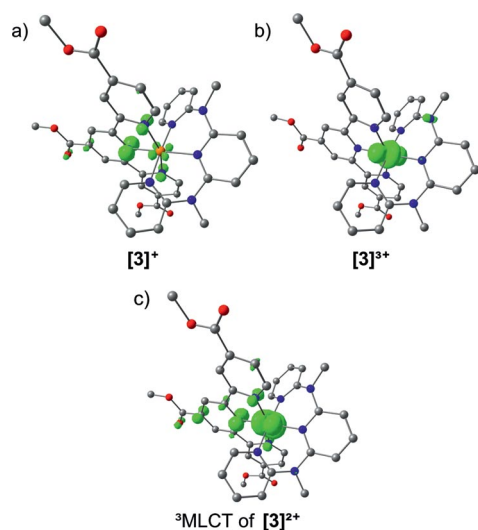


Figure 4. Spin densities of (a) one-electron-reduced complex $[3]^+$, (b) one-electron-oxidized complex $[3]^{3+}$ and (c) the lowest excited triplet species $^3\text{MLCT}$ of $[3]^{2+}$ in CH_3CN calculated by DFT (B3LYP/LANL2DZ, IEFPCM, contour value 0.01 a. u.). Hydrogen atoms are omitted.

quality, and increases the distance between ruthenium(II) complexes to avoid self-quenching processes to enhance the EQE and to prolong device lifetimes.^[18,20,44,45,64] The PEDOT:PSS and ruthenium(II) complex layers were spin-coated onto an ITO substrate. The Ag cathode was deposited in vacuo by thermal evaporation. The thicknesses of the PEDOT:PSS and the ruthenium complex:PMMA layers were determined by AFM measurements after scratching the layer with a razor (AFM: atomic force microscopy). The thicknesses are 45 ± 5 nm (PEDOT:PSS), 229 ± 19 nm (total thickness of PEDOT:PSS and ruthenium complex without PMMA), and 237 ± 23 nm (total thickness of PEDOT:PSS and ruthenium complex with PMMA). Figure 6 shows a representative AFM image of the scratched LEC with $[1](\text{PF}_6)_2$ and PMMA. AFM images for all scratched LECs are depicted in the Supporting Information (Figure S1).

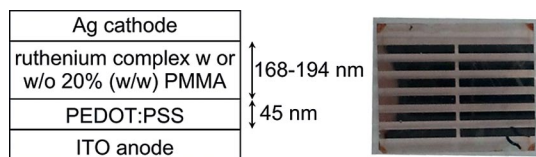


Figure 5. General device structure of the LECs and photograph of the LEC with $[1](\text{PF}_6)_2$ without PMMA.

A voltage of 3 V was applied to each cell for at least 10 min. The LEC incorporating complex $[2](\text{PF}_6)_2$ (without PMMA) shows red light emission. The other cells did not emit under these conditions. For these cells, a higher voltage on a new pixel was applied in steps of 0.5–1 V until emission was observed. LEC characteristics are summarized in Table 2. The reported voltage is the minimum voltage for which emission is observed, and all other data refer to this voltage. Cells with $[1](\text{PF}_6)_2$ without PMMA do not emit

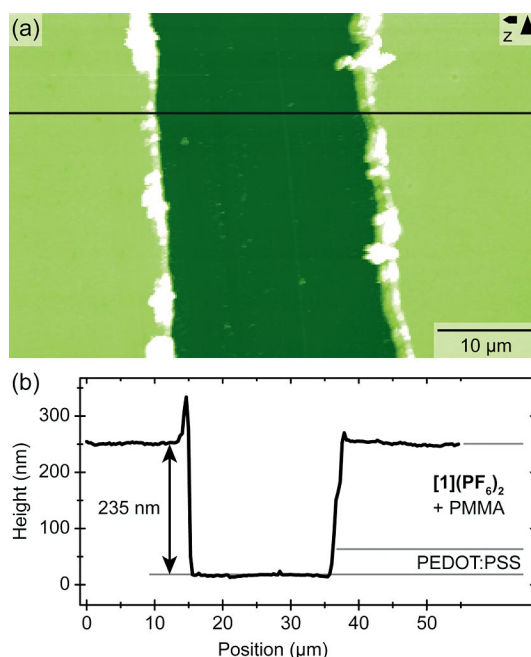


Figure 6. AFM image taken in intermittent contact mode of a scratched PEDOT:PSS/ $[1](\text{PF}_6)_2$ with PMMA layer. (a) Topographical height scan with indicated cross section. (b) Height profile along the indicated cross section.

up to a voltage of 6 V. When PMMA is present, the LEC with $[1](\text{PF}_6)_2$ emits with a turn on voltage of 4 V. The driving voltages are generally a few volts higher for cells with PMMA, which is consistent with the insulating character of PMMA.^[20] Emission wavelengths of the devices are fully comparable to the emissions in solution and differ only by $\Delta E = \pm 0.02$ eV (Tables 1 and 2, Figures S2 and S3). $[3](\text{PF}_6)_2$ features a slightly redshifted electroluminescence in LECs in the absence of PMMA (Figure S4, Tables 1 and 2). Figure 7a exemplarily depicts the emission spectra of $[2](\text{PF}_6)_2$ in CH_3CN and in LECs with and without PMMA.

The longest emission wavelength maximum ($\lambda_{\text{em,max}} = 755$ nm) was obtained for the LEC with $[3](\text{PF}_6)_2$ without PMMA at an applied voltage of 4 V. To the best of our knowledge, this is the longest emission wavelength of a LEC with a mononuclear bis(tridentate) ruthenium(II) complex. The CIE (International Commission on Illumination) coordinates^[65] of the emitted light are given in Table 2 and in all cases correspond to deep red light at the edge of the CIE chromaticity diagram. Light intensity, current density, and EQE curves are plotted against time (Supporting Information, Figures S4–S7). Exemplarily, Figure 7b shows the EQE-intensity-current density vs. time plots for the LEC with $[2](\text{PF}_6)_2$ without PMMA at an applied voltage of 3 V. All values increase at initial stages until they reach a maximum after a few minutes. Then they slowly decrease as typically observed for this kind of LECs.^[44,45] Maximum light emission occurs after $t_{\text{em,max}} = 2$ –14 min. Devices with PMMA should have a higher $t_{\text{em,max}}$ than devices without PMMA, because PMMA hinders ion migration and forma-

Table 2. LEC device characteristics for complexes [1](PF₆)₂–[3](PF₆)₂.

	[1](PF ₆) ₂ without PMMA	with PMMA ^[a]	[2](PF ₆) ₂ without PMMA	with PMMA ^[a]	[3](PF ₆) ₂ without PMMA	with PMMA ^[a]
Height of emitting layer /nm	182 ± 16	190 ± 12	168 ± 33	191 ± 31	193 ± 27	194 ± 12
<i>U</i> /V	–	4	3	6	4	5
$\lambda_{\text{em,max,LEC}}$ /nm	–	733 ^(6V)	731	722	755	745
$\lambda_{\text{em,max,acetonitrile}}$ /nm	734	734	729	729	744	744
$t_{\text{em,max}}$ /min	–	ca. 11–14	13	2	9	4
L_{max} /cd m ^{–2}	–	0.32	1.81	3.36	0.75	0.64
$t_{\text{current,max}}$ /min	–	13	31	3	8	8
$I_{\text{d,max}}$ /mA cm ^{–2}	–	313	103	518	213	231
EQE _{max} /%	–	0.001	0.016	0.028	0.007	0.013
$t_{\text{EQE,max}}$ /min	–	14–15	10	1	9	1
CIE coordinates (<i>x</i> , <i>y</i>)	–	0.709, 0.291	0.725, 0.275	0.717, 0.283	0.731, 0.269	0.729; 0.271

[a] 20% (w/w).

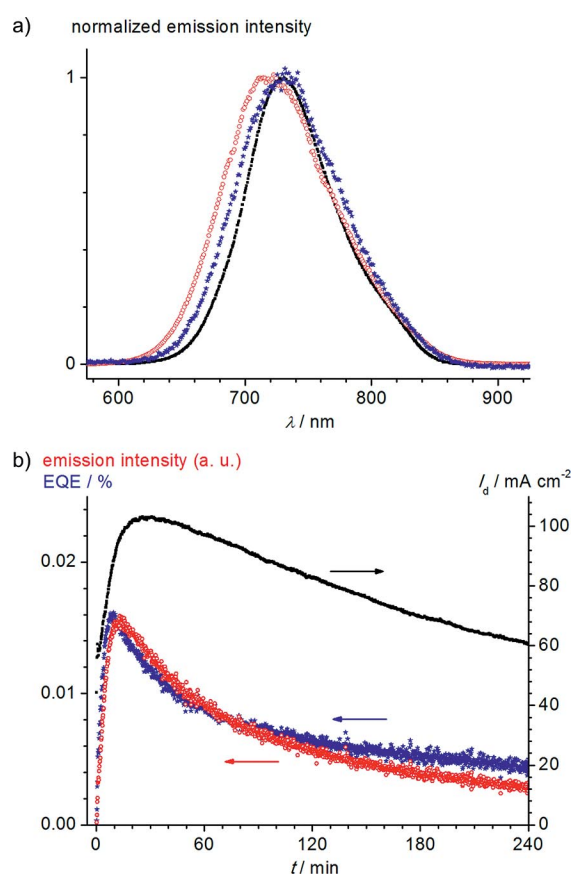


Figure 7. (a) Normalized emission spectra of [2](PF₆)₂ (black squares: CH₃CN solution; red hollow circles: LEC with PMMA, 6 V; blue stars: LEC without PMMA, 3 V). (b) Current density (black squares), emission intensity (red hollow circles), and EQE (blue stars) as a function of time in the LEC with [2](PF₆)₂ without PMMA at an applied voltage of 3 V.

tion of electric double layers. However, a smaller $t_{\text{em,max}}$ value is measured for devices with PMMA than for those without PMMA (see LECs with [2](PF₆)₂ and [3](PF₆)₂, Table 2). The higher voltages applied for devices with PMMA to compensate the insulating behavior of PMMA might be responsible for this observation.^[6] Luminances *L* were calculated with Equation (1), which assumes that the

device was a Lambertian source and a calibrated Si photodiode was placed at an angle normal to the device surface.^[66,67]

$$L = \frac{K_m \cdot I_{\text{photodiode}} \cdot R^2}{A_{\text{LEC}} \cdot A_{\text{photodiode}}} \frac{\int_{360\text{nm}}^{830\text{nm}} V(\lambda) \frac{S_{\text{emission}}(\lambda)}{S_{\text{responsivity}}(\lambda)} d\lambda}{\int_{360\text{nm}}^{830\text{nm}} S_{\text{emission}}(\lambda) d\lambda} \quad (1)$$

where $K_m = 683 \text{ lm W}^{-1}$ at 555 nm, *I*: current, *R*: distance between LEC and photodiode, A_{LEC} : area of the limiting aperture, $A_{\text{photodiode}}$: area of the photodiode, *V*(λ): photopic response curve, $S_{\text{emission}}(\lambda)$: emission spectrum, $S_{\text{responsivity}}(\lambda)$: responsivity of the Si photodiode, λ: wavelength).

The highest luminance is $L = 3.4 \text{ cd m}^{-2}$ for the LEC with [2](PF₆)₂ with PMMA at an applied voltage of 6 V. The smaller luminance of LECs with [1](PF₆)₂ ($L = 0.3 \text{ cd m}^{-2}$) is likely due to the lower luminescence quantum yield of [1](PF₆)₂ in solution (Table 2). The lower luminance of [3](PF₆)₂ ($L \approx 0.7 \text{ cd m}^{-2}$) might be due to the small overlap of its NIR emission ($\lambda_{\text{em}} \approx 750 \text{ nm}$) with the human eye response curve (Figure S8). The current density reaches its maximum after $t_{\text{current,max}} = 3\text{--}31 \text{ min}$. For LECs with complex [3](PF₆)₂ there is no clear dependency of $t_{\text{current,max}}$ on the voltage or the presence of PMMA. In contrast, $t_{\text{current,max}}$ values in LECs with [2](PF₆)₂ are smaller at high voltages (6 V, 3 min) and larger at lower voltages (3 V, 31 min), which confirms that ion migration is faster at higher voltages.^[6] Current densities are in the range $I_d = 103\text{--}518 \text{ mA cm}^{-2}$, which is consistent with previously reported LECs with a bis(terpyridine)ruthenium(II) complex (ca. 200–300 mA cm^{–2}).^[44] As expected, current densities are high for high applied voltages (Table 2). EQE values are 0.001–0.028%. The highest EQE value (0.028%) is obtained for the LEC with [2](PF₆)₂ with PMMA. LECs containing [1](PF₆)₂ only lead to a small EQE (0.001%), which is probably caused by the smaller solution quantum yield of [1](PF₆)₂ relative to those of [2](PF₆)₂ and [3](PF₆)₂ (Table 1). The maximum EQE of the LEC with [3](PF₆)₂ (0.013%) is less than the EQE for the LEC with [2](PF₆)₂ (0.028%), which is in contrast to the relative emission quan-

tum yields (Table 1 and Table 2). Possibly this observation can be explained by the redshifted emission of [3](PF₆)₂ (λ = 745–755 nm) within the LEC compared to its emission in solution (λ = 744 nm, Figure S5, Table 1 and Table 2). The low-energy emissive state might be prone to enhanced radiationless deactivation according to the energy gap law.^[58–60] Interestingly, [2](PF₆)₂ shows no redshifted emission in the LECs (Figure 7a, Table 1 and Table 2).

For OLEDs, saturation and quenching effects like triplet–triplet annihilation resulting from high luminescence lifetimes and high current densities can lead to decreasing EQEs.^[68] Typically, luminescent emitters are doped into host matrices like PMMA or CBP in order to enhance the EQE [CBP: 4,4'-bis(9-carbazolyl)-2,2'-biphenyl]. For instance, *fac*-Ir(ppy)₃ (ppy: 2-phenylpyridine) features lifetimes of 1.4 μ s (less than 0.1 w/w% in PMMA) to 630 ns (8 w/w% in CBP), which is regarded sufficiently short to avoid saturation and quenching effects up to a current density of I_d = 1000 mA cm⁻².^[69,70] Saturation thresholds for the current density also depend on the concentration of the dopant. For PtOEP (PtOEP: 2,3,7,8,12,13,17,18-octaethylporphyrine platinum) with a phosphorescence lifetime of τ \approx 30 μ s, the critical current density rises from I_d = 40 (1 w/w% in CBP) to 800 mA cm⁻² (16 w/w% in CBP).^[71] For neat films of *fac*-Ir(ppy)₃ the EQE drops to 0.8% with a concomitant drop in phosphorescence lifetime to τ \approx 100 ns relative to doped devices.^[72] This drop is caused by self-quenching due to Ir(ppy)₃–Ir(ppy)₃ exciton interactions.^[68,73] In neat films of *fac*-Ir(ppy)₃ critical current densities for quenching mechanisms like triplet–triplet annihilation are reported to be in the range I_d = 500–1400 mA cm⁻².^[74,75] However, depending on the device structure, a decrease of EQE in neat films of *fac*-Ir(ppy)₃ can already be observed at current densities of I_d \approx 300 mA cm⁻².^[76] In LECs such quenching effects have also been studied in a few cases apart from the above-mentioned deactivation due to ligand loss and the formation of aqua complexes. The cationic iridium(III) complex [Ir(ppy)₂-(pzpy)]PF₆ [pzpy: 2-(1*H*-pyrazol-1-yl)pyridine] was tested in a LEC. The doping of this complex into a PMMA film (5 w/w%) increases its luminescence quantum yield (Φ = 23 \rightarrow 61%) and lifetime (τ = 1.6 \rightarrow 3.3 μ s). However, luminescence quantum yield and lifetime drop dramatically when going from the doped (5 w/w% in PMMA) to the neat film (Φ = 3%, τ = 0.2 μ s), which is attributed to the efficient excited state quenching in the neat film.^[77] Quenching effects in LECs also depend on the thickness of the (neat) emitting layer. The EQE of a LEC with [Ru(bpy)₃](PF₆)₂ decreases monotonically from 1% for a 192 nm thick complex layer to less than 0.01% for a 46 nm thick layer. The quenching is believed to occur by triplet–triplet annihilation and higher charge carrier densities near the electrode surfaces.^[78–80] Self-quenching can be avoided by using sterically demanding substituents.^[81,82] As a result of the high local concentration (neat or 80 w/w%), high current densities (up to 518 mA cm⁻²), and high solution luminescence lifetimes (up to 841 ns), saturation and quenching effects might also be present in our LECs. Indeed, dilution with

PMMA has a positive effect on the EQE. In LECs with [2](PF₆)₂ and [3](PF₆)₂, the EQE is increased by a factor of two by using PMMA.^[20,83] The maximum values of the EQE are obtained after 1–15 min. In LECs with PMMA of [2](PF₆)₂ and [3](PF₆)₂, the maximum EQE is reached after only one minute, which is attributed to the fast ion migration and rapid device degradation due to the high applied voltages of 5–6 V.^[6]

Conclusions

Heteroleptic bis(tridentate) ruthenium(II) complexes [1](PF₆)₂–[3](PF₆)₂ (Figure 1) were used as emitters in LECs with a ITO/PEDOT:PSS/ruthenium(II) complex/Ag device structure. Red to NIR light emission was observed in the solid-state devices (λ_{em} = 722–755 nm; CIE: x = 0.709–0.731, y = 0.291–0.269). To the best of our knowledge, these are the lowest emission energies for LECs containing bis-(tridentate) ruthenium(II) complexes. The low-energy emission is favored by the pronounced push-pull character of the complexes, which results in a small HOMO–LUMO gap. PMMA as additive (20% w/w) in the ruthenium complex layer requires higher driving voltages but yields higher external quantum efficiencies. Future perspectives include the steric protection of the ruthenium core by bulkier ligands to prevent a change in the coordination sphere by ligand substitution and self-quenching as well as the usage of other counterions to investigate their effect on the LEC performance.

Experimental Section

General Procedures: Complexes [1](PF₆)₂–[3](PF₆)₂ were prepared as described previously.^[35,36,46,47] Before spin-coating, the complexes were further purified by reversed phase HPLC with a JASCO semipreparative HPLC system with a Reprosil C₁₈ column (5 μ m) by using CH₃CN/water (96:4, v/v) as an eluent (10 mL min⁻¹) and UV/Vis detection at 502–539 nm. Patterned ITO glass substrates, which were cleaned in an ultrasonic bath, sequentially with acetone, isopropyl alcohol, and deionized water, were treated with UV/O₃ for 10 min before spin-coating. PEDOT:PSS (1:6 weight%, Al 4083; suspension in water; 1.3–1.7% solid content) was filtered (HP, 0.45 μ m) and spin-coated (4000 rpm, 30 s, 4 s acceleration) onto the ITO substrate. After drying (1 h, 120 $^{\circ}$ C under reduced pressure), the substrate was transferred into an argon atmosphere. Ruthenium complexes (10 mg mL⁻¹) and PMMA (0 or 2 mg mL⁻¹, M_w 120000) were dissolved in acetonitrile in an argon atmosphere and spin-coated onto the PEDOT:PSS layer (1000 rpm, 20 s, no acceleration). Silver electrodes were vapor-deposited on the substrates under a pressure of 3×10^{-6} Torr. The current–voltage characteristics were measured by using a source measurement unit (Keithley 236). The luminance and efficiencies were calculated from photocurrent measurement data obtained with a calibrated Si photodiode (Hamamatsu S5227–1010BQ). Electroluminescence spectra of the devices were obtained by an ICCD camera through an ARC 275 monochromator. AFM measurements were conducted in intermittent contact mode with two different instruments: A Veeco Dimension AFM was used for the measurement of the total height of the PEDOT:PSS and the

emitting layers and a XE-100 AFM was used to measure the thickness of the PEDOT:PSS layer. The spin-coated PEDOT:PSS and PEDOT:PSS-ruthenium complex layers were scratched with a razor, and the thickness of the layers was determined by the measured height differences.

DFT Studies: The DFT calculations were carried out with the Gaussian 09/DFT^[84] series of programs. The LANL2DZ basis set^[84] was used in the B3LYP formulation of DFT. No symmetry constraints were imposed on the molecules. The presence of energy minima was checked by analytical frequency calculations. The integral-equation-formalism polarizable continuum model (IEFPCM, CH₃CN) was employed for solvent modeling in all calculations. All calculations were performed without explicit counterions and solvent molecules.

Supporting Information (see footnote on the first page of this article): AFM images of scratched PEDOT:PSS/ruthenium complex:PMMA layers; emission spectra of [1](PF₆)₂ and [3](PF₆)₂ in solution and in LECs; current density vs. EQE intensity curves of the LECs; human eye response curve and emission spectra of [1](PF₆)₂–[3](PF₆)₂ in LECs.

Acknowledgments

This work was supported by the Deutsche Forschungsgemeinschaft (DFG) [International Research Training Group: Self-Organized Materials for Optoelectronics (IRTG 1404)].

- [1] H. Xiang, J. Cheng, X. Ma, X. Zhou, J. J. Chruma, *Chem. Soc. Rev.* **2013**, *42*, 6128–6185.
- [2] R. D. Costa, E. Ortí, H. J. Bolink, F. Monti, G. Accorsi, N. Armaroli, *Angew. Chem.* **2012**, *124*, 8300–8334; *Angew. Chem. Int. Ed.* **2012**, *51*, 8178–8211.
- [3] R. D. Costa, E. Ortí, H. J. Bolink, *Pure Appl. Chem.* **2011**, *83*, 2115–2128.
- [4] J. Slinker, D. Bernards, P. L. Houston, H. D. Abruña, S. Bernhard, G. G. Malliaras, *Chem. Commun.* **2003**, *19*, 2392–2399.
- [5] E. Holder, B. M. W. Langeveld, U. S. Schubert, *Adv. Mater.* **2005**, *17*, 1109–1121.
- [6] J. D. Slinker, J. Rivnay, J. S. Moskowitz, J. B. Parker, S. Bernhard, H. D. Abruña, G. G. Malliaras, *J. Mater. Chem.* **2007**, *17*, 2976–2988.
- [7] Q. Pei, G. Yu, C. Zhang, Y. Yang, A. J. Heeger, *Science* **1995**, *269*, 1086–1088.
- [8] Q. Pei, Y. Yang, G. Yu, C. Zhang, A. J. Heeger, *J. Am. Chem. Soc.* **1996**, *118*, 3922–3929.
- [9] A. P. Monkman, *ISRN Mater. Sci.* **2013**, DOI: 10.1155/2013/670130.
- [10] J. Wang, A. Chepelianskii, F. Gao, N. C. Greenham, *Nat. Commun.* **2012**, *3*, DOI: 10.1038/ncomms2194.
- [11] A. Köhler, H. Bässler, *Mater. Sci. Eng.* **2009**, *R66*, 71–109.
- [12] H. Yersin, *Highly Efficient OLEDs with Phosphorescent Materials*, Wiley-VCH, Weinheim, Germany, **2008**.
- [13] J.-K. Lee, D. S. Yoo, E. S. Handy, M. F. Rubner, *Appl. Phys. Lett.* **1996**, *69*, 1686–1688.
- [14] S. Campagna, F. Puntoriero, F. Nastasi, G. Bergamini, V. Balzani, *Top. Curr. Chem.* **2007**, *280*, 117–214.
- [15] J. R. Lakowicz, *Principles of Fluorescence Spectroscopy*, Springer, New York, **2006**.
- [16] A. Juris, V. Balzani, F. Barigelli, S. Campagna, P. Belser, A. von Zelewsky, *Coord. Chem. Rev.* **1988**, *84*, 85–277.
- [17] C.-Y. Liu, A. J. Bard, *Appl. Phys. Lett.* **2005**, *87*, 061110.
- [18] H. Rudmann, S. Shimada, M. F. Rubner, *J. Am. Chem. Soc.* **2002**, *124*, 4918–4921.
- [19] S. Xun, J. Zhang, X. Li, D. Ma, Z. Y. Wang, *Synth. Met.* **2008**, *158*, 484–488.
- [20] H. Rudmann, M. F. Rubner, *J. Appl. Phys.* **2001**, *90*, 4338–4345.
- [21] C. Fu, M. Wenzel, E. Treutlein, K. Harms, E. Meggers, *Inorg. Chem.* **2012**, *51*, 10004–10011.
- [22] E. Meggers, *Chem. Eur. J.* **2010**, *16*, 752–758.
- [23] M. Maestri, N. Armaroli, V. Balzani, E. C. Constable, A. M. W. Cargill Thompson, *Inorg. Chem.* **1995**, *34*, 2759–2767.
- [24] R. Hogg, R. G. Wilkins, *J. Chem. Soc.* **1962**, 341–350.
- [25] R. H. Holyer, C. D. Hubbard, S. F. A. Kettle, R. G. Wilkins, *Inorg. Chem.* **1966**, *5*, 622–625.
- [26] A. Reynald, E. Palomares, *Eur. J. Inorg. Chem.* **2011**, *29*, 4509–4526.
- [27] C.-W. Hsu, S.-T. Ho, K.-L. Wu, Y. Chi, S.-H. Liu, P.-T. Chou, *Energy Environ. Sci.* **2012**, *5*, 7549–7554.
- [28] J.-F. Yin, M. Velayudham, D. Bhattacharya, H.-C. Lin, K.-L. Lu, *Coord. Chem. Rev.* **2012**, *256*, 3008–3035.
- [29] B. Schulze, D. Escudero, C. Friebe, R. Siebert, H. Görls, S. Sinn, M. Thomas, S. Mai, J. Popp, B. Dietzek, L. González, U. S. Schubert, *Chem. Eur. J.* **2012**, *18*, 4010–4025.
- [30] J. D. Slinker, J.-S. Kim, S. Flores-Torres, J. H. Delcamp, H. D. Abruña, R. H. Friend, G. G. Malliaras, *J. Mater. Chem.* **2007**, *17*, 76–81.
- [31] L. J. Soltzberg, J. D. Slinker, S. Flores-Torres, D. A. Bernards, G. G. Malliaras, H. D. Abruña, J.-S. Kim, R. H. Friend, M. D. Kaplan, V. Goldberg, *J. Am. Chem. Soc.* **2006**, *128*, 7761–7764.
- [32] G. Kalyuzhny, M. Buda, J. McNeill, P. Barbara, A. J. Bard, *J. Am. Chem. Soc.* **2003**, *125*, 6272–6283.
- [33] J.-P. Sauvage, J.-P. Collin, J.-C. Chambron, S. Guillerez, C. Coudret, *Chem. Rev.* **1994**, *94*, 993–1019.
- [34] Y. Liu, R. Hammit, D. A. Lutterman, R. P. Thummel, C. Turro, *Inorg. Chem.* **2007**, *46*, 6011–6021.
- [35] K. Heinze, K. Hempel, M. Beckmann, *Eur. J. Inorg. Chem.* **2006**, *10*, 2040–2050.
- [36] K. Heinze, K. Hempel, S. Tschierlei, M. Schmitt, J. Popp, S. Rau, *Eur. J. Inorg. Chem.* **2009**, *21*, 3119–3126.
- [37] K. Heinze, K. Hempel, A. Breivogel, *Z. Anorg. Allg. Chem.* **2009**, *635*, 2541–2549.
- [38] K. Lashgari, M. Kritikos, R. Norrestam, T. Norrby, *Acta Crystallogr., Sect. C* **1999**, *55*, 64–67.
- [39] M. Abrahamsson, M. Jäger, T. Österman, L. Eriksson, P. Persson, H.-C. Becker, O. Johansson, L. Hammarström, *J. Am. Chem. Soc.* **2006**, *128*, 12616–12617.
- [40] G. A. Parada, L. A. Fredin, M.-P. Santoni, M. Jäger, R. Lomoth, L. Hammarström, O. Johansson, P. Persson, S. Ott, *Inorg. Chem.* **2013**, *52*, 5128–5137.
- [41] M. Abrahamsson, M. Jäger, R. J. Kumar, T. Österman, P. Persson, H.-C. Becker, O. Johansson, L. Hammarström, *J. Am. Chem. Soc.* **2008**, *130*, 15533–15542.
- [42] F. Schramm, V. Meded, H. Fliegl, K. Fink, O. Fuhr, Z. Qu, W. Klopfer, S. Finn, T. E. Keyes, M. Ruben, *Inorg. Chem.* **2009**, *48*, 5677–5684.
- [43] W. Y. Ng, X. Gong, W. K. Chan, *Chem. Mater.* **1999**, *11*, 1165–1170.
- [44] H. J. Bolink, L. Cappelli, E. Coronado, P. Gaviña, *Inorg. Chem.* **2005**, *44*, 5966–5968.
- [45] H. J. Bolink, E. Coronado, R. D. Costa, P. Gaviña, E. Ortí, S. Tatay, *Inorg. Chem.* **2009**, *48*, 3907–3909.
- [46] A. Breivogel, M. Meister, C. Förster, F. Laquai, K. Heinze, *Chem. Eur. J.* **2013**, *19*, 13745–13760.
- [47] A. Breivogel, C. Förster, K. Heinze, *Inorg. Chem.* **2010**, *49*, 7052–7056.
- [48] A. Breivogel, K. Hempel, K. Heinze, *Inorg. Chim. Acta* **2011**, *374*, 152–162.
- [49] H. Komatsu, K. Yoshihara, H. Yamada, Y. Kimura, A. Son, S.-i. Nishimoto, K. Tanabe, *Chem. Eur. J.* **2013**, *19*, 1971–1977.
- [50] M. R. Gill, J. A. Thomas, *Chem. Soc. Rev.* **2012**, *41*, 3179–3192.
- [51] P. Ceroni, *Chem. Eur. J.* **2011**, *17*, 9560–9564.
- [52] T. N. Singh-Rachford, F. N. Castellano, *Coord. Chem. Rev.* **2010**, *254*, 2560–2573.

- [53] W. Wu, S. Ji, W. Wu, J. Shao, H. Guo, T. D. James, J. Zhao, *Chem. Eur. J.* **2012**, *18*, 4953–4964.
- [54] P. Hanczyc, B. Norden, M. Samoc, *Dalton Trans.* **2012**, *41*, 3123–3125.
- [55] M. D. Ward, *Coord. Chem. Rev.* **2007**, *251*, 1663–1677.
- [56] S. V. Eliseeva, J.-C. G. Bünzli, *Chem. Soc. Rev.* **2010**, *39*, 189–227.
- [57] J. C. G. Bünzli, S. V. Eliseeva, *J. Rare Earths* **2010**, *28*, 824–842.
- [58] T. J. Meyer, *Pure Appl. Chem.* **1986**, *58*, 1193–1206.
- [59] J. V. Caspar, T. J. Meyer, *J. Am. Chem. Soc.* **1983**, *105*, 5583–5590.
- [60] J. V. Caspar, T. J. Meyer, *J. Phys. Chem.* **1983**, *87*, 952–957.
- [61] $E(\text{vacuum})/\text{eV} = -4.68 - E(\text{SCE})/V = -5.08 - E(\text{Fc}/\text{Fc}^+)/V$.
- [62] F. Bolletta, S. Bonafede, *Pure Appl. Chem.* **1986**, *58*, 1229–1232.
- [63] F. Xu, J.-Y. Kwon, J.-H. Kim, H. U. Kim, J. M. Lim, H. Cho, C. Lee, J. Lee, J.-I. Lee, D.-H. Hwang, *Synth. Met.* **2012**, *162*, 1421–1428.
- [64] H. J. Bolink, L. Cappelli, E. Coronado, M. Grätzel, Md. K. Nazeeruddin, *J. Am. Chem. Soc.* **2006**, *128*, 46–47.
- [65] International Commission on Illumination (CIE), 1931.
- [66] P. Toivanen, J. Hovila, P. Kärh  , E. Ikonen, *Metrologia* **2000**, *37*, 527–530.
- [67] P. Toivanen, P. K  rh  , F. Manoochchri, E. Ikonen, *Metrologia* **2000**, *37*, 131–140.
- [68] H. Yersin, A. F. Rausch, R. Czerwieniec, T. Hofbeck, T. Fischer, *Coord. Chem. Rev.* **2011**, *255*, 2622–2652.
- [69] N. C. Giebink, S. R. Forrest, *Phys. Rev. B* **2008**, *77*, 235215.
- [70] T. Hofbeck, H. Yersin, *Inorg. Chem.* **2010**, *49*, 9290–9299.
- [71] M. A. Baldo, C. Adachi, S. R. Forrest, *Phys. Rev. B* **2000**, *62*, 10967–10977.
- [72] M. A. Baldo, M. E. Thompson, S. R. Forrest, *Pure Appl. Chem.* **1999**, *71*, 2095–2106.
- [73] C. Adachi, M. A. Baldo, S. R. Forrest, M. E. Thompson, *Appl. Phys. Lett.* **2000**, *77*, 904–906.
- [74] J. Kalinowski, J. M  zyk, F. Meinardi, R. Tubino, M. Cocchi, D. Virgili, *J. Appl. Phys.* **2005**, *98*, 063532.
- [75] J. Kalinowski, W. Stampor, J. Szmytkowski, D. Virgili, M. Cocchi, V. Fattori, C. Sabatini, *Phys. Rev. B* **2006**, *74*, 085316.
- [76] M. A. Baldo, S. Lamansky, P. E. Burrows, M. E. Thompson, S. R. Forrest, *Appl. Phys. Lett.* **1999**, *75*, 4–6.
- [77] L. He, L. Duan, J. Qiao, R. Wang, P. Wei, L. Wang, Y. Qiu, *Adv. Funct. Mater.* **2008**, *18*, 2123–2131.
- [78] K. W. Lee, J. D. Slinker, A. A. Gorodetsky, S. Flores-Torres, H. D. Abru  a, P. L. Houston, G. G. Malliaras, *Phys. Chem. Chem. Phys.* **2003**, *5*, 2706–2709.
- [79] S. Bernhard, X. Gao, G. G. Malliaras, H. D. Abru  a, *Adv. Mater.* **2002**, *14*, 433–436.
- [80] N. R. Armstrong, R. M. Wightman, E. M. Gross, *Annu. Rev. Phys. Chem.* **2001**, *52*, 391–422.
- [81] P. Dreyse, B. Loeb, M. Soto-Arriaza, D. Tordera, E. Ort  , J. J. Serrano-P  rez, H. J. Bolink, *Dalton Trans.* **2013**, *42*, 15502–15513.
- [82] S. Bernhard, J. A. Barron, P. L. Houston, H. D. Abru  a, J. L. Ruglovksy, X. Gao, G. G. Malliaras, *J. Am. Chem. Soc.* **2002**, *124*, 13624–13628.
- [83] D. W. Thompson, C. N. Fleming, B. D. Myron, T. J. Meyer, *J. Phys. Chem. B* **2007**, *111*, 6930–6941.
- [84] M. J. Frisch, G. W. Trucks, H. B. Schlegel, G. E. Scuseria, M. A. Robb, J. R. Cheeseman, G. Scalmani, V. Barone, B. Mennucci, G. A. Petersson, H. Nakatsuji, M. Caricato, X. Li, H. P. Hratchian, A. F. Izmaylov, J. Bloino, G. Zheng, J. L. Sonnenberg, M. Hada, M. Ehara, K. Toyota, R. Fukuda, J. Hasegawa, M. Ishida, T. Nakajima, Y. Honda, O. Kitao, H. Nakai, T. Vreven, J. A. Montgomery Jr., J. E. Peralta, F. Ogliaro, M. Bearpark, J. J. Heyd, E. Brothers, K. N. Kudin, V. N. Staroverov, R. Kobayashi, J. Normand, K. Raghavachari, A. Rendell, J. C. Burant, S. S. Iyengar, J. Tomasi, M. Cossi, N. Rega, J. M. Millam, M. Klene, J. E. Knox, J. B. Cross, V. Bakken, C. Adamo, J. Jaramillo, R. Gomperts, R. E. Stratmann, O. Yazyev, A. J. Austin, R. Cammi, C. Pomelli, J. W. Ochterski, R. L. Martin, K. Morokuma, V. G. Zakrzewski, G. A. Voth, P. Salvador, J. J. Dannenberg, S. Dapprich, A. D. Daniels, O. Farkas, J. B. Foresman, J. V. Ortiz, J. Cioslowski, D. J. Fox *Gaussian 09*, revision A.02, Gaussian, Inc., Wallingford CT, **2009**.

Received: September 19, 2013

Published Online: November 21, 2013

9.8 Anchor-Functionalized Push-Pull-Substituted Bis(tridentate) Ruthenium(II) Polypyridine Chromophores: Photostability and Evaluation as Photosensitizers

A. Breivogel, S. Wooh, J. Dietrich, T. Y. Kim, Y. S. Kang, K. Char, K. Heinze, *Eur. J. Inorg. Chem.* **2014**, 2720–2734.

DOI: 10.1002/ejic.201402091

Reprinted with permission from John Wiley and Sons, Copyright © 2014.

DOI:10.1002/ejic.201402091

Anchor-Functionalized Push-Pull-Substituted Bis(tridentate) Ruthenium(II) Polypyridine Chromophores: Photostability and Evaluation as Photosensitizers

Aaron Breivogel,^[a] Sanghyuk Wooh,^[b] Jan Dietrich,^[a] Tea Yon Kim,^[c] Yong Soo Kang,^[c] Kookheon Char,^[b] and Katja Heinze^{*[a]}

Keywords: Ruthenium / Tridentate ligands / Sensitizers / Photochemistry / N ligands

Stable push-pull substituted heteroleptic bis(tridentate) ruthenium(II) polypyridine complexes with COOH or 2,2'-bipyridine anchor groups have been prepared and characterized by ¹H, ¹³C and ¹⁵N NMR 1D and 2D spectroscopy, infrared spectroscopy, elemental analysis, high-resolution ESI mass spectrometry, electrochemistry, UV/Vis absorption spectroscopy, luminescence spectroscopy, and density functional calculations. The complexes feature a pronounced electronic directionality and high absorption wavelengths up to $\lambda_{\text{max}} = 544$ nm extending to 720 nm as a result of favorable push-pull substitutions. A remarkable photostability in the presence of water and coordinating ions (I⁻) was discovered for the tridentate complexes when compared with the standard

ruthenium sensitizer N719 and tris(bidentate) [Ru(bpy)₃](PF₆)₂, which are highly photolabile under the same conditions (photodissociation/photosubstitution). The complexes were studied as photosensitizers in dye-sensitized solar cells. The incident photon-to-current conversion efficiency follows the absorption spectra into the NIR region. However, the high positive charge of the complexes (2+) favors the recombination of the injected electrons with I₃⁻ of the redox electrolyte, which is evidenced by high dark currents and short electron recombination lifetimes, leading to low cell performances compared with cells with the negatively charged N719 dye.

Introduction

Dye-sensitized solar cells (DSSCs) were introduced in 1991 by O'Regan and Grätzel^[1] and provide a promising class of light-to-energy conversion systems.^[2–8] In a typical DSSC, molecular dyes are adsorbed onto a nanoporous inorganic semiconductor electrode (e.g., TiO₂, ZnO). After being excited by light, the dyes inject electrons into the conduction band of the semiconductor. A redox electrolyte (typically I⁻/I₃⁻) regenerates the dye and diffuses to the counter electrolyte where positive charges are collected. DSSCs are an attractive alternative to conventional silicon-based solar cells due to low-cost of fabrication and the pos-

sibility to finely tune the sensitizers, cell morphologies, and redox mediators.^[2–8] Currently, the highest power conversion efficiency amounts to $\eta = 12.3\%$ under full air mass 1.5 (AM 1.5) solar light using a designed zinc porphyrin as sensitizer in concert with an organic dye as cosensitizer.^[9] Polypyridine complexes of ruthenium(II) have emerged as a prominent class of sensitizers for DSSCs due to their useful photophysical properties,^[10] high cell efficiencies, and long-term stabilities.^[2–8] Well-known standard ruthenium(II) sensitizers for DSSCs are N719 (Bu₄N)₂[Ru(Hdcbpy)₂-(NCS)₂]^[11,12] and the so-called black dye (Bu₄N)₃[Ru(Htctpy)(NCS)₃]^[13] reaching solar cell efficiencies of $\eta = 10–11\%$ under full AM 1.5 (dcbpy = 4,4'-dicarboxy-2,2'-bipyridine, tctpy = 4,4',4''-tricarboxy-2,2';6',2''-terpyridine). However, the presence of monodentate ligands in these complexes is a key detrimental factor reducing the long-term stability in DSSCs. Monodentate ligands, such as NCS⁻ and pyridine, support thermal- and photo-induced isomerization and ligand-exchange reactions, leading to dye species with lower cell efficiencies.^[14–21] The replacement of monodentate ligands in DSSCs is realized in complexes with tris(bidentate) and bis(tridentate) coordination and offers a better opportunity for tuning the sensitizer properties.^[5,22] The two NCS⁻ ligands of N719 can be replaced by one bidentate cyclometalated 2-phenylpyridine ligand, reaching DSSC efficiencies of $\eta = 10.1\%$.^[5,20,23] In another

- [a] Institute of Inorganic Chemistry and Analytical Chemistry, Johannes Gutenberg University of Mainz, Duesbergweg 10–14, 55128 Mainz, Germany
E-mail: katja.heinze@uni-mainz.de
<http://www.ak-heinze.chemie.uni-mainz.de/>
- [b] The National Creative Research Initiative Center for Intelligent Hybrids, The WCU Program on Chemical Convergence for Energy and Environment, School of Chemical and Biological Engineering, Seoul National University, 1 Gwanak-ro, Gwanak-gu, Seoul 151-744, Korea
- [c] The WCU Department of Energy Engineering and Center for Next Generation Dye-Sensitized Solar Cells, Hanyang University, 222 Wangsimni-ro, Seongdong-gu, Seoul 133-791, Korea
- Supporting information for this article is available on the WWW under <http://dx.doi.org/10.1002/ejic.201402091>.

strategy, a NCS[−]-free complex with bidentate 2-pyridylpyrazole ligands achieves an efficiency of $\eta = 9.5\%$ in a DSSC.^[4,24] However, even ruthenium complexes with bidentate ligands such as 4,4'-bi-1,2,3-triazolate suffer from photoinduced ligand loss or photoisomerization.^[25,26] Ligand loss is also known for [Ru(bpy)₃]²⁺ in light-emitting electrochemical cells, leading to degradation products such as [Ru(bpy)₂(H₂O)₂]²⁺ and the oxido-bridged ruthenium(III) dimer [(Ru(bpy)₂(H₂O)₂)(μ-O)]⁴⁺.^[27–30] Moreover, tris(bidentate) complexes are chiral, thus diastereomers can be formed in the case of unsymmetrically substituted ligands, leading to complex synthetic procedures.^[3,31,32] The presence of stereoisomers can be circumvented with bis(tridentate) complexes such as [Ru(tpy)₂]²⁺, which are achiral, even when the ligands are functionalized unsymmetrically in the 4'-positions (tpy = 2,2',6',2''-terpyridine).^[33] Tridentate chelate complexes are expected to feature higher photo- and chemical-stability compared with bidentate chelates.^[34,35] The drawback of [Ru(tpy)₂]²⁺ is its fast excited state deactivation via ³MC states with a time constant of $\tau = 0.1–0.2$ ns,^[36–38] thus competing with electron injection into semiconductor electrodes (MC = metal-centered).^[39,40] The detrimental effect of radiationless deactivation via ³MC states can be avoided by substitution at the 4'-positions of tpy. In 4'-substituted [(EtOOC-tpy)Ru(tpy)]²⁺, the electron-withdrawing ester group stabilizes the ³MLCT state with respect to the ³MC state, thus radiationless deactivation via the latter state is hampered (MLCT = metal-to-ligand charge transfer).^[41,42] This is reflected by the enhanced excited state lifetime of $\tau = 32$ ns, which is sufficiently long for quantitative charge injection into TiO₂.^[39,40] The ester group also reduces the HOMO–LUMO gap because it effectively reduces the LUMO energy. This is beneficial due to the redshift of the absorption maximum ($\lambda = 485$ nm) compared with [Ru(tpy)₂]²⁺ ($\lambda = 476$ nm), thus enabling the harvest of lower energy photons.^[38,42] The carboxylic acid analogue [(HOOC-tpy)Ru(tpy)]²⁺ has been incorporated into DSSCs. Efficiencies were not reported, but the incident photon-to-current conversion efficiency (IPCE) shows a maximum of 35% at $\lambda = 500$ nm.^[43] The phosphonic acid derivative [(H₂O₃P-tpy)Ru(tpy)]²⁺ reaches only a low DSSC efficiency of $\eta = 0.17\%$, which has been attributed to the low injection yield.^[44] Push-pull substituted [(HOOC-tpy)Ru(tpy-NH₂)]²⁺ (**[4]**(PF₆)₂, Figure 1) features both an electron-withdrawing and an electron-donating moiety. The excited state lifetime is further enhanced ($\tau = 34$ ns) and the absorption is redshifted ($\lambda = 502$ nm) because the electron-donating NH₂ group destabilizes both the HOMO and the ³MC state.^[41,45–47] Asymmetric substitution with a carboxylic acid and an amino group offers the possibility for orthogonal functionalization. Bis(tridentate) ruthenium(II) complexes have been used in donor-acceptor arrays with photoinduced charge-separated states.^[48] Complex **[4]**-(PF₆)₂ has been covalently linked to ferrocene, Pt^{II} and Re^I complexes, which show photoinduced electron transfer.^[45,49,50] Light-induced charge separation has been achieved by using **[4]**(PF₆)₂ as a chromophore in a donor-

chromophore-acceptor nanocomposite with triphenylamine as donor and ZnO nanorods as acceptor.^[51] The push-pull character of **[4]**(PF₆)₂ can be further intensified by the inclusion of additional electron-withdrawing groups on the acceptor ligand as well as electron-donating groups on the donor ligand. This has been shown by our group employing a tpy acceptor ligand containing one or three ester groups and a ddpd donor ligand featuring two or three amine functionalities (ddpd = *N,N'*-dimethyl-*N,N'*-dipyridin-2-ylpyridine-2,6-diamine). The absorption is redshifted up to $\lambda = 546$ nm, while maintaining excited state lifetimes of $\tau > 100$ ns in spite of increased radiationless deactivation due to the energy gap law.^[41,52–54] In these dyes, a directional electron transfer is enforced by spatially separated and orthogonal frontier orbitals.^[41,55]

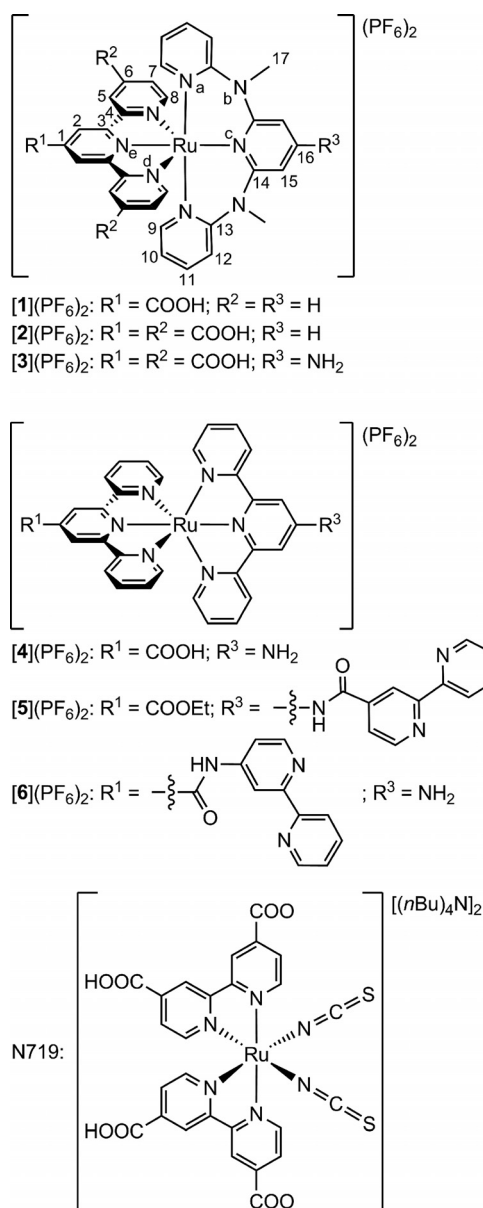


Figure 1. Bis(tridentate) ruthenium(II) oligopyridine complexes **[1]**(PF₆)₂ – **[6]**(PF₆)₂ and reference dye N719. Atom numbering for NMR assignments.

Cyclometalation is another striking tool that can be used to create a push-pull situation in ruthenium(II) complexes and to shift the absorption further into the red spectral region. Spatially separated frontier orbitals are obtained when the cyclometalated functionality is situated face to face with the anchoring ligand with the HOMO located on the cyclometalated ligand and the metal center while the LUMO is located on the anchoring ligand.^[56] The donor–acceptor motive was also realized by Berlinguette et al. in a bis(tridentate) ruthenium(II) complex with tctpy as acceptor ligand and a cyclometalating pbpy ligand with a tri-arylamine substituent (pbpy = 6-phenyl-2,2'-bipyridine). After the injection of an electron into TiO₂, the positive charge is shifted away from the TiO₂ surface towards the appended triarylamine moiety, thus avoiding charge recombination and reaching a DSSC efficiency of $\eta = 8.0\%$.^[57] Recently, bis(tridentate) ruthenium(II) complexes with a dianionic donor ligand [2,6-bis(5-pyrazolyl)pyridine] and tctpy acceptor ligand have been presented in DSSCs with efficiencies up to $\eta = 10.7\%$.^[58,59] The use of ruthenium(II) complexes with two tridentate ligands has a favorable effect on the long-term stability of DSSCs.^[4,60,61]

In this work, we present the synthesis of three novel, push-pull substituted bis(tridentate) ruthenium(II) complexes [1](PF₆)₂ – [3](PF₆)₂ together with three previously reported, push-pull-substituted bis(tridentate) complexes [4](PF₆)₂ – [6](PF₆)₂ and their performance in DSSCs in comparison with the standard ruthenium(II) sensitizer N719 (Figure 1).^[45,49,50,62] Binding to TiO₂ occurs through carboxylic acid/carboxylate groups {[1](PF₆)₂ – [4](PF₆)₂, N719} and for the first time complexes with bidentate 2,2'-bpy as anchor {[5](PF₆)₂, [6](PF₆)₂} were used in DSSCs. Dicarboxylic acid^[63] and bidentate acetylacetonato^[64,65] or catecholato^[39,66,67] anchors have been employed previously. Bidentate bpy anchors might be favored compared with monodentate pyridine anchors because dye desorption from the semiconductor is a critical issue for the long-term stability of DSSCs.^[68] The photostability under irradiation ($\lambda_{\text{exc}} = 400$ and 500 nm) of ethyl esters [1^{Et}](PF₆)₂ and [4^{Et}](PF₆)₂ was studied and compared to that of [Ru(bpy)₃](PF₆)₂ and N719. In addition, the stability of the ruthenium(III) complexes [1^{Et}]³⁺, [4^{Et}]³⁺, [Ru(bpy)₃]³⁺, and oxidized N719 was investigated by spectroelectrochemical measurements.

Results and Discussion

Synthesis and Analytical Characterization

The ester analogues of complexes [1](PF₆)₂ – [3](PF₆)₂ as well as complexes [4](PF₆)₂ – [6](PF₆)₂ have been reported previously.^[41,45,49,50,55] Complexes [1](PF₆)₂ and [2](PF₆)₂ have been synthesized by hydrolysis of their respective ester derivatives with sulfuric acid.^[41,55] [3](PF₆)₂ has been obtained in a microwave-assisted reaction of [(MeOOC)₃-tpy]-RuCl₃^[13,69–71] and ddpd-4'-phthalimide^[41] in methanol with *N*-ethylmorpholine as reducing agent. Subsequently, the ester groups and the phthalimide protecting group were hy-

drolyzed in a single step by acidic treatment. Finally, [1](PF₆)₂ – [3](PF₆)₂ were precipitated by addition of [NH₄](PF₆) and obtained as (PF₆)[−] salts. Complexes [1](PF₆)₂ – [3](PF₆)₂ were characterized by ESI and HR-ESI mass spectrometry, infrared, ¹H, ¹³C and ¹⁵N NMR 1D and 2D spectroscopy, and by elemental analysis. The ion peaks for [M – PF₆]⁺ and [M – 2PF₆]²⁺ were found in the ESI mass spectra of [1](PF₆)₂ – [3](PF₆)₂ with *m/z* values and isotope distributions being in excellent accord with theoretical values. Additionally, HRMS (ESI) clearly confirmed the molecular formulae of all complex cations (see Experimental Section). ¹H, ¹³C and ¹⁵N NMR spectroscopic data of [1](PF₆)₂ – [3](PF₆)₂ corroborate that the structural integrity remained intact during the harsh synthetic conditions (reflux, acidic medium) by showing only a single stereoisomer (*meridional*), similar to their ester derivatives (Tables S1–S3 in the Supporting Information; see Figure 1 for atom assignment).^[41,55] NMR spectra of [1](PF₆)₂ – [3](PF₆)₂ do not differ significantly from the spectra of their respective ester derivatives,^[41,55] with the exception that the resonances for the alkyl ester groups were not present. The resonances of all pyridine protons of [1](PF₆)₂ – [3](PF₆)₂ appear in the expected range between $\delta = 6.2$ and 9.2 ppm. The highest chemical shift originates from H-2 ($\delta = 8.99$ –9.15 ppm), due to the electron-withdrawing COOH moiety at the central pyridine of the tpy ligand. The addition of two carboxylic acid groups {[1](PF₆)₂ → [2](PF₆)₂} strengthens the electron-accepting character of the tpy ligand, which is reflected in the down-field shift of H-5 and H-7 by about 0.4 ppm. The protons of the NCH₃ group of the ddpd ligand appear as a singlet at $\delta = 3.4$ –3.5 ppm. The amino protons of [3](PF₆)₂ resonate at $\delta = 5.75$ ppm. The electron-donating character of the NH₂ group is clearly seen in the high-field shift of the H-15 resonance for [3](PF₆)₂ ($\delta = 6.81$ ppm) compared with [2](PF₆)₂ ($\delta = 7.58$ ppm).^[72] For [1](PF₆)₂ – [3](PF₆)₂ an interligand nuclear Overhauser effect is observed between proton H-8 of the tpy ligand and the NCH₃ protons of the ddpd ligand, supporting the twisted *meridional* coordination of the ddpd ligand, with the two NCH₃ groups lying above and below the plane of the tpy ligand.^[41,55] ¹³C{¹H} NMR spectra of [1](PF₆)₂ – [3](PF₆)₂ show resonances for all carbon atoms, including quaternary carbon atoms. All carbon atoms were assigned unambiguously on the basis of 2D NMR correlation spectroscopic methods (HMQC, HMBC) and appear with expected chemical shifts (Table S2 in the Supporting Information). Again, the electron-donating effect of the NH₂ group of [3](PF₆)₂ is revealed when comparing the chemical shifts of C-15 ($\delta = 113.7$ ([2](PF₆)₂) → 98.8 ppm ([3](PF₆)₂)). ¹⁵N NMR chemical shifts of [1](PF₆)₂ – [3](PF₆)₂ were recorded with ¹⁵N-¹H HMBC spectroscopy and also underline the electron-withdrawing effect of two additional COOH groups ($\delta(\text{N}^{\text{d}}) = 238.3$ ([1](PF₆)₂) → 249.5 ppm ([2](PF₆)₂)) and the electron-donating character of the NH₂ group ($\delta(\text{N}^{\text{c}}) = 216.3$ ([2](PF₆)₂) → 181.6 ppm ([3](PF₆)₂)). IR spectra of [1](PF₆)₂ – [3](PF₆)₂ in CsI disks were recorded, and these feature characteristic bands of the functional groups and

counterions. Broad bands at $\tilde{\nu} = 3440\text{--}3443\text{ cm}^{-1}$ arise from OH stretching vibrations. Absorption bands at $\tilde{\nu} = 1713\text{--}1728\text{ cm}^{-1}$ are assigned to C=O stretching vibrations, and very strong bands at $\tilde{\nu} = 839\text{--}843\text{ cm}^{-1}$ are caused by PF stretching vibrations of the $(\text{PF}_6)^-$ counterions.

Electrochemical Properties of $[1](\text{PF}_6)_2$ – $[3](\text{PF}_6)_2$

Cyclic and square wave voltammetry in CH_3CN and $[n\text{Bu}_4\text{N}](\text{PF}_6)$ as supporting electrolyte have been performed for complexes $[1](\text{PF}_6)_2$ – $[3](\text{PF}_6)_2$ (Figures S1–S3 in the Supporting Information). The FcH/FcH^+ redox couple was used as internal reference. Electrochemical data of $[1](\text{PF}_6)_2$ – $[6](\text{PF}_6)_2$ and N719 are summarized in Table 1. The one-electron oxidation of $[1](\text{PF}_6)_2$ – $[3](\text{PF}_6)_2$ is reversible and occurs at $E_{1/2} = 0.81, 0.87$, and 0.71 V , respectively, which essentially matches the oxidation potentials of the corresponding ester counterparts.^[41] The oxidation is assigned to the $\text{Ru}^{\text{II}}/\text{Ru}^{\text{III}}$ redox couple.^[41,55] Spin density plots of the DFT optimized one-electron oxidized complexes corroborate the ruthenium-centered oxidation (Figure 2). $[1](\text{PF}_6)_2$ ($E_{1/2} = 0.81\text{ V}$) is more easily oxidized than $[2](\text{PF}_6)_2$ ($E_{1/2} = 0.87\text{ V}$) due to the two additional electron-withdrawing COOH groups of the latter. $[3](\text{PF}_6)_2$ ($E_{1/2} = 0.71\text{ V}$) is more easily oxidized than $[2](\text{PF}_6)_2$ ($E_{1/2} = 0.87\text{ V}$) due to the electron-donating NH_2 group of $[3](\text{PF}_6)_2$. In $[3]^{3+}$, a small amount of spin density is also located on the NH_2 group, similar to complexes $[4]^{3+}$ and $[6]^{3+}$, with Mulliken spin densities on the amino nitrogen atom of 0.07, 0.11, and 0.12, respectively (Figure 2).^[45,55] Reduction of $[1](\text{PF}_6)_2$ – $[3](\text{PF}_6)_2$ is irreversible and initially occurs at $E_p = -1.50, -1.37$, and -1.53 V , respectively, and is confined to the acid-substituted tpy ligand, which is illustrated by spin density plots of the one-electron reduced species $[1]^+$, $[2]^+$, and $[3]^+$ (Figure S4 in the Supporting Information).^[41] Because the ester derivatives of $[1](\text{PF}_6)_2$ – $[3](\text{PF}_6)_2$ show reversible reductions, the irreversibility is associated with the COOH group.^[41,55] The reduced radical ligand $(\text{tpy-COOH})^-$ has a higher proton affinity compared with tpy-COOH . This might lead to the protonation reaction $(\text{tpy-COOH})^- + \text{H}^+ \rightarrow [\text{tpy-C}(\text{OH})_2]^-$ and explains the irreversibility of the reduction in complexes $[1](\text{PF}_6)_2$ – $[3](\text{PF}_6)_2$. Reductive H_2 evolution, as in the reaction $\text{R-COOH} + \text{e}^- \rightarrow \text{R-COO}^- + 1/2 \text{H}_2$, has also been reported

to be responsible for the irreversible reduction of carboxylic acids attached to bpy.^[73] Complex $[2](\text{PF}_6)_2$ is more easily reduced than $[1](\text{PF}_6)_2$ due to the additional electron-withdrawing COOH groups of the former. $[3](\text{PF}_6)_2$ is reduced at lower potential than $[2](\text{PF}_6)_2$ due to presence of the electron-donating NH_2 group.^[41]

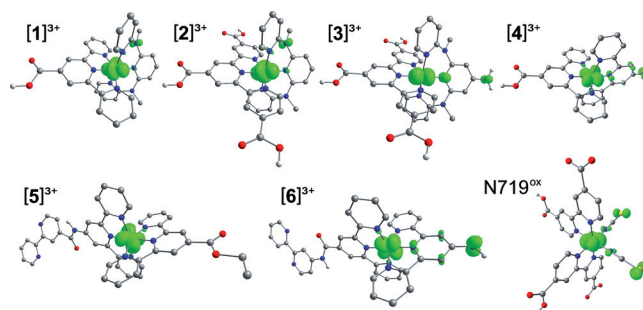


Figure 2. Spin densities of ruthenium(III) complexes $[1]^{3+}$ – $[6]^{3+}$ and one-electron oxidized N719 (contour value 0.005 a. u.; CH hydrogen atoms omitted).

Optical Properties of $[1](\text{PF}_6)_2$ – $[3](\text{PF}_6)_2$

Figure 3 depicts experimental UV/Vis spectra of $[1](\text{PF}_6)_2$ – $[3](\text{PF}_6)_2$ in CH_3CN . The data are summarized together with complexes $[4](\text{PF}_6)_2$ – $[6](\text{PF}_6)_2$ and N719 in Table 2. Intense bands at $\lambda < 400\text{ nm}$ are assigned to $\pi \rightarrow \pi^*$ transitions of the ligands. The bands in the visible spectral range are predominantly of MLCT parentage. $[1](\text{PF}_6)_2$ features its MLCT band maximum at $\lambda = 517\text{ nm}$ ($\epsilon = 8110\text{ M}^{-1}\text{ cm}^{-1}$) with a high-energy shoulder at $\lambda = 472\text{ nm}$ and two low-energy shoulders at $\lambda = 583$ and 635 nm . The spectrum of $[2](\text{PF}_6)_2$ shows two maxima at $\lambda = 537$ ($\epsilon = 6600\text{ M}^{-1}\text{ cm}^{-1}$) and 473 nm ($\epsilon = 5820\text{ M}^{-1}\text{ cm}^{-1}$) and two shoulders at $\lambda = 608$ and 661 nm . A distinct redshift compared with $[1](\text{PF}_6)_2$ can be noticed. This is due to the smaller HOMO–LUMO energy gap in the case of $[2](\text{PF}_6)_2$ caused by the additional COOH groups lowering the LUMO energy by a greater extent than the HOMO energy

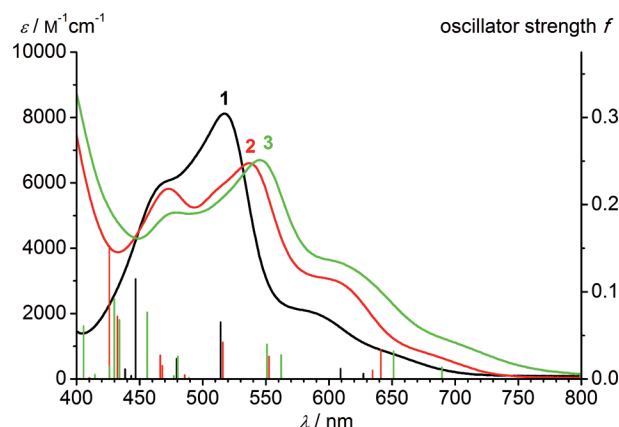


Figure 3. Experimental UV/Vis spectra in CH_3CN and calculated stick spectra (TD-DFT, B3LYP/LANL2DZ, IEFPCM in CH_3CN) of $[1]^{2+}$ – $[3]^{2+}$.

Table 1. Electrochemical data of complexes $[1](\text{PF}_6)_2$ – $[6](\text{PF}_6)_2$ and reference compound N719 in CH_3CN ($E_{1/2}$ given in V vs. FcH/FcH^+).

	$E_{1/2}$ ($\text{Ru}^{\text{II}}/\text{Ru}^{\text{III}}$)	$E_{1/2}$ (tpy/tpy^-)
$[1](\text{PF}_6)_2$	+0.810	–1.500 ^[a]
$[2](\text{PF}_6)_2$	+0.870	–1.370 ^[a]
$[3](\text{PF}_6)_2$	+0.710	–1.530 ^[a]
$[4](\text{PF}_6)_2$ ^[45]	+0.680	–1.540 ^[a]
$[5](\text{PF}_6)_2$ ^[49]	+0.915	–1.565
$[6](\text{PF}_6)_2$ ^[50]	+0.680	–1.505
N719 ^{[12][b]}	+0.500	–1.790

[a] Irreversible, E_p given. [b] In DMF.

([1]²⁺ → [2]²⁺: $\Delta E_{\text{LUMO}} = 0.30$; $\Delta E_{\text{HOMO}} = 0.19$ eV by DFT; Figure 4). For [3](PF₆)₂, the HOMO–LUMO gap is further

Table 2. UV/Vis data of complexes [1](PF₆)₂ – [6](PF₆)₂ and reference compound N719 in CH₃CN and TD-DFT data (B3LYP/LANL2DZ, IEFPCM in CH₃CN).

	Experimental $\pi \rightarrow \pi^*$ λ_{max} [nm] (ϵ [M ⁻¹ cm ⁻¹])	MLCT λ_{max} [nm] (ϵ [M ⁻¹ cm ⁻¹])	DFT ^[a] λ [nm] (f)
[1](PF ₆) ₂	319 (31200), 279 (37600), 221 (37500)	635 (970, sh), 583 (2080, sh), 517 (8110), 472 (6060, sh)	627.28 (0.0064), 609.06 (0.0119), 514.10 (0.0653), 479.27 (0.0233), 446.70 (0.1147), 438.60 (0.0114)
[2](PF ₆) ₂	340 (34400), 291 (37100), 211 (55300)	661 (1010, sh), 608 (2960, sh), 537 (6600), 473 (5820)	641.06 (0.0337), 634.53 (0.0100), 552.49 (0.0261), 515.85 (0.0423), 467.83 (0.0155), 466.40 (0.0273), 432.33 (0.0718), 425.85 (0.1511)
[3](PF ₆) ₂	340 (30400), 292 (34400), 217 (59900)	680 (1400, sh), 610 (3540, sh), 544 (6690), 480 (5090)	689.49 (0.0137), 651.28 (0.0319), 562.06 (0.0276), 550.87 (0.0400), 480.21 (0.0260), 455.99 (0.0768), 433.95 (0.0681), 426.03 (0.0142), 405.47 (0.0608)
[4](PF ₆) ₂ ^[45]	318 (41100), 306 (38000), 274 (55700), 236 (46700)	570 (1900, sh), 501 (20700), 467 (14400, sh)	585.50 (0.0053), 486.60 (0.1460), 451.84 (0.0719), 443.55 (0.0837), 439.16 (0.0402), 431.24 (0.1507)
[5](PF ₆) ₂ ^[49]	305 (56800), 276 (77800)	493 (24400)	555.74 (0.0059), 490.41 (0.0137), 475.62 (0.2638), 452.00 (0.0416), 432.90 (0.0382), 430.92 (0.2257), 427.40 (0.0372)
[6](PF ₆) ₂ ^[50]	313 (43900, sh), 278 (63900)	502 (23000)	562.43 (0.0079), 485.06 (0.1427), 457.57 (0.0134), 456.09 (0.0963), 448.27 (0.0421), 446.75 (0.0828), 435.76 (0.1837)
N719 ^[11]	312 (49100) ^[b]	535 (14700) ^[b] , 395 (14300) ^[b]	682.20 (0.0586), 653.33 (0.0131), 591.98 (0.1223), 541.43 (0.0857), 473.58 (0.0312), 455.74 (0.0595), 449.54 (0.0443), 440.46 (0.0180), 435.66 (0.0298), 433.88 (0.0260), 414.86 (0.0149), 408.02 (0.0087)

[a] Highest calculated oscillator strengths f at $\lambda > 400$ nm (TD-DFT, B3LYP/LANL2DZ, IEFPCM in CH₃CN). For a complete list see the Supporting Information. [b] In ethanol.

reduced because the addition of the electron-donating NH₂ group raises the HOMO energy more than the LUMO energy ([2]²⁺ → [3]²⁺: $\Delta E_{\text{LUMO}} = 0.05$; $\Delta E_{\text{HOMO}} = 0.22$ eV by DFT; Figure 4). This can be seen in the electronic spectra because the absorption bands of [3](PF₆)₂ are further red-shifted compared with those of [2](PF₆)₂ (Table 2, Figure 3). Calculated stick spectra were obtained by time-dependent DFT calculations including solvent modeling (TD-DFT, B3LYP/LANL2DZ, IEFPCM in CH₃CN) and these appropriately reproduce the experimental spectra (Figure 3). For example, the bands and shoulders of the experimental spectrum of [3]²⁺ at $\lambda = 680, 610, 544$ and 480 nm appear as calculated transitions at $\lambda = 689.5$ ($f = 0.0137$), 651.3 ($f = 0.0319$), 562.1 ($f = 0.0319$)/ 550.9 ($f = 0.0400$) and 480.2 ($f = 0.0260$)/ 456.0 nm ($f = 0.0768$). Absorptions at $\lambda > 400$ nm arise predominantly from transitions from metal-centered “ t_{2g} ” orbitals (HOMO, HOMO–1 and HOMO–2) to tpy-based π^* orbitals (LUMO and LUMO+1). Relevant Kohn–Sham frontier molecular orbitals are depicted for [3]²⁺ in Figure 5. The unoccupied “ e_g ”

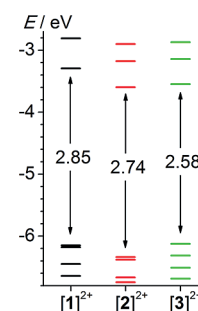


Figure 4. DFT (B3LYP/LANL2DZ, IEFPCM in CH₃CN) calculated frontier orbital energies of [1]²⁺ – [3]²⁺.

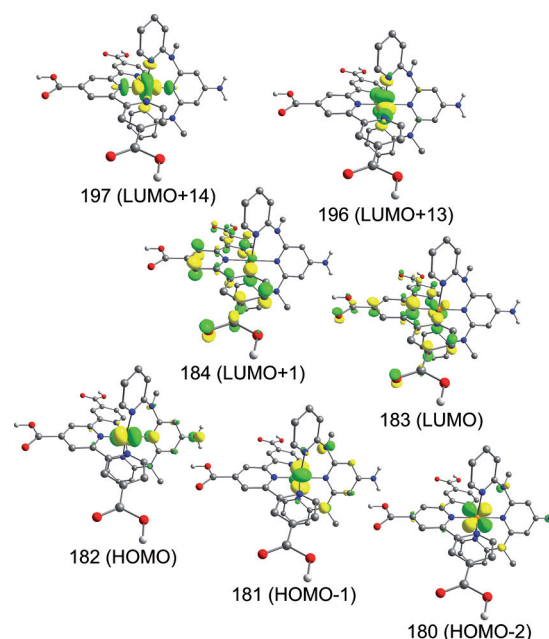


Figure 5. Relevant Kohn–Sham frontier molecular orbitals (contour value 0.06 a. u.) of [3]²⁺ (CH hydrogen atoms omitted).

orbitals of the d-manifold (LUMO+13 and LUMO+14) appear at higher energy.

In a more detailed analysis, we compare the frontier orbitals (HOMO–3 to LUMO+3) that are relevant for transitions at $\lambda > 400$ nm, as calculated by TD-DFT calculations for complexes $[1]^{2+}$ – $[6]^{2+}$ and N719 (Figures S5–S6 in the Supporting Information). HOMO, HOMO–1, and HOMO–2 of complexes $[1]^{2+}$ – $[6]^{2+}$ are located at the metal center, formally corresponding to “ t_{2g} ” orbitals. For complexes $[3]^{2+}$, $[4]^{2+}$, and $[6]^{2+}$, the p(N) orbitals of the NH_2 substituent also contribute to the HOMO.^[41,62] This is regarded as being beneficial for directional electron injection into solid semiconductors, e.g., TiO_2 .^[2–4] HOMO-3 of complexes $[1]^{2+}$ – $[4]^{2+}$ is situated at the remote amine donor ligand, which also favors directional electron injection into TiO_2 . Similarly, HOMO to HOMO–2 of N719 are metal-centered, but large contributions from the NCS^- ligands are present. HOMO-3 of N719 is even essentially NCS^- -based. LUMO to LUMO+3 of $[1]^{2+}$ – $[3]^{2+}$ and N719 are mainly located at the anchoring ligand and should therefore facilitate electron injection.^[2–4] In contrast, LUMO to LUMO+3 of $[4]^{2+}$ – $[6]^{2+}$ are distributed over both tpy ligands. In the case of $[5]^{2+}$, the LUMO is not even located on the anchor ligand as is the case for all other complexes (Figure S6). Thus, for complexes $[4]^{2+}$ – $[6]^{2+}$, the local separation of frontier orbitals is less pronounced and might retard efficient charge injection into TiO_2 .

The individual sum of oscillator strengths Σf at $\lambda > 400$ nm increases by attaching two COOH groups $\{\Sigma f = 0.2368 ([1]^{2+}) \rightarrow 0.3849 ([2]^{2+})\}$ as well as by attaching an amino group $\{\Sigma f = 0.3849 ([2]^{2+}) \rightarrow 0.4619 ([3]^{2+})\}$, which is a behavior similar to the ester derivatives and is due to the enlargement of the chromophoric system.^[41] The total experimental integrated intensity $\int I$ was calculated in the visible spectral range ($\lambda = 400$ –800 nm) on an energy scale (cm^{-1}) and increases in the same order $\{\int I = 3.77 \times 10^7 \text{ M}^{-1} \text{ cm}^{-2} ([1](\text{PF}_6)_2) \rightarrow 4.69 \times 10^7 \text{ M}^{-1} \text{ cm}^{-2} ([2](\text{PF}_6)_2) \rightarrow 5.16 \times 10^7 \text{ M}^{-1} \text{ cm}^{-2} ([3](\text{PF}_6)_2)\}$. This increased absorptivity favors photon collection over the entire spectral range.

DFT-calculated spin densities of the emissive $^3\text{MLCT}$ states of complexes $[1]^{2+}$ – $[6]^{2+}$ and N719^[12,74] are illustrated in Figure 6. For all complexes, the spin density is distributed over both the ruthenium atom and the carbonyl-substituted polypyridine ligand. For all complexes except

$[5]^{2+}$, spin density is transferred towards the anchor groups in the $^3\text{MLCT}$ state compared with the ground state. This is beneficial for efficient charge injection into semiconductors.^[2–4] For $[5]^{2+}$ however, the carbonyl-substituted terpyridine ligand is opposite to the bpy anchor group, which should be rather detrimental for charge injection (see below).^[4]

Figure 7 compares the experimental UV/Vis spectra of $[1](\text{PF}_6)_2$ – $[6](\text{PF}_6)_2$ and N719 in $\text{CH}_3\text{CN}/t\text{BuOH}$ (1:1) solution. $[2](\text{PF}_6)_2$ features a very similar absorption maximum to that of N719, with additional low energy shoulders at $\lambda = 661$ and 608 nm. The absorption maxima of $[3](\text{PF}_6)_2$ are even bathochromically shifted with respect to those of N719 (Table 2).

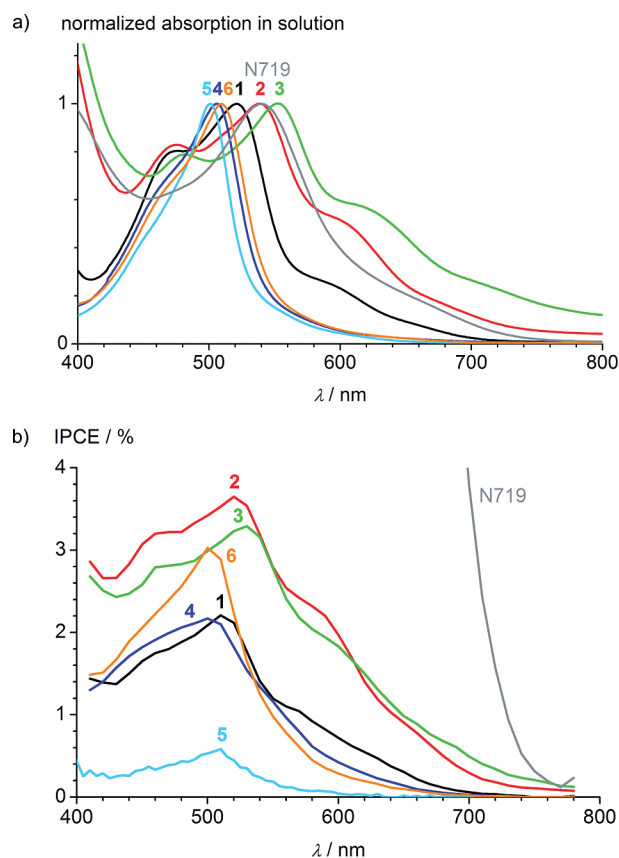


Figure 7. (a) Normalized experimental UV/Vis spectra of $[1](\text{PF}_6)_2$ – $[6](\text{PF}_6)_2$ and N719 in $\text{CH}_3\text{CN}/t\text{BuOH}$ (1:1); (b) IPCE of cells with $[1](\text{PF}_6)_2$ – $[6](\text{PF}_6)_2$ and N719.

Emission of $[1](\text{PF}_6)_2$ – $[3](\text{PF}_6)_2$ in CH_3CN at 295 K occurs at $\lambda = 732$, 743, and 771 nm, respectively. The redshift of the emission wavelength in the series $[1](\text{PF}_6)_2$, $[2](\text{PF}_6)_2$, $[3](\text{PF}_6)_2$ is due to the consecutive lowering of the HOMO–LUMO gap, as already discussed for absorption (see above, Figure 4). Emission quantum yields of $[1](\text{PF}_6)_2$ – $[3](\text{PF}_6)_2$ were measured in deaerated CH_3CN at 295 K. The quantum yield of $[3](\text{PF}_6)_2$ ($\Phi = 0.067\%$) is similar to its ester derivative ($\Phi = 0.052\%$).^[41] In contrast, the quantum yields of $[1](\text{PF}_6)_2$ ($\Phi = 0.068\%$) and $[2](\text{PF}_6)_2$ ($\Phi = 0.590\%$) are smaller by a factor of 2–7 compared with their ester derivatives,^[41,75] which is due to the presence of carboxylic acid

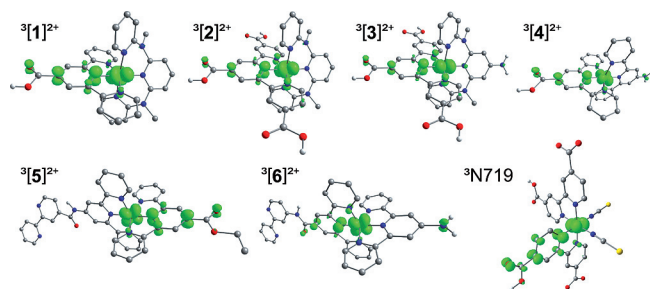


Figure 6. Spin densities of the $^3\text{MLCT}$ state of $[1]^{2+}$ – $[6]^{2+}$ and N719 (contour value 0.01 a. u.; CH hydrogen atoms omitted).

functionalities. Carboxylic acids are known to form hydrogen-bonding networks, and proton transfer along hydrogen bonds can be responsible for excited-state deactivation.^[76–80] Furthermore, excited-state deactivation can occur through high energy oscillators (O–H, N–H), typically leading to smaller quantum yields.^[41,45] For $[3](\text{PF}_6)_2$, we assume that efficient excited-state deactivation already occurs through N–H oscillators and clearly does not increase significantly by additional deactivation through the three extra O–H oscillators. This would explain the similar quantum yields of $[3](\text{PF}_6)_2$ and its ester derivative.^[41]

For example, the excited state $\text{p}K_{\text{a}}^*$ [$\text{p}K_{\text{a}}^* = \text{p}K_{\text{a}} + 0.625 \times T^{-1} \times (\tilde{\nu} - \tilde{\nu}')$] was calculated for complex $[1](\text{PF}_6)_2$ from the ground state $\text{p}K_{\text{a}}$ and the 0–0 transitions of $[1]^{2+}$ ($\tilde{\nu}/\text{cm}^{-1}$) and the deprotonated ($\tilde{\nu}/\text{cm}^{-1}$) form $[1-\text{H}]^+$.^[81] 0–0 transitions were estimated from the intersection points of the normalized absorption and emission spectrum, which were found at $\lambda = 659$ and 621 nm for $[1]^{2+}$ and $[1-\text{H}]^+$, respectively. The ground state $\text{p}K_{\text{a}}$ amounts to 2.3 and the excited state $\text{p}K_{\text{a}}^*$ to 4.3 ($T = 295$ K). A similar difference between $\text{p}K_{\text{a}}$ (3.0) and $\text{p}K_{\text{a}}^*$ (4.85) was found in $[\text{Ru}(\text{bpy})_2(\text{bpy}-4\text{-COOH})]^{2+}$.^[82] The lower acidity of the excited state compared to the ground state corroborates the metal-to-ligand charge transfer character of the excited state mentioned above.^[81]

Photostability Tests

Photostability tests were conducted to investigate possible ligand loss during DSSC operation. The ethyl ester derivatives $[1^{\text{Et}}](\text{PF}_6)_2$ and $[4^{\text{Et}}](\text{PF}_6)_2$ of carboxylic acids $[1](\text{PF}_6)_2$ and $[4](\text{PF}_6)_2$ as well as N719 and $[\text{Ru}(\text{bpy})_3](\text{PF}_6)_2$ were continuously irradiated under an Ar atmosphere in 0.1 M $[n\text{Bu}_4\text{N}]\text{I}$ in $\text{CH}_3\text{CN}/\text{H}_2\text{O}$ (98:2, v/v) at $\lambda_{\text{exc}} = 400$ and 500 nm. The solutions of $[1^{\text{Et}}](\text{PF}_6)_2$, $[4^{\text{Et}}](\text{PF}_6)_2$, N719, and $[\text{Ru}(\text{bpy})_3](\text{PF}_6)_2$ were isoabsorptive at the respective irradiation wavelength. The presence of water and potentially coordinating iodide simulates DSSCs conditions, with I^- being present in the liquid electrolyte and H_2O penetrating into the cell. The emission intensity of the complexes was measured over a period of at least 4 h and compared to the evolution of the emission intensity of N719 and $[\text{Ru}(\text{bpy})_3](\text{PF}_6)_2$ (Figure 8). In the absence of coordinating anions, $[\text{Ru}(\text{bpy})_3](\text{PF}_6)_2$ is photoinert.^[83,84] However, in the presence of coordinating anions such as Cl^- , Br^- , I^- , SCN^- , or NO_3^- , $[\text{Ru}(\text{bpy})_3]^{2+}$ readily undergoes photoinduced ligand substitution, photooxygenation (in the presence of O_2), and photoracemization.^[83–87] When irradiated at $\lambda_{\text{exc}} = 400$ nm, the normalized emission intensities of N719 and $[\text{Ru}(\text{bpy})_3](\text{PF}_6)_2$ drop within 4 h to 68 and 5% of the initial emission intensity, respectively (Figure 8, a). In contrast, for $[1^{\text{Et}}](\text{PF}_6)_2$ and $[4^{\text{Et}}](\text{PF}_6)_2$, more than 95% of the initial emission intensity is maintained after the same irradiation time under identical conditions. Irradiation at $\lambda_{\text{exc}} = 500$ nm shows similar results, with a drop in the initial emission intensity to 79 and 47% for N719 and $[\text{Ru}(\text{bpy})_3](\text{PF}_6)_2$, respectively, after 5 h (Figure 8, b). Under

the same conditions, $[1^{\text{Et}}](\text{PF}_6)_2$ and $[4^{\text{Et}}](\text{PF}_6)_2$ retain more than 97% of the initial emission intensity. The results clearly show that under the applied conditions bis(tridentate) complexes $[1^{\text{Et}}](\text{PF}_6)_2$ and $[4^{\text{Et}}](\text{PF}_6)_2$ are much more photostable than N719 and $[\text{Ru}(\text{bpy})_3](\text{PF}_6)_2$, which is a result of the tridentate coordination compared with mono- and bidentate modes.^[14–21,88]

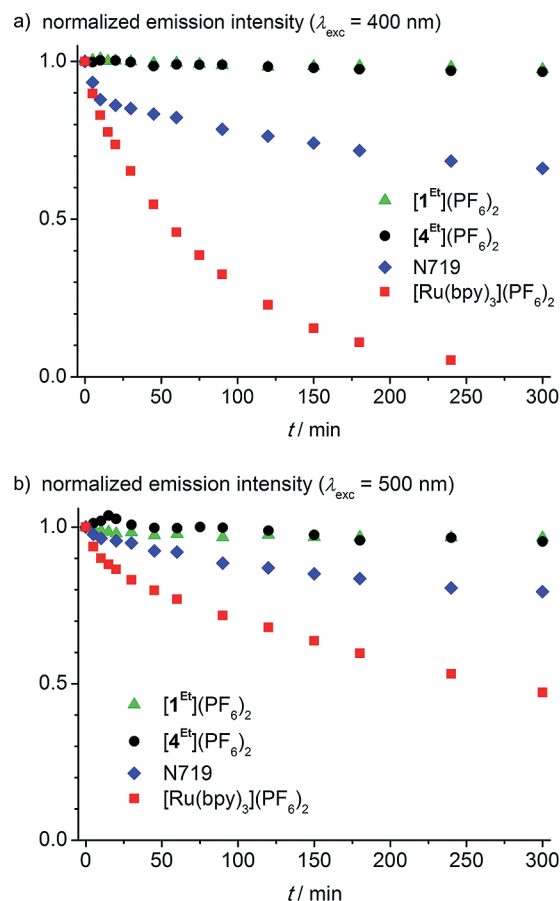


Figure 8. Normalized emission intensities of $[1^{\text{Et}}](\text{PF}_6)_2$, $[4^{\text{Et}}](\text{PF}_6)_2$, N719, and $[\text{Ru}(\text{bpy})_3](\text{PF}_6)_2$ in 0.1 M $[n\text{Bu}_4\text{N}]\text{I}$ in $\text{CH}_3\text{CN}/\text{H}_2\text{O}$ (98:2, v/v) under continuous irradiation at (a) $\lambda_{\text{exc}} = 400$ and (b) $\lambda_{\text{exc}} = 500$ nm.

Photodecomposition products of $[\text{Ru}(\text{bpy})_3]^{2+}$ were indeed detected when a solution of $[\text{Ru}(\text{bpy})_3](\text{PF}_6)_2$ (11 mM) was irradiated at $\lambda_{\text{exc}} = 400$ nm in the presence of $[n\text{Bu}_4\text{N}]\text{I}$ (2.2 equiv.) and trace amounts of H_2O . ^1H NMR spectra reveal resonances corresponding to the noncoordinated 2,2'-bipyridine ligand (Figure S7 in the Supporting Information). The ESI^+ mass spectrum after irradiation shows signals with characteristic ruthenium isotope patterns at $m/z = 559.0$ $[\text{Ru}(\text{bpy})_2(\text{H}_2\text{O})\text{I}]^+$, 541.0 $[\text{Ru}(\text{bpy})_2\text{I}]^+$, 467.1 $[\text{Ru}(\text{bpy})_2(\text{H}_2\text{O})_2(\text{OH})]^+$, and 449.1 $[\text{Ru}(\text{bpy})_2(\text{H}_2\text{O})(\text{OH})]^+$ in addition to intense signals for intact $[\text{Ru}(\text{bpy})_3]^{2+}$ (Figure S8 in the Supporting Information). Hence, one bpy ligand of $[\text{Ru}(\text{bpy})_3]^{2+}$ is efficiently photo-substituted by H_2O and/or I^- . The high photostability of ruthenium(II) complexes with bis(tridentate) coordination should thus be favorable in applications such as DSSCs and light-emitting devices.^[3,4,27–30,60,61]

Photodecomposition products of N719 could be detected when a solution of N719 (4.4 mM) was irradiated at $\lambda_{\text{exc}} = 400$ nm in the presence of $[n\text{Bu}_4\text{N}]\text{I}$ (4.5 equiv.) and H_2O . ^1H NMR spectra after irradiation show new signals with similar resonances ($\Delta\delta < 0.1$ ppm) to those obtained from N719 (Figure S9 in the Supporting Information). No signals from degradation compounds could be observed in FD, ESI⁺, or ESI[−] mass spectra. However, the small changes of the chemical shifts indicate that both dc bpy ligands remain coordinated and that NCS^- ligands are replaced by I^- or by H_2O .^[11] This is reasonable because NCS^- coordinates in a monodentate fashion and is substituted faster than the bidentate dc bpy ligand. Indeed, for N719 and related compounds, the photochemical and thermal substitution of both NCS^- by I^- and other monodentate ligands has previously been reported.^[17,19,20,89,90]

Redox Stability

The redox stability of sensitizers is an important issue in DSSCs because electron injection leads to ruthenium(III) complexes, which can be prone to ligand exchange reactions. The ethyl esters of $[\text{I}^{\text{Et}}]^{2+}$ and $[\text{4}^{\text{Et}}]^{2+}$ were oxidized and the stability of the oxidized species ($[\text{I}^{\text{Et}}]^{3+}$ and $[\text{4}^{\text{Et}}]^{3+}$) in the presence of coordinating OH^- ions was investigated by spectroelectrochemical measurements. Oxidized N719 and $[\text{Ru}(\text{bpy})_3]^{3+}$ were used for comparison. The ruthenium(II) complexes were oxidized to ruthenium(III) by gradually increasing the potential and then reduced back to the starting ruthenium(II) complexes by gradually lowering the potential. The reactions were monitored by following changes to the UV/Vis spectra. Figure 9 exemplarily shows that, upon oxidation of $[\text{4}^{\text{Et}}]^{2+}$ to $[\text{4}^{\text{Et}}]^{3+}$, the MLCT band disappears while a LMCT band at $\lambda = 729$ nm ($\epsilon = 5120 \text{ M}^{-1} \text{ cm}^{-1}$) appears.^[46] Isosbestic points at $\lambda = 581, 431, 340, 292, 283, 272$, and 241 nm reveal a clean conversion from $[\text{4}^{\text{Et}}]^{2+}$ into $[\text{4}^{\text{Et}}]^{3+}$.^[46] Upon lowering the potential, the spectra clearly show a clean reduction back to $[\text{4}^{\text{Et}}]^{2+}$ with the same isosbestic points as for the oxidation and a perfect overlap with the spectra of the initial ruthenium(II) complex could be achieved.

Experiments with $[\text{I}^{\text{Et}}](\text{PF}_6)_2$ and $[\text{Ru}(\text{bpy})_3](\text{PF}_6)_2$ show essentially the same spectral behavior upon oxidation and back reduction (Figures S10–S11 in the Supporting Information). LMCT bands for the oxidized complexes $[\text{I}^{\text{Et}}]^{3+}$, N719^{ox}, and $[\text{Ru}(\text{bpy})_3]^{3+}$ appear at $\lambda = 702$ (shoulder; $\epsilon = 770 \text{ M}^{-1} \text{ cm}^{-1}$), $\lambda = 662$ (shoulder; $\epsilon = 860 \text{ M}^{-1} \text{ cm}^{-1}$), and 662 nm ($\epsilon = 370 \text{ M}^{-1} \text{ cm}^{-1}$), respectively. The smaller LMCT band intensity of $[\text{I}^{\text{Et}}]^{3+}$, N719^{ox}, and $[\text{Ru}(\text{bpy})_3]^{3+}$ compared with NH_2 -substituted $[\text{4}^{\text{Et}}]^{3+}$ is due to the strong electron-donating character of the primary amino group of $[\text{4}^{\text{Et}}]^{3+}$. Isosbestic points for $[\text{I}^{\text{Et}}](\text{PF}_6)_2$ appear at $\lambda = 664, 423, 373, 352, 296, 285$, and 258 nm and for $[\text{Ru}(\text{bpy})_3](\text{PF}_6)_2$ at $\lambda = 573, 329, 298$, and 267 nm.

During the oxidation of N719, isosbestic points were observed at $\lambda = 316, 333$, and 550 nm (Figure S12a). However, during the back reduction, no isosbestic points were ob-

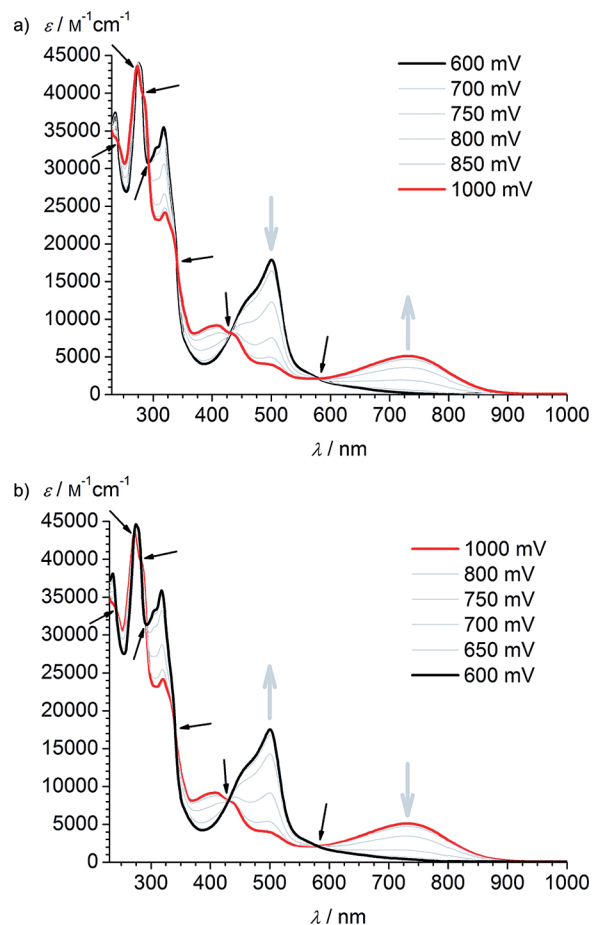


Figure 9. UV/Vis spectra of (a) the electrochemical oxidation ($E = 600 \rightarrow 1000$ mV) and (b) back reduction ($E = 1000 \rightarrow 600$ mV) of $[\text{4}^{\text{Et}}](\text{PF}_6)_2$ in an OTTE cell in 10^{-3} M NaOH and 0.1 M $[n\text{Bu}_4\text{N}](\text{PF}_6)$ in $\text{CH}_3\text{CN}/\text{H}_2\text{O}$ (98:2, v/v). Black arrows indicate isosbestic points.

served. The spectrum of N719 before oxidation ($E = 200$ mV, Figure S12 a) features maxima at $\lambda_{\text{max}} = 249$ ($\epsilon = 31810 \text{ M}^{-1} \text{ cm}^{-1}$), 308 ($\epsilon = 44640 \text{ M}^{-1} \text{ cm}^{-1}$), 374 ($\epsilon = 14090 \text{ M}^{-1} \text{ cm}^{-1}$), and 512 nm ($\epsilon = 12270 \text{ M}^{-1} \text{ cm}^{-1}$) whereas the spectrum after gradually increasing and then lowering the potential ($E = 200$ mV, Figure S12b) features maxima at $\lambda_{\text{max}} = 249$ ($\epsilon = 33190 \text{ M}^{-1} \text{ cm}^{-1}$), 307 ($\epsilon = 47040 \text{ M}^{-1} \text{ cm}^{-1}$), 372 ($\epsilon = 14700 \text{ M}^{-1} \text{ cm}^{-1}$), and 508 nm ($\epsilon = 12270 \text{ M}^{-1} \text{ cm}^{-1}$) indicating that the majority of N719 could be recovered and a small part of oxidized N719 underwent side reactions. Indeed the oxidation of the ester-protected analogue of N719 is irreversible, and desulfuration of the NCS^- ligands has been reported.^[90] In essence, $[\text{I}^{\text{Et}}]^{3+}$, $[\text{4}^{\text{Et}}]^{3+}$, and $[\text{Ru}(\text{bpy})_3]^{3+}$ are stable in the presence of coordinating OH^- . No hint of instability of the ruthenium(III) complexes could be found on the electrochemical time-scale under the applied conditions. In contrast, oxidized N719 is less stable and undergoes irreversible side reactions. Thus, compared with N719, our bis(tridentate) ruthenium(II) complexes feature a superior redox stability, which is important for applications such as DSSCs.^[2]

Device Testing

DSSCs were prepared with a FTO/TiO₂/dye/electrolyte/Pt/FTO structure. As redox electrolyte the I[−]/I₃[−] redox couple in CH₃CN was used. Ground state (¹GS) and excited state (³MLCT and ¹MLCT) energy levels of sensitizers [1](PF₆)₂ – [6](PF₆)₂ at *E* = −5.89, −4.20, −3.49 ([1](PF₆)₂), −5.95, −4.28, −3.64 ([2](PF₆)₂), −5.79, −4.18, −3.51 ([3](PF₆)₂), −5.74, −4.06, −3.26 ([4](PF₆)₂), −6.00, −4.15, −3.48 ([5](PF₆)₂), −5.58, −4.09, −3.26 eV ([6](PF₆)₂) and N719 at −5.58, −4.09, −3.26 eV are depicted together with the conduction band edge of TiO₂ (*E* = −3.94 eV) and the redox potential of the I[−]/I₃[−] redox couple (*E* = −5.24 eV), which is assumed to be responsible for dye regeneration in the I[−]/I₃[−] system (Figure 10).^[5,91] ¹GS energies were derived from experimental Ru^{II}/Ru^{III} redox potentials, ¹MLCT state energies were estimated from lowest energy absorption maxima in solution (Table 2) and ³MLCT state energies from the room temperature emission maxima in solution.^[11,45,49,50] ¹MLCT state energies are higher in energy than the TiO₂ conduction band edge by ΔE = 0.30–0.68 eV. Thus, injection of electrons into the TiO₂ conduction band is thermodynamically feasible from hot and thermally equilibrated ¹MLCT states for all tested dyes.^[39] Typically, electron injection occurs on the femto to picosecond timescale with high efficiency.^[39,40] In contrast, injection from thermally equilibrated ³MLCT states would be thermodynamically uphill for all dyes by ΔE = 0.13–0.34 eV. Injection rates from vibrationally hot ³MLCT states depend on the vibrational state and the relaxation rate to the vibrational ground state. Vibrational cooling in complexes of type [1](PF₆)₂ – [4](PF₆)₂ occurs on the timescale of several picoseconds.^[41] The ¹GS energies of all dyes is lower than the I[−]/I₂[−] redox potential by ΔE = 0.34–0.76 eV and therefore allows for the regeneration of oxidized dyes.

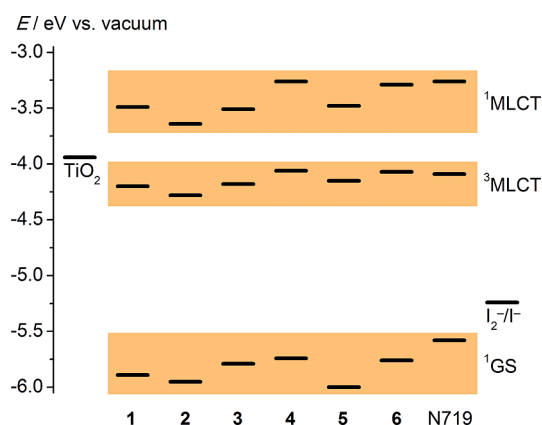


Figure 10. Energy levels of the ground state (¹GS) and excited states (¹MLCT and ³MLCT) of [1](PF₆)₂ – [6](PF₆)₂ and N719, the conduction band edge of TiO₂, and the I₂[−]/I[−] redox potential.

Dye loadings of [1](PF₆)₂ – [6](PF₆)₂ and N719 on TiO₂ were measured by the difference of absorption maxima of the dipping solution (CH₃CN/*t*BuOH, 1:1) before and after dipping of the TiO₂ electrodes. Whereas high dye loading was obtained for [1](PF₆)₂ – [4](PF₆)₂ and N719 (6–

11 × 10^{−8} mol cm^{−2}), the dye loading for [5](PF₆)₂ (1 × 10^{−8} mol cm^{−2}) and [6](PF₆)₂ (3 × 10^{−8} mol cm^{−2}) remained low (Table 3). This can be explained by the nature of the anchor group, which are 2,2′-bpy anchors for [5](PF₆)₂ and [6](PF₆)₂ and carboxylic acids and carboxylate anchors for [1](PF₆)₂ – [4](PF₆)₂ and N719. So far, only *para*-substituted pyridine anchors have been used for binding to TiO₂ and, to the best of our knowledge, this is the first example of a 2,2′-bpy anchor.^[92,93] The low dye loadings with our 2,2′-bpy anchor might have two reasons: One reason could be that both pyridines in 2,2′-bpy hinder each other sterically in binding to TiO₂ due to the 2,2′-constitution, resulting in low dye loadings for [5](PF₆)₂ and [6](PF₆)₂. A carboxylic acid/carboxylate anchor might be able to bind to TiO₂ surface atoms that are not sufficiently accessible for a 2,2′-bpy anchor. The dye loading of [6](PF₆)₂ is higher than of [5](PF₆)₂, which is due to the more electron-rich bpy moiety in [6](PF₆)₂ in which bpy is bound to the nitrogen atom of the amide functionality. In contrast, bpy is bound to the carbonyl carbon atom of the amide functionality in complex [5](PF₆)₂. The more electron-rich bpy of [6](PF₆)₂ might form stronger interactions to the electrophilic surface Ti ions of TiO₂. A second reason might be the larger area per molecule required for binding of [5](PF₆)₂ and [6](PF₆)₂ to the TiO₂ surface compared with [1](PF₆)₂ – [4](PF₆)₂ and N719, which is due to the canted orientation with respect to the surface. In addition, the 2,2′-bpy anchor has more steric bulk than a carboxylic acid/carboxylate anchor.

Table 3. Characteristics of the DSSCs with [1](PF₆)₂ – [6](PF₆)₂ and reference compound N719.

	Dye loading [mol cm ^{−2}]	<i>U</i> _{oc} [V]	<i>I</i> _{sc} [mA cm ^{−2}]	Fill factor [%]	η [%]	IPCE [%] (λ_{max} [nm])
[1](PF ₆) ₂	5.6 × 10 ^{−8}	0.41	0.50	63	0.13	2.2 (510)
[2](PF ₆) ₂	9.7 × 10 ^{−8}	0.49	0.75	70	0.26	3.6 (520)
[3](PF ₆) ₂	8.7 × 10 ^{−8}	0.45	0.74	67	0.22	3.3 (530)
[4](PF ₆) ₂	11.0 × 10 ^{−8}	0.49	0.48	62	0.15	2.2 (500)
[5](PF ₆) ₂	1.0 × 10 ^{−8}	0.44	0.24	61	0.06	0.5 (510)
[6](PF ₆) ₂	2.6 × 10 ^{−8}	0.46	0.59	61	0.18	3.0 (500)
N719	6.4 × 10 ^{−8}	0.76	9.30	71	5.03	51.6 (520)

IPCE were measured (Figure 7, b, Table 3) and these nicely follow the absorption spectrum of the respective dipping solution (Figure S13). The maximum IPCE of 3.7% was obtained for the cell with [2](PF₆)₂ at $\lambda \approx 520$ nm. For the cell with [3](PF₆)₂, the maximum IPCE (3.3%) is redshifted to $\lambda \approx 530$ nm, whereas for the cell with [1](PF₆)₂ it is blueshifted to $\lambda \approx 510$ nm. This is consistent with the tendency for λ_{max} in the solution absorption mentioned above: [3](PF₆)₂ > [2](PF₆)₂ > [1](PF₆)₂. The cell with [2](PF₆)₂ features higher IPCE and efficiency than the cell with [1](PF₆)₂ and [3](PF₆)₂. This can be ascribed to the higher dye loading (Table 3) in the case of [2](PF₆)₂ and the less intimate contact to TiO₂ in the case of [1](PF₆)₂ due to the presence of only one carboxylic acid anchor group.^[94] The IPCE maxima of cells with [4](PF₆)₂ (2.2%), [5](PF₆)₂ (0.6%), and [6](PF₆)₂ (3.0%) are at $\lambda \approx 500$ –510 nm, which is consistent with the respective absorption maxima in solu-

tion (Table 2). The reference cell with N719 features a maximum IPCE of 51.6% at $\lambda \approx 520$ nm. The maximum IPCE of the cell with $[5](PF_6)_2$ remains low (0.5% at 510 nm) due to the low dye loading (Table 3) and the poor electronic directionality of complex $[5](PF_6)_2$, as already discussed (Figure S6).

Current-voltage curves of DSSCs with $[1](PF_6)_2$ – $[6](PF_6)_2$ are depicted in Figure 11 and data are listed in Table 3. Open circuit voltages of cells with $[1](PF_6)_2$ – $[6](PF_6)_2$ reach values of $U_{oc} = 0.41$ – 0.49 V compared with $U_{oc} = 0.76$ V for the cell with N719. Short circuit currents are low for cells with $[1](PF_6)_2$ – $[6](PF_6)_2$ ($I_{sc} = 0.2$ – 0.8 mA cm⁻²) whereas the cell with N719 features a much higher value ($I_{sc} = 9.3$ mA cm⁻²). Fill factors amount to 61–71% for all cells, with the highest fill factor belonging to the one with N719. At the maximum power point, the cell with N719 has an efficiency of $\eta = 5.03$ %. Nazeeruddin, Angelis et al. have reported a maximum efficiency of 11.2% for the N719 dye, which is attributed to the optimized cell building procedure, including the addition of tetra-*n*-butylammonium chenodeoxycholic acid salt to the dipping solution.^[12] Efficiencies of cells with $[1](PF_6)_2$ – $[6](PF_6)_2$ are much lower ($\eta = 0.06$ – 0.26 %) than for the cell with N719 under the same conditions ($\eta = 5.03$ %), which is primarily due to the poor short circuit current in these cells. The low efficiency of the cell with $[5](PF_6)_2$ can further be attributed to the low dye loading (Table 3) as well as to the poor electronic directionality (Figure S6).

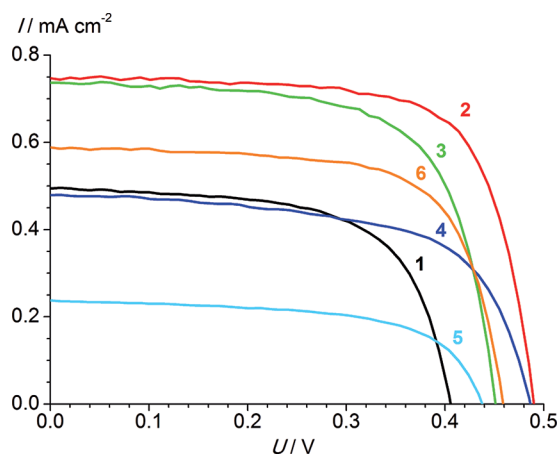


Figure 11. Current-voltage characteristics of DSSCs containing complexes $[1](PF_6)_2$ – $[6](PF_6)_2$.

A reverse bias was applied to all cells to measure the dark currents. Recombination was shown to be negligible at the TiO₂-dye interface when the I₃⁻/I⁻ redox couple was used because regeneration of the oxidized dye is significantly faster than back electron transfer from TiO₂ to the oxidized dye.^[95,96] Instead, efficient recombination is supposed to occur at the TiO₂-electrolyte interface.^[95] The recombination efficiency depends on the excitation intensity, the electrolyte composition, and the presence of dyes and additives.^[96,97] Figure 12 shows that for the cell with N719 a significantly higher voltage is necessary to produce the same amount of dark current compared with cells contain-

ing complexes $[1](PF_6)_2$ – $[6](PF_6)_2$. This can be explained by the twofold positive charge of the complex cations of $[1](PF_6)_2$ – $[6](PF_6)_2$ as compared to the twofold negative charge of N719 (Figure 1). Electrostatic interactions between the cationic complexes and I₃⁻ favor a higher concentration of I₃⁻ near the TiO₂ surface than in the bulk solution, which leads to an enhanced recombination rate.^[95,98] In contrast, the negative charge of N719 effectively repels I₃⁻ ions from the TiO₂ surface. Consequently, it is not surprising that all top-performing dyes are neutral or even negatively charged.^[6–9] Among the cells with $[1](PF_6)_2$ – $[6](PF_6)_2$, the cell with $[4](PF_6)_2$ shows the smallest dark current (Figure 12). This is possibly due to the high dye loading of $[4](PF_6)_2$, which acts as a blocking layer and reduces recombination at the TiO₂-electrolyte interface (Table 3).^[96] Indeed, the dye loading order of $[1](PF_6)_2$ – $[4](PF_6)_2$ is the inverse of the amount of dark current (Table 3, Figure 12). Regarding the low dye loading of $[5](PF_6)_2$ and $[6](PF_6)_2$, one would expect a high dark current for cells with these dyes. However, the amount of dark current of cells with $[5](PF_6)_2$ and $[6](PF_6)_2$ is moderate and can be compared to the cell with $[2](PF_6)_2$.

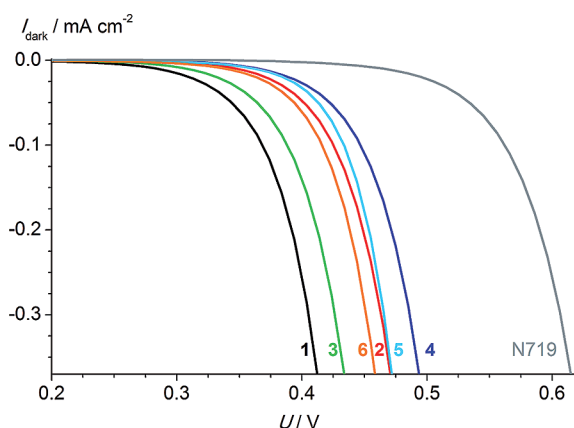


Figure 12. Dark current characteristics of DSSCs with complexes $[1](PF_6)_2$ – $[6](PF_6)_2$ and N719.

Two reasons might be responsible for this effect: (1) Dyes can also protonate (or deprotonate) the TiO₂ surface, shifting the conduction band edge of TiO₂ to lower (or higher) energy, which influences recombination rates.^[95,96,99] Protonation of TiO₂ by protons from N719 was found to increase the dark current, which might be due to the enhanced concentration of I₃⁻ near the surface.^[95,96] $[1](PF_6)_2$ – $[4](PF_6)_2$ are even more acidic than N719 [N719: $pK_{a1} = 3.5$, $pK_{a2} = 4.2$; $[4](PF_6)_2$: $pK_a = 2.7$; $[1](PF_6)_2$: $pK_a = 2.3$]^[45,100] and therefore protonate the TiO₂ surface, which lowers the energy of the conduction band. $[5](PF_6)_2$ and $[6](PF_6)_2$ cannot protonate the TiO₂ surface, which might lower the dark current in cells with these complexes. (2) The steric effect of $[5](PF_6)_2$ and $[6](PF_6)_2$ might suppress the dark current due to their steric bulk, as discussed above.

Electron recombination lifetimes τ of cells with $[1](PF_6)_2$ – $[6](PF_6)_2$ and N719 were determined experimentally by intensity-modulated photovoltage spectroscopy and the results corroborate the rationals derived from the dark

current measurements (Figure 13).^[101,102] Cells with $[1](PF_6)_2$ – $[6](PF_6)_2$ feature significantly smaller recombination lifetimes than the cell with N719. Because low recombination lifetimes result in charge carrier losses and, hence, in smaller short-circuit photocurrents,^[4] the observed recombination dynamics explains the poor performance of cells with complexes $[1](PF_6)_2$ – $[6](PF_6)_2$ compared with the cell with N719 (Table 3). The cell with $[4](PF_6)_2$ features the smallest recombination rate constant among our bis(tridentate) complexes, followed by the cell with $[2](PF_6)_2$ (Figure 12 and Figure 13). This might again be due to the high dye loading of $[4](PF_6)_2$ [and $[2](PF_6)_2$] as discussed above (Table 3).^[96] The lower dye loadings of $[1](PF_6)_2$, $[3](PF_6)_2$, $[5](PF_6)_2$, and $[6](PF_6)_2$ cannot effectively protect the TiO_2 surface from I_3^- and might be responsible for the high recombination rates. Successful strategies to suppress recombination are manifold and include the use of additional oxidic blocking layers, TiO_2 underlayers, coadsorbents, and sterically demanding dyes as surface protection.^[96,103,104]

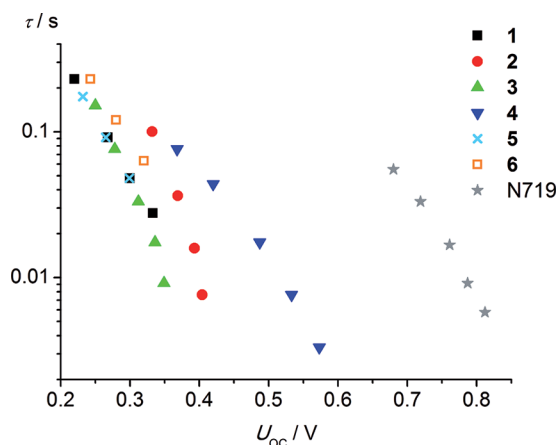


Figure 13. Electron recombination lifetimes τ vs. the open-circuit voltage U_{OC} of DSSCs with complexes $[1](PF_6)_2$ – $[6](PF_6)_2$ and N719.

Conclusions

Push-pull substituted heteroleptic bis(tridentate) ruthenium(II) polypyridine chromophores $[1](PF_6)_2$ – $[3](PF_6)_2$ (Figure 1) have been synthesized and fully characterized by ESI and HR-ESI mass spectrometry, infrared, 1H , ^{13}C and ^{15}N NMR 1D and 2D spectroscopy, elemental analysis, electrochemistry, UV/Vis absorption and emission spectroscopy. The pronounced donor–acceptor substitution induces a small HOMO–LUMO gap, which shifts the absorption to lower energy (up to $\lambda_{max} = 544$ nm and extending to 720 nm). The push-pull character is introduced by a tpy acceptor ligand featuring one or three carboxylic acid functionalities as electron-withdrawing components and a tpy/ddpd donor ligand featuring two or three amino functionalities as electron-donating components. DFT calculations show spatially separated and orthogonal frontier orbitals with a high electronic directionality. Irradiation experiments reveal a high photostability for our bis(tridentate)

complexes under conditions where N719 and tris(bidentate) $[Ru(bpy)_3](PF_6)_2$ undergo photodecomposition. Oxidation experiments revealed a superior stability of bis(tridentate) complexes as compared with N719. Complexes $[1](PF_6)_2$ – $[6](PF_6)_2$ (Figure 1) were tested as photosensitizers for TiO_2 in dye-sensitized solar cells with an I^-/I_3^- redox electrolyte. For the first time, 2,2'-bipyridine groups were used as anchors to TiO_2 $\{[5](PF_6)_2$ and $[6](PF_6)_2\}$. Power conversion efficiencies up to $\eta = 0.26\%$ under full AM 1.5 were obtained compared to $\eta = 5.0\%$ for the standard sensitizer N719 under our conditions. The twofold positive charge of our complexes contrasts with the twofold negative charge of N719. Consequently, the concentration of I_3^- near the TiO_2 electrode is increased and favors electron recombination. High dark currents and high recombination rates were measured for DSSCs with complexes $[1](PF_6)_2$ – $[6](PF_6)_2$, which rationalize the low cell performances.

Future perspectives are the use of negatively charged, cyclometalated, tridentate ligands, alkylated ligands, or triarylamine substituted ligands derived from tpy and ddpd, which can be used to redshift and broaden the absorption spectrum, to increase the push-pull characteristics and to decrease the overall positive charge of our complexes while retaining the excellent photo- and redox-stability.

Experimental Section

General Procedures: Diethyl ether was distilled from sodium, and acetonitrile from CaH_2 under an argon atmosphere. All reagents were used without further treatment from commercial suppliers (Acros and Sigma–Aldrich). Microwave heating was performed with a Discover Benchmate Plus (CEM Synthesis) single-mode microwave cavity, producing continuous irradiation at 2.455 GHz with 100 W (maximum power). NMR spectra were recorded with a Bruker Avance DRX 400 spectrometer at 400.31 MHz (1H), 100.66 MHz ($^{13}C\{^1H\}$), and 40.56 MHz (^{15}N). All resonances are reported in ppm vs. the solvent signal as an internal standard [CH_3CN (1H , $\delta = 1.94$ ppm; ^{13}C , $\delta = 1.24$ ppm)] or vs. external CH_3NO_2 [90% in $CDCl_3$, $\delta = 380.23$ ppm vs. $NH_3(l)$] and referenced to NH_3 (^{15}N , $\delta = 0$ ppm). Figure 1 shows the atom numbering for NMR signal assignment. IR spectra were recorded with a BioRad Excalibur FTS 3100 spectrometer as CsI disks. Electrochemical experiments were carried out with a Bio Logic SP-50 voltammetric analyzer using platinum wires as counter- and working-electrodes and 0.01 M $Ag/AgNO_3$ as reference electrode. The measurements were performed with a scan rate of $50\text{--}333\text{ mVs}^{-1}$ for cyclic voltammetry experiments and $100\text{--}200\text{ mVs}^{-1}$ for square-wave voltammetry experiments using 0.1 M $[nBu_4N](PF_6)$ as the supporting electrolyte and a 10^{-3} M solution of the sample in anhydrous and degassed CH_3CN . Potentials are referenced to the ferrocene/ferrocenium couple ($E_{1/2} = 86 \pm 5$ mV under our experimental conditions). UV/Vis/near-IR spectra were recorded with a Varian Cary 5000 or a Jasco V-670 spectrometer using 1.0 cm cells (Hellma, Suprasil). Emission spectra were recorded with a Varian Cary Eclipse spectrometer. Quantum yields were determined by comparing the areas under the emission spectra on an energy scale (cm^{-1}) recorded for optically matched solutions of the sample and the reference $[Ru(bpy)_3]Cl_2$ ($\Phi = 9.4\%$ in deaerated CH_3CN).^[105] ESI mass spectra were recorded with a Micromass Q-TOF-Ultima spectrometer. Elemental analyses were performed by the microana-

lytical laboratory of the chemical institutes of the University of Mainz.

Photostability: Photostability measurements were conducted at room temperature under an Ar atmosphere in 0.1 M $[n\text{Bu}_4\text{N}]\text{I}$ in $\text{CH}_3\text{CN}/\text{H}_2\text{O}$ (98:2, v/v) at $\lambda_{\text{exc}} = 400$ and 500 nm, respectively. The concentrations of the solutions were adjusted to ensure the same absorption at the corresponding excitation wavelength. The concentrations of $[\text{1}^{\text{Et}}](\text{PF}_6)_2$, $[\text{4}^{\text{Et}}](\text{PF}_6)_2$, N719, and $[\text{Ru}(\text{bpy})_3](\text{PF}_6)_2$ for the irradiation at $\lambda_{\text{exc}} = 400$ nm were 3.94×10^{-5} , 1.97×10^{-5} , 0.82×10^{-5} , and 0.96×10^{-5} M and for the irradiation at $\lambda_{\text{exc}} = 500$ nm 3.83×10^{-6} , 1.02×10^{-6} , 2.23×10^{-6} , and 9.89×10^{-6} M, respectively. As light sources, a Bivar LED (108A-713–5059, 400 nm) and a Sloan LED (L5-BG1G, 500 nm) were used in combination with a 40 W supply. Photodecomposition products of $[\text{Ru}(\text{bpy})_3](\text{PF}_6)_2$ were found when $[\text{Ru}(\text{bpy})_3](\text{PF}_6)_2$ (9.4 mg, 0.011 mmol, 1.0 equiv.) and $[n\text{Bu}_4\text{N}]\text{I}$ (9.0 mg, 0.024 mmol, 2.2 equiv.) were dissolved in CD_3CN (1.0 mL) and irradiated for 5 d at $\lambda_{\text{exc}} = 400$ nm. Before and after irradiation, NMR spectra were measured and their analysis revealed the formation of non-coordinated 2,2'-bipyridine during the irradiation. ESI⁺ mass spectra were measured with the same solution. Photodecomposition products of N719 were found when N719 (3.9 mg, 0.0033 mmol, 1.0 equiv.) and $[n\text{Bu}_4\text{N}]\text{I}$ (5.5 mg, 0.015 mmol, 4.5 equiv.) were dissolved in $\text{CD}_3\text{CN}/\text{H}_2\text{O}$ (14:1, 0.75 mL) and irradiated for 4 d at $\lambda_{\text{exc}} = 400$ nm. Before and after irradiation, NMR spectra were measured and reveal the formation of a new complex, in which presumably both NCS[−] ligands are substituted by I[−] or H₂O. No signals with ruthenium isotope pattern could be found in FD, ESI⁺, or ESI[−] mass spectra.

Redox Stability: The chemical stabilities of electrochemically oxidized complexes were measured at room temperature in a 10^{-3} M NaOH and 0.1 M $[n\text{Bu}_4\text{N}](\text{PF}_6)$ in $\text{CH}_3\text{CN}/\text{H}_2\text{O}$ (98:2, v/v) with ruthenium complex concentrations of 2×10^{-4} M. The optical path-length of the OTTE cell was 1 mm. A platinum mesh was used as working electrode, a platinum wire as counter electrode, and 0.01 M Ag/AgNO₃ as reference electrode. Electrical potentials were applied for at least 2 min before UV/Vis spectra were recorded.

DFT Calculations: Calculations were performed by using the Gaussian09/DFT^[106]series of programs. The B3LYP formulation of DFT was used, employing the LANL2DZ basis set.^[106] No symmetry constraints were imposed on the molecules. The presence of energy minima was checked by analytical frequency calculations. The integral-equation-formalism polarizable continuum model (IEFPCM in CH_3CN) was employed for solvent modeling. In TD-DFT calculations, at least 50 singlet transitions ($n \geq 50$) were calculated. All calculations were performed without explicit counterions and solvent molecules.

Materials and Fabrication of Dye-Sensitized Solar Cells: A TiO₂ blocking layer was prepared by spin coating a 2 wt.-% solution of bis(ethyl acetoacetato)-diisopropoxide titanium(IV) in *n*-butanol onto a FTO glass (TEC 8, Pilkington) followed by sintering at 500 °C for 15 min. The nanostructured TiO₂ layer was fabricated by doctor blading commercial TiO₂ paste (18NR-T, Dyesol) onto the TiO₂ layered FTO substrate followed by sintering at 500 °C for 15 min. The TiO₂ particle size was around 20 nm and the TiO₂ layer thickness was 7 μm as measured by a surface profiler (alpha-step IQ, Tencor). The TiO₂ electrodes were dipped into 0.3 mm solutions of ruthenium complexes in acetonitrile/*tert*-butyl alcohol (1:1) for 18 h at 25 °C, washed with acetonitrile and dried with an air stream. Dye loadings on TiO₂ were determined by the absorption difference of the dipping solution before and after dipping of a TiO₂ layer with a defined area of 2.6 cm². The N719 dye, bis-

(tetra-*n*-butylammonium)-*cis*-di(isothiocyanato)bis(2,2'-bipyridyl-4,4'-dicarboxylato)ruthenium(II), (Solaronix) was used as reference. For cell measurements, an active TiO₂ area of 0.25 cm² was used. Pt counter electrodes were fabricated by thermal decomposition of 0.01 M H₂PtCl₆ (Sigma–Aldrich) in isopropanol (Sigma–Aldrich) and were spun onto FTO substrates followed by sintering at 500 °C for 15 min. Two small holes were made in the Pt counter electrodes with a drill. A Surlyn film (25 μm, Solaronix) was sandwiched between the TiO₂ and the Pt electrode. The electrolyte was filled into the cell through one of the two holes and sealed with a Surlyn film and a cover glass. The electrolyte is a mixture of 1-methyl-3-propylimidazolium iodide (0.6 M) and iodine (0.05 M) in acetonitrile.

Characterization: The current-voltage curves of the cells were measured with a Keithley Model 2400 source meter and a solar simulator with a 300 W xenon arc-lamp (Newport) under 1 sun illumination (AM 1.5, 100 mW cm^{−2}). The light intensity was calibrated by a silicon solar cell (PV measurements, Inc.) A shading mask was placed on the residual area of the front side FTO substrate except for the 0.25 cm² TiO₂ active area to prevent overestimation of the power conversion efficiency. Electron recombination lifetimes were characterized by intensity-modulated photovoltage spectroscopy using IM6 (Zahner) under an open circuit condition. A white light-emitting diode (LED, $\lambda_{\text{emiss}} = 603$ nm, $\Delta\lambda = 105$ nm) was used as the modulated light source to ensure a homogeneous distribution of the illumination of the TiO₂ photoanodes. The applied light intensities ranged from 250 to 7 W m^{−2}.

Syntheses: The syntheses of $[\text{4}](\text{PF}_6)_2$ – $[\text{6}](\text{PF}_6)_2$ have been reported previously.^[45,49,50,62]

$[\text{Ru}(\text{ddpd})(\text{HOOC-tpy})](\text{PF}_6)_2$ ($[\text{1}](\text{PF}_6)_2$): $[\text{Ru}(\text{ddpd})(\text{EtOOC-tpy})](\text{PF}_6)_2$ ^[55] (119.6 mg, 0.121 mmol, 1.0 equiv.) was dissolved in CH_3CN (20 mL) and a mixture of conc. H₂SO₄ (20 mL) and water (50 mL) was added. The solution was heated to reflux (15 h). After cooling to room temperature, the mixture was neutralized with saturated NaOH solution and the solvent was removed under reduced pressure. CH_3CN (100 mL) was added, the suspension was ultrasonicated (1 min), filtered, and washed with CH_3CN (75 mL). The solvent was removed under reduced pressure and the precipitate was dissolved in water (10 mL). The pH was adjusted to 1.0 with conc. H₂SO₄. The addition of an acidic aqueous solution of $[\text{NH}_4](\text{PF}_6)$ (127.8 mg, 0.785 mmol, 6.5 equiv; 5 mL water; the pH was adjusted to 1.0 with conc. H₂SO₄) led to precipitation of a dark-purple solid, which was filtered and washed with cold water (ca. 10 mL). The solid was dissolved in CH_3CN (1 mL) and precipitated by the addition of Et₂O (10 mL). After filtration, washing with Et₂O (10 mL), and drying under reduced pressure a dark-purple solid was obtained, yield 88.3 mg (0.092 mmol, 76%). ¹H NMR (CD_3CN , 300 K): $\delta = 8.99$ (s, 2 H, H-2), 8.56 (m, 2 H, H-5), 8.27 (t, ³*J*_{H,H} = 8.2 Hz, 1 H, H-16), 8.11 (m, 2 H, H-8), 8.01 (m, 2 H, H-6), 7.61 (m, 2 H, H-11), 7.56 (d, ³*J*_{H,H} = 8.2 Hz, 2 H, H-15), 7.47 (m, 2 H, H-7), 7.17 (m, 2 H, H-12), 6.58 (m, 2 H, H-10), 6.44 (m, 2 H, H-9), 3.47 (s, 6 H, CH₃N) ppm, no resonance for OH was observed. ¹³C{¹H} NMR (CD_3CN , 300 K): $\delta = 165.7$ (s, C=O), 159.8 (s, C-13), 159.5 (s, C-3), 158.7 (s, C-4), 157.2 (s, C-14), 155.1 (s, C-8), 149.4 (s, C-9), 141.7 (s, C-16), 140.1 (s, C-11), 139.1 (s, C-6), 137.1 (s, C-1), 127.9 (s, C-7), 125.7 (s, C-5), 124.1 (s, C-2), 121.4 (s, C-10), 116.3 (s, C-12), 113.5 (s, C-15), 41.8 (s, CH₃N) ppm. ¹H-¹⁵N HMBC (CD_3CN , 300 K): $\delta = 293.6$ (N^c), 238.3 (N^d), 218.4 (N^e), 212.1 (N^a), 92.1 (N^b) ppm. MS (ESI⁺): *m/z* (%) = 335.1 (27) $[\text{M} - 2 \text{PF}_6]^{2+}$, 625.1 (7) $[\text{M} - \text{H} - \text{CO}_2 - \text{PF}_6]^+$, 815.1 (100) $[\text{M} - \text{PF}_6]^+$. HRMS (ESI⁺): *m/z* calcd. for C₃₃H₂₈F₆N₈O₂P⁹⁶Ru⁺ 809.1053; found 809.1056. IR (CsI): $\tilde{\nu} = 3443$ (br., m, OH), 3088

(w, CH), 2926 (w, CH), 1728 (m, C=O), 1601 (s, C=N), 1582 (m, C=N), 1489 (m, C=N), 1450 (s), 1364 (m), 1341 (m), 1279 (m), 1234 (m), 1138 (m), 1097 (m), 1043 (w), 1022 (w), 949 (w), 839 (vs, PF), 798 (m), 777 (m), 752 (m), 559 (s), 527 (w) cm^{-1} . UV/Vis (CH_3CN): λ_{abs} (ϵ , $\text{M}^{-1}\text{cm}^{-1}$) = 517 (8110), 319 (31200), 279 (37600), 221 (37500) nm. Emission (CH_3CN , 295 K, λ_{exc} = 517 nm): λ_{emiss} = 732 nm. $\Phi(\text{CH}_3\text{CN}$, λ_{exc} = 468 nm, 295 K): 0.068%. CV (CH_3CN): $E_{1/2}$ = +0.81 (1e, rev.), -1.50 (1e, irrev.) V vs. Fc/Fc^+ . $\text{C}_{33}\text{H}_{28}\text{F}_{12}\text{N}_8\text{O}_2\text{P}_2\text{Ru}\cdot 0.8\text{H}_2\text{O}\cdot 0.3\text{Et}_2\text{O}$: calcd. C 41.23, H 3.30, N 11.25; found C 40.94, H 2.99, N 10.87.

[Ru(ddpd){(HOOC) $_3$ -tpy}](PF $_6$) $_2$ (2**)(PF $_6$) $_2$]:** **[Ru(ddpd){(MeOOC) $_3$ -tpy}](PF $_6$) $_2$]^[41] (114.7 mg, 0.1053 mmol, 1.0 equiv.) was dissolved in CH_3CN (4 mL) and a mixture of conc. H_2SO_4 (4 mL) and water (10 mL) was added. The solution was heated to reflux (20 h). After cooling to room temperature, CH_3CN was removed under reduced pressure. The pH was adjusted to 1.0 with saturated aqueous NaOH solution. The addition of an acidic aqueous solution of $[\text{NH}_4](\text{PF}_6)$ (646.0 mg, 3.963 mmol, 37.6 equiv; 10 mL water; the pH was adjusted to 1.0 with conc. H_2SO_4) led to the precipitation of a dark-purple solid, which was filtered and washed with an acidic aqueous solution of $[\text{NH}_4](\text{PF}_6)$ (20.0 mg, 0.123 mmol, 1.2 equiv; 20 mL water; the pH was adjusted to 1.0 with conc. H_2SO_4). The solid was dried under reduced pressure to give a dark-purple powder, yield 55.5 mg (0.053 mmol, 50%). ^1H NMR (CD_3CN , 300 K): δ = 9.15 (s, 2 H, H-2), 8.97 (m, 2 H, H-5), 8.29 (t, $^3J_{\text{H,H}}$ = 8.2 Hz, 1 H, H-16), 8.26 (m, 2 H, H-8), 7.89 (m, 2 H, H-7), 7.61 (m, 2 H, H-11), 7.58 (d, $^3J_{\text{H,H}}$ = 8.2 Hz, 2 H, H-15), 7.18 (m, 2 H, H-12), 6.56 (m, 2 H, H-10), 6.36 (m, 2 H, H-9), 3.47 (s, 6 H, CH_3N) ppm, no resonance for OH was observed. $^{13}\text{C}\{^1\text{H}\}$ NMR (CD_3CN , 300 K): δ = 165.1 (s, C=O^{center}), 164.7 (s, C=O^{outer}), 159.7 (s, C-3), 159.6 (s, C-13), 159.2 (s, C-4), 157.1 (s, C-14), 155.8 (s, C-8), 149.2 (s, C-9), 142.1 (s, C-16), 140.4 (s, C-11), 140.1 (s, C-6), 136.6 (s, C-1), 127.1 (s, C-7), 125.0 (s, C-2), 124.9 (s, C-5), 121.6 (s, C-10), 116.6 (s, C-12), 113.7 (s, C-15), 41.7 (s, CH_3N) ppm. ^1H - ^{15}N HMBC (CD_3CN , 300 K): δ = 293.9 (N^{e}), 249.5 (N^{d}), 216.3 (N^{c}), 209.0 (N^{a}) ppm, N^{b} was not observed. MS (ESI⁺): m/z (%) = 379.1 (100) [$M - 2 \text{PF}_6$]²⁺, 903.1 (80) [$M - \text{PF}_6$]⁺. HRMS (ESI⁺): m/z calcd. for $\text{C}_{35}\text{H}_{28}\text{F}_6\text{N}_9\text{O}_6\text{P}^{\text{Ru}+}$ 897.0850; found 897.0836. IR (CsI): $\tilde{\nu}$ = 3440 (br., m, OH), 3105 (w, CH), 2928 (w, CH), 2855 (w, CH), 1726 (m, C=O), 1605 (m, C=N), 1543 (w, C=N), 1489 (w, C=N), 1450 (m), 1404 (m), 1360 (vs), 1234 (s), 1138 (m), 1115 (m), 1099 (s), 843 (vs, PF), 800 (w), 777 (m), 752 (w), 679 (w), 615 (w), 559 (w) cm^{-1} . UV/Vis (CH_3CN): λ_{abs} (ϵ , $\text{M}^{-1}\text{cm}^{-1}$) = 537 (6600), 473 (5820), 340 (34400), 291 (37100), 211 (55300) nm. Emission (CH_3CN , 295 K, λ_{exc} = 537 nm): λ_{emiss} = 743 nm. $\Phi(\text{CH}_3\text{CN}$, λ_{exc} = 467.5 nm, 295 K): 0.59%. CV (CH_3CN): $E_{1/2}$ = +0.87 (1e, rev.), -1.37 (1e, irrev.) V vs. Fc/Fc^+ . $\text{C}_{35}\text{H}_{28}\text{F}_{12}\text{N}_8\text{O}_6\text{P}_2\text{Ru}\cdot 0.3\text{H}_2\text{O}$: calcd. C 39.92, H 2.74, N 10.64; found C 40.51, H 3.36, N 10.36.**

[Ru(ddpd-NH $_2$){(HOOC) $_3$ -tpy}](PF $_6$) $_2$ (3**)(PF $_6$) $_2$]:** **{(MeOOC) $_3$ -tpy}RuCl $_3$ }[^{13,69–71}] (222.3 mg, 0.3616 mmol, 1.00 equiv.) and ddpd-4'-phthalimide^[41] (162.7 mg, 0.3728 mmol, 1.03 equiv.) were suspended in methanol (20 mL), ultrasonicated (1 min), and *N*-ethylmorpholine (0.40 mL, 3.2 mmol, 8.7 equiv.) was added. The dark-green to brown mixture was heated to reflux in a laboratory microwave oven for 45 min (75 °C). After cooling to room temperature, the mixture was filtered through Celite (1.5 cm; Ø 3.0 cm) and rinsed with methanol. The solvent was removed under reduced pressure and the residue was dissolved in conc. $\text{HCl}/\text{H}_2\text{O}$ (2:1, 150 mL) and heated to reflux (15 h). After cooling to room temperature, the pH was carefully adjusted to 0.9 with saturated NaOH solution. The addition of an acidic aqueous solution of $[\text{NH}_4](\text{PF}_6)$ (1.0 g, 6.1 mmol, 17 equiv., 100 mL H_2O , adjusted to pH 0.9 with conc. H_2SO_4) led to the precipitation of a dark-purple**

solid, which was filtered and washed with an acidic aqueous solution of $[\text{NH}_4](\text{PF}_6)$ (100 mg, 0.613 mmol, 1.7 equiv., 100 mL H_2O , adjusted to pH 0.9 with conc. H_2SO_4). The solid was dried under reduced pressure to give a dark-purple powder, yield 95.1 mg (0.0895 mmol, 25%). ^1H NMR (CD_3CN , 300 K): δ = 9.12 (s, 2 H, H-2), 8.94 (m, 2 H, H-5), 8.30 (m, 2 H, H-8), 7.89 (m, 2 H, H-7), 7.58 (m, 2 H, H-11), 7.12 (m, 2 H, H-12), 6.81 (s, 2 H, H-15), 6.52 (m, 2 H, H-10), 6.29 (m, 2 H, H-9), 5.75 (br. s, 2 H, NH_2), 3.36 (s, 6 H, CH_3N) ppm, no resonance for OH was observed. $^{13}\text{C}\{^1\text{H}\}$ NMR (CD_3CN , 300 K): δ = 165.3 (s, C=O^{center}), 164.8 (s, C=O^{outer}), 160.0 (s, C-13), 159.8 (s, C-4), 159.5 (s, C-3), 159.3 (s, C-16), 156.7 (s, C-14), 155.7 (s, C-8), 149.2 (s, C-9), 140.3 (s, C-11), 139.7 (s, C-6), 135.5 (s, C-1), 127.0 (s, C-7), 124.9 (s, C-2), 124.7 (s, C-5), 121.2 (s, C-10), 116.5 (s, C-12), 98.8 (s, C-15), 41.3 (s, CH_3N) ppm. ^1H - ^{15}N HMBC (CD_3CN , 300 K): δ = 296.9 (N^{e}), 249.9 (N^{d}), 210.0 (N^{a}), 181.6 (N^{c}), 72.2 (NH_2) ppm, N^{b} was not observed. MS (ESI⁺): m/z (%) = 386.6 (38) [$M - 2 \text{PF}_6$]²⁺, 918.1 (100) [$M - \text{PF}_6$]⁺. HRMS (ESI⁺): m/z calcd. for $\text{C}_{35}\text{H}_{29}\text{F}_6\text{N}_9\text{O}_6\text{P}^{\text{Ru}+}$ 912.0959; found 912.0914. IR (CsI): $\tilde{\nu}$ = 3443 (br., s, OH), 3098 (w, CH), 2959 (w, CH), 2926 (w, CH), 2855 (w, CH), 1713 (m, C=O), 1605 (vs, NH, C=N), 1539 (m, C=N), 1462 (s), 1437 (m), 1404 (s), 1360 (vs), 1234 (m), 1167 (m), 1117 (m), 1097 (vs), 968 (w), 841 (vs, PF), 781 (m), 756 (m), 727 (w), 696 (w), 683 (w), 667 (w), 648 (w), 613 (s), 561 (s), 530 (w), 505 (w), 482 (w), 451 (w), 347 (w) cm^{-1} . UV/Vis (CH_3CN): λ_{abs} (ϵ , $\text{M}^{-1}\text{cm}^{-1}$) = 544 (6690), 480 (5090), 340 (30400), 292 (34400), 217 (59900) nm. Emission (CH_3CN , 295 K, λ_{exc} = 544 nm): λ_{emiss} = 771 nm. $\Phi(\text{CH}_3\text{CN}$, λ_{exc} = 509 nm, 295 K): 0.067%. CV (CH_3CN): $E_{1/2}$ = +0.71 (1e, rev.), -1.53 (1e, irrev.) V vs. Fc/Fc^+ . $\text{C}_{35}\text{H}_{29}\text{F}_{12}\text{N}_9\text{O}_6\text{P}_2\text{Ru}\cdot 3\text{CH}_3\text{OH}$: calcd. C 39.39, H 3.57, N 10.88; found C 39.96, H 3.67, N 11.22.

Supporting Information (see footnote on the first page of this article): Tabulated ^1H , ^{13}C and ^{15}N NMR chemical shifts in CD_3CN ; cyclic and square-wave voltammograms of **1** and **3**; spin densities of **1**²⁺ – **6**²⁺ and reduced N719; frontier molecular orbitals of **1**²⁺ – **6**²⁺ and N719. ^1H NMR spectra of **[Ru(bpy) $_3$](PF $_6$) $_2$]/**[nBu $_4$ N]I** before and after irradiation. ESI mass spectrum of **[Ru(bpy) $_3$](PF $_6$) $_2$]/**[nBu $_4$ N]I** after irradiation. ^1H NMR spectra of N719/**[nBu $_4$ N]I** before and after irradiation. UV/Vis spectra of the electrochemical oxidation and back reduction of **1** and **3**; **[Ru(bpy) $_3$](PF $_6$) $_2$ and N719 in the presence of NaOH; IPCE plots of cells with **1** and **3** and N719; DFT (B3LYP/LANL2DZ, IEFPCM, CH_3CN) optimized geometries of **1**²⁺ – **6**²⁺ and N719 (singlet) and **1**³⁺ – **6**³⁺, and oxidized N719 (doublet); results of TD-DFT calculations of **1**²⁺ – **6**²⁺ and N719 (singlet).******

Acknowledgments

This work was supported by the International Research Training Group (IRTG 1404): Self Organized Materials for Optoelectronics supported by the Deutsche Forschungsgemeinschaft (DFG).

- [1] B. O'Regan, M. Grätzel, *Nature* **1991**, 353, 737–740.
- [2] A. Hagfeld, G. Boschloo, L. Sun, L. Kloo, H. Pettersson, *Chem. Rev.* **2010**, 110, 6595–6663.
- [3] A. Reynal, E. Palomares, *Eur. J. Inorg. Chem.* **2011**, 29, 4509–4526.
- [4] J.-F. Yin, M. Velayudham, D. Bhattacharya, H.-C. Lin, K.-L. Lu, *Coord. Chem. Rev.* **2012**, 256, 3008–3035.
- [5] P. G. Bomben, K. C. D. Robson, B. D. Koivisto, C. P. Berlinguette, *Coord. Chem. Rev.* **2012**, 256, 1438–1450.

- [6] C. A. Bignozzi, R. Argazzi, R. Boaretto, E. Busatto, S. Carli, F. Ronconi, S. Caramori, *Coord. Chem. Rev.* **2013**, *257*, 1472–1492.
- [7] B. Bozic-Weber, E. C. Constable, C. E. Housecroft, *Coord. Chem. Rev.* **2013**, *257*, 3089–3106.
- [8] T. Chen, L. Qiu, Z. Yang, H. Peng, *Chem. Soc. Rev.* **2013**, *42*, 5031–5041.
- [9] A. Yella, H.-W. Lee, H. N. Tsao, C. Yi, A. K. Chandiran, M. K. Nazeeruddin, E. W.-G. Diau, C.-Y. Yeh, S. M. Zakeeruddin, M. Grätzel, *Science* **2011**, *334*, 629–634.
- [10] S. Campagna, F. Puntoriero, F. Nastasi, G. Bergamini, V. Balzani, *Top. Curr. Chem.* **2007**, *280*, 117–214.
- [11] M. K. Nazeeruddin, S. M. Zakeeruddin, R. Humphry-Baker, M. Jirousek, P. Liska, N. Vlachopoulos, V. Shklover, C.-H. Fischer, M. Grätzel, *Inorg. Chem.* **1999**, *38*, 6298–6305.
- [12] M. K. Nazeeruddin, F. D. Angelis, S. Fantacci, A. Selloni, G. Viscardi, P. Liska, S. Ito, B. Takeru, M. Grätzel, *J. Am. Chem. Soc.* **2005**, *127*, 16835–16847.
- [13] M. K. Nazeeruddin, P. Péchy, T. Renouard, S. M. Zakeeruddin, R. Humphrey-Baker, P. Comte, P. Liska, L. Cevey, E. Costa, V. Shklover, L. Spiccia, G. B. Deacon, C. A. Bignozzi, M. Grätzel, *J. Am. Chem. Soc.* **2001**, *123*, 1613–1624.
- [14] T. P. Brewster, W. Ding, N. D. Schley, N. Hazari, V. S. Batista, R. H. Crabtree, *Inorg. Chem.* **2011**, *50*, 11938–11946.
- [15] S. Betanzos-Lara, L. Salassa, A. Habtemariam, O. Novakova, A. M. Pizarro, G. J. Clarkson, B. Liskova, V. Brabec, P. J. Sadler, *Organometallics* **2012**, *31*, 3466–3479.
- [16] S. Kämper, A. Paretzki, J. Fiedler, S. Zális, W. Kaim, *Inorg. Chem.* **2012**, *51*, 2097–2104.
- [17] G. Xue, Y. Guo, T. Yu, J. Guan, X. Yu, J. Zhang, J. Liu, Z. Zou, *Int. J. Electrochem. Sci.* **2012**, *7*, 1496–1511.
- [18] A. Bahreman, B. Limburg, M. A. Siegler, E. Bouwman, S. Bonnet, *Inorg. Chem.* **2013**, *52*, 9456–9469.
- [19] P. T. Nguyen, B. X. T. Lam, A. R. Andersen, P. E. Hansen, T. Lund, *Eur. J. Inorg. Chem.* **2011**, 2533–2539.
- [20] C. Dragonetti, A. Valore, A. Colombo, D. Roberto, V. Trifiletti, N. Manfredi, M. M. Salamone, R. Ruffo, A. Abboto, *J. Organomet. Chem.* **2012**, *714*, 88–93.
- [21] M. M. R. Choudhuri, R. J. Crutchley, *Inorg. Chem.* **2013**, *52*, 14404–14410.
- [22] C.-H. Siu, C.-L. Ho, J. He, T. Chen, X. Cui, J. Zhao, W.-Y. Wong, *J. Organomet. Chem.* **2013**, *748*, 75–83.
- [23] T. Bessho, E. Yoneda, J.-H. Yum, M. Guglielmi, I. Tavernelli, H. Imai, U. Rothlisberger, M. K. Nazeeruddin, M. Grätzel, *J. Am. Chem. Soc.* **2009**, *131*, 5930–5934.
- [24] K.-L. Wu, H.-C. Hsu, K. Chen, Y. Chi, M.-W. Chung, W.-H. Liu, P.-T. Chou, *Chem. Commun.* **2010**, *46*, 5124–5126.
- [25] C. E. Welby, C. R. Rice, P. I. P. Elliott, *Angew. Chem. Int. Ed.* **2013**, *52*, 10826–10829; *Angew. Chem.* **2013**, *125*, 11026–11029.
- [26] K. Garg, J. T. Engle, C. J. Ziegler, J. J. Rack, *Chem. Eur. J.* **2013**, *19*, 11686–11695.
- [27] J. D. Slinker, J. Rivnay, J. S. Moskowitz, J. B. Parker, S. Bernhard, H. D. Abruña, G. G. Malliaras, *J. Mater. Chem.* **2007**, *17*, 2976–2988.
- [28] J. D. Slinker, J.-S. Kim, S. Flores-Torres, J. H. Delcamp, H. D. Abruña, R. H. Friend, G. G. Malliaras, *J. Mater. Chem.* **2007**, *17*, 76–81.
- [29] L. J. Soltzberg, J. D. Slinker, S. Flores-Torres, D. A. Bernards, G. G. Malliaras, H. D. Abruña, J.-S. Kim, R. H. Friend, M. D. Kaplan, V. Goldberg, *J. Am. Chem. Soc.* **2006**, *128*, 7761–7764.
- [30] G. Kalyuzhny, M. Buda, J. McNeill, P. Barbara, A. J. Bard, *J. Am. Chem. Soc.* **2003**, *125*, 6272–6283.
- [31] C. Fu, M. Wenzel, E. Treutlein, K. Harms, E. Meggers, *Inorg. Chem.* **2012**, *51*, 10004–10011.
- [32] E. Meggers, *Chem. Eur. J.* **2010**, *16*, 752–758.
- [33] M. Maestri, N. Armaroli, V. Balzani, E. C. Constable, A. M. W. Cargill Thompson, *Inorg. Chem.* **1995**, *34*, 2759–2767.
- [34] R. Hogg, R. G. Wilkins, *J. Chem. Soc.* **1962**, 341–350.
- [35] R. H. Holyer, C. D. Hubbard, S. F. A. Kettle, R. G. Wilkins, *Inorg. Chem.* **1966**, *5*, 622–625.
- [36] J.-P. Sauvage, J.-P. Collin, J.-C. Chambron, S. Guillerez, C. Coudret, V. Balzani, F. Barigelletti, L. D. Cola, L. Flamigni, *Chem. Rev.* **1994**, *94*, 993–1019.
- [37] L. Hammarström, O. Johansson, *Coord. Chem. Rev.* **2010**, *254*, 2546–2559.
- [38] Y. Liu, R. Hammitt, D. A. Lutterman, R. P. Thummel, C. Turro, *Inorg. Chem.* **2007**, *46*, 6011–6021.
- [39] T. Banerjee, S. Kaniyankandy, A. Das, H. N. Ghosh, *Inorg. Chem.* **2013**, *52*, 5366–5377.
- [40] E. Jakubikova, R. C. Snoeberger, V. S. Batista, R. L. Martin, E. R. Batista, *J. Phys. Chem. A* **2009**, *113*, 12532–12540.
- [41] A. Breivogel, M. Meister, C. Förster, F. Laquei, K. Heinze, *Chem. Eur. J.* **2013**, *19*, 13745–13760.
- [42] H. J. Bolink, L. Cappelli, E. Coronado, P. Gaviña, *Inorg. Chem.* **2005**, *44*, 5966–5968.
- [43] S. H. Wadman, J. M. Kroon, K. Bakker, M. Lutz, A. L. Spek, G. P. M. van Klink, G. van Koten, *Chem. Commun.* **2007**, *19*, 1907–1909.
- [44] C. Houarner-Rassin, F. Chaignon, C. She, D. Stockwell, E. Blart, P. Buvat, T. Lian, F. Odobel, *J. Photochem. Photobiol. A* **2007**, *192*, 56–65.
- [45] K. Heinze, K. Hempel, M. Beckmann, *Eur. J. Inorg. Chem.* **2006**, 2040–2050.
- [46] A. Breivogel, K. Hempel, K. Heinze, *Inorg. Chim. Acta* **2011**, *374*, 152–162.
- [47] K. Heinze, K. Hempel, A. Breivogel, *Z. Anorg. Allg. Chem.* **2009**, *635*, 2541–2549.
- [48] R. J. Kumar, S. Karlsson, D. Streich, A. R. Jensen, M. Jäger, H.-C. Becker, J. Bergquist, O. Johansson, L. Hammarström, *Chem. Eur. J.* **2010**, *16*, 2830–2842.
- [49] J. Dietrich, U. Thorenz, C. Förster, K. Heinze, *Inorg. Chem.* **2013**, *52*, 1248–1264.
- [50] J. Dietrich, A. Wünsche von Leupoldt, M. Grabolle, U. Resch-Genger, K. Heinze, *Eur. J. Inorg. Chem.* **2013**, 3009–3019.
- [51] L. zur Borg, A. L. Domanski, A. Breivogel, M. Bürger, R. Berger, K. Heinze, R. Zentel, *J. Mater. Chem.* **2013**, *1*, 1223–1230.
- [52] T. J. Meyer, *Pure Appl. Chem.* **1986**, *58*, 1193–1206.
- [53] J. V. Caspar, T. J. Meyer, *J. Am. Chem. Soc.* **1983**, *105*, 5583–5590.
- [54] J. V. Caspar, T. J. Meyer, *J. Phys. Chem.* **1983**, *87*, 952–957.
- [55] A. Breivogel, C. Förster, K. Heinze, *Inorg. Chem.* **2010**, *49*, 7052–7056.
- [56] B. D. Koivisto, K. C. D. Robson, C. P. Berlinguette, *Inorg. Chem.* **2009**, *48*, 9644–9652.
- [57] K. C. D. Robson, B. D. Koivisto, A. Yella, B. Sporinova, M. K. Nazeeruddin, T. Baumgartner, M. Grätzel, C. P. Berlinguette, *Inorg. Chem.* **2011**, *50*, 5494–5508.
- [58] C.-C. Chou, K.-L. Wu, Y. Chi, W.-P. Hu, S. J. Yu, G.-H. Lee, C.-L. Lin, P.-T. Chou, *Angew. Chem. Int. Ed.* **2011**, *50*, 2054–2058; *Angew. Chem.* **2011**, *123*, 2102–2106.
- [59] C.-C. Chou, F.-C. Hu, H.-H. Yeh, H.-P. Wu, Y. Chi, J. N. Clifford, E. Palomares, S.-H. Liu, P.-T. Chou, G.-H. Lee, *Angew. Chem. Int. Ed.* **2014**, *53*, 178–183; *Angew. Chem.* **2014**, *126*, 182–187.
- [60] C.-W. Hsu, S.-T. Ho, K.-L. Wu, Y. Chi, S.-H. Liu, P.-T. Chou, *Energy Environ. Sci.* **2012**, *5*, 7549–7554.
- [61] B. Schulze, D. Escudero, C. Friebe, R. Siebert, H. Görls, S. Sinn, M. Thomas, S. Mai, J. Popp, B. Dietzek, L. González, U. S. Schubert, *Chem. Eur. J.* **2012**, *18*, 4010–4025.
- [62] K. Heinze, K. Hempel, S. Tschierlei, M. Schmitt, J. Popp, S. Rau, *Eur. J. Inorg. Chem.* **2009**, 3119–3126.
- [63] W. B. Heuer, H.-L. Xia, W. Ward, Z. Zhou, W. H. Pearson, M. A. Siegler, A. A. N. Sarjeant, M. Abrahamsson, G. J. Meyer, *Inorg. Chem.* **2012**, *51*, 3981–3988.
- [64] S. Zhang, Y. Peng, W. Jiang, X. Liu, X. Song, B. Pan, H.-Q. Yu, *Chem. Commun.* **2014**, *50*, 1086–1088.
- [65] W. R. McNamara, R. C. Snoeberger III, G. Li, J. M. Schleicher, C. W. Cady, M. Poyatos, C. A. Schmuttenmaer, R. H.

- Crabtree, G. W. Brudvig, V. S. Batista, *J. Am. Chem. Soc.* **2008**, *130*, 14329–14338.
- [66] T. Banerjee, S. Rawalekar, A. Das, H. N. Ghosh, *Eur. J. Inorg. Chem.* **2011**, 4187–4197.
- [67] E. Franzmann, F. Khalil, C. Weidmann, M. Schröder, M. Rohnke, J. Janek, B. M. Smarsly, W. Maison, *Chem. Eur. J.* **2011**, *17*, 8596–8603.
- [68] M. I. Asghar, K. Miettunen, J. Halme, P. Vahermaa, M. Toivola, K. Aitola, P. Lund, *Energy Environ. Sci.* **2010**, *3*, 418–426.
- [69] J. Dehaut, J. Husson, L. Guyard, *Green Chem.* **2011**, *13*, 3337–3340.
- [70] L. Giribabu, T. Bessho, M. Srinivasu, C. Vijaykumar, Y. Soujanya, V. G. Reddy, P. Y. Reddy, J.-H. Yum, M. Grätzel, M. K. Nazeeruddin, *Dalton Trans.* **2011**, *40*, 4497–4504.
- [71] M. K. Nazeeruddin, P. Péchy, M. Grätzel, *Chem. Commun.* **1997**, *18*, 1705–1706.
- [72] M. Hesse, H. Meier, B. Zeeh, *Spektroskopische Methoden in der Organischen Chemie*, Thieme, Stuttgart, Germany, **1991**.
- [73] W.-S. Han, J.-K. Han, H.-Y. Kim, M. J. Choi, Y.-S. Kang, C. Pac, S. O. Kang, *Inorg. Chem.* **2011**, *50*, 3271–3280.
- [74] F. D. Angelis, S. Fantacci, E. Mosconi, M. K. Nazeeruddin, M. Grätzel, *J. Phys. Chem. C* **2011**, *115*, 8825–8831.
- [75] A. Breivogel, M. Park, D. Lee, S. Klassen, A. Kühnle, C. Lee, K. Char, K. Heinze, *Eur. J. Inorg. Chem.* **2014**, 288–295.
- [76] G. R. Desiraju, *Angew. Chem. Int. Ed. Engl.* **1995**, *34*, 2311–2327; *Angew. Chem.* **1995**, *107*, 2541–2558.
- [77] K. Heinze, K. Hempel, *Chem. Eur. J.* **2009**, *15*, 1346–1358.
- [78] C. Turro, S. H. Bossmann, Y. Jenkins, J. K. Barton, N. J. Turro, *J. Am. Chem. Soc.* **1995**, *117*, 9026–9032.
- [79] Y. Nosenko, G. Wiosna-Sałyga, M. Kunitski, I. Petkova, A. Singh, W. J. Buma, R. P. Thummel, B. Brutschy, J. Waluk, *Angew. Chem. Int. Ed.* **2008**, *47*, 6037–6040; *Angew. Chem.* **2008**, *120*, 6126–6129.
- [80] M. Marazzi, U. Sancho, O. Castaño, W. Domcke, L. M. Frutos, *J. Phys. Chem. Lett.* **2010**, *1*, 425–428.
- [81] G. Y. Zheng, Y. Wang, D. P. Rillema, *Inorg. Chem.* **1996**, *35*, 7118–7123.
- [82] P. A. Lay, W. H. F. Sasse, *Inorg. Chem.* **1984**, *23*, 4125–4127.
- [83] R. J. Watts, *J. Chem. Educ.* **1983**, *60*, 834–842.
- [84] B. Durham, J. V. Caspar, J. K. Nagle, T. J. Meyer, *J. Am. Chem. Soc.* **1982**, *104*, 4803–4810.
- [85] Z. J. Fuller, W. D. Bare, K. A. Kneas, W.-Y. Xu, J. N. Demas, B. A. DeGraff, *Anal. Chem.* **2003**, *75*, 2670–2677.
- [86] W. M. Wallace, P. E. Hoggard, *Inorg. Chem.* **1979**, *18*, 2934–2935.
- [87] T. E. Keyes, E. Gicquel, L. Guerin, R. J. Forster, V. Hultgren, A. M. Bond, A. G. Wedd, *Inorg. Chem.* **2003**, *42*, 7897–7905.
- [88] M. Abrahamsson, M. Jäger, R. J. Kumar, T. Österman, P. Persson, H.-C. Becker, O. Johansson, L. Hammarström, *J. Am. Chem. Soc.* **2008**, *130*, 15533–15542.
- [89] O. Kohle, M. Grätzel, A. F. Meyer, T. B. Meyer, *Adv. Mater.* **1997**, *9*, 904–906.
- [90] G. Wolfbauer, A. M. Bond, D. R. MacFarlane, *Inorg. Chem.* **1999**, *38*, 3836–3846.
- [91] G. Boschloo, A. Hagfeld, *Acc. Chem. Res.* **2009**, *42*, 1819–1826.
- [92] Y. Ooyama, T. Nagano, S. Inoue, I. Imae, K. Komaguchi, J. Ohshita, Y. Harima, *Chem. Eur. J.* **2011**, *17*, 14837–14843.
- [93] Y. Ooyama, S. Inoue, T. Nagano, K. Kushimoto, J. Ohshita, I. Imae, K. Komaguchi, Y. Harima, *Angew. Chem. Int. Ed.* **2011**, *50*, 7429–7433; *Angew. Chem.* **2011**, *123*, 7567–7571.
- [94] S. H. Wadman, J. M. Kroon, K. Bakker, M. Lutz, A. L. Spek, G. P. M. van Klink, G. van Koten, *Chem. Commun.* **2007**, 1907–1909.
- [95] A. J. Frank, N. Kopidakis, J. van de Lagemaat, *Coord. Chem. Rev.* **2004**, *248*, 1165–1179.
- [96] S. Ito, P. Liska, P. Comte, R. Charvet, P. Péchy, U. Bach, L. Schmidt-Mende, S. M. Zakeeruddin, A. Kay, M. K. Nazeeruddin, M. Grätzel, *Chem. Commun.* **2005**, 4351–4353.
- [97] S. A. Haque, Y. Tachibana, R. L. Willis, J. E. Moser, M. Grätzel, D. R. Klug, J. R. Durrant, *J. Phys. Chem. B* **2000**, *104*, 538–547.
- [98] S. Caramori, J. Husson, M. Beley, C. A. Bignozzi, R. Argazzi, P. C. Gros, *Chem. Eur. J.* **2010**, *16*, 2611–2618.
- [99] M. K. Nazeeruddin, R. Humphry-Baker, P. Liska, M. Grätzel, *J. Phys. Chem. B* **2003**, *107*, 8981–8987.
- [100] G. Pizzoli, M. G. Lobello, B. Carlotti, F. Elisei, M. K. Nazeeruddin, G. Vitillaro, F. D. Angelis, *Dalton Trans.* **2012**, *41*, 11841–11848.
- [101] G. Schlichthörl, S. Y. Huang, J. Sprague, A. J. Frank, *J. Phys. Chem. B* **1997**, *101*, 8141–8155.
- [102] J. Bisquert, F. Fabregat-Santiago, I. Mora-Seró, G. Garcia-Belmonte, S. Giménez, *J. Phys. Chem. A* **2009**, *113*, 17278–17290.
- [103] E. Palomares, J. N. Clifford, S. A. Haque, T. Lutz, J. R. Durrant, *Chem. Commun.* **2002**, 1464–1465.
- [104] Y.-G. Lee, S. Park, W. Cho, T. Son, P. Sudhagar, J. H. Jung, S. Wooh, K. Char, Y. S. Kang, *J. Phys. Chem. C* **2012**, *116*, 6770–6777.
- [105] K. Suzuki, A. Kobayashi, S. Kaneko, K. Takehira, T. Yoshihara, H. Ishida, Y. Shiina, S. Oishi, S. Tobita, *Phys. Chem. Chem. Phys.* **2009**, *11*, 9850–9860.
- [106] M. J. Frisch, G. W. Trucks, H. B. Schlegel, G. E. Scuseria, M. A. Robb, J. R. Cheeseman, G. Scalmani, V. Barone, B. Mennucci, G. A. Petersson, H. Nakatsuji, M. Caricato, X. Li, H. P. Hratchian, A. F. Izmaylov, J. Bloino, G. Zheng, J. L. Sonnenberg, M. Hada, M. Ehara, K. Toyota, R. Fukuda, J. Hasegawa, M. Ishida, T. Nakajima, Y. Honda, O. Kitao, H. Nakai, T. Vreven, J. A. Montgomery Jr., J. E. Peralta, F. Ogliaro, M. Bearpark, J. J. Heyd, E. Brothers, K. N. Kudin, V. N. Staroverov, R. Kobayashi, J. Normand, K. Raghavachari, A. Rendell, J. C. Burant, S. S. Iyengar, J. Tomasi, M. Cossi, N. Rega, J. M. Millam, M. Klene, J. E. Knox, J. B. Cross, V. Bakken, C. Adamo, J. Jaramillo, R. Gomperts, R. E. Stratmann, O. Yazyev, A. J. Austin, R. Cammi, C. Pomelli, J. W. Ochterski, R. L. Martin, K. Morokuma, V. G. Zakrzewski, G. A. Voth, P. Salvador, J. J. Dannenberg, S. Dapprich, A. D. Daniels, O. Farkas, J. B. Foresman, J. V. Ortiz, J. Cioslowski, D. J. Fox, *Gaussian 09*, revision A.02, Gaussian, Inc., Wallingford CT, **2009**.

Received: February 21, 2014
Published Online: April 28, 2014

10 Supporting Information

10.1 Explanatory Notes for the Supporting Information

In the following the full supporting information of all manuscripts and publications is reproduced herein expect published DFT optimized cartesian coordinates and published results of TD-DFT calculations. This is for the sake of clarity. The data can be found in the online supporting information of the respective journal.

10.2 Thermal and Photo Reactivity of a Donor-Acceptor-Substituted Bis(terpyridine) Ruthenium(III) Complex in Acidic Solutions

A. Breivogel, K. Heinze.

-to be submitted-

Thermal and Photo Reactivity of a Donor-Acceptor-Substituted Bis(terpyridine) Ruthenium(III) Complex in Acidic Solutions

Aaron Breivogel, and Katja Heinze*

Supporting Information

Table of Contents:

- 1) Figures S1 – S8
- 2) Preparation and characterization of the IrCl(PEt₃)₃ solution and Figure S9.
- 3) DFT (B3LYP/LANL2DZ, IEFPCM, H₂O) optimized geometries of [1]²⁺, [1]³⁺, [1 – H]²⁺, [1 – 2 H]⁺, [Ru(κ²-H₂N-tpy)(κ³-HOOC-tpy)(H₂O)]³⁺ and "[Ru(κ³-H₂N-tpy)(κ³-HOOC-tpy)]³⁺ + H₂O".
- 4) Results of TD-DFT calculations of [1]²⁺ and [1]³⁺.

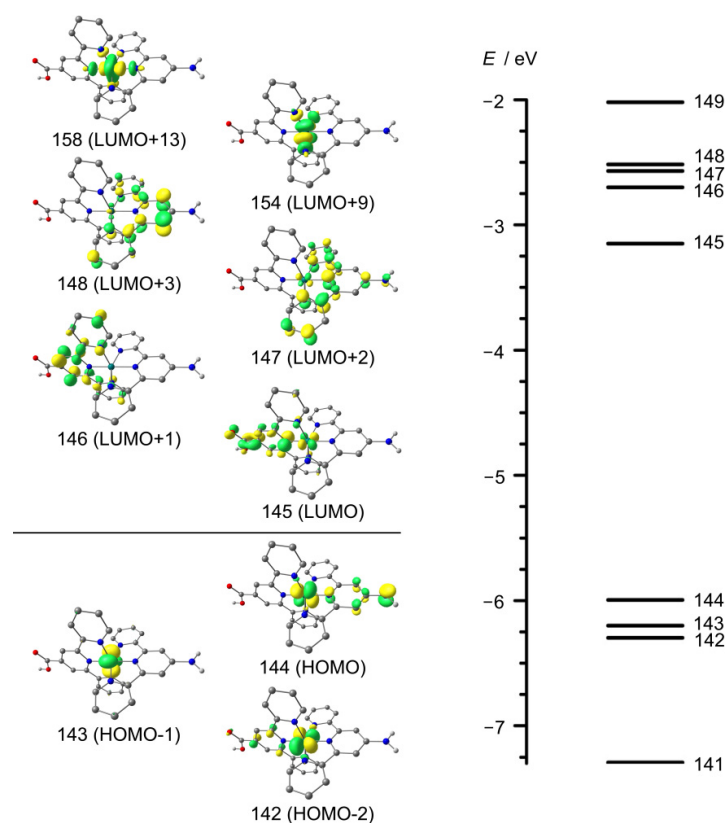


Figure S1. Relevant DFT-calculated Kohn-Sham frontier molecular orbitals (B3LYP/LANL2DZ, IEFPCM, H₂O, contour value 0.06 a.u., CH hydrogen atoms omitted) and energy levels of frontier molecular orbitals of [1]²⁺.

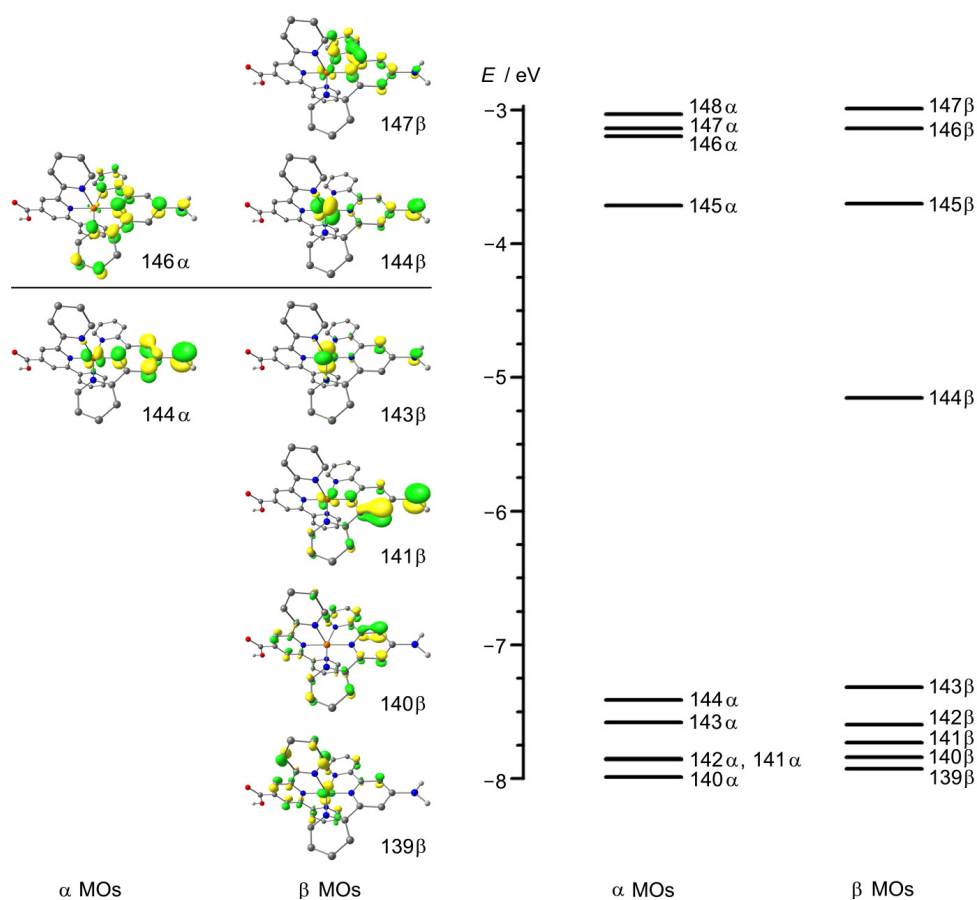


Figure S2. Relevant DFT-calculated Kohn-Sham frontier molecular orbitals (B3LYP/LANL2DZ, IEFPCM, H₂O, contour value 0.06 a.u., CH hydrogen atoms omitted) and energy levels of frontier molecular orbitals of [1]³⁺.

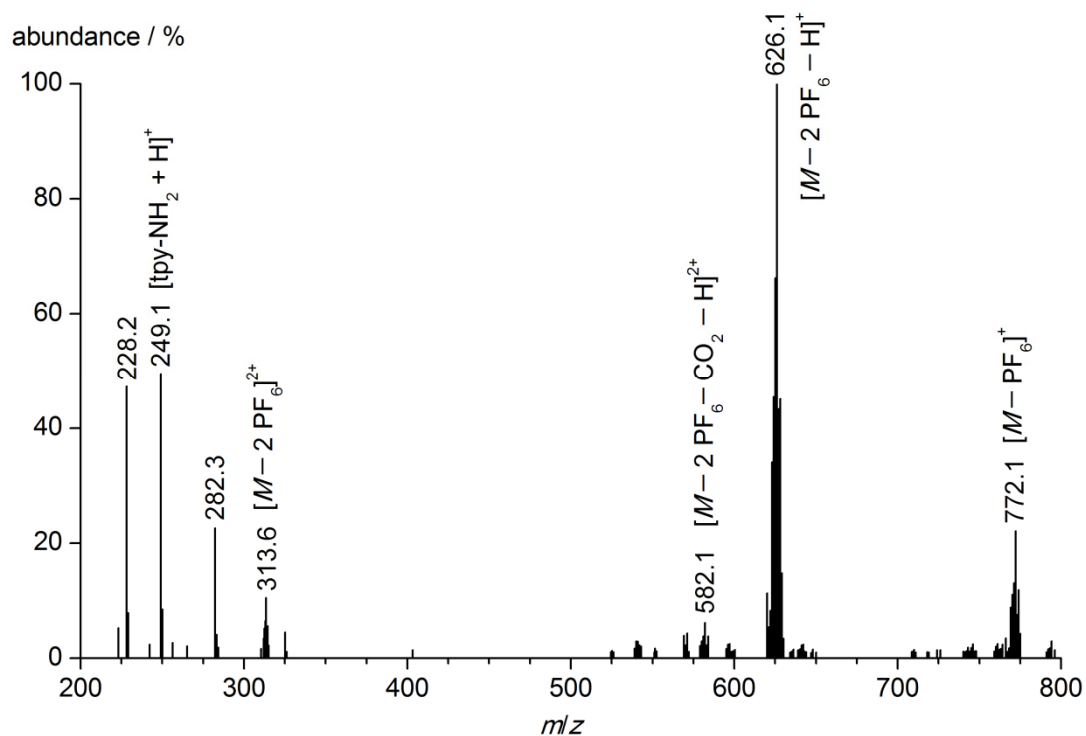


Figure S3. ESI⁺ mass spectrum of [1](PF₆)₂ 0.5 M TFA in CH₃CN:H₂O (200:1) before addition of (NH₄)₂[Ce(NO₃)₆].

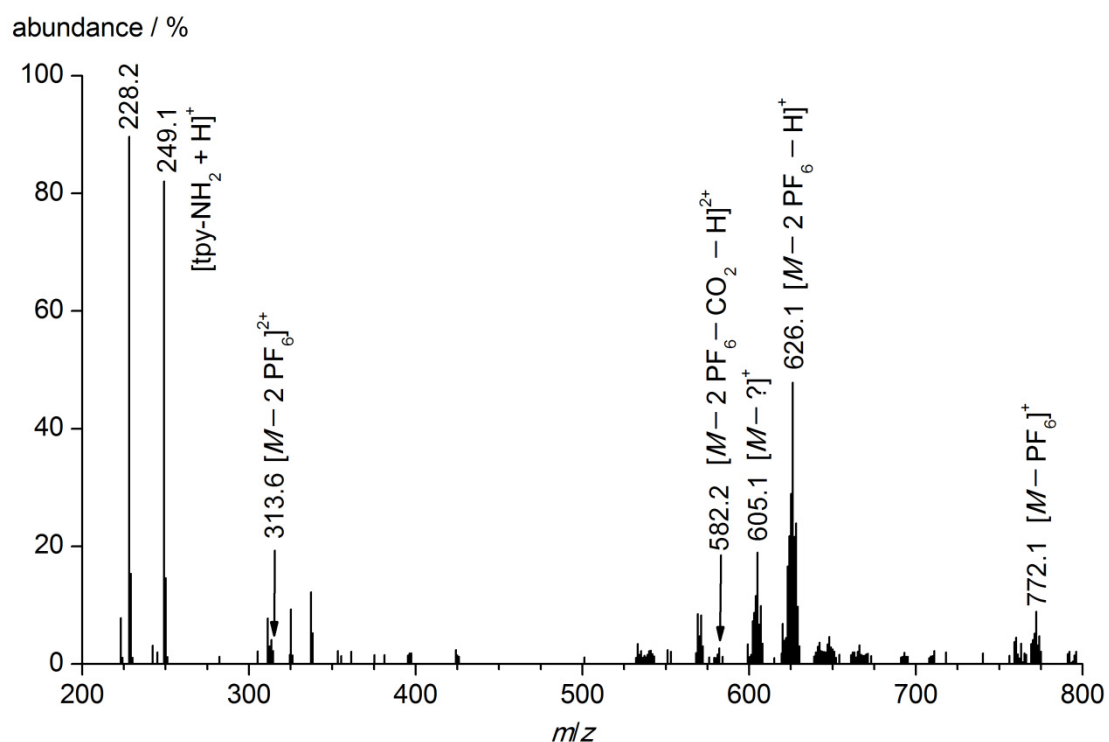


Figure S4. ESI⁺ mass spectrum of [1](PF₆)₂ 0.5 M TFA in CH₃CN:H₂O (200:1) 2 d after oxidation with 2.0 equiv (NH₄)₂[Ce(NO₃)₆].

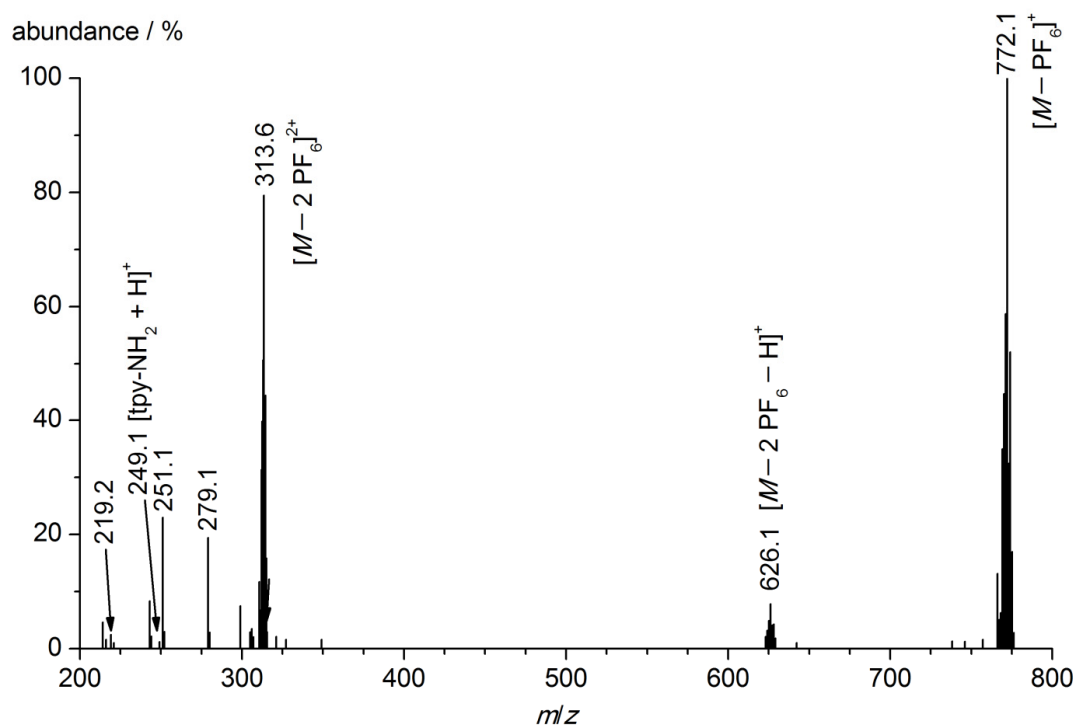


Figure S5. ESI⁺ mass spectrum of [1](PF₆)₂ in 0.5 M HNO₃ in H₂O before addition of (NH₄)₂[Ce(NO₃)₆].

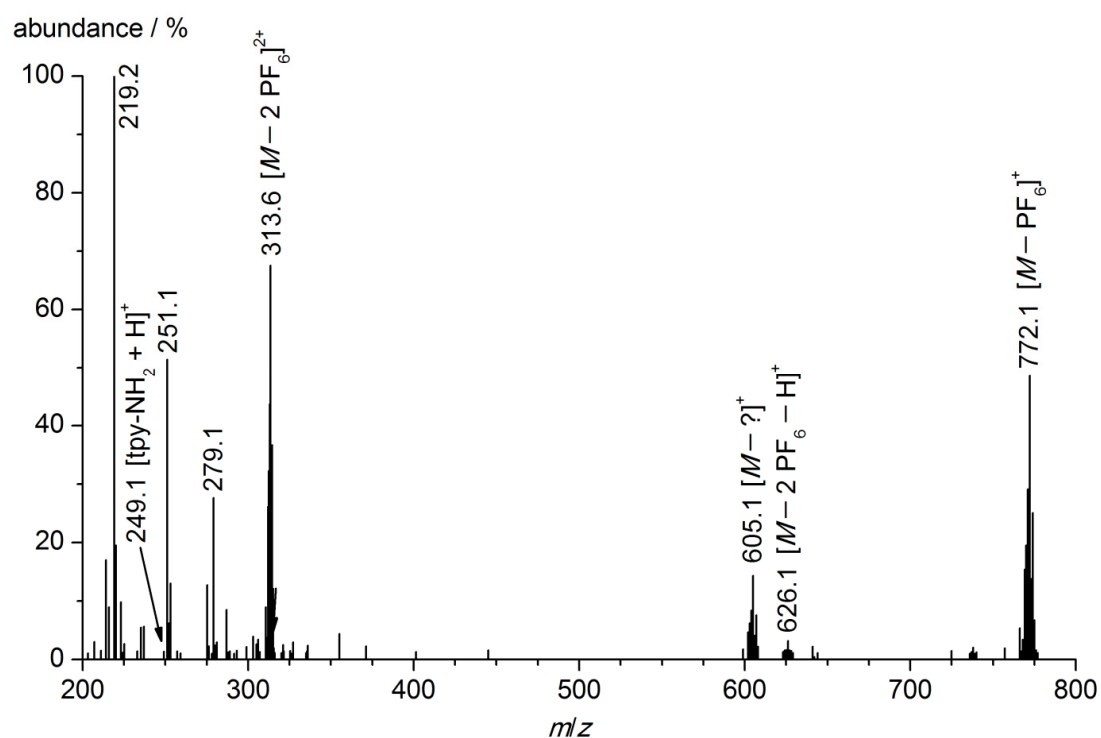


Figure S6. ESI⁺ mass spectrum of [1](PF₆)₂ in 0.5 M HNO₃ in H₂O 2 d after oxidation with 2.0 equiv (NH₄)₂[Ce(NO₃)₆].

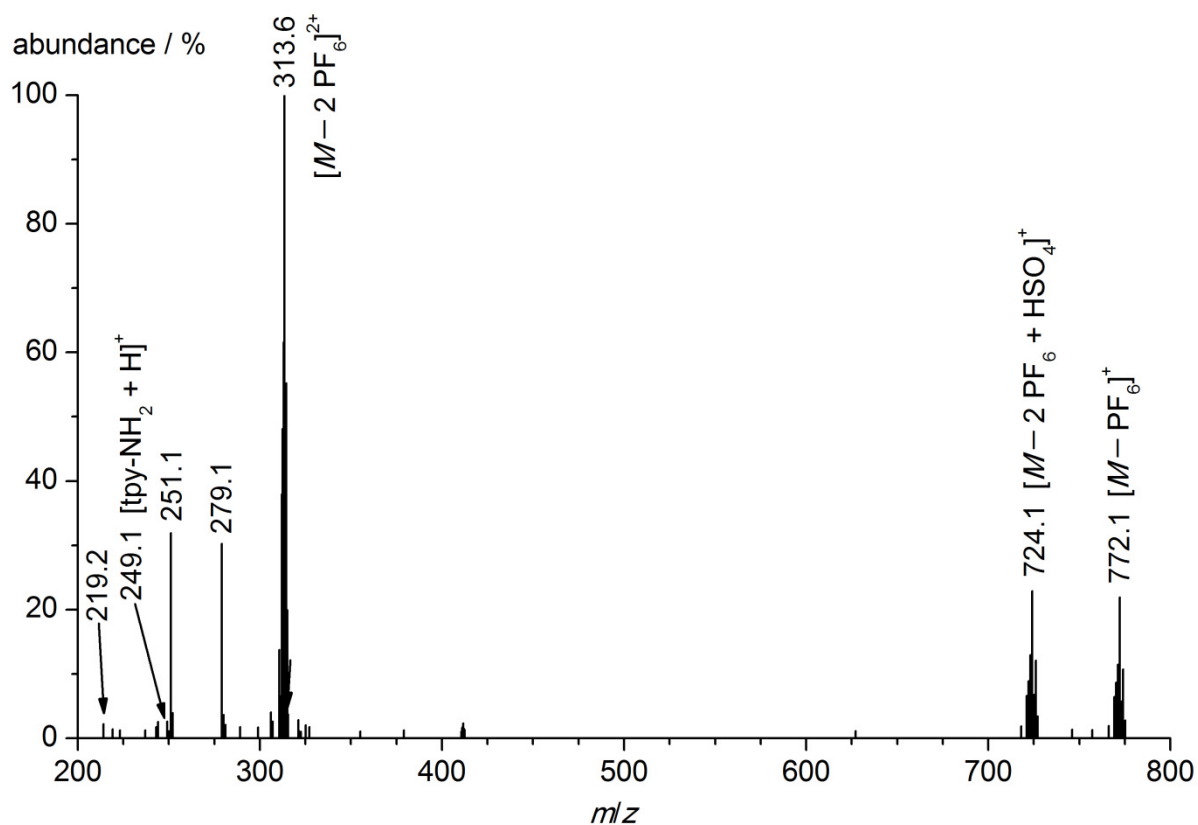


Figure S7. ESI⁺ mass spectrum of [1](PF₆)₂ in 0.1 M H₂SO₄ in H₂O before addition of Ce(SO₄)₂ • 4 H₂O.

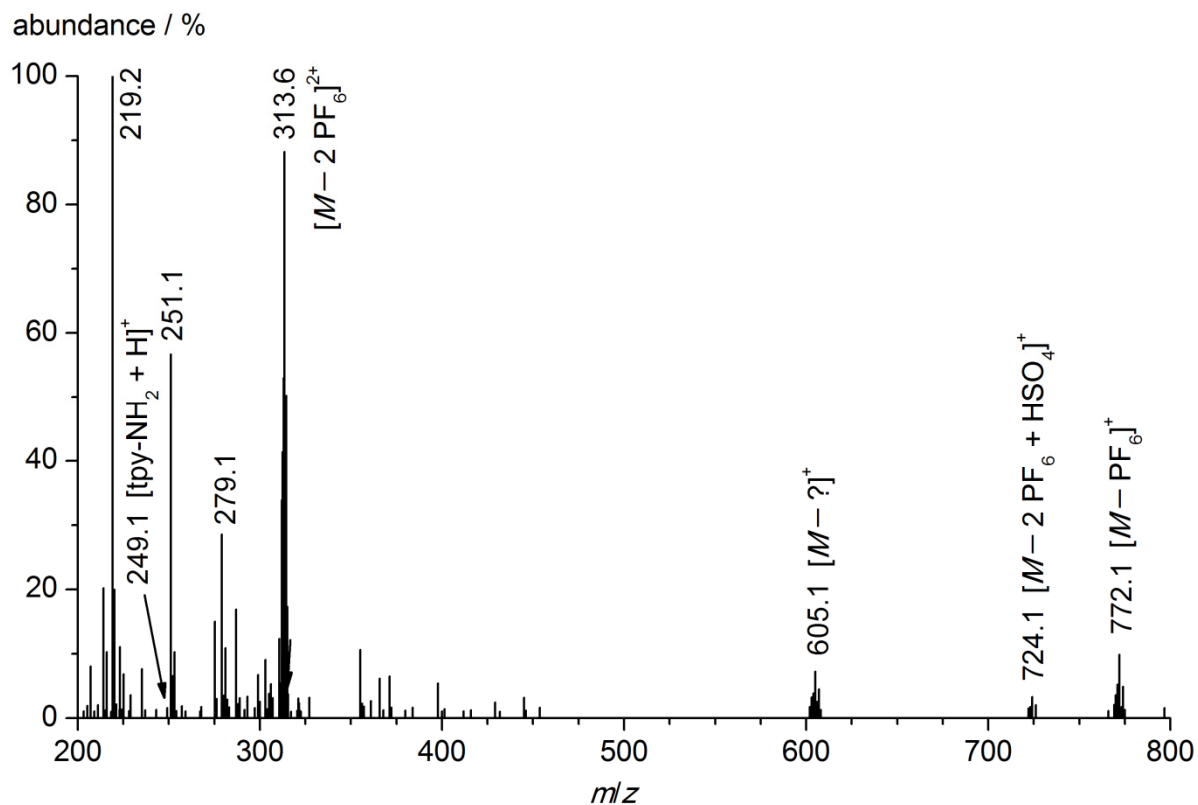


Figure S8. ESI⁺ mass spectrum of [1](PF₆)₂ in 0.1 M H₂SO₄ in H₂O 2 d after oxidation with 2.0 equiv Ce(SO₄)₂ • 4 H₂O.

Preparation of the IrCl(PET₃)₃ solution^[1]: [Ir(COE)₂Cl]₂ (178.3 mg, 0.199 mmol, 1.0 equiv) was dissolved in abs. THF (17 ml; COE = cyclooctene). The orange solution turned red when a solution of PET₃ (1 M in THF, 1.2 ml, 1.2 mmol, 6.0 equiv) was added. The mixture was stirred for 4 h at room temperature. Then the solvent and excess PET₃ were removed under reduced pressure. The red solid was dissolved in 7.2 ml d₈-THF and a red solution of IrCl(PET₃)₃ was obtained (55 mM). IrCl(PET₃)₃ reversibly reacts with O₂ under formation of IrCl(O₂)(PET₃)₃.^[2] Figure S9 shows ³¹P-NMR spectra before and after bubbling an excess of air through the solution.

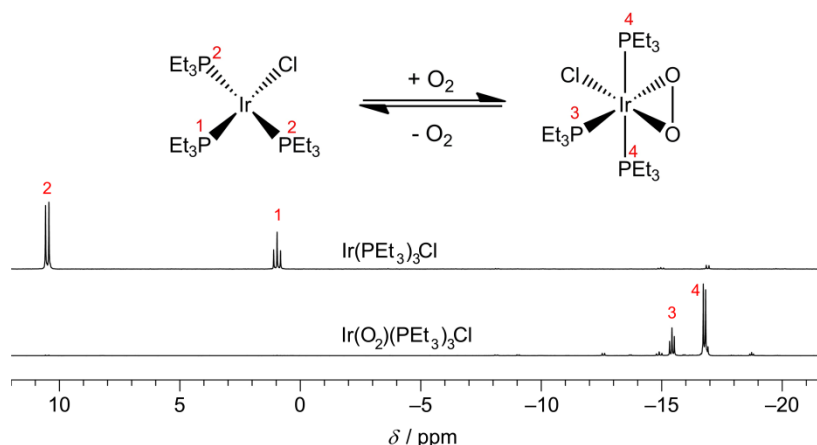


Figure S9. ³¹P-NMR spectra, structures and phosphorus atom numbering of IrCl(PET₃)₃ and IrCl(O₂)(PET₃)₃ in d₈-THF.

IrCl(PET₃)₃ and its oxygen adduct IrCl(O₂)(PET₃)₃ show the following ³¹P-NMR characteristics in accordance with literature data^[2]:

IrCl(PET₃)₃: ³¹P-NMR (d₈-THF, 162 MHz): $\delta = 10.5$ (d, 24.0 Hz, 2 P, P²), 9.0 ppm (t, 24.0 Hz, 1 P, P¹).

IrCl(O₂)(PET₃)₃: ³¹P-NMR (d₈-THF, 162 MHz): $\delta = -15.5$ (t, 15.6 Hz, 1 P, P³), -16.8 ppm (d, 15.6 Hz, 2 P, P⁴).

[1] A. L. Casalnuovo, J. C. Calabrese, D. Milstein, *J. Am. Chem. Soc.* **1988**, *110*, 6738–6744.

[2] S. W. Kohl, L. Weiner, L. Schwartzburd, L. Konstantinovski, L. J. W. Shimon, Y. Ben-David, M. A. Iron, D. Milstein, *Science* **2009**, *324*, 74–77.

DFT-optimized Cartesian Coordinates of [I]²⁺ (singlet) in H₂O in Å.

6	2.345932000	1.227034000	0.000056000
6	3.745880000	1.259502000	0.000365000
6	4.457632000	0.040748000	-0.000607000
6	3.767095000	-1.189673000	-0.001892000
6	2.365520000	-1.177243000	-0.002196000
7	1.693729000	0.019176000	-0.001193000
1	4.294158000	2.194070000	0.001415000
1	4.324431000	-2.117441000	-0.002560000
6	-0.835580000	3.076620000	0.002348000
6	-0.460851000	4.427858000	0.003143000
6	0.907443000	4.756607000	0.002939000
6	1.858166000	3.722892000	0.001951000
6	1.429494000	2.385531000	0.001186000
7	0.079193000	2.072608000	0.001377000
1	1.227783000	5.793175000	0.003513000
1	-1.878145000	2.782458000	0.002503000
1	-1.226590000	5.195430000	0.003888000
1	2.916408000	3.956674000	0.001746000
6	1.467855000	-2.350346000	-0.003413000
6	1.917532000	-3.680929000	-0.004957000
6	0.983156000	-4.729462000	-0.006189000

6	-0.390209000	-4.422276000	-0.005929000
6	-0.786061000	-3.077170000	-0.004353000
7	0.112761000	-2.058854000	-0.003045000
1	1.319705000	-5.760874000	-0.007345000
1	2.979327000	-3.898074000	-0.005214000
1	-1.143852000	-5.201712000	-0.006903000
1	-1.833062000	-2.799455000	-0.004113000
6	-2.983720000	-0.020585000	1.194604000
6	-4.378794000	-0.033018000	1.229899000
6	-5.109048000	-0.038835000	0.003570000
6	-4.380885000	-0.030577000	-1.223984000
6	-2.985756000	-0.018227000	-1.190997000
7	-2.317904000	-0.013952000	0.001238000
1	-4.913161000	-0.038252000	2.173097000
1	-4.916806000	-0.033900000	-2.166312000
6	0.186433000	0.006603000	3.076521000
6	-0.199143000	0.003739000	4.424349000
6	-1.569786000	-0.007922000	4.740206000
6	-2.510304000	-0.016414000	3.696871000
6	-2.072287000	-0.012993000	2.363113000
7	-0.719180000	-0.001370000	2.063633000
1	-1.900198000	-0.010319000	5.773655000
1	1.232300000	0.015463000	2.794756000
1	0.560457000	0.010505000	5.197878000
1	-3.570482000	-0.025372000	3.920904000
6	-2.076289000	-0.008267000	-2.361029000
6	-2.516561000	-0.009302000	-3.694056000
6	-1.577793000	0.001323000	-4.738951000
6	-0.206622000	0.012755000	-4.425363000
6	0.181212000	0.013196000	-3.078183000
7	-0.722688000	0.003047000	-2.063788000
1	-1.909929000	0.000720000	-5.771849000
1	-3.577117000	-0.018091000	-3.916305000
1	0.551691000	0.021151000	-5.200140000
1	1.227546000	0.021834000	-2.798148000
44	-0.295512000	0.003541000	-0.000426000
8	6.613661000	1.148068000	0.000993000
6	5.945539000	0.095901000	-0.000097000
8	6.523325000	-1.152892000	-0.000961000
7	-6.479088000	-0.052174000	0.004733000
1	-7.003176000	-0.059026000	0.869213000
1	7.507019000	-1.110604000	-0.000592000
1	-7.004664000	-0.057368000	-0.858853000

DFT-optimized Cartesian Coordinates of $[1]^{3+}$ (doublet) in H_2O in Å.

6	2.339086000	1.039146000	-0.685533000
6	3.739758000	1.074493000	-0.729207000
6	4.463091000	0.088631000	-0.031293000
6	3.792121000	-0.906525000	0.704129000
6	2.389118000	-0.896918000	0.720919000
7	1.708088000	0.061586000	0.028784000
1	4.274110000	1.835121000	-1.284964000
1	4.359712000	-1.655902000	1.239366000
6	-0.870021000	2.516129000	-1.690720000
6	-0.520860000	3.628289000	-2.470061000
6	0.838217000	3.912334000	-2.686782000
6	1.812614000	3.076093000	-2.115372000
6	1.411503000	1.975842000	-1.345461000
7	0.072179000	1.705452000	-1.144978000
1	1.136203000	4.766336000	-3.285152000
1	-1.907136000	2.268239000	-1.506695000

1	-1.303911000	4.248245000	-2.890377000
1	2.865052000	3.282726000	-2.267564000
6	1.510705000	-1.837403000	1.440767000
6	1.968807000	-2.888834000	2.246231000
6	1.038235000	-3.711290000	2.904151000
6	-0.334712000	-3.458362000	2.743588000
6	-0.742064000	-2.392859000	1.927970000
7	0.158100000	-1.603877000	1.287274000
1	1.380219000	-4.528150000	3.530181000
1	3.031124000	-3.064935000	2.364798000
1	-1.084390000	-4.066563000	3.235833000
1	-1.791538000	-2.172277000	1.781441000
6	-3.047620000	0.619232000	0.881476000
6	-4.430285000	0.593050000	0.841876000
6	-5.087221000	-0.159489000	-0.190182000
6	-4.289174000	-0.867637000	-1.153707000
6	-2.910685000	-0.811622000	-1.062421000
7	-2.311269000	-0.076752000	-0.058078000
1	-5.023263000	1.128601000	1.573175000
1	-4.777814000	-1.434219000	-1.936843000
6	0.018097000	1.834016000	2.523547000
6	-0.439460000	2.620729000	3.592072000
6	-1.822798000	2.765103000	3.788306000
6	-2.711738000	2.117848000	2.911674000
6	-2.202654000	1.343295000	1.860725000
7	-0.837079000	1.211158000	1.676822000
1	-2.205606000	3.367499000	4.604990000
1	1.077151000	1.701628000	2.342299000
1	0.278919000	3.102258000	4.245130000
1	-3.781402000	2.219432000	3.050170000
6	-1.938074000	-1.482072000	-1.960884000
6	-2.305505000	-2.297673000	-3.038495000
6	-1.305970000	-2.894669000	-3.828407000
6	0.043684000	-2.662829000	-3.516973000
6	0.357266000	-1.838748000	-2.424889000
7	-0.604120000	-1.259323000	-1.665899000
1	-1.580086000	-3.527515000	-4.665550000
1	-3.350693000	-2.471569000	-3.263944000
1	0.844059000	-3.105619000	-4.098027000
1	1.386567000	-1.643156000	-2.153487000
44	-0.343847000	-0.000946000	0.018047000
8	6.602531000	0.991666000	-0.722116000
6	5.958249000	0.132976000	-0.095147000
8	6.538920000	-0.884108000	0.616252000
7	-6.436200000	-0.202405000	-0.258185000
1	-7.017448000	0.294498000	0.407405000
1	7.522858000	-0.865411000	0.579343000
1	-6.913190000	-0.730631000	-0.980240000

DFT-optimized Cartesian Coordinates of $[1 - H]^{2+}$ (doublet) in H_2O in Å.

6	2.377101000	1.013332000	-0.668955000
6	3.778779000	1.032189000	-0.707309000
6	4.499932000	0.046337000	-0.005207000
6	3.804674000	-0.934696000	0.729049000
6	2.402460000	-0.916682000	0.739834000
7	1.729948000	0.044846000	0.042725000
1	4.332688000	1.780679000	-1.260428000
1	4.378176000	-1.678981000	1.267726000
6	-0.815690000	2.534668000	-1.673416000
6	-0.452427000	3.644414000	-2.448336000
6	0.911256000	3.910439000	-2.663619000

6	1.874029000	3.059699000	-2.095083000
6	1.459640000	1.961031000	-1.328811000
7	0.116285000	1.708595000	-1.131234000
1	1.220599000	4.762803000	-3.258818000
1	-1.855851000	2.298766000	-1.490046000
1	-1.226746000	4.276672000	-2.866608000
1	2.929768000	3.251271000	-2.244188000
6	1.509866000	-1.846644000	1.457062000
6	1.953317000	-2.901940000	2.266703000
6	1.012825000	-3.713664000	2.922773000
6	-0.357869000	-3.447628000	2.757825000
6	-0.750971000	-2.380043000	1.939338000
7	0.159778000	-1.601642000	1.298906000
1	1.344533000	-4.533049000	3.551294000
1	3.013989000	-3.086564000	2.386990000
1	-1.114994000	-4.047645000	3.248808000
1	-1.797636000	-2.148704000	1.788300000
6	-3.032962000	0.627495000	0.862096000
6	-4.416298000	0.605842000	0.813787000
6	-5.068218000	-0.143749000	-0.222693000
6	-4.266087000	-0.854059000	-1.180787000
6	-2.887331000	-0.801402000	-1.080521000
7	-2.294076000	-0.068959000	-0.072864000
1	-5.012413000	1.142796000	1.541590000
1	-4.751239000	-1.419283000	-1.967160000
6	0.029757000	1.828567000	2.522308000
6	-0.430115000	2.615938000	3.589357000
6	-1.814093000	2.765139000	3.778739000
6	-2.701323000	2.122518000	2.896947000
6	-2.190164000	1.347003000	1.847485000
7	-0.823870000	1.209909000	1.671169000
1	-2.198623000	3.368026000	4.594306000
1	1.088873000	1.690885000	2.344345000
1	0.286557000	3.094241000	4.246710000
1	-3.771319000	2.228142000	3.030107000
6	-1.909434000	-1.473442000	-1.974149000
6	-2.272431000	-2.284210000	-3.056914000
6	-1.269700000	-2.880764000	-3.843416000
6	0.078902000	-2.653131000	-3.524219000
6	0.388300000	-1.833973000	-2.427108000
7	-0.576011000	-1.255765000	-1.670987000
1	-1.540785000	-3.509708000	-4.684539000
1	-3.316721000	-2.454269000	-3.289473000
1	0.881218000	-3.095220000	-4.103176000
1	1.416090000	-1.639839000	-2.148383000
44	-0.323185000	-0.001760000	0.017989000
8	6.591218000	0.958849000	-0.754994000
6	6.036521000	0.042728000	-0.037284000
8	6.615892000	-0.876875000	0.656064000
7	-6.418193000	-0.182116000	-0.300060000
1	-7.001617000	0.316883000	0.361604000
1	-6.891791000	-0.708194000	-1.025488000

DFT-optimized Cartesian Coordinates of $[1 - 2 \text{ H}]^+$ (doublet) in H_2O in Å.

6	-2.354807000	1.196201000	-0.007843000
6	-3.757813000	1.218302000	-0.010102000
6	-4.466861000	-0.000135000	-0.005773000
6	-3.757735000	-1.218517000	0.000699000
6	-2.354733000	-1.196312000	0.002612000
7	-1.695544000	-0.000031000	-0.001650000
1	-4.321707000	2.143137000	-0.015157000

1	-4.321581000	-2.143390000	0.004068000
6	0.814288000	3.071276000	-0.012058000
6	0.428859000	4.419245000	-0.017688000
6	-0.941394000	4.736782000	-0.020334000
6	-1.884451000	3.695719000	-0.017261000
6	-1.446611000	2.362234000	-0.011613000
7	-0.095461000	2.062843000	-0.009040000
1	-1.269644000	5.770826000	-0.024615000
1	1.859463000	2.787636000	-0.009721000
1	1.189413000	5.191677000	-0.019843000
1	-2.944772000	3.918674000	-0.019121000
6	-1.446470000	-2.362279000	0.009083000
6	-1.884229000	-3.695790000	0.014471000
6	-0.941108000	-4.736782000	0.020679000
6	0.429123000	-4.419148000	0.021477000
6	0.814470000	-3.071153000	0.015905000
7	-0.095338000	-2.062792000	0.009738000
1	-1.269298000	-5.770846000	0.024875000
1	-2.944536000	-3.918823000	0.013913000
1	1.189723000	-5.191522000	0.026302000
1	1.859626000	-2.787437000	0.016529000
6	2.979720000	-0.005418000	-1.204260000
6	4.364031000	-0.005644000	-1.232273000
6	5.116919000	-0.000040000	0.011111000
6	4.358481000	0.005494000	1.246991000
6	2.975382000	0.005363000	1.215383000
7	2.301977000	0.000008000	0.003738000
1	4.905951000	-0.009971000	-2.172394000
1	4.912872000	0.009684000	2.178052000
6	-0.193729000	-0.014215000	-3.076047000
6	0.187173000	-0.019897000	-4.425185000
6	1.557023000	-0.020809000	-4.745541000
6	2.503148000	-0.016126000	-3.707298000
6	2.068620000	-0.010564000	-2.372521000
7	0.718137000	-0.009543000	-2.070252000
1	1.882783000	-0.025092000	-5.780445000
1	-1.237848000	-0.013372000	-2.788110000
1	-0.574772000	-0.023451000	-5.196265000
1	3.562311000	-0.016789000	-3.936209000
6	2.060991000	0.010606000	2.380080000
6	2.491948000	0.016236000	3.716115000
6	1.542977000	0.021022000	4.751569000
6	0.173804000	0.020174000	4.427349000
6	-0.203363000	0.014447000	3.077285000
7	0.711419000	0.009660000	2.073878000
1	1.865813000	0.025325000	5.787407000
1	3.550763000	0.016859000	3.946666000
1	-0.590193000	0.023813000	5.196413000
1	-1.246694000	0.013669000	2.786490000
44	0.333881000	0.000043000	0.001077000
8	-6.574519000	1.156473000	-0.016102000
6	-6.002325000	-0.000205000	-0.008205000
8	-6.574424000	-1.156942000	-0.002256000
7	6.461372000	0.000483000	0.093263000
1	6.909218000	-0.003548000	-0.837938000

DFT-optimized Cartesian Coordinates of $[\text{Ru}(\kappa^2\text{-H}_2\text{N-tpy})(\kappa^3\text{-HOOC-tpy})(\text{H}_2\text{O})]^{3+}$ (doublet) in H_2O in Å.

6	-2.528788000	1.228951000	0.418211000
6	-3.909906000	1.429337000	0.292727000
6	-4.663957000	0.494960000	-0.445550000
6	-4.046609000	-0.620696000	-1.041993000

6	-2.657994000	-0.776191000	-0.898003000
7	-1.953797000	0.146242000	-0.183950000
1	-4.408483000	2.275737000	0.748936000
1	-4.643985000	-1.331892000	-1.596759000
6	0.683358000	2.283634000	1.883320000
6	0.372386000	3.429128000	2.631127000
6	-0.953381000	3.895736000	2.641661000
6	-1.937778000	3.202500000	1.912813000
6	-1.575857000	2.063867000	1.182525000
7	-0.262537000	1.625177000	1.169014000
1	-1.221987000	4.778825000	3.211402000
1	1.688148000	1.882230000	1.848526000
1	1.154026000	3.932794000	3.187483000
1	-2.965298000	3.545625000	1.924453000
6	-1.824848000	-1.864522000	-1.451941000
6	-2.330202000	-2.917305000	-2.226683000
6	-1.450185000	-3.897822000	-2.718466000
6	-0.079482000	-3.800227000	-2.426121000
6	0.373921000	-2.726802000	-1.644173000
7	-0.473209000	-1.783765000	-1.165758000
1	-1.830102000	-4.716559000	-3.319897000
1	-3.388230000	-2.977353000	-2.450535000
1	0.631625000	-4.531388000	-2.792107000
1	1.423898000	-2.615033000	-1.409338000
6	3.304158000	0.166376000	-0.518955000
6	4.510538000	-0.535635000	-0.597531000
6	4.681222000	-1.784593000	0.060298000
6	3.609722000	-2.209525000	0.888128000
6	2.420439000	-1.485856000	0.912420000
7	2.200061000	-0.349962000	0.142437000
1	5.331280000	-0.123520000	-1.172155000
1	3.716651000	-3.109497000	1.479880000
6	2.427899000	3.347346000	-2.357521000
6	3.549567000	4.154001000	-2.151006000
6	4.593837000	3.649120000	-1.355117000
6	4.495429000	2.356194000	-0.812246000
6	3.356709000	1.564184000	-1.067155000
7	2.359939000	2.100697000	-1.824780000
1	5.471321000	4.253482000	-1.150859000
1	1.572141000	3.670270000	-2.937676000
1	3.591412000	5.144527000	-2.586942000
1	5.284802000	1.974548000	-0.177881000
6	1.317649000	-1.878965000	1.823163000
6	1.471468000	-2.789569000	2.883975000
6	0.385474000	-3.058858000	3.731184000
6	-0.841545000	-2.407317000	3.508316000
6	-0.941817000	-1.514641000	2.437171000
7	0.112656000	-1.259215000	1.617457000
1	0.498477000	-3.757566000	4.553268000
1	2.423144000	-3.270993000	3.066529000
1	-1.701695000	-2.582299000	4.143589000
1	-1.868951000	-0.997756000	2.228411000
8	-6.736137000	1.691419000	-0.066289000
6	-6.138487000	0.725137000	-0.570846000
8	-6.756588000	-0.250871000	-1.307343000
7	5.826583000	-2.506240000	-0.062788000
1	6.589812000	-2.185984000	-0.645036000
1	-7.727119000	-0.108508000	-1.396256000
1	5.949974000	-3.385040000	0.423616000
44	0.036013000	-0.039396000	-0.068002000
1	1.405432000	1.560687000	-1.950646000
1	-0.632442000	1.154297000	-2.318534000

8 0.163482000 0.948394000 -1.789268000

DFT-optimized Cartesian Coordinates of "[Ru(κ^3 -H₂N-tpy)(κ^3 -HOOC-tpy)]³⁺ + H₂O" (doublet) in H₂O in Å.

6	-2.255210000	-0.095835000	1.223861000
6	-3.650869000	-0.213871000	1.263436000
6	-4.352203000	-0.352928000	0.051528000
6	-3.664856000	-0.359978000	-1.175894000
6	-2.267526000	-0.239205000	-1.161610000
7	-1.606993000	-0.124922000	0.024696000
1	-4.198513000	-0.199847000	2.197784000
1	-4.215626000	-0.456252000	-2.102223000
6	0.913505000	0.320855000	3.036137000
6	0.542108000	0.422064000	4.384127000
6	-0.818827000	0.343315000	4.725933000
6	-1.772659000	0.166624000	3.709140000
6	-1.350186000	0.068565000	2.376245000
7	-0.008627000	0.142659000	2.055567000
1	-1.133978000	0.420366000	5.760855000
1	1.952730000	0.374394000	2.738704000
1	1.308905000	0.559883000	5.137311000
1	-2.826241000	0.110511000	3.954979000
6	-1.375578000	-0.211890000	-2.334963000
6	-1.815668000	-0.269762000	-3.664347000
6	-0.876133000	-0.205182000	-4.707376000
6	0.488346000	-0.079824000	-4.394309000
6	0.877645000	-0.025441000	-3.048579000
7	-0.030773000	-0.095555000	-2.041625000
1	-1.204456000	-0.248190000	-5.740169000
1	-2.872190000	-0.358562000	-3.886303000
1	1.244806000	-0.023699000	-5.168222000
1	1.920351000	0.067206000	-2.773297000
6	3.099225000	1.124915000	-0.074121000
6	4.483456000	1.138899000	-0.090854000
6	5.196291000	-0.105422000	-0.040146000
6	4.451911000	-1.333381000	0.029301000
6	3.069604000	-1.286935000	0.044486000
7	2.415814000	-0.072657000	-0.007984000
1	5.033477000	2.070725000	-0.143121000
1	4.982617000	-2.276917000	0.071320000
6	-0.060849000	3.023940000	-0.153708000
6	0.346765000	4.367920000	-0.221378000
6	1.716705000	4.674036000	-0.239845000
6	2.653187000	3.625604000	-0.191422000
6	2.200720000	2.301892000	-0.124946000
7	0.845346000	2.015785000	-0.106177000
1	2.054651000	5.703596000	-0.291398000
1	-1.118800000	2.769000000	-0.140813000
1	-0.406591000	5.146489000	-0.258323000
1	3.714626000	3.842180000	-0.206062000
6	2.149367000	-2.449583000	0.118917000
6	2.578941000	-3.781044000	0.183758000
6	1.626757000	-4.814077000	0.258936000
6	0.260664000	-4.488407000	0.268815000
6	-0.115910000	-3.138206000	0.200623000
7	0.799652000	-2.141823000	0.125458000
1	1.949336000	-5.848437000	0.309737000
1	3.636022000	-4.017704000	0.177936000
1	-0.504494000	-5.253548000	0.327689000
1	-1.159546000	-2.851759000	0.207584000
8	-6.499764000	-0.485589000	1.165080000

6	-5.841697000	-0.478822000	0.109796000
8	-6.405690000	-0.583527000	-1.135486000
7	6.548310000	-0.126336000	-0.057280000
1	7.091070000	0.728159000	-0.105680000
1	-7.386821000	-0.663704000	-1.105979000
1	7.064845000	-0.997689000	-0.024643000
44	0.442632000	-0.052313000	0.009353000
1	-3.656912000	3.048101000	-0.982642000
1	-3.654450000	3.192280000	0.606575000
8	-3.151029000	2.868133000	-0.165969000

Results of the TD-DFT (singlet) calculation of $[1]^{2+}$ in H_2O .

Excited State 1:	Singlet-A	1.9750 eV	627.78 nm	f=0.0000	<S**2>=0.000
141 ->145	-0.10870				
144 ->145	0.69246				
Excited State 2:	Singlet-A	2.1153 eV	586.12 nm	f=0.0052	<S**2>=0.000
143 ->145	0.69916				
Excited State 3:	Singlet-A	2.5469 eV	486.80 nm	f=0.1455	<S**2>=0.000
142 ->145	0.57686				
143 ->146	0.31690				
143 ->148	-0.11544				
144 ->147	0.20329				
Excited State 4:	Singlet-A	2.5876 eV	479.15 nm	f=0.0007	<S**2>=0.000
144 ->146	0.68512				
144 ->148	-0.12805				
Excited State 5:	Singlet-A	2.7334 eV	453.59 nm	f=0.0001	<S**2>=0.000
143 ->147	0.51478				
144 ->146	0.12725				
144 ->148	0.45975				
Excited State 6:	Singlet-A	2.7443 eV	451.79 nm	f=0.0721	<S**2>=0.000
143 ->146	-0.24029				
143 ->148	0.27371				
144 ->147	0.59561				
Excited State 7:	Singlet-A	2.7968 eV	443.31 nm	f=0.0831	<S**2>=0.000
143 ->147	-0.47471				
144 ->148	0.50770				
Excited State 8:	Singlet-A	2.8227 eV	439.25 nm	f=0.0399	<S**2>=0.000
142 ->146	0.68338				
142 ->148	-0.13124				
Excited State 9:	Singlet-A	2.8327 eV	437.69 nm	f=0.0000	<S**2>=0.000
142 ->147	0.70338				
Excited State 10:	Singlet-A	2.8766 eV	431.00 nm	f=0.1498	<S**2>=0.000
142 ->145	-0.23294				
143 ->146	0.55124				
143 ->148	0.35878				
Excited State 11:	Singlet-A	2.9978 eV	413.59 nm	f=0.0002	<S**2>=0.000
142 ->146	0.13946				
142 ->148	0.68534				
Excited State 12:	Singlet-A	3.2041 eV	386.95 nm	f=0.0000	<S**2>=0.000
142 ->145	0.26190				
143 ->146	-0.17335				
143 ->148	0.51695				
143 ->153	0.19386				
144 ->147	-0.27442				
Excited State 13:	Singlet-A	3.3095 eV	374.63 nm	f=0.0000	<S**2>=0.000
144 ->149	0.69057				
Excited State 14:	Singlet-A	3.5000 eV	354.24 nm	f=0.0025	<S**2>=0.000
144 ->150	0.70082				
Excited State 15:	Singlet-A	3.5055 eV	353.69 nm	f=0.0000	<S**2>=0.000
143 ->154	0.68831				
Excited State 16:	Singlet-A	3.5162 eV	352.61 nm	f=0.0227	<S**2>=0.000

139 ->145	-0.25148			
143 ->149	0.64439			
Excited State 17:	Singlet-A	3.6070 eV	343.73 nm	f=0.0000 <S**2>=0.000
141 ->145	0.69083			
144 ->145	0.10958			
Excited State 18:	Singlet-A	3.6122 eV	343.24 nm	f=0.0862 <S**2>=0.000
142 ->149	0.68142			
Excited State 19:	Singlet-A	3.6767 eV	337.22 nm	f=0.0172 <S**2>=0.000
140 ->145	0.68809			
143 ->149	0.10246			
Excited State 20:	Singlet-A	3.6851 eV	336.45 nm	f=0.0047 <S**2>=0.000
143 ->150	0.18307			
144 ->151	0.67215			
Excited State 21:	Singlet-A	3.6985 eV	335.23 nm	f=0.0019 <S**2>=0.000
142 ->154	-0.16061			
144 ->153	0.67319			
Excited State 22:	Singlet-A	3.7257 eV	332.78 nm	f=0.0433 <S**2>=0.000
143 ->150	0.66581			
144 ->151	-0.19306			
Excited State 23:	Singlet-A	3.7552 eV	330.17 nm	f=0.0536 <S**2>=0.000
139 ->145	-0.30303			
142 ->150	0.53909			
142 ->153	-0.12772			
143 ->149	-0.10597			
144 ->154	-0.25204			
Excited State 24:	Singlet-A	3.7665 eV	329.18 nm	f=0.2028 <S**2>=0.000
139 ->145	0.52022			
142 ->150	0.20038			
143 ->149	0.22205			
143 ->152	-0.17578			
144 ->154	-0.23572			
144 ->158	-0.13462			
Excited State 25:	Singlet-A	3.7762 eV	328.33 nm	f=0.0000 <S**2>=0.000
144 ->152	0.69464			
Excited State 26:	Singlet-A	3.7887 eV	327.25 nm	f=0.0455 <S**2>=0.000
139 ->145	0.10903			
141 ->154	-0.12333			
142 ->150	0.40099			
142 ->153	0.15864			
144 ->154	0.47164			
144 ->158	0.17466			
Excited State 27:	Singlet-A	3.8519 eV	321.88 nm	f=0.0173 <S**2>=0.000
140 ->147	0.23051			
143 ->151	0.65801			
Excited State 28:	Singlet-A	3.9279 eV	315.65 nm	f=0.0000 <S**2>=0.000
142 ->151	0.70602			
Excited State 29:	Singlet-A	3.9370 eV	314.92 nm	f=0.0001 <S**2>=0.000
142 ->154	0.62189			
142 ->158	-0.26124			
144 ->153	0.15388			
Excited State 30:	Singlet-A	3.9710 eV	312.23 nm	f=0.0709 <S**2>=0.000
139 ->145	0.17217			
142 ->153	-0.44057			
143 ->152	0.48006			
144 ->154	0.10257			
144 ->158	0.14432			
Excited State 31:	Singlet-A	3.9882 eV	310.88 nm	f=0.0706 <S**2>=0.000
139 ->145	0.11096			
142 ->153	0.45465			
143 ->152	0.45862			
144 ->158	-0.21776			
Excited State 32:	Singlet-A	4.0502 eV	306.12 nm	f=0.0085 <S**2>=0.000

142 ->152	0.69614		
Excited State 33:	Singlet-A	4.0790 eV	303.95 nm f=0.0377 <S**2>=0.000
140 ->147	0.15337		
141 ->146	0.58621		
141 ->148	0.32934		
143 ->151	-0.11653		
Excited State 34:	Singlet-A	4.1049 eV	302.04 nm f=0.0022 <S**2>=0.000
140 ->146	-0.11582		
141 ->147	0.54619		
143 ->153	0.37082		
144 ->147	0.11367		
144 ->155	-0.10703		
Excited State 35:	Singlet-A	4.1417 eV	299.35 nm f=0.0818 <S**2>=0.000
140 ->147	0.26880		
141 ->146	-0.37987		
141 ->148	0.50095		
143 ->151	-0.12920		
Excited State 36:	Singlet-A	4.1720 eV	297.18 nm f=0.0001 <S**2>=0.000
139 ->146	-0.13244		
140 ->146	0.66731		
140 ->148	-0.12635		
141 ->147	0.12697		
Excited State 37:	Singlet-A	4.2541 eV	291.45 nm f=0.3151 <S**2>=0.000
140 ->147	0.57867		
141 ->148	-0.34301		
143 ->151	-0.16253		
Excited State 38:	Singlet-A	4.2675 eV	290.53 nm f=0.0008 <S**2>=0.000
136 ->145	0.65669		
136 ->149	0.22666		
Excited State 39:	Singlet-A	4.2763 eV	289.94 nm f=0.0130 <S**2>=0.000
141 ->158	-0.16381		
142 ->153	0.20544		
144 ->154	-0.30325		
144 ->158	0.56756		
Excited State 40:	Singlet-A	4.2922 eV	288.86 nm f=0.0180 <S**2>=0.000
140 ->146	0.10292		
140 ->148	0.19368		
141 ->147	-0.37843		
142 ->145	-0.12919		
143 ->153	0.49101		
Excited State 41:	Singlet-A	4.3518 eV	284.90 nm f=0.0465 <S**2>=0.000
139 ->147	0.70015		
Excited State 42:	Singlet-A	4.4032 eV	281.58 nm f=0.0314 <S**2>=0.000
137 ->145	-0.20112		
139 ->146	0.51274		
139 ->148	0.38877		
140 ->146	0.10739		
140 ->148	0.15620		
Excited State 43:	Singlet-A	4.4537 eV	278.39 nm f=0.0000 <S**2>=0.000
138 ->145	0.70297		
Excited State 44:	Singlet-A	4.4662 eV	277.60 nm f=0.0925 <S**2>=0.000
137 ->145	0.30491		
139 ->146	-0.30659		
139 ->148	0.49830		
140 ->148	0.22595		
Excited State 45:	Singlet-A	4.5271 eV	273.87 nm f=0.1573 <S**2>=0.000
139 ->148	-0.26896		
140 ->148	0.57427		
141 ->147	0.14123		
143 ->153	-0.18681		
144 ->155	-0.12126		
Excited State 46:	Singlet-A	4.6147 eV	268.67 nm f=0.0024 <S**2>=0.000

142 ->154	0.25091				
142 ->158	0.64013				
Excited State 47:	Singlet-A	4.6307 eV	267.74 nm	f=0.3221	<S**2>=0.000
137 ->145	0.58807				
139 ->146	0.30995				
139 ->148	-0.11426				
Excited State 48:	Singlet-A	4.7889 eV	258.90 nm	f=0.0000	<S**2>=0.000
141 ->149	0.67820				
143 ->158	-0.14964				
Excited State 49:	Singlet-A	4.8280 eV	256.80 nm	f=0.0000	<S**2>=0.000
141 ->149	0.15706				
143 ->158	0.66443				
Excited State 50:	Singlet-A	4.8325 eV	256.56 nm	f=0.0156	<S**2>=0.000
139 ->149	0.32655				
140 ->149	0.60284				

Results of the TD-DFT (doublet) calculation of [1]³⁺ in H₂O.

Excited State 1:	2.008-A	0.3658 eV	3388.97 nm	f=0.0009	<S**2>=0.758
139B ->144B	0.26181				
141B ->144B	-0.19275				
143B ->144B	0.91551				
143B ->147B	-0.10577				
Excited State 2:	2.007-A	0.5367 eV	2310.28 nm	f=0.0000	<S**2>=0.757
127B ->144B	0.10736				
137B ->144B	-0.10498				
142B ->144B	0.96680				
142B ->147B	-0.11855				
Excited State 3:	2.122-A	1.8129 eV	683.89 nm	f=0.1535	<S**2>=0.876
144A ->146A	0.18133				
141B ->144B	0.93145				
143B ->144B	0.21801				
Excited State 4:	2.110-A	1.8555 eV	668.19 nm	f=0.0118	<S**2>=0.863
139B ->144B	0.48220				
140B ->144B	0.83199				
143B ->144B	-0.20153				
Excited State 5:	2.042-A	2.0387 eV	608.17 nm	f=0.0011	<S**2>=0.793
139B ->144B	0.81370				
140B ->144B	-0.52923				
141B ->144B	0.13497				
143B ->144B	-0.17997				
Excited State 6:	3.092-A	2.6440 eV	468.92 nm	f=0.0061	<S**2>=2.140
140A ->147A	0.12066				
141A ->145A	-0.18966				
141A ->147A	0.16086				
142A ->145A	-0.29651				
143A ->145A	0.11777				
143A ->147A	-0.16660				
138B ->144B	0.53468				
139B ->146B	-0.17131				
140B ->146B	0.16444				
142B ->145B	0.50119				
143B ->145B	-0.25299				
143B ->146B	0.15189				
Excited State 7:	2.586-A	2.6460 eV	468.58 nm	f=0.0013	<S**2>=1.422
141A ->145A	0.14130				
141A ->147A	-0.11314				
142A ->145A	0.22506				
138B ->144B	0.81745				
139B ->146B	0.10435				
140B ->146B	-0.11907				
142B ->145B	-0.28673				

143B ->145B	0.18022				
143B ->146B	-0.10932				
Excited State 8:	3.309-A	2.6728 eV	463.88 nm	f=0.0006	<S**2>=2.488
142A ->145A	-0.23286				
143A ->145A	-0.31601				
140B ->145B	0.21285				
141B ->145B	-0.13785				
142B ->145B	0.23888				
143B ->145B	0.77350				
Excited State 9:	2.050-A	2.7676 eV	447.98 nm	f=0.0000	<S**2>=0.801
137B ->144B	0.98046				
142B ->144B	0.12704				
Excited State 10:	3.456-A	2.8968 eV	428.00 nm	f=0.0000	<S**2>=2.737
128A ->150A	-0.11573				
140A ->149A	0.10119				
140A ->150A	-0.29653				
143A ->149A	0.18061				
143A ->150A	-0.51427				
144A ->150A	-0.16550				
139B ->152B	0.19455				
141B ->152B	-0.12517				
143B ->149B	-0.10247				
143B ->152B	0.58235				
143B ->154B	0.27497				
Excited State 11:	2.568-A	2.9434 eV	421.23 nm	f=0.0001	<S**2>=1.398
141A ->145A	-0.28017				
142A ->145A	0.14813				
143A ->145A	0.69651				
144A ->145A	0.16119				
139B ->145B	0.28202				
140B ->145B	-0.16188				
143B ->145B	0.47082				
Excited State 12:	3.417-A	3.0158 eV	411.11 nm	f=0.0075	<S**2>=2.669
138A ->145A	0.14716				
140A ->147A	-0.11423				
141A ->147A	-0.25876				
142A ->145A	-0.23245				
142A ->147A	0.12603				
143A ->146A	0.13532				
143A ->147A	0.33923				
143A ->148A	-0.13566				
137B ->145B	-0.13941				
139B ->146B	0.19530				
140B ->146B	-0.24146				
140B ->147B	-0.10522				
142B ->145B	0.49361				
143B ->146B	-0.37841				
143B ->148B	-0.11454				
Excited State 13:	3.373-A	3.0429 eV	407.46 nm	f=0.0059	<S**2>=2.594
136A ->146A	-0.13093				
139A ->146A	0.15298				
140A ->148A	-0.16651				
141A ->148A	0.33865				
142A ->148A	-0.13341				
143A ->147A	0.12169				
143A ->148A	0.37896				
144A ->146A	0.11787				
144A ->148A	0.17445				
134B ->144B	0.13486				
138B ->144B	0.13186				
138B ->147B	-0.15508				
139B ->147B	0.13004				

139B ->148B	-0.11718				
140B ->147B	0.21938				
140B ->148B	-0.29254				
141B ->148B	-0.10323				
142B ->145B	0.14644				
143B ->146B	-0.10926				
143B ->147B	-0.24039				
143B ->148B	0.33938				
Excited State 14:	3.217-A	3.0813 eV	402.38 nm	f=0.0054	<S**2>=2.337
139A ->148A	0.14126				
141A ->146A	0.19346				
143A ->146A	0.34775				
143A ->147A	-0.12636				
143A ->148A	0.10827				
144A ->145A	-0.24086				
144A ->146A	0.27921				
144A ->148A	-0.20096				
135B ->144B	-0.26193				
138B ->148B	-0.12251				
139B ->144B	0.10581				
140B ->147B	-0.12880				
141B ->148B	-0.19969				
143B ->147B	0.47774				
143B ->148B	0.19931				
Excited State 15:	2.510-A	3.0832 eV	402.13 nm	f=0.0002	<S**2>=1.325
136A ->145A	0.10065				
139A ->145A	0.13035				
140A ->145A	0.15936				
141A ->145A	0.13064				
144A ->145A	0.89167				
139B ->145B	-0.15911				
140B ->145B	0.11879				
143B ->147B	0.13156				
Excited State 16:	3.055-A	3.1709 eV	391.00 nm	f=0.0008	<S**2>=2.083
140A ->145A	0.45147				
141A ->145A	0.28698				
142A ->145A	-0.13040				
143A ->145A	0.53433				
144A ->145A	-0.24683				
139B ->145B	-0.40701				
140B ->145B	0.33275				
142B ->146B	0.10895				
Excited State 17:	3.453-A	3.1864 eV	389.11 nm	f=0.0010	<S**2>=2.731
127A ->150A	-0.10798				
138A ->150A	0.10979				
141A ->150A	-0.24585				
142A ->149A	0.20008				
142A ->150A	-0.57020				
142B ->149B	-0.10855				
142B ->152B	0.61066				
142B ->154B	0.28870				
Excited State 18:	2.041-A	3.2040 eV	386.96 nm	f=0.0000	<S**2>=0.792
136B ->144B	0.99860				
Excited State 19:	2.304-A	3.2309 eV	383.74 nm	f=0.0252	<S**2>=1.078
142A ->145A	0.11810				
144A ->146A	0.42397				
134B ->144B	-0.22185				
135B ->144B	0.79032				
141B ->147B	0.13368				
143B ->147B	0.17595				
Excited State 20:	2.543-A	3.2503 eV	381.45 nm	f=0.0239	<S**2>=1.367
139A ->148A	0.10151				

141A ->146A	0.13863	
143A ->146A	0.25853	
144A ->146A	-0.46182	
144A ->148A	-0.24144	
134B ->144B	0.43694	
135B ->144B	0.48031	
141B ->144B	0.13202	
141B ->148B	-0.28629	
Excited State 21:	2.809-A	3.3091 eV 374.68 nm f=0.0256 <S**2>=1.723
141A ->145A	0.11404	
141A ->148A	-0.11786	
142A ->145A	0.27456	
143A ->146A	0.11624	
143A ->148A	-0.15315	
144A ->148A	0.53025	
131B ->144B	-0.12220	
134B ->144B	0.40026	
141B ->147B	-0.17554	
141B ->148B	0.29260	
142B ->145B	0.19186	
143B ->147B	0.16959	
143B ->148B	0.31225	
Excited State 22:	2.538-A	3.3234 eV 373.07 nm f=0.0714 <S**2>=1.360
141A ->145A	0.18912	
142A ->145A	0.45056	
143A ->146A	-0.19706	
144A ->146A	0.22140	
144A ->148A	-0.36023	
126B ->144B	-0.10475	
134B ->144B	0.35127	
135B ->144B	-0.18647	
141B ->147B	0.22787	
142B ->145B	0.32912	
143B ->146B	0.29040	
143B ->148B	-0.17173	
Excited State 23:	2.083-A	3.3374 eV 371.50 nm f=0.0008 <S**2>=0.835
127B ->144B	-0.16182	
128B ->144B	-0.10050	
130B ->144B	0.16340	
132B ->144B	-0.15240	
133B ->144B	0.91000	
134B ->144B	-0.13166	
142B ->144B	0.10096	
142B ->147B	0.12584	
Excited State 24:	2.034-A	3.3931 eV 365.40 nm f=0.0001 <S**2>=0.784
128A ->150A	0.10177	
140A ->150A	0.30191	
143A ->149A	-0.19602	
143A ->150A	0.57043	
143A ->155A	-0.11938	
144A ->150A	0.13240	
139B ->152B	0.16283	
141B ->145B	-0.10377	
141B ->152B	-0.10802	
143B ->149B	-0.11152	
143B ->152B	0.53291	
143B ->154B	0.24984	
Excited State 25:	2.375-A	3.4026 eV 364.38 nm f=0.0004 <S**2>=1.160
141A ->145A	-0.12162	
142A ->145A	-0.31509	
143A ->146A	-0.28799	
144A ->146A	0.15601	

133B ->144B	0.11419	
134B ->144B	0.57490	
139B ->146B	-0.12350	
141B ->147B	0.12836	
141B ->148B	0.10331	
142B ->145B	-0.28324	
143B ->146B	-0.39710	
143B ->147B	0.18850	
143B ->148B	-0.12237	
Excited State 26:	2.279-A	3.5016 eV 354.08 nm f=0.0192 <S**2>=1.049
141A ->146A	-0.17362	
142A ->150A	-0.10596	
143A ->146A	-0.44952	
143A ->147A	0.13111	
144A ->146A	-0.34208	
144A ->148A	-0.18543	
128B ->144B	-0.12354	
129B ->144B	-0.10320	
134B ->144B	-0.15452	
139B ->147B	0.16466	
140B ->147B	0.12409	
141B ->148B	-0.11907	
143B ->144B	0.13443	
143B ->147B	0.49394	
143B ->148B	0.34590	
Excited State 27:	2.826-A	3.5159 eV 352.64 nm f=0.0056 <S**2>=1.746
140A ->145A	0.10080	
141A ->145A	0.13970	
140B ->145B	-0.12894	
141B ->145B	0.92432	
142B ->146B	0.15841	
143B ->145B	0.16012	
Excited State 28:	2.274-A	3.5402 eV 350.22 nm f=0.0357 <S**2>=1.042
136A ->150A	-0.11486	
139A ->150A	-0.12264	
140A ->145A	0.21511	
141A ->145A	0.37874	
142A ->145A	-0.12406	
144A ->149A	0.10654	
144A ->150A	-0.28530	
139B ->145B	0.29855	
140B ->145B	-0.46496	
141B ->145B	-0.29446	
142B ->146B	0.47264	
Excited State 29:	2.935-A	3.5863 eV 345.72 nm f=0.0298 <S**2>=1.904
140A ->147A	-0.20064	
141A ->147A	-0.14104	
142A ->145A	-0.36314	
142A ->147A	0.10984	
143A ->148A	0.14571	
144A ->150A	-0.17518	
126B ->144B	0.10141	
134B ->144B	0.13766	
139B ->146B	0.33439	
140B ->146B	-0.19878	
142B ->145B	-0.12745	
142B ->146B	-0.17647	
143B ->146B	0.59614	
143B ->147B	0.15818	
Excited State 30:	2.614-A	3.5994 eV 344.45 nm f=0.0042 <S**2>=1.458
133A ->150A	0.12250	
136A ->150A	0.18790	

139A ->150A	0.20730
141A ->145A	-0.12436
143A ->150A	-0.10825
144A ->149A	-0.18908
144A ->150A	0.50478
133B ->144B	0.12475
139B ->146B	0.11905
142B ->146B	0.51083
142B ->147B	-0.28502
142B ->148B	-0.11665
143B ->146B	0.19046
Excited State 31:	2.761-A 3.6193 eV 342.56 nm f=0.0183 <S**2>=1.656
136A ->150A	0.11842
139A ->150A	0.13189
141A ->145A	0.18827
142A ->146A	0.16014
144A ->149A	-0.11672
144A ->150A	0.32618
127B ->144B	-0.16047
133B ->144B	-0.21421
139B ->145B	0.12364
140B ->145B	-0.15368
142B ->144B	0.13619
142B ->147B	0.64238
142B ->148B	0.35417
Excited State 32:	3.373-A 3.6349 eV 341.09 nm f=0.0033 <S**2>=2.595
140A ->145A	-0.29119
141A ->145A	0.36535
142A ->145A	-0.13490
143A ->145A	0.16462
139B ->145B	0.58287
140B ->145B	0.54706
143B ->145B	-0.14313
Excited State 33:	2.477-A 3.6474 eV 339.93 nm f=0.0154 <S**2>=1.284
140A ->145A	-0.30875
141A ->145A	0.51338
142A ->145A	-0.19004
142A ->147A	0.15467
143A ->145A	0.12840
144A ->150A	0.18833
139B ->145B	-0.23445
140B ->145B	-0.39499
142B ->146B	-0.39712
142B ->147B	-0.18493
142B ->148B	-0.20720
Excited State 34:	3.158-A 3.6584 eV 338.90 nm f=0.0095 <S**2>=2.243
139A ->148A	-0.18786
140A ->146A	0.41850
140A ->148A	-0.11131
141A ->146A	-0.29707
143A ->146A	0.46315
144A ->147A	0.10864
144A ->148A	-0.17145
139B ->147B	0.28695
140B ->147B	0.36175
141B ->148B	0.10902
143B ->147B	0.12838
143B ->148B	-0.21507
Excited State 35:	2.823-A 3.6680 eV 338.02 nm f=0.0178 <S**2>=1.743
139A ->146A	-0.10496
139A ->148A	-0.10190
140A ->147A	-0.12715

140A ->148A	0.18342
141A ->148A	-0.14974
143A ->146A	0.16940
143A ->147A	-0.22174
144A ->147A	-0.21358
144A ->148A	-0.31514
139B ->148B	0.20734
140B ->146B	-0.10778
140B ->148B	0.23925
141B ->147B	0.14980
141B ->148B	0.16854
143B ->146B	-0.14723
143B ->147B	-0.33599
143B ->148B	0.49374
Excited State 36: 2.777-A 3.6886 eV 336.13 nm f=0.0863 <S**2>=1.678	
138A ->147A	0.11174
140A ->145A	0.57849
141A ->147A	0.13170
142A ->147A	0.27901
143A ->145A	-0.18413
144A ->150A	0.16844
130B ->144B	-0.10100
137B ->146B	-0.10745
139B ->145B	0.34466
142B ->146B	-0.36306
143B ->149B	0.18611
Excited State 37: 3.466-A 3.6975 eV 335.32 nm f=0.0002 <S**2>=2.754	
137A ->145A	0.64327
137A ->149A	0.25929
137A ->154A	-0.13375
137A ->159A	0.12887
136B ->145B	-0.60761
136B ->149B	-0.25818
136B ->154B	0.10442
136B ->159B	-0.12562
Excited State 38: 2.322-A 3.7110 eV 334.10 nm f=0.0010 <S**2>=1.098	
139A ->147A	0.12243
144A ->146A	0.18867
144A ->147A	0.90395
144A ->148A	-0.15602
143B ->148B	0.16108
Excited State 39: 3.396-A 3.7378 eV 331.70 nm f=0.0095 <S**2>=2.633	
140A ->145A	0.18296
140A ->155A	-0.25395
141A ->155A	0.10023
142A ->155A	0.20584
143A ->149A	0.11905
143A ->155A	-0.46898
144A ->155A	-0.14945
139B ->155B	0.17325
141B ->155B	-0.10650
142B ->146B	-0.10470
142B ->147B	-0.13903
142B ->148B	-0.10181
142B ->155B	-0.24661
143B ->149B	-0.10726
143B ->155B	0.54683
Excited State 40: 3.333-A 3.7452 eV 331.04 nm f=0.0205 <S**2>=2.527	
134A ->151A	-0.11770
135A ->149A	-0.10684
138A ->147A	-0.25401
140A ->145A	0.32754

140A ->154A	0.16247
141A ->145A	-0.12597
141A ->154A	0.13172
142A ->155A	-0.13700
143A ->149A	0.21694
143A ->150A	0.11130
143A ->155A	0.16223
133B ->150B	0.10704
135B ->149B	-0.10232
137B ->146B	0.25566
139B ->154B	-0.17266
140B ->145B	-0.16789
140B ->154B	0.11571
142B ->146B	-0.16583
142B ->148B	-0.10768
142B ->150B	0.10288
142B ->155B	0.16464
143B ->149B	-0.28288
143B ->155B	-0.19713
Excited State 41: 3.450-A	3.7580 eV 329.92 nm f=0.0000 <S**2>=2.726
128A ->155A	-0.10066
138A ->155A	0.10536
140A ->155A	-0.14790
141A ->155A	-0.22194
142A ->155A	-0.52854
143A ->155A	-0.21703
142B ->152B	0.12443
142B ->155B	0.63175
143B ->155B	0.26339
Excited State 42: 2.522-A	3.7653 eV 329.28 nm f=0.0007 <S**2>=1.340
141A ->146A	0.36079
142A ->146A	0.87440
142A ->147A	-0.12800
142B ->147B	-0.19219
Excited State 43: 2.765-A	3.8051 eV 325.84 nm f=0.0352 <S**2>=1.661
139A ->146A	-0.10283
140A ->147A	0.36154
140A ->148A	0.11157
141A ->147A	0.18067
141A ->148A	-0.12315
142A ->147A	-0.11645
143A ->146A	0.15224
143A ->147A	0.61337
143A ->148A	0.13632
144A ->147A	-0.14239
126B ->144B	0.10614
131B ->144B	0.13066
137B ->145B	-0.10879
139B ->146B	-0.13749
142B ->145B	-0.11047
143B ->146B	0.18770
143B ->148B	0.14781
143B ->150B	0.15292
Excited State 44: 2.209-A	3.8087 eV 325.53 nm f=0.0013 <S**2>=0.970
142A ->147A	0.12262
127B ->144B	-0.35135
128B ->144B	-0.25294
130B ->144B	0.75166
132B ->144B	0.28978
133B ->144B	-0.14389
142B ->147B	-0.26924
Excited State 45: 2.938-A	3.8446 eV 322.49 nm f=0.0012 <S**2>=1.908

130B ->144B	-0.14613
132B ->144B	-0.14972
142B ->146B	-0.17132
142B ->147B	-0.48784
142B ->148B	0.79837
Excited State 46:	3.257-A 3.8510 eV 321.95 nm f=0.0062 <S**2>=2.402
129A ->147A	-0.10828
138A ->145A	0.49979
140A ->148A	-0.10099
143A ->147A	-0.35202
143A ->148A	-0.14291
131B ->144B	0.27412
137B ->145B	-0.47258
143B ->148B	0.12364
143B ->150B	0.11168
Excited State 47:	2.226-A 3.8702 eV 320.36 nm f=0.0007 <S**2>=0.989
144A ->148A	0.22108
127B ->144B	0.10916
128B ->144B	-0.18069
129B ->144B	-0.57438
131B ->144B	0.67093
132B ->144B	0.11771
Excited State 48:	2.427-A 3.8839 eV 319.22 nm f=0.0291 <S**2>=1.222
138A ->145A	0.14483
139A ->146A	-0.10668
140A ->148A	0.26634
141A ->148A	-0.16837
143A ->147A	-0.15474
143A ->148A	0.48991
144A ->146A	-0.14148
144A ->147A	0.10203
144A ->148A	0.22580
126B ->144B	-0.36068
128B ->144B	-0.10106
131B ->144B	-0.15619
134B ->144B	-0.17491
141B ->147B	0.22403
143B ->147B	0.10495
143B ->148B	-0.30332
143B ->153B	-0.12053
Excited State 49:	2.314-A 3.8992 eV 317.97 nm f=0.0201 <S**2>=1.089
138A ->145A	-0.13695
142A ->150A	0.17608
144A ->146A	-0.17155
126B ->144B	-0.25726
127B ->144B	-0.23415
128B ->144B	0.45334
129B ->144B	0.35388
131B ->144B	0.38179
137B ->145B	0.14624
141B ->146B	-0.10928
141B ->147B	0.24331
142B ->152B	0.14495
143B ->147B	0.22593
143B ->148B	0.12755
Excited State 50:	2.154-A 3.9215 eV 316.16 nm f=0.0289 <S**2>=0.910
141A ->147A	0.15542
142A ->147A	0.36853
127B ->144B	0.34077
128B ->144B	0.16720
129B ->144B	0.10568
132B ->144B	0.69256

133B ->144B	0.17356
139B ->145B	-0.10195
142B ->146B	0.11614
142B ->147B	0.15366
142B ->148B	0.26673
Excited State 51: 2.394-A 3.9244 eV 315.93 nm f=0.0965 <S**2>=1.182	
141A ->147A	0.30638
142A ->147A	0.66361
142A ->148A	-0.16198
125B ->144B	0.10804
127B ->144B	-0.15008
132B ->144B	-0.42499
139B ->145B	-0.19845
142B ->146B	0.20020
143B ->149B	-0.14801
Excited State 52: 2.739-A 3.9655 eV 312.66 nm f=0.0402 <S**2>=1.626	
139A ->146A	-0.12540
140A ->146A	-0.20781
140A ->148A	-0.16260
141A ->146A	0.21919
141A ->148A	0.13269
142A ->150A	-0.14352
143A ->146A	0.16728
143A ->148A	-0.26217
144A ->146A	-0.14711
126B ->144B	-0.32354
128B ->144B	-0.13151
129B ->144B	-0.18135
131B ->144B	-0.16104
139B ->148B	-0.16561
140B ->148B	-0.18914
141B ->146B	-0.20796
141B ->147B	0.29384
141B ->148B	0.34341
142B ->152B	-0.12462
143B ->151B	-0.12138
Excited State 53: 2.503-A 3.9753 eV 311.89 nm f=0.0059 <S**2>=1.316	
136A ->146A	-0.13336
140A ->146A	0.11917
141A ->146A	-0.19471
143A ->148A	-0.36754
144A ->146A	-0.16950
144A ->148A	0.18623
126B ->144B	0.45307
131B ->144B	-0.14979
141B ->147B	0.51021
141B ->148B	-0.21789
Excited State 54: 3.311-A 4.0051 eV 309.57 nm f=0.0049 <S**2>=2.490	
132A ->145A	0.15641
132A ->149A	0.12483
134A ->145A	0.29438
138A ->145A	0.15843
140A ->151A	0.19437
141A ->149A	-0.11071
141A ->151A	0.12494
142A ->149A	-0.21829
143A ->147A	0.22278
129B ->144B	0.12747
132B ->145B	-0.16498
132B ->149B	-0.12798
133B ->145B	-0.26674
137B ->145B	-0.15199

139B ->146B	0.10199
139B ->150B	-0.20995
139B ->153B	-0.10561
141B ->148B	0.12681
142B ->149B	0.30895
142B ->154B	0.12201
143B ->146B	-0.13536
143B ->150B	-0.17778
Excited State 55:	2.718-A 4.0237 eV 308.14 nm f=0.0114 <S**2>=1.597
139A ->153A	0.10836
140A ->146A	-0.15173
141A ->146A	0.25316
142A ->146A	-0.10731
142A ->150A	0.20843
143A ->147A	-0.15705
143A ->148A	0.13646
144A ->146A	-0.12593
126B ->144B	0.38296
141B ->146B	-0.14067
141B ->147B	-0.21697
141B ->148B	0.25991
142B ->145B	0.10339
142B ->149B	-0.14865
142B ->152B	0.17652
143B ->147B	0.21236
143B ->148B	-0.12593
143B ->153B	-0.11587
Excited State 56:	2.019-A 4.0289 eV 307.73 nm f=0.0002 <S**2>=0.770
137A ->145A	0.64634
137A ->149A	0.18379
136B ->145B	0.67950
136B ->149B	0.20658
Excited State 57:	2.689-A 4.0349 eV 307.28 nm f=0.0010 <S**2>=1.558
141A ->148A	0.35548
142A ->147A	0.19693
142A ->148A	0.87458
Excited State 58:	2.051-A 4.0492 eV 306.19 nm f=0.0062 <S**2>=0.802
125B ->144B	0.95603
Excited State 59:	3.050-A 4.0678 eV 304.80 nm f=0.0062 <S**2>=2.076
136A ->146A	-0.12208
139A ->146A	0.15437
139A ->153A	0.14009
140A ->146A	-0.13591
140A ->152A	0.13766
140A ->153A	0.10349
141A ->146A	-0.12472
141A ->152A	-0.10565
142A ->150A	-0.22421
143A ->146A	0.19952
143A ->148A	-0.19711
144A ->146A	0.10711
129B ->144B	0.20436
131B ->144B	0.11234
138B ->147B	-0.16480
139B ->151B	-0.12833
140B ->147B	-0.10423
140B ->151B	-0.14392
141B ->146B	0.35275
141B ->147B	-0.11529
141B ->148B	-0.12909
142B ->149B	0.11148
142B ->152B	-0.19646

142B ->154B	-0.10080				
143B ->150B	0.12599				
Excited State 60:	3.132-A	4.0812 eV	303.79 nm	f=0.0001	<S**2>=2.203
133A ->152A	-0.10326				
135A ->152A	-0.10262				
136A ->146A	-0.13549				
136A ->148A	-0.10159				
139A ->145A	-0.23108				
139A ->151A	0.10056				
139A ->152A	0.15657				
139A ->153A	-0.11200				
140A ->146A	0.14086				
140A ->152A	-0.19190				
141A ->152A	0.14773				
142A ->150A	-0.10994				
143A ->146A	-0.16387				
143A ->148A	-0.14467				
144A ->148A	-0.13196				
128B ->144B	-0.20324				
129B ->144B	0.15514				
131B ->144B	0.20987				
134B ->151B	0.11672				
138B ->148B	-0.17519				
138B ->151B	0.11449				
139B ->151B	0.12935				
140B ->151B	0.15711				
141B ->148B	0.31767				
141B ->151B	0.13669				
143B ->148B	-0.14230				
143B ->150B	0.13719				
143B ->151B	0.10782				
Excited State 61:	2.588-A	4.0844 eV	303.55 nm	f=0.0007	<S**2>=1.424
132A ->145A	-0.12337				
139A ->145A	0.59235				
141A ->149A	0.10050				
142A ->150A	-0.15796				
144A ->145A	-0.10548				
126B ->144B	0.11688				
128B ->144B	-0.34539				
129B ->144B	0.38471				
130B ->144B	-0.10387				
131B ->144B	0.24084				
132B ->145B	0.12647				
142B ->152B	-0.19048				
Excited State 62:	2.789-A	4.0861 eV	303.43 nm	f=0.0006	<S**2>=1.694
132A ->145A	0.11667				
136A ->145A	0.11366				
139A ->145A	0.71376				
143A ->148A	-0.12850				
144A ->145A	-0.12884				
126B ->144B	-0.12265				
128B ->144B	0.22951				
129B ->144B	-0.27611				
131B ->144B	-0.13675				
132B ->145B	-0.12010				
142B ->152B	0.12196				
143B ->150B	0.10416				
Excited State 63:	2.488-A	4.1145 eV	301.34 nm	f=0.0017	<S**2>=1.297
132A ->145A	-0.12135				
138A ->145A	0.12791				
141A ->146A	-0.12435				
142A ->150A	-0.23544				

126B ->144B	0.24598
128B ->144B	0.50058
129B ->144B	-0.25998
130B ->144B	0.16130
132B ->145B	0.12188
137B ->145B	-0.12155
140B ->146B	0.12111
141B ->146B	0.21408
141B ->148B	0.26917
142B ->152B	-0.26366
142B ->155B	0.11047
Excited State 64: 3.179-A 4.1204 eV 300.91 nm f=0.0003 <S**2>=2.276	
132A ->145A	0.16139
138A ->145A	-0.10365
138A ->151A	0.13255
140A ->149A	-0.20251
140A ->153A	-0.11875
140A ->154A	-0.10243
141A ->149A	-0.17477
142A ->149A	0.15468
142A ->151A	0.17422
142A ->154A	0.10679
143A ->147A	-0.11601
143A ->148A	0.19635
143A ->149A	0.12815
126B ->144B	0.27814
132B ->145B	-0.15955
137B ->145B	0.10702
137B ->150B	-0.13540
139B ->149B	0.25281
139B ->153B	0.10290
139B ->154B	0.10281
140B ->149B	-0.19758
140B ->150B	-0.10581
141B ->148B	0.12520
142B ->150B	-0.17554
142B ->154B	-0.12790
Excited State 65: 2.783-A 4.1295 eV 300.24 nm f=0.0018 <S**2>=1.687	
141A ->146A	0.17493
142A ->150A	0.16157
128B ->144B	-0.14733
141B ->146B	0.80602
141B ->147B	0.26150
141B ->148B	0.20991
142B ->152B	0.17191
142B ->155B	-0.10565
Excited State 66: 3.387-A 4.1391 eV 299.54 nm f=0.0003 <S**2>=2.617	
132A ->145A	-0.21381
134A ->145A	-0.15884
134A ->149A	-0.11021
138A ->145A	0.12801
138A ->151A	0.13832
140A ->149A	-0.19759
140A ->151A	0.12934
140A ->153A	0.10493
140A ->154A	-0.11581
141A ->149A	-0.19562
141A ->151A	0.16229
141A ->154A	-0.12213
142A ->145A	-0.10977
142A ->149A	0.10541
143A ->148A	-0.11228

143A ->149A	0.14117
126B ->144B	-0.14763
128B ->145B	0.11664
132B ->145B	0.21718
133B ->145B	0.12991
133B ->149B	0.10470
137B ->145B	-0.13612
137B ->150B	-0.13956
139B ->149B	0.24427
139B ->150B	-0.13342
139B ->154B	0.11977
140B ->149B	-0.19798
140B ->150B	0.10784
142B ->150B	-0.18195
142B ->154B	0.12882
143B ->149B	-0.11385
Excited State 67: 2.569-A 4.1651 eV 297.67 nm f=0.0665 <S**2>=1.400	
139A ->146A	0.12497
140A ->146A	0.26503
141A ->146A	0.49833
141A ->147A	-0.15492
142A ->146A	-0.21857
142A ->150A	-0.20259
144A ->148A	0.13259
126B ->144B	0.11553
128B ->144B	0.17170
138B ->147B	-0.10374
139B ->146B	-0.17327
139B ->147B	0.10190
140B ->146B	-0.29657
140B ->147B	0.24698
140B ->148B	0.15773
141B ->147B	0.19404
141B ->148B	-0.15188
142B ->152B	-0.20255
Excited State 68: 2.856-A 4.1918 eV 295.78 nm f=0.0591 <S**2>=1.789	
139A ->146A	-0.12673
140A ->146A	0.60398
140A ->147A	-0.17175
141A ->146A	0.23564
142A ->146A	-0.12058
142A ->155A	0.16609
143A ->146A	-0.11624
139B ->146B	0.24820
140B ->146B	0.35981
140B ->147B	-0.23868
140B ->151B	-0.11608
140B ->153B	-0.10021
142B ->155B	0.17846
Excited State 69: 3.101-A 4.2227 eV 293.61 nm f=0.0277 <S**2>=2.154	
136A ->146A	-0.20851
139A ->146A	0.44415
139A ->152A	-0.18767
140A ->151A	0.12571
140A ->153A	-0.16174
141A ->147A	-0.10989
141A ->151A	-0.14346
141A ->153A	0.17546
143A ->153A	0.11441
144A ->146A	-0.11719
138B ->147B	-0.27336
138B ->148B	-0.17594

138B ->151B	-0.13934
139B ->146B	0.15339
139B ->150B	-0.12877
139B ->153B	0.14938
140B ->146B	0.29286
140B ->147B	-0.11842
140B ->150B	-0.16470
140B ->153B	0.18835
141B ->147B	0.10445
141B ->148B	0.11653
141B ->151B	-0.15884
Excited State 70: 3.246-A 4.2300 eV 293.11 nm f=0.0199 <S**2>=2.383	
140A ->146A	-0.21909
140A ->147A	-0.34913
141A ->146A	0.11548
141A ->147A	0.39785
141A ->148A	-0.12828
142A ->147A	-0.15349
142A ->155A	-0.17063
143A ->147A	0.14109
143A ->151A	0.10231
139B ->146B	0.26329
139B ->147B	0.17175
139B ->148B	0.10674
140B ->146B	0.33095
140B ->147B	0.21459
140B ->148B	0.24457
142B ->155B	-0.16454
143B ->150B	-0.13373
Excited State 71: 2.209-A 4.2521 eV 291.58 nm f=0.0020 <S**2>=0.970	
139A ->146A	0.10703
140A ->147A	-0.37566
141A ->147A	0.42460
141A ->148A	-0.10522
141A ->155A	0.11126
142A ->147A	-0.15640
142A ->155A	0.25740
139B ->146B	-0.30938
139B ->148B	-0.10106
140B ->146B	-0.42017
140B ->147B	-0.21284
140B ->148B	-0.16871
142B ->155B	0.25080
143B ->150B	-0.14360
Excited State 72: 2.863-A 4.2600 eV 291.04 nm f=0.0224 <S**2>=1.799	
135A ->145A	-0.11163
138A ->147A	-0.21359
141A ->154A	0.12052
142A ->147A	0.10760
143A ->154A	-0.13767
127B ->144B	0.41623
130B ->144B	0.30757
132B ->144B	-0.24085
133B ->146B	0.10094
137B ->146B	0.18721
140B ->154B	0.10341
143B ->149B	0.54828
143B ->154B	0.17971
Excited State 73: 2.541-A 4.2694 eV 290.40 nm f=0.0155 <S**2>=1.364	
138A ->147A	0.17647
143A ->154A	0.10551
127B ->144B	0.58251

129B ->144B	0.11268
130B ->144B	0.41237
132B ->144B	-0.31152
137B ->146B	-0.15769
143B ->149B	-0.37347
143B ->154B	-0.14217
Excited State 74:	2.222-A 4.2808 eV 289.63 nm f=0.0811 <S**2>=0.984
127A ->155A	0.10044
140A ->146A	-0.17415
140A ->147A	0.10329
141A ->146A	0.10222
141A ->155A	0.22329
142A ->155A	0.51792
139B ->146B	0.17176
140B ->147B	0.38033
140B ->148B	0.23083
142B ->155B	0.49974
143B ->150B	0.10645
143B ->151B	-0.11449
Excited State 75:	3.008-A 4.3215 eV 286.90 nm f=0.0358 <S**2>=2.012
139A ->152A	-0.11923
140A ->147A	-0.17581
140A ->148A	0.18260
141A ->147A	0.29579
141A ->148A	0.14613
141A ->153A	0.11128
142A ->147A	-0.12547
143A ->151A	-0.18631
137B ->145B	0.16731
138B ->151B	-0.11928
139B ->146B	0.31570
139B ->147B	-0.39011
139B ->148B	-0.11540
140B ->147B	0.19454
140B ->153B	0.14378
141B ->151B	-0.10188
143B ->150B	0.43887
Excited State 76:	2.838-A 4.3436 eV 285.44 nm f=0.0123 <S**2>=1.764
138A ->145A	-0.11021
139A ->146A	-0.16575
140A ->146A	-0.13680
140A ->147A	-0.19616
140A ->148A	0.31433
141A ->148A	0.30441
142A ->148A	-0.13891
143A ->151A	-0.11969
139B ->146B	-0.19194
139B ->147B	0.50444
139B ->148B	0.28746
140B ->146B	0.19613
140B ->147B	-0.22524
140B ->148B	-0.14246
143B ->150B	0.23501
143B ->153B	-0.10032
Excited State 77:	2.879-A 4.3519 eV 284.90 nm f=0.0001 <S**2>=1.822
138B ->145B	0.99330
Excited State 78:	2.036-A 4.3658 eV 283.99 nm f=0.0001 <S**2>=0.787
126A ->155A	0.12605
133A ->155A	0.17086
136A ->155A	0.25666
139A ->155A	0.29818
143A ->155A	-0.16950

144A ->150A	-0.12028
144A ->155A	0.78030
123B ->144B	0.14194
124B ->144B	0.22187
Excited State 79:	3.078-A 4.3692 eV 283.77 nm f=0.0120 <S**2>=2.119
138A ->145A	0.11645
140A ->147A	0.24166
140A ->148A	0.44758
141A ->148A	0.45982
141A ->151A	-0.12712
142A ->148A	-0.20822
143A ->148A	-0.14711
143A ->151A	0.15075
139B ->147B	-0.18506
140B ->150B	-0.14813
142B ->149B	-0.17179
143B ->150B	-0.35447
143B ->153B	-0.13693
Excited State 80:	2.159-A 4.3897 eV 282.45 nm f=0.0325 <S**2>=0.916
138A ->145A	0.34927
140A ->147A	0.41559
141A ->147A	0.25083
142A ->147A	-0.12201
143A ->147A	-0.12504
137B ->145B	0.33908
139B ->146B	0.37677
139B ->147B	0.40396
140B ->146B	-0.23398
140B ->147B	-0.25946
Excited State 81:	2.702-A 4.4287 eV 279.96 nm f=0.0624 <S**2>=1.575
134A ->147A	0.19963
135A ->145A	0.26122
143A ->149A	0.43277
143A ->150A	0.13606
143A ->154A	0.10490
144A ->149A	0.26732
133B ->146B	-0.18102
135B ->145B	0.33007
135B ->149B	-0.10742
139B ->154B	0.10900
143B ->149B	0.49571
Excited State 82:	2.554-A 4.4343 eV 279.60 nm f=0.0236 <S**2>=1.380
138A ->145A	0.13101
139A ->146A	-0.14113
140A ->147A	0.14366
140A ->148A	-0.27191
141A ->148A	-0.14505
143A ->153A	0.13076
139B ->147B	-0.17781
139B ->148B	0.63204
140B ->147B	0.17801
140B ->148B	-0.45826
142B ->149B	-0.10003
143B ->153B	-0.14311
Excited State 83:	3.190-A 4.4402 eV 279.23 nm f=0.0136 <S**2>=2.294
132A ->145A	0.21258
134A ->145A	-0.15895
135A ->147A	-0.10424
136A ->146A	0.11862
139A ->146A	0.29868
140A ->148A	0.23586
141A ->151A	0.10681

143A ->151A	-0.10056
143A ->152A	-0.10056
143A ->153A	-0.13777
132B ->145B	-0.20989
133B ->145B	0.18642
137B ->145B	0.11025
139B ->147B	-0.12013
139B ->148B	0.31259
140B ->147B	0.12140
140B ->148B	-0.13192
140B ->150B	0.13476
141B ->147B	0.11911
143B ->150B	-0.25557
143B ->151B	0.17861
143B ->153B	0.30253
Excited State 84: 3.341-A 4.4511 eV 278.55 nm f=0.0177 <S**2>=2.540	
132A ->145A	-0.12606
133A ->148A	0.11114
135A ->146A	0.19576
136A ->148A	-0.10989
136A ->153A	-0.10666
140A ->146A	-0.16657
141A ->152A	-0.16522
143A ->152A	-0.34218
132B ->145B	0.12362
134B ->148B	0.12405
135B ->147B	-0.12007
138B ->153B	0.12084
139B ->148B	-0.10942
140B ->148B	0.12587
140B ->151B	-0.17403
141B ->151B	-0.16922
143B ->151B	0.54188
Excited State 85: 2.569-A 4.4547 eV 278.32 nm f=0.0011 <S**2>=1.399	
136A ->145A	-0.58339
139A ->145A	0.17775
144A ->149A	0.66295
144A ->150A	0.22591
Excited State 86: 2.910-A 4.4593 eV 278.03 nm f=0.0361 <S**2>=1.868	
127A ->145A	0.12982
130A ->145A	0.16889
132A ->145A	-0.21059
132A ->149A	-0.12791
138A ->145A	0.23258
140A ->151A	-0.10904
127B ->145B	-0.12699
130B ->145B	-0.16055
132B ->145B	0.20722
132B ->149B	0.14522
137B ->145B	0.36494
139B ->147B	-0.10288
139B ->148B	0.14994
142B ->149B	0.52624
142B ->152B	0.12077
143B ->150B	-0.17620
Excited State 87: 2.700-A 4.4817 eV 276.65 nm f=0.1190 <S**2>=1.573	
132A ->145A	-0.17189
134A ->145A	0.13280
136A ->146A	0.18288
138A ->145A	-0.24382
139A ->146A	0.28558
140A ->147A	0.13124

140A ->148A	0.37536
141A ->148A	-0.11526
143A ->151A	0.21715
122B ->144B	-0.11099
132B ->145B	0.16630
133B ->145B	-0.18889
137B ->145B	-0.25194
140B ->148B	-0.30383
141B ->147B	0.11250
143B ->150B	0.24033
143B ->153B	0.15732
Excited State 88: 2.598-A 4.5121 eV 274.78 nm f=0.0013 <S**2>=1.437	
136A ->145A	0.70991
139A ->145A	-0.10155
143A ->149A	-0.11453
143A ->155A	0.11739
144A ->149A	0.56273
144A ->150A	0.17928
143B ->155B	0.11862
Excited State 89: 2.401-A 4.5163 eV 274.53 nm f=0.0349 <S**2>=1.191	
130A ->145A	0.10477
136A ->145A	-0.11108
138A ->145A	-0.26169
140A ->148A	-0.23963
141A ->147A	0.10065
141A ->148A	0.29639
142A ->148A	-0.11674
142A ->149A	-0.13102
143A ->148A	0.16153
143A ->151A	-0.10646
144A ->146A	-0.10854
144A ->149A	-0.10004
144A ->152A	0.13601
122B ->144B	0.10771
137B ->145B	-0.18593
139B ->146B	0.10375
139B ->147B	-0.10671
139B ->148B	0.36946
140B ->146B	-0.13153
140B ->147B	-0.20835
140B ->148B	0.27929
142B ->149B	-0.13532
143B ->153B	0.29833
Excited State 90: 3.196-A 4.5385 eV 273.18 nm f=0.0002 <S**2>=2.303	
129A ->146A	0.11800
131A ->146A	-0.11646
136A ->148A	-0.14924
139A ->148A	0.60922
139A ->151A	-0.10710
139A ->153A	0.12019
140A ->146A	0.15123
140A ->152A	0.13514
141A ->146A	-0.11890
141A ->152A	-0.15285
129B ->147B	0.10274
138B ->147B	0.18693
138B ->148B	-0.28227
139B ->147B	0.15042
139B ->151B	-0.14359
140B ->147B	0.11894
140B ->151B	-0.16801
143B ->151B	-0.26655

Excited State 91: 2.711-A 4.5748 eV 271.02 nm f=0.0688 <S**2>=1.587

134A ->145A	-0.20608
138A ->145A	-0.13728
141A ->147A	0.11993
143A ->151A	0.42463
144A ->151A	0.33811
130B ->145B	0.11634
133B ->145B	0.14067
137B ->145B	-0.18684
139B ->148B	0.10836
142B ->149B	0.53096
143B ->150B	0.13617

Excited State 92: 3.094-A 4.5811 eV 270.64 nm f=0.0185 <S**2>=2.143

134A ->147A	-0.17682
135A ->145A	-0.38755
138A ->147A	0.10494
143A ->149A	0.62221
143A ->150A	0.17525
143A ->154A	0.14245
133B ->146B	0.18466
135B ->145B	-0.29284
137B ->146B	-0.13203
142B ->150B	0.14330
143B ->154B	-0.19919

Excited State 93: 2.707-A 4.6008 eV 269.48 nm f=0.0389 <S**2>=1.581

127A ->145A	0.11175
130A ->145A	0.16220
136A ->146A	-0.20034
138A ->145A	-0.10954
139A ->146A	-0.23619
139A ->147A	-0.12527
141A ->148A	-0.13819
142A ->149A	-0.21082
143A ->153A	-0.10485
144A ->151A	0.58161
127B ->145B	-0.12052
130B ->145B	-0.16121
133B ->145B	0.10515
140B ->148B	-0.13258
141B ->148B	-0.10251
142B ->149B	-0.18239
143B ->150B	-0.24949

Excited State 94: 2.872-A 4.6015 eV 269.44 nm f=0.0536 <S**2>=1.812

134A ->145A	0.19110
135A ->147A	0.11324
136A ->146A	-0.11210
138A ->145A	0.27870
141A ->147A	-0.13741
142A ->149A	0.19786
143A ->153A	-0.23649
144A ->151A	0.38355
144A ->152A	0.12014
133B ->145B	-0.21439
135B ->146B	0.10520
137B ->145B	0.20015
139B ->146B	-0.16383
142B ->149B	-0.19314
143B ->150B	0.26265
143B ->151B	-0.10393
143B ->153B	0.30913

Excited State 95: 2.548-A 4.6265 eV 267.99 nm f=0.1021 <S**2>=1.373

136A ->146A	0.30207
-------------	---------

139A ->146A	0.26549
139A ->147A	-0.16673
140A ->148A	-0.12904
141A ->148A	0.13460
143A ->151A	-0.29917
143A ->153A	0.28562
144A ->151A	0.52475
144A ->152A	-0.11590
122B ->144B	-0.11257
138B ->147B	0.18531
140B ->148B	0.11500
141B ->147B	0.11117
141B ->148B	0.15244
143B ->153B	-0.16342
Excited State 96: 2.082-A 4.6441 eV 266.97 nm f=0.0010 <S**2>=0.834	
136A ->145A	-0.23454
140A ->155A	0.25092
143A ->150A	0.14326
143A ->155A	0.58385
144A ->155A	0.11239
124B ->144B	-0.19452
127B ->144B	0.12060
139B ->155B	0.13940
141B ->152B	-0.10369
141B ->155B	-0.11807
142B ->150B	0.11415
143B ->152B	0.10675
143B ->155B	0.56539
Excited State 97: 2.851-A 4.6627 eV 265.90 nm f=0.0034 <S**2>=1.782	
143A ->149A	-0.14332
137B ->150B	-0.12221
139B ->149B	0.16334
140B ->149B	-0.15450
142B ->150B	0.86334
142B ->153B	-0.15165
143B ->154B	-0.15530
Excited State 98: 2.913-A 4.6745 eV 265.23 nm f=0.0064 <S**2>=1.872	
143A ->149A	0.17966
124B ->144B	-0.10228
137B ->146B	-0.19861
139B ->149B	-0.11100
140B ->149B	0.11050
142B ->150B	0.23332
142B ->153B	-0.10621
143B ->149B	-0.15621
143B ->151B	-0.10205
143B ->152B	-0.37767
143B ->154B	0.72252
Excited State 99: 3.075-A 4.6797 eV 264.94 nm f=0.0586 <S**2>=2.114	
133A ->148A	-0.16222
135A ->146A	-0.25219
136A ->148A	0.29142
139A ->146A	-0.10418
139A ->148A	0.38242
144A ->152A	-0.18505
134B ->147B	0.16947
134B ->148B	-0.17036
135B ->147B	0.24952
139B ->147B	0.11034
143B ->151B	0.50098
143B ->153B	0.25307
143B ->154B	0.12899

10.3 Dinuclear Bis(terpyridine)ruthenium(II) Complexes by Amide Coupling of Ruthenium Amino Acids: Synthesis and Properties

A. Breivogel, K. Hempel, K. Heinze, *Inorg. Chim. Acta* **2011**, 374, 152–162.

DOI: 10.1016/j.ica.2011.03.046

Reprinted with permission from Elsevier, Copyright © 2011.

DFT-optimized (B3LYP/LANL2DZ) cartesian coordinates of **3a** and **3b** (singlet) and **1b**⁺, **3a**⁺ and **3b**⁺ (doublet) can be found in the online supporting information.

Dinuclear Bis(terpyridine)ruthenium(II) Complexes by Amide Coupling of Ruthenium Amino Acids: Synthesis and Properties

Aaron Breivogel^a, Klaus Hempel^b, Katja Heinze^{*a}

Supporting Information

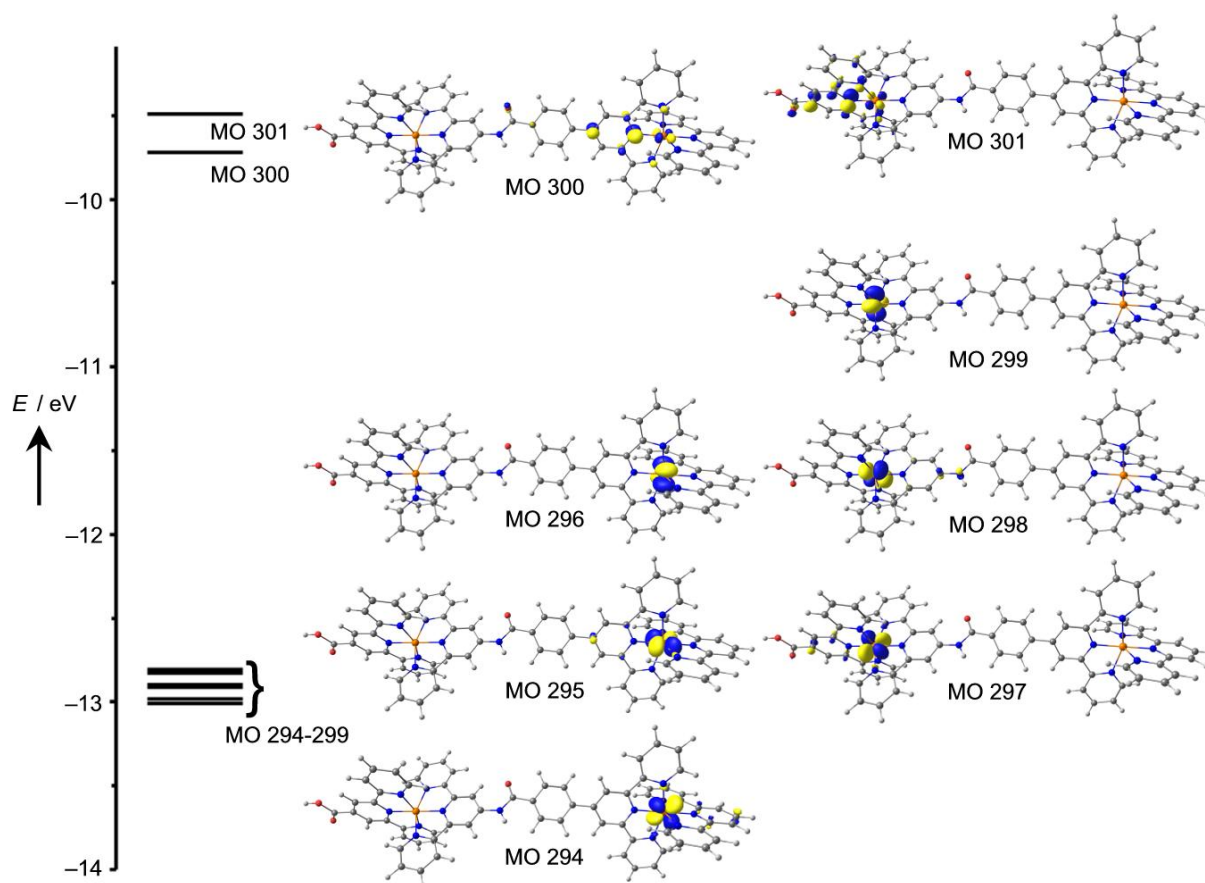


Fig. S1. MO scheme of **3a** (contour level 0.07 a.u.).

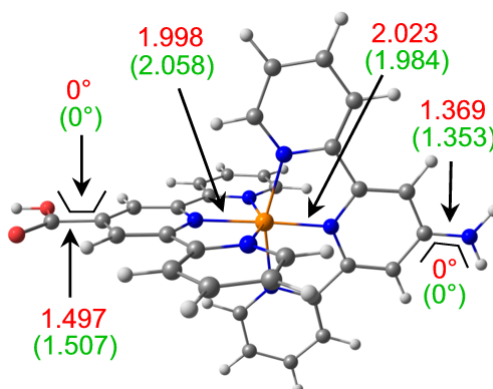


Fig. S2. Relevant DFT calculated metrical parameters of a model of **1b** (red) and **[1b]⁺** (green, in parentheses) (distances in Å).

10.4 Light-induced Charge Separation in a Donor-Chromophore-Acceptor Nanocomposite Poly[TPA-Ru(tpy)₂]@ZnO

L. zur Borg, A. L. Domanski, A. Breivogel, M. Bürger, R. Berger, K. Heinze, R. Zentel, *J. Mater. Chem. C* **2013**, *1*, 1223–1230.

DOI: 10.1039/c2tc00535b

Reprinted with permission from The Royal Society of Chemistry, Copyright © 2013.

Supporting Information

Light-Induced Charge Separation in a Donor-Chromophore-Acceptor Nanocomposite Poly[TPA-Ru(tpy)₂]@ZnO

- Fig. S1** FT-IR spectrum of [(H₂N-Gly-CONH-tpy)Ru(tpy-CONH-Gly-COOH)](PF₆)₂ (**A**)
- Fig. S2** ¹⁹F NMR spectra of **P2** and **P3a**
- Fig. S3** FT-IR spectra of **P2**, **P3a** and **P3b**
- Fig. S4** TEM images
- Fig. S5** Topography image of **P3a**@ZnO
- Fig. S6** KPFM images of **P3b**@ZnO
- Fig. S7** Atom numbering of **A** used for NMR assignments
- Fig. S8** UV-Vis spectrum of **P3b** in THF

Fig. S1 FT-IR spectrum of $[(\text{H}_2\text{N}-\text{CH}_2-\text{CONH-tpy})\text{Ru}(\text{tpy}-\text{CONH}-\text{CH}_2-\text{COOH})](\text{PF}_6)_2$ (A).

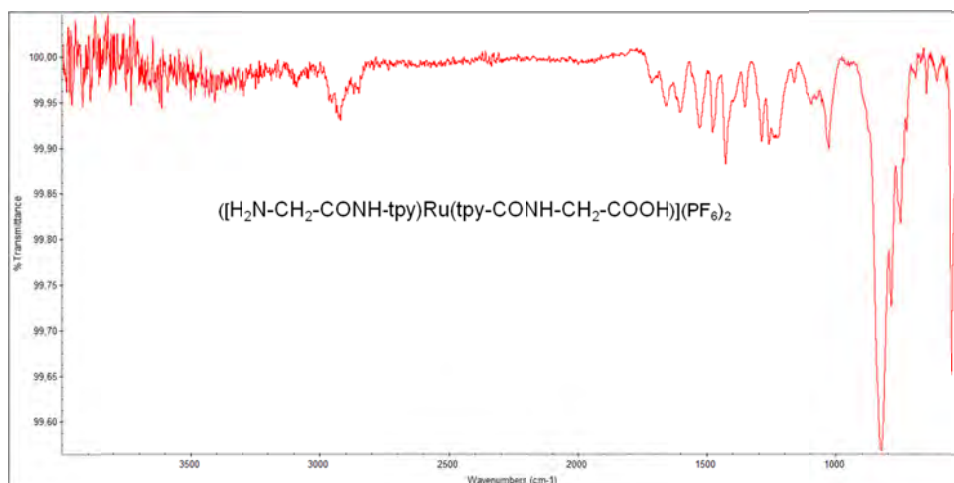


Fig. S2 FT-IR spectra of P2 and P3a and 3b.

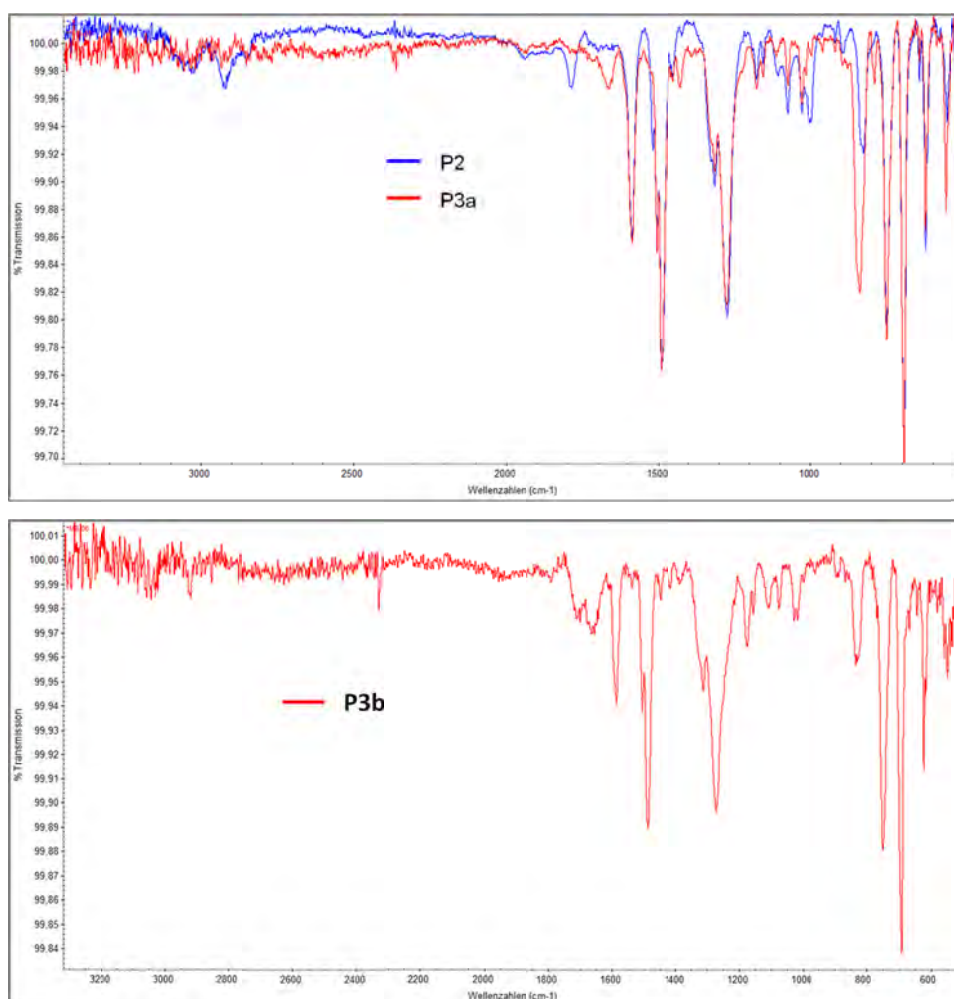


Fig. S3 ^{19}F NMR spectra of P2 and P3a in CDCl_3 .

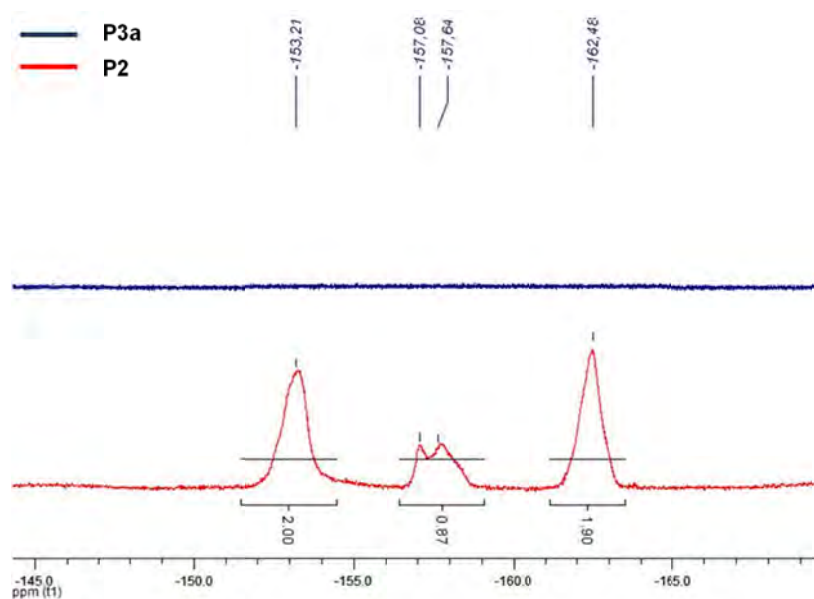


Fig. S4 TEM images of a) pristine ZnO. b) and c) P3a@ZnO, drop cast from THF.

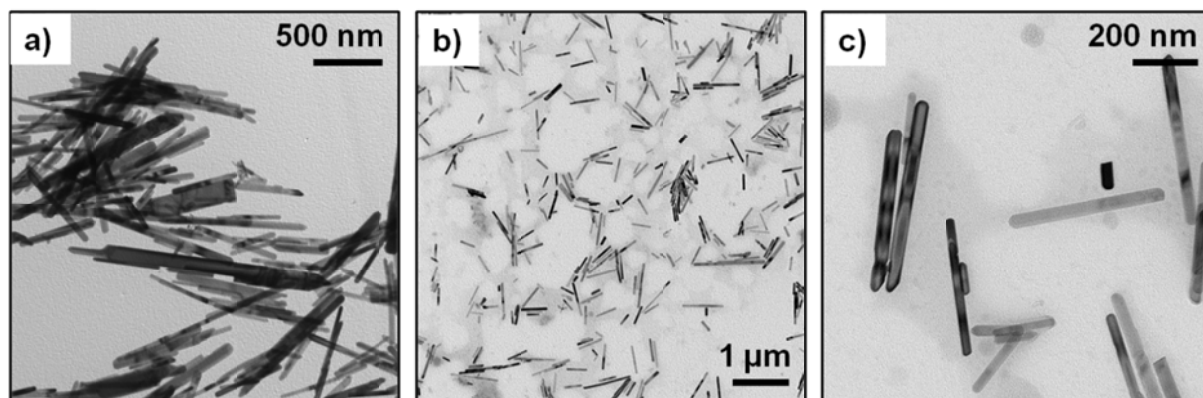


Fig. S5 Topography image of P3a@ZnO.

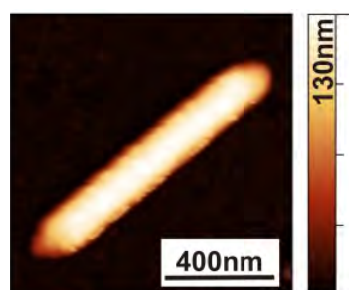


Fig. S6 KPFM images of P3b@ZnO. a) Topography b) Surface potential map recorded in darkness. c) Surface potential map recorded under laser illumination of a wavelength of 488 nm. d) Line profile of the surface potential across the particle indicated by the line in the respective surface potential map. No photo-response was observed for this D-A system.

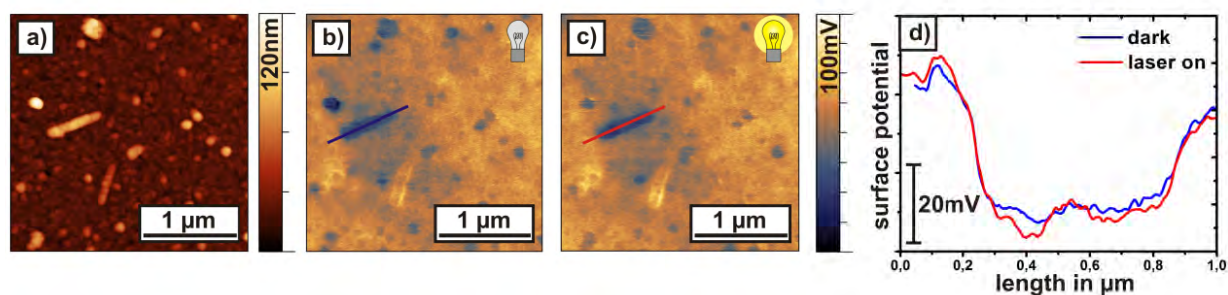


Fig. S7 Atom numbering of A used for NMR assignments.

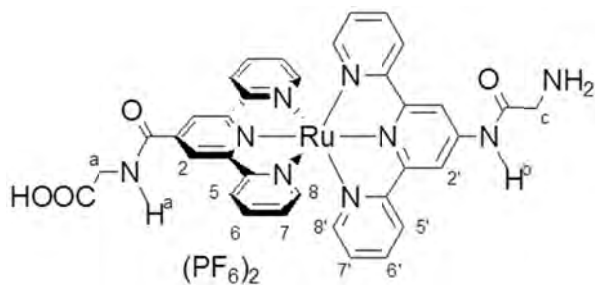
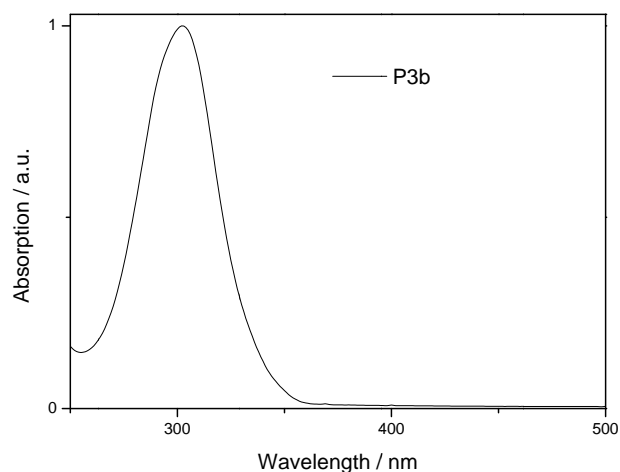


Fig. S8 UV-Vis spectrum of P3b in THF.



10.5 A Heteroleptic Bis(tridentate)ruthenium(II) Polypyridine Complex with Improved Photophysical Properties and Integrated Functionalizability

A. Breivogel, C. Förster, K. Heinze, *Inorg. Chem.* **2010**, 49, 7052–7056.

DOI: 10.1021/ic1007236

Reprinted with permission from the American Chemical Society, Copyright © 2010.

DFT-optimized (B3LYP/LANL2DZ, IEFPCM in CH₃CN) cartesian coordinates of *cis-fac*-[Ru(dddpd)₂]²⁺, *trans-fac*-[Ru(dddpd)₂]²⁺, *mer*-[Ru(dddpd)₂]²⁺, [**8**]²⁺ (singlet ground state and ³MLCT state) and results of the TD-DFT (B3LYP/LANL2DZ, gasphase and IEFPCM in CH₃CN) calculation of [**8**]²⁺ (singlet) can be found in the online supporting information.

A Heteroleptic Bis(tridentate)ruthenium(II) Polypyridine Complex with Improved Photophysical Properties and Integrated Functionalizability

Aaron Breivogel, Christoph Förster, Katja Heinze*

Supporting Information

- X-ray crystal data of **8**
- Spectroscopic data of **8**
- Cartesian Coordinates of *cis-fac*-[Ru(ddpd)₂]²⁺, *trans-fac*-[Ru(ddpd)₂]²⁺, *mer*-[Ru(ddpd)₂]²⁺, **8** (singlet ground state), **8** (³MLCT state)
- Graphical representation of the frontier orbitals of **8**
- Results of the TD-DFT (singlets) calculation of **8** (gas phase)
- Results of the TD-DFT (singlets) calculation of **8** (CH₃CN).
- Cartesian Coordinates of Ni(CO)₃L complexes (L = κN(central pyridine)-ddpd, κN(terminal pyridine)-ddpd, NMe₃, NHC (1,3-dimethyl-2,3-dihydro-1*H*-imidazol-2-ylidene), PMe₃, PH₃, PF₃, pyridine, methyl(1-methyl-1*H*-pyridin-2-ylidene)amine)

Figure S1. Atom numbering of the dication of **8**.

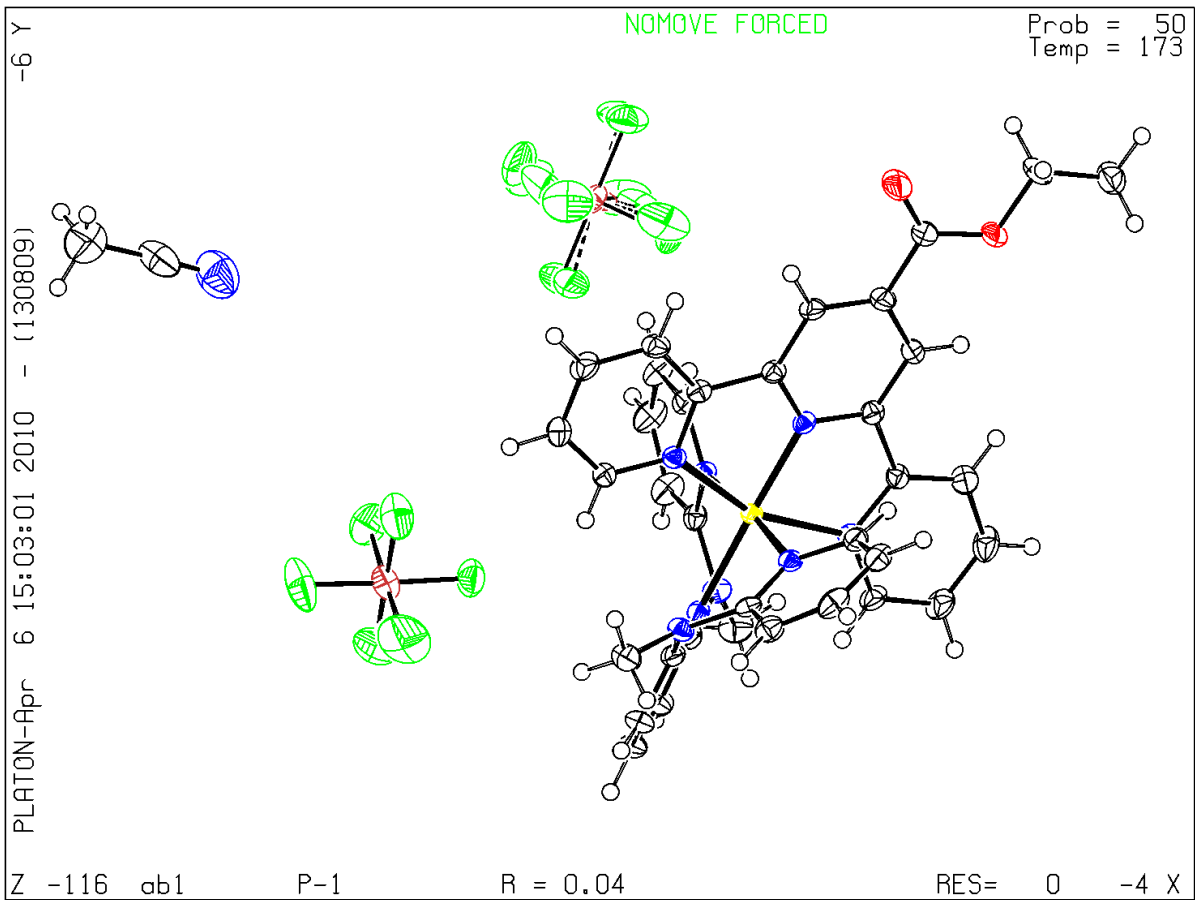
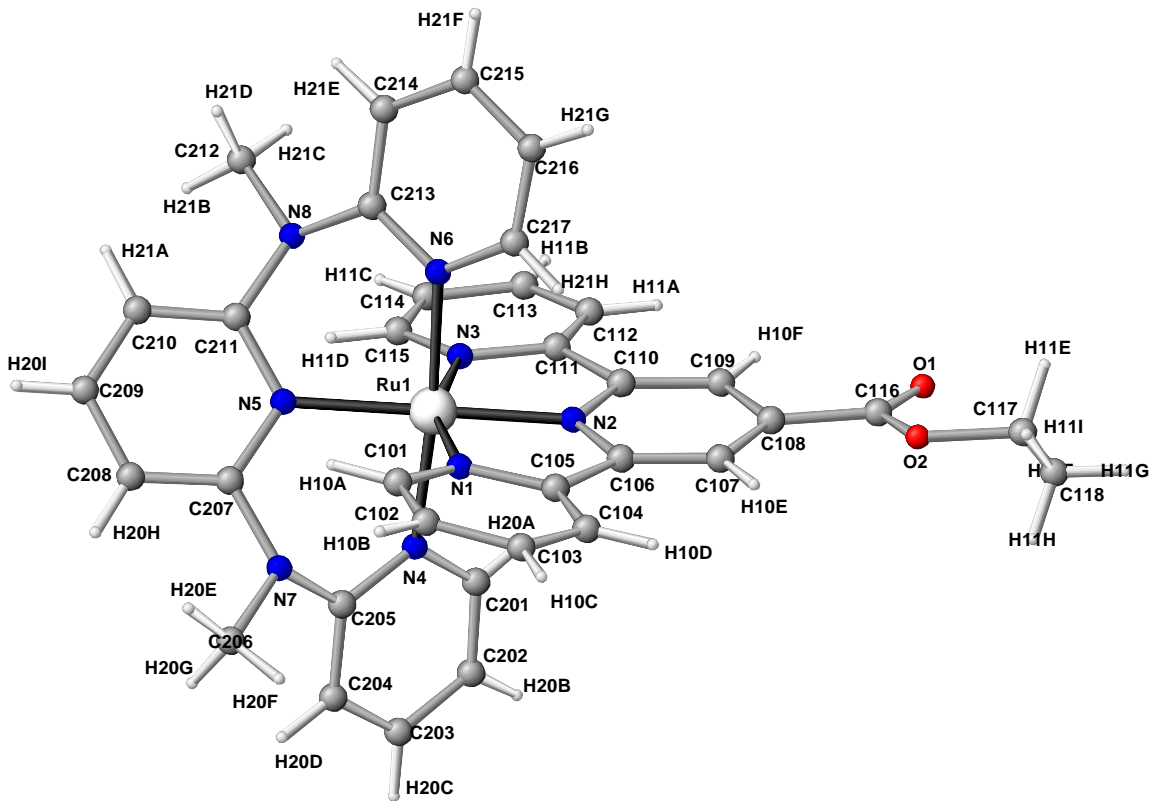


Table S1. Crystal and structure refinement data for **8**.

	8
Empirical formula	C ₃₇ H ₃₅ F ₁₂ N ₉ O ₂ P ₂ Ru
Formula weight	1028.75
Crystal color, habit	orange-brown plate
Crystal dimensions / mm	0.20 × 0.20 × 0.10
Crystal system	triclinic
Space group	<i>P</i> 1-bar
<i>a</i> / Å	11.9005(9)
<i>b</i> / Å	13.2663(10)
<i>c</i> / Å	14.7564(11)
α / °	68.413(2)
β / °	73.337(2)
γ / °	73.704(2)
<i>V</i> / Å ³	2034.8(3)
<i>Z</i>	2
<i>F</i> (000)	1036
Density (calcd) / g cm ⁻³	1.679
Absorption coefficient μ / mm ⁻¹	0.567 (MULABS)
Theta range / °	1.52 – 28.12
Index ranges	–15 ≤ <i>h</i> ≤ 15 –17 ≤ <i>k</i> ≤ 17 –19 ≤ <i>l</i> ≤ 19
Reflections collected	44719
Independent reflections	9793 (<i>R</i> _{int} = 0.1026)
Observed reflections	9793
Parameters	632
Max. / min. transmission	1.2702 / 0.8205
Goodness-of-fit on <i>F</i> ²	0.931
Largest difference peak and hole / e Å ⁻³	0.51 / –1.26
<i>R</i> ₁ (<i>I</i> > 2σ(<i>I</i>))	0.0391
<i>R</i> ₁ (all data)	0.0781
<i>wR</i> ₂ (<i>I</i> > 2σ(<i>I</i>))	0.0614
<i>wR</i> ₂ (all data)	0.0842

Table S2. Bond lengths / Å and angles / ° of **8**.

Ru(1)–N(2)	1.944(2)
Ru(1)–N(6)	2.072(2)
Ru(1)–N(4)	2.076(2)
Ru(1)–N(3)	2.078(2)
Ru(1)–N(5)	2.078(2)
Ru(1)–N(1)	2.079(2)
N(1)–C(101)	1.348(3)
N(1)–C(105)	1.378(3)
N(2)–C(110)	1.360(3)
N(2)–C(106)	1.366(3)
N(3)–C(115)	1.349(3)
N(3)–C(111)	1.373(3)
C(101)–C(102)	1.378(4)
C(101)–H(10A)	0.9500
C(102)–C(103)	1.382(4)
C(102)–H(10B)	0.9500
C(103)–C(104)	1.384(4)
C(103)–H(10C)	0.9500
C(104)–C(105)	1.379(4)
C(104)–H(10D)	0.9500
C(105)–C(106)	1.479(4)
C(106)–C(107)	1.376(3)
C(107)–C(108)	1.388(4)
C(107)–H(10E)	0.9500
C(108)–C(109)	1.397(4)
C(108)–C(116)	1.488(4)
C(109)–C(110)	1.379(3)
C(109)–H(10F)	0.9500
C(110)–C(111)	1.476(4)
C(111)–C(112)	1.382(4)
C(112)–C(113)	1.381(4)
C(112)–H(11A)	0.9500
C(113)–C(114)	1.383(4)
C(113)–H(11B)	0.9500
C(114)–C(115)	1.373(4)
C(114)–H(11C)	0.9500
C(115)–H(11D)	0.9500
C(116)–O(1)	1.210(3)
C(116)–O(2)	1.329(3)
C(117)–O(2)	1.457(3)
C(117)–C(118)	1.497(4)
C(117)–H(11E)	0.9900
C(117)–H(11F)	0.9900
C(118)–H(11G)	0.9800
C(118)–H(11H)	0.9800
C(118)–H(11I)	0.9800
N(4)–C(201)	1.352(3)
N(4)–C(205)	1.357(3)
N(5)–C(211)	1.360(3)
N(5)–C(207)	1.361(3)
N(6)–C(213)	1.349(3)
N(6)–C(217)	1.359(3)
C(201)–C(202)	1.363(4)
C(201)–H(20A)	0.9500
C(202)–C(203)	1.374(4)
C(202)–H(20B)	0.9500
C(203)–C(204)	1.375(4)
C(203)–H(20C)	0.9500
C(204)–C(205)	1.391(4)
C(204)–H(20D)	0.9500
C(205)–N(7)	1.401(3)
N(7)–C(207)	1.412(3)
N(7)–C(206)	1.473(3)
C(206)–H(20E)	0.9800
C(206)–H(20F)	0.9800
C(206)–H(20G)	0.9800
C(207)–C(208)	1.384(4)
C(208)–C(209)	1.378(4)

C(208)-H(20H) 0.9500
 C(209)-C(210) 1.370(4)
 C(209)-H(20I) 0.9500
 C(210)-C(211) 1.381(3)
 C(210)-H(21A) 0.9500
 C(211)-N(8) 1.410(3)
 N(8)-C(213) 1.407(3)
 N(8)-C(212) 1.478(3)
 C(212)-H(21B) 0.9800
 C(212)-H(21C) 0.9800
 C(212)-H(21D) 0.9800
 C(213)-C(214) 1.395(3)
 C(214)-C(215) 1.370(4)
 C(214)-H(21E) 0.9500
 C(215)-C(216) 1.387(4)
 C(215)-H(21F) 0.9500
 C(216)-C(217) 1.367(4)
 C(216)-H(21G) 0.9500
 C(217)-H(21H) 0.9500
 P(1)-F(13) 1.565(5)
 P(1)-F(16) 1.576(4)
 P(1)-F(15) 1.582(5)
 P(1)-F(14) 1.587(5)
 P(1)-F(12) 1.598(5)
 P(1)-F(11) 1.603(5)
 P(1A)-F(14A) 1.566(12)
 P(1A)-F(15A) 1.582(12)
 P(1A)-F(16A) 1.582(12)
 P(1A)-F(13A) 1.583(13)
 P(1A)-F(12A) 1.589(13)
 P(1A)-F(11A) 1.610(13)
 P(2)-F(26) 1.571(2)
 P(2)-F(24) 1.583(2)
 P(2)-F(23) 1.595(2)
 P(2)-F(25) 1.597(2)
 P(2)-F(22) 1.602(2)
 P(2)-F(21) 1.6022(18)
 N(300)-C(301) 1.134(5)
 C(301)-C(302) 1.452(6)
 C(302)-H(30A) 0.9800
 C(302)-H(30B) 0.9800
 C(302)-H(30C) 0.9800

N(2)-Ru(1)-N(6) 91.95(8)
 N(2)-Ru(1)-N(4) 92.92(8)
 N(6)-Ru(1)-N(4) 174.70(8)
 N(2)-Ru(1)-N(3) 79.57(8)
 N(6)-Ru(1)-N(3) 88.88(8)
 N(4)-Ru(1)-N(3) 89.94(8)
 N(2)-Ru(1)-N(5) 178.29(9)
 N(6)-Ru(1)-N(5) 87.68(8)
 N(4)-Ru(1)-N(5) 87.51(8)
 N(3)-Ru(1)-N(5) 102.09(8)
 N(2)-Ru(1)-N(1) 79.68(8)
 N(6)-Ru(1)-N(1) 90.94(8)
 N(4)-Ru(1)-N(1) 92.00(8)
 N(3)-Ru(1)-N(1) 159.22(8)
 N(5)-Ru(1)-N(1) 98.66(8)
 C(101)-N(1)-C(105) 117.4(2)
 C(101)-N(1)-Ru(1) 129.34(19)
 C(105)-N(1)-Ru(1) 113.22(16)
 C(110)-N(2)-C(106) 121.1(2)
 C(110)-N(2)-Ru(1) 119.27(17)
 C(106)-N(2)-Ru(1) 119.59(17)
 C(115)-N(3)-C(111) 116.7(2)
 C(115)-N(3)-Ru(1) 129.85(18)
 C(111)-N(3)-Ru(1) 113.38(16)
 N(1)-C(101)-C(102) 123.1(3)
 N(1)-C(101)-H(10A) 118.5
 C(102)-C(101)-H(10A) 118.5
 C(101)-C(102)-C(103) 119.2(3)

C(101)-C(102)-H(10B) 120.4
 C(103)-C(102)-H(10B) 120.4
 C(102)-C(103)-C(104) 118.8(3)
 C(102)-C(103)-H(10C) 120.6
 C(104)-C(103)-H(10C) 120.6
 C(105)-C(104)-C(103) 119.8(3)
 C(105)-C(104)-H(10D) 120.1
 C(103)-C(104)-H(10D) 120.1
 N(1)-C(105)-C(104) 121.6(2)
 N(1)-C(105)-C(106) 114.7(2)
 C(104)-C(105)-C(106) 123.7(2)
 N(2)-C(106)-C(107) 120.3(2)
 N(2)-C(106)-C(105) 112.6(2)
 C(107)-C(106)-C(105) 126.8(2)
 C(106)-C(107)-C(108) 119.4(2)
 C(106)-C(107)-H(10E) 120.3
 C(108)-C(107)-H(10E) 120.3
 C(107)-C(108)-C(109) 119.7(2)
 C(107)-C(108)-C(116) 122.7(2)
 C(109)-C(108)-C(116) 117.5(2)
 C(110)-C(109)-C(108) 119.4(2)
 C(110)-C(109)-H(10F) 120.3
 C(108)-C(109)-H(10F) 120.3
 N(2)-C(110)-C(109) 120.1(2)
 N(2)-C(110)-C(111) 113.0(2)
 C(109)-C(110)-C(111) 126.9(2)
 N(3)-C(111)-C(112) 122.1(2)
 N(3)-C(111)-C(110) 114.5(2)
 C(112)-C(111)-C(110) 123.4(2)
 C(113)-C(112)-C(111) 119.9(3)
 C(113)-C(112)-H(11A) 120.1
 C(111)-C(112)-H(11A) 120.1
 C(112)-C(113)-C(114) 118.3(3)
 C(112)-C(113)-H(11B) 120.9
 C(114)-C(113)-H(11B) 120.9
 C(115)-C(114)-C(113) 119.6(3)
 C(115)-C(114)-H(11C) 120.2
 C(113)-C(114)-H(11C) 120.2
 N(3)-C(115)-C(114) 123.4(3)
 N(3)-C(115)-H(11D) 118.3
 C(114)-C(115)-H(11D) 118.3
 O(1)-C(116)-O(2) 124.4(2)
 O(1)-C(116)-C(108) 122.8(3)
 O(2)-C(116)-C(108) 112.8(2)
 O(2)-C(117)-C(118) 107.5(2)
 O(2)-C(117)-H(11E) 110.2
 C(118)-C(117)-H(11E) 110.2
 O(2)-C(117)-H(11F) 110.2
 C(118)-C(117)-H(11F) 110.2
 H(11E)-C(117)-H(11F) 108.5
 C(117)-C(118)-H(11G) 109.5
 C(117)-C(118)-H(11H) 109.5
 H(11G)-C(118)-H(11H) 109.5
 C(117)-C(118)-H(11I) 109.5
 H(11G)-C(118)-H(11I) 109.5
 H(11H)-C(118)-H(11I) 109.5
 C(116)-O(2)-C(117) 115.3(2)
 C(201)-N(4)-C(205) 117.9(2)
 C(201)-N(4)-Ru(1) 121.68(17)
 C(205)-N(4)-Ru(1) 120.40(17)
 C(211)-N(5)-C(207) 117.8(2)
 C(211)-N(5)-Ru(1) 121.56(16)
 C(207)-N(5)-Ru(1) 120.61(18)
 C(213)-N(6)-C(217) 117.9(2)
 C(213)-N(6)-Ru(1) 121.10(16)
 C(217)-N(6)-Ru(1) 120.51(18)
 N(4)-C(201)-C(202) 123.7(3)
 N(4)-C(201)-H(20A) 118.1
 C(202)-C(201)-H(20A) 118.1
 C(201)-C(202)-C(203) 118.3(3)
 C(201)-C(202)-H(20B) 120.8

C(203)-C(202)-H(20B) 120.8
 C(202)-C(203)-C(204) 119.5(3)
 C(202)-C(203)-H(20C) 120.3
 C(204)-C(203)-H(20C) 120.3
 C(203)-C(204)-C(205) 120.0(3)
 C(203)-C(204)-H(20D) 120.0
 C(205)-C(204)-H(20D) 120.0
 N(4)-C(205)-C(204) 120.6(2)
 N(4)-C(205)-N(7) 117.9(2)
 C(204)-C(205)-N(7) 121.5(2)
 C(205)-N(7)-C(207) 121.9(2)
 C(205)-N(7)-C(206) 115.7(2)
 C(207)-N(7)-C(206) 115.8(2)
 N(7)-C(206)-H(20E) 109.5
 N(7)-C(206)-H(20F) 109.5
 H(20E)-C(206)-H(20F) 109.5
 N(7)-C(206)-H(20G) 109.5
 H(20E)-C(206)-H(20G) 109.5
 H(20F)-C(206)-H(20G) 109.5
 N(5)-C(207)-C(208) 122.4(2)
 N(5)-C(207)-N(7) 117.2(2)
 C(208)-C(207)-N(7) 120.4(2)
 C(209)-C(208)-C(207) 118.7(3)
 C(209)-C(208)-H(20H) 120.7
 C(207)-C(208)-H(20H) 120.7
 C(210)-C(209)-C(208) 119.7(3)
 C(210)-C(209)-H(20I) 120.2
 C(208)-C(209)-H(20I) 120.2
 C(209)-C(210)-C(211) 119.7(3)
 C(209)-C(210)-H(21A) 120.2
 C(211)-C(210)-H(21A) 120.2
 N(5)-C(211)-C(210) 121.8(2)
 N(5)-C(211)-N(8) 117.5(2)
 C(210)-C(211)-N(8) 120.7(2)
 C(213)-N(8)-C(211) 123.0(2)
 C(213)-N(8)-C(212) 116.0(2)
 C(211)-N(8)-C(212) 115.5(2)
 N(8)-C(212)-H(21B) 109.5
 N(8)-C(212)-H(21C) 109.5
 H(21B)-C(212)-H(21C) 109.5
 N(8)-C(212)-H(21D) 109.5
 H(21B)-C(212)-H(21D) 109.5
 H(21C)-C(212)-H(21D) 109.5
 N(6)-C(213)-C(214) 121.0(2)
 N(6)-C(213)-N(8) 118.5(2)
 C(214)-C(213)-N(8) 120.5(2)
 C(215)-C(214)-C(213) 119.9(3)
 C(215)-C(214)-H(21E) 120.0
 C(213)-C(214)-H(21E) 120.0
 C(214)-C(215)-C(216) 119.4(3)
 C(214)-C(215)-H(21F) 120.3
 C(216)-C(215)-H(21F) 120.3
 C(217)-C(216)-C(215) 118.2(3)
 C(217)-C(216)-H(21G) 120.9
 C(215)-C(216)-H(21G) 120.9
 N(6)-C(217)-C(216) 123.4(3)
 N(6)-C(217)-H(21H) 118.3
 C(216)-C(217)-H(21H) 118.3
 F(13)-P(1)-F(16) 89.8(4)
 F(13)-P(1)-F(15) 179.2(4)
 F(16)-P(1)-F(15) 91.0(4)
 F(13)-P(1)-F(14) 89.8(4)
 F(16)-P(1)-F(14) 179.6(4)
 F(15)-P(1)-F(14) 89.4(4)
 F(13)-P(1)-F(12) 89.9(5)
 F(16)-P(1)-F(12) 89.7(4)
 F(15)-P(1)-F(12) 90.2(4)
 F(14)-P(1)-F(12) 90.3(4)
 F(13)-P(1)-F(11) 90.6(5)
 F(16)-P(1)-F(11) 90.6(5)
 F(15)-P(1)-F(11) 89.3(5)

F(14)-P(1)-F(11)	89.5(5)
F(12)-P(1)-F(11)	179.4(6)
F(14A)-P(1A)-F(15A)	92.3(12)
F(14A)-P(1A)-F(16A)	175.2(12)
F(15A)-P(1A)-F(16A)	92.3(11)
F(14A)-P(1A)-F(13A)	90.4(11)
F(15A)-P(1A)-F(13A)	177.1(13)
F(16A)-P(1A)-F(13A)	85.0(11)
F(14A)-P(1A)-F(12A)	90.2(12)
F(15A)-P(1A)-F(12A)	93.1(12)
F(16A)-P(1A)-F(12A)	91.1(13)
F(13A)-P(1A)-F(12A)	87.9(12)
F(14A)-P(1A)-F(11A)	89.0(13)
F(15A)-P(1A)-F(11A)	89.3(13)
F(16A)-P(1A)-F(11A)	89.5(12)
F(13A)-P(1A)-F(11A)	89.8(13)
F(12A)-P(1A)-F(11A)	177.6(16)
F(26)-P(2)-F(24)	91.86(14)
F(26)-P(2)-F(23)	178.61(13)
F(24)-P(2)-F(23)	89.13(12)
F(26)-P(2)-F(25)	91.54(14)
F(24)-P(2)-F(25)	91.20(12)
F(23)-P(2)-F(25)	89.41(12)
F(26)-P(2)-F(22)	90.24(14)
F(24)-P(2)-F(22)	177.72(13)
F(23)-P(2)-F(22)	88.76(12)
F(25)-P(2)-F(22)	89.65(12)
F(26)-P(2)-F(21)	89.96(12)
F(24)-P(2)-F(21)	89.76(11)
F(23)-P(2)-F(21)	89.07(10)
F(25)-P(2)-F(21)	178.18(13)
F(22)-P(2)-F(21)	89.33(10)
N(300)-C(301)-C(302)	176.9(5)
C(301)-C(302)-H(30A)	109.5
C(301)-C(302)-H(30B)	109.5
H(30A)-C(302)-H(30B)	109.5
C(301)-C(302)-H(30C)	109.5
H(30A)-C(302)-H(30C)	109.5
H(30B)-C(302)-H(30C)	109.5

Figure S2. IR spectrum of **8** in KBr.

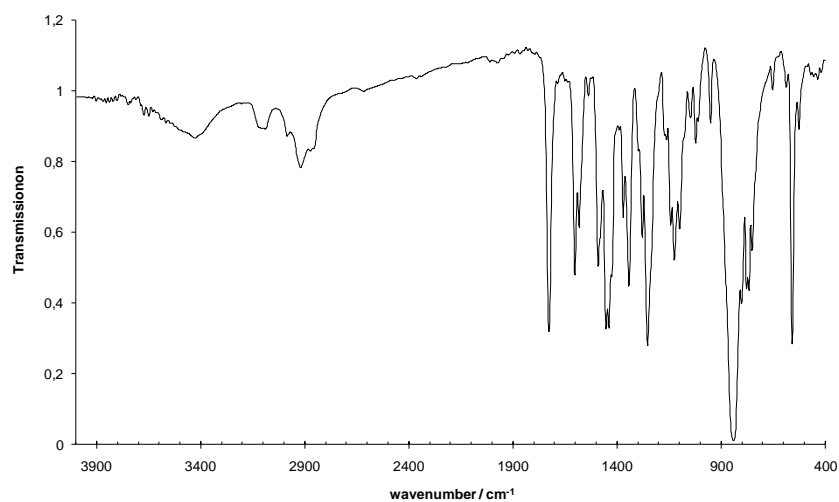


Figure S3. UV/Vis absorption and emission spectrum ($\lambda_{\text{exc}} = 517$ nm) of **8** in CH₃CN at 295 K.

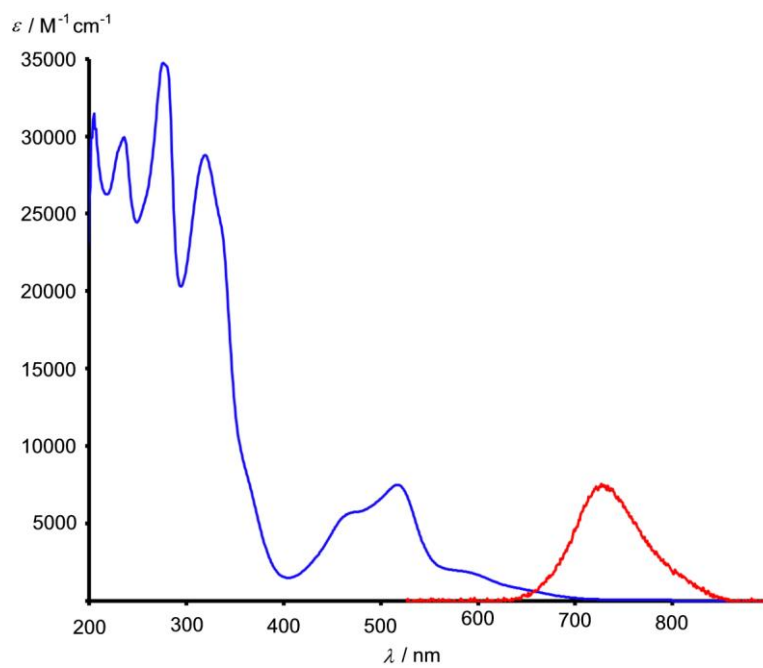


Figure S4. ^1H NMR spectrum of **8** in CD_3CN (top: full spectrum; bottom: zoom).

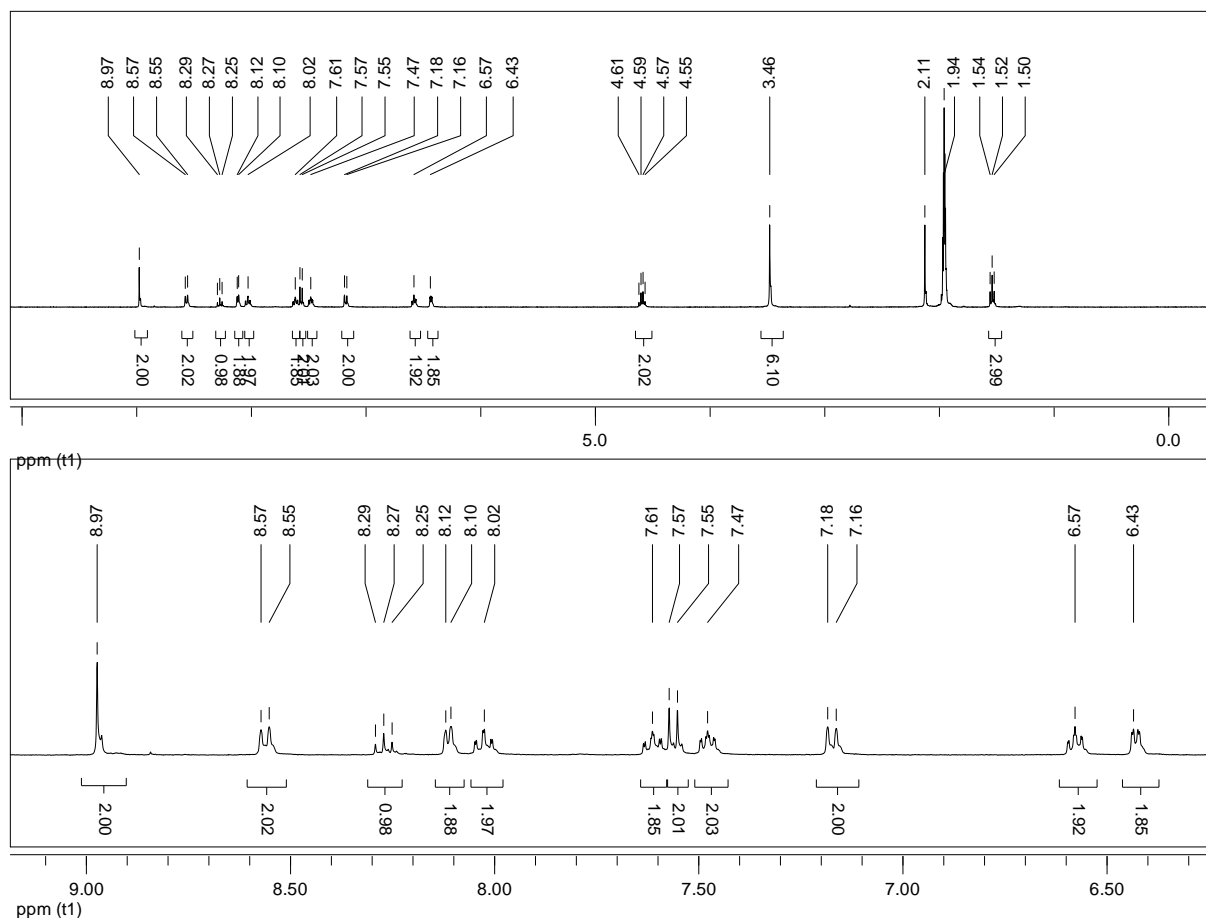


Figure S5. $^{13}\text{C}\{^1\text{H}\}$ NMR spectrum of **8** in CD_3CN (top: full spectrum; bottom: zoom).

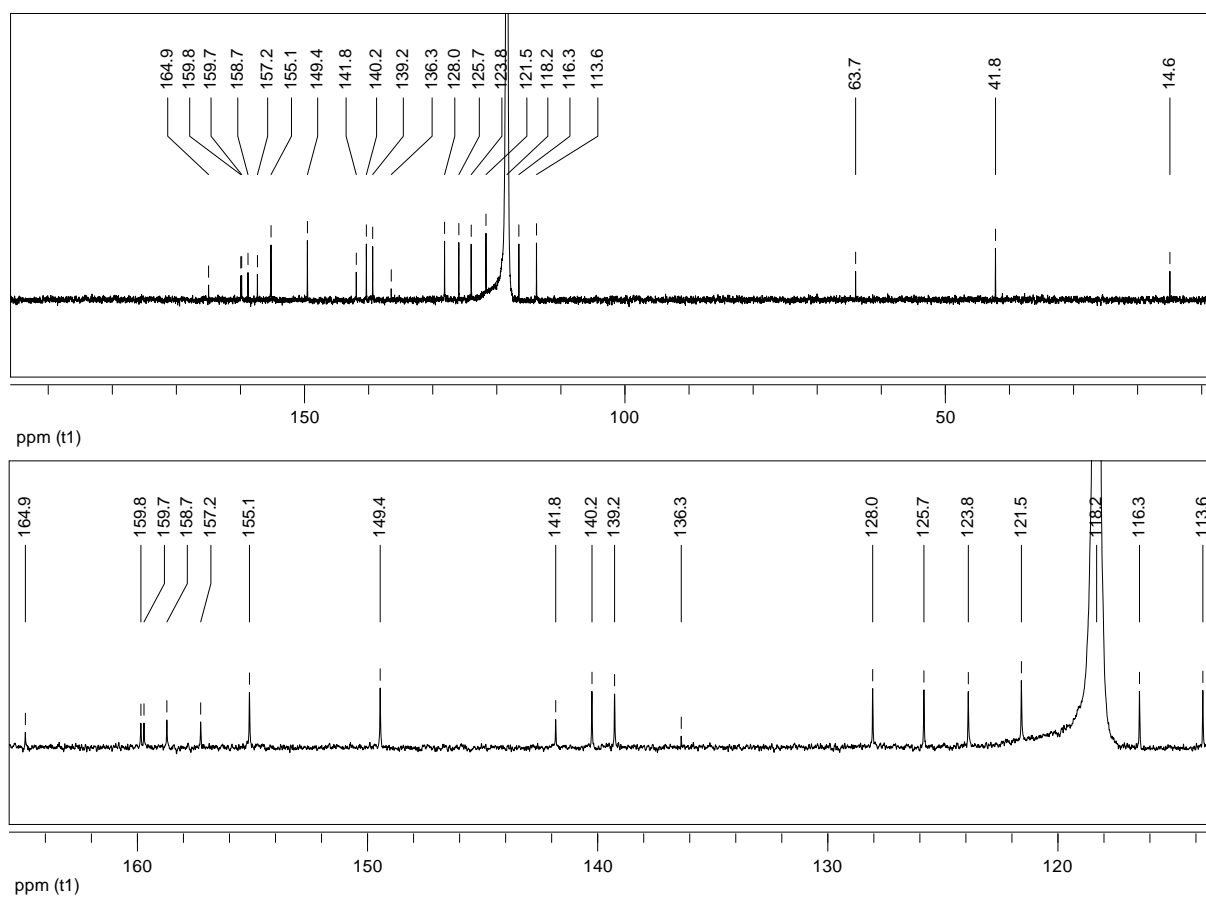


Figure S6. HH-COSY of **8** in CD₃CN.

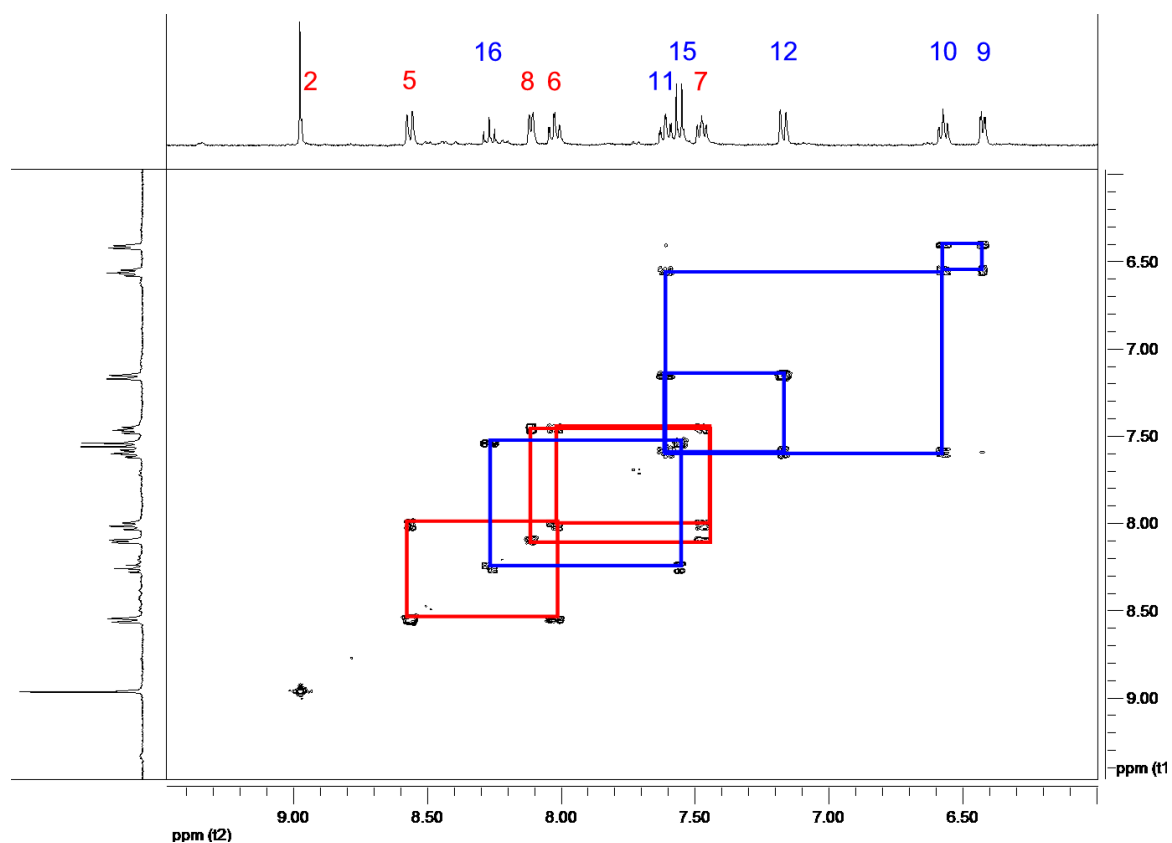


Figure S7. NOESY of **8** in CD₃CN.

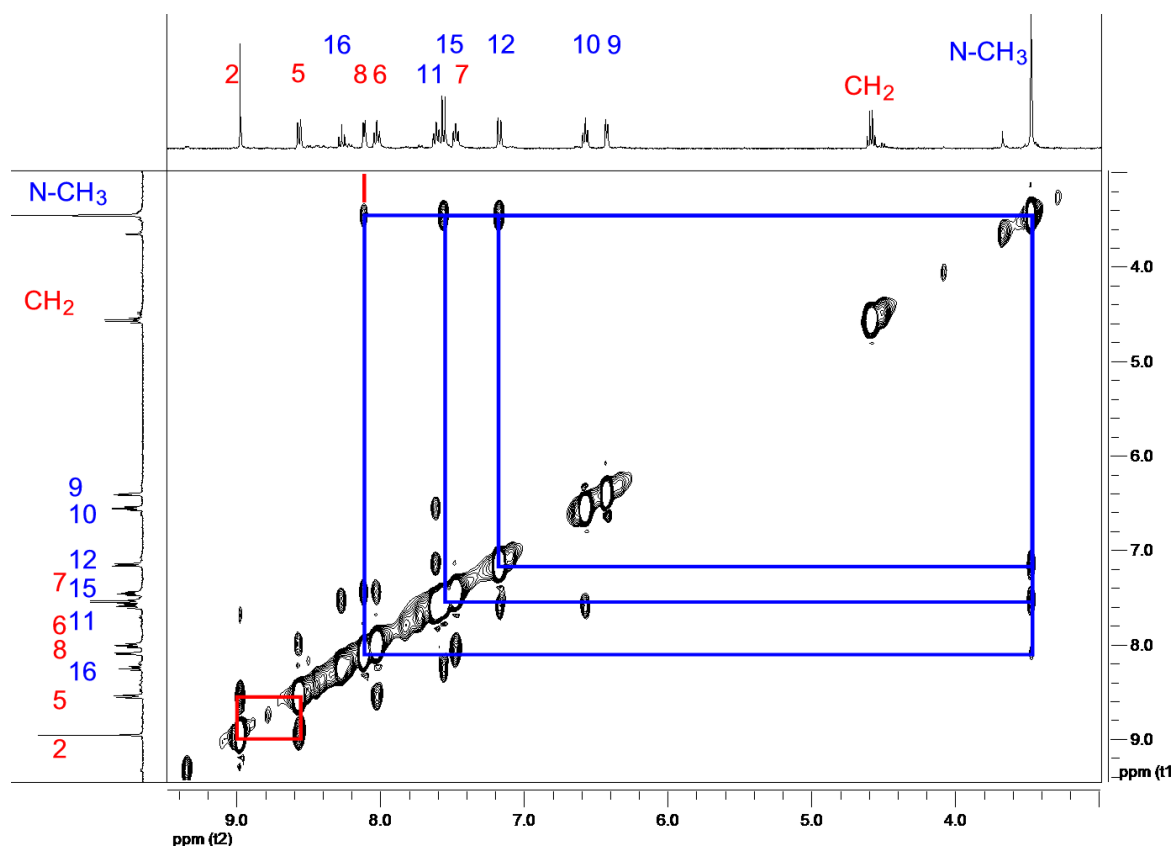


Figure S8. CH-COSY of **8** in CD₃CN.

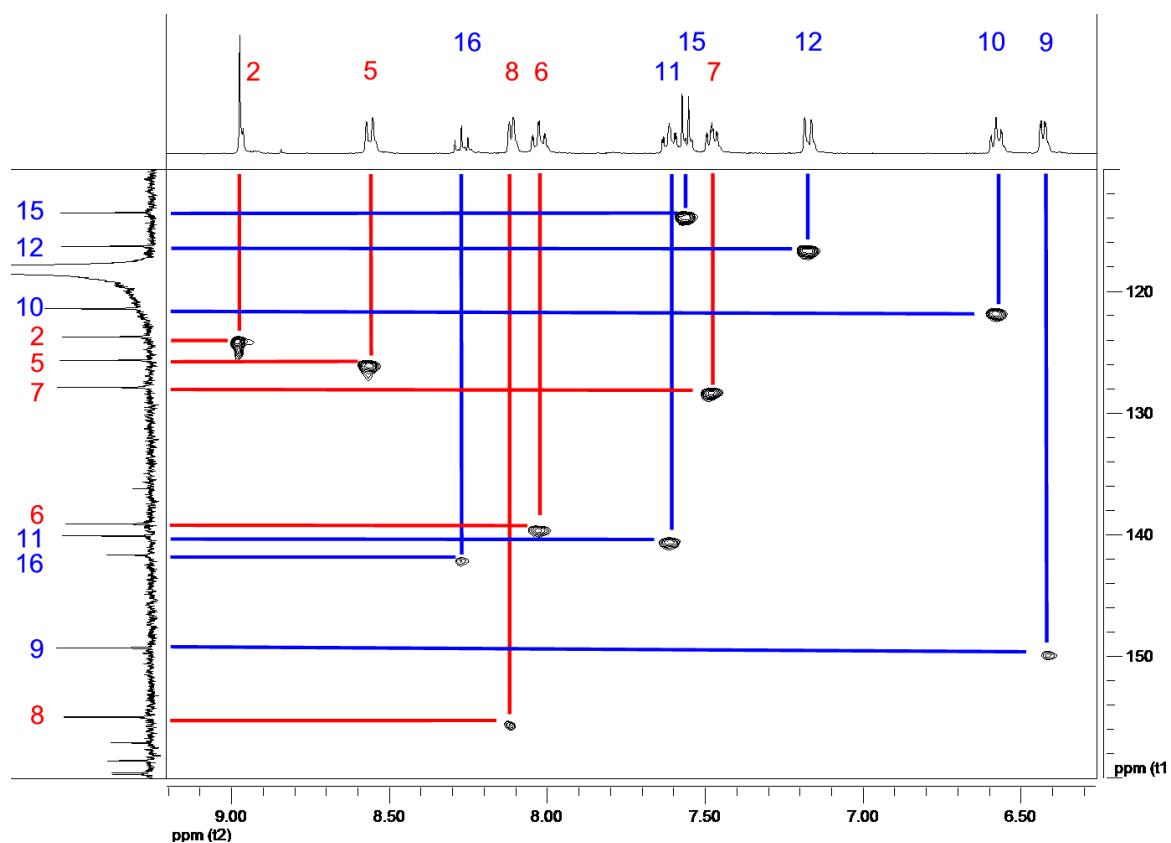


Figure S9. ¹³C-¹H HMBC of **8** in CD₃CN.

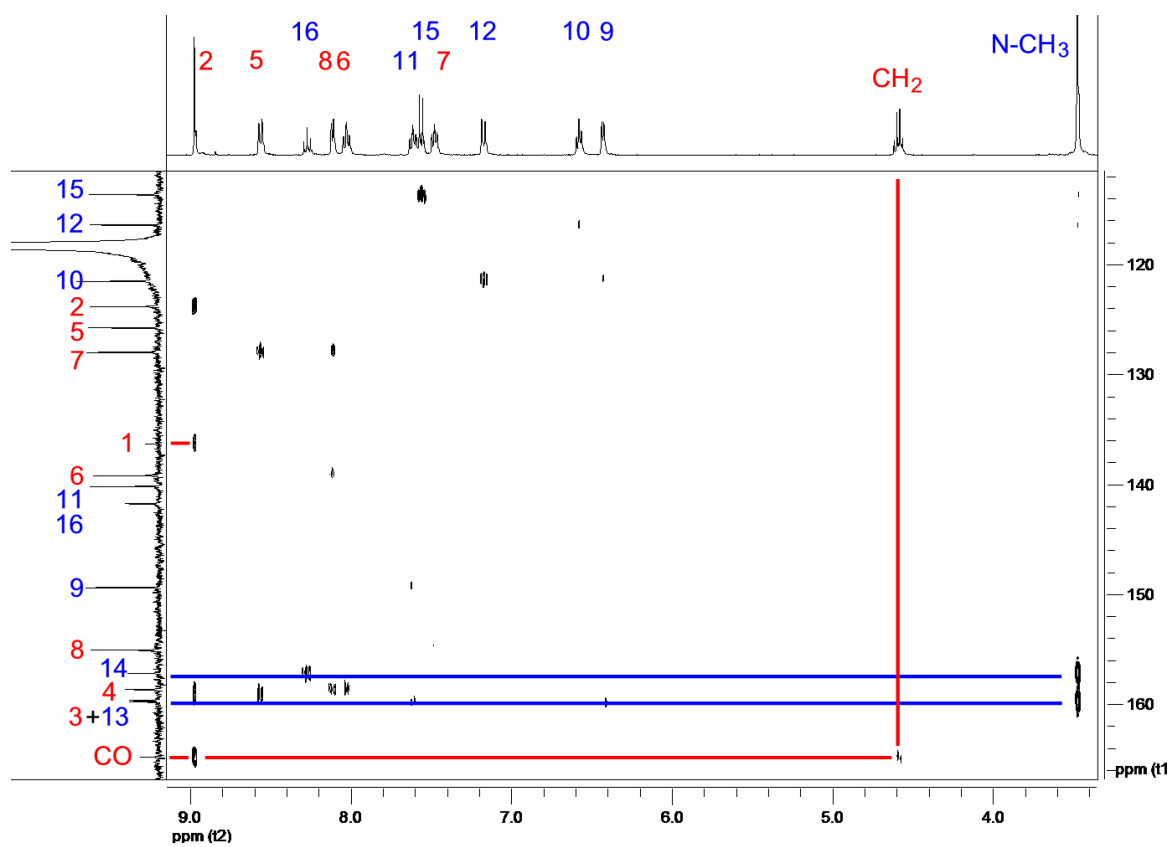
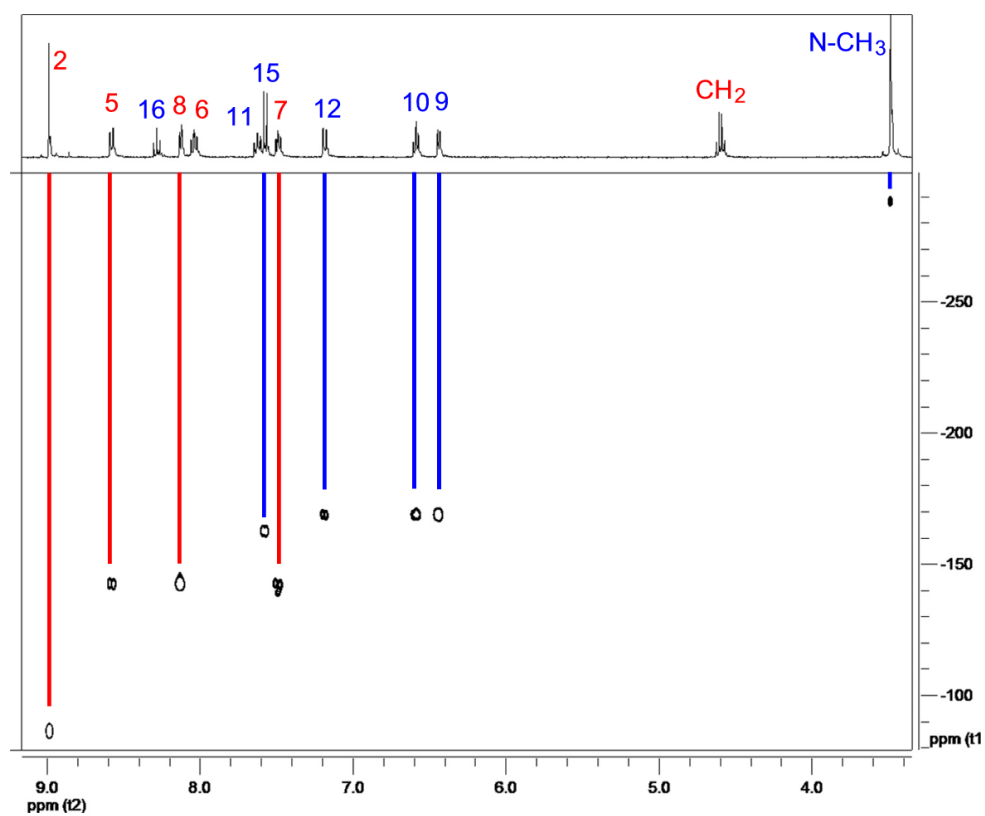
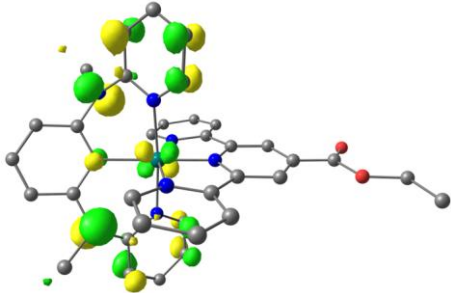
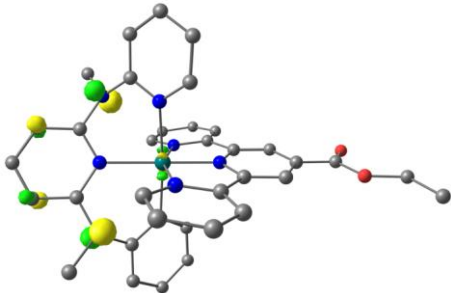
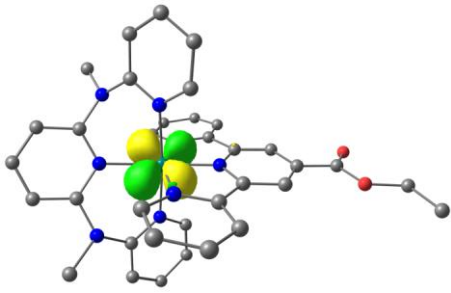
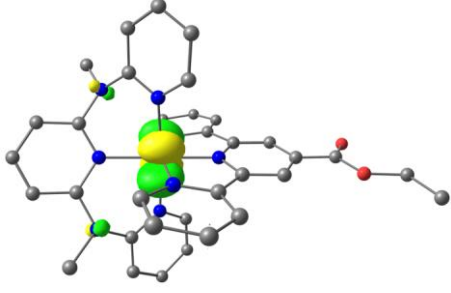
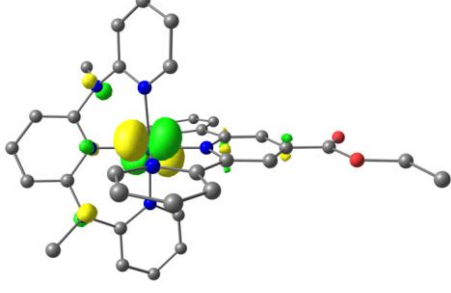
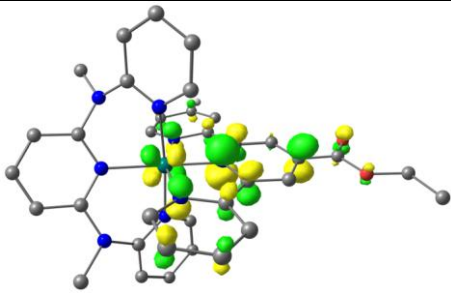
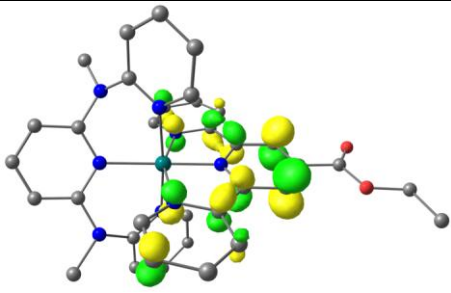
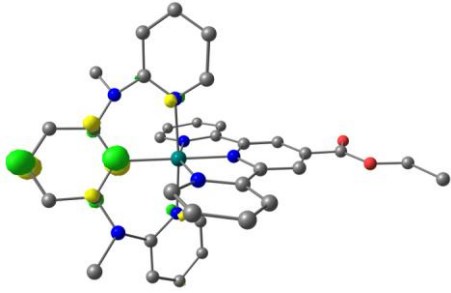
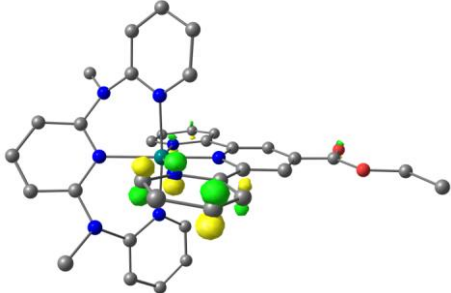
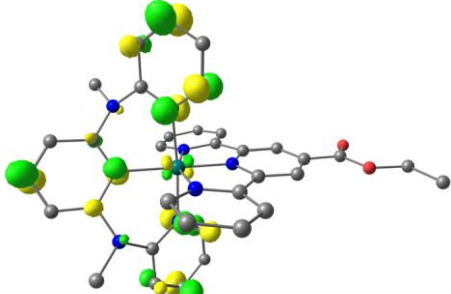


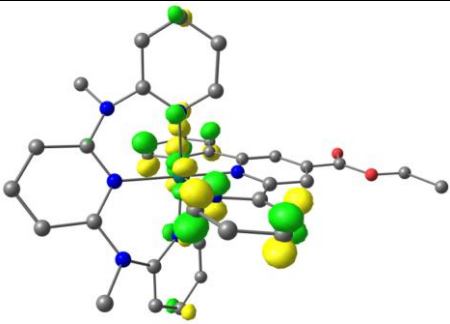
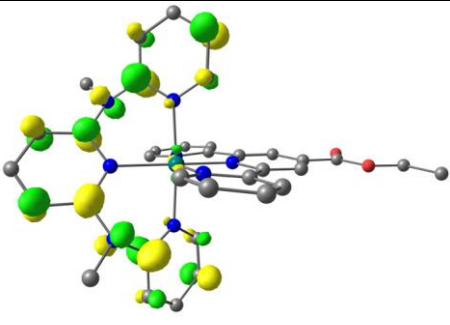
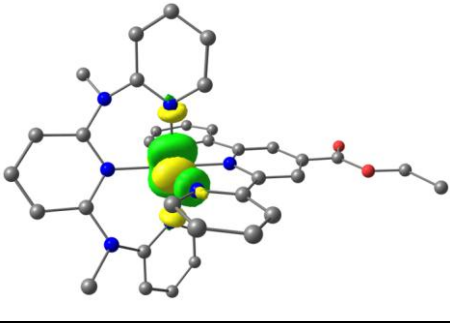
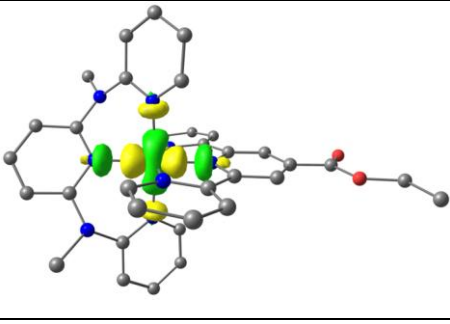
Figure S10. ^{15}N - ^1H HMBC of **8** in CD_3CN .



Graphical representation of some relevant frontier orbitals of 8.

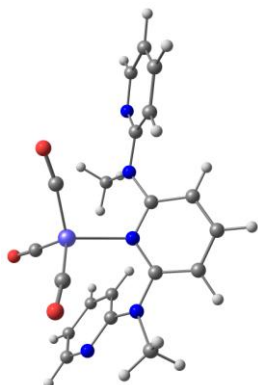
#MO	E / eV	contour value 0.06 a.u.	qualitative description
160	-11.884		ddpd (NMe+py_{terminal}) + d_{yz}
161	-11.352		ddpd (NMe+py_{central}) + d_{xy}
162	-11.083		d_{xz}
163	-10.838		ddpd (NMe) + d_{xy}
164	-10.798 (HOMO)		ddpd (NMe) + d_{yz}

165	-7.779 (LUMO)		$\pi^*(\text{tpy-COOEt})$
166	-7.424		$\pi^*(\text{tpy-COOEt})$
167	-6.618		$\pi^*(\text{ddpd})$
168	-6.577		$\pi^*(\text{tpy-COOEt})$
169	-6.548		$\pi^*(\text{tpy-COOEt+ddpd})$
170	-6.452		$\pi^*(\text{ddpd})$

171	-6.357		$\pi^*(\text{tpy-COOEt}+\text{ddpd})$
172	-6.187		$\pi^*(\text{tpy-COOEt})$
173	-6.020		$\pi^*(\text{ddpd})$
174	-5.723		$\pi^*(\text{ddpd})$
175	-5.679		$\pi^*(\text{ddpd})$
176	-5.110		$\mathbf{d}_{x^2-y^2}^2$
177	-4.794		$\pi^*(\text{tpy-COOEt})$
178	-4.619		\mathbf{d}_z^2

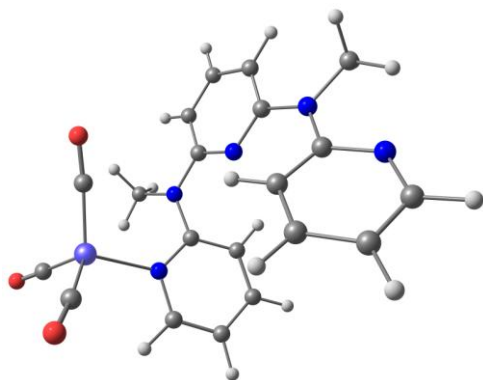
Cartesian Coordinates of Ni(CO)₃L complexes

L = $\kappa N(\text{central pyridine})\text{-ddpd}$: $\tilde{\nu} = 2017 \text{ cm}^{-1}$; $d(\text{C-O}) = 1.1776 \text{ \AA}$



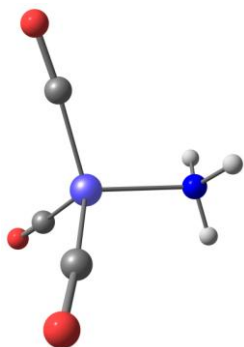
6	-1.192199000	1.057845000	-0.602639000
6	-1.697181000	2.378356000	-0.678960000
6	-0.825367000	3.446807000	-0.438169000
6	0.535284000	3.204164000	-0.201082000
6	0.989100000	1.865741000	-0.169386000
7	0.113752000	0.811282000	-0.268176000
1	-2.728587000	2.551799000	-0.958313000
1	1.235503000	4.022932000	-0.094502000
6	-5.473083000	-0.958263000	-1.281627000
6	-6.146247000	-0.278924000	-0.254916000
6	-5.377153000	0.527369000	0.612285000
6	-3.995895000	0.635688000	0.417157000
6	-3.402769000	-0.066240000	-0.666871000
7	-4.137655000	-0.856671000	-1.490775000
1	-5.845745000	1.047151000	1.443935000
1	-6.008550000	-1.610381000	-1.967309000
1	-7.218301000	-0.389967000	-0.128411000
1	-3.386454000	1.215258000	1.101170000
6	3.040139000	0.557851000	-0.674111000
6	2.548525000	0.002814000	-1.884719000
6	3.311231000	-0.975008000	-2.534425000
6	4.542699000	-1.385650000	-1.982674000
6	4.958791000	-0.771504000	-0.791233000
7	4.230954000	0.174948000	-0.152067000
1	2.951583000	-1.409635000	-3.463633000
1	1.608958000	0.338984000	-2.304192000
1	5.154917000	-2.145707000	-2.456725000
1	5.902433000	-1.037881000	-0.321846000
7	-2.008536000	-0.051463000	-0.909034000
6	-1.454588000	-1.144950000	-1.744886000
1	-0.367283000	-1.103242000	-1.694291000
1	-1.795653000	-2.112858000	-1.369475000
1	-1.798518000	-1.043614000	-2.780800000
7	2.355807000	1.593773000	0.018702000
6	3.157844000	2.527373000	0.842551000
1	2.571550000	2.862134000	1.703304000
1	4.037020000	1.987238000	1.192814000
1	3.487830000	3.402031000	0.262402000
1	-1.192113000	4.468281000	-0.496084000
28	0.485328000	-0.897765000	1.134868000
6	-1.150388000	-1.362065000	1.777693000
6	1.504902000	-0.140656000	2.438177000
6	1.314170000	-2.312051000	0.352032000
8	-2.130302000	-1.759076000	2.297063000
8	2.144125000	0.250679000	3.346037000
8	1.835560000	-3.299150000	-0.023109000

L = κN (terminal pyridine)-ddpd: $\tilde{\nu} = 2016 \text{ cm}^{-1}$; $d(\text{C-O}) = 1.1780 \text{ \AA}$



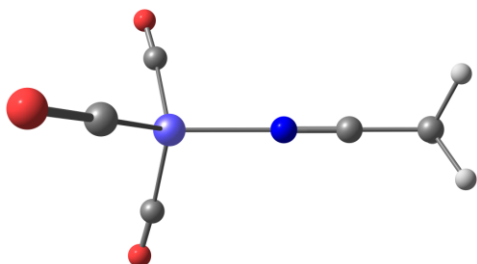
6	-2.738332000	1.560588000	-0.186873000
6	-3.012743000	2.931350000	-0.457625000
6	-1.997339000	3.866410000	-0.217368000
6	-0.745507000	3.468484000	0.279624000
6	-0.552959000	2.085098000	0.515395000
7	-1.528110000	1.175449000	0.284611000
1	-3.964883000	3.252281000	-0.856848000
1	0.031290000	4.197700000	0.466482000
6	-4.447703000	-2.956659000	-0.249348000
6	-3.243545000	-3.600233000	-0.571880000
6	-2.121379000	-2.785573000	-0.832208000
6	-2.231142000	-1.391457000	-0.754678000
6	-3.489759000	-0.823767000	-0.417448000
7	-4.570423000	-1.610624000	-0.174332000
1	-1.166782000	-3.230798000	-1.101512000
1	-5.351406000	-3.525300000	-0.042735000
1	-3.189562000	-4.683032000	-0.624343000
1	-1.377504000	-0.756595000	-0.934651000
6	0.790332000	0.276276000	1.523583000
6	-0.109657000	-0.161232000	2.524586000
6	0.088290000	-1.399677000	3.140482000
6	1.199453000	-2.182246000	2.761478000
6	2.036526000	-1.700322000	1.752561000
7	1.826899000	-0.510169000	1.113385000
1	-0.595247000	-1.741432000	3.912634000
1	-0.939140000	0.476955000	2.801142000
1	1.407794000	-3.140147000	3.226517000
1	2.895712000	-2.270938000	1.419187000
7	-3.731575000	0.581361000	-0.374195000
6	-5.126955000	1.045590000	-0.540957000
1	-5.273430000	1.517152000	-1.522974000
1	-5.777095000	0.176909000	-0.455264000
1	-5.388039000	1.764344000	0.244408000
7	0.681281000	1.582486000	0.973534000
6	1.830164000	2.497523000	1.119693000
1	1.645656000	3.239585000	1.911368000
1	2.714485000	1.916006000	1.381052000
1	2.037042000	3.023169000	0.181172000
1	-2.181427000	4.918039000	-0.422480000
28	2.897774000	-0.278308000	-0.705140000
6	1.970163000	0.849428000	-1.792671000
6	4.564682000	0.324220000	-0.311884000
6	2.946051000	-1.940390000	-1.447871000
8	5.665810000	0.700454000	-0.125179000
8	3.019127000	-2.969049000	-2.017776000
8	1.432128000	1.562188000	-2.559520000

L = NH₃: $\tilde{\nu} = 2022 \text{ cm}^{-1}$; d(C-O) = 1.1779 Å



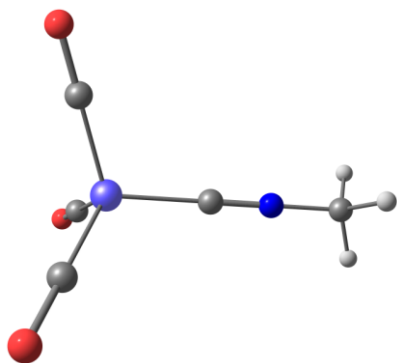
7	0.010502000	0.006530000	2.247972000
28	0.000827000	-0.000425000	0.113981000
6	1.741517000	-0.076465000	-0.406532000
6	-0.938262000	-1.471886000	-0.395239000
6	-0.808274000	1.544182000	-0.401231000
8	-1.537721000	-2.401312000	-0.800521000
8	-1.320030000	2.523850000	-0.808483000
8	2.844968000	-0.126842000	-0.815548000
1	0.439625000	-0.861521000	2.565872000
1	0.551497000	0.813916000	2.554989000
1	-0.955418000	0.073256000	2.566290000

L = CH₃CN: $\tilde{\nu} = 2029 \text{ cm}^{-1}$; d(C-O) = 1.1759 Å



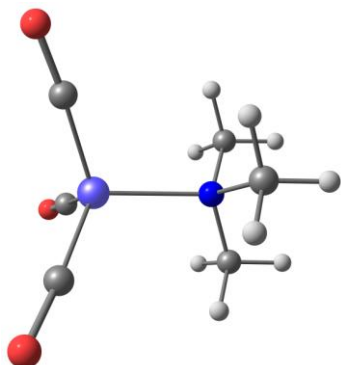
28	-0.493126000	0.000188000	0.000042000
6	-1.019284000	-0.764509000	1.570875000
6	-1.014613000	-0.978525000	-1.448953000
6	-1.013966000	1.744563000	-0.124384000
8	-1.422046000	-1.248258000	2.564164000
8	-1.414117000	-1.597775000	-2.365347000
8	-1.413083000	2.847898000	-0.203117000
6	4.191001000	-0.001721000	0.002217000
1	4.571096000	0.593705000	0.839816000
1	4.570675000	-1.024970000	0.099109000
1	4.570967000	0.425908000	-0.932317000
6	2.726395000	-0.001323000	0.002291000
7	1.553079000	-0.000820000	0.002048000

L = CH₃NC: $\tilde{\nu} = 2026 \text{ cm}^{-1}$; d(C-O) = 1.1746 Å



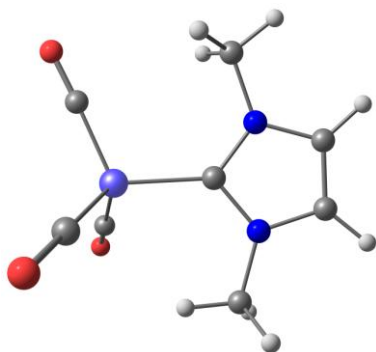
28	-0.457112000	0.000276000	-0.000197000
6	-1.034001000	-0.136895000	1.734395000
6	-1.028171000	-1.436217000	-0.985532000
6	-1.035554000	1.569530000	-0.750348000
6	1.459999000	0.002733000	0.000894000
8	-1.406675000	-0.225082000	2.844827000
8	-1.397053000	-2.356070000	-1.616016000
8	-1.409862000	2.574065000	-1.230495000
7	2.645858000	0.003477000	0.001129000
6	4.076084000	0.003322000	0.001596000
1	4.452180000	0.841387000	0.598785000
1	4.451976000	-0.932919000	0.428959000
1	4.452567000	0.101326000	-1.022680000

L = NMe₃: $\tilde{\nu} = 2018 \text{ cm}^{-1}$; d(C-O) = 1.1783 Å



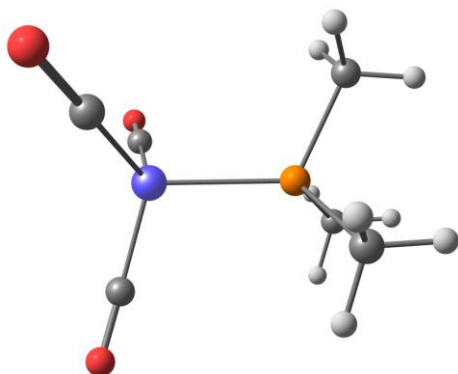
7	1.630255000	-0.002271000	0.000256000
28	-0.533608000	0.001320000	-0.000344000
6	-1.061949000	1.729122000	-0.180847000
6	-1.067140000	-1.018648000	-1.404455000
6	-1.067223000	-0.705530000	1.584770000
8	-1.493372000	-1.666204000	-2.291811000
8	-1.492311000	-1.152815000	2.588585000
8	-1.483529000	2.823384000	-0.295984000
6	2.126237000	0.542377000	-1.302423000
1	1.755592000	1.562183000	-1.438914000
1	3.230184000	0.553920000	-1.333168000
1	1.754163000	-0.075589000	-2.124431000
6	2.126374000	0.852475000	1.124144000
1	1.754058000	0.461197000	2.075083000
1	3.230298000	0.872020000	1.151229000
1	1.755971000	1.873940000	1.000063000
6	2.122907000	-1.404137000	0.178729000
1	1.743234000	-2.032970000	-0.631549000
1	3.226735000	-1.440883000	0.174784000
1	1.757468000	-1.803735000	1.128904000

L = NHC (1,3-dimethyl-2,3-dihydro-1*H*-imidazol-2-ylidene): $\tilde{\nu} = 2003 \text{ cm}^{-1}$; $d(\text{C-O}) = 1.1795 \text{ \AA}$



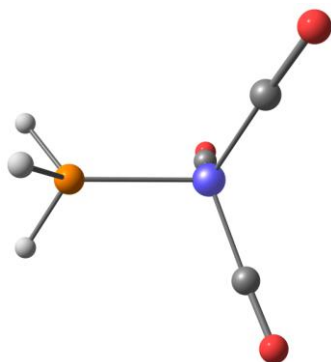
28	-0.999909000	-0.038726000	0.005330000
6	-1.773367000	1.604051000	-0.131304000
6	-1.488999000	-1.035589000	-1.439149000
6	-1.488024000	-0.803448000	1.584151000
8	-1.794347000	-1.667664000	-2.386652000
8	-1.790182000	-1.283721000	2.617791000
8	-2.315954000	2.648117000	-0.221294000
6	0.999683000	0.065109000	-0.000221000
6	3.185074000	0.815152000	-0.016069000
6	3.226755000	-0.553869000	-0.011355000
1	3.982625000	1.540060000	-0.021738000
1	4.066378000	-1.229766000	-0.013203000
7	1.827590000	1.176617000	-0.008208000
7	1.893589000	-0.995136000	0.000280000
6	1.352213000	2.566868000	-0.007142000
1	0.778788000	2.775658000	-0.914669000
1	0.714855000	2.748781000	0.862212000
1	2.212862000	3.241013000	0.034267000
6	1.513720000	-2.412900000	0.000235000
1	0.435997000	-2.484981000	0.146771000
1	1.776067000	-2.882138000	-0.955295000
1	2.023158000	-2.940771000	0.814279000

L = PMe₃; $\tilde{\nu} = 2017 \text{ cm}^{-1}$; d(C-O) = 1.1774 Å



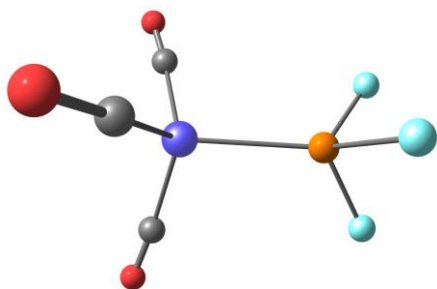
28	-0.847940000	0.002154000	-0.000741000
6	-1.341633000	-0.783905000	1.560879000
6	-1.340990000	1.747530000	-0.102242000
6	-1.337773000	-0.961554000	-1.460422000
8	-1.677544000	2.873887000	-0.168144000
8	-1.671240000	-1.583737000	-2.402781000
8	-1.678242000	-1.294500000	2.567013000
6	2.364086000	0.807528000	1.490935000
1	2.045422000	0.296488000	2.405199000
1	3.456268000	0.754842000	1.407903000
1	2.056757000	1.856181000	1.558346000
6	2.354032000	-1.696646000	-0.041598000
1	2.038980000	-2.228499000	-0.945164000
1	3.447198000	-1.608441000	-0.035660000
1	2.033777000	-2.278701000	0.828799000
6	2.368328000	0.883224000	-1.443663000
1	2.050087000	1.930604000	-1.464236000
1	3.460359000	0.838070000	-1.354179000
1	2.062725000	0.412731000	-2.383810000
15	1.527376000	0.001609000	0.000767000

L = PH₃; $\tilde{\nu} = 2033 \text{ cm}^{-1}$; d(C-O) = 1.1752 Å



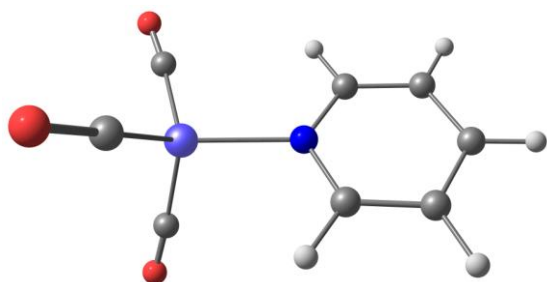
28	0.181192000	0.001745000	-0.000798000
6	0.650749000	1.739721000	-0.271771000
6	0.683806000	-0.626292000	1.632568000
6	0.676566000	-1.092629000	-1.368541000
8	1.054681000	-1.027119000	2.673219000
8	1.043177000	-1.789048000	-2.241334000
8	1.000852000	2.848351000	-0.443658000
15	-2.210295000	-0.022743000	0.008572000
1	-2.911744000	-1.101275000	0.643921000
1	-2.933601000	1.053412000	0.623122000
1	-2.930017000	-0.042118000	-1.232625000

L = PF₃: $\tilde{\nu} = 2068 \text{ cm}^{-1}$; d(C-O) = 1.1682 Å



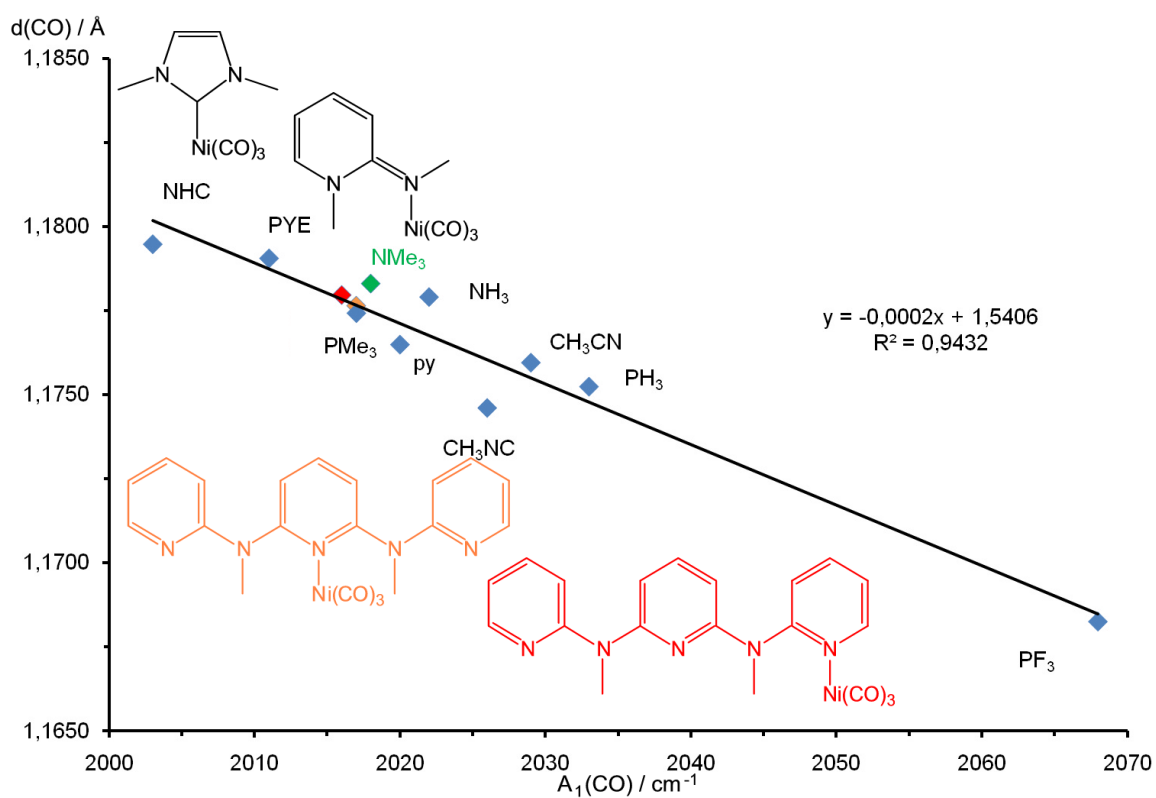
28	0.795350000	0.000773000	-0.000169000
6	1.307127000	-0.688236000	1.624481000
6	1.307109000	-1.061834000	-1.409283000
6	1.301104000	1.753870000	-0.215532000
8	1.705158000	-1.723465000	-2.285942000
8	1.695383000	2.845303000	-0.349779000
8	1.705110000	-1.117212000	2.635532000
15	-1.506495000	-0.002249000	0.000480000
9	-2.371505000	-0.585592000	1.348650000
9	-2.370092000	1.457763000	-0.168657000
9	-2.370584000	-0.877472000	-1.179874000

L = pyridine: $\tilde{\nu} = 2020 \text{ cm}^{-1}$; d(C-O) = 1.1765 Å



6	-1.756714000	-1.132832000	0.000494000
6	-3.159507000	-1.176693000	0.000397000
6	-3.879971000	0.032151000	-0.000549000
6	-3.163814000	1.243057000	-0.001302000
6	-1.760138000	1.204903000	-0.001153000
7	-1.059619000	0.037248000	-0.000313000
1	-4.966436000	0.030146000	-0.000682000
1	-3.666515000	-2.136425000	0.001040000
1	-3.674181000	2.201019000	-0.002007000
1	-1.176271000	2.118286000	-0.001691000
28	1.025497000	-0.002772000	-0.000123000
6	1.524415000	-0.872345000	1.519160000
6	1.524310000	-0.900744000	-1.502698000
6	1.643434000	1.707106000	-0.015834000
8	1.906568000	-1.474600000	-2.457106000
8	2.128279000	2.780695000	-0.025176000
8	1.905281000	-1.428758000	2.484359000
1	-1.166273000	-2.042450000	0.001276000

Correlation of A_1 stretching frequencies with C-O distances in $\text{Ni}(\text{CO})_3\text{L}$ complexes



10.6 Excited State Tuning of Bis(tridentate) Ruthenium(II) Polypyridine Chromophores by Push-Pull Effects and Bite Angle Optimization: A Comprehensive Experimental and Theoretical Study

A. Breivogel, M. Meister, C. Förster, F. Laquai, K. Heinze, *Chem. Eur. J.* **2013**, *19*, 13745–13760.

DOI: 10.1002/chem.201302231

Reprinted with permission from John Wiley and Sons, Copyright © 2013.

DFT-optimized (B3LYP/LANL2DZ, IEFPCM in CH₃CN) cartesian coordinates of $[\mathbf{1} - \mathbf{7}]^0$ (singlet and triplet), $[\mathbf{1} - \mathbf{7}]^+ [\mathbf{1} - \mathbf{7}]^{2+}$ (singlet ground state and ³MLCT state), $[\mathbf{1} - \mathbf{7}]^{2+}$ (³MC and ³TS state, except for $[\mathbf{4}]^{2+}$), $[\mathbf{1} - \mathbf{7}]^{3+}$, $[\mathbf{1} - \mathbf{7}]^{4+}$ and results of the TD-DFT (B3LYP/LANL2DZ, IEFPCM in CH₃CN) calculation of $[\mathbf{1} - \mathbf{7}]^{2+}$ (singlet) can be found in the online supporting information.

Supporting Information

© Copyright Wiley-VCH Verlag GmbH & Co. KGaA, 69451 Weinheim, 2013

Excited State Tuning of Bis(tridentate) Ruthenium(II) Polypyridine Chromophores by Push–Pull Effects and Bite Angle Optimization: A Comprehensive Experimental and Theoretical Study

**Aaron Breivogel,^[a] Michael Meister,^[b] Christoph Förster,^[a] Frédéric Laquai,^[b] and
Katja Heinze*^[a]**

chem_201302231_sm_miscellaneous_information.pdf

Table of Contents:

- 1) Description of the synthetic strategy and syntheses of **8**, 4-amino-2,6-dibromopyridine, **9** and **10**
- 2) Figures S1 – S49
- 3) Tables S1 – S11
- 4) DFT (B3LYP/LANL2DZ, IEFPCM in CH₃CN) optimized geometries of [**1** – **7**]⁰ (singlet and triplet), [**1** – **7**]⁺ (doublet), [**1** – **7**]²⁺ (singlet, ³MLCT, ³MC (not for [**4**]²⁺), ³TS (not for [**4**]²⁺)), [**1** – **7**]³⁺ (doublet) and [**1** – **7**]⁴⁺ (triplet)
- 5) Results of TD-DFT calculations of [**1** – **7**]²⁺ (singlet)

Synthesis strategy. Initial attempts to synthesize an amino substituted ddpd ligand analogously to the straightforward synthesis of **11** in a metal free amination using 4-amino-2,6-dibromopyridine or 4-amino-2,6-dichloropyridine and *N*-methylpyridine-2-ylamine failed although a similar procedure for the amination of 4-amino-2,6-dichloropyridine with pyrrolidine had been reported.^[1] This is probably due to the electron donating character of the NH₂ group which prevents a nucleophilic attack of *N*-methylpyridine-2-ylamine. Furthermore, the amine group itself can act as nucleophile. Hence, a strategy is necessary to prevent nucleophilic reactivity of the primary amino group and to activate the dibromopyridine. Attempts to employ a nitro group as latent amine by using 2,6-dibromo-4-nitropyridine in a metal free amination reaction with *N*-methylpyridine-2-ylamine using sodium hydride as base only resulted in *ipso* substitution of the nitro group before the desired bromine substitution.^[1,2,3,4] Finally, we chose the phthalimido group as protecting group because of its less electron withdrawing character compared to the nitro group which should inhibit the undesired *ipso* substitution. The phthalimido protecting group is introduced straightforwardly by treating 4-amino-2,6-dichloropyridine or its dibromo derivative with phthalic anhydride giving *N*-protected **8** and **9** in 56 % and 65 % yield, respectively. Amination of **8** or **9** with *N*-methylpyridine-2-ylamine using sodium hydride or potassium bis(trimethylsilyl) amide (KHMDs) as base in dioxane or in *N*-methylpyridine-2-ylamine as solvent using different reaction times and temperatures without a metal catalyst did not yield the desired ligand **10**. However, using Pd₂(dba)₃ (dba = dibenzylidene acetone) together with P(^{*t*}Bu)₃ as precatalyst and KO^{*t*}Bu as base **10** is successfully obtained from **8** or **9** in 5 % and 26 % yields, respectively (Scheme 2). Harsher reaction conditions are required for the chloro compound **8** compared to the bromo derivative **9** due to the lower reactivity of the chloro derivative **8** in the oxidative addition to the catalytically active palladium species. However, the starting material for **8**, 4-amino-2,6-dichloropyridine, is commercially available while the bromo derivative 4-amino-2,6-dibromopyridine, has to be prepared in three steps from 2,6-dibromopyridine rendering the dichloro starting material attractive in spite of its lower reactivity.^[5,6]

Synthesis of 2,6-dichloro-4-phthalimidopyridine (8). Phthalic anhydride (2.338 g, 15.78 mmol, 1.0 equiv) and 4-amino-2,6-dichloropyridine (3.287 g, 20.17 mmol, 1.3 equiv) were placed in a flask and acetic acid (100 ml) was added. The mixture was stirred at room temperature and ultrasonicated until the starting materials were completely dissolved. The yellow solution was heated to reflux for 6 h and cooled to room temperature. During the cooling process a colorless solid precipitated. The solid was filtered, washed with 60 ml of petroleum ether 40 – 60 and dried under reduced pressure. A colourless solid was obtained. Single crystals for X-ray diffraction analysis were obtained by slow evaporation of an acetone solution of **8**. Yield: 2.609 g (8.9 mmol, 56%). ¹H NMR (d₆-DMSO, 300 K): δ = 8.06-8.04 (m, 2 H, H²), 7.98-7.96 (m, 2 H, H¹), 7.80 (s, 2 H, H⁶) ppm. ¹³C{¹H} NMR (d₆-DMSO, 300 K): δ = 165.5 (C⁴), 149.4 (s, C⁷), 144.1 (s, C⁵), 135.3 (s, C¹), 131.0 (s, C³), 124.0 (s, C²), 119.3 (s, C⁶) ppm. ¹H-¹⁵N HMBC (d₆-DMSO, 300 K): δ = 294.1 (N^a), 167.6 (N^b) ppm. MS (FD): *m/z* 292.3 (100%) [M]⁺. IR (CsI): $\tilde{\nu}$ 3130 (w, CH), 3099 (w, CH), 1788 (m, C=O), 1761 (m, C=O), 1736 (vs, C=O), 1580 (vs, C=N), 1549 (s, C=N), 1468 (w), 1433 (s), 1377 (vs), 1354 (vs, C-N), 1232 (s, C-N), 1167 (m, C-N), 1143 (w, C-N), 1121 (w, C-N), 1097 (m, C-N, C-Cl), 1074 (m, C-N, C-Cl), 988 (w), 932 (w), 885 (w, C=C), 858 (m, C=C), 824 (m, C=C), 798 (w, C=C), 789 (w), 714 (s), 663 (w), 638 (m), 613 (w), 596 (w), 532 (w), 453 (w), 361 (w), 270 (w) cm⁻¹. Elemental analysis calcd (%) for C₁₃H₆Cl₂N₂O₂: C 53.27, H 2.06, N 9.56; found: C 52.90, H 2.20, N 8.92.

Synthesis of 4-amino-2,6-dibromopyridine. 4-amino-2,6-Dibromopyridine was synthesized by modification of a literature procedure.^[5] 2,6-Dibromo-4-nitropyridine-*N*-oxide^[6] (303 mg, 1.08 mmol, 1.0 equiv) and iron powder (301 mg, 5.39 mmol, 5.0 equiv) were suspended in acetic acid. The grey suspension was heated to 100 °C and stirred for 1 h. During the heating process the mixture turned brown. After cooling to room temperature the mixture was cooled with an ice bath and the pH was adjusted to 14 with a concentrated NaOH solution. The mixture was extracted with diethylether (5 × 10 – 15 ml). The combined organic phases were dried over Na₂SO₄, filtered and the solvent was removed in vacuo. A colorless solid was obtained. Yield: 0.24 g, (0.95 mmol, 88%). ¹H NMR (CD₂Cl₂, 300 K): δ = 6.69 (s, 2 H, H^{aromatic}), 4.43 (s, 2 H, NH₂) ppm. MS (FD): *m/z* 251.9 (100%) [M]⁺.

Synthesis of 2,6-dibromo-4-phthalimidopyridine (9). Phthalic anhydride (2.80 g, 18.9 mmol, 1.0 equiv) and 4-amino-2,6-dibromopyridine (5.94 g, 23.6 mmol, 1.2 equiv) were placed in a flask and

acetic acid (150 ml) was added. The mixture was stirred at room temperature and ultrasonicated. The starting materials did not dissolve completely. The yellowish suspension was heated to reflux for 6 h. Before starting to reflux, all the components were dissolved (at 60-70 °C) and a yellow solution was obtained. The mixture was cooled to room temperature. During the cooling process a colorless solid precipitated. The solid was filtered, washed with 50 ml of petroleum ether 40 – 60 and dried in a vacuo. A colorless solid was obtained. Single crystals for X-ray diffraction analysis were obtained by slow evaporation of an acetone solution of **9**. Yield: 4.67 g (12.2 mmol, 65%). ¹H NMR (d₆-DMSO, 300 K): δ = 8.06-8.03 (m, 2 H, H²), 7.98-7.95 (m, 2 H, H¹), 7.94 (s, 2 H, H⁶) ppm. ¹³C{¹H} NMR (d₆-DMSO, 300 K): δ = 165.5 (C⁴), 143.1 (s, C⁵), 139.8 (s, C⁷), 135.3 (s, C¹), 131.1 (s, C³), 123.9 (s, C²), 123.3 (s, C⁶) ppm. ¹H-¹⁵N HMBC (d₆-DMSO, 300 K): δ = 260.5 (N^a), 166.8 (N^b) ppm. MS (FD): *m/z* 382.1 (100%) [M]⁺. IR (CsI): $\tilde{\nu}$ 3140 (w, CH), 3117 (w, CH), 3090 (w, CH), 3062 (w, CH), 1790 (vs, C=O), 1757 (s, C=O), 1734 (s, C=O), 1570 (s, C=N), 1535 (vs, C=N), 1468 (m, C=N), 1423 (vs), 1348 (vs, C-N), 1231 (vs, C-N), 1165 (s, C-N), 1126 (s, C-N), 1096 (s, C-N), 1070 (vs, C-N, C-Br), 1016 (w), 982 (m), 962 (w), 906 (w, C=C), 883 (m, C=C), 860 (s, C=C), 824 (w, C=C), 800 (m, C=C), 770 (s), 717 (vs), 665 (w), 635 (vs), 590 (m), 563 (w), 532 (m), 405 (w), 362 (m), 330 (w), 289 (w), 224 (w) cm⁻¹. Elemental analysis calcd (%) for C₁₃H₆Br₂N₂O₂: C 40.87, H 1.58, N 7.33; found: C 41.79, H 1.57, N 7.43.

Synthesis of ddpd-phthalimide (10) from 2,4-dibromo-4-phthalimidopyridine (9). Under an argon atmosphere KO^tBu (814.2 mg, 7.6 mmol, 2.6 equiv) was dissolved in absolute dioxane (50 ml). While adding methylaminopyridine (0.80 ml, 7.8 mmol, 2.8 equiv) the solution turned yellow. Pd₂(dba)₃ (128.2 mg, 0.14 mmol, 0.05 equiv) was added and a black suspension was obtained. Then a solution of P(^tBu)₃ (1 M in toluene, 0.50 ml, 0.50 mmol, 0.18 equiv) was added and the reaction mixture turned into a green-brown solution. 2,6-Dibromo-4-phthalimidopyridine (**9**, 1.060 g, 2.8 mmol, 1.0 equiv) was added and dissolved completely. The green-brown solution was heated to 80 °C for 48 h. The reaction mixture was a brown solution containing a brown solid. The solvent was removed under reduced pressure. The residue was purified by column chromatography (silica gel, petroleum ether 40 – 60/ethyl acetate 1:2), yielding a light yellow solid. Yield: 312.1 mg (7.2 mmol, 26%). ¹H NMR (CD₃CN, 300 K): δ = 8.33 (m, 2 H, H⁸), 7.90 (m, 2 H, H¹¹), 7.85 (s, 2 H, H¹²), 7.64 (m, 2 H, H⁶), 7.38 (m, 2 H, H⁵), 6.96 (m, 2 H, H⁷), 6.79 (s, 2 H, H²), 3.55 (s, 6 H, CH₃) ppm. ¹³C{¹H} NMR (CD₃CN, 300 K): δ = 167.6 (s, C⁹), 158.4 (s, C⁴), 157.6 (s, C³), 148.9 (s, C⁸), 143.0 (s, C¹), 138.0 (s, C⁶), 135.7 (s, C¹²), 132.7 (s, C¹⁰), 124.4 (s, C¹¹), 118.6 (s, C⁷), 117.1 (s, C⁵), 102.8 (s, C²), 36.3 (s, CH₃) ppm. ¹H-¹⁵N HMBC (CD₃CN, 300 K): δ = 287.9 (N^{pyridine,outer}), 250.1 (N^{pyridine,center}), 169.0 (N^{phthalimide}), 98.7 (NCH₃) ppm. MS (FD): *m/z* 436.5 (100%) [M]⁺. HR-MS (ESI⁺): Calcd for C₂₅H₂₀N₆NaO₂⁺: *m/z* 459.1545. Obsd: *m/z* 459.1559. IR (CsI): $\tilde{\nu}$ 3055 (w, CH), 2957 (s, CH), 2926 (s, CH), 2854 (s, CH), 1768 (m, C=O), 1726 (vs, C=O), 1599 (s, C=N), 1472 (vs, CH₃, C=N), 1421 (vs, CH₃), 1364 (vs, C-N, CH₃), 1333 (s, C-N), 1290 (s, C-N), 1240 (s, C-N), 1175 (m, C-N), 1144 (m, C-N), 1111 (s, C-N), 1080 (m, C-N), 989 (m), 961 (w), 881 (m), 851 (w), 798 (m), 777 (s), 743 (m), 716 (s), 673 (w), 636 (w), 619 (m), 555 (w), 532 (w), 409 (w), 361 (w) cm⁻¹. Elemental analysis calcd (%) for C₂₅H₂₀N₆O₂: C 68.80, H 4.62, N 19.25; found: C 68.57, H 4.65, N 18.34.

Synthesis of ddpd-phthalimide (10) from 2,6-dichloro-4-phthalimidopyridine (8). Under an argon atmosphere KO^tBu (411.0 mg, 3.66 mmol, 2.6 equiv) was dissolved in absolute dioxane (50 ml). While adding methylaminopyridine (0.40 ml, 3.9 mmol, 2.8 equiv) the solution turned yellow. Pd₂(dba)₃ (66.8 mg, 0.073 mmol, 0.05 equiv) was added and a black suspension was obtained. Then a solution of P(^tBu)₃ (1 M in toluene, 0.40 ml, 0.40 mmol, 0.30 equiv) was added and the reaction mixture turned into a green-brown solution. 2,6-Dichloro-4-phthalimidopyridine (**8**, 410.1 mg, 1.4 mmol, 1.0 equiv) was added and dissolved completely. The green-brown solution was heated (80 °C for 48 h). An aliquot was taken from the reaction mixture and filtered. An FD mass spectrum of the solution did not show a signal for the product, only signals of the starting materials could be found. Therefore, the heating of the mixture was continued (90 °C for 48 h). The reaction mixture now was a brown solution containing a brown solid. The solvent was removed under reduced pressure. The remaining dark brown oil was dissolved in very few dichloromethane and purified by column chromatography (silica gel, petroleum ether 40 – 60/ethyl acetate 1:2). A yellow oil was obtained, which was dissolved in THF (2 ml) and ice cold petroleum ether 40 – 60 was added. The mixture was stored at –30 °C for 18 h. The clear solution was decanted and the solid was dried in a vacuo and

purified by column chromatography (silica gel, 1:3:0.05 petroleum ether 40-60/ethyl acetate/triethylamine). A light yellow solid was obtained. Yield: 19.2 mg (0.0669 mmol, 5%).

- [1] M. Menichincheri, D. F. Bassini, M. Gude, M. Angiolini, *Tetrahedron Lett.* **2003**, *44*, 519–522.
- [2] R. Shetty, D. Nguyen, D. Flubacher, F. Ruggle, A. Schumacher, M. Kelly, E. Michelotti, *Tetrahedron Lett.* **2007**, *48*, 113–117.
- [3] H. Abe, N. Masuda, M. Waki, M. Inouye, *J. Am. Chem. Soc.* **2005**, *127*, 16189–16196.
- [4] J. C. Rodriguez-Ubis, R. Sedano, G. Barroso, O. Juanes, E. Brunet, *Helv. Chim. Acta* **1997**, *80*, 86–96.
- [5] M. van Ammers, H. J. den Hertog, *Recl. Trav. Chim. Pays-Bas* **1958**, *77*, 340–345.
- [6] U. Neumann, F. Vögtle, *Chem. Ber.* **1989**, *122*, 589–591.

Figure S1. IR spectrum of **8** in CsI.

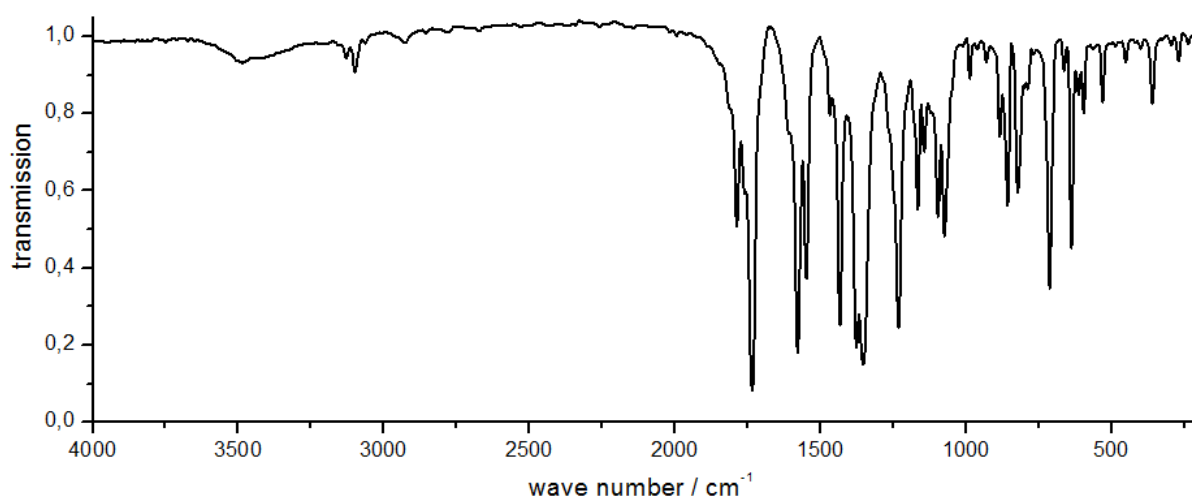


Figure S2. IR spectrum of **9** in CsI.

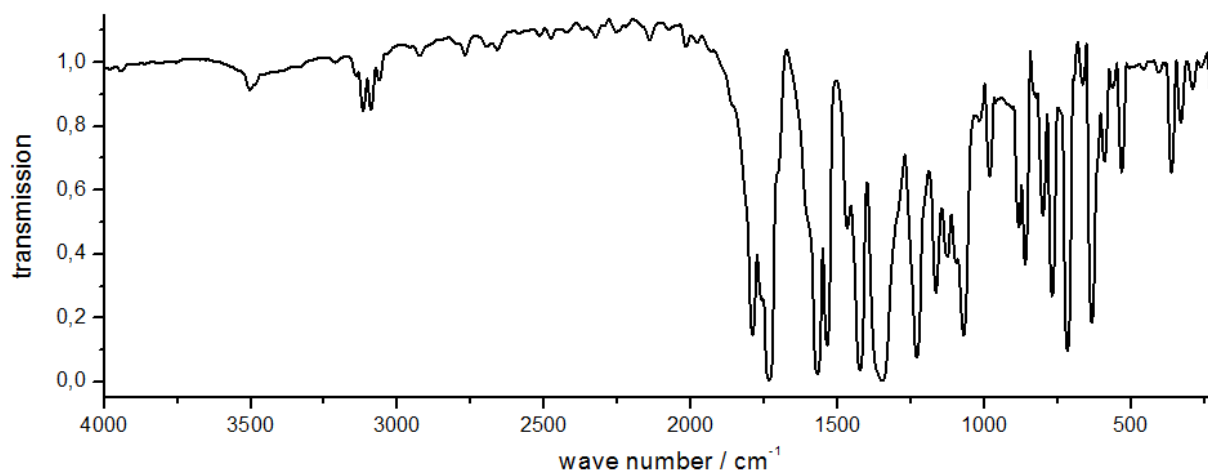


Figure S3. IR spectrum of **10** in CsI.

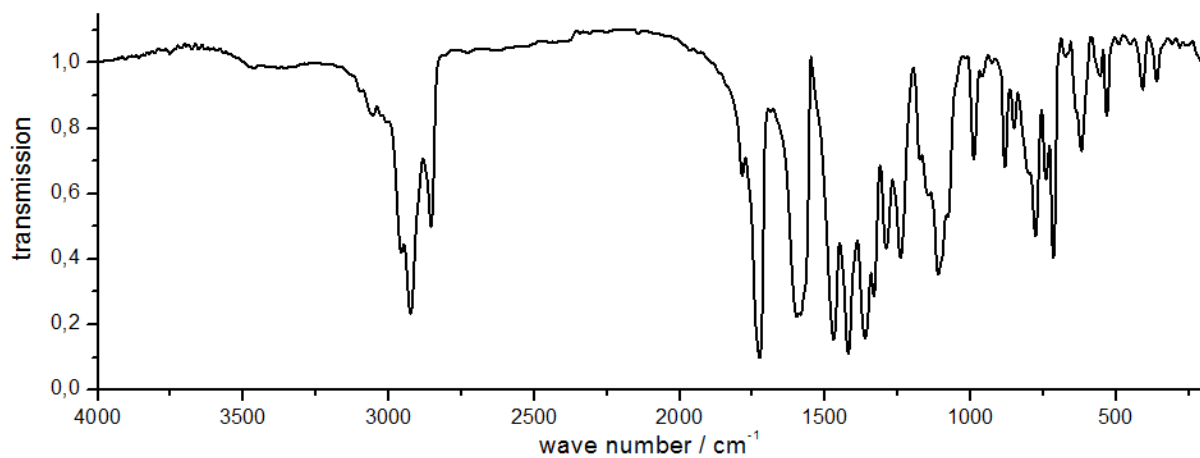


Figure S4. IR spectrum of **11** between KBr plates.

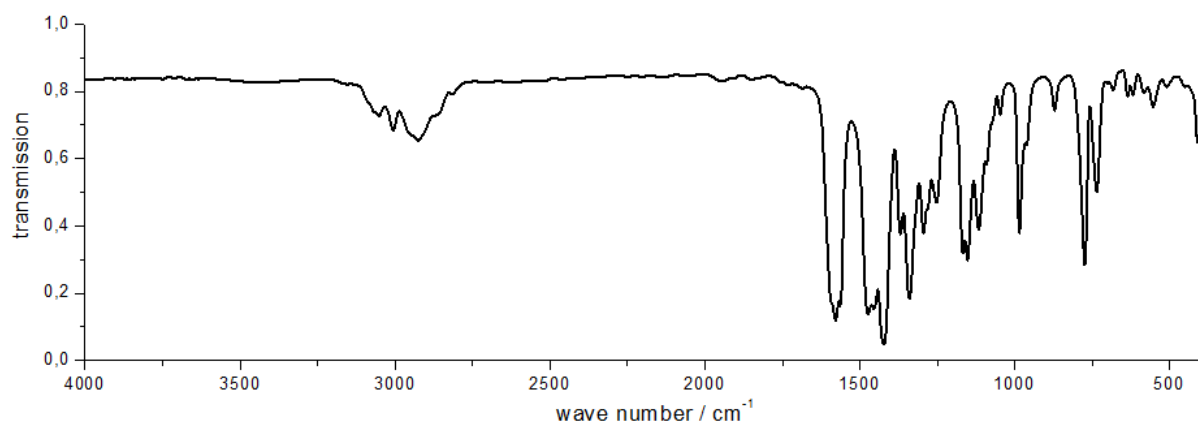


Figure S5. ¹H-NMR spectrum of **8** in d₆-DMSO (top: full spectrum; inset: zoom).

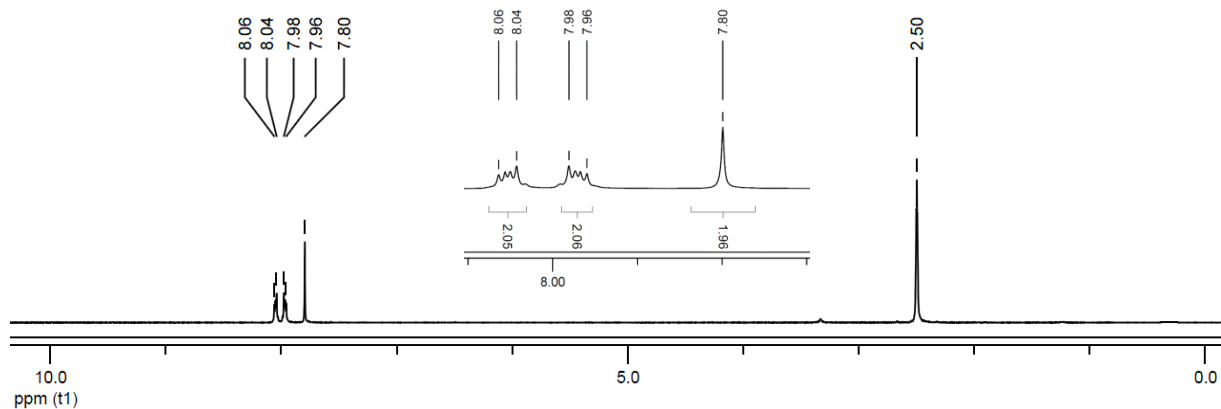


Figure S6. ¹H-NMR spectrum of **9** in d₆-DMSO (top: full spectrum; inset: zoom).

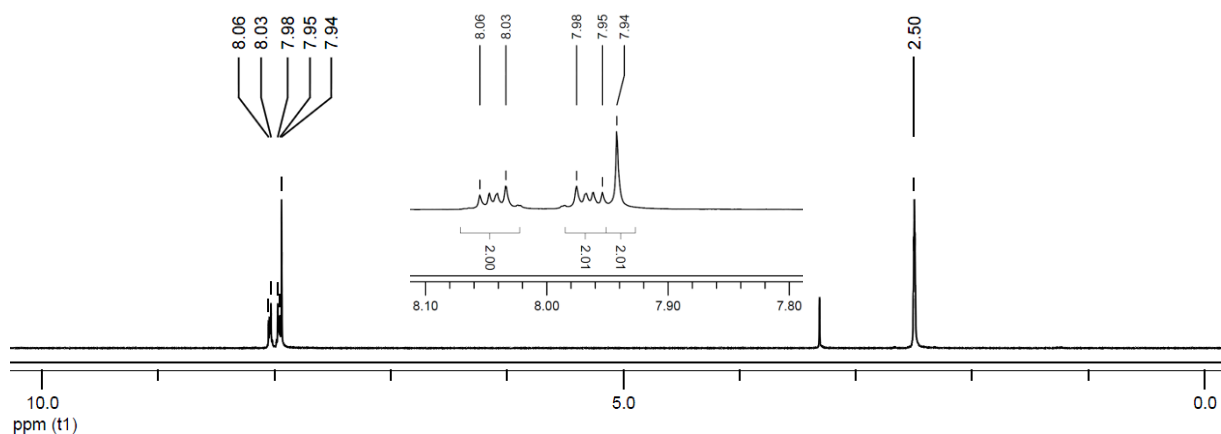


Figure S7. ^1H -NMR spectrum of **10** in CD_3CN (top: full spectrum; bottom: zoom).

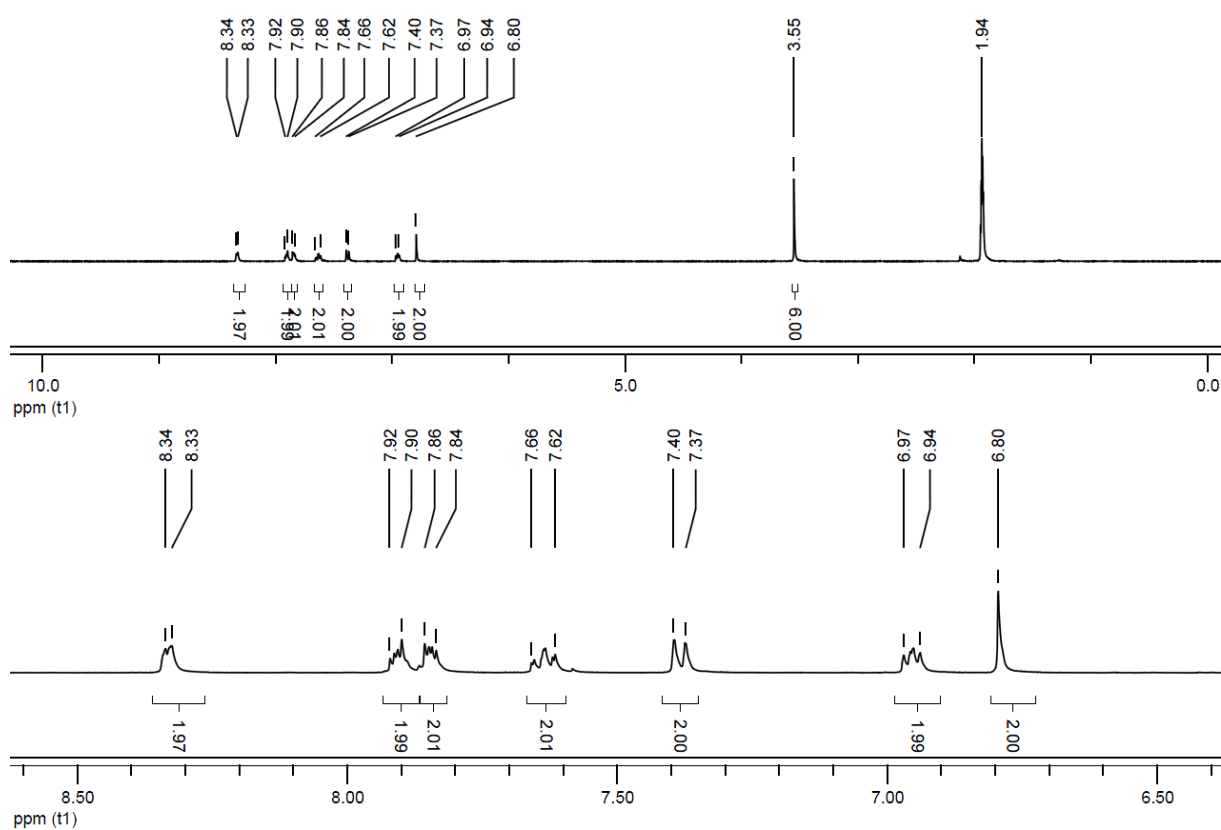


Figure S8. ^1H -NMR spectrum of **11** in CD_3CN (top: full spectrum; bottom: zoom).

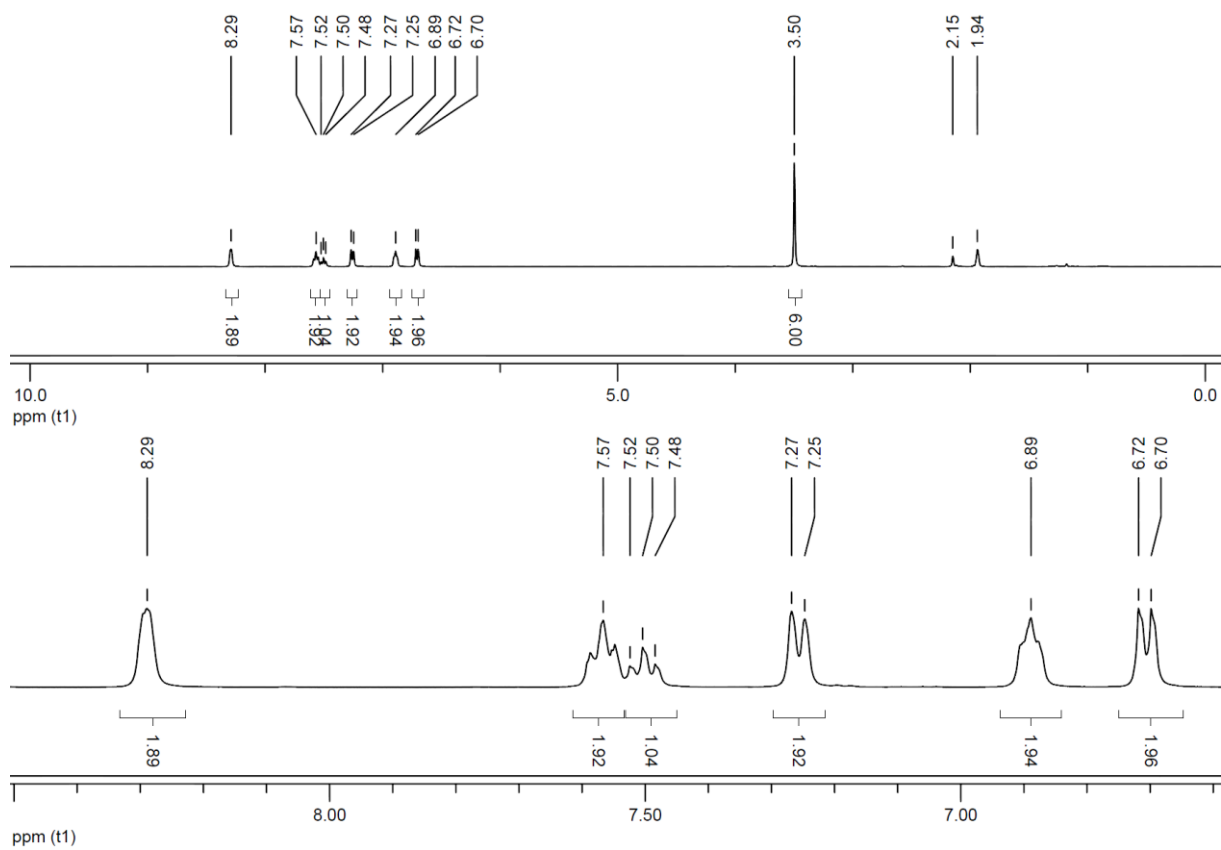


Figure S9. $^{13}\text{C}\{^1\text{H}\}$ NMR spectrum of **8** in $\text{d}_6\text{-DMSO}$.

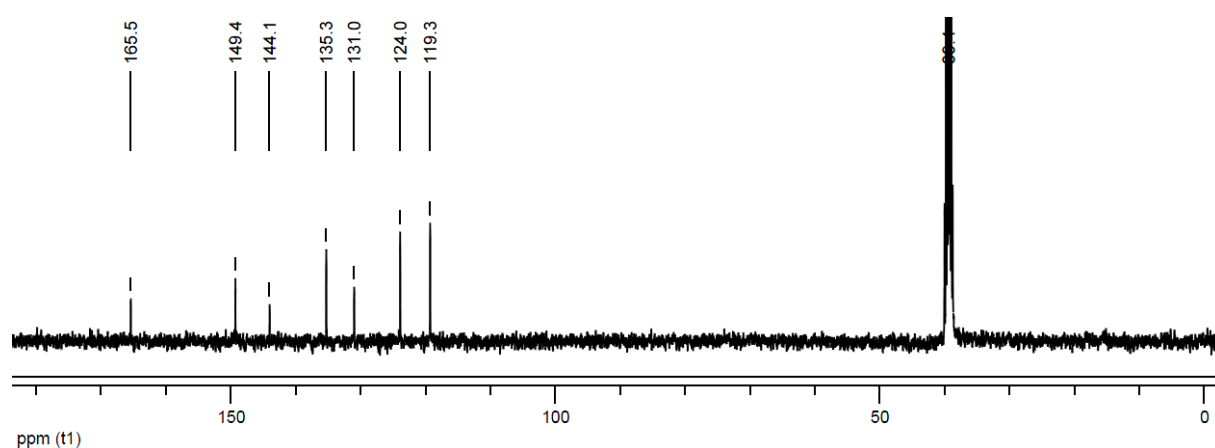


Figure S10. $^{13}\text{C}\{^1\text{H}\}$ NMR spectrum of **9** in $\text{d}_6\text{-DMSO}$.

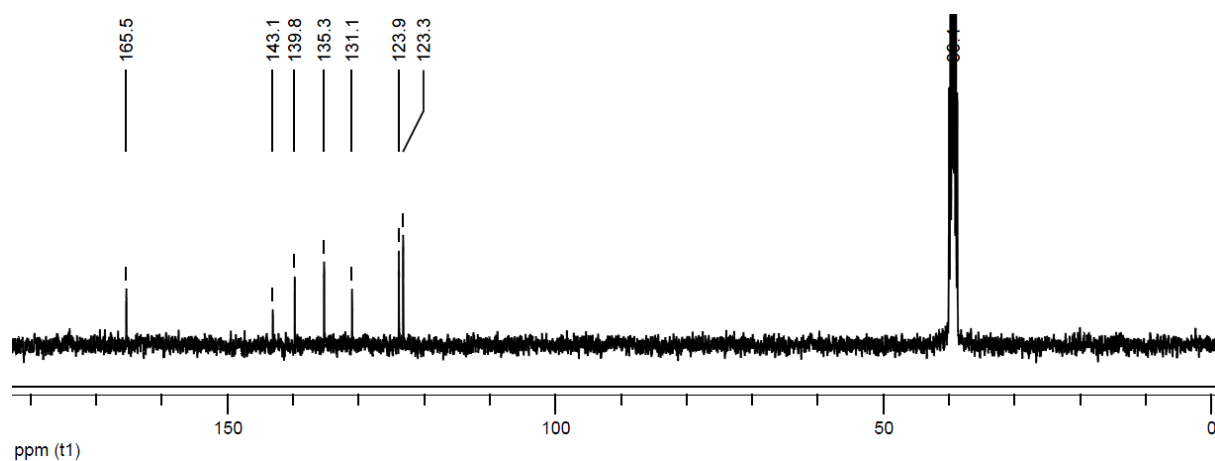


Figure S11. $^{13}\text{C}\{^1\text{H}\}$ NMR spectrum of **10** in CD_3CN .

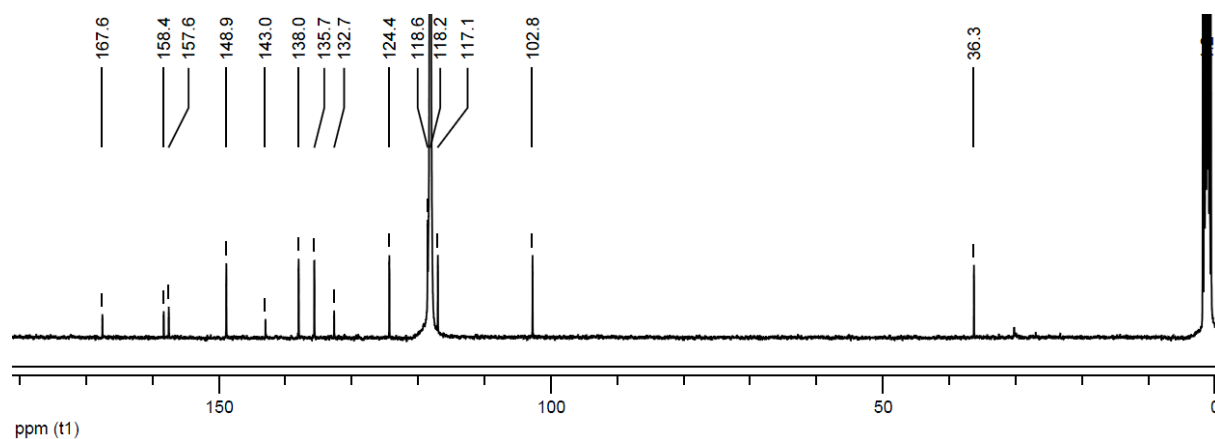


Figure S12. $^{13}\text{C}\{^1\text{H}\}$ NMR spectrum of **11** in CD_3CN .

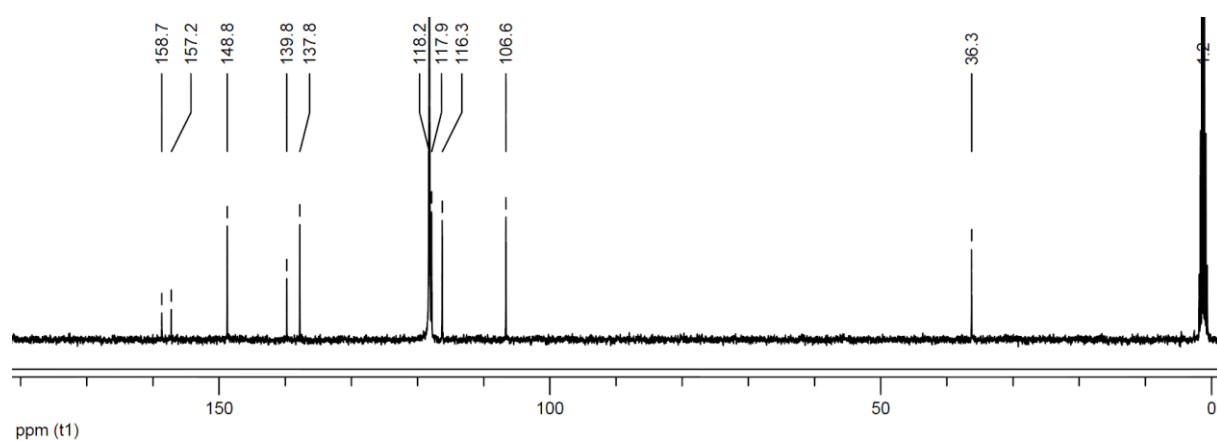


Figure S13. $^{15}\text{N}\text{-}^1\text{H}$ HMBC of **8** in d_6DMSO .

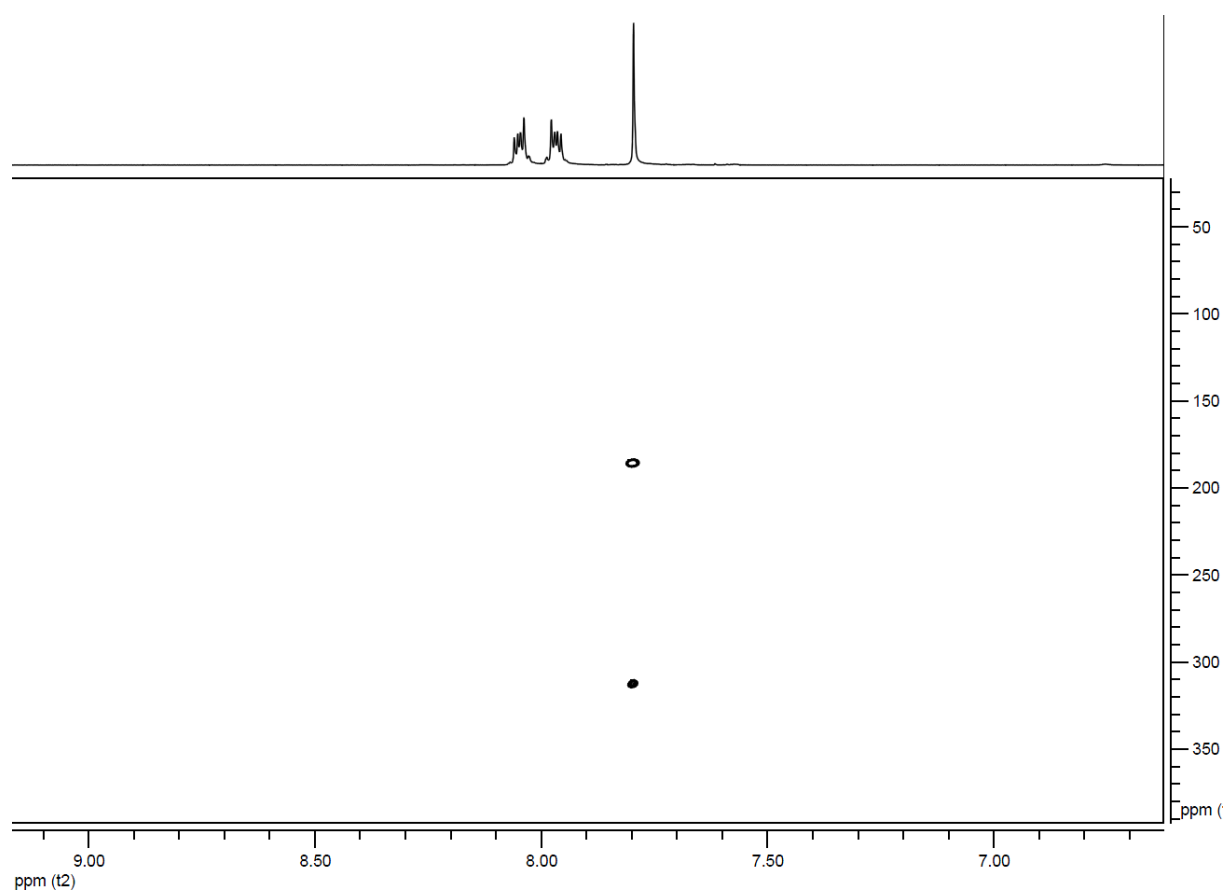


Figure S14. ^{15}N - ^1H HMBC of **9** in d_6DMSO .

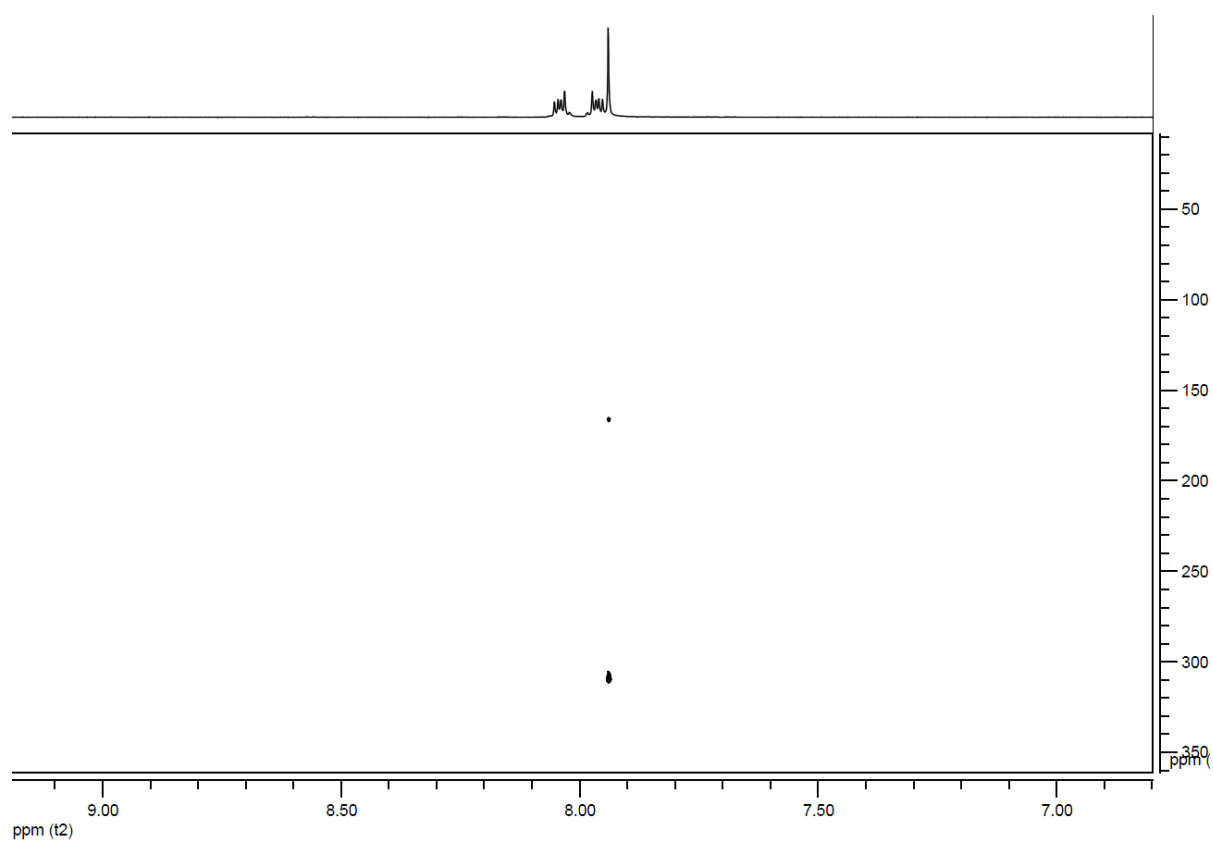


Figure S15. ^{15}N - ^1H HMBC of **10** in CD_3CN .

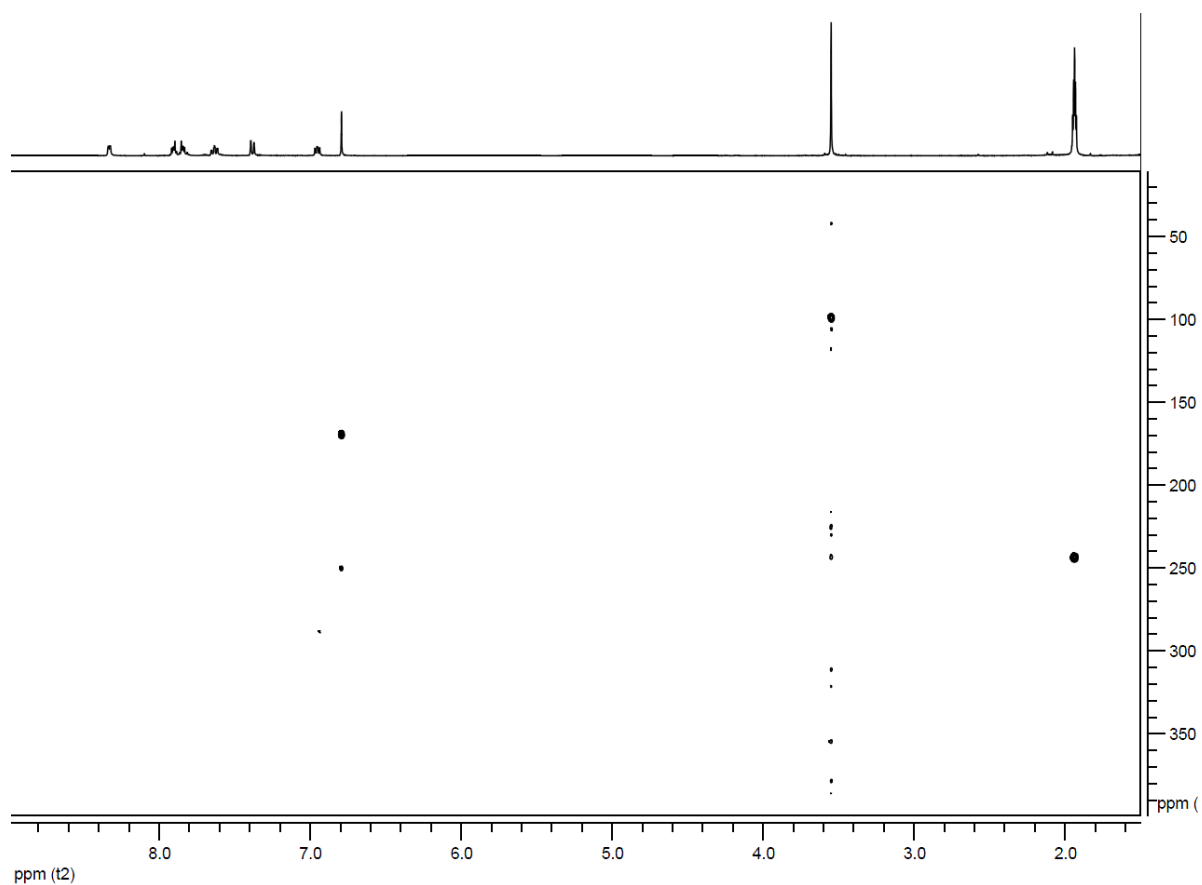


Figure S16. ^{15}N - ^1H HMBC of **11** in CD_3CN .

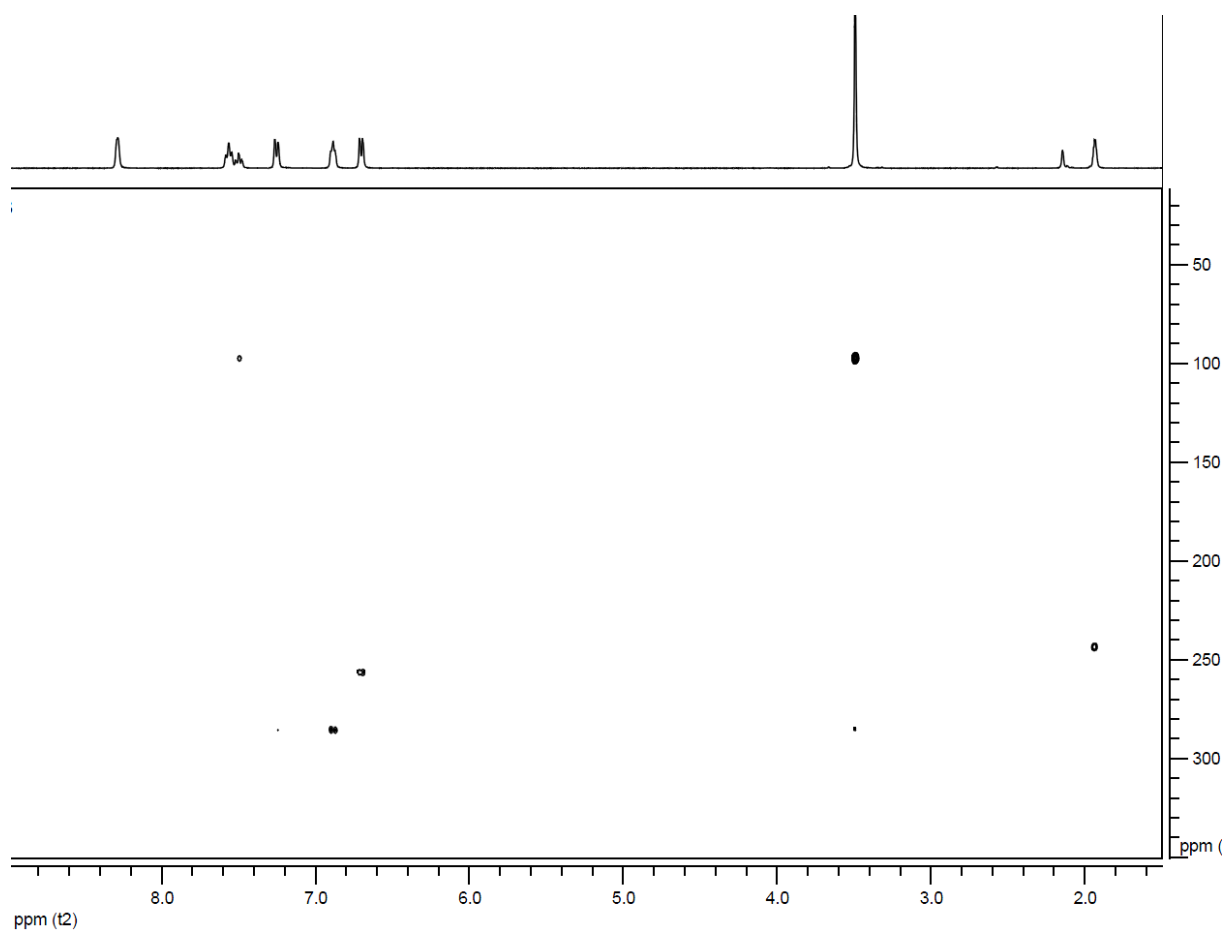


Figure S17. Ellipsoid view and atom numbering of **8** (50% probability, 296 K).

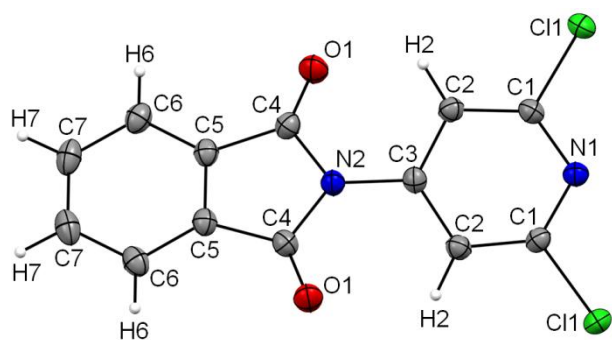


Figure S18. Ellipsoid view and atom numbering of **9** (50% probability, 173 K).

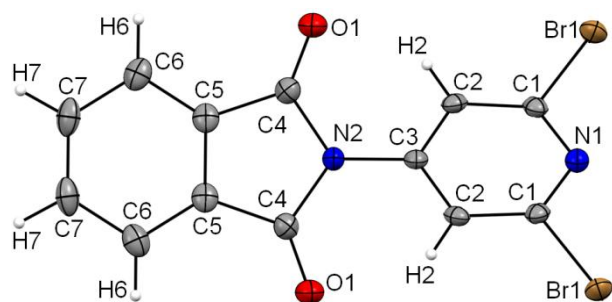


Figure S19. ^1H -NMR spectrum of $[\mathbf{2}](\text{PF}_6)_2$ in CD_3CN (top: full spectrum; bottom: zoom).

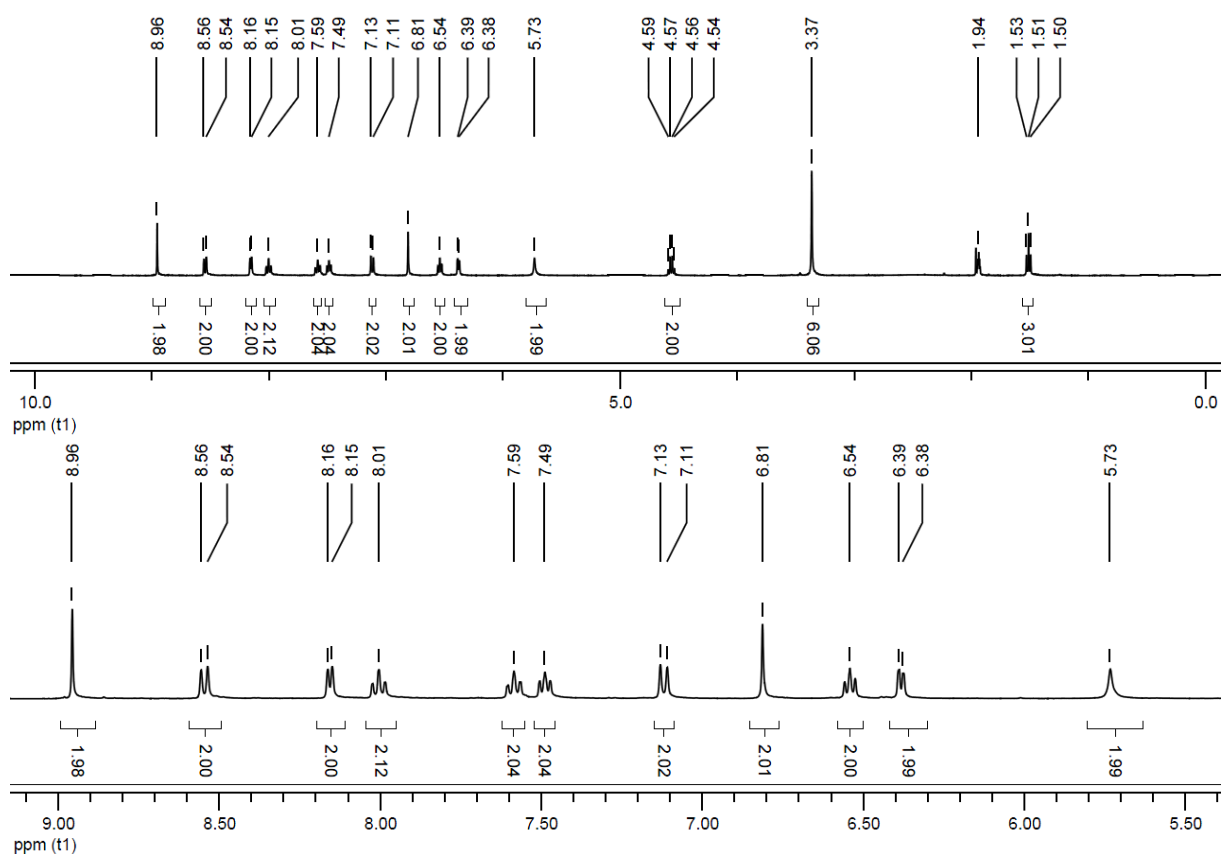


Figure S20. ^1H -NMR spectrum of $[\mathbf{3}](\text{PF}_6)_2$ in CD_3CN (top: full spectrum; bottom: zoom).

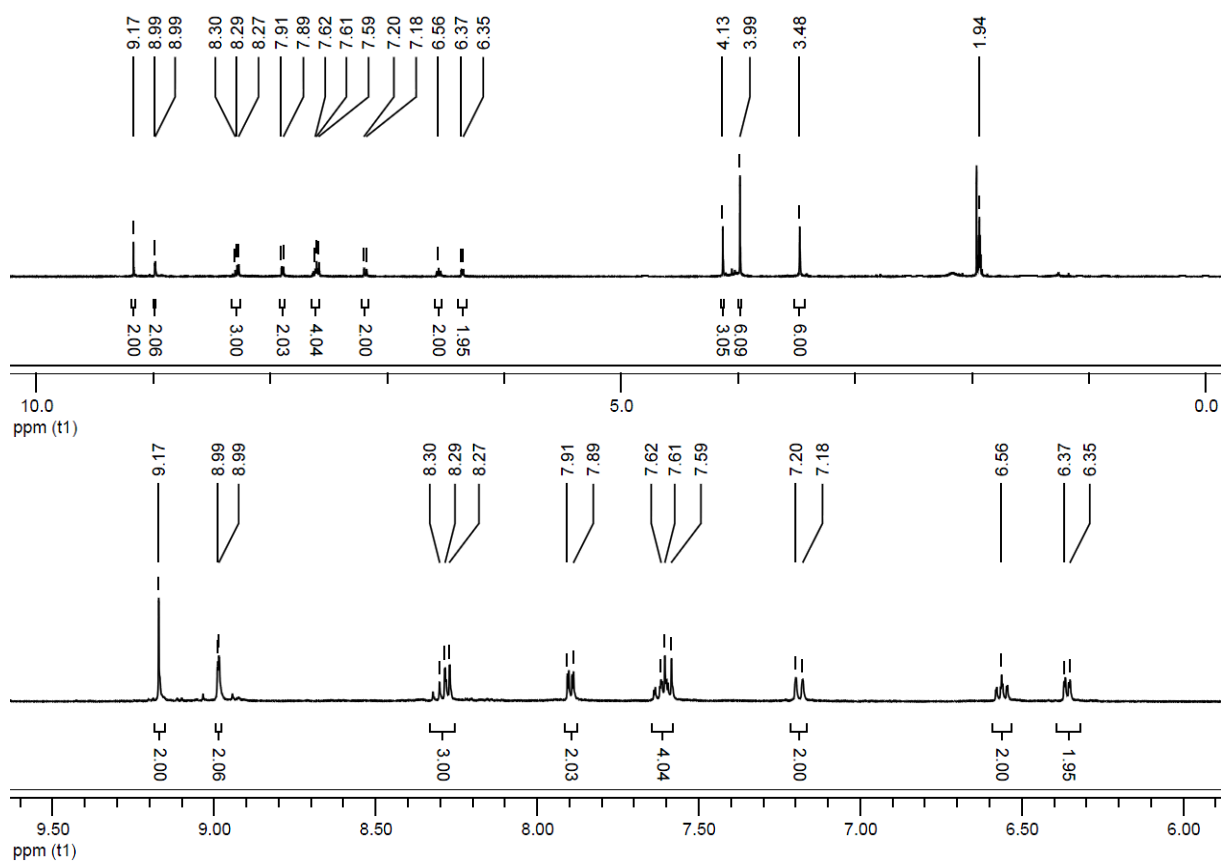


Figure S21. ^1H -NMR spectrum of $[\mathbf{4}](\text{PF}_6)_2$ in CD_3CN (top: full spectrum; bottom: zoom).

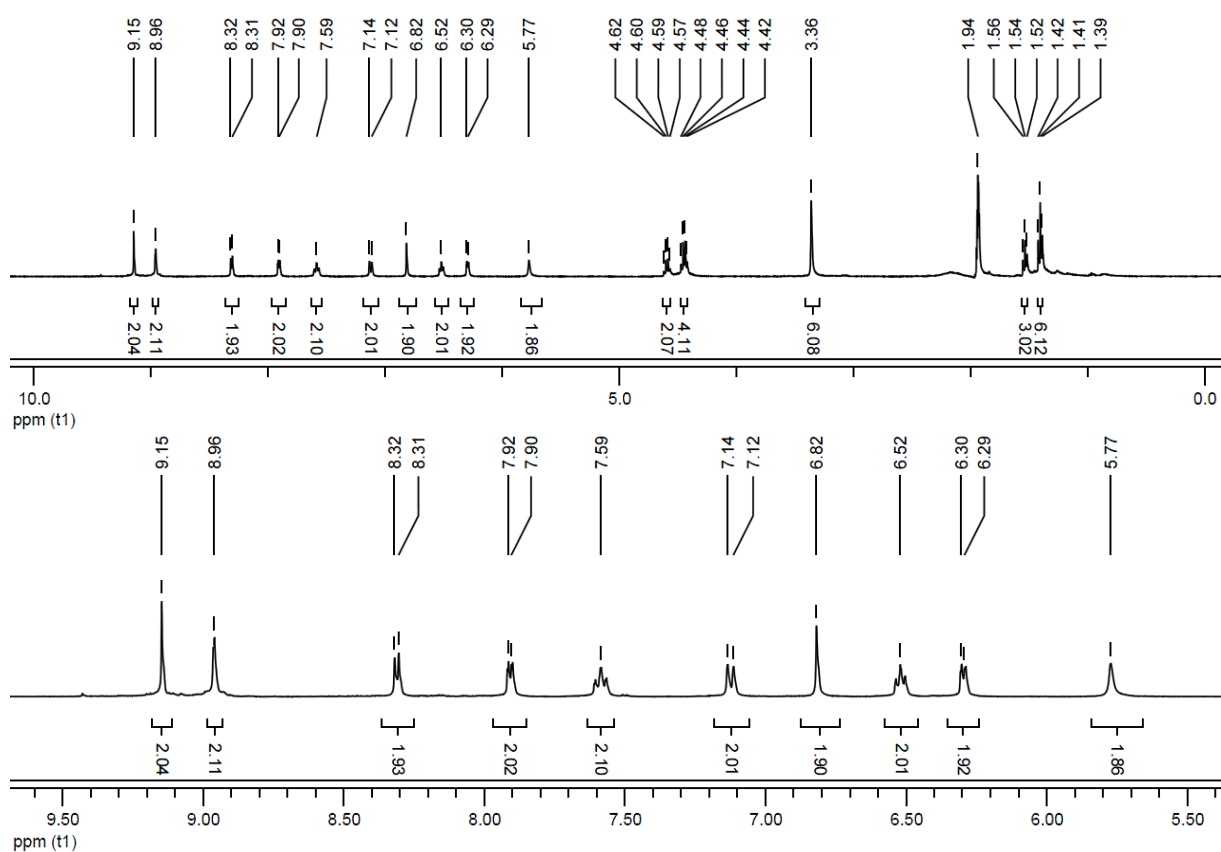


Figure S22. $^{13}\text{C}\{^1\text{H}\}$ NMR spectrum of $[\mathbf{2}](\text{PF}_6)_2$ in CD_3CN (top: full spectrum; bottom: zoom).

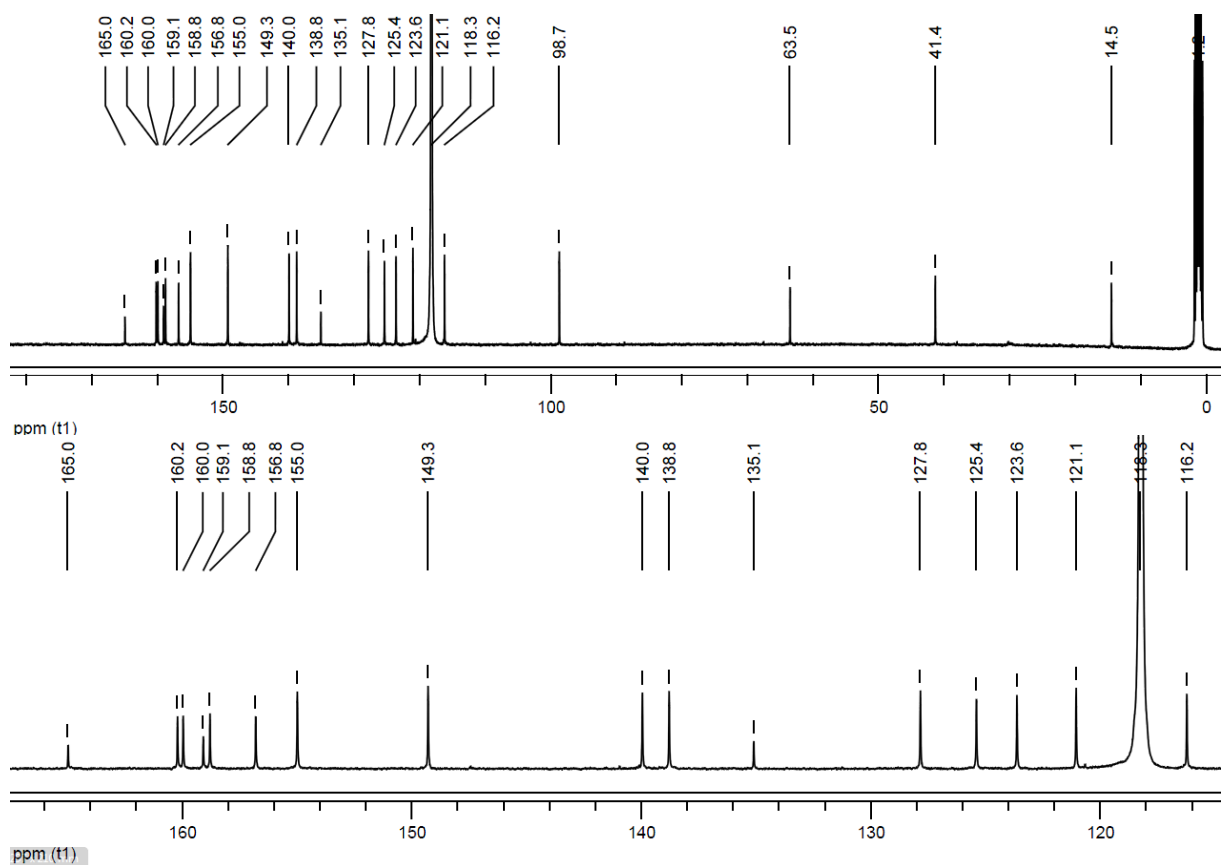


Figure S23. $^{13}\text{C}\{^1\text{H}\}$ NMR spectrum of $[\mathbf{3}](\text{PF}_6)_2$ in CD_3CN (top: full spectrum; bottom: zoom).

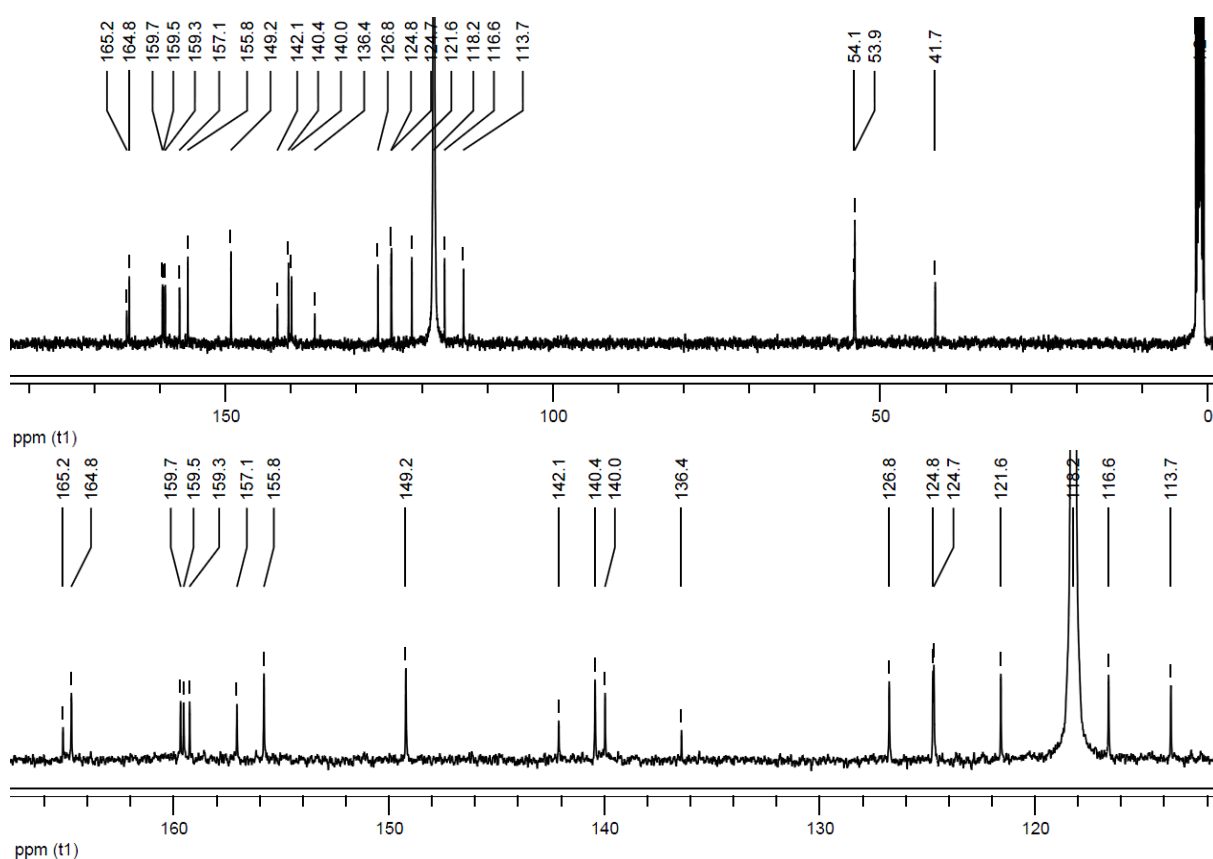


Figure S24. $^{13}\text{C}\{^1\text{H}\}$ NMR spectrum of $[\mathbf{4}](\text{PF}_6)_2$ in CD_3CN (top: full spectrum; bottom: zoom).

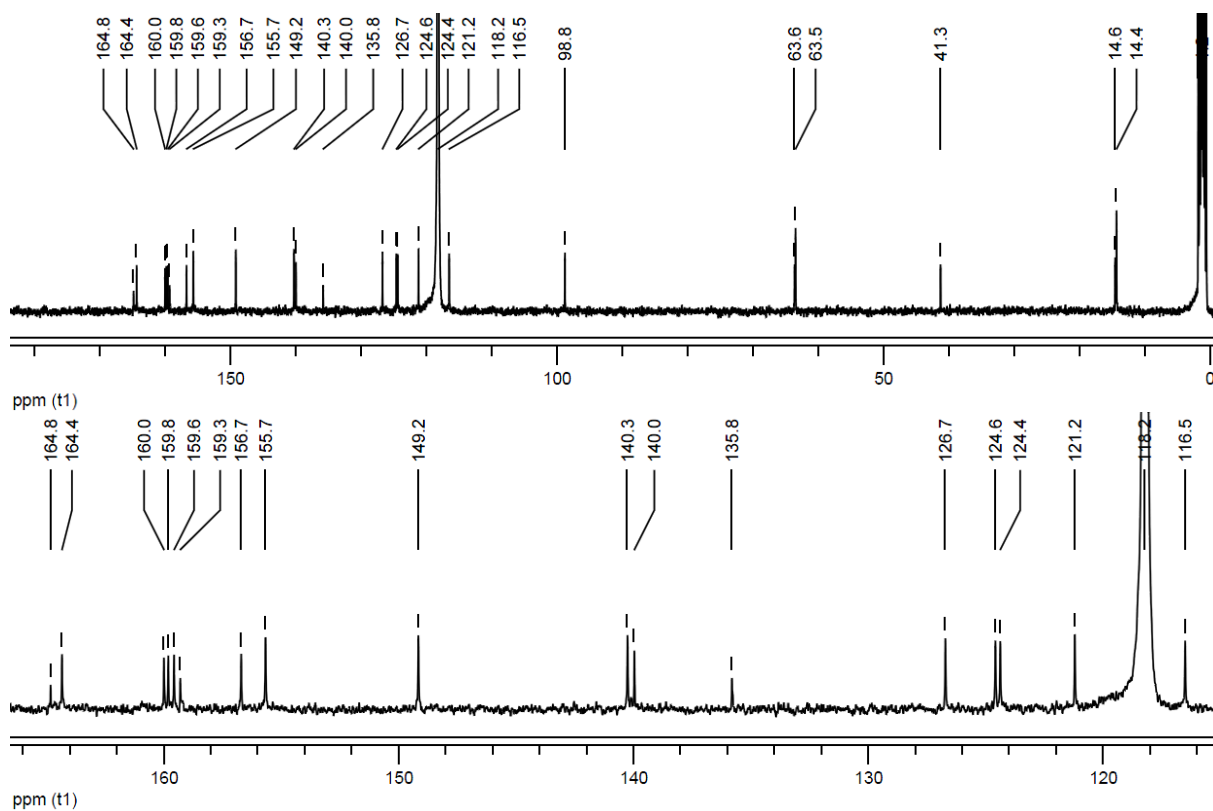


Figure S25. ^{15}N - ^1H HMBC of $[2](\text{PF}_6)_2$ in CD_3CN .

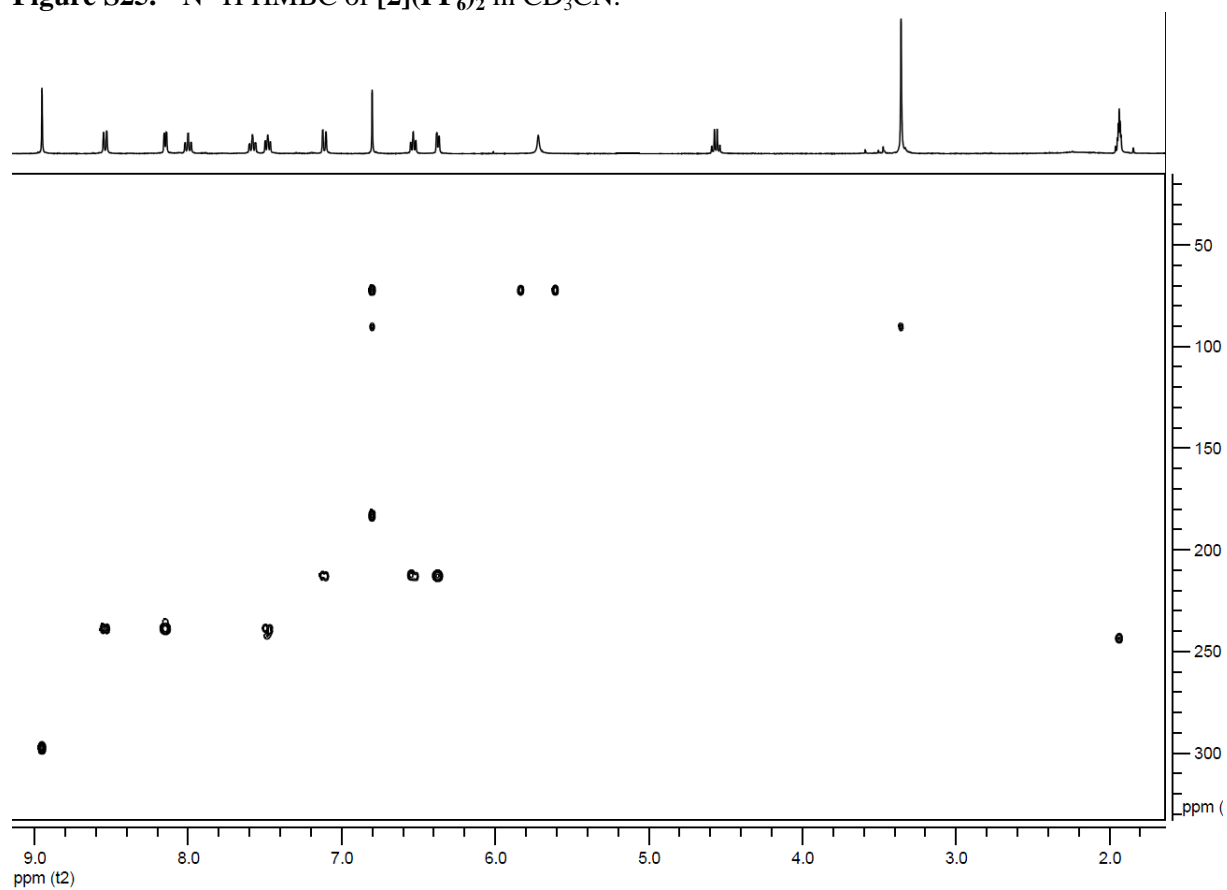


Figure S26. ^{15}N - ^1H HMBC of $[3](\text{PF}_6)_2$ in CD_3CN .

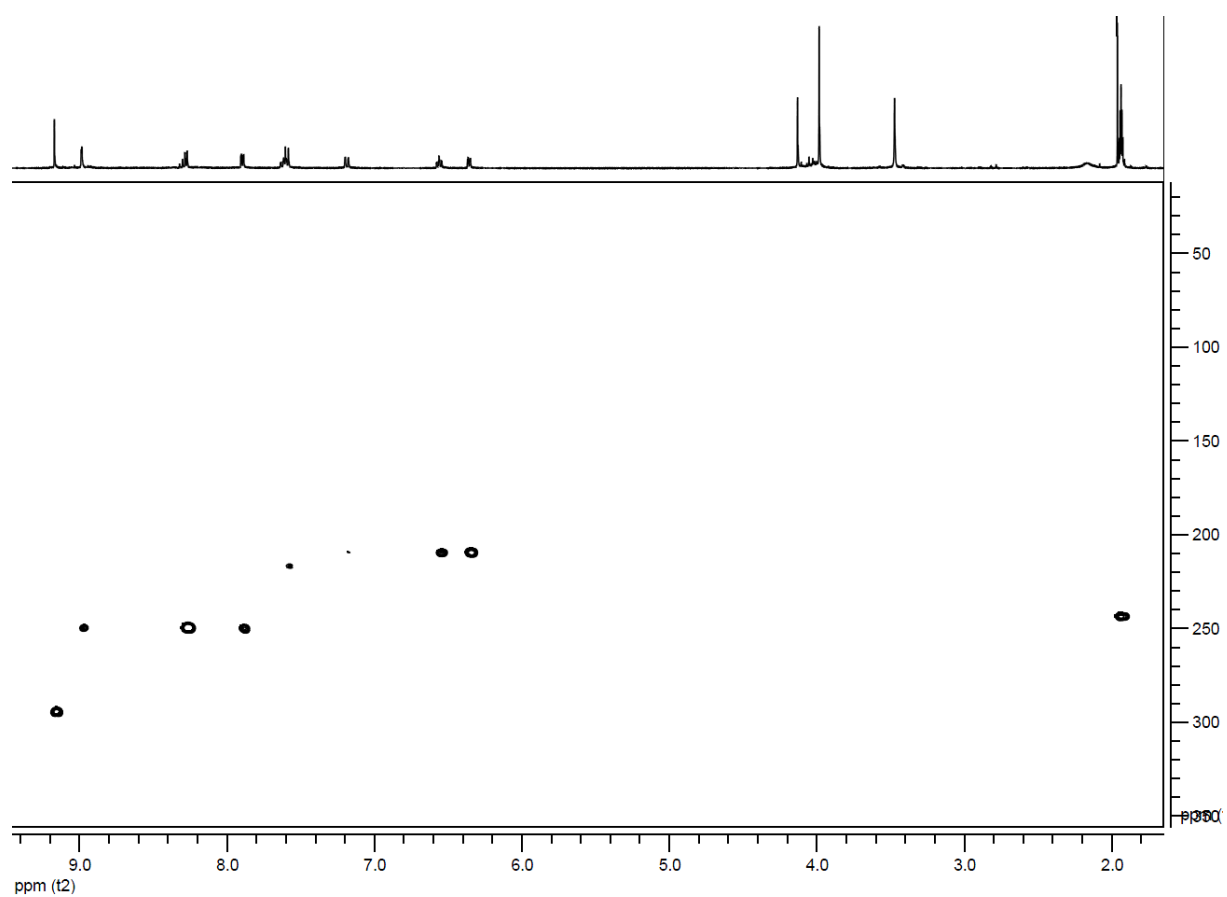


Figure S27. ^{15}N - ^1H HMBC of $[\mathbf{4}](\text{PF}_6)_2$ in CD_3CN .

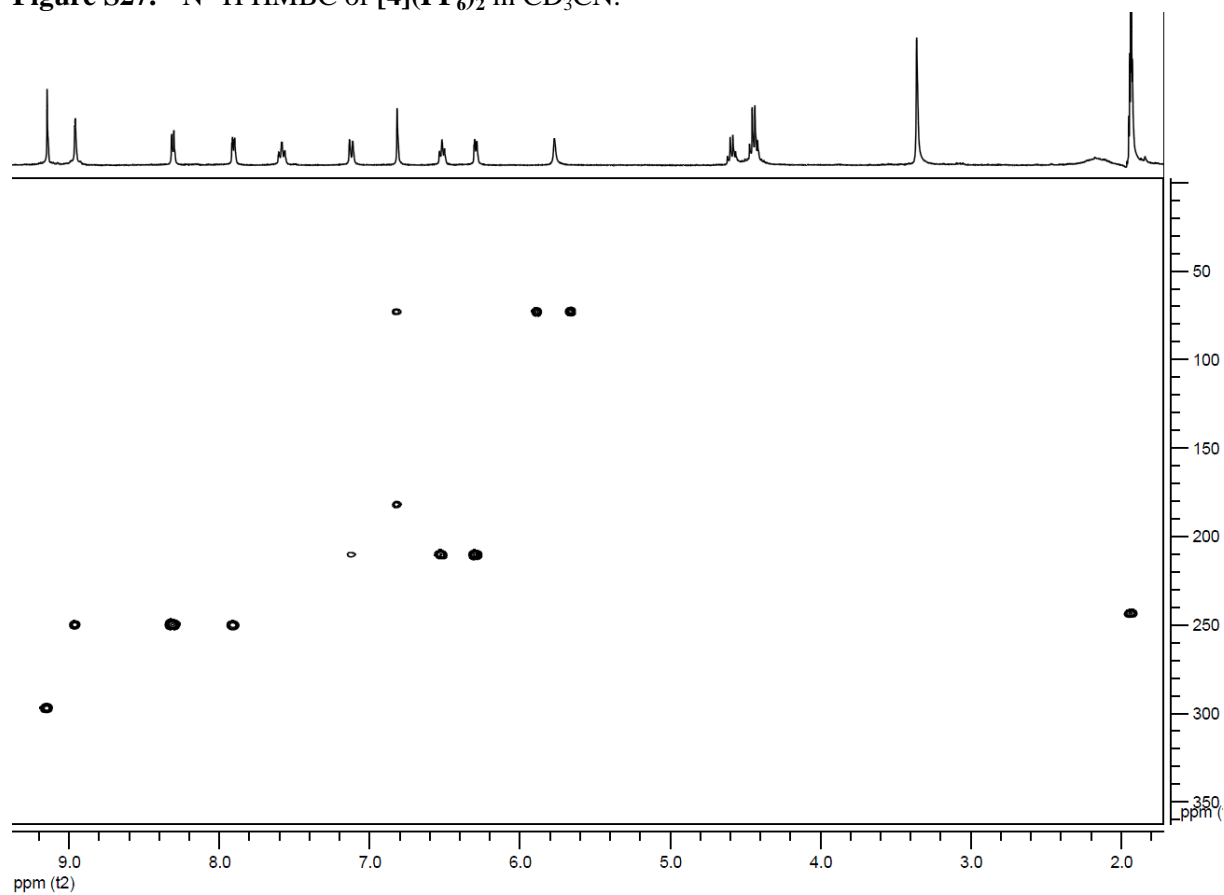


Figure S28. IR spectrum of $[\mathbf{2}](\text{PF}_6)_2$ in CsI.

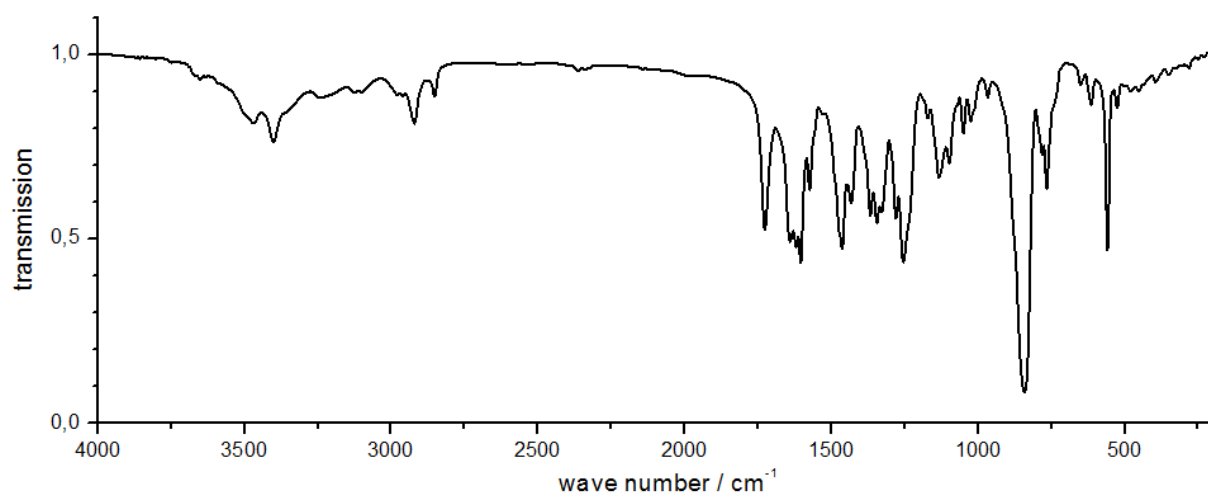


Figure S29. IR spectrum of $[3](\text{PF}_6)_2$ in CsI.

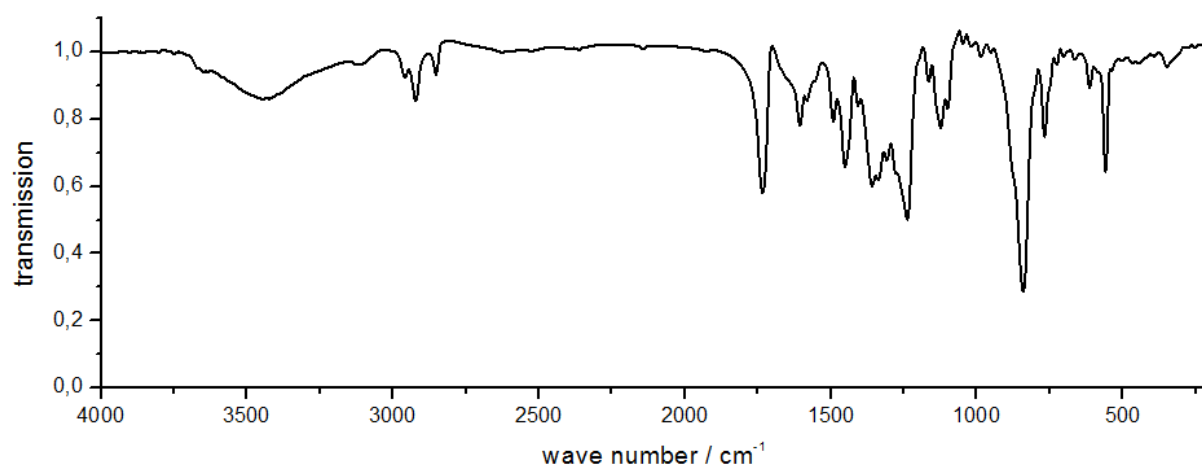


Figure S30. IR spectrum of $[4](\text{PF}_6)_2$ in CsI.

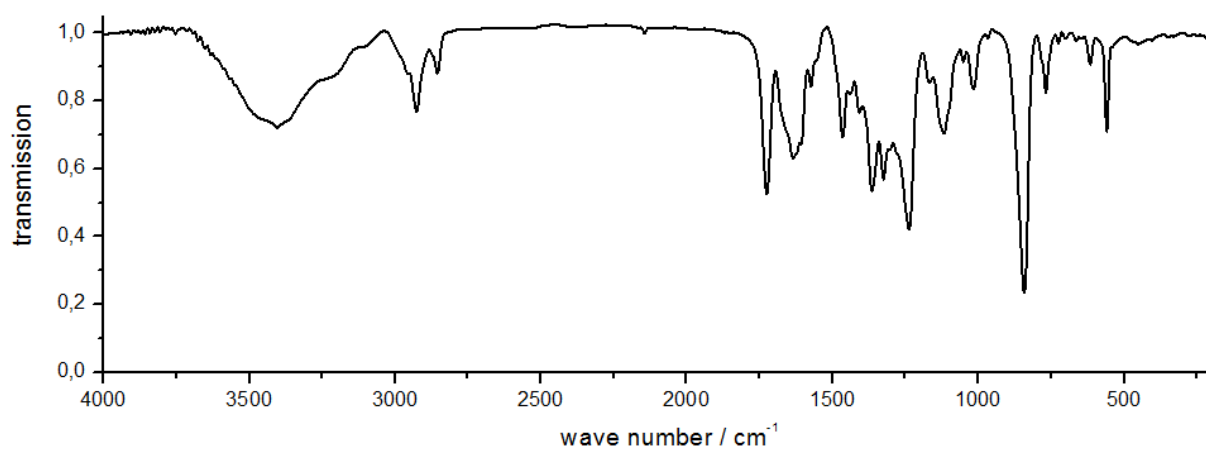


Figure S31. Ellipsoid view of $[2](\text{PF}_6)_2$ (50% probability, 173 K).

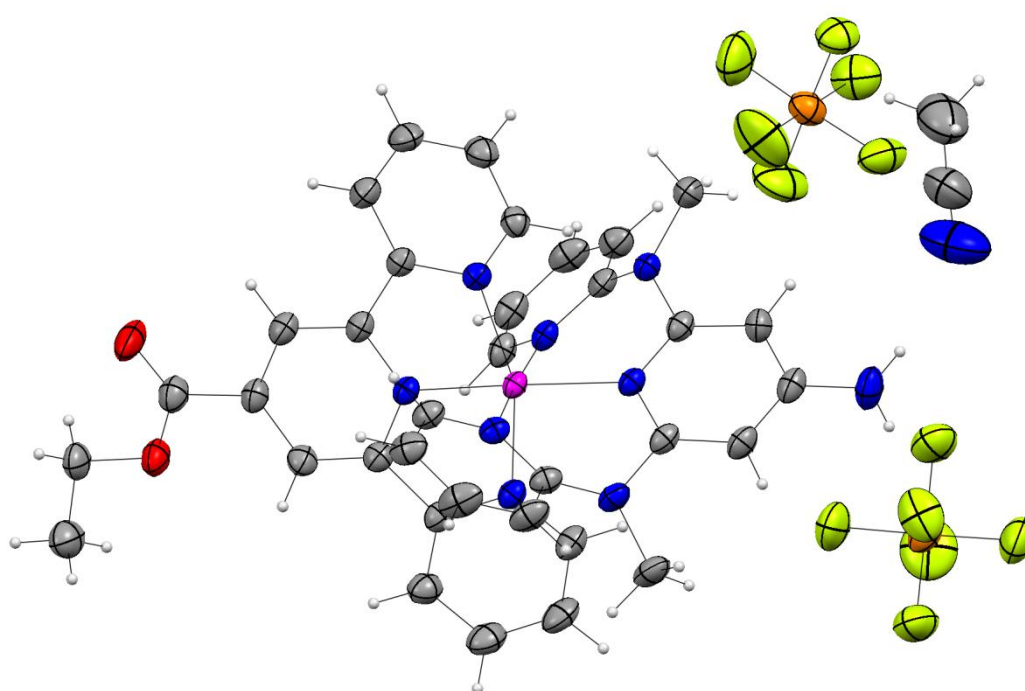


Figure S32. Ellipsoid view of $[3](\text{PF}_6)_2$ (50% probability, 173 K).

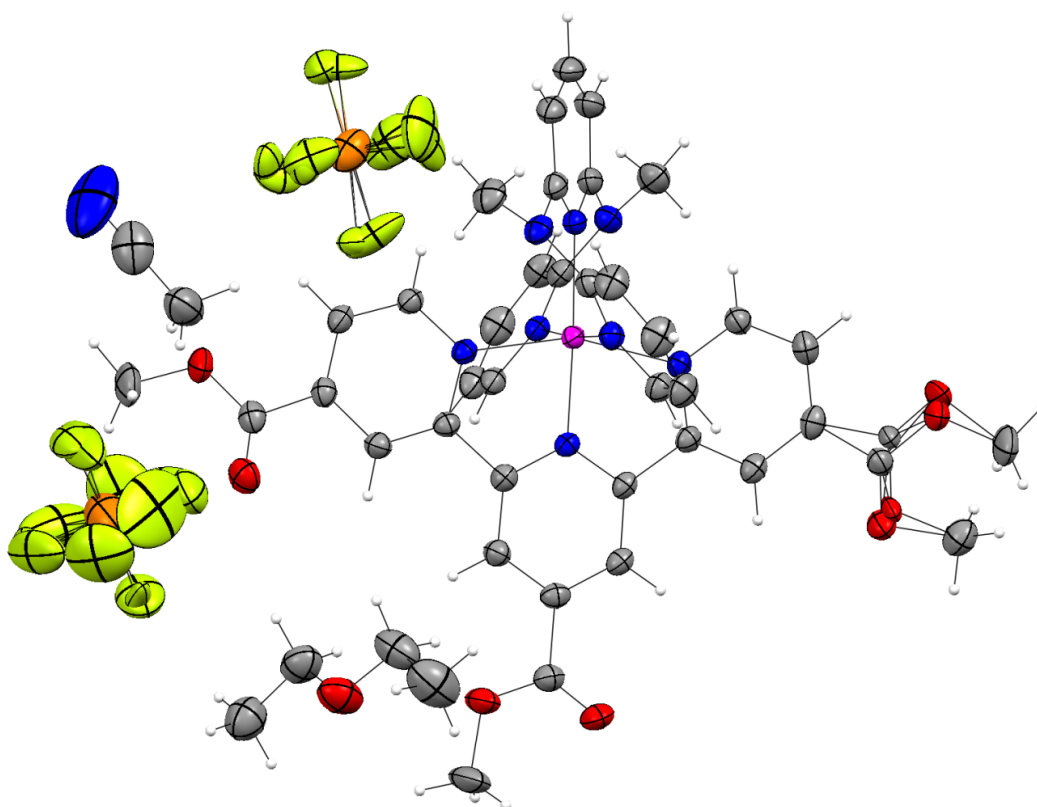


Figure S33. ^1H NMR spectra of selected signals of $[2](\text{PF}_6)_2$ CD_3CN without and with Δ -TRISPHAT.

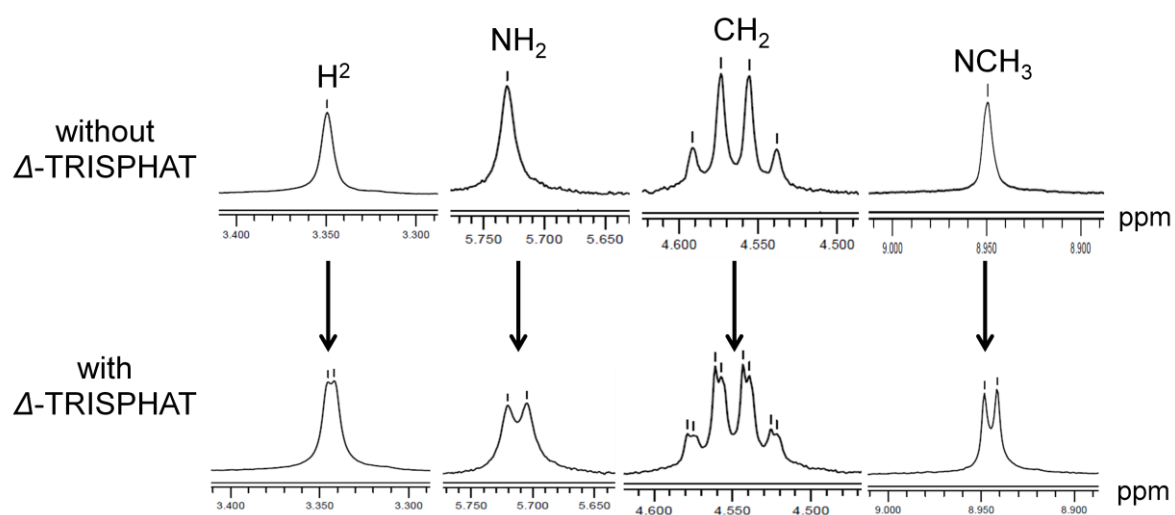
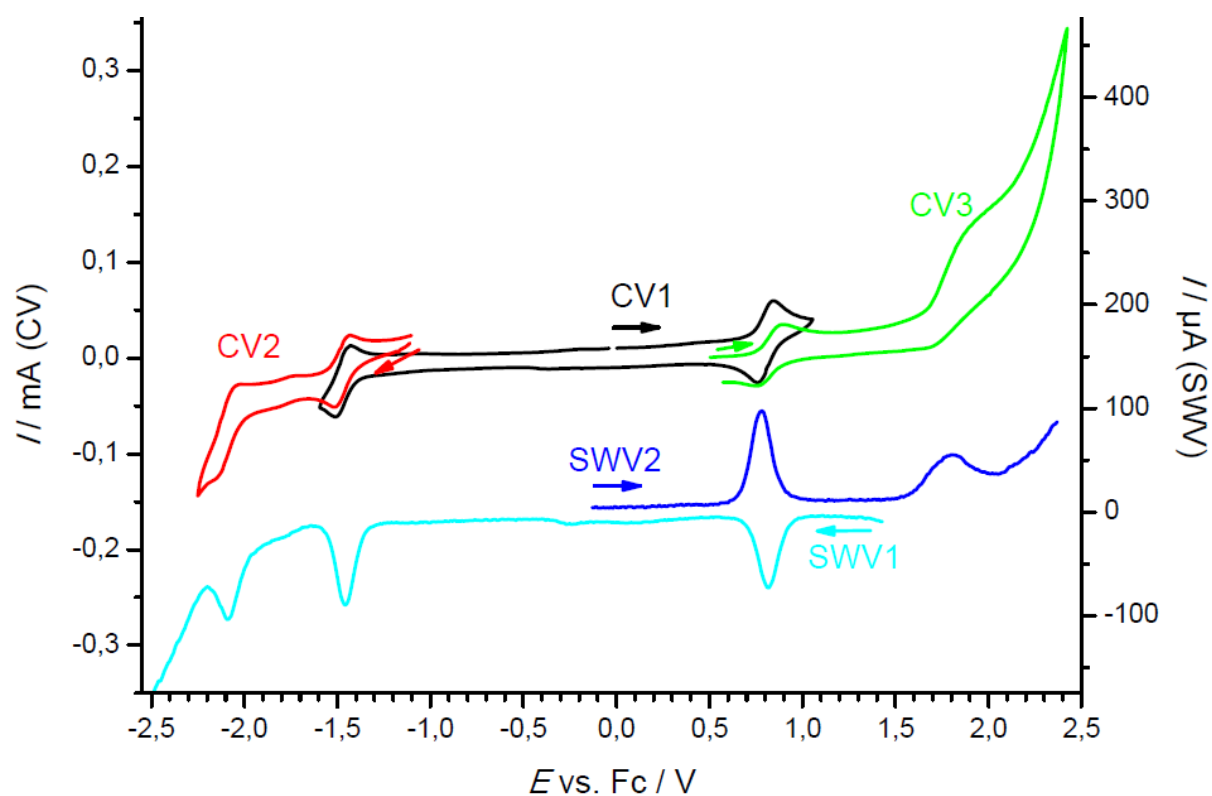
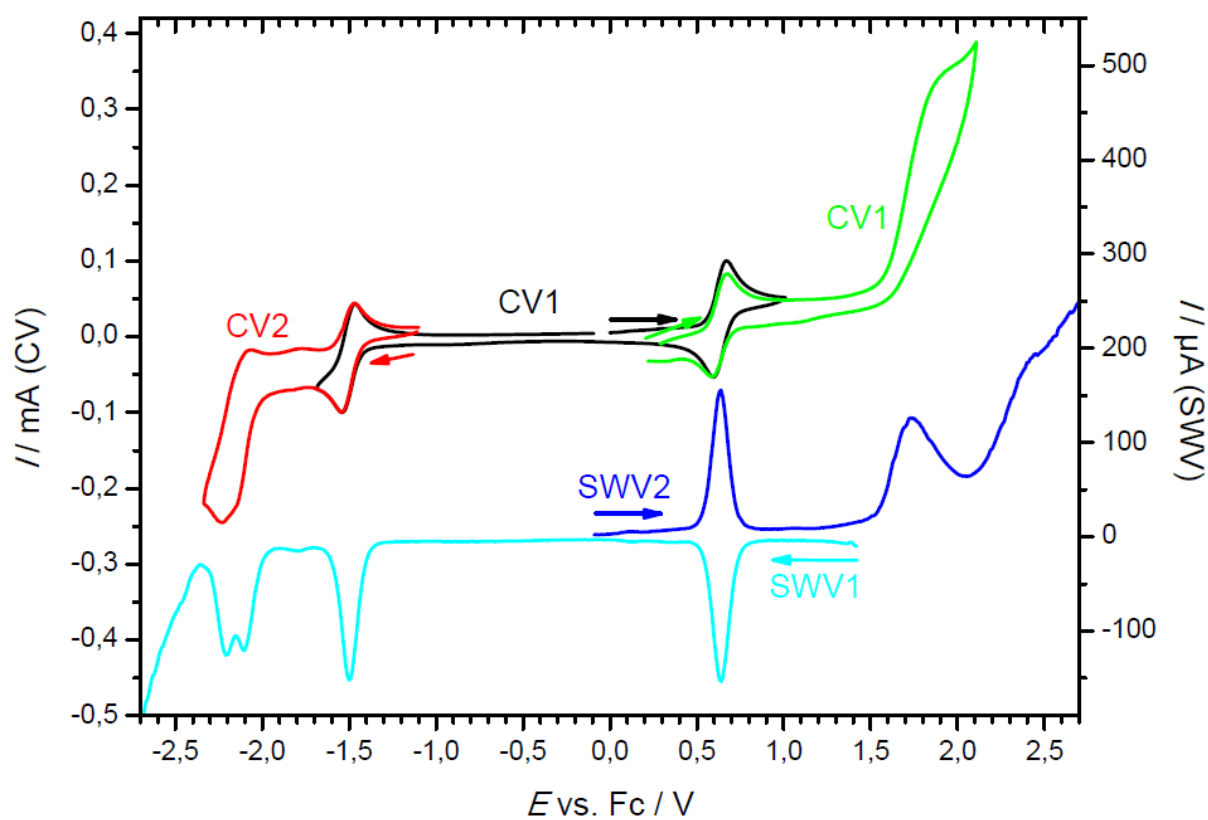


Figure S34. Cyclic voltammograms (CV) and square wave voltammograms (SWV) of **[1](PF₆)₂**^[a].



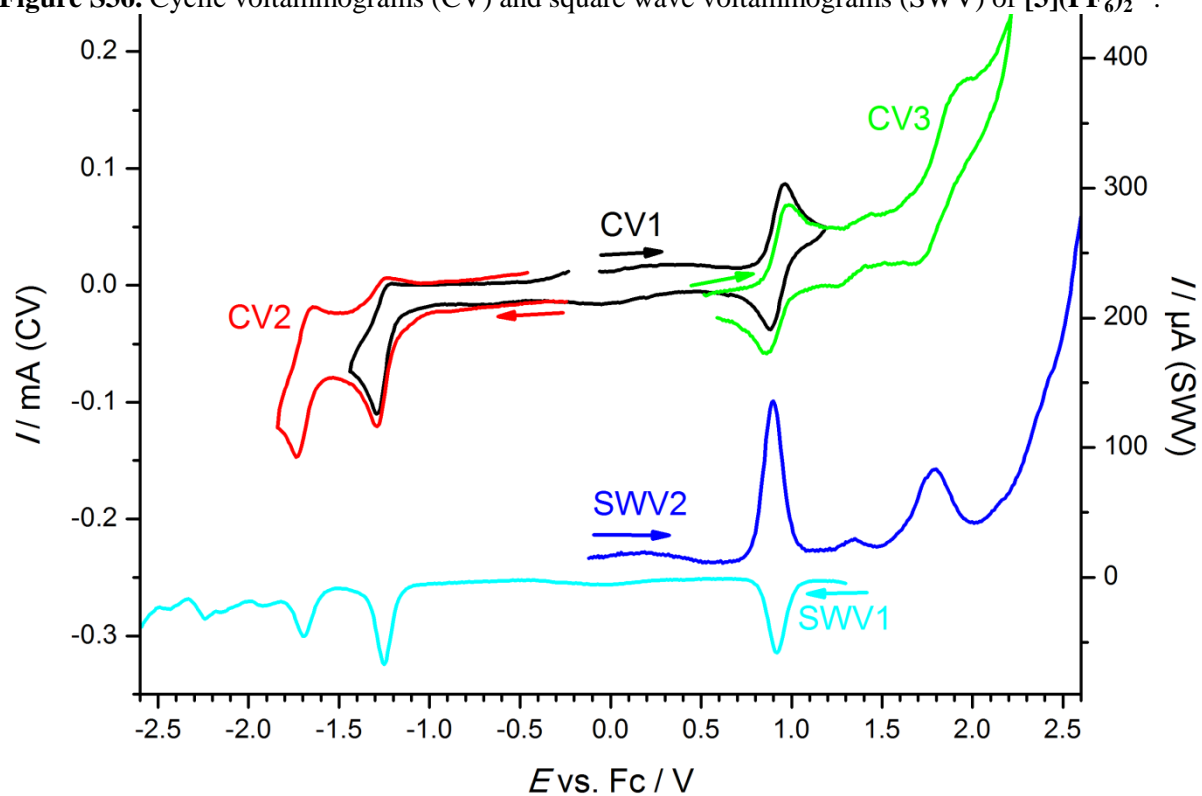
[a] in CH₃CN; 0.1 M (*n*Bu₄)(PF₆); in V versus Fc/Fc⁺.

Figure S35. Cyclic voltammograms (CV) and square wave voltammograms (SWV) of **[2](PF₆)₂**^[a].



[a] in CH₃CN; 0.1 M (*n*Bu₄)(PF₆); in V versus Fc/Fc⁺.

Figure S36. Cyclic voltammograms (CV) and square wave voltammograms (SWV) of $[3](PF_6)_2^{[a]}$.



[a] in CH_3CN ; 0.1 M $(nBu_4)(PF_6)$; in V versus Fc/Fc^+ .

Figure S37. Spin density of one-electron oxidized species $[1]^{3+} - [4]^{3+}$ and reference compounds $[5]^{3+} - [7]^{3+}$ in CH_3CN (b3lyp/lanl2dz, iefpcm, contour value 0.01 a. u.). Hydrogen atoms are omitted for clarity.

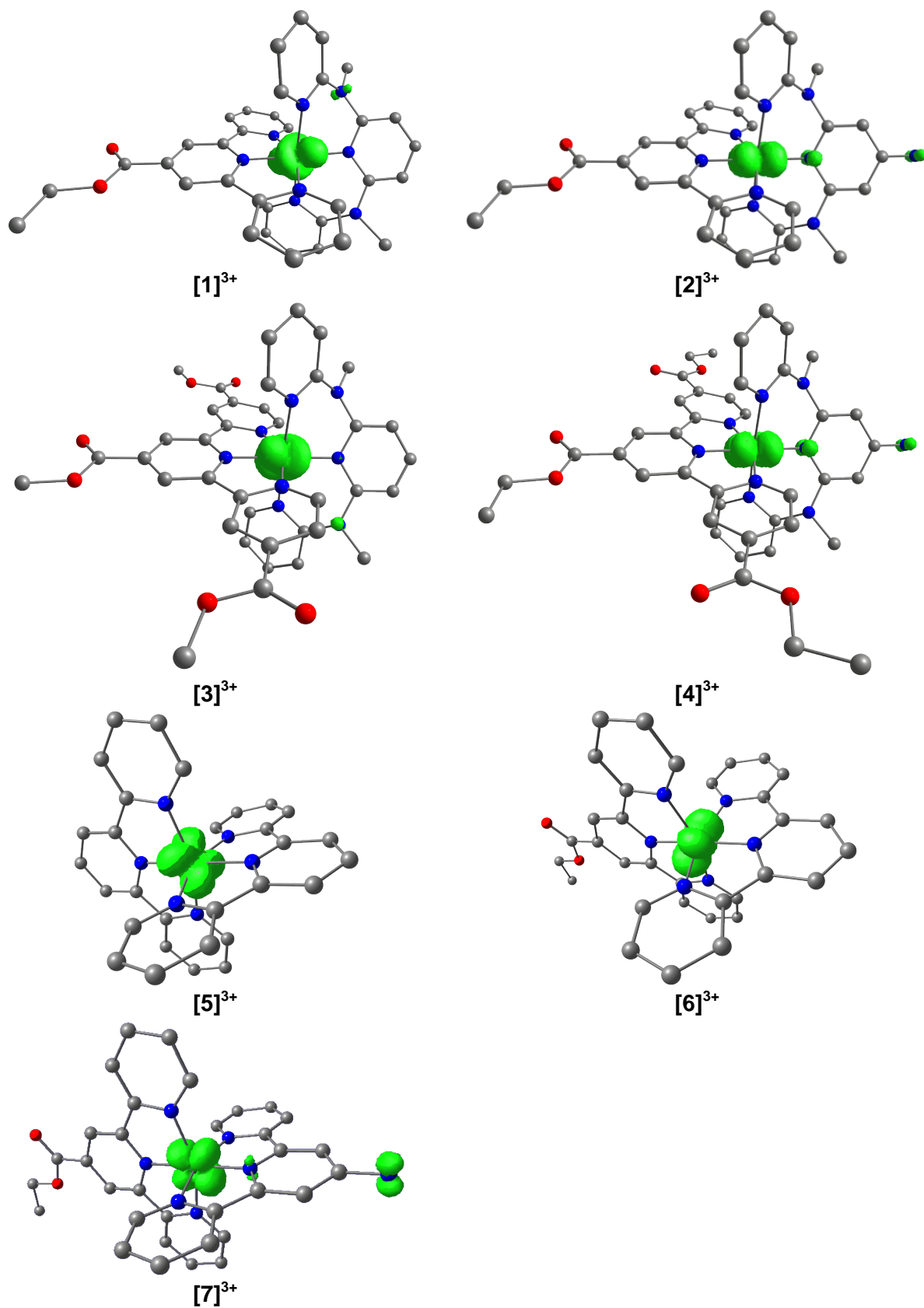


Figure S38. Spin density of two-electron oxidized species $[1]^{4+}$ – $[4]^{4+}$ and reference compounds $[5]^{4+}$ – $[7]^{4+}$ in CH_3CN (b3lyp/lanl2dz, iefpcm, contour value 0.01 a. u.). Hydrogen atoms are omitted for clarity.

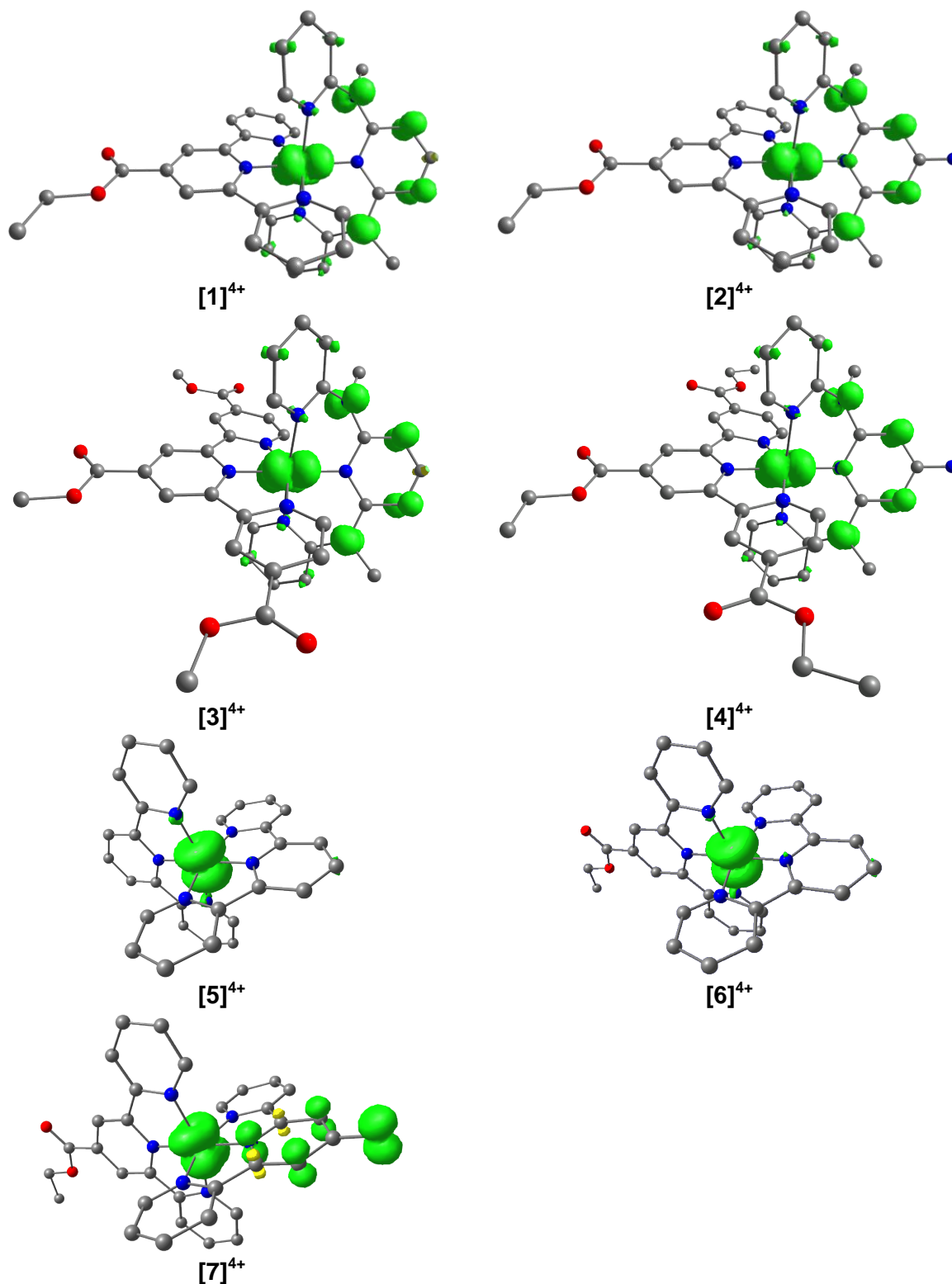


Figure S39. Spin density of one-electron reduced species $[1]^+ - [4]^+$ and reference compounds $[5]^+ - [7]^+$ in CH_3CN (b3lyp/lanl2dz, iefpcm, contour value 0.01 a. u.). Hydrogen atoms are omitted for clarity.

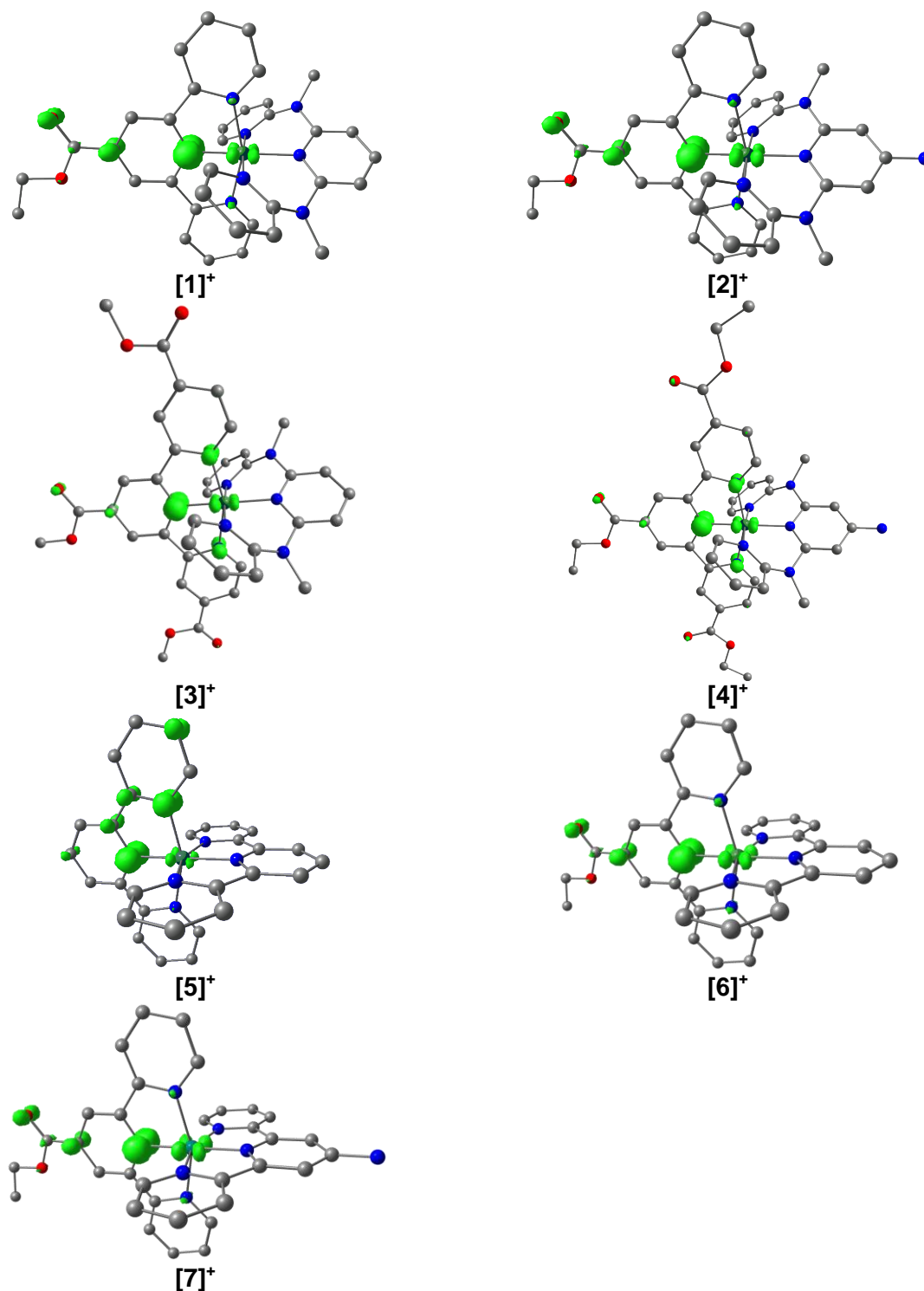
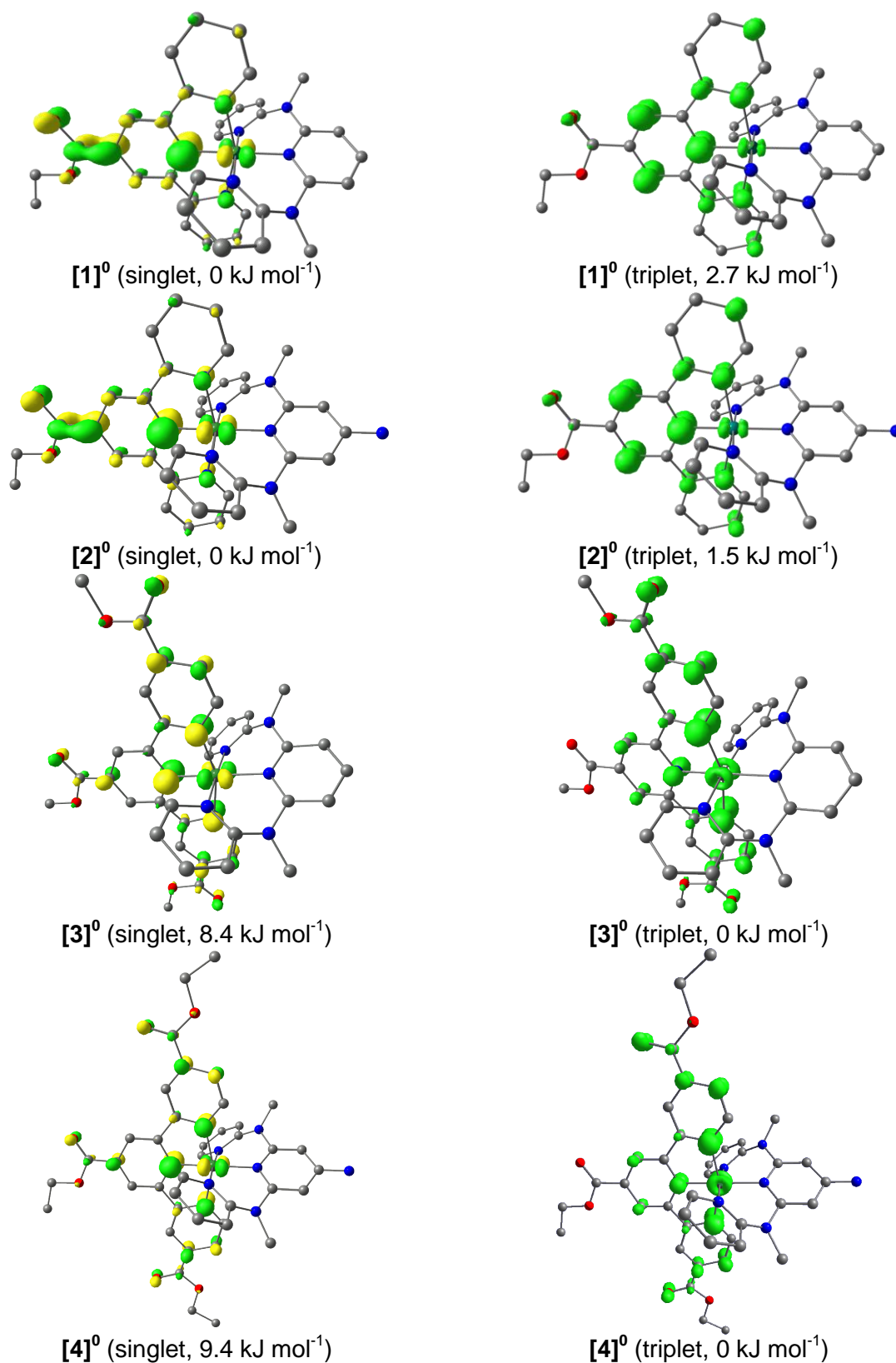


Figure S40. Two-electron reduced species $[1]^0 - [4]^0$ and reference compounds $[5]^0 - [7]^0$ CH_3CN (b3lyp/lanl2dz, iefpcm). Left: HOMOs of singlet species ($M = 1$, contour value 0.06 a. u.). Right: Spin density of triplet species ($M = 3$, contour value 0.01 a. u.). In parentheses is shown the relative energy of singlet and triplet species. Hydrogen atoms are omitted for clarity.



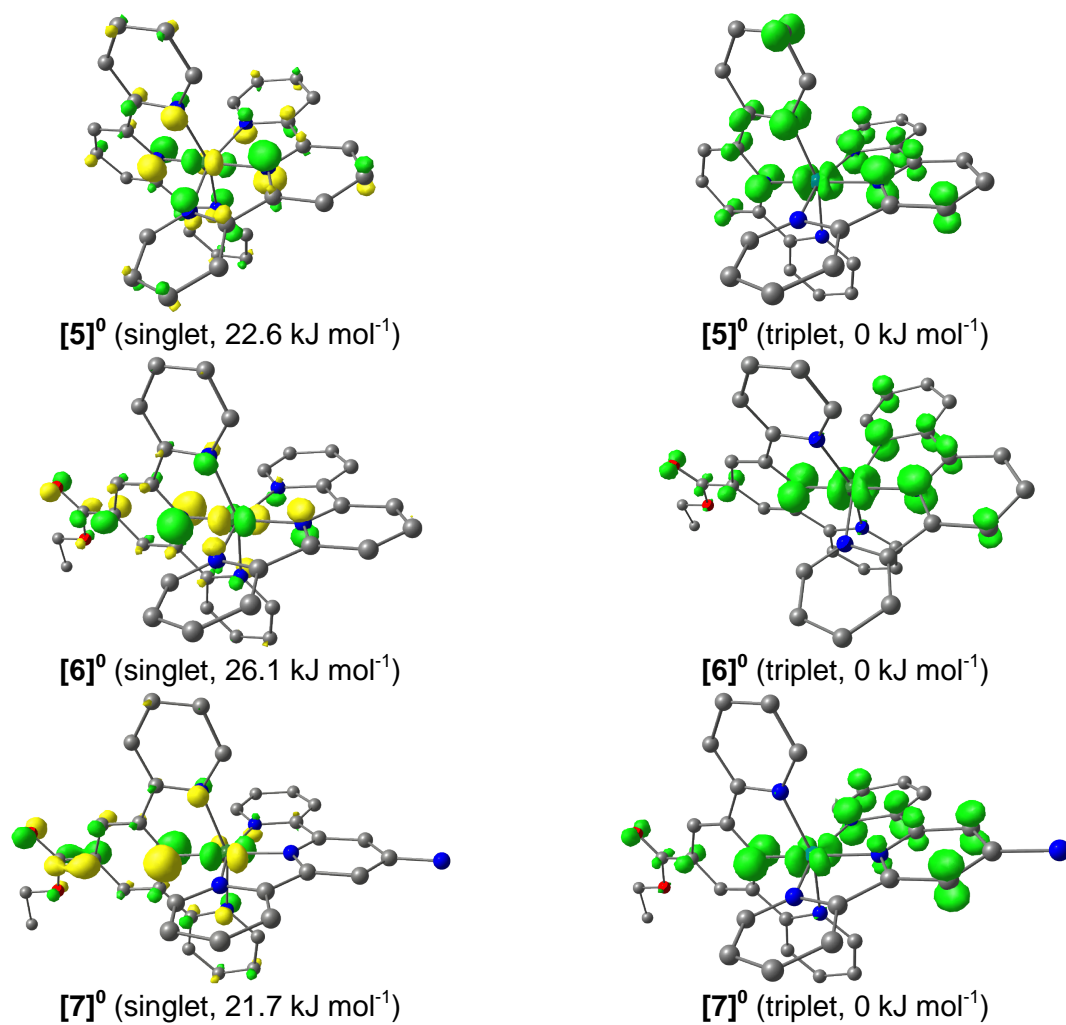


Figure S41. X-band EPR spectrum of $[2]^{3+}$ in 0.5 M trifluoroacetic acid in CH_3CN at 77 K. Black: measurement; red: simulation.

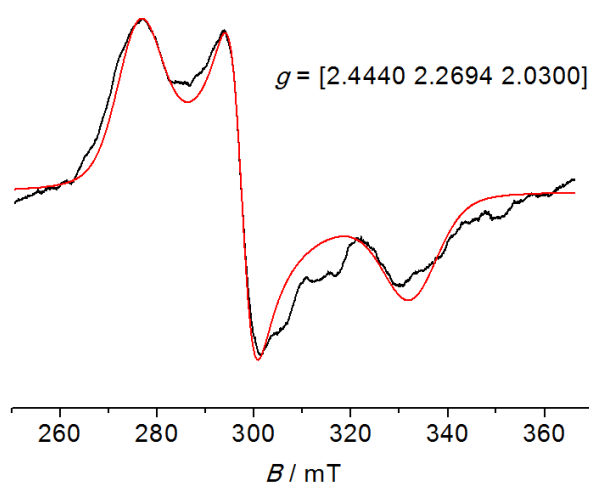


Figure S42. X-band EPR spectrum of $[2]^+$ in CH_3CN at 77 K. Black: measurement; red: simulation.

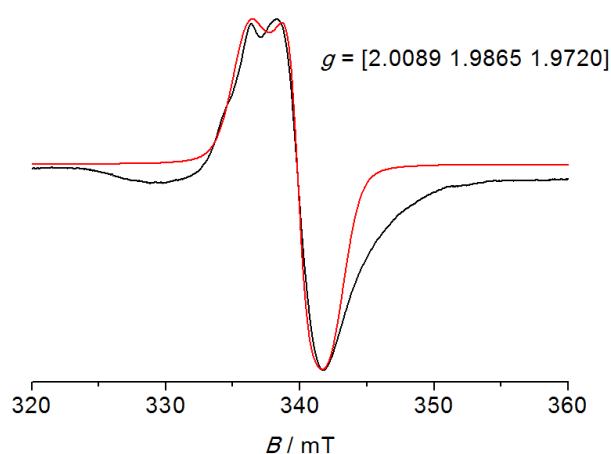


Figure S43. Transient absorption spectra of $[1](\text{PF}_6)_2$ in PrCN at room temperature (pulse $\lambda_{\text{exc}} = 425$ nm, 1900 nJ).

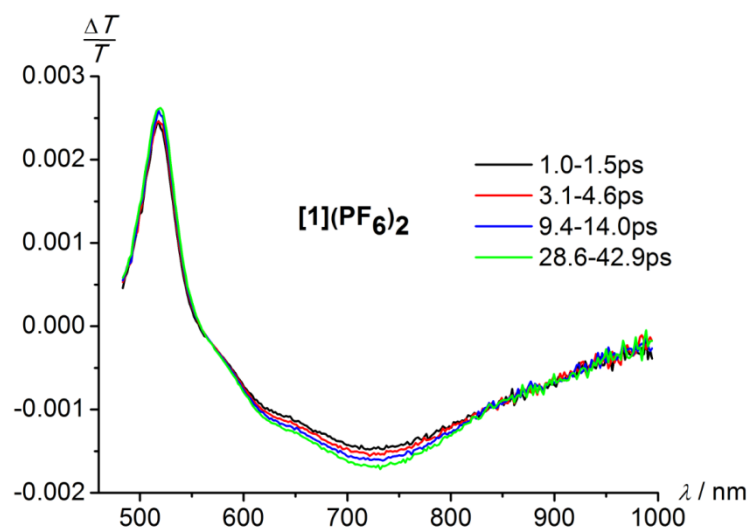


Figure S44. Transient absorption spectra of $[3](\text{PF}_6)_2$ in PrCN at room temperature (pulse $\lambda_{\text{exc}} = 400$ nm, 2200 nJ).

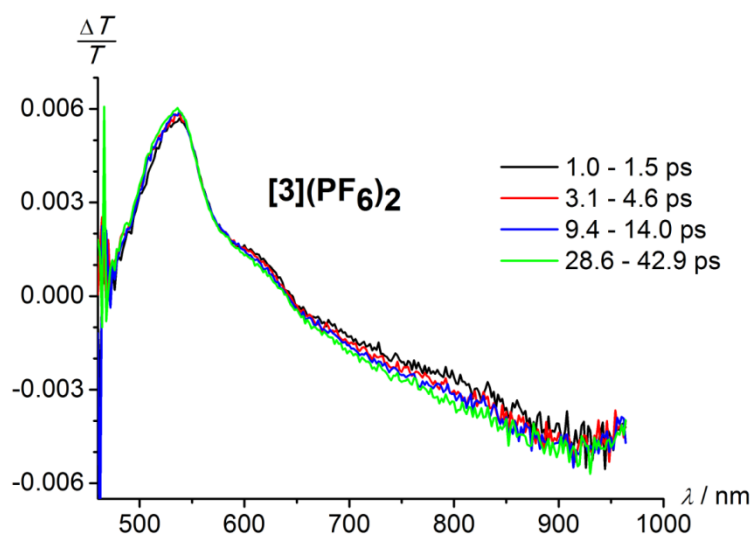


Figure S45. Transient absorption spectra of $[4](PF_6)_2$ in PrCN at room temperature (pulse $\lambda_{exc} = 420$ nm, 3800 nJ).

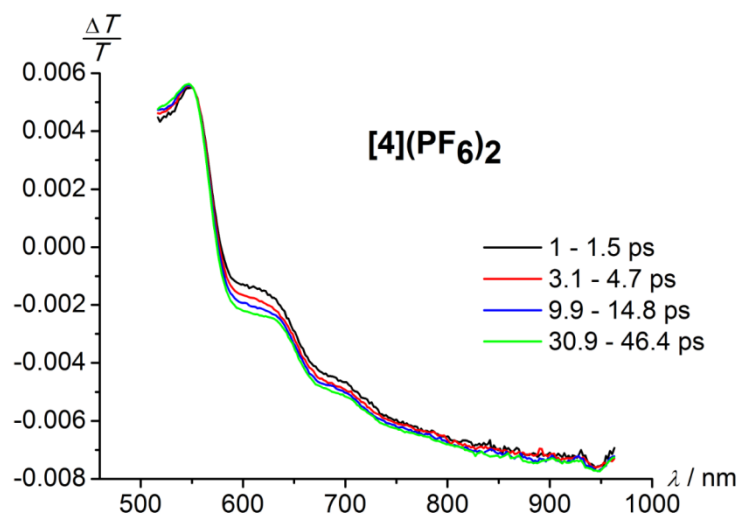


Figure S46. Transient absorption spectra of $[6](PF_6)_2$ in PrCN at room temperature (pulse $\lambda_{exc} = 425$ nm, 2050 nJ).

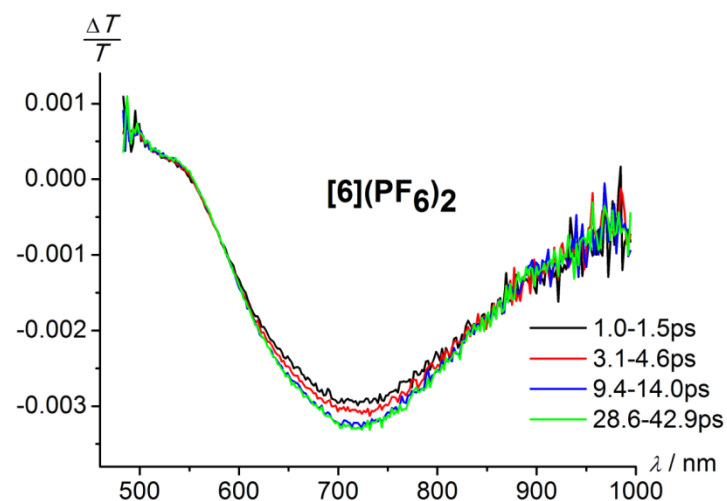


Figure S47. UV/Vis spectra of reduced and oxidized $[2](PF_6)_2$ in different solvents.

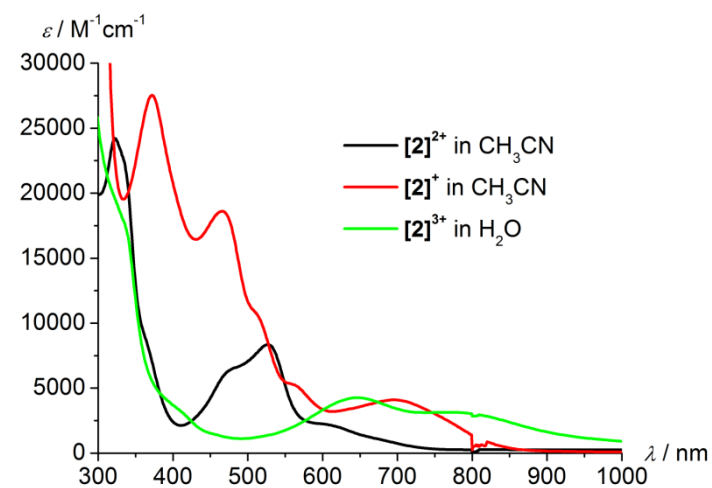


Figure S48. IR spectrum (CsI) of $[2^D](PF_6)_2$.

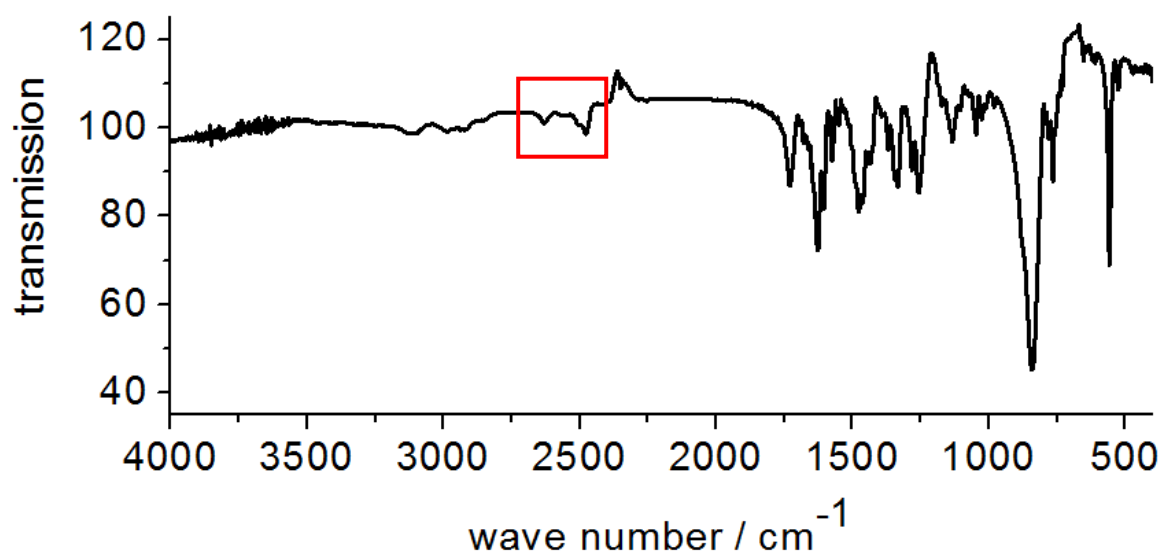


Figure S49. IR spectrum (CsI) of $[4^D](PF_6)_2$.

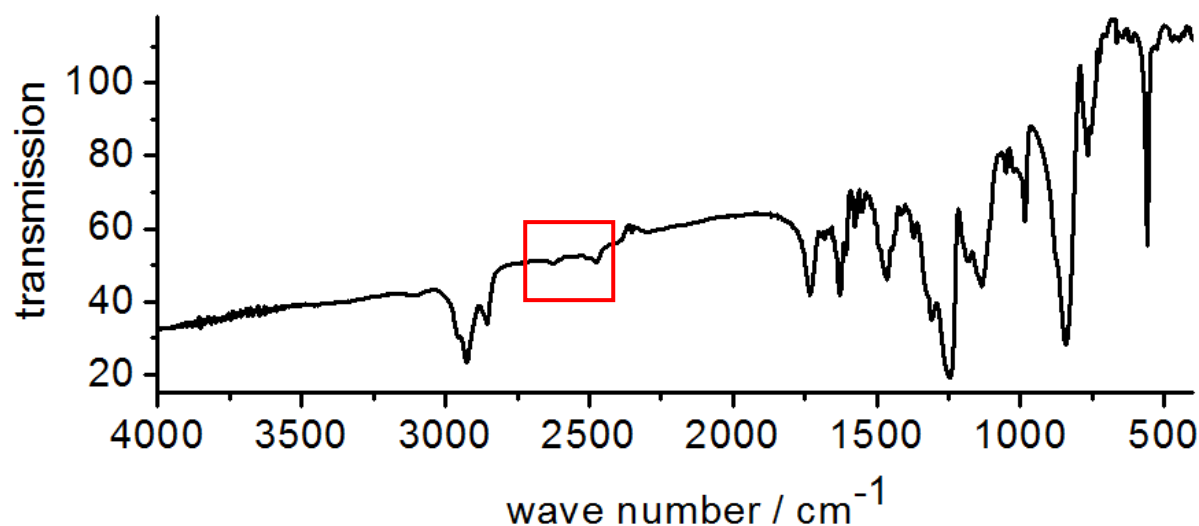


Table S1. Crystal and structure refinement data for **8** and **9** from X-ray analysis.

	8	9
Empirical formula	C ₁₃ H ₆ Cl ₂ N ₂ O ₂	C ₁₃ H ₆ Br ₂ N ₂ O ₂
Formula weight	293.10	382.02
Crystal color, habit	colourless block	colourless plate
Crystal dimensions / mm	0.85 x 0.52 x 0.30	0.98 x 0.37 x 0.10
Crystal system	orthorhombic	orthorhombic
Space group	Pbcn	Pbcn
<i>a</i> / Å	7.2514(5)	7.2704(14)
<i>b</i> / Å	12.1612(8)	12.246(2)
<i>c</i> / Å	13.5025(9)	14.167(3)
α / °	90	90
β / °	90	90
γ / °	90	90
<i>V</i> / Å ³	1190.73(14)	1261.3(4)
<i>Z</i>	4	4

$F(000)$	592	736
Density (calcd) / g cm ⁻³	1.635	2.012
Absorption coefficient μ / mm ⁻¹	0.542 (MULABS)	6.424 (MULABS)
Theta range / °	3.02 – 27.94	2.88 – 27.87
Index ranges	-9 ≤ h ≤ 9	-9 ≤ h ≤ 9
	-15 ≤ k ≤ 15	-16 ≤ k ≤ 16
	-17 ≤ l ≤ 17	-18 ≤ l ≤ 17
Reflections collected	12886	11138
Independent reflections	1424 ($R_{\text{int}} = 0.0868$)	1513 ($R_{\text{int}} = 0.1152$)
Observed reflections	1424	1513
Parameters	89	88
Max. / min. transmission	0.8543 / 0.6558	0.5659 / 0.0616
Goodness-of-fit on F^2	1.080	1.048
Largest difference peak and hole / e Å ⁻³	0.385 / -0.360	1.258 / -1.038
R_1 ($I > 2\sigma(I)$)	0.0302	0.0478
R_1 (all data)	0.0331	0.0684
wR_2 ($I > 2\sigma(I)$)	0.0732	0.1316
wR_2 (all data)	0.0752	0.1494

Table S2. Bond lengths / Å and angles / ° of **8** from X-ray crystal analysis.

Cl(1)-C(1)	1.7376(11)
O(1)-C(4)	1.2038(14)
N(2)-C(3)	1.4163(19)
N(2)-C(4)#1	1.4232(13)
N(2)-C(4)	1.4232(13)
C(5)-C(5)#1	1.386(2)
C(5)-C(6)	1.3877(16)
C(5)-C(4)	1.4830(15)
C(1)-N(1)	1.3305(13)
C(1)-C(2)	1.3841(15)
C(2)-C(3)	1.3929(13)
C(2)-H(2)	0.9300
C(3)-C(2)#1	1.3929(13)
C(6)-C(7)	1.3928(17)
C(6)-H(6)	0.9300
C(7)-C(7)#1	1.395(3)
C(7)-H(7)	0.9300
N(1)-C(1)#1	1.3305(13)
C(3)-N(2)-C(4)#1	124.24(6)
C(3)-N(2)-C(4)	124.24(6)
C(4)#1-N(2)-C(4)	111.52(13)
C(5)#1-C(5)-C(6)	121.65(7)
C(5)#1-C(5)-C(4)	109.03(6)
C(6)-C(5)-C(4)	129.32(11)
N(1)-C(1)-C(2)	125.61(10)
N(1)-C(1)-Cl(1)	114.77(8)
C(2)-C(1)-Cl(1)	119.62(8)
C(1)-C(2)-C(3)	116.43(10)
C(1)-C(2)-H(2)	121.8
C(3)-C(2)-H(2)	121.8
O(1)-C(4)-N(2)	125.28(11)
O(1)-C(4)-C(5)	129.50(10)
N(2)-C(4)-C(5)	105.21(9)
C(2)#1-C(3)-C(2)	120.31(14)

C(2)#1-C(3)-N(2)	119.84(7)
C(2)-C(3)-N(2)	119.84(7)
C(5)-C(6)-C(7)	117.02(12)
C(5)-C(6)-H(6)	121.5
C(7)-C(6)-H(6)	121.5
C(6)-C(7)-C(7)#1	121.32(7)
C(6)-C(7)-H(7)	119.3
C(7)#1-C(7)-H(7)	119.3
C(1)#1-N(1)-C(1)	115.59(13)

Table S3. Bond lengths / Å and angles / ° of **9** from X-ray crystal analysis.

Br(1)-C(1)	1.899(5)
O(1)-C(4)	1.210(7)
N(1)-C(1)	1.329(6)
N(1)-C(1)#1	1.329(6)
N(2)-C(4)	1.419(6)
N(2)-C(4)#1	1.419(6)
N(2)-C(3)	1.423(9)
C(1)-C(2)	1.395(7)
C(2)-C(3)	1.389(6)
C(2)-H(2)	0.9500
C(3)-C(2)#1	1.389(6)
C(4)-C(5)	1.488(7)
C(5)-C(5)#1	1.374(11)
C(5)-C(6)	1.397(7)
C(6)-C(7)	1.403(8)
C(6)-H(6)	0.9500
C(7)-C(7)#1	1.372(13)
C(7)-H(7)	0.9500
C(1)-N(1)-C(1)#1	116.6(6)
C(4)-N(2)-C(4)#1	111.4(6)
C(4)-N(2)-C(3)	124.3(3)
C(4)#1-N(2)-C(3)	124.3(3)
N(1)-C(1)-C(2)	124.9(5)
N(1)-C(1)-Br(1)	115.6(4)
C(2)-C(1)-Br(1)	119.5(4)
C(3)-C(2)-C(1)	116.2(5)
C(3)-C(2)-H(2)	121.9
C(1)-C(2)-H(2)	121.9
C(2)#1-C(3)-C(2)	121.1(6)
C(2)#1-C(3)-N(2)	119.5(3)
C(2)-C(3)-N(2)	119.5(3)
O(1)-C(4)-N(2)	125.5(5)
O(1)-C(4)-C(5)	129.2(5)
N(2)-C(4)-C(5)	105.2(5)
C(5)#1-C(5)-C(6)	122.3(3)
C(5)#1-C(5)-C(4)	109.0(3)
C(6)-C(5)-C(4)	128.6(5)
C(5)-C(6)-C(7)	115.4(6)
C(5)-C(6)-H(6)	122.3
C(7)-C(6)-H(6)	122.3
C(7)#1-C(7)-C(6)	122.2(4)
C(7)#1-C(7)-H(7)	118.9
C(6)-C(7)-H(7)	118.9

Table S4. ^1H NMR data of $[1](\text{PF}_6)_2 - [4](\text{PF}_6)_2$ in CD_3CN , 400 MHz.

	$[1](\text{PF}_6)_2$	$[2](\text{PF}_6)_2$	$[3](\text{PF}_6)_2$	$[4](\text{PF}_6)_2$
H^2	8.97 (s, 2 H)	8.95 (s, 2 H)	9.17 (s, 2 H)	9.15 (s, 2 H)
H^5	8.56 (s, 2 H)	8.54 (s, 2 H)	8.99 (m, 2 H)	8.96 (m, 2 H)
H^6	8.02 (m, 2 H)	8.00 (m, 2 H)	-	-
H^7	7.47 (m, 2 H)	7.48 (m, 2 H)	7.91 (m, 2 H)	7.91 (m, 2 H)
H^8	8.11 (m, 2 H)	8.15 (m, 2 H)	8.28 (m, 2 H)	8.31 (m, 2 H)
H^9	6.42 (m, 2 H)	6.38 (m, 2 H)	6.36 (m, 2 H)	6.30 (m, 2 H)
H^{10}	6.57 (m, 2 H)	6.54 (m, 2 H)	6.56 (m, 2 H)	6.52 (m, 2 H)
H^{11}	7.61 (m, 2 H)	7.58 (m, 2 H)	7.62 (m, 2 H)	7.59 (m, 2 H)
H^{12}	7.17 (m, 2 H)	7.12 (m, 2 H)	7.19 (m, 2 H)	7.13 (m, 2 H)
H^{15}	7.56 (d, $^3J_{\text{HH}} = 8.2$ Hz, 2 H)	6.80 (s, 2 H)	7.60 (d, $^3J_{\text{HH}} = 8.2$ Hz, 2 H)	6.82 (s, 2 H)
H^{16}	8.27 (t, $^3J_{\text{HH}} = 8.2$ Hz, 1 H)	-	8.30 (t, $^3J_{\text{HH}} = 8.2$ Hz, 1 H)	-
NH_2	-	5.72 (br, s, 2 H)	-	5.77 (br, s, 2 H)
NCH_3	3.46 (s, 6 H)	3.36 (s, 6 H)	3.48 (s, 6 H)	3.36 (s, 6 H)
$\text{CH}_2\text{CH}_3^{\text{center}}$	1.52 (t, $^3J_{\text{HH}} = 7.1$ Hz, 3 H)	1.51 (t, $^3J_{\text{HH}} = 7.1$ Hz, 3 H)	-	1.54 (t, $^3J_{\text{HH}} = 7.1$ Hz, 3 H)
$\text{CH}_2\text{CH}_3^{\text{outer}}$	-	-	-	1.41 (q, $^3J_{\text{HH}} = 7.1$ Hz, 6 H)
$\text{CH}_2\text{CH}_3^{\text{center}}$	4.58 (q, $^3J_{\text{HH}} = 7.1$ Hz, 2 H)	4.57 (q, $^3J_{\text{HH}} = 7.1$ Hz, 2 H)	-	4.60 (q, $^3J_{\text{HH}} = 7.1$ Hz, 2 H)
$\text{CH}_2\text{CH}_3^{\text{outer}}$	-	-	-	4.45 (q, $^3J_{\text{HH}} = 7.1$ Hz, 4 H)
$\text{OCH}_3^{\text{center}}$	-	-	4.13 (s, 3 H)	-
$\text{OCH}_3^{\text{outer}}$	-	-	3.99 (s, 6 H)	-

Table S5. $^{13}\text{C}\{^1\text{H}\}$ NMR data of $[1](\text{PF}_6)_2 - [4](\text{PF}_6)_2$ in CD_3CN , 101 MHz.

	$[1](\text{PF}_6)_2$	$[2](\text{PF}_6)_2$	$[3](\text{PF}_6)_2$	$[4](\text{PF}_6)_2$
C^1	136.3	135.1	136.4	135.8
C^2	123.8	123.6	124.8	124.6
C^3	159.7	159.1	159.3	159.6
C^4	158.7	158.8	159.7	159.8
C^5	125.7	125.4	124.7	124.4
C^6	139.2	138.8	140.0	140.0
C^7	128.0	127.8	126.8	126.7
C^8	155.1	155.0	155.8	155.7
C^9	149.4	149.3	149.2	149.2
C^{10}	121.5	121.1	121.6	121.2
C^{11}	140.2	140.0	140.4	140.3
C^{12}	116.3	116.2	116.6	116.5
C^{13}	159.8	160.2	159.5	160.0
C^{14}	157.2	156.8	157.1	156.7
C^{15}	113.6	98.7	113.7	98.8
C^{16}	141.8	160.0	142.1	159.3
$\text{CO}^{\text{center}}$	164.9	165.0	165.2	164.8
CO^{outer}	-	-	164.8	164.4
NCH_3	41.8	41.4	41.7	41.3
$\text{CH}_2\text{CH}_3^{\text{center}}$	14.6	14.5	-	14.6
$\text{CH}_2\text{CH}_3^{\text{outer}}$	-	-	-	14.4
$\text{CH}_2\text{CH}_3^{\text{center}}$	63.7	63.5	-	63.6
$\text{CH}_2\text{CH}_3^{\text{outer}}$	-	-	-	63.5
$\text{OCH}_3^{\text{center}}$	-	-	54.1	-
$\text{OCH}_3^{\text{outer}}$	-	-	53.9	-

Table S6. ^{15}N NMR data of $[1](\text{PF}_6)_2 - [4](\text{PF}_6)_2$, **10** and **11** in CD_3CN , 41 MHz.

	$[1](\text{PF}_6)_2$	$[2](\text{PF}_6)_2$	$[3](\text{PF}_6)_2$	$[4](\text{PF}_6)_2$	10	11	EtOOC-tpy (in d_6 -DMSO)
N^{a}	211.6	212.7	209.2	209.9	287.9	285.4	-
N^{b}	92.1	90.1	92.0	89.5	98.7	97.1	-
N^{c}	218.0	183.1	216.2	181.7	250.1	256.1	-
N^{d}	238.0	238.6	249.1	249.7	-	-	301.5
N^{e}	294.4	297.2	294.4	296.6	-	-	306.6
NH_2	-	72.1	-	72.7	-	-	-
phthalimide	-	-	-	-	169.0	-	-

Table S7. Crystal and structure refinement data for $[2](\text{PF}_6)_2$ and $[3](\text{PF}_6)_2$ from X-ray analysis.

	$[2](\text{PF}_6)_2$	$[3](\text{PF}_6)_2$
Empirical formula	$\text{C}_{37}\text{H}_{36}\text{F}_{12}\text{N}_{10}\text{O}_2\text{P}_2\text{Ru}$	$\text{C}_{44}\text{H}_{47}\text{F}_{12}\text{N}_9\text{O}_7\text{P}_2\text{Ru}$
Formula weight	1043.77	1204.92
Crystal color, habit	brown block	black block
Crystal dimensions / mm	0.43 x 0.20 x 0.17	0.25 x 0.11 x 0.11
Crystal system	triclinic	triclinic
Space group	$P\bar{1}$	$P\bar{1}$
$a / \text{\AA}$	12.0041(5)	12.0767(3)
$b / \text{\AA}$	13.4065(5)	15.4254(4)
$c / \text{\AA}$	14.8818(6)	15.7197(4)
$\alpha / ^\circ$	68.1070(10)	64.4150(10)
$\beta / ^\circ$	72.3710(10)	86.9760(10)
$\gamma / ^\circ$	73.7940(10)	69.4790(10)
$V / \text{\AA}^3$	2080.16(14)	2456.73(11)
Z	2	2
$F(000)$	1052	1224
Density (calcd) / g cm^{-3}	1.666	1.629
Absorption coefficient μ / mm^{-1}	0.556 (MULABS)	0.490 (MULABS)
Theta range / $^\circ$	1.51 – 27.97	2.45 – 27.98
Index ranges	$-15 \leq h \leq 15$ $-17 \leq k \leq 17$ $-19 \leq l \leq 19$	$-15 \leq h \leq 15$ $-20 \leq k \leq 17$ $-20 \leq l \leq 20$
Reflections collected	43817	45957
Independent reflections	9967 ($R_{\text{int}} = 0.0373$)	11811 ($R_{\text{int}} = 0.0376$)
Observed reflections	9967	11811
Parameters	585	841
Max. / min. transmission	0.910 / 0.875	0.9481 / 0.8873
Goodness-of-fit on F^2	1.019	0.944
Largest difference peak and hole / e \AA^{-3}	0.837 / -0.398	0.453 / -0.331
R_1 ($I > 2\sigma(I)$)	0.0316	0.0300
R_1 (all data)	0.0414	0.0432
wR_2 ($I > 2\sigma(I)$)	0.0816	0.0704
wR_2 (all data)	0.0855	0.0745

Table S8. Bond lengths / \AA and angles / $^\circ$ of $[2](\text{PF}_6)_2$ from X-ray crystal analysis.

Ru(1)-N(2)	1.9465(16)
Ru(1)-N(4)	2.0750(16)
Ru(1)-N(6)	2.0766(16)
Ru(1)-N(1)	2.0804(17)
Ru(1)-N(5)	2.0806(16)
Ru(1)-N(3)	2.0869(16)

N(1)-C(101)	1.348(3)
N(1)-C(105)	1.370(3)
N(2)-C(106)	1.366(3)
N(2)-C(110)	1.368(2)
N(3)-C(115)	1.343(3)
N(3)-C(111)	1.375(2)
N(4)-C(201)	1.354(3)
N(4)-C(205)	1.358(2)
N(5)-C(207)	1.362(2)
N(5)-C(211)	1.362(3)
N(6)-C(213)	1.350(3)
N(6)-C(217)	1.361(3)
N(7)-C(205)	1.403(3)
N(7)-C(207)	1.422(3)
N(7)-C(206)	1.479(2)
N(8)-C(213)	1.409(3)
N(8)-C(211)	1.416(2)
N(8)-C(212)	1.473(3)
N(9)-C(209)	1.364(3)
N(9)-H(9A)	0.8800
N(9)-H(9B)	0.8800
O(1)-C(116)	1.210(3)
O(2)-C(116)	1.323(3)
O(2)-C(117)	1.459(3)
C(101)-C(102)	1.390(3)
C(101)-H(101)	0.9500
C(102)-C(103)	1.378(4)
C(102)-H(102)	0.9500
C(103)-C(104)	1.388(3)
C(103)-H(103)	0.9500
C(104)-C(105)	1.384(3)
C(104)-H(104)	0.9500
C(105)-C(106)	1.481(3)
C(106)-C(107)	1.384(3)
C(107)-C(108)	1.394(3)
C(107)-H(107)	0.9500
C(108)-C(109)	1.399(3)
C(108)-C(116)	1.493(3)
C(109)-C(110)	1.380(3)
C(109)-H(109)	0.9500
C(110)-C(111)	1.480(3)
C(111)-C(112)	1.388(3)
C(112)-C(113)	1.378(3)
C(112)-H(112)	0.9500
C(113)-C(114)	1.382(3)
C(113)-H(113)	0.9500
C(114)-C(115)	1.388(3)
C(114)-H(114)	0.9500
C(115)-H(115)	0.9500
C(117)-C(118)	1.493(3)
C(117)-H(11A)	0.9900
C(117)-H(11B)	0.9900
C(118)-H(11C)	0.9800
C(118)-H(11D)	0.9800
C(118)-H(11E)	0.9800
C(201)-C(202)	1.372(3)

C(201)-H(201)	0.9500
C(202)-C(203)	1.387(3)
C(202)-H(202)	0.9500
C(203)-C(204)	1.376(3)
C(203)-H(203)	0.9500
C(204)-C(205)	1.397(3)
C(204)-H(204)	0.9500
C(206)-H(20A)	0.9800
C(206)-H(20B)	0.9800
C(206)-H(20C)	0.9800
C(207)-C(208)	1.372(3)
C(208)-C(209)	1.393(3)
C(208)-H(208)	0.9500
C(209)-C(210)	1.405(3)
C(210)-C(211)	1.376(3)
C(210)-H(210)	0.9500
C(212)-H(21A)	0.9800
C(212)-H(21B)	0.9800
C(212)-H(21C)	0.9800
C(213)-C(214)	1.404(3)
C(214)-C(215)	1.378(3)
C(214)-H(214)	0.9500
C(215)-C(216)	1.383(4)
C(215)-H(215)	0.9500
C(216)-C(217)	1.371(3)
C(216)-H(216)	0.9500
C(217)-H(217)	0.9500
P(1)-F(6)	1.571(2)
P(1)-F(4)	1.5809(19)
P(1)-F(5)	1.5899(19)
P(1)-F(2)	1.5952(17)
P(1)-F(3)	1.5961(18)
P(1)-F(1)	1.6037(16)
P(2)-F(10)	1.5770(18)
P(2)-F(12)	1.5845(18)
P(2)-F(9)	1.5905(17)
P(2)-F(7)	1.5956(17)
P(2)-F(11)	1.5980(16)
P(2)-F(8)	1.6127(17)
N(10)-C(300)	1.146(5)
C(300)-C(301)	1.418(5)
C(301)-H(30A)	0.9800
C(301)-H(30B)	0.9800
C(301)-H(30C)	0.9800
N(2)-Ru(1)-N(4)	92.88(7)
N(2)-Ru(1)-N(6)	92.02(6)
N(4)-Ru(1)-N(6)	174.83(6)
N(2)-Ru(1)-N(1)	79.80(7)
N(4)-Ru(1)-N(1)	91.53(6)
N(6)-Ru(1)-N(1)	90.94(7)
N(2)-Ru(1)-N(5)	178.19(7)
N(4)-Ru(1)-N(5)	87.33(6)
N(6)-Ru(1)-N(5)	87.83(6)
N(1)-Ru(1)-N(5)	98.39(6)
N(2)-Ru(1)-N(3)	79.74(7)

N(4)-Ru(1)-N(3)	90.38(6)
N(6)-Ru(1)-N(3)	88.88(6)
N(1)-Ru(1)-N(3)	159.53(7)
N(5)-Ru(1)-N(3)	102.05(6)
C(101)-N(1)-C(105)	117.89(18)
C(101)-N(1)-Ru(1)	128.94(15)
C(105)-N(1)-Ru(1)	113.13(13)
C(106)-N(2)-C(110)	121.29(17)
C(106)-N(2)-Ru(1)	119.25(13)
C(110)-N(2)-Ru(1)	119.39(14)
C(115)-N(3)-C(111)	117.73(17)
C(115)-N(3)-Ru(1)	129.36(14)
C(111)-N(3)-Ru(1)	112.90(13)
C(201)-N(4)-C(205)	117.78(17)
C(201)-N(4)-Ru(1)	121.55(13)
C(205)-N(4)-Ru(1)	120.62(14)
C(207)-N(5)-C(211)	116.83(17)
C(207)-N(5)-Ru(1)	121.21(14)
C(211)-N(5)-Ru(1)	121.82(12)
C(213)-N(6)-C(217)	118.09(17)
C(213)-N(6)-Ru(1)	121.02(13)
C(217)-N(6)-Ru(1)	120.63(14)
C(205)-N(7)-C(207)	122.30(17)
C(205)-N(7)-C(206)	116.09(17)
C(207)-N(7)-C(206)	115.46(17)
C(213)-N(8)-C(211)	122.15(17)
C(213)-N(8)-C(212)	116.24(17)
C(211)-N(8)-C(212)	115.65(16)
C(209)-N(9)-H(9A)	120.0
C(209)-N(9)-H(9B)	120.0
H(9A)-N(9)-H(9B)	120.0
C(116)-O(2)-C(117)	115.90(17)
N(1)-C(101)-C(102)	122.6(2)
N(1)-C(101)-H(101)	118.7
C(102)-C(101)-H(101)	118.7
C(103)-C(102)-C(101)	119.1(2)
C(103)-C(102)-H(102)	120.5
C(101)-C(102)-H(102)	120.5
C(102)-C(103)-C(104)	119.2(2)
C(102)-C(103)-H(103)	120.4
C(104)-C(103)-H(103)	120.4
C(105)-C(104)-C(103)	119.4(2)
C(105)-C(104)-H(104)	120.3
C(103)-C(104)-H(104)	120.3
N(1)-C(105)-C(104)	121.74(19)
N(1)-C(105)-C(106)	114.95(18)
C(104)-C(105)-C(106)	123.21(19)
N(2)-C(106)-C(107)	120.03(18)
N(2)-C(106)-C(105)	112.62(17)
C(107)-C(106)-C(105)	127.10(19)
C(106)-C(107)-C(108)	119.2(2)
C(106)-C(107)-H(107)	120.4
C(108)-C(107)-H(107)	120.4
C(107)-C(108)-C(109)	120.24(19)
C(107)-C(108)-C(116)	121.9(2)
C(109)-C(108)-C(116)	117.79(19)

C(110)-C(109)-C(108)	118.98(19)
C(110)-C(109)-H(109)	120.5
C(108)-C(109)-H(109)	120.5
N(2)-C(110)-C(109)	120.24(19)
N(2)-C(110)-C(111)	112.53(17)
C(109)-C(110)-C(111)	127.21(18)
N(3)-C(111)-C(112)	121.51(19)
N(3)-C(111)-C(110)	115.11(17)
C(112)-C(111)-C(110)	123.31(19)
C(113)-C(112)-C(111)	119.8(2)
C(113)-C(112)-H(112)	120.1
C(111)-C(112)-H(112)	120.1
C(112)-C(113)-C(114)	118.8(2)
C(112)-C(113)-H(113)	120.6
C(114)-C(113)-H(113)	120.6
C(113)-C(114)-C(115)	119.3(2)
C(113)-C(114)-H(114)	120.4
C(115)-C(114)-H(114)	120.4
N(3)-C(115)-C(114)	122.8(2)
N(3)-C(115)-H(115)	118.6
C(114)-C(115)-H(115)	118.6
O(1)-C(116)-O(2)	124.9(2)
O(1)-C(116)-C(108)	122.8(2)
O(2)-C(116)-C(108)	112.30(19)
O(2)-C(117)-C(118)	107.26(19)
O(2)-C(117)-H(11A)	110.3
C(118)-C(117)-H(11A)	110.3
O(2)-C(117)-H(11B)	110.3
C(118)-C(117)-H(11B)	110.3
H(11A)-C(117)-H(11B)	108.5
C(117)-C(118)-H(11C)	109.5
C(117)-C(118)-H(11D)	109.5
H(11C)-C(118)-H(11D)	109.5
C(117)-C(118)-H(11E)	109.5
H(11C)-C(118)-H(11E)	109.5
H(11D)-C(118)-H(11E)	109.5
N(4)-C(201)-C(202)	124.00(19)
N(4)-C(201)-H(201)	118.0
C(202)-C(201)-H(201)	118.0
C(201)-C(202)-C(203)	117.9(2)
C(201)-C(202)-H(202)	121.1
C(203)-C(202)-H(202)	121.1
C(204)-C(203)-C(202)	119.5(2)
C(204)-C(203)-H(203)	120.2
C(202)-C(203)-H(203)	120.2
C(203)-C(204)-C(205)	119.9(2)
C(203)-C(204)-H(204)	120.1
C(205)-C(204)-H(204)	120.1
N(4)-C(205)-C(204)	120.9(2)
N(4)-C(205)-N(7)	118.37(17)
C(204)-C(205)-N(7)	120.72(18)
N(7)-C(206)-H(20A)	109.5
N(7)-C(206)-H(20B)	109.5
H(20A)-C(206)-H(20B)	109.5
N(7)-C(206)-H(20C)	109.5
H(20A)-C(206)-H(20C)	109.5

H(20B)-C(206)-H(20C)	109.5
N(5)-C(207)-C(208)	123.4(2)
N(5)-C(207)-N(7)	117.05(17)
C(208)-C(207)-N(7)	119.52(17)
C(207)-C(208)-C(209)	119.52(19)
C(207)-C(208)-H(208)	120.2
C(209)-C(208)-H(208)	120.2
N(9)-C(209)-C(208)	121.0(2)
N(9)-C(209)-C(210)	121.3(2)
C(208)-C(209)-C(210)	117.75(19)
C(211)-C(210)-C(209)	119.6(2)
C(211)-C(210)-H(210)	120.2
C(209)-C(210)-H(210)	120.2
N(5)-C(211)-C(210)	122.87(18)
N(5)-C(211)-N(8)	117.20(17)
C(210)-C(211)-N(8)	119.93(19)
N(8)-C(212)-H(21A)	109.5
N(8)-C(212)-H(21B)	109.5
H(21A)-C(212)-H(21B)	109.5
N(8)-C(212)-H(21C)	109.5
H(21A)-C(212)-H(21C)	109.5
H(21B)-C(212)-H(21C)	109.5
N(6)-C(213)-C(214)	120.85(19)
N(6)-C(213)-N(8)	118.79(17)
C(214)-C(213)-N(8)	120.3(2)
C(215)-C(214)-C(213)	119.6(2)
C(215)-C(214)-H(214)	120.2
C(213)-C(214)-H(214)	120.2
C(214)-C(215)-C(216)	119.5(2)
C(214)-C(215)-H(215)	120.2
C(216)-C(215)-H(215)	120.2
C(217)-C(216)-C(215)	118.3(2)
C(217)-C(216)-H(216)	120.9
C(215)-C(216)-H(216)	120.9
N(6)-C(217)-C(216)	123.5(2)
N(6)-C(217)-H(217)	118.3
C(216)-C(217)-H(217)	118.3
F(6)-P(1)-F(4)	92.00(13)
F(6)-P(1)-F(5)	92.28(13)
F(4)-P(1)-F(5)	91.68(11)
F(6)-P(1)-F(2)	90.12(13)
F(4)-P(1)-F(2)	177.40(11)
F(5)-P(1)-F(2)	89.74(11)
F(6)-P(1)-F(3)	177.87(13)
F(4)-P(1)-F(3)	89.25(11)
F(5)-P(1)-F(3)	89.41(12)
F(2)-P(1)-F(3)	88.59(10)
F(6)-P(1)-F(1)	89.80(11)
F(4)-P(1)-F(1)	88.94(10)
F(5)-P(1)-F(1)	177.81(12)
F(2)-P(1)-F(1)	89.55(9)
F(3)-P(1)-F(1)	88.50(9)
F(10)-P(2)-F(12)	92.45(12)
F(10)-P(2)-F(9)	91.37(10)
F(12)-P(2)-F(9)	90.93(11)
F(10)-P(2)-F(7)	90.30(11)

F(12)-P(2)-F(7)	177.23(12)
F(9)-P(2)-F(7)	89.39(10)
F(10)-P(2)-F(11)	89.93(10)
F(12)-P(2)-F(11)	89.58(11)
F(9)-P(2)-F(11)	178.58(10)
F(7)-P(2)-F(11)	90.04(10)
F(10)-P(2)-F(8)	179.28(12)
F(12)-P(2)-F(8)	88.25(11)
F(9)-P(2)-F(8)	88.80(10)
F(7)-P(2)-F(8)	89.01(10)
F(11)-P(2)-F(8)	89.89(10)
N(10)-C(300)-C(301)	176.3(4)
C(300)-C(301)-H(30A)	109.5
C(300)-C(301)-H(30B)	109.5
H(30A)-C(301)-H(30B)	109.5
C(300)-C(301)-H(30C)	109.5
H(30A)-C(301)-H(30C)	109.5
H(30B)-C(301)-H(30C)	109.5

Table S9. Bond lengths / Å and angles / ° of [3](PF₆)₂ from X-ray crystal analysis.

Ru(1)-N(2)	1.9481(14)
Ru(1)-N(1)	2.0777(15)
Ru(1)-N(8)	2.0784(15)
Ru(1)-N(4)	2.0800(15)
Ru(1)-N(6)	2.0858(15)
Ru(1)-N(3)	2.0921(15)
O(1)-C(4)	1.199(2)
O(2)-C(4)	1.328(2)
O(2)-C(5)	1.457(2)
N(1)-C(1)	1.349(2)
N(1)-C(7)	1.371(2)
N(2)-C(14)	1.359(2)
N(2)-C(8)	1.364(2)
N(3)-C(21)	1.344(2)
N(3)-C(15)	1.381(2)
N(4)-C(22)	1.352(2)
N(4)-C(26)	1.353(2)
N(5)-C(26)	1.409(2)
N(5)-C(28)	1.415(3)
N(5)-C(27)	1.471(3)
N(6)-C(32)	1.354(2)
N(6)-C(28)	1.358(2)
N(7)-C(34)	1.412(2)
N(7)-C(32)	1.412(3)
N(7)-C(33)	1.472(3)
N(8)-C(34)	1.345(2)
N(8)-C(38)	1.360(2)
C(1)-C(2)	1.383(3)
C(1)-H(1A)	0.9500
C(2)-C(3)	1.388(3)
C(2)-H(2A)	0.9500
C(3)-C(6)	1.388(3)
C(3)-C(4)	1.502(3)
C(5)-H(5A)	0.9800
C(5)-H(5B)	0.9800

C(5)-H(5C)	0.9800
C(6)-C(7)	1.387(3)
C(6)-H(6A)	0.9500
C(7)-C(8)	1.471(3)
C(8)-C(9)	1.371(3)
C(9)-C(10)	1.393(3)
C(9)-H(9A)	0.9500
C(10)-C(13)	1.389(3)
C(10)-C(11)	1.499(2)
C(11)-O(3)	1.195(2)
C(11)-O(4)	1.331(2)
O(4)-C(12)	1.448(2)
C(12)-H(12A)	0.9800
C(12)-H(12B)	0.9800
C(12)-H(12C)	0.9800
C(13)-C(14)	1.385(2)
C(13)-H(13A)	0.9500
C(14)-C(15)	1.474(3)
C(15)-C(16)	1.380(3)
C(16)-C(17)	1.383(3)
C(16)-H(16A)	0.9500
C(17)-C(20)	1.382(3)
C(17)-C(18)	1.508(4)
C(17)-C(18A)	1.518(9)
C(18)-O(5)	1.196(2)
C(18)-O(6)	1.332(2)
O(6)-C(19)	1.449(2)
C(19)-H(19A)	0.9800
C(19)-H(19B)	0.9800
C(19)-H(19C)	0.9800
C(18A)-O(5A)	1.196(2)
C(18A)-O(6A)	1.332(2)
O(6A)-C(19A)	1.448(2)
C(19A)-H(19D)	0.9800
C(19A)-H(19E)	0.9800
C(19A)-H(19F)	0.9800
C(20)-C(21)	1.391(3)
C(20)-H(20A)	0.9500
C(21)-H(21A)	0.9500
C(22)-C(23)	1.373(3)
C(22)-H(22A)	0.9500
C(23)-C(24)	1.382(3)
C(23)-H(23A)	0.9500
C(24)-C(25)	1.373(3)
C(24)-H(24A)	0.9500
C(25)-C(26)	1.393(3)
C(25)-H(25A)	0.9500
C(27)-H(27A)	0.9800
C(27)-H(27B)	0.9800
C(27)-H(27C)	0.9800
C(28)-C(29)	1.387(3)
C(29)-C(30)	1.368(3)
C(29)-H(29A)	0.9500
C(30)-C(31)	1.375(3)
C(30)-H(30A)	0.9500
C(31)-C(32)	1.391(3)

C(31)-H(31A)	0.9500
C(33)-H(33A)	0.9800
C(33)-H(33B)	0.9800
C(33)-H(33C)	0.9800
C(34)-C(35)	1.402(3)
C(35)-C(36)	1.370(3)
C(35)-H(35A)	0.9500
C(36)-C(37)	1.378(3)
C(36)-H(36A)	0.9500
C(37)-C(38)	1.370(3)
C(37)-H(37A)	0.9500
C(38)-H(38A)	0.9500
P(1)-F(4)	1.574(2)
P(1)-F(3)	1.586(2)
P(1)-F(1)	1.5881(19)
P(1)-F(6)	1.5973(19)
P(1)-F(2)	1.598(2)
P(1)-F(5)	1.604(2)
P(1A)-F(4A)	1.574(2)
P(1A)-F(3A)	1.586(2)
P(1A)-F(1A)	1.588(2)
P(1A)-F(6A)	1.597(2)
P(1A)-F(2A)	1.598(2)
P(1A)-F(5A)	1.604(2)
P(2)-F(9)	1.513(5)
P(2)-F(8)	1.536(4)
P(2)-F(12)	1.566(6)
P(2)-F(11)	1.595(4)
P(2)-F(10)	1.609(4)
P(2)-F(7)	1.619(7)
P(2A)-F(10A)	1.402(12)
P(2A)-F(7A)	1.38(2)
P(2A)-F(9A)	1.538(12)
P(2A)-F(11A)	1.590(12)
P(2A)-F(12A)	1.635(14)
P(2A)-F(8A)	1.668(12)
O(10)-C(41)	1.417(3)
O(10)-C(40)	1.422(3)
C(39)-C(40)	1.495(4)
C(39)-H(39A)	0.9800
C(39)-H(39B)	0.9800
C(39)-H(39C)	0.9800
C(40)-H(40A)	0.9900
C(40)-H(40B)	0.9900
C(41)-C(42)	1.504(4)
C(41)-H(41A)	0.9900
C(41)-H(41B)	0.9900
C(42)-H(42A)	0.9800
C(42)-H(42B)	0.9800
C(42)-H(42C)	0.9800
N(9)-C(44)	1.125(4)
C(43)-C(44)	1.438(4)
C(43)-H(43A)	0.9800
C(43)-H(43B)	0.9800
C(43)-H(43C)	0.9800

N(2)-Ru(1)-N(1)	79.84(6)
N(2)-Ru(1)-N(8)	93.08(6)
N(1)-Ru(1)-N(8)	89.97(6)
N(2)-Ru(1)-N(4)	92.05(6)
N(1)-Ru(1)-N(4)	92.08(6)
N(8)-Ru(1)-N(4)	174.74(6)
N(2)-Ru(1)-N(6)	177.18(6)
N(1)-Ru(1)-N(6)	97.43(6)
N(8)-Ru(1)-N(6)	87.59(6)
N(4)-Ru(1)-N(6)	87.34(6)
N(2)-Ru(1)-N(3)	79.31(6)
N(1)-Ru(1)-N(3)	159.10(6)
N(8)-Ru(1)-N(3)	89.80(6)
N(4)-Ru(1)-N(3)	90.00(6)
N(6)-Ru(1)-N(3)	103.44(6)
C(4)-O(2)-C(5)	115.64(18)
C(1)-N(1)-C(7)	117.70(16)
C(1)-N(1)-Ru(1)	129.52(12)
C(7)-N(1)-Ru(1)	112.73(12)
C(14)-N(2)-C(8)	120.91(15)
C(14)-N(2)-Ru(1)	120.10(12)
C(8)-N(2)-Ru(1)	118.98(12)
C(21)-N(3)-C(15)	117.11(16)
C(21)-N(3)-Ru(1)	130.17(13)
C(15)-N(3)-Ru(1)	112.71(11)
C(22)-N(4)-C(26)	117.40(16)
C(22)-N(4)-Ru(1)	122.10(13)
C(26)-N(4)-Ru(1)	120.49(13)
C(26)-N(5)-C(28)	121.22(16)
C(26)-N(5)-C(27)	115.79(17)
C(28)-N(5)-C(27)	116.66(17)
C(32)-N(6)-C(28)	118.19(16)
C(32)-N(6)-Ru(1)	121.50(13)
C(28)-N(6)-Ru(1)	120.20(13)
C(34)-N(7)-C(32)	121.66(16)
C(34)-N(7)-C(33)	115.71(17)
C(32)-N(7)-C(33)	115.80(16)
C(34)-N(8)-C(38)	117.85(16)
C(34)-N(8)-Ru(1)	121.45(12)
C(38)-N(8)-Ru(1)	120.59(13)
N(1)-C(1)-C(2)	122.74(17)
N(1)-C(1)-H(1A)	118.6
C(2)-C(1)-H(1A)	118.6
C(1)-C(2)-C(3)	119.48(18)
C(1)-C(2)-H(2A)	120.3
C(3)-C(2)-H(2A)	120.3
C(2)-C(3)-C(6)	118.35(17)
C(2)-C(3)-C(4)	123.74(18)
C(6)-C(3)-C(4)	117.89(18)
O(1)-C(4)-O(2)	125.59(19)
O(1)-C(4)-C(3)	122.97(19)
O(2)-C(4)-C(3)	111.43(18)
O(2)-C(5)-H(5A)	109.5
O(2)-C(5)-H(5B)	109.5
H(5A)-C(5)-H(5B)	109.5
O(2)-C(5)-H(5C)	109.5

H(5A)-C(5)-H(5C)	109.5
H(5B)-C(5)-H(5C)	109.5
C(7)-C(6)-C(3)	119.76(18)
C(7)-C(6)-H(6A)	120.1
C(3)-C(6)-H(6A)	120.1
N(1)-C(7)-C(6)	121.66(17)
N(1)-C(7)-C(8)	115.33(16)
C(6)-C(7)-C(8)	122.97(17)
N(2)-C(8)-C(9)	120.28(17)
N(2)-C(8)-C(7)	112.73(16)
C(9)-C(8)-C(7)	126.73(17)
C(8)-C(9)-C(10)	119.57(17)
C(8)-C(9)-H(9A)	120.2
C(10)-C(9)-H(9A)	120.2
C(13)-C(10)-C(9)	119.85(17)
C(13)-C(10)-C(11)	118.90(17)
C(9)-C(10)-C(11)	121.24(17)
O(3)-C(11)-O(4)	125.45(16)
O(3)-C(11)-C(10)	123.65(17)
O(4)-C(11)-C(10)	110.88(16)
C(11)-O(4)-C(12)	116.29(16)
O(4)-C(12)-H(12A)	109.5
O(4)-C(12)-H(12B)	109.5
H(12A)-C(12)-H(12B)	109.5
O(4)-C(12)-H(12C)	109.5
H(12A)-C(12)-H(12C)	109.5
H(12B)-C(12)-H(12C)	109.5
C(14)-C(13)-C(10)	118.96(17)
C(14)-C(13)-H(13A)	120.5
C(10)-C(13)-H(13A)	120.5
N(2)-C(14)-C(13)	120.40(16)
N(2)-C(14)-C(15)	112.48(15)
C(13)-C(14)-C(15)	127.10(17)
C(16)-C(15)-N(3)	121.88(17)
C(16)-C(15)-C(14)	122.94(17)
N(3)-C(15)-C(14)	115.16(16)
C(15)-C(16)-C(17)	120.03(18)
C(15)-C(16)-H(16A)	120.0
C(17)-C(16)-H(16A)	120.0
C(20)-C(17)-C(16)	118.53(18)
C(20)-C(17)-C(18)	127.3(2)
C(16)-C(17)-C(18)	114.1(2)
C(20)-C(17)-C(18A)	109.0(4)
C(16)-C(17)-C(18A)	132.5(4)
C(18)-C(17)-C(18A)	18.4(4)
O(5)-C(18)-O(6)	125.0(2)
O(5)-C(18)-C(17)	125.6(3)
O(6)-C(18)-C(17)	109.4(2)
C(18)-O(6)-C(19)	115.7(2)
O(6)-C(19)-H(19A)	109.5
O(6)-C(19)-H(19B)	109.5
H(19A)-C(19)-H(19B)	109.5
O(6)-C(19)-H(19C)	109.5
H(19A)-C(19)-H(19C)	109.5
H(19B)-C(19)-H(19C)	109.5
O(5A)-C(18A)-O(6A)	125.3(2)

O(5A)-C(18A)-C(17)	129.4(6)
O(6A)-C(18A)-C(17)	105.2(6)
C(18A)-O(6A)-C(19A)	116.0(2)
O(6A)-C(19A)-H(19D)	109.5
O(6A)-C(19A)-H(19E)	109.5
H(19D)-C(19A)-H(19E)	109.5
O(6A)-C(19A)-H(19F)	109.5
H(19D)-C(19A)-H(19F)	109.5
H(19E)-C(19A)-H(19F)	109.5
C(17)-C(20)-C(21)	119.28(18)
C(17)-C(20)-H(20A)	120.4
C(21)-C(20)-H(20A)	120.4
N(3)-C(21)-C(20)	123.08(18)
N(3)-C(21)-H(21A)	118.5
C(20)-C(21)-H(21A)	118.5
N(4)-C(22)-C(23)	123.84(19)
N(4)-C(22)-H(22A)	118.1
C(23)-C(22)-H(22A)	118.1
C(22)-C(23)-C(24)	118.2(2)
C(22)-C(23)-H(23A)	120.9
C(24)-C(23)-H(23A)	120.9
C(25)-C(24)-C(23)	119.3(2)
C(25)-C(24)-H(24A)	120.3
C(23)-C(24)-H(24A)	120.3
C(24)-C(25)-C(26)	119.7(2)
C(24)-C(25)-H(25A)	120.2
C(26)-C(25)-H(25A)	120.2
N(4)-C(26)-C(25)	121.50(18)
N(4)-C(26)-N(5)	117.52(17)
C(25)-C(26)-N(5)	120.95(18)
N(5)-C(27)-H(27A)	109.5
N(5)-C(27)-H(27B)	109.5
H(27A)-C(27)-H(27B)	109.5
N(5)-C(27)-H(27C)	109.5
H(27A)-C(27)-H(27C)	109.5
H(27B)-C(27)-H(27C)	109.5
N(6)-C(28)-C(29)	122.04(19)
N(6)-C(28)-N(5)	117.37(16)
C(29)-C(28)-N(5)	120.58(18)
C(30)-C(29)-C(28)	118.8(2)
C(30)-C(29)-H(29A)	120.6
C(28)-C(29)-H(29A)	120.6
C(29)-C(30)-C(31)	120.44(19)
C(29)-C(30)-H(30A)	119.8
C(31)-C(30)-H(30A)	119.8
C(30)-C(31)-C(32)	118.6(2)
C(30)-C(31)-H(31A)	120.7
C(32)-C(31)-H(31A)	120.7
N(6)-C(32)-C(31)	121.90(19)
N(6)-C(32)-N(7)	117.66(16)
C(31)-C(32)-N(7)	120.44(18)
N(7)-C(33)-H(33A)	109.5
N(7)-C(33)-H(33B)	109.5
H(33A)-C(33)-H(33B)	109.5
N(7)-C(33)-H(33C)	109.5
H(33A)-C(33)-H(33C)	109.5

H(33B)-C(33)-H(33C)	109.5
N(8)-C(34)-C(35)	121.21(18)
N(8)-C(34)-N(7)	118.32(17)
C(35)-C(34)-N(7)	120.43(18)
C(36)-C(35)-C(34)	119.4(2)
C(36)-C(35)-H(35A)	120.3
C(34)-C(35)-H(35A)	120.3
C(35)-C(36)-C(37)	119.9(2)
C(35)-C(36)-H(36A)	120.0
C(37)-C(36)-H(36A)	120.0
C(38)-C(37)-C(36)	118.14(19)
C(38)-C(37)-H(37A)	120.9
C(36)-C(37)-H(37A)	120.9
N(8)-C(38)-C(37)	123.48(19)
N(8)-C(38)-H(38A)	118.3
C(37)-C(38)-H(38A)	118.3
F(4)-P(1)-F(3)	91.47(14)
F(4)-P(1)-F(1)	91.13(17)
F(3)-P(1)-F(1)	89.86(12)
F(4)-P(1)-F(6)	89.95(16)
F(3)-P(1)-F(6)	90.52(13)
F(1)-P(1)-F(6)	178.84(17)
F(4)-P(1)-F(2)	178.42(13)
F(3)-P(1)-F(2)	89.90(13)
F(1)-P(1)-F(2)	89.67(14)
F(6)-P(1)-F(2)	89.24(14)
F(4)-P(1)-F(5)	88.87(15)
F(3)-P(1)-F(5)	179.53(17)
F(1)-P(1)-F(5)	90.46(11)
F(6)-P(1)-F(5)	89.16(12)
F(2)-P(1)-F(5)	89.76(15)
F(4A)-P(1A)-F(3A)	91.47(15)
F(4A)-P(1A)-F(1A)	91.12(17)
F(3A)-P(1A)-F(1A)	89.86(13)
F(4A)-P(1A)-F(6A)	89.96(16)
F(3A)-P(1A)-F(6A)	90.52(13)
F(1A)-P(1A)-F(6A)	178.84(17)
F(4A)-P(1A)-F(2A)	178.43(14)
F(3A)-P(1A)-F(2A)	89.90(14)
F(1A)-P(1A)-F(2A)	89.66(14)
F(6A)-P(1A)-F(2A)	89.24(14)
F(4A)-P(1A)-F(5A)	88.87(16)
F(3A)-P(1A)-F(5A)	179.54(16)
F(1A)-P(1A)-F(5A)	90.46(12)
F(6A)-P(1A)-F(5A)	89.16(12)
F(2A)-P(1A)-F(5A)	89.76(15)
F(9)-P(2)-F(8)	94.5(3)
F(9)-P(2)-F(12)	89.1(4)
F(8)-P(2)-F(12)	89.7(3)
F(9)-P(2)-F(11)	176.5(4)
F(8)-P(2)-F(11)	88.7(3)
F(12)-P(2)-F(11)	89.5(3)
F(9)-P(2)-F(10)	88.3(3)
F(8)-P(2)-F(10)	177.2(4)
F(12)-P(2)-F(10)	90.7(3)
F(11)-P(2)-F(10)	88.5(3)

F(9)-P(2)-F(7)	88.5(3)
F(8)-P(2)-F(7)	88.1(3)
F(12)-P(2)-F(7)	176.6(4)
F(11)-P(2)-F(7)	93.1(3)
F(10)-P(2)-F(7)	91.6(3)
F(10A)-P(2A)-F(7A)	85.5(13)
F(10A)-P(2A)-F(9A)	94.6(10)
F(7A)-P(2A)-F(9A)	92.0(11)
F(10A)-P(2A)-F(11A)	97.8(11)
F(7A)-P(2A)-F(11A)	91.1(11)
F(9A)-P(2A)-F(11A)	167.5(12)
F(10A)-P(2A)-F(12A)	88.6(9)
F(7A)-P(2A)-F(12A)	173.2(14)
F(9A)-P(2A)-F(12A)	91.8(7)
F(11A)-P(2A)-F(12A)	86.3(7)
F(10A)-P(2A)-F(8A)	177.5(10)
F(7A)-P(2A)-F(8A)	97.0(13)
F(9A)-P(2A)-F(8A)	85.0(10)
F(11A)-P(2A)-F(8A)	82.6(8)
F(12A)-P(2A)-F(8A)	88.9(7)
C(41)-O(10)-C(40)	113.1(2)
C(40)-C(39)-H(39A)	109.5
C(40)-C(39)-H(39B)	109.5
H(39A)-C(39)-H(39B)	109.5
C(40)-C(39)-H(39C)	109.5
H(39A)-C(39)-H(39C)	109.5
H(39B)-C(39)-H(39C)	109.5
O(10)-C(40)-C(39)	109.5(2)
O(10)-C(40)-H(40A)	109.8
C(39)-C(40)-H(40A)	109.8
O(10)-C(40)-H(40B)	109.8
C(39)-C(40)-H(40B)	109.8
H(40A)-C(40)-H(40B)	108.2
O(10)-C(41)-C(42)	110.8(2)
O(10)-C(41)-H(41A)	109.5
C(42)-C(41)-H(41A)	109.5
O(10)-C(41)-H(41B)	109.5
C(42)-C(41)-H(41B)	109.5
H(41A)-C(41)-H(41B)	108.1
C(41)-C(42)-H(42A)	109.5
C(41)-C(42)-H(42B)	109.5
H(42A)-C(42)-H(42B)	109.5
C(41)-C(42)-H(42C)	109.5
H(42A)-C(42)-H(42C)	109.5
H(42B)-C(42)-H(42C)	109.5
C(44)-C(43)-H(43A)	109.5
C(44)-C(43)-H(43B)	109.5
H(43A)-C(43)-H(43B)	109.5
C(44)-C(43)-H(43C)	109.5
H(43A)-C(43)-H(43C)	109.5
H(43B)-C(43)-H(43C)	109.5
N(9)-C(44)-C(43)	177.4(4)

	Ru-N1	Ru-N2	Ru-N3	Ru-N4	Ru-N5	Ru-N6	N1-Ru-N2	N2-Ru-N3	N4-Ru-N5	N5-Ru-N6	N1-C-C-N2	N2-C-C-N3
[1] ²⁺ - ¹ GS	2.12	1.98	2.12	2.12	2.11	2.12	79.2	79.2	87.6	87.6	-1.4	-1.4
[1] ²⁺ - ³ MLCT	2.12	2.01	2.12	2.12	2.09	2.10	78.0	77.9	88.2	88.2	-1.5	-2.4
[1] ²⁺ - ³ TS	2.31	2.16	2.30	2.15	2.10	2.11	72.7	73.2	87.1	88.2	10.9	-17.9
[1] ²⁺ - ³ MC	2.36	2.23	2.38	2.13	2.11	2.11	71.1	71.2	87.9	87.9	1.9	-14.3
[2] ²⁺ - ¹ GS	2.11	1.98	2.12	2.12	2.11	2.12	79.3	79.3	87.3	87.3	-1.3	-1.2
[2] ²⁺ - ³ MLCT	2.12	2.02	2.12	2.11	2.06	2.11	77.5	77.5	88.6	88.6	-1.8	-1.9
[2] ²⁺ - ³ TS	2.33	2.19	2.33	2.14	2.09	2.11	72.1	72.4	87.3	88.1	9.5	-17.9
[2] ²⁺ - ³ MC	2.37	2.23	2.38	2.12	2.09	2.11	71.0	71.2	87.4	87.7	-0.8	-13.6
[3] ²⁺ - ¹ GS	2.11	1.98	2.11	2.12	2.11	2.12	79.3	79.3	87.6	87.5	-1.3	-1.2
[3] ²⁺ - ³ MLCT	2.11	2.02	2.11	2.12	2.09	2.10	77.9	77.8	88.2	88.3	-1.0	-2.8
[3] ²⁺ - ³ TS	2.35	2.19	2.35	2.14	2.10	2.11	71.3	71.8	87.1	87.6	3.3	-16.8
[3] ²⁺ - ³ MC	2.35	2.23	2.38	2.13	2.11	2.11	70.8	71.1	87.3	87.8	1.1	-14.1
[4] ²⁺ - ¹ GS	2.11	1.98	2.11	2.12	2.11	2.12	79.3	79.4	87.3	87.3	-1.1	-0.9
[4] ²⁺ - ³ MLCT	2.11	2.03	2.11	2.11	2.05	2.11	77.5	77.5	88.6	88.6	-1.7	-1.7
[4] ²⁺ - ³ TS	n. a.	n. a.	n. a.	n. a.	n. a.	n. a.	n. a.	n. a.	n. a.	n. a.	n. a.	n. a.
[4] ²⁺ - ³ MC	n. a.	n. a.	n. a.	n. a.	n. a.	n. a.	n. a.	n. a.	n. a.	n. a.	n. a.	n. a.
[5] ²⁺ - ¹ GS	2.11	2.01	2.11	2.11	2.01	2.11	78.9	78.9	78.9	78.9	0.0	0.0
[5] ²⁺ - ³ MLCT	2.10	2.05	2.10	2.12	1.98	2.10	77.6	77.6	79.7	79.5	-0.4	0.4
[5] ²⁺ - ³ TS	2.20	2.07	2.15	2.11	2.02	2.18	75.4	76.0	79.5	77.4	-10.6	11.2
[5] ²⁺ - ³ MC	2.36	2.16	2.35	2.14	2.01	2.15	72.6	72.6	79.2	77.8	-10.6	10.6
[6] ²⁺ - ¹ GS	2.10	2.00	2.10	2.11	2.01	2.11	79.0	79.0	78.8	78.8	0.0	0.0
[6] ²⁺ - ³ MLCT	2.10	2.02	2.10	2.10	2.02	2.12	77.8	77.9	79.0	79.9	1.3	-1.7
[6] ²⁺ - ³ TS	2.25	2.10	2.25	2.18	2.02	2.13	74.3	74.5	77.4	79.4	12.2	-12.7
[6] ²⁺ - ³ MC	2.34	2.14	2.34	2.16	2.02	2.14	72.9	73.0	77.7	79.2	10.9	-11.0
[7] ²⁺ - ¹ GS	2.10	1.99	2.10	2.11	2.02	2.11	79.2	79.2	78.4	78.4	0.0	0.0
[7] ²⁺ - ³ MLCT	2.11	2.04	2.10	2.11	1.99	2.12	77.0	77.1	79.4	79.8	0.3	-0.3
[7] ²⁺ - ³ TS	2.29	2.15	2.30	2.15	2.01	2.13	72.9	72.9	77.8	79.2	12.6	-12.8
[7] ²⁺ - ³ MC	2.33	2.17	2.33	2.14	2.01	2.13	72.2	72.3	77.9	79.1	11.2	-11.4

Table S10. Selected bond lengths / Å and angles / ° of DFT (B3LYP/LANL2DZ, IEFPCM in CH₃CN) calculated singlet ground state (¹GS) and triplet excited states (³MLCT, ³MC, ³TS) of [1]²⁺ – [7]²⁺.

Table S11. Selected Mulliken spin densities of DFT (B3LYP/LANL2DZ, IEFPCM in CH₃CN) calculated triplet excited states (³MLCT, ³MC, ³TS) of [1]²⁺ – [7]²⁺.

	Ru	ligand 1	ligand 2
		tpy	ddpd or second tpy
[1] ²⁺ - ³ MLCT	0.89	1.04	0.07
[1] ²⁺ - ³ TS	1.60	0.38	0.02
[1] ²⁺ - ³ MC	1.80	0.19	0.01
[2] ²⁺ - ³ MLCT	0.86	1.03	0.11
[2] ²⁺ - ³ TS	1.67	0.30	0.03
[2] ²⁺ - ³ MC	1.81	0.17	0.02
[3] ²⁺ - ³ MLCT	0.89	1.04	0.07
[3] ²⁺ - ³ TS	1.72	0.27	0.01
[3] ²⁺ - ³ MC	1.78	0.21	0.01
[4] ²⁺ - ³ MLCT	0.85	1.03	0.12
[4] ²⁺ - ³ TS	n. a.	n. a.	n. a.
[4] ²⁺ - ³ MC	n. a.	n. a.	n. a.
[5] ²⁺ - ³ MLCT	0.86	0.05	1.09
[5] ²⁺ - ³ TS	1.31	0.60	0.09
[5] ²⁺ - ³ MC	1.75	0.21	0.04
[6] ²⁺ - ³ MLCT	0.91	1.05	0.04
[6] ²⁺ - ³ TS	1.50	0.44	0.06
[6] ²⁺ - ³ MC	1.73	0.22	0.05
[7] ²⁺ - ³ MLCT	0.85	1.02	0.13
[7] ²⁺ - ³ TS	1.59	0.33	0.08
[7] ²⁺ - ³ MC	1.69	0.24	0.07

10.7 Push-Pull Design of Bis(tridentate) Ruthenium(II) Polypyridine Chromophores as Deep Red Light Emitters in Light-Emitting Electrochemical Cells

A. Breivogel, M. Park, D. Lee, S. Klassen, A. Kühnle, C. Lee, K. Char, K. Heinze, *Eur. J. Inorg. Chem.* **2014**, 288–295.

DOI: 10.1002/ejic.201301226

Reprinted with permission from John Wiley and Sons, Copyright © 2013.

SUPPORTING INFORMATION

DOI: 10.1002/ejic.201301226

Title: Push-Pull Design of Bis(tridentate) Ruthenium(II) Polypyridine Chromophores as Deep Red Light Emitters in Light-Emitting Electrochemical Cells

Author(s): Aaron Breivogel, Myeongjin Park, Donggu Lee, Stefanie Klassen, Angelika Kühnle, Changhee Lee, Kookheon Char, Katja Heinze*

Table of Contents:

- 1) AFM images of scratched PEDOT:PSS/ruthenium complex:PMMA layers (Figure S1)
- 2) Emission spectra of **[1](PF₆)₂** and **[3](PF₆)₂** in solution and in LECs (Figures S2 – S3)
- 3) Current density-EQE-intensity curves of the LECs (Figures S4 – S7)
- 4) Human eye response curve and emission spectra of **[1](PF₆)₂** – **[3](PF₆)₂** in LECs (Figure S8)

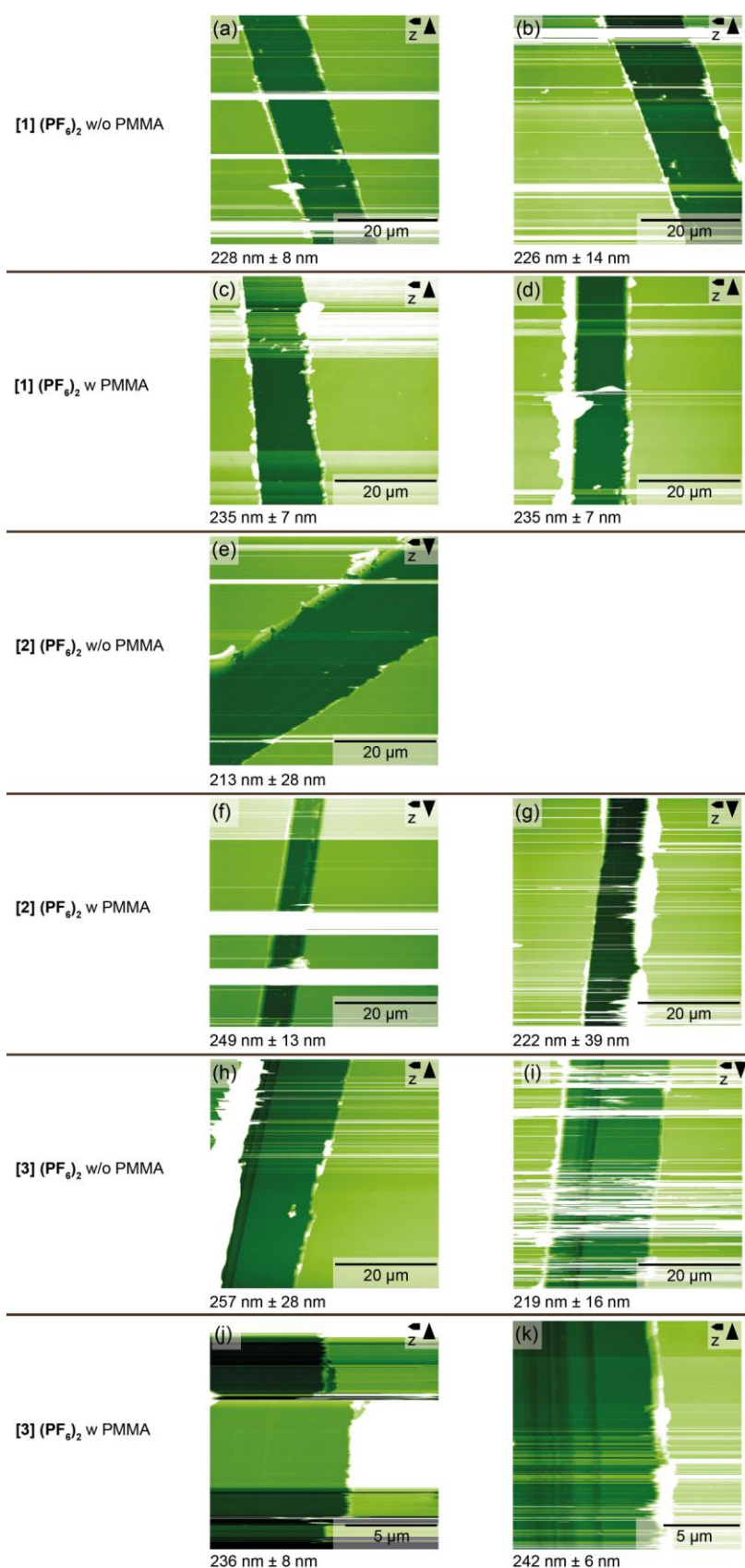


Figure S1. Representative intermittent contact mode images showing scratched PEDOT:PSS/ruthenium(II) complex:PMMA samples with varying compositions. The horizontal stripes arise from material attaching to and detaching from the cantilever tip. The given thickness values are determined by height histograms taken in areas without stripe artifacts.

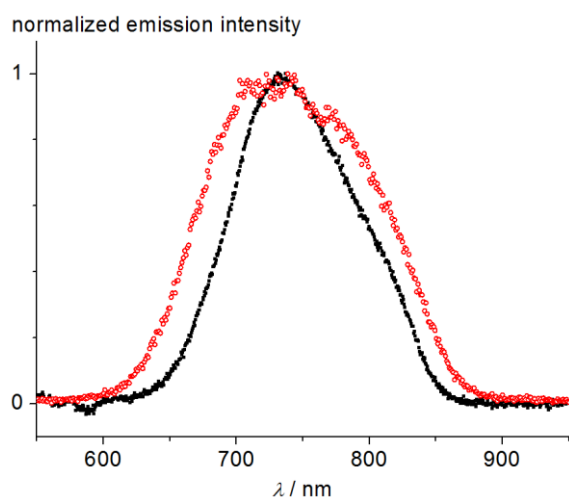


Figure S2. Normalized emission spectra of $[1](PF_6)_2$ (black squares: CH_3CN solution at 297 K; red hollow circles: LEC with PMMA, 6 V).

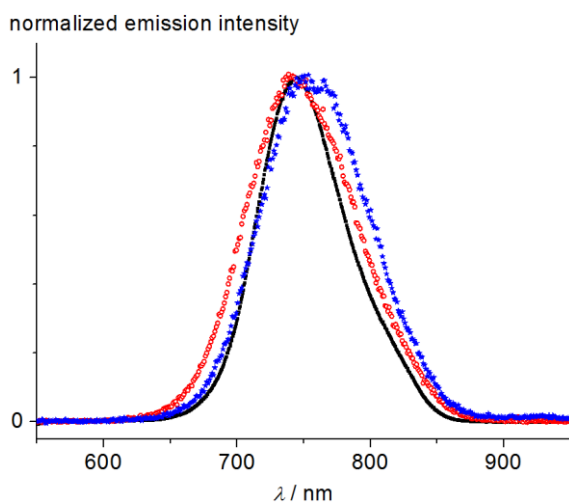


Figure S3. Normalized emission spectra of $[3](PF_6)_2$ (black squares: CH_3CN solution at 297 K; red hollow circles: LEC with PMMA, 5 V; blue stars: LEC without PMMA, 4 V)

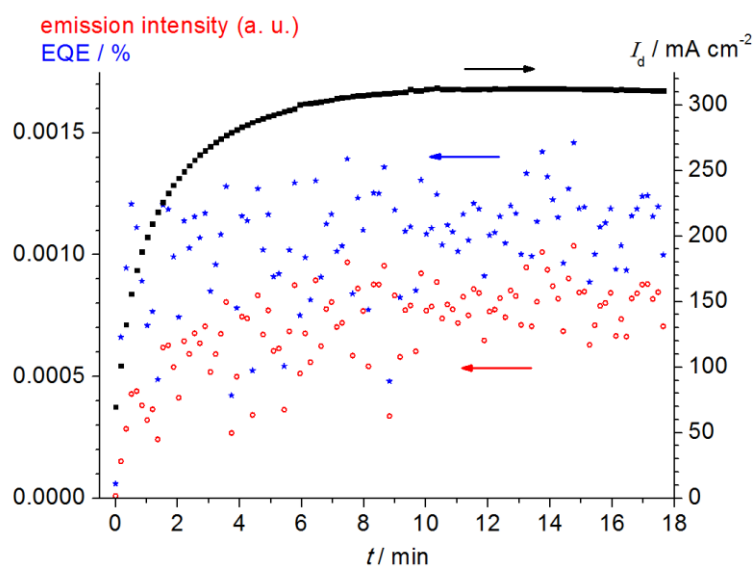


Figure S4. Current density (black squares), emission intensity (red hollow circles) and EQE (blue stars) vs. time in the LEC with $[1](PF_6)_2$ with PMMA at an applied voltage of 4 V.

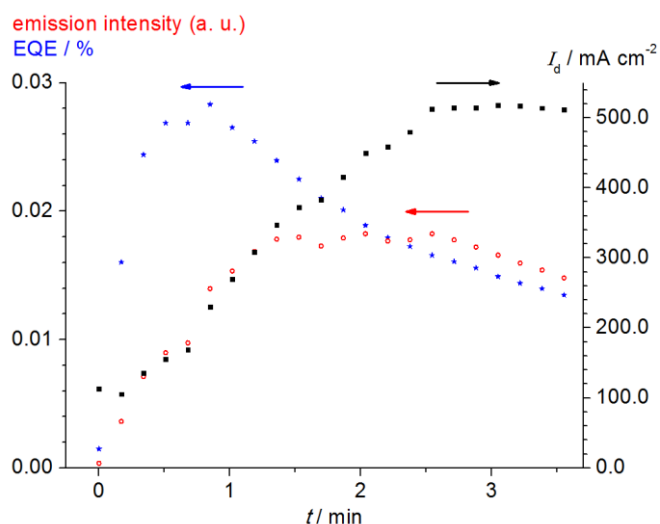


Figure S5. Current density (black squares), emission intensity (red hollow circles) and EQE (blue stars) vs. time in the LEC with $[2](\text{PF}_6)_2$ with PMMA at an applied voltage of 6 V.

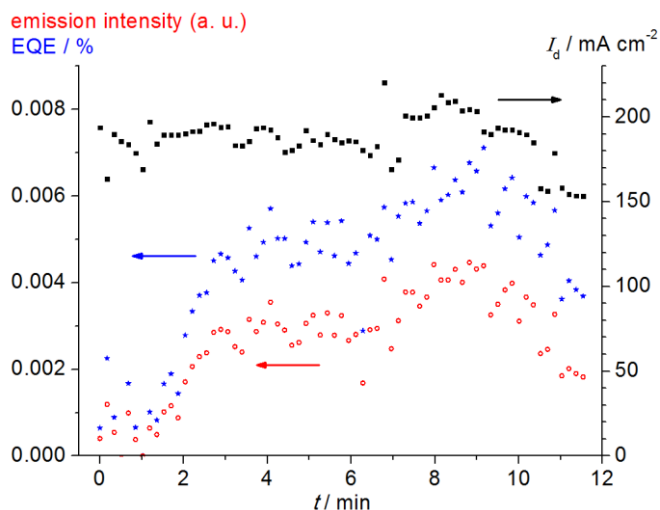


Figure S6. Current density (black squares), emission intensity (red hollow circles) and EQE (blue stars) vs. time in the LEC with $[3](\text{PF}_6)_2$ without PMMA at an applied voltage of 4 V.

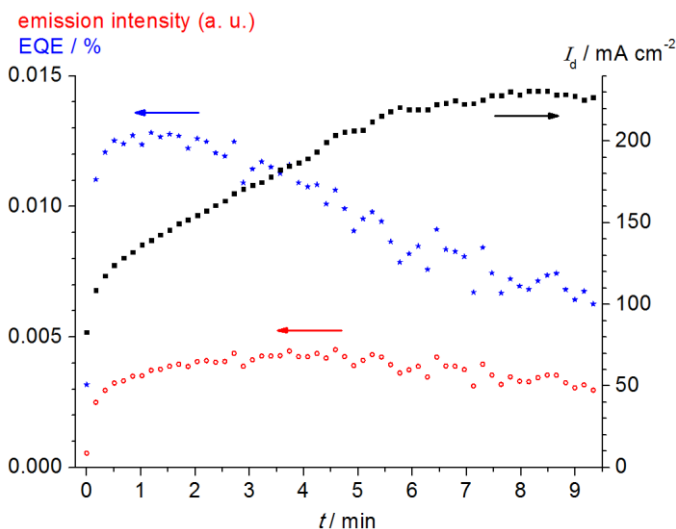


Figure S7. Current density (black squares), emission intensity (red hollow circles) and EQE (blue stars) vs. time in the LEC with $[3](\text{PF}_6)_2$ with PMMA at an applied voltage of 5 V.

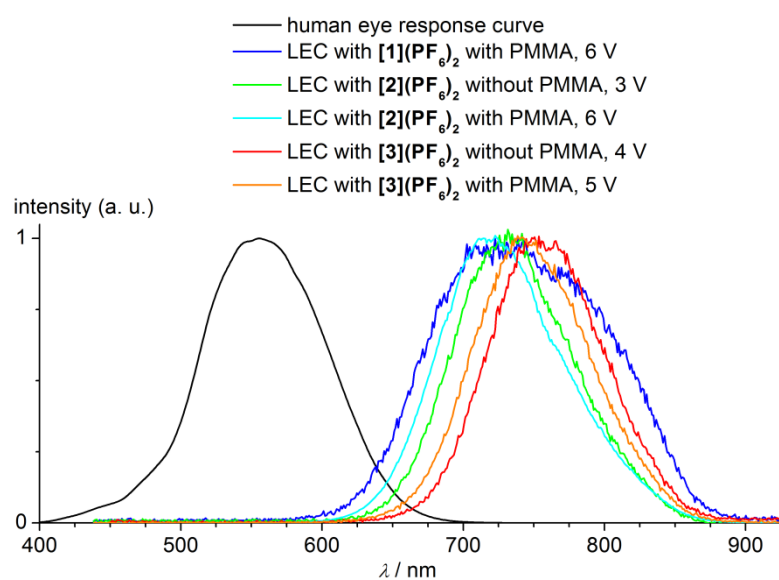


Figure S8. Comparison of the human eye response curve (photopic response curve) with normalized emission spectra of LECs of [1](PF₆)₂ – [3](PF₆)₂.

10.8 Anchor-Functionalized Push-Pull-Substituted Bis(tridentate) Ruthenium(II) Polypyridine Chromophores: Photostability and Evaluation as Photosensitizers

A. Breivogel, S. Wooh, J. Dietrich, T. Y. Kim, Y. S. Kang, K. Char, K. Heinze, *Eur. J. Inorg. Chem.* **2014**, 2720–2734.

DOI: 10.1002/ejic.2014020919

Reprinted with permission from John Wiley and Sons, Copyright © 2014.

DFT-optimized (B3LYP/LANL2DZ, IEFPCM in CH₃CN) cartesian coordinates of [**1** – **6**]³⁺ and reduced N719 (doublet), [**1** – **6**]²⁺ and N719 (singlet), [**1** – **6**]³⁺ and oxidized N719 (doublet) and results of the TD-DFT (B3LYP/LANL2DZ, IEFPCM in CH₃CN) calculation of [**1** – **6**]²⁺ (singlet) can be found in the online supporting information.

SUPPORTING INFORMATION

DOI: 10.1002/ejic.201402091

Title: Anchor-Functionalized Push-Pull-Substituted Bis(tridentate) Ruthenium(II) Polypyridine Chromophores: Photostability and Evaluation as Photosensitizers

Author(s): Aaron Breivogel, Sanghyuk Wooh, Jan Dietrich, Tea Yon Kim, Yong Soo Kang, Kookheon Char, Katja Heinze*

Table of Contents:

- 1) Tabulated ^1H , ^{13}C and ^{15}N NMR chemical shifts in CD_3CN (Tables S1 – S3).
- 2) Figures S1 – S13
- 3) DFT (B3LYP/LANL2DZ, IEFPCM, CH_3CN) optimized geometries of
 - $[\mathbf{1}]^{2+}$ – $[\mathbf{6}]^{2+}$ and N719 (singlet)
 - $[\mathbf{1}]^{3+}$ – $[\mathbf{6}]^{3+}$ and oxidized N719 (doublet)
 - $[\mathbf{1}]^+$ – $[\mathbf{6}]^+$ and reduced N719 (doublet)
- 4) Results of TD-DFT calculations of $[\mathbf{1}]^{2+}$ – $[\mathbf{6}]^{2+}$ and N719 (singlet).

Table S1. ^1H NMR data (δ / ppm) of [1](PF₆)₂ – [3](PF₆)₂ in CD₃CN, 400 MHz.

	[1](PF ₆) ₂	[2](PF ₆) ₂	[3](PF ₆) ₂
H ²	8.99 (s, 2 H)	9.15 (s, 2 H)	9.12 (s, 2 H)
H ⁵	8.56 (m, 2 H)	8.97 (m, 2 H)	8.94 (m, 2 H)
H ⁶	8.01 (m, 2 H)	-	-
H ⁷	7.47 (m, 2 H)	7.89 (m, 2 H)	7.89 (m, 2 H)
H ⁸	8.11 (m, 2 H)	8.26 (m, 2 H)	8.30 (m, 2 H)
H ⁹	6.44 (m, 2 H)	6.36 (m, 2 H)	6.29 (m, 2 H)
H ¹⁰	6.58 (m, 2 H)	6.56 (m, 2 H)	6.52 (m, 2 H)
H ¹¹	7.61 (m, 2 H)	7.61 (m, 2 H)	7.58 (m, 2 H)
H ¹²	7.17 (m, 2 H)	7.18 (m, 2 H)	7.12 (m, 2 H)
H ¹⁵	7.56 (d, $^3J_{\text{HH}} = 8.2$ Hz, 2 H)	7.58 (d, $^3J_{\text{HH}} = 8.2$ Hz, 2 H)	6.81 (s, 2 H)
H ¹⁶	8.27 (t, $^3J_{\text{HH}} = 8.2$ Hz, 1 H)	8.29 (t, $^3J_{\text{HH}} = 8.2$ Hz, 1 H)	-
NH ₂	-	-	5.75 (br, s, 2 H)
NCH ₃	3.47 (s, 6 H)	3.47 (s, 6 H)	3.36 (s, 6 H)

Table S2. $^{13}\text{C}\{^1\text{H}\}$ NMR data (δ / ppm) of [1](PF₆)₂ – [3](PF₆)₂ in CD₃CN, 101 MHz.

	[1](PF ₆) ₂	[2](PF ₆) ₂	[3](PF ₆) ₂
C ¹	137.1	136.6	135.5
C ²	124.1	125.0	124.9
C ³	159.5	159.7	159.5
C ⁴	158.7	159.2	159.8
C ⁵	125.7	124.9	124.7
C ⁶	139.1	140.1	139.7
C ⁷	127.9	127.1	127.0
C ⁸	155.1	155.8	155.7
C ⁹	149.4	149.2	149.2
C ¹⁰	121.4	121.6	121.2
C ¹¹	140.1	140.4	140.3
C ¹²	116.3	116.6	116.5
C ¹³	159.8	159.6	160.0
C ¹⁴	157.2	157.1	156.7
C ¹⁵	113.5	113.7	98.8
C ¹⁶	141.7	142.1	159.3
CO ^{center}	165.7	165.1	165.3
CO ^{outer}	-	164.7	164.8
NCH ₃	41.8	41.7	41.3

Table S3. ^{15}N NMR data (δ / ppm) of [1](PF₆)₂ – [3](PF₆)₂ in CD₃CN, 41 MHz.

	[1](PF ₆) ₂	[2](PF ₆) ₂	[3](PF ₆) ₂
N ^a	212.1	209.0	210.0
N ^b	92.1	not observed	not observed
N ^c	218.4	216.3	181.6
N ^d	238.3	249.5	249.9
N ^e	293.6	293.9	296.9
NH ₂	-	-	72.2

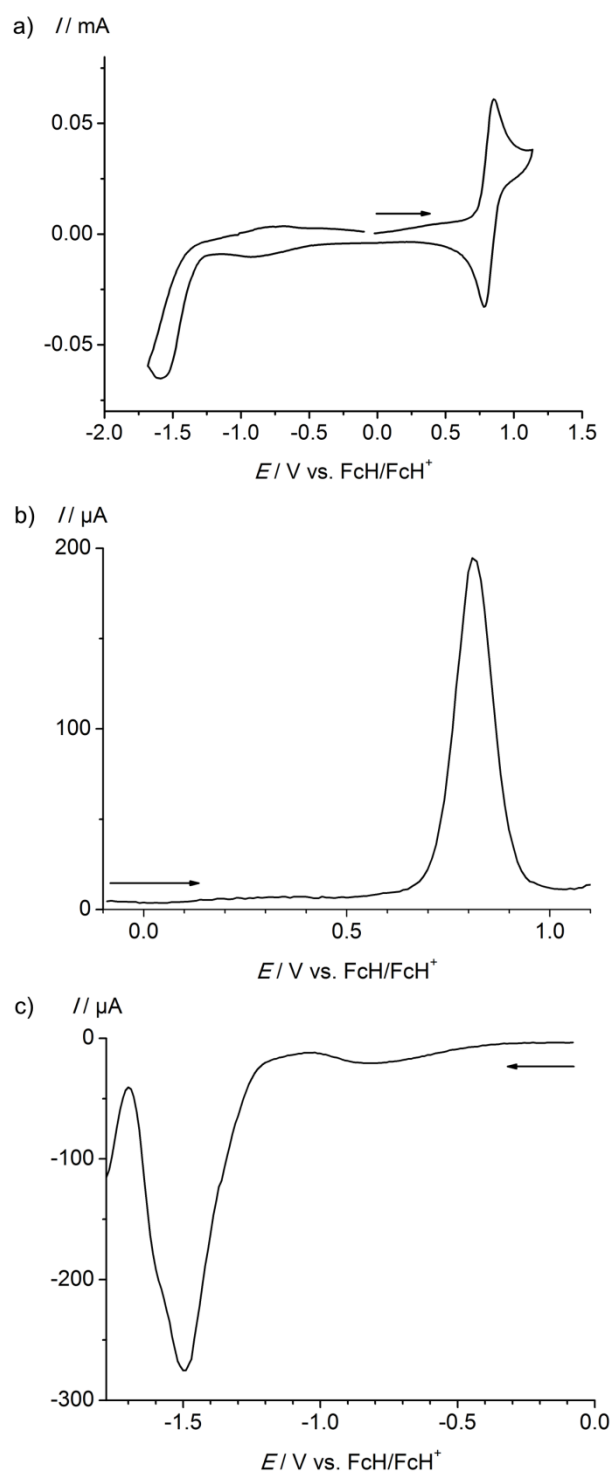


Figure S1. Cyclic voltammogram (a) and square wave voltammograms (b, c) of $[1](PF_6)_2$ in CH_3CN ; $0.1\text{ M } [n-Bu_4](PF_6)$.

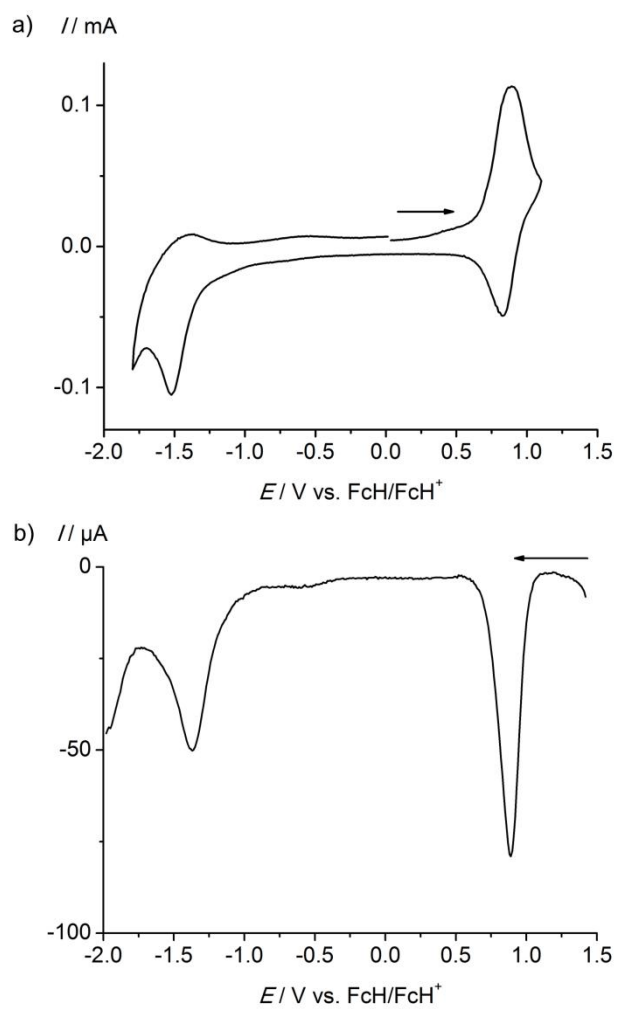


Figure S2. Cyclic voltammogram (a) and square wave voltammogram (b) of $[\mathbf{2}](\text{PF}_6)_2$ in CH_3CN ; 0.1 M $[n\text{-Bu}_4](\text{PF}_6)$.

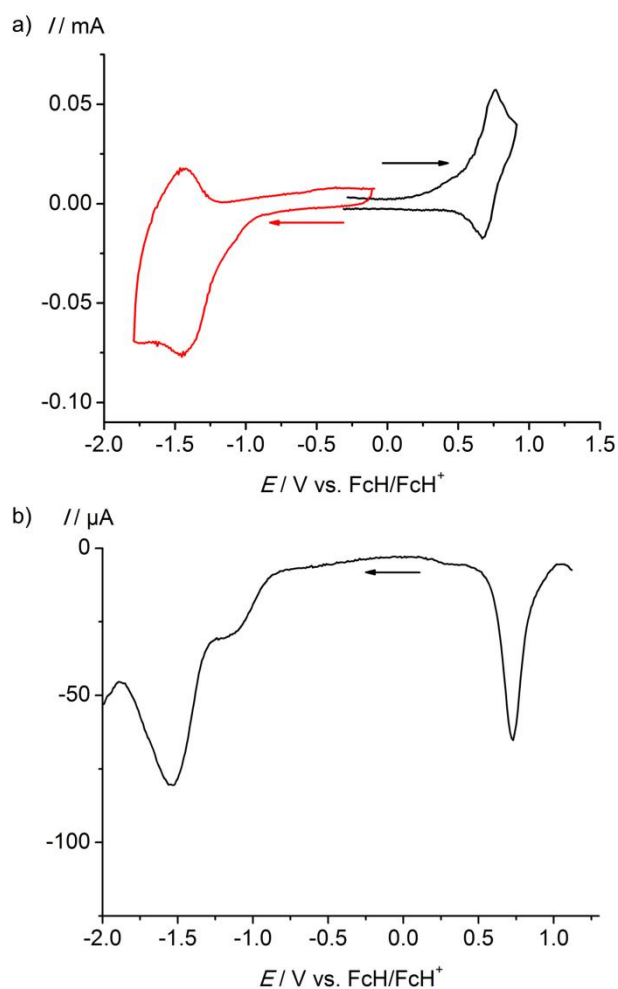


Figure S3. Cyclic voltammograms (a) and square wave voltammogram (b) of $[3](\text{PF}_6)_2$ in CH_3CN ; 0.1 M $[n\text{-Bu}_4](\text{PF}_6)$.

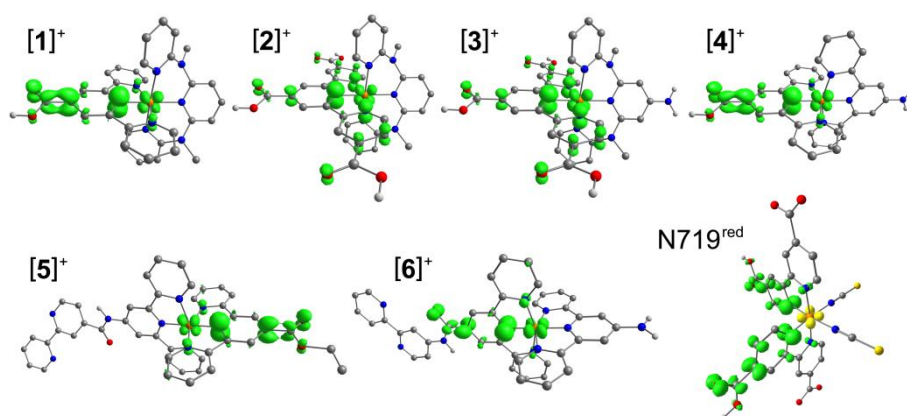


Figure S4. Spin densities of $[1]^+ - [6]^+$ and one-electron reduced N719 (contour value 0.005 a. u.; CH hydrogen atoms omitted).

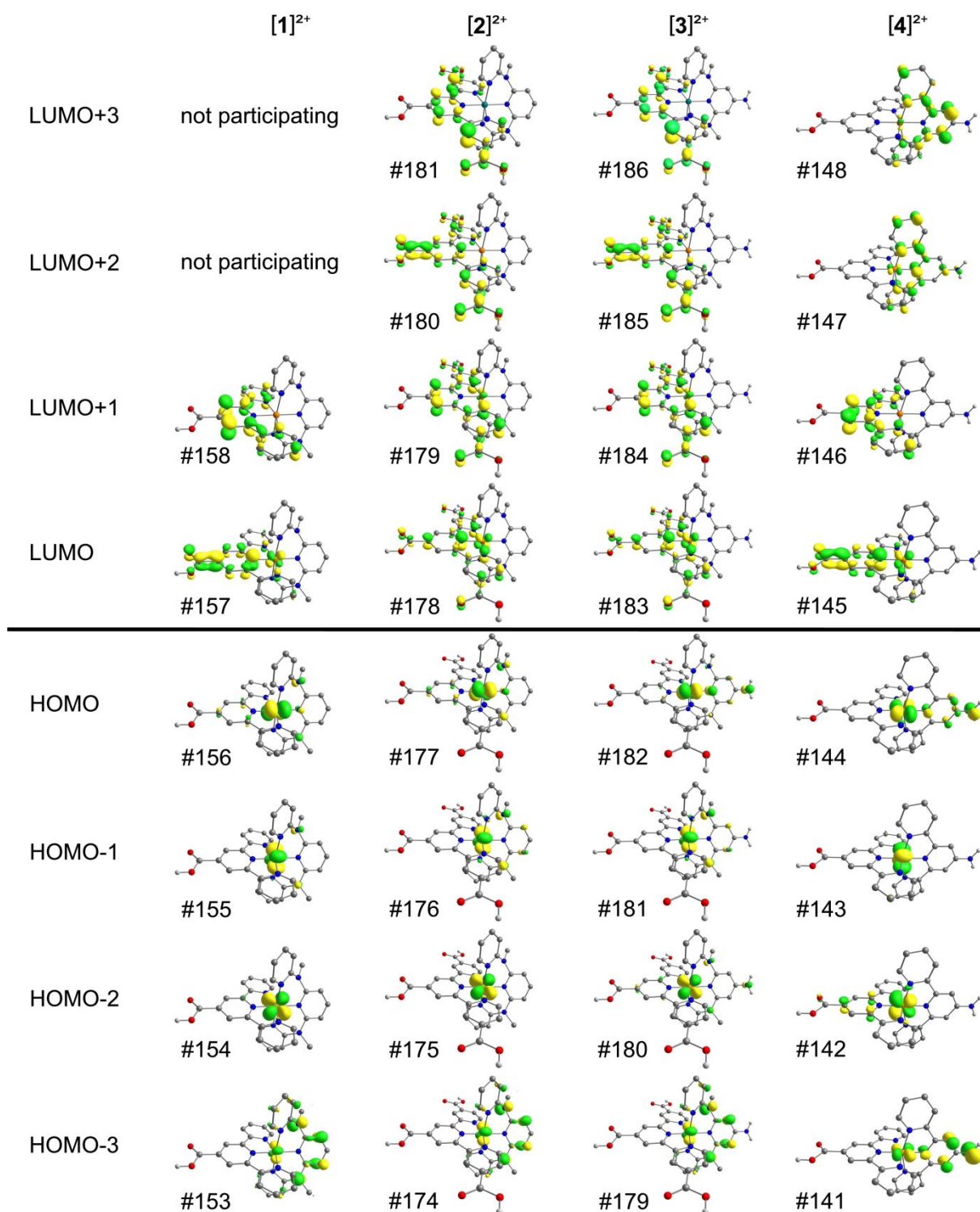


Figure S5. Relevant DFT calculated frontier orbitals (HOMO-3 to LUMO+3) of [1]²⁺ – [4]²⁺ for transitions with $\lambda > 400$ nm (contour value 0.06 a. u.; CH hydrogen atoms omitted).

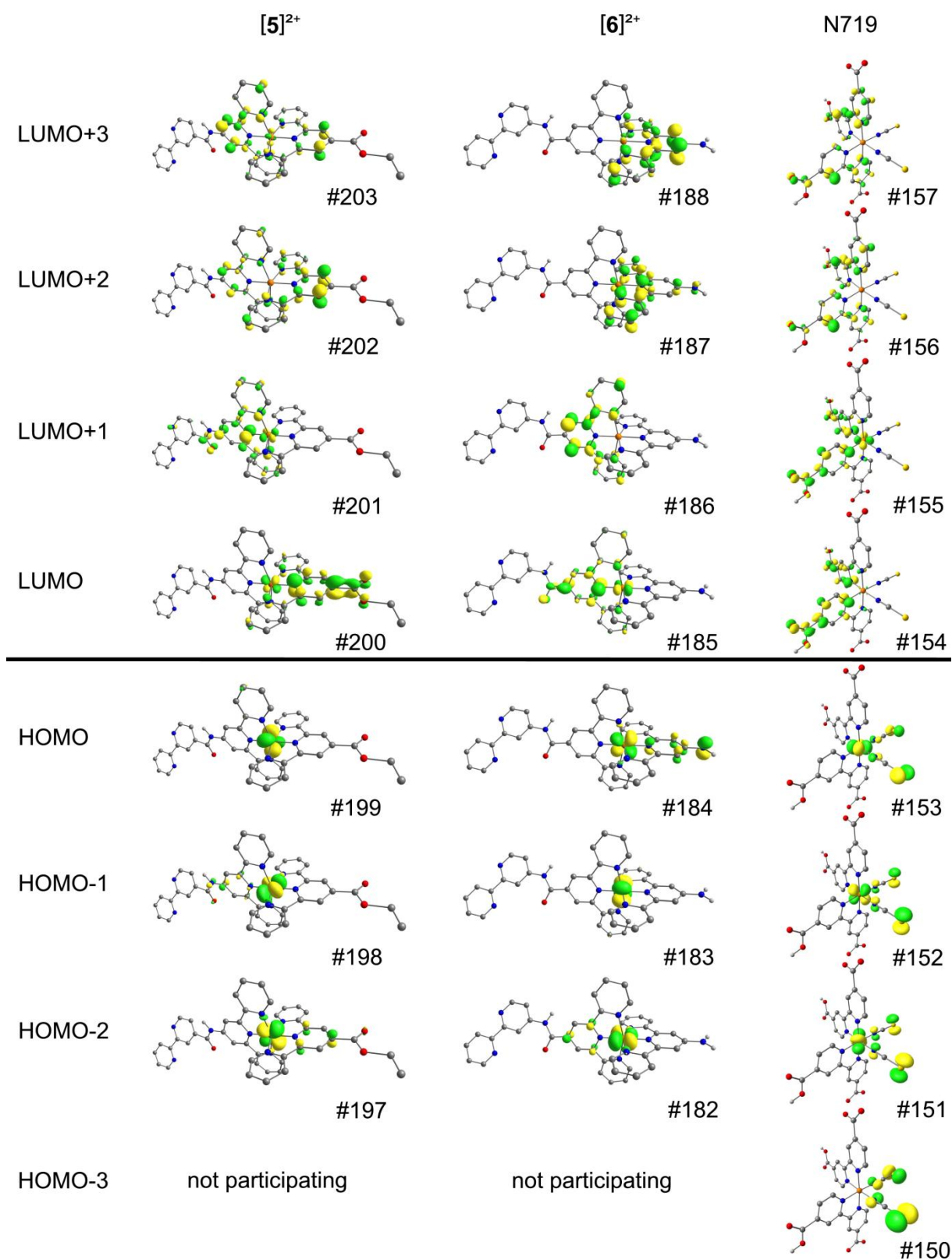


Figure S6. Relevant DFT calculated frontier orbitals (HOMO-3 to LUMO+3) of [5]²⁺, [6]²⁺ and N719 for transitions with $\lambda > 400$ nm (contour value 0.06 a. u.; CH hydrogen atoms omitted).

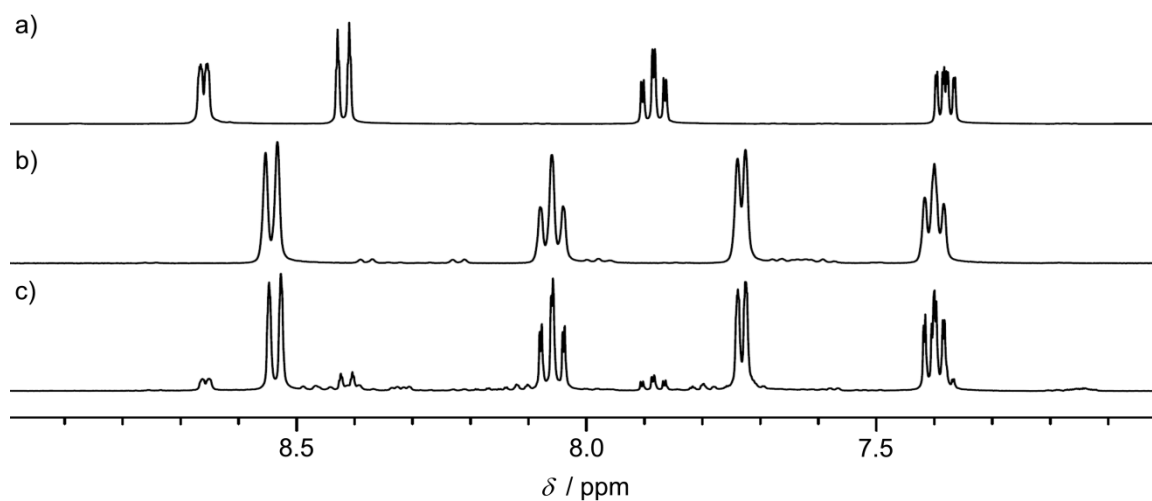


Figure S7. ^1H -NMR spectra in CD_3CN : a) free bpy and the mixture of $[\text{Ru}(\text{bpy})_3](\text{PF}_6)_2$ and 2.2 equiv $[n\text{-Bu}_4\text{N}]\text{I}$ b) before and c) after irradiation.

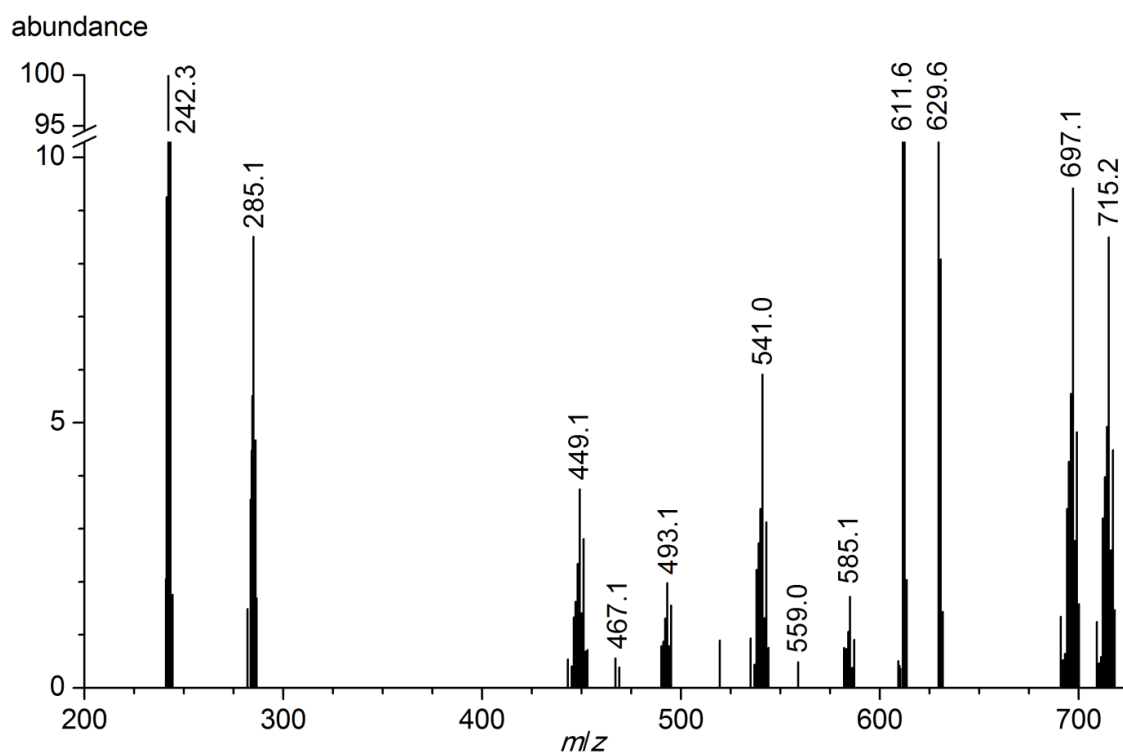


Figure S8. ESI $^+$ mass spectrum of the mixture of $[\text{Ru}(\text{bpy})_3](\text{PF}_6)_2$ and 2.2 equiv $[n\text{-Bu}_4\text{N}]\text{I}$ in CD_3CN after irradiation.

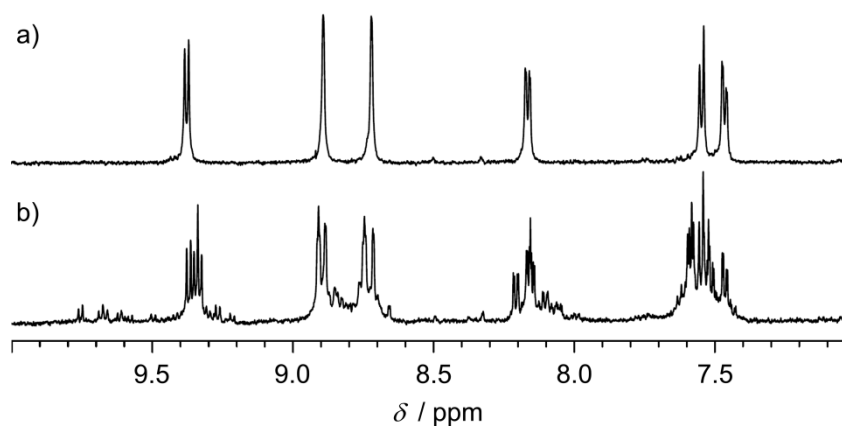


Figure S9. ^1H -NMR spectra in $\text{CD}_3\text{CN}:\text{H}_2\text{O}$ (14:1): N719 and 4.5 equiv $[n\text{-Bu}_4\text{N}]\text{I}$ a) before and b) after irradiation.

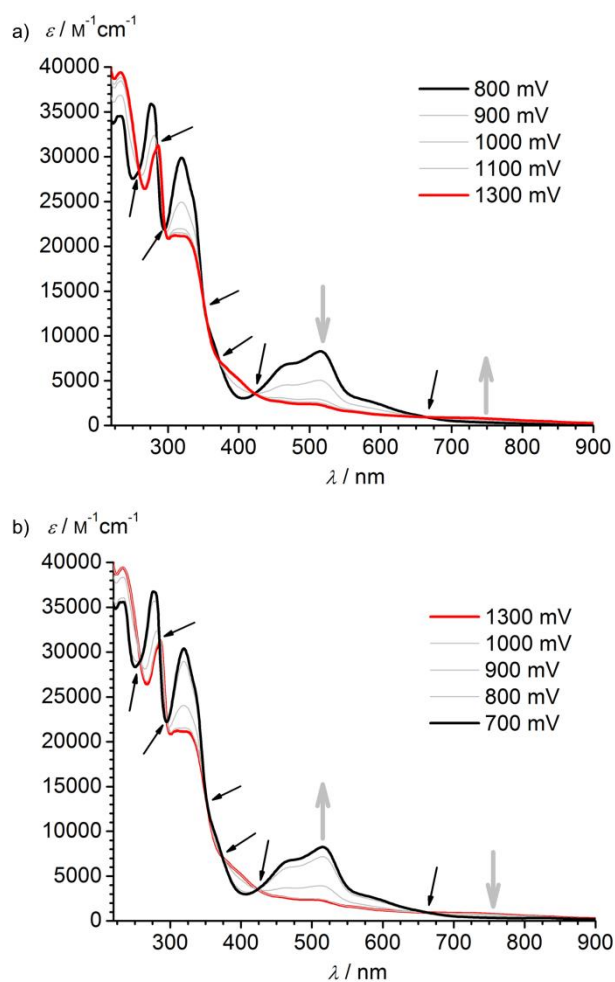


Figure S10. UV/Vis spectra of a) the electrochemical oxidation ($E = 800 \rightarrow 1300$ mV) and b) back reduction ($E = 1300 \rightarrow 700$ mV) of $[1^{\text{Et}}](\text{PF}_6)_2$ in an OTTE cell in 10^{-3} M NaOH and 0.1 M $[n\text{-Bu}_4\text{N}](\text{PF}_6)$ in $\text{CH}_3\text{CN}:\text{H}_2\text{O}$ (98:2, v%). Black arrows indicate isosbestic points.

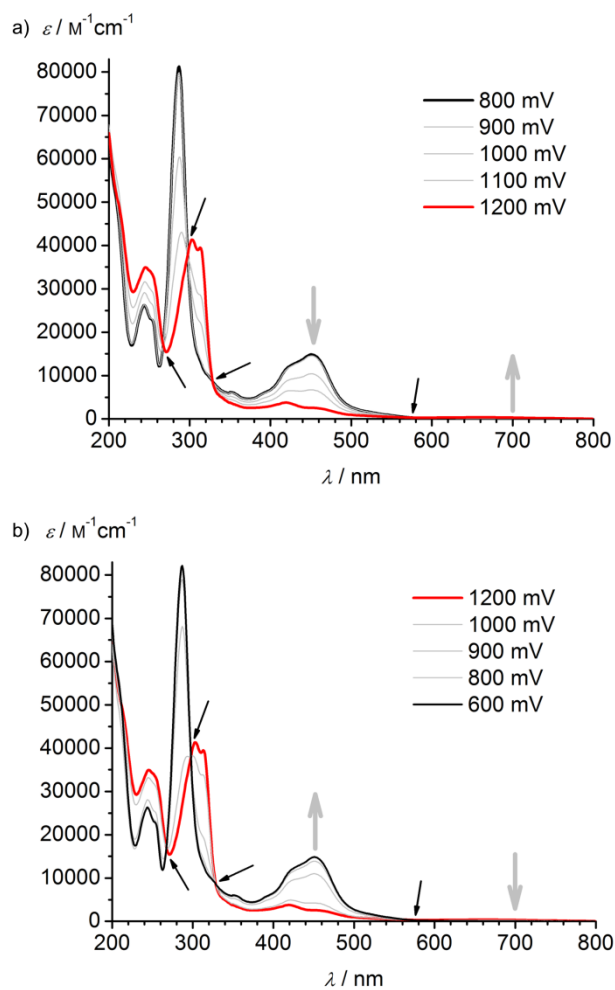


Figure S11. UV/Vis spectra of a) the electrochemical oxidation ($E = 800 \rightarrow 1200 \text{ mV}$) and b) back reduction ($E = 1200 \rightarrow 600 \text{ mV}$) of $[\text{Ru}(\text{bpy})_3](\text{PF}_6)_2$ in an OTTLE cell in 10^{-3} M NaOH and $0.1 \text{ M } [n\text{-Bu}_4\text{N}](\text{PF}_6)$ in $\text{CH}_3\text{CN}:\text{H}_2\text{O}$ (98:2, v%). Black arrows indicate isosbestic points.

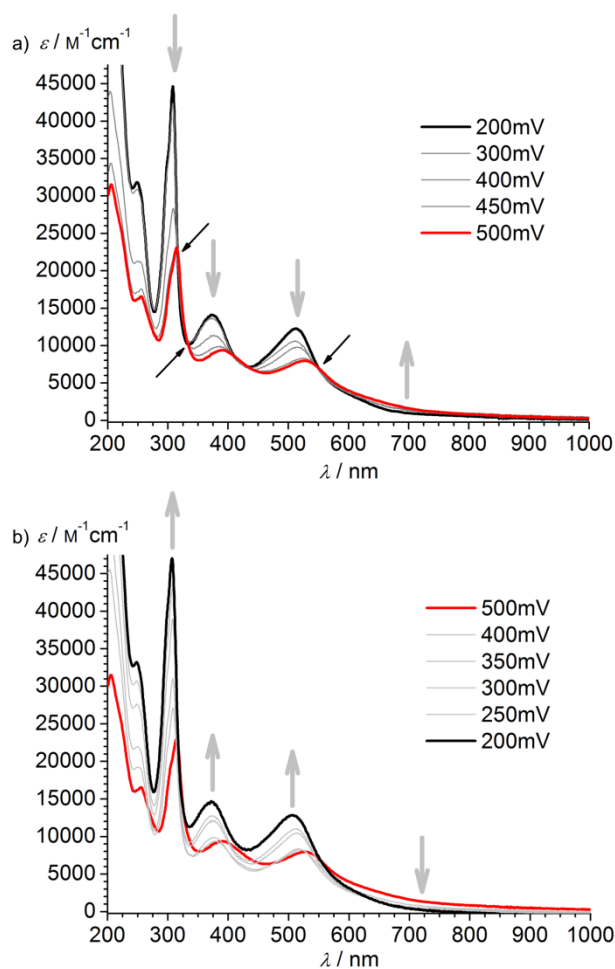


Figure S12. UV/Vis spectra of a) the electrochemical oxidation ($E = 200 \rightarrow 500 \text{ mV}$) and b) back reduction ($E = 500 \rightarrow 200 \text{ mV}$) of N719 in an OTTLE cell in 10^{-3} M NaOH and $0.1 \text{ M } [n\text{-Bu}_4\text{N}](\text{PF}_6)$ in $\text{CH}_3\text{CN}:\text{H}_2\text{O}$ (98:2, v%). Black arrows indicate isosbestic points.

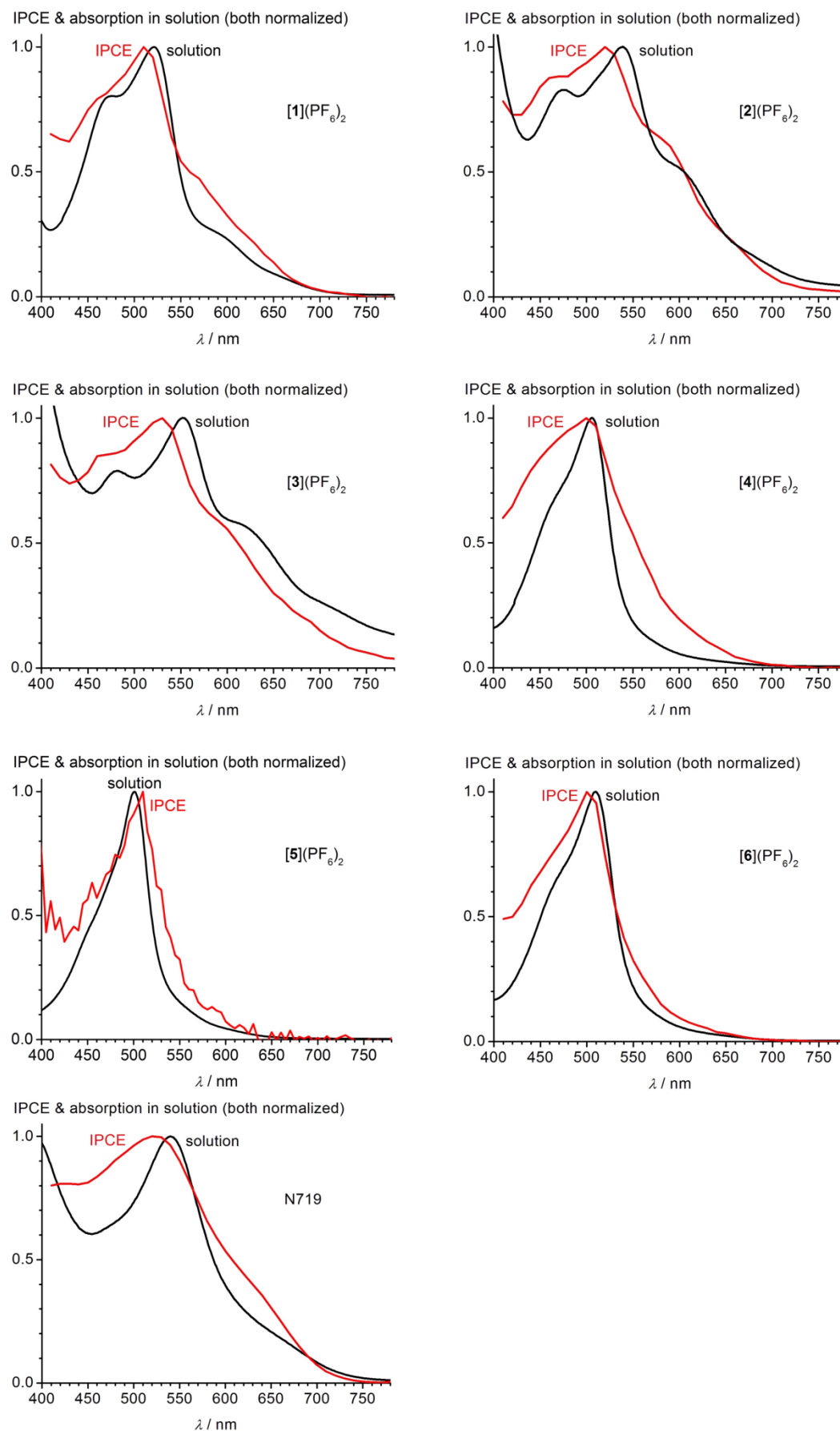


Figure S13. IPCE plots of cells with [1](PF₆)₂ – [6](PF₆)₂ and N719 and solution absorption spectra of the respective complexes in CH₃CN:BuOH (1:1).

11 Summary and Outlook

Polypyridine complexes of ruthenium(II) have unique and tunable electrochemical and photophysical properties such as high redox stability, visible light absorption, room temperature emission in fluid solution combined with high thermal and chemical robustness.^[1] They are applied in a plethora of applications, e.g. dye-sensitized solar cells (DSSC),^[2–4] light-emitting devices,^[5–8] photodynamic therapy^[9–11] and as photocatalysts for water splitting,^[34,35] hydrogen production,^[36–40] CO₂ reduction^[38–40] and organic redox reactions.^[39,41–45] One of the most famous ruthenium(II) polypyridine complexes is [Ru(bpy)₃]²⁺ (bpy = 2,2'-bipyridine). Excitation of [Ru(bpy)₃]²⁺ with visible light leads to instantaneous population of the ¹MLCT state followed by quantitative ISC to the ³MLCT state (Figure 29a, MLCT = metal-to-ligand charge transfer, ISC = intersystem crossing).^[1] At room temperature the ³MLCT state is emissive with a long lifetime of $\tau_{\text{RT}} \approx 1 \mu\text{s}$ and a high luminescence quantum yield of $\Phi_{\text{RT}} \approx 10\%$ which explains the use of [Ru(bpy)₃]²⁺ as photoredox catalyst and as emitter in light-emitting devices.^[47] The properties of [Ru(bpy)₃]²⁺ can be fine tuned via ligand design. However, the intrinsic Δ , Λ chirality of tris(bidentate) [Ru(bpy)₃]²⁺ leads to stereoisomers when the bpy ligands are substituted unsymmetrically which heavily complicates synthetic procedures.^[48–50] In contrast, bis(tridentate) [Ru(tpy)₂]²⁺ (**1**)²⁺, Figure 30) is achiral, even in the case of unsymmetrical substitution of the tpy 4'-positions (tpy = 2,2';6',2''-terpyridine).^[47] Furthermore, the stronger chelate effect is favorable in terms of chemical, photo and redox stability.^[52,53,78] Unfortunately, [Ru(tpy)₂]²⁺ features poor excited state properties ($\tau_{\text{RT}} \approx 0.1 - 0.2 \text{ ns}$, $\Phi_{\text{RT}} \leq 0.0007\%$) due to effective radiationless deactivation of the ³MLCT state via thermally accessible ³MC states (Figure 29b, MC = metal-centered).^[54–56]

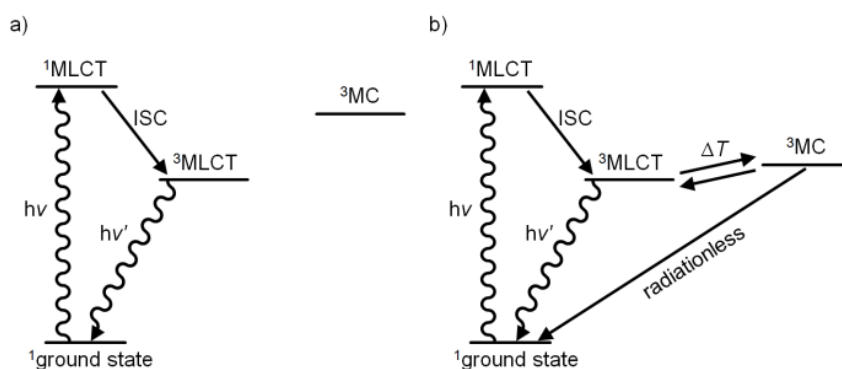


Figure 29. Qualitative Jablonski diagrams of a) [Ru(bpy)₃]²⁺ and b) [Ru(tpy)₂]²⁺ (MLCT = metal-to-ligand charge transfer, ISC = intersystem crossing, MC = metal-centered, bpy = 2,2'-bipyridine, tpy = 2,2';6',2''-terpyridine).

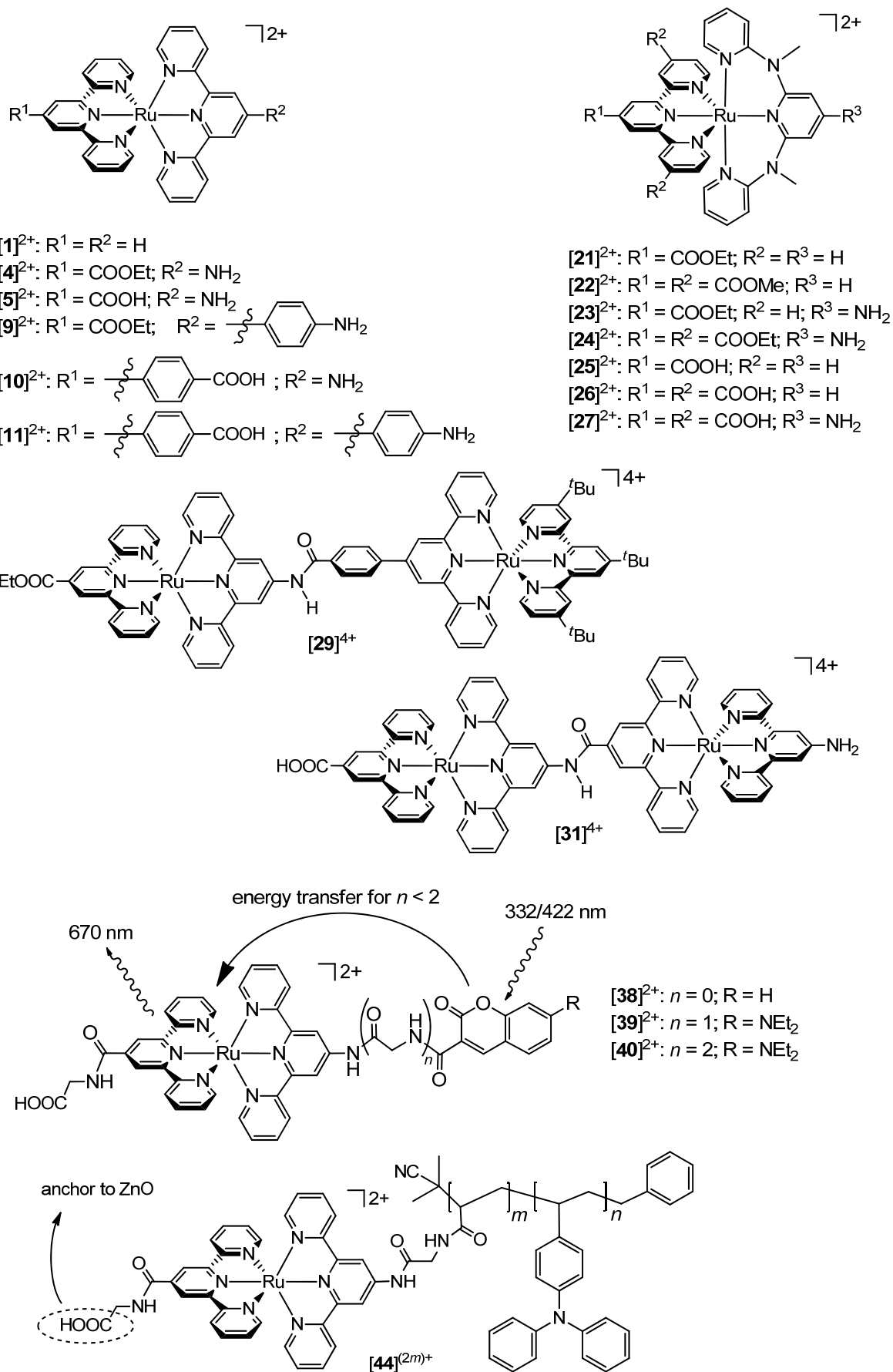


Figure 30. Bis(tridentate) polypyridine complexes of ruthenium(II) and their amide conjugates.

Amino acid ester $[4]^{2+}$ features substituents at the 4'-position of both tpy ligands (Figure 30). The electron-withdrawing COOEt group lowers the energy of the $^3\text{MLCT}$ state while the electron-donating NH_2 group shifts the ^3MC state to higher energy resulting in improved excited state properties ($\tau_{\text{RT}} \approx 34$ ns, $\Phi_{\text{RT}} = 0.27\%$).^[61] $[4]^{2+}$ can be hydrolyzed to the carboxylic acid $[5]^{2+}$ (Figure 30) enabling selective functionalization either at the C- or at the N-terminus. The formal addition of *para*-phenylene spacers to $[4]^{2+}/[5]^{2+}$ results in complexes $[9 - 11]^{2+}$ (Figure 30).^[62] $[9 - 11]^{2+}$ feature enhanced extinction coefficients compared to the respective *para*-phenylene-free complex ($[4]^{2+}/[5]^{2+}$). However, the ring planes of the phenylene ring and the central pyridyl ring of a tpy ligand are twisted which dilutes the effect of donor and acceptor substituents. Hence, $^3\text{MLCT}$ lifetimes and phosphorescence quantum yields of $[9 - 11]^{2+}$ are smaller compared to the *para*-phenylene-free analogues $[4]^{2+}$ and $[5]^{2+}$.

The N-Ru-N ligand bite angles of bis(terpyridine) complexes of ruthenium(II) are typically around 79° . Enlargement of the bite angles to 90° creates a stronger ligand field splitting due to the higher overlap between Ru d orbitals and pyridine nitrogen lone pairs. A stronger ligand field increases the ^3MC – $^3\text{MLCT}$ energy difference making ^3MC states less accessible.^[56] However, ligands with large bite angles can form stereoisomers (*mer*, *cis-fac*, *trans-fac*).^[85]

In this work, complexes $[21]^{2+}$ and $[22]^{2+}$ (Figure 30) have been synthesized and characterized. In these complexes the problem of stereoisomers is overcome by the use of a tpy acceptor ligand in combination with a ddpd donor ligand (ddpd = *N,N'*-dimethyl-*N,N'*-dipyridin-2-ylpyridine-2,6-diamine) because the tpy ligand only allows for the *meridional* coordination. The ddpd ligand features N-Ru-N bite angles of 88° . The donor-acceptor substitution in $[21]^{2+}$ and $[22]^{2+}$ leads to small HOMO–LUMO gaps and spatially separated frontier orbitals which is favorable for low-energy absorption and the use as photosensitizers in dye-sensitized solar cells. The high $^3\text{MLCT}$ lifetimes and phosphorescence quantum yields of $[21]^{2+}$ ($\tau_{\text{RT}} = 722$ ns, $\Phi_{\text{RT}} = 0.45\%$) and $[22]^{2+}$ ($\tau_{\text{RT}} = 841$ ns, $\Phi_{\text{RT}} = 1.1\%$) confirm the effectiveness of the bite angle enlargement strategy.^[57] $[23]^{2+}$ and $[24]^{2+}$ (Figure 30) feature additional NH_2 groups at the 4'-position of the ddpd ligand. The donor-acceptor substitution is even more pronounced inducing smaller HOMO–LUMO gaps compared to the NH_2 -free analogues $[21]^{2+}$ and $[22]^{2+}$. However, $^3\text{MLCT}$ lifetimes and phosphorescence quantum yields of $[23]^{2+}$ ($\tau_{\text{RT}} = 149$ ns, $\Phi_{\text{RT}} = 0.042\%$) and $[24]^{2+}$ ($\tau_{\text{RT}} = 136$ ns, $\Phi_{\text{RT}} = 0.052\%$) are smaller compared to the NH_2 -free analogues.^[57] There are two reasons for this: The small HOMO-LUMO gap induces fast radiationless deactivation of the $^3\text{MLCT}$ state due to the energy gap law.^[73,87,88] Secondly, the presence of high-energy oscillators (N–H) provides an additional path for radiationless deactivation to the ground state. Deuteration ($\text{NH}_2 \rightarrow \text{ND}_2$) removes this effect and enhances the quantum yields by a factor of about 2.^[57] Excited states of $[4]^{2+}$ and $[21 - 24]^{2+}$ were studied experimentally by transient absorption measurements revealing excited state dynamics with a lifetime in the ps regime which might be associated with localization of the electron on the tpy-COOEt ligand, ISC or vibrational relaxation within $^1/3\text{MLCT}$ states.^[57] Lifetime and transient absorption experiments

were measured in collaboration with the group of Dr. Frédéric Laquai together with Dr. Michael Meister. ^3MC , $^3\text{MLCT}$ and the connecting transition state ^3TS were calculated via DFT methods and nicely explain the trends of experimental $^3\text{MLCT}$ lifetimes of $[\mathbf{1}]^{2+}$, $[\mathbf{2}]^{2+}$, $[\mathbf{4}]^{2+}$ and $[\mathbf{21} - \mathbf{24}]^{2+}$ (DFT = density functional theory).^[57] In the future $[\mathbf{21}]^{2+}$ and $[\mathbf{22}]^{2+}$ will be used as sensitizers for photoredox catalysis.

$[\mathbf{4}]^{2+}$, $[\mathbf{21}]^{2+}$ and $[\mathbf{22}]^{2+}$ have been used and characterized as emitters in light-emitting electrochemical cells with an ITO/PEDOT:PSS/ruthenium(II) complex/Ag device structure in a collaboration with the groups of Prof. Dr. Kookheon Char, Prof. Dr. Changhee Lee and Prof. Dr. Angelika Kühnle together with Myeongjin Park, Dongu Lee and Stefanie Klassen. Deep red light emission up to a maximum emission wavelength of 755 nm is achieved when an external voltage is applied. The small external quantum efficiencies (EQE) of $\leq 0.03\%$ is rationalized by radiationless deactivation predicted by the energy gap law and by saturation and quenching effects in the emitting layer. The EQE increases by admixture of PMMA to the emitting ruthenium complexes.^[107] Future work will be focused on the steric protection of the ruthenium core by bulky ligands to prevent self-quenching and the effect of counterion exchange.

Compared to $[\text{Ru}(\text{bpy})_3]^{2+}$ bis(tridentate) complexes $[\mathbf{4}]^{2+}$ and $[\mathbf{21}]^{2+}$ feature an enhanced photostability in the presence of H_2O and coordinating I^- ions which is favorable for applications in DSSCs.^[78] $[\mathbf{21}]^{2+}$, $[\mathbf{22}]^{2+}$ and $[\mathbf{24}]^{2+}$ can be hydrolyzed to their respective carboxylic acids in order to obtain $[\mathbf{25} - \mathbf{27}]^{2+}$ (Figure 30). $[\mathbf{5}]^{2+}$, derivatives of $[\mathbf{5}]^{2+}$ featuring 2,2'-bipyridine anchor substituents (kindly donated by Jan Dietrich, AK Heinze) and $[\mathbf{25} - \mathbf{27}]^{2+}$ have been incorporated as sensitizers in dye-sensitized solar cells with an I^-/I_3^- redox electrolyte. DSSC fabrication and characterization were conducted in collaborations with the groups of Prof. Dr. Kookheon Char and Prof. Dr. Yong Soo Kang together with Dr. Sanghyuk Wooh and Tea Yon Kim. The COOH and 2,2'-bipyridine groups serve as anchor to the nanoporous TiO_2 electrode. The incident photon-to-current efficiency (IPCE) follows the solution absorption spectrum of the complexes. Power conversion efficiencies of the cells remain low ($\eta_{\text{max}} = 0.26\%$). This is ascribed to the twofold positive charge of the complexes which increases the I_3^- concentration near the TiO_2 electrode favoring electron recombination. This was shown by dark current measurements and electron recombination lifetime measurements. A twofold negatively charged ruthenium(II) complex (N719) was used as reference and reaches a power conversion efficiency of $\eta = 5.03\%$ under the same conditions.^[78] Future perspectives include the reduction of the overall complex charge by negatively charged, cyclometalated, tridentate ligands. Triarylamine substituted ligands will be employed in order to further redshift the absorption spectrum and to enhance extinction coefficients. In addition, other redox electrolytes such as polypyridine complexes of $\text{Co}^{2+/3+}$ will be used in order to suppress electron recombination.

Dinuclear complexes $[\mathbf{29}]^{4+}$ and $[\mathbf{31}]^{4+}$ (Figure 30), kindly donated by Dr. Klaus Hempel (AK Heinze), have been synthesized from mononuclear complexes by standard solution peptide chemistry methods. The mixed valence behavior of the one-electron oxidized forms $[\mathbf{29}]^{5+}$ and $[\mathbf{31}]^{5+}$ has been studied.

Electrochemical and UV/Vis/NIR spectroscopic measurements reveal that $[29]^{5+}$ and $[31]^{5+}$ are valence localized showing no metal-metal interaction (Robin-Day-Class I^[94]). In both complexes, $[29]^{5+}$ and $[31]^{5+}$, the ruthenium center with the donor-substituted tpy ligand (^tBu- or NH₂-substituents) is oxidized to ruthenium(III) while the other ruthenium(II) center remains unaffected.^[26] This redox asymmetry vanishes when the substituents are adjusted and results will be reported in due course by Christoph Kreitner (AK Heinze).^[160]

Peptidic arrays such as $[38]^{2+}$, $[39]^{2+}$ and $[40]^{2+}$ (Figure 30) including amino acid $[5]^{2+}$ are also available via solid-phase peptide synthesis (SPPS). The bis(tpy) ruthenium(II) core of $[5]^{2+}$ is connected to coumarin chromophores via amide bridges consisting of a different number ($n = 0 - 2$) of glycine units.^[18,20] For short amide bridges with $n = 0$ ($[38]^{2+}$) and $n = 1$ ($[39]^{2+}$; both kindly donated by Dr. Klaus Hempel, AK Heinze) excitation of the coumarin chromophore leads to efficient energy transfer from the coumarin to the bis(tpy) ruthenium chromophore. This is evident from the phosphorescence of the ruthenium chromophore and the quenching of the coumarin fluorescence.^[18] For longer bridges ($n = 2$; $[40]^{2+}$; prepared in this work) energy transfer is hampered which is evident from the intense fluorescence of the coumarin chromophore while no emission from the ruthenium chromophore is detected when the coumarin is excited.^[20] Future applications deal with more sophisticated energy transfer systems featuring multichromophore systems for dye-sensitized solar cells and light-to-chemical energy conversion systems with 0 – 1 amino acids between the energy donor and the acceptor.

Amino acid $[5]^{2+}$ has been used as chromophore in light-induced charge separation in a donor-chromophore-acceptor nanocomposite in a collaboration with the groups of Prof. Dr. Rudolf Zentel and Dr. Rüdiger Berger together with Dr. Lisa zur Borg, Mareike Bürger and Anna Domanski. A TPA-containing block-copolymer acts as electron donor and ZnO nanorods as electron acceptor (TPA = triphenylamine). In this work $[5]^{2+}$ is functionalized by SPPS and connected to the TPA-containing block-copolymer (provided by Prof. Dr. Rudolf Zentel together with Dr. Lisa zur Borg) to obtain $[44]^{(2m)+}$ (Figure 30). The COOH groups serve as anchors to the ZnO nanorods. In $[44]^{(2m)+}@ZnO$ the phosphorescence of the ruthenium(II) chromophore is completely quenched. Irradiation into the absorption band of the ruthenium(II) chromophore leads to electron injection into the ZnO nanorods. The electron holes are transferred to the TPA units of the block-copolymer. The positive charge of the polymer is detected by Kelvin probe force microscopy measured by the group of Dr. Rüdiger Berger together with Anna Domanski.^[100] In the future sophisticated nanoscale charge separation systems will be used in solid state dye-sensitized solar cells.

The ruthenium(II) complex $[5]^{2+}$ can be oxidized in acidic media by Ce^{IV} leading to the ruthenium(III) complex $[5]^{3+}$. $[5]^{3+}$ features a LMCT band around 730 nm. EPR spectra and DFT calculations reveal a ruthenium-centered oxidation with smaller contributions from the NH₂ nitrogen atom. After oxidation of $[5]^{2+}$ to $[5]^{3+}$ in acidic media, the ruthenium(III) complex undergoes slow spontaneous back reduction to $[5]^{2+}$ without addition of a reducing agent which is shown by mass spectrometry, UV/Vis

and NMR spectroscopy. The rate of back reduction is enhanced in the presence of light. However, the responsible reducing agent is yet unidentified. The oxidation of H₂O to O₂ was ruled out by oxygen measurements using different methods. It is assumed that upon degradation a small fraction of [5]³⁺ undergoes irreversible side reactions which provide enough electrons for the reduction of the majority ($\approx 91 \pm 3\%$) of [5]³⁺ to [5]²⁺. DFT calculations indicate that chelate decoordination and protonation of an outer pyridine ring of the tpy ligand in [5]³⁺ in concert with the attack of water to the ruthenium atom might be responsible for irreversible side reactions such as ligand loss and oxidative ligand decomposition e.g. to CO₂. Further investigations are necessary to clarify the mechanism of the back reduction.^[74]

12 List of Publications

A. Breivogel, K. Heinze, **2014**, to be submitted. Thermal and Photo Reactivity of a Donor-Acceptor-Substituted Bis(terpyridine) Ruthenium(III) Complex in Acidic Solutions.

A. Breivogel, C. Kreitner, K. Heinze, *Eur. J. Inorg. Chem.* **2014**, accepted. Redox and Photochemistry of Bis(terpyridine)ruthenium(II) Amino Acids and their Amide Conjugates – from Understanding to Applications.

A. Breivogel, S. Wooh, J. Dietrich, T. Y. Kim, Y. S. Kang, K. Char, K. Heinze, *Eur. J. Inorg. Chem.* **2014**, 2720–2734. Anchor-Functionalized Push-Pull-Substituted Bis(tridentate) Ruthenium(II) Polypyridine Chromophores: Photostability and Evaluation as Photosensitizers. DOI: 10.1002/ejic.201402091.

A. Breivogel, M. Park, D. Lee, S. Klassen, A. Kühnle, C. Lee, K. Char, K. Heinze, *Eur. J. Inorg. Chem.* **2014**, 288–295. Push-Pull Design of Bis(tridentate) Ruthenium(II) Polypyridine Chromophores as Deep Red Light Emitters in Light-Emitting Electrochemical Cells. DOI: 10.1002/ejic.201301226.

A. Breivogel, M. Meister, C. Förster, F. Laquai, K. Heinze, *Chem. Eur. J.* **2013**, *19*, 13745–13760. Excited State Tuning of Bis(tridentate) Ruthenium(II) Polypyridine Chromophores by Push-Pull Effects and Bite Angle Optimization: A Comprehensive Experimental and Theoretical Study. DOI: 10.1002/chem.201302231.

L. zur Borg, A. L. Domanski, A. Breivogel, M. Bürger, R. Berger, K. Heinze, R. Zentel, *J. Mater. Chem. C* **2013**, *1*, 1223–1230. Light-induced Charge Separation in a Donor-Chromophore-Acceptor Nanocomposite Poly[TPA-Ru(tpy)₂]₂@ZnO. DOI: 10.1039/c2tc00535b.

A. Breivogel, K. Hempel, K. Heinze, *Inorg. Chim. Acta* **2011**, *374*, 152–162. Dinuclear Bis(terpyridine)ruthenium(II) Complexes by Amide Coupling of Ruthenium Amino Acids: Synthesis and Properties. DOI: 10.1016/j.ica.2011.03.046.

A. Breivogel, C. Förster, K. Heinze, *Inorg. Chem.* **2010**, *49*, 7052–7056. A Heteroleptic Bis(tridentate)ruthenium(II) Polypyridine Complex with Improved Photophysical Properties and Integrated Functionalizability. DOI: 10.1021/ic1007236.

K. Heinze, K. Hempel, A. Breivogel, *Z. Anorg. Allg. Chem.* **2009**, *635*, 2541–2549. Synthesis and Characterization of Extended Bis(terpyridine)ruthenium Amino Acids. DOI: 10.1002/zaac.200900303.

13 Oral and Poster Presentations

- 03.2014 Poster *Novel Iron(II) Complexes – A Way to 3d Metal Complex Chromophores* at the Koordinationschemiker-Treffen in Kaiserslautern
- 08.2013 Oral presentation *Ruthenium Complexes for Applications in Solar Cells and Light-Emitting Devices* at Laytec in Berlin
- 03.2013 Oral presentation *Ruthenium Complexes for Applications in Solar Cells and Light-Emitting Devices* at the Seoul National University in Seoul (South Korea)
- 02.2013 Poster *New Ruthenium Chromophores for Solar Cells and Light-Emitting Devices* at the IRTG conference in Seoul (South Korea)
- 09.2012 Oral presentation *Molecular Ruthenium Chromophores* at the Seoul National University in Seoul (South Korea)
- 02.2012 Poster *Light-Induced Charge Separation in a ZnO-Bis(terpyridine)ruthenium-TPA Polymer Composite* at the Koordinationschemiker-Treffen in Dortmund
- 11.2011 Poster *Light-Induced Charge Separation in a ZnO-Bis(terpyridine)ruthenium-TPA Polymer Composite* at the pacific polymer conference in Jeju (South Korea)
- 07.2011 Oral presentation *Novel Ruthenium Chromophores with Optimized Properties* in the Max-Planck-Institut für Polymerforschung in Mainz
- 06.2011 Oral presentation *Novel Ruthenium Chromophores with Optimized Properties* at the IRTG conference in Mainz
- 01.2011 Poster *New Ruthenium Chromophores with Optimized Properties* at the IRTG conference in Seoul (South Korea)
- 02.2010 Poster *Neue Rutheniumchromophore mit maßgeschneiderten Eigenschaften* at the Koordinationschemiker-Treffen in Mainz
- 02.2009 Oral presentation *Solid-Phase Synthesis of Peptide Libraries Combining α -Amino Acids with Inorganic and Organic Chromophores* at the Koordinationschemiker-Treffen in Erlangen

14 Acknowledgment/Dank

Ich danke....

...besonders Prof. Dr. Katja Heinze für die Promotionsstelle in ihrem Arbeitskreis, die spannenden Themen und für die exzellente wissenschaftliche Betreuung.

...Prof. Dr. Kookheon Char für die 6-monatige, freundliche Aufnahme in seinem Arbeitskreis in der Seoul National University in Seoul.

...meinen Kooperationspartnern Prof. Dr. Kookheon Char, Prof. Dr. Rudolf Zentel, Prof. Dr. Changhee Lee, Prof. Dr. Angelika Kühnle, Prof. Dr. Yong Soo Kang, Dr. Christoph Förster, Dr. Frédéric Laquai, Dr. Rüdiger Berger, Dr. Michael Meister, Dr. Sanghyuk Wooh, Dr. Klaus Hempel, Dr. Lisa zur Borg, Mareike Bürger, Anna Domanski, Jan Dietrich, Stefanie Klassen, Christoph Kreitner, Myeongjin Park, Dongu Lee und Tea Yon Kim für die erfolgreiche und interessante Zusammenarbeit.

...dem gesamten Arbeitskreis Heinze für die gegenseitige Unterstützung, die Diskussionen und die gute Stimmung im Labor ("immer cool keepen").

...meinen Arbeitskollegen Jascha Melomedov (Stichwort: Käsebroten) und Kristina Hüttinger (Ey, was guckst du?) für die Freundschaft und die gemeinsamen Freizeitaktivitäten.

...dem "IRTG 1404 - Self Organized Materials for Optoelectronics" von der Deutschen Forschungsgemeinschaft für die Finanzierung und die einzigartigen Auslandserfahrungen.

...Dr. Christoph Förster für das Lösen der Kristallstrukturen.

...Dr. Mihail Mondeshki für die großartige Unterstützung bei den NMR-Experimenten.

...Dr. Norbert Hanold und Petra Auerbach für das Messen der Massenspektren.

...dem Mikroanalytischen Labor des Institutes für Organische Chemie.

...meinen Forschungspraktikanten Julia Beer, Stefan Jaschonek, Kathrin Koch, Pia Glawion, Tanja Becker, Philip Spang, Matthias Worm, Johanna Götzinger und Mareike Bürger.

...Dr. Lisa zur Borg und Dr. Philipp Schattling für die Hilfe beim Sprung in die koreanische Kultur.

...meinen Eltern dafür, dass sie immer zu mir halten und sowieso für alles.

...meiner Oma für die große Fürsorge.

...meiner Schwester Rabea für den geschwisterlichen Zusammenhalt.

...meiner Freundin Denise für all die schönen Momente.

15 Literature

- [1] S. Campagna, F. Puntoriero, F. Nastasi, G. Bergamini, V. Balzani, *Top. Curr. Chem.* **2007**, *280*, 117–214.
- [2] B. O'Regan, M. Grätzel, *Nature* **1991**, *353*, 737–740.
- [3] J.-F. Yin, M. Velayudham, D. Bhattacharya, H.-C. Lin, K.-L. Lu, *Coord. Chem. Rev.* **2012**, *256*, 3008–3035.
- [4] P. G. Bomben, K. C. D. Robson, B. D. Koivisto, C. P. Berlinguette, *Coord. Chem. Rev.* **2012**, *256*, 1438–1450.
- [5] R. D. Costa, E. Ortí, H. J. Bolink, F. Monti, G. Accorsi, N. Armaroli, *Angew. Chem.* **2012**, *124*, 8300–8334; *Angew. Chem. Int. Ed.* **2012**, *51*, 8178–8211.
- [6] P. Dreyse, B. Loeb, M. Soto-Arriaza, D. Tordera, E. Ortí, J. J. Serrano-Pérez, H. J. Bolink, *Dalton Trans.* **2013**, *42*, 15502–15513.
- [7] H. J. Bolink, E. Coronado, R. D. Costa, P. Gaviña, E. Ortí, S. Tatay, *Inorg. Chem.* **2009**, *48*, 3907–3909.
- [8] H. J. Bolink, L. Cappelli, E. Coronado, P. Gaviña, *Inorg. Chem.* **2005**, *44*, 5966–5968.
- [9] L. Marcélis, J. Ghesquière, K. Garnir, A. K.-D. Mesmaeker, C. Moucheron, *Coord. Chem. Rev.* **2012**, *256*, 1569–1582.
- [10] M. R. Gill, J. A. Thomas, *Chem. Soc. Rev.* **2012**, *41*, 3179–3192.
- [11] H. Komatsu, K. Yoshihara, H. Yamada, Y. Kimura, A. Son, S.-i. Nishimoto, K. Tanabe, *Chem. Eur. J.* **2013**, *19*, 1971–1977.
- [12] D. Maity, C. Bhaumik, D. Mondal, S. Baitalik, *Dalton Trans.* **2014**, *43*, 1829–1845.
- [13] Z.-B. Zheng, Z.-M. Duan, Y.-Y. Ma, K.-Z. Wang, *Inorg. Chem.* **2013**, *52*, 2306–2316.
- [14] M. Li, Q. Liang, M. Zheng, C. Fang, S. Peng, M. Zhao, *Dalton Trans.* **2013**, *42*, 13509–13515.
- [15] S. A. Poteet, F. M. MacDonnell, *Dalton Trans.* **2013**, *42*, 13305–13307.
- [16] H. Chen, X. Li, Y. Wu, W. Gao, R. Bai, *Dalton Trans.* **2012**, *41*, 13292–13297.
- [17] R. Zhang, Z. Ye, G. Wang, W. Zhang, J. Yuan, *Chem. Eur. J.* **2010**, *16*, 6884–6891.
- [18] K. Heinze, K. Hempel, *Chem. Eur. J.* **2009**, *15*, 1346–1358.
- [19] R. Horvath, J. Lombard, J.-C. Leprêtre, M.-N. Collomb, A. Deronizer, J. Chauvin, K. C. Gordon, *Dalton Trans.* **2013**, *42*, 16527–16537.
- [20] A. Breivogel, C. Kreitner, K. Heinze, *Eur. J. Inorg. Chem.* **2014**, accepted.
- [21] S. Roeser, M. Z. Ertem, C. Cady, R. Lomoth, J. Benet-Buchholz, L. Hammarström, B. Sarkar, W. Kaim, C. J. Cramer, A. Llobet, *Inorg. Chem.* **2012**, *51*, 320–327.
- [22] L.-Z. Sui, W.-W. Yang, C.-J. Yao, H.-Y. Xie, Y.-W. Zhong, *Inorg. Chem.* **2012**, *51*, 1590–1598.
- [23] O. S. Wenger, *Chem. Soc. Rev.* **2012**, *41*, 3772–3779.
- [24] H.-J. Nie, X. Chen, C.-J. Yao, Y.-W. Zhong, G. R. Hutchison, J. Yao, *Chem. Eur. J.* **2012**, *18*, 14497–14509.
- [25] C.-J. Yao, Y.-W. Zhong, J. Yao, *Inorg. Chem.* **2013**, *52*, 4040–4045.
- [26] A. Breivogel, K. Hempel, K. Heinze, *Inorg. Chim. Acta* **2011**, *374*, 152–162.
- [27] P. Ceroni, *Chem. Eur. J.* **2011**, *17*, 9560–9564.

- [28] T. N. Singh-Rachford, F. N. Castellano, *Coord. Chem. Rev.* **2010**, *254*, 2560–2573.
- [29] W. Wu, S. Ji, W. Wu, J. Shao, H. Guo, T. D. James, J. Zhao, *Chem. Eur. J.* **2012**, *18*, 4953–4964.
- [30] P. Hanczyc, B. Norden, M. Samoc, *Dalton Trans.* **2012**, *41*, 3123–3125.
- [31] P. Ceroni, G. Bergamini, V. Balzani, *Angew. Chem.* **2009**, *121*, 8668–8670; *Angew. Chem. Int. Ed.* **2009**, *48*, 8516–8518.
- [32] J. Lee, H. Chang, S. Kim, G. S. Bang, H. Lee, *Angew. Chem.* **2009**, *121*, 8653–8656; *Angew. Chem. Int. Ed.* **2009**, *48*, 8501–8504.
- [33] K. Terada, K. Kanaizuka, V. M. Iyer, M. Sannodo, S. Saito, K. Kobayashi, M.-a. Haga, *Angew. Chem.* **2011**, *123*, 6411–6415; *Angew. Chem. Int. Ed.* **2011**, *50*, 6287–6291.
- [34] R. H. Crabtree *Energy Production and Storage: Inorganic Chemical Strategies for a Warming World*; Wiley-VCH: Weinheim, Germany, **2010**.
- [35] X. Liu, F. Wang, *Coord. Chem. Rev.* **2012**, *256*, 1115–1136.
- [36] W. T. Eckenhoff, R. Eisenberg, *Dalton Trans.* **2012**, *41*, 13004–13021.
- [37] T. Stoll, M. Gennari, I. Serrano, J. Fortage, J. Chauvin, F. Odobel, M. Rebarz, O. Poizat, M. Sliwa, A. Deronizer, M.-N. Collomb, *Chem. Eur. J.* **2013**, *19*, 782–792.
- [38] M. Schulz, M. Karnahl, M. Schwalbe, J. G. Vos, *Coord. Chem. Rev.* **2012**, *256*, 1682–1705.
- [39] A. Inagaki, M. Akita, *Coord. Chem. Rev.* **2010**, *254*, 1220–1239.
- [40] Z. Chen, P. Kang, M.-T. Zhang, T. J. Meyer, *Chem. Commun.* **2014**, *50*, 335–337.
- [41] S. Ohzu, T. Ishizuka, Y. Hirai, S. Fukuzumi, T. Kojima, *Chem. Eur. J.* **2013**, *19*, 1563–1567.
- [42] H. Nitadori, T. Takahashi, A. Inagaki, M. Akita, *Inorg. Chem.* **2012**, *51*, 51–62.
- [43] P. Guillo, O. Hamelin, P. Batat, G. Jonusauskas, N. D. McClenaghan, S. Ménage, *Inorg. Chem.* **2012**, *51*, 2222–2230.
- [44] F. Li, M. Yu, Y. Jiang, F. Huang, Y. Li, B. Zhang, L. Sun, *Chem. Commun.* **2011**, *47*, 8949–8951.
- [45] D. Chao, W.-F. Fu, *Dalton Trans.* **2014**, *43*, 306–310.
- [46] C. K. Prier, D. A. Rankic, D. W. C. MacMillan, *Chem. Rev.* **2013**, *113*, 5322–5363.
- [47] A. Juris, V. Balzani, F. Barigelletti, S. Campagna, P. Belser, A. von Zelewsky, *Coord. Chem. Rev.* **1988**, *84*, 85–277.
- [48] A. Reynal, E. Palomares, *Eur. J. Inorg. Chem.* **2011**, 4509–4526.
- [49] C. Fu, M. Wenzel, E. Treutlein, K. Harms, E. Meggers, *Inorg. Chem.* **2012**, *51*, 10004–10011.
- [50] E. Meggers, *Chem. Eur. J.* **2010**, *16*, 752–758.
- [51] M. Maestri, N. Armaroli, V. Balzani, E. C. Constable, A. M. W. Cargill Thompson, *Inorg. Chem.* **1995**, *34*, 2759–2767.
- [52] R. Hogg, R. G. Wilkins, *J. Chem. Soc.* **1962**, 341–350.
- [53] R. H. Holyer, C. D. Hubbard, S. F. A. Kettle, R. G. Wilkins, *Inorg. Chem.* **1966**, *5*, 622–625.
- [54] J.-P. Sauvage, J.-P. Collin, J.-C. Chambron, S. Guillerez, C. Coudret, V. Balzani, F. Barigelletti, L. D. Cola, L. Flamigni, *Chem. Rev.* **1994**, *94*, 993–1019.
- [55] Y. Liu, R. Hammitt, D. A. Lutterman, R. P. Thummel, C. Turro, *Inorg. Chem.* **2007**, *46*, 6011–6021.
- [56] L. Hammarström, O. Johansson, *Coord. Chem. Rev.* **2010**, *254*, 2546–2559.

- [57] A. Breivogel, M. Meister, C. Förster, F. Laquai, K. Heinze, *Chem. Eur. J.* **2013**, *19*, 13745–13760.
- [58] K. Suzuki, A. Kobayashi, S. Kaneko, K. Takehira, T. Yoshihara, H. Ishida, Y. Shiina, S. Oishi, S. Tobita, *Phys. Chem. Chem. Phys.* **2009**, *11*, 9850–9860.
- [59] B. D. Koivisto, K. C. D. Robson, C. P. Berlinguette, *Inorg. Chem.* **2009**, *48*, 9644–9652.
- [60] V. Duprez, M. Biancardo, F. C. Krebs, *Sol. Energy Mater. Sol. Cells* **2007**, *91*, 230–237.
- [61] K. Heinze, K. Hempel, M. Beckmann, *Eur. J. Inorg. Chem.* **2006**, 2040–2050.
- [62] K. Heinze, K. Hempel, A. Breivogel, *Z. Anorg. Allg. Chem.* **2009**, *635*, 2541–2549.
- [63] K. Heinze, K. Hempel, S. Tschierlei, M. Schmitt, J. Popp, S. Rau, *Eur. J. Inorg. Chem.* **2009**, 3119–3126.
- [64] Y.-Q. Fang, N. J. Taylor, G. S. Hanan, F. Loiseau, R. Passalacqua, S. Campagna, H. Nierengarten, A. V. Dorsselaer, *J. Am. Chem. Soc.* **2002**, *124*, 7912–7913.
- [65] Y.-Q. Fang, N. J. Taylor, F. Laverdière, G. S. Hanan, F. Loiseau, F. Nastasi, S. Campagna, H. Nierengarten, E. Leize-Wagner, A. V. Dorsselaer, *Inorg. Chem.* **2007**, *46*, 2854–2863.
- [66] A. Harriman, M. Hissler, A. Khatyr, R. Ziessel, *Chem. Commun.* **1999**, *8*, 735–736.
- [67] M. Hissler, A. Harriman, A. Khatyr, R. Ziessel, *Chem. Eur. J.* **1999**, *5*, 3366–3381.
- [68] A. C. Benniston, A. Harriman, D. J. Lawrie, A. Mayeux, *Phys. Chem. Chem. Phys.* **2004**, *6*, 51–57.
- [69] D. G. Brown, N. Sanguantrakun, B. Schulze, U. S. Schubert, C. P. Berlinguette, *J. Am. Chem. Soc.* **2012**, *134*, 12354–12357.
- [70] M. Abrahamsson, M. Jäger, T. Österman, L. Eriksson, P. Persson, H.-C. Becker, O. Johansson, L. Hammarström, *J. Am. Chem. Soc.* **2006**, *128*, 12616–12617.
- [71] M. Abrahamsson, M. Jäger, R. J. Kumar, T. Österman, P. Persson, H.-C. Becker, O. Johansson, L. Hammarström, *J. Am. Chem. Soc.* **2008**, *130*, 15533–15542.
- [72] F. Schramm, V. Meded, H. Fliegl, K. Fink, O. Fuhr, Z. Qu, W. Kloppe, S. Finn, T. E. Keyes, M. Ruben, *Inorg. Chem.* **2009**, *48*, 5677–5684.
- [73] J. V. Caspar, T. J. Meyer, *J. Am. Chem. Soc.* **1983**, *105*, 5583–5590.
- [74] A. Breivogel, K. Heinze, **2014**, to be submitted.
- [75] M. D. Kärkäs, T. Åkermark, H. Chen, J. Sun, B. Åkermark, *Angew. Chem.* **2013**, *125*, 4283–4287; *Angew. Chem. Int. Ed.* **2013**, *52*, 4189–4193.
- [76] N. G. Connelly, W. E. Geiger, *Chem. Rev.* **1996**, *96*, 877–910.
- [77] J. Dietrich, U. Thorenz, C. Förster, K. Heinze, *Inorg. Chem.* **2013**, *52*, 1248–1264.
- [78] A. Breivogel, S. Wooh, J. Dietrich, T. Y. Kim, Y. S. Kang, K. Char, K. Heinze, *Eur. J. Inorg. Chem.* **2014**, 2720–2734.
- [79] S. Ji, W. Wu, W. Wu, H. Guo, J. Zhao, *Angew. Chem.* **2011**, *123*, 1664–1667; *Angew. Chem. Int. Ed.* **2011**, *50*, 1626–1629.
- [80] J. Wang, G. S. Hanan, F. Loiseau, S. Campagna, *Chem. Commun.* **2004**, *18*, 2068–2069.
- [81] Y. Chi, P.-T. Chou, *Chem. Soc. Rev.* **2010**, *39*, 638–655.
- [82] V. Frieze, S. Nag, J. Wang, M.-P. Santoni, A. Rodrigue-Witchel, G. S. Hanan, F. Schaper, *Eur. J. Inorg. Chem.* **2011**, 39–44.
- [83] W. Ghattas, H. Müller-Bunz, M. Albrecht, *Organometallics* **2010**, *29*, 6782–6789.
- [84] G. A. Parada, L. A. Fredin, M.-P. Santoni, M. Jäger, R. Lomoth, L. Hammarström, O. Johansson, P. Persson, S. Ott, *Inorg. Chem.* **2013**, *52*, 5128–5137.

- [85] M. Jäger, R. J. Kumar, H. Görls, J. Bergquist, O. Johansson, *Inorg. Chem.* **2009**, *48*, 3228–3238.
- [86] A. Breivogel, C. Förster, K. Heinze, *Inorg. Chem.* **2010**, *49*, 7052–7056.
- [87] T. J. Meyer, *Pure Appl. Chem.* **1986**, *58*, 1193–1206.
- [88] J. V. Caspar, T. J. Meyer, *J. Phys. Chem.* **1983**, *87*, 952–957.
- [89] R. J. Watts, *J. Chem. Educ.* **1983**, *60*, 834–842.
- [90] B. Durham, J. V. Caspar, J. K. Nagle, T. J. Meyer, *J. Am. Chem. Soc.* **1982**, *104*, 4803–4810.
- [91] Z. J. Fuller, W. D. Bare, K. A. Kneas, W.-Y. Xu, J. N. Demas, B. A. DeGraff, *Anal. Chem.* **2003**, *75*, 2670–2677.
- [92] W. M. Wallace, P. E. Hoggard, *Inorg. Chem.* **1979**, *18*, 2934–2935.
- [93] T. E. Keyes, E. Gicquel, L. Guerin, R. J. Forster, V. Hultgren, A. M. Bond, A. G. Wedd, *Inorg. Chem.* **2003**, *42*, 7897–7905.
- [94] M. B. Robin, P. Day, *Adv. Inorg. Chem. Radiochem.* **1968**, *10*, 247–422.
- [95] E. Bayer, *Angew. Chem.* **1991**, *103*, 117–133; *Angew. Chem. Int. Ed. Engl.* **1991**, *30*, 113–129.
- [96] M. Grötli, C. H. Gotfredsen, J. Rademann, J. Buchardt, A. J. Clark, J. Ø. Duus, M. Meldal, *J. Comb. Chem.* **2000**, *2*, 108–119.
- [97] *Fmoc Solid Phase Peptide Synthesis* (Eds.: W. C. Chan, P. D. White), Oxford University Press, Oxford **2000**.
- [98] A. Barbieri, B. Ventura, R. Ziessel, *Coord. Chem. Rev.* **2012**, *256*, 1732–1741.
- [99] A. Barbieri, B. Ventura, F. Barigelletti, A. D. Nicola, M. Quesada, R. Ziessel, *Inorg. Chem.* **2004**, *43*, 7359–7368.
- [100] L. zur Borg, A. L. Domanski, A. Breivogel, M. Bürger, R. Berger, K. Heinze, R. Zentel, *J. Mater. Chem. C* **2013**, *1*, 1223–1230.
- [101] K. C. D. Robson, B. D. Koivisto, A. Yella, B. Sporinova, M. K. Nazeeruddin, T. Baumgartner, M. Grätzel, C. P. Berlinguette, *Inorg. Chem.* **2011**, *50*, 5494–5508.
- [102] C.-C. Chou, K.-L. Wu, Y. Chi, W.-P. Hu, S. J. Yu, G.-H. Lee, C.-L. Lin, P.-T. Chou, *Angew. Chem.* **2011**, *123*, 2102–2106; *Angew. Chem. Int. Ed.* **2011**, *50*, 2054–2058.
- [103] C.-C. Chou, F.-C. Hu, H.-H. Yeh, H.-P. Wu, Y. Chi, J. N. Clifford, E. Palomares, S.-H. Liu, P.-T. Chou, G.-H. Lee, *Angew. Chem.* **2014**, *126*, 182–187; *Angew. Chem. Int. Ed.* **2014**, *53*, 178–183.
- [104] S. Caramori, J. Husson, M. Beley, C. A. Bignozzi, R. Argazzi, P. C. Gros, *Chem. Eur. J.* **2010**, *16*, 2611–2618.
- [105] J. Dietrich, A. Wünsche von Leupoldt, M. Grabolle, U. Resch-Genger, K. Heinze, *Eur. J. Inorg. Chem.* **2013**, 3009–3019.
- [106] W. Y. Ng, X. Gong, W. K. Chan, *Chem. Mater.* **1999**, *11*, 1165–1170.
- [107] A. Breivogel, M. Park, D. Lee, S. Klassen, A. Kühnle, C. Lee, K. Char, K. Heinze, *Eur. J. Inorg. Chem.* **2014**, 288–295.
- [108] A. Abbotto, N. Manfredi, *Dalton Trans.* **2011** *40*, 12421–12438.
- [109] O. K. Varghese, C. A. Grimes, *Sol. Energy Mater. Sol. Cells* **2008**, *92*, 374–384.
- [110] M. K. Nazeeruddin, P. Péchy, T. Renouard, S. M. Zakeeruddin, R. Humphrey-Baker, P. Comte, P. Liska, L. Cevey, E. Costa, V. Shklover, L. Spiccia, G. B. Deacon, C. A. Bignozzi, M. Grätzel, *J. Am. Chem. Soc.* **2001**, *123*, 1613–1624.
- [111] M. K. Nazeeruddin, S. M. Zakeeruddin, R. Humphrey-Baker, M. Jirousek, P. Liska, N. Vlachopoulos, V. Shklover, C.-H. Fischer, M. Grätzel, *Inorg. Chem.* **1999**, *38*, 6298–6305.

- [112] M. K. Nazeeruddin, F. D. Angelis, S. Fantacci, A. Selloni, G. Viscardi, P. Liska, S. Ito, B. Takeru, M. Grätzel, *J. Am. Chem. Soc.* **2005**, *127*, 16835–16847.
- [113] S. Ghosh, G. K. Chaitanya, K. Bhanuprakash, M. K. Nazeeruddin, M. Grätzel, P. Y. Reddy, *Inorg. Chem.* **2006**, *45*, 7600–7611.
- [114] Y. Cao, Y. Bai, Q. Yu, Y. Cheng, S. Liu, D. Shi, F. Gao, P. Wang, *J. Phys. Chem. C* **2009**, *113*, 6290–6297.
- [115] T. P. Brewster, W. Ding, N. D. Schley, N. Hazari, V. S. Batista, R. H. Crabtree, *Inorg. Chem.* **2011**, *50*, 11938–11946.
- [116] S. Betanzos-Lara, L. Salassa, A. Habtemariam, O. Novakova, A. M. Pizarro, G. J. Clarkson, B. Liskova, V. Brabec, P. J. Sadler, *Organometallics* **2012**, *31*, 3466–3479.
- [117] S. Kämper, A. Paretzki, J. Fiedler, S. Zális, W. Kaim, *Inorg. Chem.* **2012**, *51*, 2097–2104.
- [118] G. Xue, Y. Guo, T. Yu, J. Guan, X. Yu, J. Zhang, J. Liu, Z. Zou, *Int. J. Electrochem. Sci.* **2012**, *7*, 1496–1511.
- [119] A. Bahreman, B. Limburg, M. A. Siegler, E. Bouwman, S. Bonnet, *Inorg. Chem.* **2013**, *52*, 9456–9469.
- [120] P. T. Nguyen, B. X. T. Lam, A. R. Andersen, P. E. Hansen, T. Lund, *Eur. J. Inorg. Chem.* **2011**, 2533–2539.
- [121] C. Dragonetti, A. Valore, A. Colombo, D. Roberto, V. Trifiletti, N. Manfredi, M. M. Salamone, R. Ruffo, A. Abboto, *J. Organomet. Chem.* **2012**, *714*, 88–93.
- [122] M. M. R. Choudhuri, R. J. Crutchley, *Inorg. Chem.* **2013**, *52*, 14404–14410.
- [123] T. Bessho, E. Yoneda, J.-H. Yum, M. Guglielmi, I. Tavernelli, H. Imai, U. Rothlisberger, M. K. Nazeeruddin, M. Grätzel, *J. Am. Chem. Soc.* **2009**, *131*, 5930–5934.
- [124] C.-H. Siu, C.-L. Ho, J. He, T. Chen, X. Cui, J. Zhao, W.-Y. Wong, *J. Organomet. Chem.* **2013**, *748*, 75–83.
- [125] B. D. Koivisto, K. C. D. Robson, C. P. Berlinguette, *Inorg. Chem.* **2009**, *48*, 9644–9652.
- [126] K. C. D. Robson, B. D. Koivisto, A. Yella, B. Sporinova, M. K. Nazeeruddin, T. Baumgartner, M. Grätzel, C. P. Berlinguette, *Inorg. Chem.* **2011**, *50*, 5495–5508.
- [127] K.-L. Wu, H.-C. Hsu, K. Chen, Y. Chi, M.-W. Chung, W.-H. Liu, P.-T. Chou, *Chem. Commun.* **2010**, *46*, 5124–5126.
- [128] C. E. Welby, C. R. Rice, P. I. P. Elliott, *Angew. Chem.* **2013**, *125*, 11026–11029; *Angew. Chem. Int. Ed.* **2013**, *52*, 10826–10829.
- [129] K. Garg, J. T. Engle, C. J. Ziegler, J. J. Rack, *Chem. Eur. J.* **2013**, *19*, 11686–11695.
- [130] C.-W. Hsu, S.-T. Ho, K.-L. Wu, Y. Chi, S.-H. Liu, P.-T. Chou, *Energy Environ. Sci.* **2012**, *5*, 7549–7554.
- [131] B. Schulze, D. Escudero, C. Friebe, R. Siebert, H. Görls, S. Sinn, M. Thomas, S. Mai, J. Popp, B. Dietzek, L. González, U. S. Schubert, *Chem. Eur. J.* **2012**, *18*, 4010–4025.
- [132] A. Yella, H.-W. Lee, H. N. Tsao, C. Yi, A. K. Chandiran, M. K. Nazeeruddin, E. W.-G. Diau, C.-Y. Yeh, S. M. Zakeeruddin, M. Grätzel, *Science* **2011**, *334*, 629–634.
- [133] P. L. Burn, P. Meredith, *NPG Asia Materials* **2014**, *6*, e79, DOI:10.1038/am.2013.74.
- [134] H. J. Snaith, *J. Phys. Chem. Lett.* **2013**, *4*, 3623–3630.
- [135] N.-G. Park, *J. Phys. Chem. Lett.* **2013**, *4*, 2423–2429.
- [136] M. Liu, M. B. Johnston, H. J. Snaith, *Nature* **2013**, *501*, 395–398.
- [137] Q. Pei, G. Yu, C. Zhang, Y. Yang, A. J. Heeger, *Science* **1995**, *269*, 1086–1088.
- [138] Q. Pei, Y. Yang, G. Yu, C. Zhang, A. J. Heeger, *J. Am. Chem. Soc.* **1996**, *118*, 3922–3929.

- [139] H. Xiang, J. Cheng, X. Ma, X. Zhou, J. J. Chruma, *Chem. Soc. Rev.* **2013**, *42*, 6128–6185.
- [140] R. D. Costa, E. Ortí, H. J. Bolink, *Pure Appl. Chem.* **2011**, *83*, 2115–2128.
- [141] J. Slinker, D. Bernards, P. L. Houston, H. D. Abruña, S. Bernhard, G. G. Malliaras, *Chem. Commun.* **2003**, *19*, 2392–2399.
- [142] E. Holder, B. M. W. Langeveld, U. S. Schubert, *Adv. Mater.* **2005**, *17*, 1109–1121.
- [143] J. D. Slinker, J. Rivnay, J. S. Moskowitz, J. B. Parker, S. Bernhard, H. D. Abruña, G. G. Malliaras, *J. Mater. Chem.* **2007**, *17*, 2976–2988.
- [144] International Commission on Illumination (CIE), 1931.
- [145] http://upload.wikimedia.org/wikipedia/commons/6/60/CIE1931xy_CIERGB.svg, 04.03.2014.
- [146] P. Toivanen, J. Hovila, P. Kärhä, E. Ikonen, *Metrologia* **2000**, *37*, 527–530.
- [147] P. Toivanen, P. Kärhä, F. Manoochchri, E. Ikonen, *Metrologia* **2000**, *37*, 131–140.
- [148] A. P. Monkman, *ISRN Materials Science* **2013**, DOI:10.1155/2013670130.
- [149] J. Wang, A. Chepelianskii, F. Gao, N. C. Greenham, *Nat. Commun.* **2012**, DOI:10.1038/ncomms2194.
- [150] A. Köhler, H. Bässler, *Mater. Sci. Eng.* **2009**, *R 66*, 71–109.
- [151] H. Yersin, *Highly Efficient OLEDs with Phosphorescent Materials*; Wiley-VCH: Weinheim, Germany, **2008**.
- [152] J.-K. Lee, D. S. Yoo, E. S. Handy, M. F. Rubner, *Appl. Phys. Lett.* **1996**, *69*, 1686–1688.
- [153] C.-Y. Liu, A. J. Bard, *Appl. Phys. Lett.* **2005**, *87*, 061110.
- [154] J. D. Slinker, J.-S. Kim, S. Flores-Torres, J. H. Delcamp, H. D. Abruña, R. H. Friend, G. G. Malliaras, *J. Mater. Chem.* **2007**, *17*, 76–81.
- [155] L. J. Soltzberg, J. D. Slinker, S. Flores-Torres, D. A. Bernards, G. G. Malliaras, H. D. Abruña, J.-S. Kim, R. H. Friend, M. D. Kaplan, V. Goldberg, *J. Am. Chem. Soc.* **2006**, *128*, 7761–7764.
- [156] G. Kalyuzhny, M. Buda, J. McNeill, P. Barbara, A. J. Bard, *J. Am. Chem. Soc.* **2003**, *125*, 6272–6283.
- [157] H. Yersin, A. F. Rausch, R. Czerwieniec, T. Hofbeck, T. Fischer, *Coord. Chem. Rev.* **2011**, *255*, 2622–2652.
- [158] S. Bernhard, J. A. Barron, P. L. Houston, H. D. Abruña, J. L. Ruglovksy, X. Gao, G. G. Malliaras, *J. Am. Chem. Soc.* **2002**, *124*, 13624–13628.
- [159] T. Sajoto, P. I. Djurovich, A. B. Tamayo, J. Oxgaard, W. A. Goddard, M. E. Thompson, *J. Am. Chem. Soc.* **2009**, *131*, 9813–9822.
- [160] C. Kreitner, K. Heinze, to be submitted.